

Vroegtijdig thermomechanisch gedrag van betonnen Supercontainers
voor de berging van radioactief afval

Early-Age Thermo-Mechanical Behaviour of Concrete Supercontainers
for Radwaste Disposal

Bart Craeye

Promotor: prof. dr. ir. G. De Schutter
Proefschrift ingediend tot het behalen van de graad van
Doctor in de Ingenieurswetenschappen: Bouwkunde

Vakgroep Bouwkundige Constructies
Voorzitter: prof. dr. ir. L. Taerwe
Faculteit Ingenieurswetenschappen
Academiejaar 2009 - 2010



ISBN 978-90-8578-331-2
NUR 955
Wettelijk depot: D/2010/10.500/7

Supervisor

Prof. dr. ir. Geert De Schutter

Research institute

Magnel Laboratory for Concrete Research
Department of Structural Engineering
Faculty of Engineering
Ghent University, Belgium



Examination committee

Prof. dr. ir. Luc Taerwe (chairman)	Ghent University Faculty of Engineering	Department of Structural Engineering
Prof. dr. ir. Nele De Belie (secretary)	Ghent University Faculty of Engineering	Department of Structural Engineering
Prof. dr. ir. Geert De Schutter (supervisor)	Ghent University Faculty of Engineering	Department of Structural Engineering
Prof. dr. ir. Anne-Mieke Poppe	Ghent University Faculty of Engineering	Department of Structural Engineering
Prof. dr. ir. Julien De Rouck	Ghent University Faculty of Engineering	Department of Civil Engineering
Prof. dr. ir. John Van Tomme	Royal Military Academy Brussels	Department of Civil and Material Engineering
Dr. Lou Areias	SCK·CEN Mol	Belgian Nuclear Research Center
Dr. Robert Gens	ONDRAF/NIRAS Brussels	Belgian Agency for Radioactive Waste and Enriched Fissile Materials

Copyright © Bart Craeye 2010

All rights reserved. No parts of this publication may be reproduced, stored in a retrieval system or transmitted in any form or by any means electronic, mechanical, photocopying, recording or otherwise, without the prior written permission of the author and his supervisor.

Alle rechten voorbehouden. Dit werk of delen ervan, mogen onder geen enkele voorwaarde en ook niet voor persoonlijk gebruik worden uitgeleend, gekopieerd of op één of andere manier vermenigvuldigd, zonder voorafgaande, schriftelijke toestemming, van de auteur en zijn promotor.

DANKWOORD

Silent gratitude isn't much use to anyone
[G.B. Stern]

Na pakweg duizend tweehonderd vierendertig dagen bloed, zweet en tranen is het zover! Aan de hand van dit boek tracht ik een antwoord te formuleren op een veel gestelde vraag: 'Bart, wat doe jij zoal aan de Universiteit Gent?'. Wel, zonder jullie hulp zou ik deze woorden zelf niet hoeven te formuleren. Via deze weg, tracht ik het merendeel van jullie allen te bedanken.

Vooreerst wens ik mijn promotor, prof. Geert De Schutter, te bedanken. Hij was het die destijds met een afstudeerwerk omtrent de autogene krimp van jong beton mijn interesse rond deze materie heeft doen aanwakkeren, en hij was het die mij de kans gegeven heeft om dit doctoraatsonderzoek aan te vangen. Geert, steeds stond uw deur open om betontechnologische problemen aan te kaarten, maar tevens kon ik steeds op veel begrip en steun rekenen daarbuiten. Bedankt ook voor het vele naleeswerk van tal van papers die mij de kans gaven een stukje van de wereld te bewonderen. Naast uw uitermate professionele begeleiding, zal vooral uw menselijkheid mij steeds bijblijven. Dank!

Dank aan Hughes Van Humbeeck, William Wacquier (ONDRAF/NIRAS), Alain Van Cotthem, Loïc Villers, Deborah Stinghamer (TECHNUM/Tractebel Engineering) voor de verduidelijking en de sturing tijdens de vele vergaderingen die dit onderzoek in goede banen geleid hebben. Tevens dank aan Lou Areias (SCK·CEN) voor de uitstekende samenwerking die tot stand is gekomen ter voorbereiding en ter realisatie van de eerste Half-Scale Container. Ik hoop dan ook een vruchtbaar vervolg te kunnen breien aan onze brainstorm activiteiten. Tevens dank aan Geert De Mets (HOLCIM), Nele De Smet, Kristof Soenen (Kesteleyn NV) en Koenraad Boel (Ready Beton) voor de levering van het cement, het vervaardigen van het beton en het verpompen van de specie om de betonnen mastodont te verwezenlijken. Ook dank aan Christian Lefevre (SCK·CEN) voor het zorgvuldig plaatsen van het spinnenweb aan bedrading en instrumentatie in de container. Dankzij Isabelle Gérardy en Francois Tondeur (ISIB) ontstond de (betaalbare) mogelijkheid om het gedrag van verhardend beton onder gamma straling te bestuderen en ik wens dan ook mijn appreciatie naar hen toe uit te drukken: merci à vous!

Dankwoord

Lopende door de gangen van Magnel kon ik ook steeds op jullie steun, advies, deskundigheid en hulp rekenen. De recepties, de BBQ's, de sportnamiddagen en de nevenactiviteiten (en effecten) zullen mij steeds bijblijven. Bedankt Anibal, Annielo, Anne-Mieke, Arnold, Bart, Brenda, Christel, Dorleta, Elke, Frederik, Gao, Gert, Jan, Kathelijn, Katrien, Kim, Lander, Lin, Liu (lees: Jan Koen Leo), Lu, Mariette, Marijke, Mieke, Mu, Nicolas, Peter, Pepa, Philip, Qiang, Robby, Tan, Veerle, Viviane, Wang en Willem. Mijn kantoorgenoten Pieter en Geoffrey: bedankt voor mij wegwijst te maken in de (vaak tot frustraties leidende) wereld van de computer, voor het helpen zoeken naar Engelse woordjes die op dat moment net niet het puntje van mijn tong wouden verlaten, voor het verzorgen van de kantoorplanten als ik er even niet was, voor de afwisseling tijdens het schrijven, voor de babbels,... kortom voor jullie gezelschap. Dank aan Dimitri en Emmanuel, voor het helpen verzorgen van de vele oefeningensessies Betontechnologie en Sterkteleer en voor de randanimatie gedurende deze lessen, voor de bezoeken aan de cementfabriek te Obourg, en voor het gezelschap tijdens de trip naar respectievelijk Beijing en Cape Town. Ook dank aan het professoren corps voor het aanleren van handige tips and tricks: prof. Luc Taerwe, prof. Nele De Belie en prof. Stijn Matthijs. Tommy, bedankt om, in niet altijd ideale omstandigheden, steeds een gepaste planning te verzorgen voor het uitvoeren van de vele proeven. Sandra, bedankt voor het vervaardigen van de slijpplaatjes en de assistentie tijdens de microscopie sessies. Ook een 'welgemeende thank you' aan de technische staf van het labo: Dieter, Jan, Marc, Nathan, Nicolas, Peter, Peter, Stefan en Tom. Steeds kon ik rekenen op jullie vakkundigheid en assisteerden jullie mij bij het opstellen van de proeven en het maken van het beton, om mij zo even te doen vergeten dat ik wel degelijk beschik over twee prachtexemplaren linkerhanden.

Naast de werkvloer diende er ook voldoende tijd vrijgemaakt te worden voor de nodige portie sport, spel, ontspanning en muziek. De wekelijkse minivoetbalpartijtjes met Sparta Cool Cast, met als hoogtepunt de verlossende titel in 2009 (de vele nederlagen in het huidige seizoen nemen we er graag bij),... het wist mij steeds te animeren. Ook de maten van FC Bonanza en van de supportersclub wil ik bedanken voor het leuke gezelschap en de (soms kritische) babbels tijdens trainingen, wedstrijden en de niet te versmaden derde helft. Ook merci, gasten van Mr. Panter voor onze wekelijkse repetities en onze legendarische sporadische optredens, voor het componeren van tal van toffe deuntjes en natuurlijk voor de release van onze EP, 'Silence in Stereo'. Voor de rest bestaat er geen betere ontspanning als een feestje met jullie.

Daarom, bedankt Antoon, Bart, Bjorn, Ben, Bruno, Bram, Christophe, Ellen, Els, Els, Evelien, Fabian, Frank, Fred, Geert, Hedwig, Ief, Jan, Kris, Kristof, Koen, Koen, Kurt, Kurt, Laura, Liesbeth, Lisa, Maarten, Peter, Pieter, Pieter-Jan, Rik, Saartje, Siska, Sofie, Sofia, Stefan, Stefanie, Stijn, Thomas, Thomas, Tim, Tim, Tommy, Veerle, Ward...

Dimi, steeds en onvoorwaardelijk kon ik op jou rekenen, zowel op een gemeente als op een enigszins 'lossere' manier. Zelfs het delen van een huis krijgt ons niet kapot. Maat, bedankt gewoon voor alles!

Dankwoord

Naast de vriendenkring wens ik een onmetelijke dankbaarheid te tonen aan mijn familie. Mama en papa, zonder jullie zou ik hier nooit staan. Nooit heb ik iets tekort geschoten, altijd kozen jullie mijn kant en respecteerden jullie mijn beslissingen. Hoewel jullie het niet makkelijk gehad hebben, weet ik dat we er samen met ons gezin doorkomen!

Zus, Fieke, woorden komen te kort om te beschrijven hoe trots ik wel ben op jou. De afgelopen jaren had je steeds een luisterend oor ter beschikking en apprecieerde ik de raad van mijn grote zus. Hoewel ik binnenkort richting Antwerpen vertrek, zal ik steeds trachten tijd vrij te maken om een lunch in het UZ te verorberen, of om nogmaals getuige te zijn van wederom een pracht prestatie tijdens een van je musicals.

Ook een bloem van dank aan Frank, Robbe, Stijn en Vera voor het warme nest, voor de assistentie in de huishoudelijke taakjes en voor de vele lekkere maaltijden.

Wat me brengt naar misschien wel de mooiste bloem van allemaal. Ellen, vanaf dag één ben jij getuige geweest van hoe zwaar zo'n doctoraatsonderzoek wel kan zijn, maar steeds ben jij mijn steun en toeverlaat geweest op momenten dat het even wat minder ging. Je deinsde niet terug als 'koppige Bart' weer eens zijn kopke liet zien of liet hangen, en je opperde steeds voor conversatie om zo samen tot een oplossing te komen. Door jou ben ik grotendeels de 'man' geworden die hier nu staat. Zelfs met 'ik zie je graag' beschrijf ik nog maar een deel van hoe graag ik je echt wel zie...

Bedankt allemaal!

Bart,

Gent, 2 februari 2010

*I can no other answer make, but thanks, and thanks
[W. Shakespeare]*

Dankwoord

Ter nagedachtenis van mijn lieve zus Leen † 17 april 2000

*Nu 't rouwrumoer rondom jou is verstomd,
de stoet voorbij is, de schuifelende voeten,
nu voel ik dat er 'n diepe stilte komt
en in die stilte zal ik je opnieuw ontmoeten.
En telkens weer zal ik je tegenkomen,
we zeggen veel te gauw: het is voorbij.
Hij heeft alleen je lichaam weggenomen,
niet wie je was en ook niet wat je zei.
Ik zal nog altijd grapjes met je maken,
we zullen samen door het stille landschap gaan.
Nu je mijn handen niet meer aan kunt raken,
raak je mijn hart nog duidelijker aan.*

[T. Hermans]

TABLE OF CONTENTS

Dankwoord
Table of contents
List of symbols and abbreviations
Summary - Samenvatting

Chapter 1: Introduction and objectives

1	Introduction	1
2	The Belgian reference concept: the Supercontainer	2
3	Objectives	4
	References	5

Chapter 2: Radioactivity and radioactive waste

1	Radioactivity	7
1.1	Definition of radioactivity	7
1.2	Types of ionizing radiation	8
1.2.1	<i>Alpha radiation</i>	8
1.2.2	<i>Beta radiation</i>	9
1.2.3	<i>Electromagnetic radiation: gamma rays and X-rays</i>	10
1.2.4	<i>Neutrons</i>	11
1.3	The unity of radioactivity	11
1.3.1	<i>Activity</i>	12
1.3.2	<i>Absorbed dose D and equivalent dose H_T</i>	12
1.3.3	<i>Effective dose E_T</i>	14
1.3.4	<i>Radioactive decay</i>	14
2	Radiological protection	17
3	Radioactive waste	18
3.1	The Nuclear Fuel Cycle	18
3.2	Classification of radioactive waste	18
3.3	Radioactive waste according to present activity	20
3.4	Vitrified HLW versus Spent Fuel	21
	References	24

Chapter 3: Disposal of radioactive waste

1	Radwaste Management	25
2	The Belgian reference concept for the disposal of High Level Waste and Spent Fuel assemblies: the Supercontainer	27
2.1	Supercontainer design concept	27
2.2	Design functions	30
2.2.1	<i>The overpack</i>	30
2.2.2	<i>The buffer</i>	31
2.2.3	<i>The envelope</i>	36
2.3	The Host Rock formation	38
3	International policy on geological disposal	40
	References	43

Chapter 4: Parameters affecting the buffer

1	Temperature effects	45
1.1	Fundamentals of heat transfer	45
1.1.1	<i>Conduction</i>	45
1.1.2	<i>Convection</i>	46
1.1.3	<i>Radiation</i>	47
1.1.4	<i>Combined mechanisms of heat transfer</i>	49
1.2	Thermal analysis of the Supercontainer concept	50
1.3	Thermal power of vitrified HLW and SF assemblies	51
1.4	Effect of temperature on mechanical properties	54
1.5	Effect of temperature on thermal properties	59
1.5.1	<i>Specific heat</i>	59
1.5.2	<i>Thermal conductivity</i>	60
1.5.3	<i>Coefficient of thermal expansion (CTE)</i>	61
2	Irradiation Effects	62
2.1	Radiation originating from the waste canisters	62
2.2	Irradiation-induced physical degradation	62
2.3	Radiolytic Gas Generation	66
2.3.1	<i>Introduction and Definition</i>	66
2.3.2	<i>Primary and secondary radiolysis reactions</i>	67
2.3.3	<i>Gas transport mechanisms</i>	68
2.3.4	<i>Design concept assumptions</i>	69
2.3.5	<i>Internal pressure build-up due to radiolysis</i>	70
2.3.6	<i>Parameters influencing the radiolysis process</i>	72
3	Gas production and gas transport due to corrosion	76
3.1	Introduction	76
3.2	Corrosion before penetration of external fluids	76
3.3	Corrosion after penetration of external fluids	78

4	Water content and transport	81
5	Redox and pH	82
5.1	Redox	82
5.2	pH	82
6	Mechanical processes	83
7	Microbial activity	84
8	Concrete mineralogy and degradation mechanisms	86
8.1	Concrete mineralogy	86
8.2	Degradation mechanisms	86
	References	91

Chapter 5: Reference concrete compositions

1	Early-age behaviour of massive concrete	97
1.1	Introduction	97
1.2	Properties of young concrete	98
1.3	Crack creating actions	100
1.3.1	<i>Situation</i>	100
1.3.2	<i>Shrinkage of concrete</i>	100
1.3.3	<i>Creep of concrete</i>	103
1.3.4	<i>Plastic settlement of fresh concrete</i>	103
1.3.5	<i>Thermal stresses</i>	103
1.4	Early-age cracking of concrete	103
1.5	Crack reducing or crack preventing measures	105
2	SCC: a comparison with TVC	106
2.1	Origin and background of Self-Compacting Concrete	106
2.2	Characterization of Self-Compacting Concrete	107
2.2.1	<i>The definition of Self-Compacting Concrete</i>	107
2.2.2	<i>The properties of fresh Self-Compacting Concrete</i>	107
2.2.3	<i>The constituent materials of Self-Compacting Concrete</i>	109
2.2.4	<i>The advantages and disadvantages of Self-Compacting Concrete</i>	112
3	Special Protection Concrete	113
3.1	Definition of Special Protection Concrete	113
3.2	Formulating the composition of SPC	113
3.3	Properties of SPC	114
4	Engineered Cementitious Composites	117
5	Concrete Buffer Composition	119
5.1	Introduction and restrictions	119
5.2	The pH of the concrete buffer	120
5.3	Compatibility with the Host Rock	120
5.4	Limitation of the hydration heat	121
5.5	Sufficient mechanical strength	121
5.6	Ettringite formation and sulphate attack	122

5.7	Permeability, water content and desired degree of saturation	122
5.8	Choice of cement	123
5.9	Choice of aggregates	124
5.10	Choice of admixtures	124
5.11	Reference concrete compositions of the concrete buffer	126
	References	127

Chapter 6: Thermo-mechanical and fresh properties

1	Goal and methodology	131
2	Principles, test procedures and previous studies	133
2.1	Concrete compositions and mixing procedure	133
2.2	Fresh concrete properties	137
2.2.1	<i>Fresh properties of SCC</i>	137
2.2.2	<i>Fresh properties of TVC</i>	140
2.2.3	<i>Previous studies</i>	141
2.3	Thermal properties	143
2.3.1	<i>Specific heat</i>	143
2.3.2	<i>Thermal conductivity</i>	144
2.3.3	<i>Coefficient of thermal expansion</i>	145
2.3.4	<i>Heat production</i>	148
2.4	Maturity-related properties	153
2.5	Mechanical properties	158
2.5.1	<i>Autogenous deformation</i>	158
2.5.2	<i>Creep behaviour</i>	161
2.5.3	<i>Compressive strength</i>	164
2.5.4	<i>Tensile strength</i>	167
2.5.5	<i>Modulus of elasticity</i>	171
2.5.6	<i>Poisson's ratio</i>	174
2.5.7	<i>Time zero</i>	175
3	Results and Discussion	179
3.1	Fresh concrete properties	179
3.1.1	<i>Fresh properties of SCC</i>	179
3.1.2	<i>Fresh properties of TVC</i>	180
3.2	Thermal properties	185
3.2.1	<i>Specific heat</i>	185
3.2.2	<i>Thermal conductivity</i>	185
3.2.3	<i>Coefficient of thermal expansion</i>	187
3.2.4	<i>Heat production</i>	188
3.3	Maturity-related properties	190
3.4	Mechanical properties	194
3.4.1	<i>Autogenous deformation</i>	194
3.4.2	<i>Creep behaviour</i>	195

3.4.3	<i>Compressive strength</i>	200
3.4.4	<i>Tensile strength</i>	200
3.4.5	<i>Modulus of elasticity</i>	200
3.4.6	<i>Poisson's ratio</i>	201
3.4.7	<i>Time zero</i>	202
4	Conclusion	204
	References	205

Chapter 7: Effect of radwaste on strength of the Supercontainer

1	Goal and methodology	211
2	Previous results and testing procedure	212
2.1	Effect of gamma irradiation on strength of concrete	212
2.1.1	<i>Previous results</i>	212
2.1.2	<i>MBE method</i>	213
2.1.3	<i>Testing procedure</i>	215
2.2	Effect of heat on strength of concrete	223
2.2.1	<i>Previous results</i>	223
2.2.2	<i>Testing procedure</i>	225
3	Results and discussion	227
3.1	Effect of gamma radiation on strength of the Supercontainer	227
3.2	Effect of heat on strength of the Supercontainer	228
4	Conclusion	238
	References	239

Chapter 8: Thermo-mechanical behaviour of the Supercontainer

1	Goal and methodology	243
2	The numerical simulation tool HEAT/MLS	245
3	Pre-processing	248
3.1	Implementation of the concrete properties	248
3.1.1	<i>Thermal properties</i>	248
3.1.2	<i>Maturity-related properties</i>	248
3.1.3	<i>Mechanical properties</i>	248
3.2	Geometry and boundary conditions	251
4	Post-processing	254
4.1	Overview	254
4.2	Phase 1 of the simulations: casting of the buffer (out of hot cell)	256
4.2.1	<i>Reference simulation 20 °C with SCC</i>	256
4.2.1.1	<i>Temperature T</i>	256
4.2.1.2	<i>Stresses S_{zz}, S_{yy}, S_{xx}, S_{xy}</i>	259
4.2.1.3	<i>Cracking criteria: $S/(0.7 \cdot f_a) < 1$</i>	263
4.2.1.4	<i>Displacement U_x</i>	265
4.2.2	<i>Sensitivity analysis: changing the concrete parameters</i>	267

4.2.2.1	<i>The effect of the autogenous deformation and the creep behaviour</i>	267
4.2.2.2	<i>The effect of the exothermal hydration reaction</i>	269
4.2.2.3	<i>The use of other types of concrete</i>	270
4.2.3	<i>Sensitivity analysis: changing the dimensions of the buffer</i>	274
4.2.3.1	<i>Temperature T</i>	275
4.2.3.2	<i>Stresses S_{zz}</i>	278
4.2.3.3	<i>Cracking criteria: $S_{zz}/(0.7 \cdot f_{ct}) < 1$</i>	279
4.2.3.4	<i>Displacement U_x</i>	279
4.2.4	<i>Sensitivity analysis: changing the environmental conditions</i>	281
4.2.4.1	<i>Temperature T</i>	282
4.2.4.2	<i>Stresses S_{zz}</i>	283
4.2.4.3	<i>Cracking criteria: $S_{zz}/(0.7 \cdot f_{ct}) < 1$</i>	285
4.2.4.4	<i>Displacement U_x</i>	286
4.2.5	<i>Alternative casting condition</i>	288
4.2.5.1	<i>Temperature T</i>	288
4.2.5.2	<i>Stresses S_{zz}</i>	291
4.2.5.3	<i>Cracking criteria: $S_{zz}/(0.7 \cdot f_{ct}) < 1$</i>	293
4.2.5.4	<i>Displacement U_x</i>	293
4.2.6	<i>Casting of the buffer out of hot cell: main conclusions</i>	295
4.3	<i>Phase 2 of the simulations: insertion, filler and lid (in hot cell)</i>	298
4.3.1	<i>Early-age behaviour of the buffer</i>	299
4.3.1.1	<i>Temperature T</i>	299
4.3.1.2	<i>Stresses S_{zz}, S_{yy}, S_{xx}</i>	304
4.3.1.3	<i>Cracking criteria: $S/(0.7 \cdot f_{ct}) < 1$</i>	309
4.3.1.4	<i>Displacement U_x</i>	312
4.3.2	<i>Early-age behaviour of the filler and the lid</i>	315
4.3.2.1	<i>Temperature T</i>	315
4.3.2.2	<i>Stresses S_{zz}</i>	315
4.3.2.3	<i>Cracking criteria: $S_{zz}/(0.7 \cdot f_{ct}) < 1$</i>	316
4.3.2.4	<i>Displacement U_x</i>	317
4.3.3	<i>Insertion of the radwaste in hot cell: main conclusions</i>	317
4	Conclusion	323
	References	324

Chapter 9: Half-Scale Tests: Validation of the simulation results

1	Goal and methodology	327
2	Test set-up	330
2.1	Mixing, casting-pumping and hardening procedure	330
2.2	Fresh properties of SCC	334
2.3	Instrumentation test set-up	334
2.3.1	<i>Temperature, wind velocity and RH instrumentation</i>	335
2.3.2	<i>Radial and axial displacement</i>	336

2.3.3	<i>Radial, axial and tangential deformation</i>	337
2.4	Strength tests	337
3	Results and discussion	340
3.1	Fresh properties of SCC	340
3.2	Validation of the simulation results	342
3.2.1	<i>Pre-processing: geometry, boundary conditions and concrete properties</i>	342
3.2.2	<i>Validation of the temperature development</i>	345
3.2.3	<i>Validation of the displacement</i>	350
3.2.4	<i>The deformation of the steel formwork and the HC</i>	353
3.2.5	<i>Stress calculation in the HC</i>	356
3.2.6	<i>Strength development of the SCC</i>	360
3.2.7	<i>Cracking behaviour of the HC</i>	363
4	Conclusion	367
	References	369

Chapter 10: Conclusions and future research

1	Conclusions and discussion	369
1.1	Objective of the doctoral research	369
1.2	The studied concrete compositions	369
1.3	Conclusions of the laboratory characterization program	370
1.4	Conclusions of the simulation results and the Half-Scale Tests	371
2	Future research	374

Curriculum Vitae and Publications

LIST OF SYMBOLS AND ABBREVIATIONS

1 Symbols

A	= Activity of a radioactive matter (Bq)
	= Shortened notation of Al_2O_3
A_a	= Absorption coefficient of the aggregates (%)
A_c	= The surface of a concrete sample on which a load is applied (m^2)
A_{ct}	= The section of a concrete sample where tensile rupture occurs (m^2)
A_m	= The surface of a mortar sample on which a load is applied (m^2)
A_0	= Initial activity of a radioactive matter (Bq)
α	= Type of radiation
α_h	= Degree of hydration (-)
α_T	= Coefficient of thermal expansion ($\mu m/m/^\circ C$)
α_0	= Percolation threshold (-)
B	= Constant value (-)
Bq	= Becquerel, measure of radioactivity decay
β_T	= Temperature dependent residual resistance factor (-)
β^+	= Type of radioactive decay
β^-	= Type of radioactive decay
C	= Amount of cement (kg/m^3)
	= Shortened notation for CaO
c_p	= Specific heat of concrete ($J/(kg \cdot ^\circ C)$)
c_T	= Heat capacity of concrete ($J/(m^3 \cdot ^\circ C)$)
D	= Absorbed dose (Gy)
D_i^e	= Effective mass transport coefficient (m^2/s)
dm	= Mass of an element (kg)
dN	= Amount of nuclear mutations (-)
Dr	= Dose rate (Gy/s)
d_s	= Distance from the irradiation source (cm)
dt	= Time interval (s)
$D_{T,R}$	= Average absorbed dose of radioactive type R in tissue T (Gy)
dE	= Amount of absorbed energy (J)
Δl	= Length change (μm)
ΔT	= Temperature gradient ($^\circ C$)
$\Delta \epsilon_l$	= Longitudinal deformation gradient ($\mu m/m$)
$\Delta \epsilon_t$	= Transversal deformation gradient ($\mu m/m$)

$\Delta\sigma$	= Stress gradient (MPa)
E	= Apparent activation energy (kJ/mol)
E_c	= Modulus of elasticity of concrete (GPa)
E_k	= Kinetic energy (J)
	= Spring stiffness of branch k (Maxwell) (GPa)
E_p	= Specific energy level of photons (eV)
E_s	= Modulus of elasticity of steel (GPa)
E_T	= Effective dose (Sv)
e^+	= Positron
eV	= ElectronVolts (1.6×10^{-16} J)
e^-	= Electron
ε	= Uni-axial strain ($\mu\text{m/m}$)
ε_f	= Final value of the autogenous deformation curve ($\mu\text{m/m}$)
ε_p	= Swelling peak in the autogenous deformation curve ($\mu\text{m/m}$)
ε_{c0}	= Elastic strain when creep load is applied ($\mu\text{m/m}$)
ε_{c0r}	= Strain decrease after removal of creep load ($\mu\text{m/m}$)
ε_T	= Thermal deformation ($\mu\text{m/m}$)
ε_u	= Ultimate strain ($\mu\text{m/m}$)
ε_x	= Radial deformation ($\mu\text{m/m}$)
ε_y	= Axial deformation ($\mu\text{m/m}$)
ε_z	= Tangential deformation ($\mu\text{m/m}$)
F	= Shortened notation of Fe_2O_3
f_c	= Cylindrical compressive strength of concrete (MPa)
F_c	= Maximal load at rupture of concrete in compressive behaviour (kN)
$f_{\text{ccub}100}$	= Compressive strength of concrete cube, side 100 mm (MPa)
$f_{\text{ccub}100,T}$	= Compressive strength of concrete cube, side 100 mm, at temperature T (MPa)
$f_{\text{ccub}150}$	= Compressive strength of concrete cube, side 150 mm (MPa)
$f_{\text{ccub}200}$	= Compressive strength of concrete cube, side 200 mm (MPa)
f_{ck}	= Characteristic concrete compressive strength (MPa)
f_{ct}	= Pure tensile strength of concrete (MPa)
F_{ct}	= Maximal load at rupture of concrete in pure tensile behaviour (kN)
f_{ctsp}	= Splitting tensile strength of concrete (MPa)
F_{ctsp}	= Maximal load at rupture of concrete in splitting tensile behaviour (kN)
$f_{ct,act}$	= Actual tensile strength of the structure (MPa)
$f_{ct,lab}$	= Tensile strength determined in laboratory conditions (MPa)
$f_{ct,\infty}$	= Long-term tensile strength (MPa)
$f_{c,prism}$	= Compressive strength of concrete prisms (MPa)
F_d	= Height of the splitting plane (mm)
F_i	= Local force behind mass transport
F_l	= Length of the splitting plane (mm)
F_m	= Maximal load at rupture of mortar in compressive behaviour (kN)
$f_{m,irr}$	= Compressive strength of irradiated mortar sample (MPa)
$f_{m,ref}$	= Compressive strength of reference mortar sample (MPa)
f_{Rc}	= Relative compressive strength ratio (-)

f_{Rct}	= Relative splitting tensile strength ratio (-)
G	= Amount of aggregates (kg/m^3)
Gy/s	= Gray per second, measure of absorbed radiation dose
$g(\theta,t)$	= Temperature dependency function (-)
γ	= Type of radiation
γ_{cr}	= Cracking index (-)
H	= Shortened notation of H_2O
h	= Planck constant ($3.626 \times 10^{-34} J \cdot s$)
h_c	= Convective heat transfer coefficient ($W/(m^2 \cdot ^\circ C)$)
H_T	= Total equivalent absorbed dose (Sv)
	= Heat production source (W/m^2)
$H_{T,R}$	= Equivalent absorbed dose of radioactive type R in tissue T (Sv)
HT	= Halving thickness of an absorbing medium (cm)
k	= Thermal conductivity ($W/(m \cdot ^\circ C)$)
k_c	= Temperature dependent coefficient (-)
L	= Length of cylindrical conductor (m)
l_0	= Initial length of the material (m)
λ	= Desintegration constant (s^{-1})
λ'	= Wavelength (m)
M	= Maturity of concrete (h)
M_d	= Mass of dry aggregates (g)
M_f	= Final mass of concrete sample (kg)
M_w	= Mass of wet aggregates (g)
M_0	= Initial mass of concrete sample (kg)
μ	= Attenuation coefficient of the absorbing material (cm^{-1})
n	= Neutron
N	= Amount of radioactive atoms or energetic photons (-)
N_0	= Initial amount of radioactive atoms or energetic photons (-)
ν_c	= Poisson's ratio of concrete (-)
ν	= Frequency of a wave (Hz)
$\bar{\nu}$	= Antineutrino
$\nu \cdot$	= Neutrino
p	= Proton
P	= Total porosity (%)
	= Amount of powder (kg/m^3)
P_i	= Initial internal pressure (Pa)
P_{max}	= Maximal pressure build-up (Pa)
P_{tot}	= Total pressure build-up (Pa)
Q	= Amount of (hydration) heat production (J/g)
	= Heater power of heat source (W/m)
q	= Rate of convective heat transfer (W)
	= Rate of conductive heat transfer (W)
	= Rate of radiant energy (W)
	= Heat production rate (J/(g·h))
Q_k	= Maximal available kinetic energy for radiation (J)

q_{\max}	= Maximal heat production rate (J/(g·h))
$q_{\max,10^{\circ}\text{C}}$	= Maximal heat production rate at 10 °C (J/(g·h))
$q_{\max,20^{\circ}\text{C}}$	= Maximal heat production rate at 20 °C (J/(g·h))
$q_{\max,30^{\circ}\text{C}}$	= Maximal heat production rate at 30 °C (J/(g·h))
Q_{\max}	= Maximal heat of hydration (J/g)
Q_{tot}	= Total amount of hydration heat (J/g)
Q_{TP}	= Thermal power output of radioactive waste (W/tHM)
$q_{20^{\circ}\text{C}}$	= Heat production rate at 20 °C (J/(g·h))
$Q_{72\text{h}}$	= Accumulated adiabatic heat of hydration after 72 hours (J/g)
θ	= Temperature (°C)
θ_0	= Starting or initial temperature (°C)
r	= Reaction degree of the hydration process (-)
R	= Universal gas constant (0.0831 kJ/(mol·K))
r_i	= Inner radius of cylindrical conductor (m)
r_o	= Outer radius of cylindrical conductor (m)
$r_{q_{\max,20^{\circ}\text{C}}}$	= Reaction degree at appearance of the maximal heat production rate at 20 °C (-)
R_{thermal}	= Thermal resistance (°C/W)
ρ_c	= Volumetric weight of concrete (kg/m ³)
s	= Standard deviation on the mean value (-)
S	= Shortened notation of SiO ₂
	= Saturation degree (-)
S_{ij}	= Stress in the i-direction (MPa)
$S_{ii,\max}$	= Maximal stress in the i-direction (MPa)
S_s	= Specific surface of the aggregates (m ² /kg)
S_{xx}	= Normal stress in the radial x-direction (MPa)
S_{xy}	= Shear stress in the x-y-plane (MPa)
S_{yy}	= Normal stress in the axial y-direction (MPa)
S_{zz}	= Normal stress in the tangential z-direction (MPa)
Sv/h	= Sievert per hour, radiation dose equivalent
σ	= Uni-axial load (kN)
	= Stefan-Boltzmann constant (5.676 x 10 ⁻⁸ W/(m ² ·°C ⁴))
σ_c	= Concrete stress (MPa)
σ_t	= Internal splitting tensile stress (MPa)
σ_0	= Applied creep stress (MPa)
t	= Time interval (s)
T	= Temperature (°C, K)
t_{con}	= Casting time (s)
T_h	= Highest fluorescence threshold (-)
t_i	= Thickness of layer i (m)
T_{in}	= Inner temperature in the opening of the HC (°C)
T_l	= Lowest fluorescence threshold (-)
t_{\max}	= Time of appearance of the maximal value of a certain quantity (h)
T_{\max}	= Maximal temperature (°C)
T_{out}	= Outer or ambient temperature around the HC (°C)

t_p	= Time of appearance of the autogenous deformation peak (h)
t_{qmax}	= Time of appearance of the maximal heat production rate (h)
$t_{qmax,10^{\circ}C}$	= Time of appearance of the maximal heat production rate at 10 °C (h)
$t_{qmax,20^{\circ}C}$	= Time of appearance of the maximal heat production rate at 20 °C (h)
$t_{qmax,30^{\circ}C}$	= Time of appearance of the maximal heat production rate at 30 °C (h)
T_{ref}	= Reference temperature (°C, K)
t_0	= Time zero (h)
	= Time of placement of creep load (h)
t_1	= Time of removal of creep load (h)
$T_{1/2}$	= Half-life of radioactive material (s)
T_{72h}	= Temperature after 72 hours (°C)
τ_k	= Retardation time of branch k (Maxwell) (h)
U_{max}	= Maximal displacement (mm)
U_x	= Radial displacement (mm)
U_y	= Axial displacement (mm)
VW	= Volumetric weight (kg/m ³)
W	= Amount of water (kg/m ³)
	= Wind velocity (m/s)
WC	= Water content (%)
WL	= Weight loss (kg)
W_{MBE}	= Amount of water added to the SCC based mortar composition (kg/m ³)
W_{out}	= Outer or ambient wind velocity (m/s)
w_R	= Radiation type weighing factor (-)
W_{SCC}	= Amount of water added to the SCC composition (kg/m ³)
w_T	= Tissue weighing factor (-)
W_{tot}	= Total amount of water (kg/m ³)
x	= Coordinate of the Fourier equation (m)
X	= Type of radiation
x_i	= Fluorescence in each point within the zones in between the thresholds (-)
y	= Coordinate of the Fourier equation (m)
y_i	= Number of dots with a specific fluorescence (-)
Z	= Number of protons in the nucleus (-)
#	= Number of the amount of testes samples (-)

2 Abbreviations

AAR	= Alkali Aggregate Reaction
AC	= Aluminate Cement
ACI	= American Concrete Institute
ALARA	= As Low As Reasonable Achievable
ALI	= Annual Limits on Intake (mSv/year)
ANE	= Anemometer
AS	= Autogenous Shrinkage
ASR	= Alkali Silica Reaction
BBRI	= Belgian Building Research Institute
BFS	= Blast Furnace Slag
BFSC	= Blast Furnace Slag Cement
CC	= Composite Cement
CEA	= Commissariat à l' Énergie Atomique
CEM I	= Another appellation for Ordinary Portland Cement
CH	= Calcium Hydroxide
CSH	= Calcium Silicate Hydrate
CTE	= Coefficient of Thermal Expansion
C ₃ A	= Tricalcium Aluminate
C ₄ AF	= Tetracalcium Alumino Ferrite
C ₂ S	= Dicalcium Silicate
C ₃ S	= Tricalcium Silicate
DD	= Displacement Difference
EBS	= Engineered Barrier System
ECC	= Engineered Cementitious Composites
EDX	= Energy Dispersive X-rays
EDZ	= Excavation Disturbed Zone
EFNARC	= European Federation for Specialists Construction Chemicals and Concrete Systems
FA	= Fly Ash
FANC	= Federal Agency for Nuclear Control
FB	= Final Batch
FBFC	= Franco-Belge de Fabrication de Combustibles
HADES	= High Activity Disposal Experimental Site
HC	= Half-Scale Container
HLW	= High Level Waste
HPC	= High Performance Concrete
HSR	= High Sulphate Resistance
IAEA	= International Atomic Energy Agency
ICRP	= International Commission on Radiological Protection
IF	= Interface of the buffer and the overpack
ILW	= Intermediate Level Waste
ISIB	= Institut Supérieur des Ingénieurs de Bruxelles
JNC	= Japan Nuclear Cycle Development Institute
LA	= Low Alkali amount

LF	= Limestone Filler
LH	= Low Heat production
LL	= Long-Lived
LLW	= Low Level Waste
LVDT	= Linear Variable Displacement Transducer
M	= Middle of the buffer
MBE	= Mortier de Béton Equivalent
MFS	= Melamine Formaldehyde Sulphonate
MOX	= Mixed Oxide Fuel
NAGRA	= Nationale Genossenschaft für die Lagerung Radioaktiver Abfälle
NIREX	= Nuclear Industry Radioactive Waste Executive
NFS	= Naphthalene Formaldehyde Sulphonate
NPP	= Nuclear Power Plant
NSSP	= Non Steady-State Probe
ONDRAF/ NIRAS	= Belgian Agency for Radioactive Waste and Enriched Fissile Materials/ Nationale Instelling voor Radioactief Afval en verrijkte Splijtstoffen
OPC	= Ordinary Portland Cement
PA	= Passing Ability
PCL	= Precast Lid
R	= Radiation type
RH	= Relative Humidity
rpm	= Rotations per minute
SCC	= Self-Compacting Concrete
SCK-CEN	= Studiecentrum voor Kernenergie/Centre d'Étude de l'énergie Nucléaire
SEM	= Scanning Electron Microscopy
SF	= Spent Fuel = Silica Fume = Slump Flow
SG	= Strain Gauge
SP	= Superplasticizer
SPC	= Special Protection Concrete
SRB	= Sulphate Reducing Bacteria
SS	= Sieve Stability
T	= Tissue
TB	= Trial Batch
TC	= Thermocouple
TD	= Temperature Difference
tHM	= Tons of Heavy Metal
THM	= Thermal Hygral Mechanical
TM	= Thermal Mechanical
TSA	= Thaumasite Sulphate Attack
TVC	= Traditional Vibrated Concrete
UOX	= Urate Oxidase
UV	= Ultra Violet

VF = V-Funnel
VMA = Viscosity Modifying Agent
W/C = Water to Cement ratio
W/P = Water to Powder ratio

SUMMARY

Radioactivity plays a major role in numerous applications, relevant for the existence of human-beings: provision of electricity by means of nuclear power plants, treatment of diseases and other medical applications, industrial programs, research activities, military applications, aerospace science, etc. As a consequence, several types and considerable amounts of radioactive waste are present worldwide. The past decades, solutions are being searched and disposal possibilities are investigated to counteract the presence of these radioactive waste forms. Nowadays, the Belgian reference design concept for the disposal of High Level Waste (HLW) and Spent Fuel (SF) assemblies, is based on cylindrical Supercontainers, deeply disposed in clayey Host Rock layers.

The Supercontainer is based on the use of an integrated waste package composed of a carbon steel overpack surrounded by a concrete buffer based on Ordinary Portland Cement. Two types of concrete are being considered for the buffer: a Self-Compacting Concrete (SCC) and a Traditional Vibrated Concrete (TVC). Preference is given to the SCC.

This doctoral research study project focuses on the early-age thermo-mechanical behaviour of the concrete buffer of the Supercontainer during the four construction stages: (i) the fabrication of the buffer inside a cylindrical stainless steel envelope, (ii) the insertion of the heat-emitting overpack containing the radioactive waste canisters, (iii) the filling of the remaining annular gap under thermal load and in the presence of a radiation source and (iv) the closure of the Supercontainer by fitting the lid (Chapter 1). The feasibility of construction of the Supercontainer and the early-age cracking behaviour of the concrete buffer, can be seen as the two main objectives of this study. Through-going macrocracks in the concrete buffer must be avoided at all times, because they will ease considerably migration and other possible transport mechanisms of potentially aggressive species (present in the Host Rock) through the Supercontainer, once placed in the disposal galleries. This will have a detrimental effect on the durability of the Supercontainer.

To a certain extent, everything around us is radioactive. In Chapter 2, the principles of radioactivity, the different types of radiation, the radiological protection mechanisms and the various types of radioactive waste are explained. Based on their activity and the half-life of the included radionuclides, conditioned waste is subdivided into different categories. The main intention of the Supercontainer is to deeply dispose vitrified, heat-

emitting HLW and SF assemblies. Only gamma rays can penetrate through the carbon steel overpack, alpha and beta particles are blocked and the flux of neutrons is considered low enough to be neglected. The thickness of the concrete buffer layers is calculated to provide sufficient attenuation of the gamma photons during transportation. Therefore, a thickness of approximately 70 centimeters is satisfactory.

Worldwide, various disposal concepts are suggested and investigated, depending on the type of Host Rock present at the country. The main purpose of disposal is to isolate the waste and its radioactivity from the human environment for time periods sufficiently long enough to enable disadvantageous impact on life at Earth's surface. Therefore, in the Belgian reference design concept, the HLW and the SF assemblies are surrounded by an Engineered Barrier System: (i) the carbon steel overpack contains the waste canisters, (ii) the concrete buffer surrounds the overpack, and (iii) a stainless steel envelope encloses the buffer. Each of these layers have their specific functions. The concrete buffer has to facilitate handling and underground transportation into the deep disposal galleries (operational safety) and it needs to create a favourable chemical environment, with high pH, to prevent or slow down the corrosion processes of the different metallic parts of the Supercontainer (Chapter 3).

The concrete study investigates the three concrete layers present in the Supercontainer: the buffer, the filler and the lid. Several parameters have an effect on the concrete, its properties and the durability during its expected lifetime. Due to the heat-emitting radioactive waste, heat and radiation are introduced into the system, leading towards a temperature elevation and irradiation of the different concrete layers. Hydrolysis of the pore water, internal gas pressure build-up and degradation of the mechanical strength are known processes caused by those two parameters. Other durability related issues, such as gas production due to corrosion, microbial activity and other degradation mechanisms are briefly discussed in Chapter 4.

The two types of concrete considered for the cementitious buffer around the overpack, SCC and TVC, have their specific needs in order to guaranty the operational safety and the long-term safety. In Chapter 5, the process of choosing a reference SCC and TVC composition is explained, taking into account the early-age behaviour of massive concrete structures and the restrictions the compositions need to follow. These requirements significantly differ from the prescriptions used in classical structures. To create the high pH of the cementitious buffer (for corrosion protection purposes), OPC is used in combination with limestone aggregates and limestone filler. The hydration heat production needs to be limited to avoid early-age thermal cracking of the massive concrete buffer. Also high sulphate attack resistance is highly desired and the Alkali Aggregate Reaction cannot be overlooked. Finally, compared to TVC, more limestone filler and a higher superplasticizer amount is used, in order to make the composition self-compacting.

To determine the most relevant thermal, mechanical and maturity-related properties of SCC and TVC, and to come to a good comparison of the test results of the two compositions, an extensive laboratory characterization program is executed (Chapter

6). Compared to TVC, SCC acts more like an insulator due to the lower value for thermal conductivity, and SCC has a higher value of the adiabatic hydration heat production. The mechanical strength properties, such as the compressive strength, the tensile strength, autogenous shrinkage and creep behaviour, however, are also higher in case of SCC. The higher amount of fine materials, such as limestone filler, added to SCC in order to make it self-compacting, can be an explanation for the differences between SCC and TVC.

Once the buffer is cast and cured until a sufficient degree of hardening is attained, the heat-emitting HLW or SF assemblies will be inserted into the buffer. As a consequence, the buffer, the filler and the lid come into direct contact with the overpack containing the radwaste, they suffer from elevated temperatures up to 100 °C and they are irradiated by gamma photons. The effect of gamma radiation (with a relevant dose rate) on the mechanical strength of hardening SCC based mortar, and the influence of elevated temperatures (between 20 °C and 105 °C) on the mechanical strength of hardened concrete is investigated in Chapter 7. Indications of a possible compressive strength loss up to 15 % – 20 % appear, linked with an increasing capillary porosity trend (without statistical significance), investigated by means of fluorescence microscopy.

The main purpose of the doctoral research is to evaluate the possible early-age cracking risk of the concrete buffer of the Supercontainer during the construction stage out of hot cell and the construction stages in hot cell (when the radwaste is inserted). The comprehensiveness of the behaviour of the hardening SCC and TVC is obtained by means of finite element simulations via HEAT/MLS (Chapter 8), and by means of Half-Scale Tests for the validation of the simulation results (Chapter 9). The obtained concrete properties are implemented into the material database of the simulation tool, and stress calculations are performed.

For the first construction stage, no early-age cracking is expected. Via a sensitivity analysis, the effect of changed material properties, changed dimensions of the buffer and altered ambient boundary conditions is studied. Especially the exothermal hydration reaction of the cement leads towards high tensile stresses near the outer surface, and in some cases (e.g. high ambient wind velocity or high environmental temperatures in the vicinity of the buffer, poor insulation conditions, increased thickness of the buffer due to design alterations, etc.) adequate measures need to be taken in order to prevent early-age cracking. The main mechanism behind early-age cracking is the thermal gradient between the middle of the buffer and the outer surface, but also the convective heat transfer coefficient at the interface of the outer surface of the Supercontainer and the environment, and the thermal conductivity of the concrete buffer strongly affect the early-age cracking risk. In order to validate the first stage simulation results, and for the evaluation of the construction feasibility, Half-Scale Tests are conducted. Therefore, the casting of the buffer is executed in practice, and a system of registration equipment is provided. The obtained temperature development, the displacement and the deformation data proceeding the casting of the Half-Scale Container are compared with the simulation results of an identical casting situation. A

rather good comparison is obtained: especially good similarities are obtained on behalf of the critical thermal gradient. The visual inspection indicates that no early-age macrocracks appear in the first construction stage of the buffer, and the conclusions drawn by means of the simulation tool HEAT/MLS are safe and conservative. The Half-Scale Tests also revealed some difficulties appearing during mixing and pumping of the considerable amount of SCC needed for the casting of the buffer, e.g. the determination of the water content of the aggregates, the pumping of the concrete in one fluent movement, the manual addition of limestone powder during the mixing of the concrete, etc.

Also the construction stages in hot cell, i.e. the insertion of the heat-emitting overpack and the closure of the Supercontainer by casting the filler and the lid, are simulated once the buffer is in a certain state of hardening. Three main mechanisms cause an internal stress build-up in the buffer of the Supercontainer: (i) the hydration heat due to the hardening filler and lid, (ii) the heat originating from the heat-emitting radioactive waste, and (iii) the expansive behaviour of the overpack containing the radwaste. Although the reality is underestimated via the first simulation method (no early-age cracking is expected), where the effect of the overpack is only implemented as a boundary condition (via the convective heat transfer coefficient), the effect of altered casting situations is investigated. Different conclusions can be drawn: a prolongation of the preceding cooling period of the radwaste has a beneficial effect, the insertion of SF assemblies instead of HLW affects the cracking risk negatively, the use of a TVC buffer or a precast lid does not have an influence on the internal stress build-up inside the buffer, and delaying the insertion time also does not have a considerable effect on the early-age behaviour of the Supercontainer. It is better, and more realistic to also consider the expansive behaviour of the overpack, obtained via implementing the overpack as a macro layer (the second simulation type). In that case, a considerable cracking risk near the outer surface of the buffer is found, mainly depending on the coefficient of thermal expansion of the overpack. Especially tangential cracks (due to the axial stresses) can appear, which is confirmed by the Half-Scale Tests. In practice, it is better to use a carbon steel overpack instead of a stainless steel overpack, in combination with a cooling period of 70 years to overcome cracking. The internal eigenstresses, present in the buffer after the first construction stage out of hot cell, counteract the stress creation due to the three previously mentioned stress creating mechanisms and a significant safety barrier is obtained, to counteract the negative effect of heat and radiation on the strength of the concrete buffer. The presence of the stainless steel envelope reduces the tensile stresses due to the prevention of the expansive behaviour of the buffer and the introduction of additional beneficial compressive stresses. Also the appliance of a top force (e.g. by screwing a top plate on the mantle of the envelope) can also induce beneficial compressive stresses that counteract the tensile stress build-up in the buffer. No cracking is expected in the filler, which is compressed due to the expansive behaviour of the overpack and the hindering of its own displacement by the surrounding buffer. Also early-age cracking is not at state in case of the lid, which is confirmed by means of the Half-Scale Tests.

SAMENVATTING

Radioactiviteit neemt een belangrijke plaats in bij tal van toepassingen die relevant zijn voor het bestaan van de mensheid: de voorziening van elektriciteit met behulp van kerncentrales, de behandeling van ziektes en de toepassing in andere medische applicaties, industriële activiteiten en onderzoeksactiviteiten, militaire toepassingen, de ruimtevaart, enz. Bijgevolg is er wereldwijd een aanzienlijke hoeveelheid radioactief afval geproduceerd in uiteenlopende vormen. De afgelopen decennia werd er intensief gezocht naar mogelijke oplossingen die antwoord dienen te bieden omtrent de opslagproblematiek van het radioactief afval. Vandaag bestaat het Belgisch referentieconcept, voor de opslag en de berging van hoogactief en langlevend afval, uit cilindrische Supercontainers. Deze betonnen mastodonten zullen geborgen worden in stabiele (kleiachtige) geologische bodemlagen nadat de extreme periodes van radioactiviteit van het afval danig zijn afgezwakt door radioactief verval.

De Supercontainer bestaat in de eerste plaats uit een koolstofstalen verpakking die het radioactief afval insluit tijdens de thermische fase, en deze verpakking is omgeven door een betonnen buffer (met gebruik van Portland cement). Tot slot wordt de betonnen matrix omgeven door een cilindrische roestvrij stalen beslagring. Twee betonsoorten worden beschouwd voor gebruik in de buffer: een zelfverdichtend beton (SCC) en een traditioneel verdicht beton (TVC). De voorkeur gaat uit naar het gebruik van SCC. De Supercontainer wordt aan de oppervlakte gebouwd en na de finalisering van de constructie getransporteerd naar de ondergrondse galerijen.

Dit doctoraatsonderzoek bestudeert het vroegtijdig thermomechanisch gedrag van de betonnen buffer van de Supercontainer tijdens de vier constructiefases: (i) de fabricatie van de buffer in de cilindrische roestvrij stalen beslagring, (ii) de plaatsing van het warmteafgevend afval (omgeven door de koolstofstalen verpakking), (iii) de vulling van de overblijvende ruimte tussen de verpakking en de buffer en (iv) de plaatsing van het deksel en de sluiting van de Supercontainer (Hoofdstuk 1). De constructieve uitvoerbaarheid van de Supercontainer en de studie van het vroegtijdig scheurgedrag van de betonnen buffer worden als de hoofdobjectieven van deze studie beschouwd. Macroscheuren doorheen het beton van de buffer dienen te allen tijde vermeden te worden om transport van potentiële agressieve stoffen (aanwezig in de geologische bodemformatie) en migratie van schadelijke radioactieve straling doorheen de Supercontainer tegen te gaan.

In zekere mate is alles rondom ons radioactief. In Hoofdstuk 3 worden de principes van radioactiviteit, de verscheidene stralingstypes, het mechanisme van radioprotectie en de verschillende soorten radioactief afval besproken. Geconditioneerd afval wordt onderverdeeld in verschillende categorieën, gebaseerd op de activiteit en de halfwaardetijd van de aanwezige radionucliden. Enkel gamma straling kan doorheen het koolstofstalen vat penetreren, de alfa en bèta deeltjes worden afgezwakt of gestopt (attenuatie) en de neutronenflux is laag genoeg om verwaarloosd te worden. De dikte van de betonnen buffer wordt berekend zodat de attenuatie van de gamma fotonen voldoende groot is gedurende het transport van de Supercontainer. Een dikte van 70 centimeter is toereikend.

Wereldwijd is het onderzoek naar mogelijke bergingsoplossingen vooral afhankelijk van de beschikbare geologische bodemformatie. Het hoofddoel van de berging is het garanderen van de isolatie van het radioactief afval en om de radioactiviteit in het afval veilig te laten vervallen zonder schade te berokkenen aan de mens en het milieu. In het Belgisch referentieconcept wordt het hoogactief en langlevend afval omgeven door meerdere barrières, die samen het 'Engineered Barrier System' vormen: (i) de koolstofstalen verpakking met daarin de radioactieve afvalvaten, (ii) de betonnen buffer die het koolstofstalen vat omgeeft, en (iii) een roestvast stalen omhulsel. Elke barrière van het systeem heeft specifieke functies. De betonnen buffer moet het transport en de bediening van de Supercontainer naar de ondergrondse galerijen vereenvoudigen (operationele veiligheid) en creëert een gunstig alkalisch klimaat (met hoge pH), dat de corrosie van de verschillende metallische onderdelen van de Supercontainer vertraagt of zelfs verhindert (Hoofdstuk 3).

De betonstudie onderzoekt de drie betonnen lagen die aanwezig zijn in de Supercontainer: de buffer, de filler en het deksel. Verscheidene parameters hebben een effect op het beton, de betoneigenschappen en de duurzaamheid. Door de aanwezigheid van het warmteafgevend radioactief afval wordt er warmte en straling ingeleid in het systeem, waardoor de drie betonnen lagen onderworpen worden aan een temperatuurverhoging en aan gamma bestraling. De hydrolyse van het poriënwater, interne opbouw van gasdruk en degradatie van de mechanische sterkte zijn gekende gevolgen van het bestralings- en verwarmingseffect. Andere aan duurzaamheid gerelateerde kwesties, zoals corrosie gerelateerde gasproductie en microbiële activiteit worden besproken in Hoofdstuk 4.

De twee, voor de cementgebonden buffer beschouwde, betonsoorten, SCC en TVC, hebben hun specifieke vereisten om operationele veiligheid en veiligheid op lange termijn te kunnen garanderen. In Hoofdstuk 5 worden de betonsamenstellingen van SCC en TVC bepaald, rekening houdend met specifieke vereisten en eisen betreffende vroegtijdige scheurpreventie. Er bestaat een significant verschil tussen de eisen gedefinieerd voor klassieke constructies, en de eisen nodig om de veiligheid van de Supercontainer te garanderen. Portland cement, in combinatie met kalksteen granulaten, wordt gebruikt in de beide betonsamenstellingen, om de gunstige hoge pH te realiseren ter preventie van corrosie. Bovendien is het gewenst dat de warmteproductie ten gevolge van de hydratatiereacties beperkt blijft om het

vroegtijdig thermisch scheurgedrag van de massieve betonnen buffer te beperken. Wegens duurzaamheidseisen dient de samenstelling bovendien te beschikken over een hoge sulfaatweerstand en dient de alkali silica reactie bekeken te worden. Om de zelfverdichtende eigenschap van het SCC te verwezenlijken, worden additionele hoeveelheden kalksteenpoeder en superplastificeerder toegevoegd.

Aan de hand van een uitgebreid programma van laboratoriumproeven zijn de relevante thermische, mechanische en maturiteit gerelateerde eigenschappen van SCC en TVC bepaald en vergeleken (Hoofdstuk 6). In vergelijking met TVC, heeft SCC een lagere thermische conductiviteit, waardoor het een groter isolerend vermogen heeft. Tevens is er een hogere productie van gecumuleerde adiabatische hydratatie-warmte vastgesteld bij SCC, in combinatie met hogere mechanische sterkte (zowel in trek als in druk), hogere autogene krimp en groter kruipgedrag. Dit verschil in eigenschappen kan vooral toegeschreven worden aan de grotere hoeveelheid aan fijner materiaal (zoals kalksteenpoeder) dat is toegevoegd aan SCC om de samenstelling zelfverdichtend te maken.

Eens de buffer gestort is, en het beton reeds een voldoende maturiteit en graad van verharding bereikt heeft, zal het warmteafgevend hoogactief afval in de buffer geplaatst worden. Hierdoor komen de buffer, de filler en het deksel in direct contact met het koolstofstalen vat dat warmte en gamma straling uitstraalt afkomstig van het afval. Het effect van gamma straling (met relevant stralingsdebiet) op de mechanische eigenschappen van verhardend SCC mortel, en de invloed van verhoogde temperaturen (tussen 20 °C en 105 °C) op de mechanische eigenschappen van reeds verhard beton, wordt besproken in Hoofdstuk 7. Er zijn indicaties van een mogelijk (druk)sterkte verlies tot 15 tot 20 %. Dit sterkteverlies kan te wijten zijn aan een toenemende trend in capillaire porositeit van de matrix, waarbij echter geen statistische significantie gevonden werd (bestudeerd aan de hand van fluorescentiemicroscopie).

Het hoofddoel van dit doctoraatsonderzoek bestaat er in om het risico op vroegtijdig scheuren van de betonnen buffer van de Supercontainer te evalueren, en dit zowel tijdens de constructiestappen in hot cell als daarbuiten. Het gedrag van het verhardend SCC en TVC wordt bestudeerd aan de hand van simulaties via HEAT/MLS (Hoofdstuk 8), en met behulp van Half-Scale Tests ter validatie van de bekomen gesimuleerde resultaten (Hoofdstuk 9). De bekomen betoneigenschappen zijn geïmplementeerd in de materialen database van de gebruikte simulatie tool, en spannings- en sterkteberekeningen worden uitgevoerd.

Er wordt geen vroegtijdige scheurvorming verwacht tijdens de eerste constructiestap. De desbetreffende sensitiviteitsanalyse analyseert vervolgens de invloed van gewijzigde materiaaleigenschappen, van gewijzigde dimensies van de buffer en van variaties in de randvoorwaarden op de bekomen resultaten. Vooral de exotherme hydratatiereactie van het cement leidt tot hoge trekspanningen ter hoogte van het buitenoppervlak van de buffer. In sommige situaties (bijvoorbeeld bij aanwezigheid van hoge externe windsnelheden of hoge buitentemperaturen) dienen er adequate maatregelen genomen te worden om vroegtijdig scheuren van het beton te voorkomen.

De thermisch gradiënt, die ontstaat ten gevolge van het temperatuurverschil tussen het inwendige beton van de buffer en het buitenoppervlak van de buffer, is de voornaamste oorzaak van het vroegtijdig scheurgedrag. Daarnaast spelen de convectiecoëfficiënt ter hoogte van de interface van het uitwendige oppervlak van de Supercontainer met de omgeving, en de thermische geleidbaarheid van de betonnen buffer een belangrijke rol in het vroegtijdig scheurgedrag. Om tot een validatie te komen van de eerste constructiefase en om de uitvoerbaarheid van de constructie van de buffer te bepalen, zijn er Half-Scale Tests uitgevoerd. Hierbij worden de temperatuursontwikkeling en het verloop van de verplaatsing en de vervorming van een in de praktijk gestorte buffer geregistreerd aan de hand van een uitgebreide test set-up en vergeleken met de bekomen simulatieresultaten. Een goede overeenkomst wordt bekomen, vooral wat betreft de kritieke thermische gradiënt. Bovendien toont een visuele inspectie van de buffer aan dat vroegtijdige macroscheuren niet voorkomen in de eerste constructiefase, en dat bijgevolg het eindige elementenprogramma HEAT/MLS veilige en conservatieve besluitvorming toelaat. Enkele moeilijkheden gedurende het mengen en tijdens het verpompen van het verse beton, die verbetering vragen in de toekomst, zijn geïdentificeerd tijdens de Half-Scale tests: de bepaling van het watergehalte van de gebruikte granulaten, het verpompen van het beton in één vloeiende beweging, het handmatig toevoegen van het kalksteenpoeder, enz.

Tot slot worden de verschillende constructiestappen in de hot cell, namelijk het inbrengen van het warmteafgevend afval en de sluiting van de Supercontainer door het storten van de filler en het deksel, gesimuleerd vanaf het moment dat de buffer een bepaalde verhardingsgraad bereikt heeft. De interne spanningsopbouw in de buffer van de Supercontainer is gerelateerd aan drie mechanismen: (i) de hydratatiewarmte afkomstig van de hydraterende filler en het hydraterend deksel, (ii) de warmte afkomstig van het radioactief afval, en (iii) het uitzettingsgedrag van het koolstofstalen vat dat het radioactief afval insluit. De eerste simulaties, die enkel de eerste twee mechanismen beschouwen en het koolstofstalen vat enkel als randvoorwaarde in rekening brengen, onderschatten de werkelijkheid: er wordt geen vroegtijdige scheurvorming verwacht. Via deze simulaties wordt de invloed van gewijzigde stortsituatie bestudeerd, en enkele conclusies kunnen getrokken worden: een langere afkoelingsperiode van het warmteafgevend afval is gunstig, er is een verhoogd scheurrisico indien SF ingebracht wordt, het gebruik van een TVC buffer of een geprefabriceerd deksel heeft weinig invloed op de interne spanningsopbouw in de buffer, en het uitstellen van het inbrengen van het afval heeft eveneens geen significante invloed op het vroegtijdig gedrag van de Supercontainer. Het is bijgevolg realistischer om het uitzettingsgedrag van het radioactief afvalvat eveneens in rekening te brengen, door dit vat als een macro element te implementeren in de simulaties (tweede simulatietype). Hierbij wordt er wel een aanzienlijk scheurrisico aangetroffen aan de buitenkant van de buffer, dat vooral afhankelijk is van de thermische uitzettingscoëfficiënt van het vat. Vooral tangentiële scheuren kunnen aangetroffen worden (ten gevolge van axiale spanningen). Deze bevinding wordt bovendien bevestigd door de Half-Scale tests. Om scheurvorming te vermijden, wordt in de praktijk aangeraden om een koolstofstalen vat te gebruiken in plaats van een roestvast stalen vat, en dit in combinatie met een afkoelingsperiode van het radioactief afval van

70 jaar. De inwendige eigenspanningen, aanwezig in de buffer na de eerste constructiestap buiten de hot cell, heffen de spanningsontwikkelingen ten gevolge van de drie vernoemde mechanismen gedeeltelijk op, en er is voldoende veiligheidsmarge om het mogelijke sterkteverlies van de buffer ten gevolge van de warmte en de bestraling op te vangen. De aanwezigheid van het roestvast stalen omhulsel veroorzaakt een reductie van de trekspanningen door introductie van gunstige additionele drukspanningen, die ontstaan door de belemmering van de uitzetting van de buffer. De toepassing van een last aan de bovenkant van de Supercontainer (bijvoorbeeld door het opschroeven van een stalen deksel aan de mantel van het roestvast stalen omhulsel) kan eveneens gunstige drukspanningen opwekken die de opbouw van trekspanningen in de buffer tegenwerkt. Scheurvorming in de filler, die samengedrukt wordt door de combinatie van de uitzetting van het vat en de eigen verhinderde vervorming door het omgevende beton, wordt niet verwacht. Scheurvorming van het deksel is niet van toepassing, wat bovendien bevestigd wordt door de Half-Scale tests.

CHAPTER 1:

INTRODUCTION AND OBJECTIVES

1 Introduction

The ongoing battle against global warming, the threat of fossil fuels exhaustion and the development of renewable energies nowadays are very hot topics which are being discussed worldwide. To comply with the popular energy demand and to reduce the carbon energies, the promotion of nuclear energy once again cannot be overlooked. Nuclear power is entering its renaissance age. Leaving out of consideration whether nuclear power is a good or a bad thing, matter of fact is: several types and considerable amounts of radioactive wastes are present worldwide. This waste originates from different producers and various applications: nuclear power plants (in Belgium, more than 50 % of the electricity production is provided via NPP's), medical applications and treatment of diseases, industry, research centres, military applications, aerospace technology, etc.

The past decades worldwide research started to investigate the possibilities and solutions for decommissioning the long-term radioactive waste. The back-end of the management of radioactive waste is its disposal. Disposal is defined as the placement of waste in approved repositories without the intention of retrieval [Rahman, 2008]. The maintenance and the guaranty of safety towards the disposal concept, both on the short term as on the long term, is inevitable. The general goal and the vision on deep geological disposal consists of a safe isolation of radioactivity towards people and their environment and this for a long period of time and to minimize the amount of radioactive waste [Umeki, 2008]. The radioactive waste management policy must prevent, at all times, contact of radioactive waste with the biosphere.

The Supercontainer is the current Belgian reference concept for the final disposal of heat-emitting waste designed by ONDRAF/NIRAS, the Belgian Agency for Radioactive Waste and Enriched Fissile Materials. The concept is based on a multiple barrier system where every component has its own specific safety function requirements [Bel et al., 2005].

2 The Belgian reference concept: the Supercontainer

During the past 25 years several preliminary repository concepts were studied. Today, the Supercontainer is considered to be the most promising Belgian reference design concept for the final disposal of heat-emitting waste designed by ONDRAF/NIRAS. In this reference concept, the vitrified High Level Waste (HLW) and Spent Fuel (SF) assemblies are encapsulated into a watertight carbon steel overpack surrounded by a cylindrical concrete buffer and an outer stainless steel envelope (Figure 1.1). This approach using several protecting layers is better known as an Engineered Barrier System (EBS). After construction of the Supercontainer, it will be transported into underground galleries and disposed in a deep clay layer (Host Rock) after backfilling the disposal gallery (Figure 1.2).

The carbon steel overpack, surrounded by the concrete buffer, is used to provide the confinement of the waste. The concrete buffer provides a favourable chemical environment and ensures a uniform corrosion mechanism for the overpack on a long-term safety approach. In a short-term view, the buffer should ensure operational shielding during fabrication and transportation. The Supercontainer provides complete containment of the radionuclides and other contaminants at least through the thermal phase (statement of ONDRAF/NIRAS). The disposal galleries should have sufficient strength in order to avoid a collapse. The clay layers must have a beneficial behaviour and retention capacity towards radionuclides migration. A wide range of experiments have been conducted in the past decades to counteract the limited range of experience and knowledge concerning the long-term behaviour of clay materials, in contact with highly alkaline matter, such as concrete, and under elevated temperature. Radionuclides must be confined during the thermal phase (HEATING 1 and HEATING 2, statement of ONDRAF/NIRAS). In such a way, the most important function of the Supercontainer is defined: the encapsulation of radioactive waste. The Supercontainer must also provide radiological protection during transportation.

On a long-term approach the conceptual evolution of the Supercontainer can be subdivided into four different phases:

- Phase 1: Fabrication of the Supercontainer.
- Phase 2: Heating under aerobic conditions (HEATING 1).
- Phase 3: Heating under anaerobic conditions (HEATING 2).
- Phase 4: Cooling under anaerobic conditions (COOLING), the pore water of the Host Rock comes into contact with the Supercontainer.

This study examines the early-age thermo-mechanical behaviour of the Supercontainer during construction or fabrication (Phase 1).

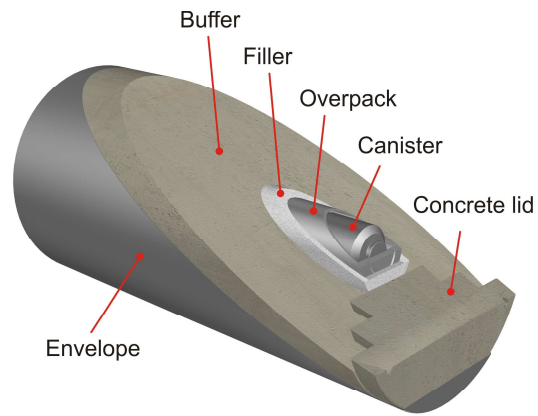


Figure 1.1: The Belgian Supercontainer concept: 3D view [source: ONDRAF/NIRAS]

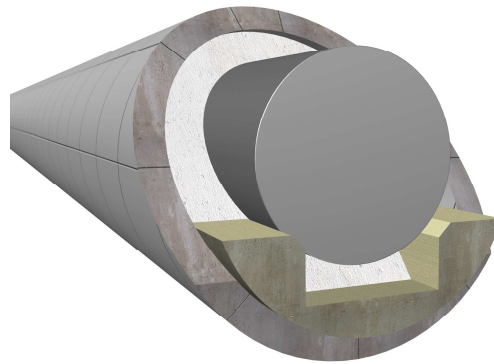


Figure 1.2: The Belgian Supercontainer concept: 3D view of the disposal gallery [source: ONDRAF/NIRAS]

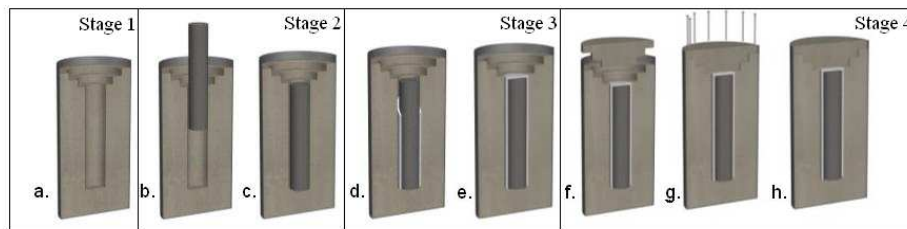


Figure 1.3: The four construction stages of the Supercontainer (steps b to h performed in hot cell) [source: ONDRAF/NIRAS]

3 Objectives

In the framework of the feasibility demonstration program of the Belgian Supercontainer concept, extensive laboratory tests and finite element calculations were performed to accurately simulate the Thermal (Hygral) Mechanical (THM) behaviour of the Supercontainer concrete buffer during construction and to predict and prevent early-age crack formation.

A laboratory test program has been set up and large scale tests are performed, to allow the characterization of the mechanical, thermal and maturity-related behaviour of two types of concrete currently considered for the choice of the cementitious buffer: a Self-Compacting Concrete (SCC) and a Traditional Vibrated Concrete (TVC). The measured data are used to simulate the behaviour of the concrete buffer during construction by using a 2.5D thermal and crack modelling program. This includes the fabrication of the concrete buffer, the emplacement of the heat-emitting waste canisters, and the closure of the container (Figure 1.3, Table 1.1). It is possible to take into account different casting conditions and to examine changes in concrete properties, environmental conditions and dimensions via a sensitivity analysis. The objective is to prevent through-going cracks in the concrete buffer, which will considerably ease the transport mechanisms inside the Supercontainer and reduce the radiological shielding role of the buffer.

The final objective of the doctoral thesis is to demonstrate the feasibility to construct the buffer with the explicit demand of crack avoidance during construction. The necessity of concrete reinforcement in order to prevent thermal cracking during construction must be determined by means of this study.

Table 1.1: The four construction stages of the Supercontainer (short-term approach)

Four construction stages (Figure 1.3)	
Stage 1	Fabrication of the concrete buffer inside a steel envelope (a)
Stage 2	Emplacement of the carbon steel overpack containing the waste canisters inside the concrete buffer (b,c)
Stage 3	Filling the remaining annular gap with the filler under thermal load (d,e)
Stage 4	Closure by fitting the lid (f,g,h)

References

Bel J., Van Cotthem A., De Bock C. (2005), *Construction, operation and closure of the Belgian repository for long-lived radioactive waste*, Proceedings of the 10th International Conference on Environmental Remediation and Radioactive Waste Management, ICEM05, Glasgow, Scotland, 7p.

Rahman A. (2008), *Decommissioning and Radioactive Waste Management*, Whittles Publishing, Scotland, UK.

Umeki H. (2008), *Safety Aspects of cementitious systems*, Cement and Cementitious Materials in the geological disposal of radioactive waste, ITC School International Course, Eurojoki, Finland.

CHAPTER 2:

RADIOACTIVITY AND RADIOACTIVE WASTE

To a certain extent, everything around us is radioactive. Even our own human body emanates a small amount of radioactivity. Radioactivity is a natural phenomenon happening at the infinitesimally small level of the nucleus. Man did not invent this phenomenon, he discovered it by observation towards the end of the 19th century. Since then, the knowledge concerning radioactive materials expanded, leading to peaceful improvements towards medical science, energy production and industry. Unfortunately every advantage has its downsides: the use of nuclear weapons or the inevitable creation of nuclear waste is like a blot on the escutcheon of nuclear science. However, nowadays valuable solutions exist to ensure a good handling of nuclear waste and to prevent the possible harmful consequences of radioactivity on mankind and its environment.

1 Radioactivity

1.1 Definition of radioactivity

Radioactivity is a natural phenomenon that occurs at the level of the building blocks of matter, the infinitely small: i.e. the nuclei of atoms [source: website ONDRAF/NIRAS.]. To understand the phenomenon, we must get right to the heart of the matter. Generally, atoms are stable. For an atom to be stable, there must be an equilibrium between the numbers of different particles in its nucleus. In some atoms, that equilibrium is disrupted. There are too many protons compared to the number of neutrons, or too many neutrons compared with the number of protons, or even too many of both. In other words: there is an overdose of energy in the nucleus. This nucleus is then described as unstable or radioactive. Sooner or later every unstable nucleus will undergo changes in order to get rid of the excess energy. The energy is expelled in the form of particles or pure energy (electromagnetic waves). This spontaneous process is known as radioactive decay. Energy is expelled until a new equilibrium is established in the nucleus. This can take place in several stages. The

activity of an amount of radioactive material gradually diminishes until it has virtually disappeared. Decay continues until the unstable nucleus has become stable and non-radioactive.

The radiation deriving from radioactive materials gives off energy. When this radiation passes through matter, it reacts with atoms or molecules of this matter and transfers some of its energy to them. An electron can be shut away from an atom or a molecule, or can be absorbed by it. In this way an electrically charged atom or molecule, an ion, is created. This phenomenon is called ionization. Radiation emitted by radioactive materials is called ionizing radiation, because it creates ionization by contact with the matter and the matter gets irradiated. Ionizing radiation emits so much energy that it can alter the structure of the matter into which it penetrates.

Two types of ionization can be distinguished:

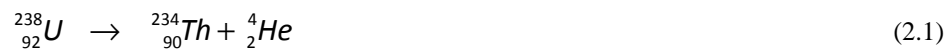
- Direct ionization: electrons are released by means of electrical interactions (Coulomb forces).
- Indirect ionization: this is caused by non-charged particles or electromagnetic radiation. Charged particles are formed and ionized directly by means of interaction processes.

1.2 Types of ionizing radiation

Different types of radiation can be described: alpha and beta radiation, gamma rays, X-rays and neutrons [Reynaert and Thierens, 2008, Rahman, 2008].

1.2.1 Alpha radiation

One of the ways in which an unstable radioactive atom can decay, is by emitting an alpha particle. Alpha radiation consists of rather large particles: helium atoms with two neutrons and two protons that are released with alpha decay. Alpha decay can be seen as a form of nuclear fission where the parent atom splits into two daughter products. For example:



Most of the produced helium comes from the alpha decay of underground deposits of minerals containing uranium and thorium. The helium is brought to surface as a by-product of natural gas production.

Alpha radiation has a corpuscular character and is directly ionizing. The alpha particles are mono-energetic. This type of radiation can only occur with heavy nuclides with a large amount of protons ($Z > 82$, lead: $Z = 82$, $Z =$ number of protons in the nucleus).

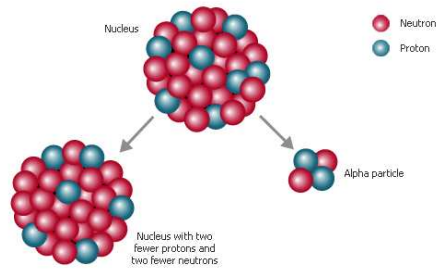


Figure 2.1: Emission of an alpha particle by the parent nucleus. The atom transmutes into an atom of a different element [source: website encyclopaedia Encarta]

Alpha radiation is not highly penetrable and is easily blocked because of their relatively large mass. It has a short range. Even a thin slice of paper or a small layer of air can stop the alpha particles, who have a typical kinetic energy level of 5 MeV and a velocity of 15 000 km/s.

1.2.2 Beta radiation

In nuclear physics, beta decay is a type of radioactive decay in which a beta particle (an electron or a positron) is emitted. The beta radiation consists of smaller particles released after beta decay.

The electrons and positrons of the beta radiation also have a corpuscular character and they are directly ionizing. Kinetic energy of beta particles has a continuous spectrum ranging from 0 to the maximal available energy (Q_k), which depends on parent and daughter nuclear states participating in the decay. Typically Q_k is of the order of 1 MeV, but it can range from a few keV to a few tens of MeV.

In β^- decay, the weak interaction converts a neutron (n) into a proton (p) while emitting an electron (e^-) and an antineutrino, an uncharged elementary particle with negligible mass. This can only occur if the amount of neutrons is larger than the amount of protons. For example:



In β^+ decay, energy is used to convert a proton (p) into a neutron (n), a positron (e^+) and a neutrino, an uncharged elementary particle with negligible mass. The β^+ decay requires energy, the mass of the neutron being bigger than the mass of the proton.

An example:



Beta particles with a speed of 270 000 km/s can be stopped by steel or aluminium with a thickness of a couple of mm, or by an air layer with a thickness of 3 meter.

1.2.3 Electromagnetic radiation: gamma rays and X-rays

The nucleus is often found in an excited state after alpha or beta decay. To achieve the lowest state of energy and repair the initial state of equilibrium, electromagnetic rays are emitted: gamma rays. An example:



Sometimes the energy is expelled in the form of electrons leaving the nucleus. An internal conversion process starts, leading to the appearance of X-rays. Nucleons in atoms have certain energy levels which are much higher than those of electrons. When a nucleon moves from a higher energy level towards a lower energy level, gamma rays are emitted in the order of keV or more (1 eV equals 1.6×10^{-16} J). X-rays originate from the transition of atomic electrons from a higher energy state to a lower energy state and hence the X-ray energy level is lower than the gamma ray energy level. Gamma emission and internal conversion are competitive reactions.

The electromagnetic radiation in general consists of waves which are characterized by a wavelength λ' , and a frequency, ν . The quantum of an electromagnetic radiation is known as photon and its energy level is given by:

$$E_k = h \cdot \nu \quad (2.5)$$

where: $h = \text{the Planck constant } (= 6.626 \times 10^{-34} \text{ J}\cdot\text{s})$
 $\nu = \text{the frequency of the wave (Hz)}$

These electromagnetic rays have no mass, have an undular-corpuseular character and are indirectly ionizing. X-rays and gamma rays have a very high frequency ($> 10^{18}$ Hz) and consequently their photon energies are also high. If the energy of the photon is higher than the binding energy of an electron in a target atom, ionisation of the target atom is caused. Gamma rays have the highest frequency (above 10^{19} Hz) and energy level (above 100 keV), and also the shortest wavelength (below about 10 picometers), in the electromagnetic spectrum and travel with the speed of light (300 000 km/s). Because the wavelength of gamma radiation is so short, a single incident photon can impart significant damage to a living cell and cause serious damage when absorbed by living tissue. Gamma rays have a large penetration depth. They can only be stopped by heavy matter such as iron, concrete or lead with a sufficient thickness. The electromagnetic radiation can easily travel several hundred of meters through air.

1.2.4 Neutrons

Neutrons are uncharged particles that are indirectly ionizing. They occur after spontaneous reaction, but especially after nuclear fission in nuclear reactors. For example:



Notice that one neutron is used, but three neutrons are produced. These three neutrons, if they encounter other ${}^{235}\text{U}$ atoms, can initiate other fissions, producing even more neutrons. In terms of nuclear chemistry, it is a continuing cascade of nuclear fissions called a chain reaction.

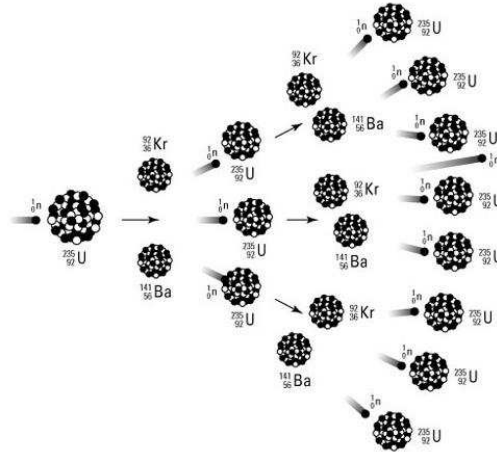


Figure 2.2: Chain reaction in a nuclear reactor [source: website CliffsNotes.com]

Neutrons can be characterized according to their kinetic energy E_k level:

- Slow neutrons: $E_k < 0.5 \text{ eV}$
- Medium fast neutrons: $0.5 \text{ eV} < E_k < 200 \text{ keV}$
- Fast neutrons: $200 \text{ keV} < E_k < 20 \text{ MeV}$
- Relativistic neutrons: $20 \text{ MeV} < E_k$

As neutrons are uncharged particles, they do not react electrically with the electron cloud of the atom. They undergo physical collisions with atomic nuclei losing energy in every encounter.

1.3 The unity of radioactivity

The following explanation is based on an application of the Royal Decree of 20th of July 2001, dealing with the protection of the Belgian population, employees and environment against the dangers of ionizing radiation [website FANC, Federal Agency for Nuclear Control].

1.3.1 Activity

The activity A of a radioactive matter with a certain energy level is expressed as the total amount of spontaneous mutations of radioactive nuclei from that certain energy level in a certain amount of time:

$$A = \frac{dN}{dt} = \lambda \cdot N \quad (2.7)$$

where: dN = expectation of total amount of spontaneous mutations of nuclei (-)
 dt = time interval (s)
 N = amount of radioactive atoms at time t (-)
 λ = disintegration constant (s^{-1} , h^{-1} , d^{-1} , y^{-1})

The unity of activity is better known as Becquerel (Bq). One Becquerel equals one decomposition per second. For example, the water in the oceans has an activity of 12 Bq per litre, the human body has an activity of 120 Bq per kilogram. The progress of the amount of radioactive atoms with time is given by equation (2.8). Substituting (2.8) in (2.7) leads to equation (2.9) giving the exponential decrease of the activity A of a radioactive matter with time.

$$N(t) = N_0 \cdot e^{-\lambda t} \quad (2.8)$$

where: N_0 = amount of radioactive atoms at time $t = 0$ (-)
 λ = disintegration constant (s^{-1} , h^{-1} , d^{-1} , y^{-1})
 t = time (s, h, d, y)

$$A(t) = A_0 \cdot e^{-\lambda t} \quad (2.9)$$

where: A_0 = the activity of a radioactive matter at time $t = 0$ (Bq)

1.3.2 Absorbed dose D and equivalent dose H_T

The absorbed dose D is the total absorbed energy $d\mathcal{E}$ per unity of mass dm :

$$D = \frac{d\mathcal{E}}{dm} \quad (2.10)$$

where: $d\mathcal{E}$ = amount of energy transferred by the ionizing radiation (J)
 dm = mass of the element (kg)

The unity of the absorbed dose is Gray (Gy). One Gray equals one Joule per kilogram.

Biological radiation damage does not only depend on the absorbed dose D , also the type of ionizing radiation has a significant influence. Some types of radiation cause more ionisation: alpha radiation causes more damage than gamma radiation. Therefore a new variable was brought into life: the equivalent dose $H_{T,R}$.

$$H_{T,R} = w_R \cdot D_{T,R} \quad (2.11)$$

where: w_R = radiation type weighing factor (-)
 Values of w_R are given in Table 2.2 according to ICRP 30 reports (International Commission on Radiological Protection)
 $D_{T,R}$ = average absorbed dose in a tissue or organ T of the body due to a radiation type R (Gy)

Table 2.1: Radiation type weighing factor [according to ICRP 30 reports]

Radiation type	w_R
X- γ	1
β^- - β^+	1
n	5 – 10
α	20

The unity of the equivalent dose is Sievert (Sv). When the radiation field is composed by more than one radiation type with different w_R -values, the total equivalent dose is obtained by using equation (2.12), expressed in Sievert.

$$H_T = \sum w_R \cdot D_{T,R} \quad (2.12)$$

If the obtained equivalent dose over a certain amount of time τ due to a certain radiation type at a certain point of time t_0 is desired, equation (2.12) needs to be integrated over that time period:

$$H_T(\tau) = \int_{t_0}^{t_0+\tau} H_T(t) \cdot dt \quad (2.13)$$

If τ is not specified, a duration of 50 years for adults and 70 years for children is specified.

1.3.3 Effective dose E_T

Finally the effective dose E_T is the sum of all equivalent doses in all tissues and organs of the human body caused by internal and external contamination:

$$E_T = \sum w_T \cdot H_T = \sum w_T \cdot \sum w_R \cdot D_{T,R} \quad (2.14)$$

where: w_T = tissue weighing factor of the organ or tissue T (-),
Values of w_T are given in Table 2.2 according to ICRP 30 reports
(International Commission on Radiological Protection)

The integrated effective dose in the various tissues and organs T can be calculated according to equation (2.15):

$$E(\tau) = \sum w_T \cdot H_T(\tau) \quad (2.15)$$

1.3.4 Radioactive decay

Just as a fire dies down as time passes, the activity of radioactive materials does to. Each time an atomic nucleus of a radioactive substance emits energy to attain better equilibrium between the number of protons and neutrons, another variant is created, which may or may not be radioactive. An ever-decreasing amount of the original radioactive material thus remains. This is called radioactive decay. The time it takes for the activity to reduce to half of its initial value, is called the half-life $T_{1/2}$ of a radioactive material (Figure 2.3). To calculate $T_{1/2}$ equation (2.16) is used.

$$T_{1/2} = \frac{\ln 2}{\lambda} \quad (2.16)$$

where: λ = disintegration constant (s^{-1} , h^{-1} , d^{-1} , y^{-1})

After 10 half-life periods, only about one thousandth ($1/2^{10}$) of the original activity is left. Each radioactive material is specified by its own half-life. Some have half-lives of just a few seconds, others of thousands or even millions of years. Some examples of radioactive materials and their half-lives are given in Table 2.3.

Table 2.2: Tissue weighing factor of the organ or tissue T [according to ICRP 30 reports]

Organ or tissue	w_T
Bladder	0.05
Red bone marrow	0.12
Bone surface	0.01
Colon	0.12
Ovary	0.2
Breast	0.05
Oesophagus	0.05
Liver	0.05
Lung	0.12
Skin	0.01
Stomach	0.12
Thyroid	0.05
Rest of body	0.05
Total body	1

Table 2.3: Radioactive materials and their half-life [website ONDRAF/NIRAS]

	Field of application	Half-life
Iodine-123	Nuclear medicine: diagnostics	13 hours
Iridium-192	Nuclear medicine: therapy	74 days
Cobalt-60	Nuclear medicine: therapy	5.27 years
Caesium-137	Nuclear medicine: therapy Important fission product	30 years
Carbon-14	Age determination of materials	5 730 years
Plutonium-239	Production of nuclear fuel	24 065 years
Uranium-235	Production of nuclear fuel	704 000 000 years

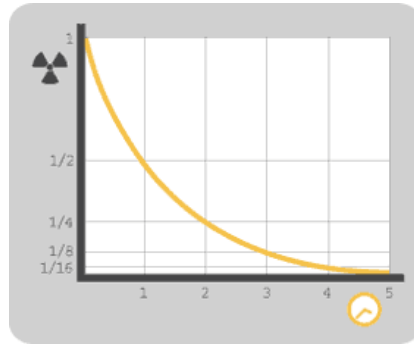


Figure 2.3: The principle of half-life [source: website ONDRAF/NIRAS]



Figure 2.4: The three principle of protection against radiation [source: website ONDRAF/NIRAS]

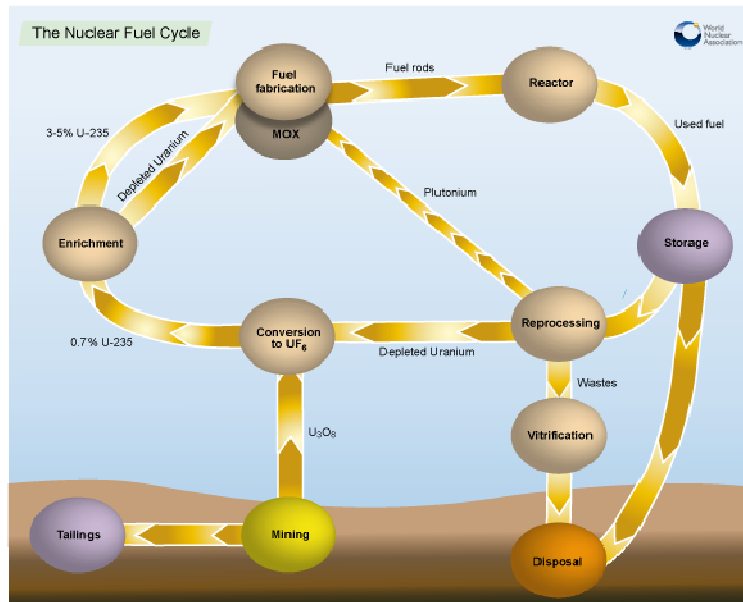


Figure 2.5: The Nuclear Fuel Cycle [source: World Nuclear Association]

2 Radiological protection

The subject matter of radiological protection deals with ways and means of protecting human beings and their descendants, both individually and collectively, as well as the environment, from the harmful effects of ionizing radiation. Radiological protection aims to do more good than harm to individuals as well as to society [Rahman, 2008].

The tools and techniques available to protect us against ionizing radiation are based on the following three principles (Figure 2.4):

- Exposure time: the shorter the exposure time, the smaller the dose.
- Distance from source: the further away the radioactive source, the smaller the dose.
- Shielding and containment: water, glass, lead, concrete and many other materials shield from radiation effectively. The encapsulation or containment of radioactive substances in such materials prevents them from being dispersed into the environment. Adapted clothes and masks limit the risk of contamination.

In Belgium, the population and the workers are protected by the ARAB/RGPT (Belgian legislation and general regulations on safety and health protection at work) and by the Royal Decree of 20th of July 2001, dealing with the protection of the Belgian population, employees and environment against the dangers of ionizing radiation.

Three important principles are handled:

- Principle of justification of practice: the advantages of radioactivity must be exceeded by the disadvantages.
- Principle of optimizing the protection: the absorbed dose must be kept as low as reasonable achievable (ALARA) taking into account the economical and social factors.
- Principle of individual dose limits determined for the population and the employees.

On the basis of recommendations of the ICRP in 1990 and according to the ICRP 30 reports, different ALI values (Annual Limits on Intake) are determined. A total tolerable effective dose E_T of 1 mSv/year may not be exceeded for the population. People who are exposed to radiation by virtue of one's profession may be subjected to a total effective dose E_T of 20 mSv/year. The equivalent dose, cumulated over a period of 50 years, $H_T(\tau)$ should not exceed 0.5 Sv for each tissue or organ. These values are in addition to the cosmic (background) radiation present in nature and soil, that can reach a value up to 10 mSv/year .

3 Radioactive waste

3.1 The Nuclear Fuel Cycle

Radioactive waste originates in every stage of the nuclear fuel cycle: from the excavation of uranium ore, to the dismantlement of nuclear power plants (NPP's), until the disposal in deep geological layers (Figure 2.5). The amount and the radioactivity varies with the type of radioactive waste. Various types of radioactive waste in various physical and chemical forms were and are produced in Belgium. This waste originates from different producers and can be subdivided into three major categories:

- Generation of electricity by means of nuclear energy. Almost 80 % of the radwaste in Belgium derives from the energy producing companies: NPP's in Doel (4 reactors) and Tihange (3 reactors), production of nuclear fuel by FBFC International in Dessel, and research at a nuclear level at SCK-CEN, Mol.
- Utilization of radioactivity in medical applications and hospitals, industry and agriculture. On a daily basis, radioactive materials and ionizing beams are used in hospitals to detect (scanner) and treat diseases (cancer). In order to make the medical instrumentation sterile, radioactivity is being used. Germ-control and the prolongation of the conservation of food is an other branch for the use of radioactivity. In the industry, the examination of welded joints and the detection of construction faults are examples of execution by means of radioactive beams and electromagnetic radiation.
- The shut down and dismantling of nuclear installations creates additional radwaste.

3.2 Classification of radioactive waste

Radioactive waste can be classified in many different ways: according to source, physical state (solid-liquid-gas), level of radioactivity, half-life, final disposal route or radiotoxicity. The two most significant and widely used parameters which are taken into account for waste classification are (i) the half-lives, and (ii) the activity concentrations. Looking at the short-term management, the classification only takes into account the activity of the radwaste. Three activity levels can be distinguished: (i) Low Level Waste (LLW), (ii) Intermediate Level Waste (ILW) and (iii) High Level Waste (HLW).

The LLW has a contact dose rate smaller than 5 mSv/h. Only minimal shielding is necessary during processing. Approximately 75 % of the total volume of radioactive waste has a low activity according to ONDRAF/NIRAS.

The contact dose rate of the ILW, representing 24 % of the total radwaste volume, lies in between 5 mSv/h and 2 Sv/h. This waste form must be totally encapsulated and shielded with thick concrete and leaded layers and must be handled from a certain distance.

Roughly 95 % of the total activity of the radioactive waste in Belgium is represented by less than 1 % of the total amount (ONDRAF/NIRAS statement): waste which is very radioactive and in which temperature may rise significantly as a result of its radioactivity. The HLW has a contact dose rate higher than 2 Sv/h, emits heat and needs careful handling and sufficient shielding.

On a long-term base, the classification of the radioactive waste takes into account both the activity and the half-life of the radioactive materials, leading towards three categories: (i) A-level waste, (ii) B-level waste or (iii) C-level waste, according to Table 2.4. The half-life consideration is consistent with the disposal route: Long-Lived (LL) require long-term isolation from humans and the environment, preferably in geological structures. Based on the half-life of the radionuclides that need to be confined, the type of solution needed for the long-term disposal is determined.

The A-level waste originates from NPP's, nuclear medical applications, agriculture and industry. The dismantling of a NPP delivers the largest amount of A-level waste. These wastes are generated from normal plant operations, routine maintenance work, refuelling operations and consist of protective clothes and shoes, disposable handkerchiefs, etc. It contains small amounts of radionuclides with short or intermediate half-life (< 30 years). The amount of alpha radiation is limited. In the Belgian concept, this type of waste will be preferably stored on ground level during the time it takes for the activity to drop with a factor 1000 [Bel et al., 2005]. In June 2006, the Belgian Federal Government decided to dispose the A-level waste in Dessel (Figure 2.6).

Table 2.4: The Belgian Waste Classification: three types of radioactive waste

	Activity		
	Low Level	Intermediate Level	High Level
Short-lived (SL) : Half-life < 30 years	A	A	C
Long-Lived (LL) : Half-life > 30 years	B	B	C

Serious amounts of radionuclides and alpha radiation with half-lives larger than 30 years is subdivided in B-level category. Due to the longer period of time for radioactive decay, the reference solution in the Belgian concept for the disposal of B-level waste is the geological disposal by means of concrete Monoliths [Bel et al., 2005]. The general design principle is to enclose a number of waste packages by a sufficiently thick concrete layer (Monolith) to reduce the dose rate at 1 m from the outer surface to a maximum of 25 µSv/h (Figure 2.7).

In comparison with B-level waste, the C-level waste has a higher concentration of beta and gamma radiation, resulting in the heat emitted by this type of waste. It can also have a considerable amount of alpha radiation, explaining the long half-life in some cases. C-level waste mostly originates from fission products and from the reprocessing of nuclear fuel and untreated SF.

ONDRAF/NIRAS is responsible for the inventory and the estimation of the total amount of radioactive waste present in Belgium. Previous assessments, based on data facts of 1st of January 2001, indicate that the total volume amounts up to 70 500 m³ A-level, 8900 m³ B-level, and 2100 m³ – 4700 m³ C-level waste in the year 2070.

3.3 Radioactive waste according to present activity

Waste with high activity and within the fuel cycle contains three key types of radionuclides:

- Activation products: these arise from interaction of neutrons with reactor materials. Some important activation products are ¹⁴C, ³⁶Cl, ⁶⁰Co, ⁵⁹Ni or ⁶³Ni.
- Fission products: these arise when a nuclide undergoes fission. Some important fission products are ⁹⁰Sr, ⁹⁰Zr, ⁹⁹Tc, ¹²⁹I, ¹³⁷Cs or ^{137m}Ba. They are radionuclides with a relatively short half-life.
- Actinides: these radionuclides are produced when fertile isotopes, like ²³⁸U, absorb neutrons that lead to the production of trans-uranic actinides, such as ²³⁹Pu (T_{1/2}: 24390 y), ²⁴⁰Pu (T_{1/2}: 6540 y), ²⁴¹Pu (T_{1/2}: 15 y), ²⁴²Pu (T_{1/2}: 3.9·10⁵ y), ²⁴¹Am (T_{1/2}: 462 y) or ²³⁷Np (T_{1/2}: 2.2·10⁶ y). The decrease of activity of these actinides can be very slow.

The energy of radiation originating from radioactive decay produces the heat emitted by vitrified HLW and SF assemblies. This process is dominated by a few radionuclides, such as ⁶⁰Co (~ 5·10⁻¹³ W/Bq), ⁹⁰Sr (~ 1.8·10⁻¹³ W/Bq), ¹³⁷Cs (~ 1.35·10⁻¹³ W/Bq) or ^{137m}Ba (~ 1.35·10⁻¹³ W/Bq). Some actinides such as ²⁴¹Am, ²⁴⁰Pu or ²³⁹Pu with a heat production of approximately 8.9·10⁻¹² W/Bq only arise in the SF assemblies, explaining the higher and longer lasting heat production of the SF in comparison with vitrified HLW.

Relative activity (in comparison with the radiotoxicity of the mined uranium ore) of vitrified HLW is most likely expected to last a couple of thousands of years (Figure 2.8). The first hundreds of years, the activity of the fission products and activation products has the greatest impact on the total activity. When the activity of the fission products drops, the actinides and its daughters have the highest contribution to the total activity. The same behaviour is noticed for SF, except for the much higher original relative activity (factor 100), and the lower radioactive decay (factor 100) due to the higher amount of certain actinides. Relative activity (in comparison with the radiotoxicity of the mined uranium ore) of SF assemblies is most likely expected to last a couple of hundreds of thousands of years.

3.4 Vitrified HLW versus Spent Fuel

The current Belgian reference design for heat-emitting HLW and SF assemblies is based on the so-called Supercontainer concept [Bel et al., 2005]. The same design principle occurs as for the concrete Monoliths. The dimensions and the weight of the Supercontainer also depend on the type of radioactive material that needs to be disposed: (i) Vitrified HLW, (ii) Spent Fuel (UOX) or (iii) Mixed Oxide Fuel (MOX) (Chapter 3). MOX is a nuclear fuel composed of a mixture of plutonium oxide and natural uranium oxide, reprocessed uranium or depleted uranium. MOX originates from the separation of still fissile materials from the Spent Fuel. The Supercontainer is intended for the disposal of Vitrified HLW and for direct disposal of SF assemblies (Table 2.4, category C).

SF and vitrified HLW are durable waste forms that will dissolve and release radionuclides very slowly (i.e. over periods of tens to hundreds of thousands of years or, in the case of SF, even longer) under the conditions expected to exist in the repository. SF is irradiated nuclear fuel that has not been chemically reprocessed. HLW is primary waste, either liquid or solid, that arises from the chemical reprocessing of SF.

Vitrified HLW consists of an amorphous structure of glass holding large quantities of radionuclides, with many different types of glass formulations (e.g. borosilicate glass). The waste loadings of the radionuclides is about 10 % – 20 % of the total weight of the waste package. The glass matrix with its vitrified fission products is surrounded by a stainless steel overpack (Figure 2.9). The thermal loading per unit mass of vitrified HLW is lower compared to SF caused by the removal of some heat-producing actinides in case of HLW. The heat output depends on the aging before reprocessing, the storage before disposal, the inventory and the total mass.

As a waste form, the SF rods can be subdivided into multiple radioactive sources (Figure 2.9). The UO₂ matrix consist of volatile fission products migrated to voids, cracks, gaps and grain boundaries and 5-metal particles. A ¹⁴C crud at the outer surface of the rod can be formed from the irradiation of coolant water. Concerning the radiation field of SF, it initially has a high alpha, beta and gamma content. After 1000 years, mostly alpha irradiation remains.

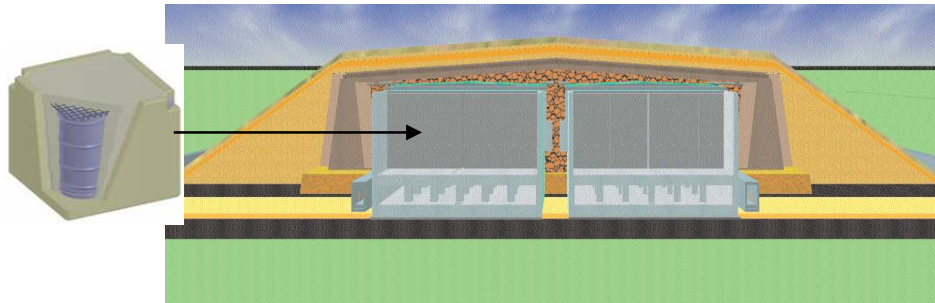


Figure 2.6: 3D view of the Belgian concept for A-level waste [source: ONDRAF/NIRAS]

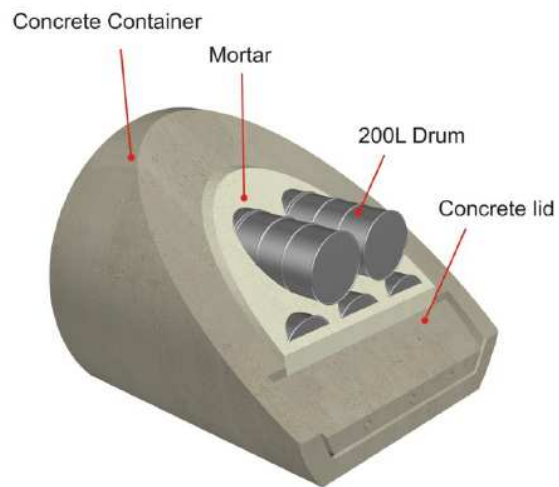


Figure 2.7: The Belgian concept for disposal of B-level waste: 3D view of the Monolith [source: ONDRAF/NIRAS]

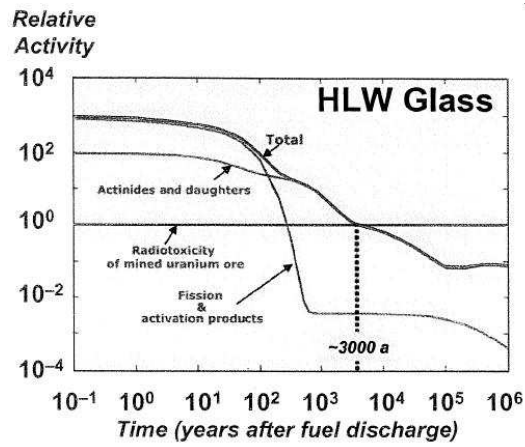


Figure 2.8: Time dependent 'Relative Hazard' of vitrified HLW [Apted, 2008b]

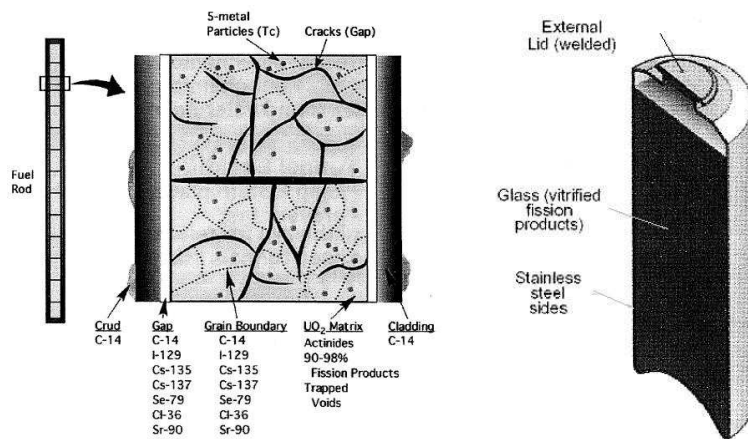


Figure 2.9: Spent Fuel (left) and vitrified HLW (right) as a waste form [Apted, 2008b]

References

Apted M. (2008), *Chemical, Thermal and Hazaed Characteristics of Spent Nuclear Fuel and HLW*, Geological Disposal of High-Level Waste, ITC School International Course, Las Vegas, USA.

Apted M. (2008b), *Design Concepts for Repositories and Underground Storage*, Geological Disposal of High-Level Waste, ITC School International Course, Las Vegas, USA.

Bel J., Van Cotthem A., De Bock C. (2005), *Construction, operation and closure of the Belgian repository for long-lived radioactive waste*, Proceedings of the 10th International Conference on Environmental Remediation and Radioactive Waste Management, ICEM05, Glasgow, Scotland, 7p.

International Commission on Radiological Protection (1990), *Recommendations of the International Commission on Radiological Protection*, ICRP Publication 60, Annuals of the ICRP, Vol. 21, No 1-3.

Rahman A. (2008), *Decommissioning and Radioactive Waste Management*, Whittles Publishing, Scotland, UK.

Reynaert N., Thierens H. (2008), *Environmental impact of radiation and sound (in Dutch)*, Ghent University.

CHAPTER 3:

DISPOSAL OF RADIOACTIVE WASTE

The management of radioactive waste is inescapably linked with its disposal. Disposal is defined as the emplacement of waste in an approved repository without the intention of retrieving it [Rahman, 2008]. Before the disposal, radioactive waste is subjected to a number of pre-disposal management steps: (i) collection, (ii) characterization, (iii) sorting, (iv) pre-treatment, (v) treatment and conditioning, (vi) storage and (vii) transportation as well as the cleanup activities. The goal is to prepare the waste for the long-term containment in a disposal facility and to isolate the waste from the human environment.

1 Radwaste Management

The two basic safety objectives for the disposal of radioactive waste are listed according to IAEA (1994):

- Protection of human beings and the environment from the harmful effects of wastes, either radiological or non-radiological.
- Disposal of the waste in such a way that the transfer of responsibility to future generations is minimised.

According to Chapman (2008) the objectives of geological disposal are:

- Isolate radioactivity from people by deep burial in the Host Rock.
- Maintain a stable geological cocoon for the engineered containment system for hundreds of thousands of years.
- Contain radioactivity for many thousands of years until 99.9 % of the radioactivity has decayed.
- Prevent any releases in harmful concentrations reaching people and the environment.

A considerable amount of work is already done and some work is still ongoing in order to overcome the disposal problemacy and to realise applicable safety standards in the pre-closure or operational phase and the post-closure phase. The concept and practices of radioactive waste disposal are intricately linked with the waste categories (Chapter 2). Low Level Waste (LLW) with a short half-life requires isolation for a relatively

short period of time (hundred of years) and hence may be disposed at surface facilities (surface disposal). LLW with longer half-life require a longer period of isolation and more severe criteria must be considered, which can be realised by means of near-surface disposal. Long-lived Intermediate Level Waste (ILW) and High Level Waste (HLW), independent of the half-life, require a long period of isolation. This can be achieved by deep underground disposal, better known as geological disposal. There are various disposal options, based on different criteria such as waste category and the considered and available Host Rock. Our focus lies on the geological disposal of HLW.

The isolation of radioactive waste from the human environment is achieved by applying the general principle of defence in depth [Rahman, 2008]. The higher the activity-level or the longer the half-life of the waste, the more rigorous is the application of defence in depth principle. A multiple barrier concept is used to isolate the HLW and the long-lived ILW. The multiple barriers of the geological repository consist of (i) an Engineered Barrier System (EBS) comprising the waste form, the waste containers, the buffer mass and the backfill material, (ii) the natural barrier comprising site geology (Host Rock), and (iii) the biosphere comprising atmosphere, soil and surface waters. The idea is that the combination of the EBS and the natural barrier will offer a barrier that is robust enough and will contain activity for a sufficiently long period of time during which activity will decay sufficiently to have any significant impact on either human beings or on the environment. Containment of radioactive waste is assured, in first instance, by the EBS of the disposal facility, including the waste form itself and the complete set of man-made barriers placed around it. Next, the natural barrier assures containment of the radioactive substances that can escape from the EBS after some time. The depth of disposal and the characteristics of the host formation further must guarantee isolation of the waste from the biosphere and from potentially disturbing factors, such as climate changes. Each barrier has its specific safety functions. The bedrock should (i) isolate the EBS from the biosphere, (ii) remain geomechanically stable, (iii) provide a favourable geochemistry for the EBS and (iv) limit groundwater flow. The tunnel backfill keeps the EBS in place, keeps the tunnel stable and prevents fast pathways for release. The mass transport inside the buffer is diffusion limited. The buffer isolates the waste containing canister from the Host Rock, conducts heat and filters colloids. Finally the waste canister provides aid during the emplacement of the waste, also conducts heat, isolates waste from the ground water and must withstand mechanical loads [Apted, 2008].

Disposal of radioactive waste aims at containing and isolating it over time periods sufficiently long enough to preclude any adverse impact on life at the Earth's surface (10^4 , 10^5 , 10^6 ... years).

2 The Belgian reference concept for the disposal of High Level Waste and Spent Fuel assemblies: the Supercontainer

2.1 Supercontainer design concept

During the past 25 years several preliminary repository concepts were studied. Today, the Supercontainer is considered to be the most promising Belgian reference design concept for the final disposal of heat-emitting waste designed by ONDRAF/NIRAS, the Belgian Agency for Radioactive Waste and Enriched Fissile Materials. The Supercontainer is intended for the disposal of heat-emitting vitrified High Level Waste and for the direct disposal of Spent Fuel assemblies (UOX, MOX). Depending on the type of waste that needs to be disposed off, the dimensions of the Supercontainer vary (Figure 3.1a, Table 3.1).

In this concept (Figure 3.1b, Figure 3.1c, Figure 3.1d), the vitrified waste canisters or SF assemblies will be surrounded by a carbon steel overpack, a concrete buffer and a stainless steel envelope. The Supercontainer will be constructed at surface level, before being transported underground for disposal. The waste forms first are enclosed in a carbon steel overpack of about 30 mm thick. This overpack has to prevent contact of the waste with the water coming from the host formation during the thermal phase i.e. several 100's of years for vitrified HLW, and several 1000's of years for SF.

Table 3.1: Dimensions and weight of the Supercontainer

	Vitrified HLW	UOX	MOX
Length	4.2 m	max 6.2 m	6.1 m
Outer diameter	2.0 m	2.1 m	1.6 m
Weight	30 t	max 60 t	max 31 t
Canisters or SF assemblies	2	4	1

For corrosion protection purposes, the overpack is enveloped by a high pH concrete buffer (high alkaline concrete) based on Ordinary Portland Cement (OPC). A protective oxidizing layer is formed on the metal surfaces of the overpack due to the reaction with the highly alkaline pore water. This passivating layer is believed to be either ferrous hydroxide or a lime-rich iron oxide complex. It protects the metal against corrosion, even in the presence of oxygen, but it is only stable for pH values in excess

of 9 [De Belie, 2007]. The concrete buffer passivates the outer surface of the overpack. This buffer, with a thickness of about 70 cm, also performs as a well-defined radiological protection buffer for the workers, simplifying underground waste transportation operations. It can easily be cast in the desired cylindrical form. Concrete is a well studied matter with a broadly ranged experience field. The thickness of the Supercontainer is determined by radiological protection aspects related to the tolerable dose limits (Chapter 2). The buffer is surrounded by a stainless steel cylindrical envelope. The concrete buffer is used to provide the confinement.

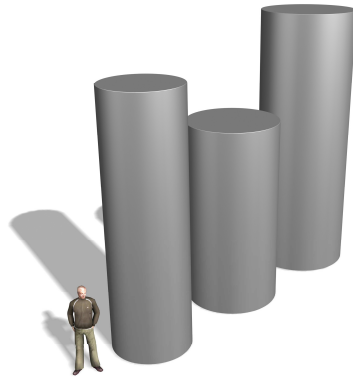


Figure 3.1a: 3D view of the Supercontainer for the disposal of UOX (right), vitrified HLW (middle) and MOX (left) [source: ONDRAF/NIRAS]

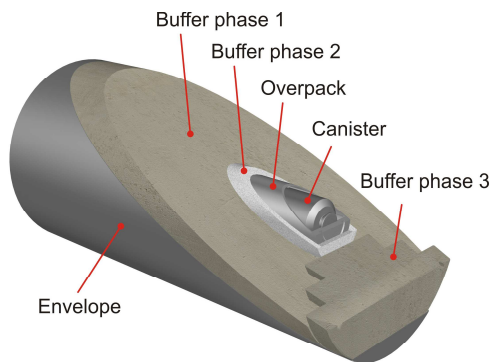


Figure 3.1b: 3D view of the Supercontainer for vitrified HLW [source: ONDRAF/NIRAS]

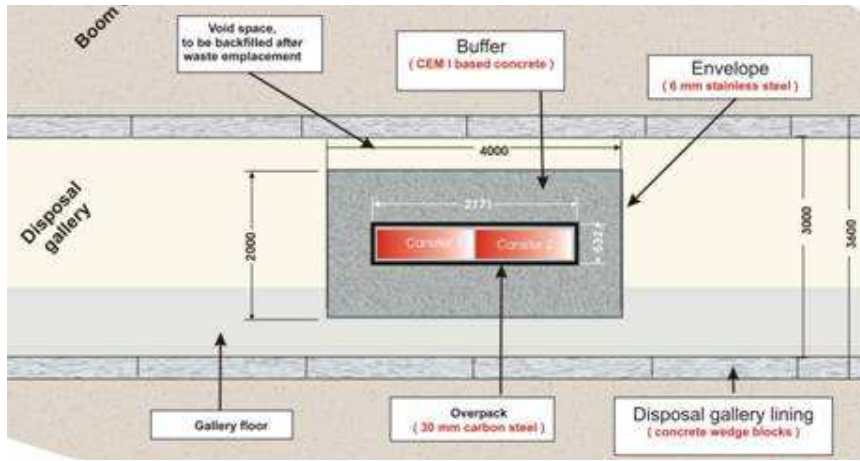


Figure 3.1c: Side view of the disposal gallery for vitrified HLW [source: ONDRAF/NIRAS]

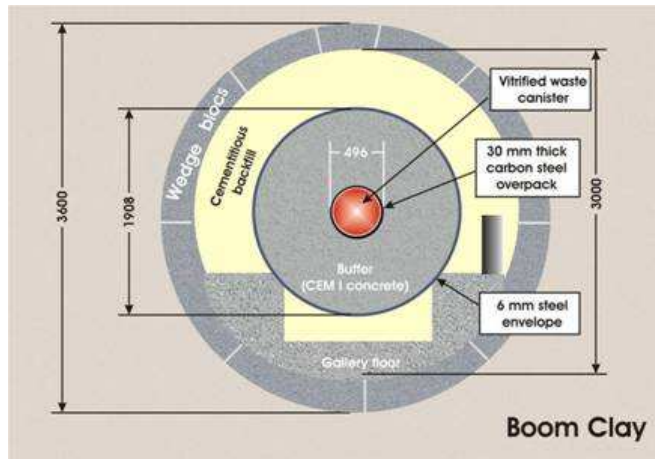


Figure 3.1d: Cross-section of the disposal gallery for vitrified HLW [source: ONDRAF/NIRAS]

Once the primary waste is post-conditioned, the Supercontainer will be transported and disposed in the underground disposal galleries (Figure 3.2) and the remaining annular gap will be backfilled. The disposal galleries should have sufficient strength in order to avoid a collapse. The geological clay layers have a beneficial behaviour and retention capacity towards radionuclides migration (the overpack must confine the radionuclides at least during the thermal phase). Because clay is the main barrier against radionuclide migration, the materials of the Supercontainer should not induce large perturbation towards the retention capacity of the Host Rock.

To conclude, the two main objectives of the Supercontainer are given:

- Provide confinement of the radionuclides during the thermal phase (long-term safety function).
- Provide radiological shielding (nuclear operational safety function). The thickness of the Supercontainer (approximately 70 cm) is determined by dose rate calculations.

2.2 Design functions

In the Supercontainer concept, the vitrified HLW canisters, or the SF assemblies will be surrounded by (i) the carbon steel overpack, (ii) the concrete buffer and (iii) the stainless steel envelope (Figure 3.1c). The main functions of the three Supercontainer components will be discussed. The Supercontainer is constructed at ground level before being transported underground for disposal (Figure 3.2) [Galson Sciences Report, 2005].

2.2.1 *The overpack*

The overpack, manufactured from 30 mm thick carbon steel, will surround the vitrified HLW canisters or SF assemblies and provides the main barrier against radionuclide release during the thermal phase. Carbon steel is chosen over a low-alloy steel because of its better resistance to sulphide attack and because of its more predictable behaviour. A thickness of 16 mm for the overpack is calculated to resist to the mechanical and thermal stresses. An additional thickness (14 mm) is foreseen for corrosion purposes.

The overpack will be inserted into the center of the concrete buffer. Good quality concrete surrounding the overpack is particularly favourable for controlling and limiting corrosion because it will lead to passivation of the steel. Under all redox states, the corrosion rate is expected to be sufficiently low, less than 2.5 μm per year. Consequently there is a sufficient certainty level that the overpack will not fail during the thermal period (Chapter 4).

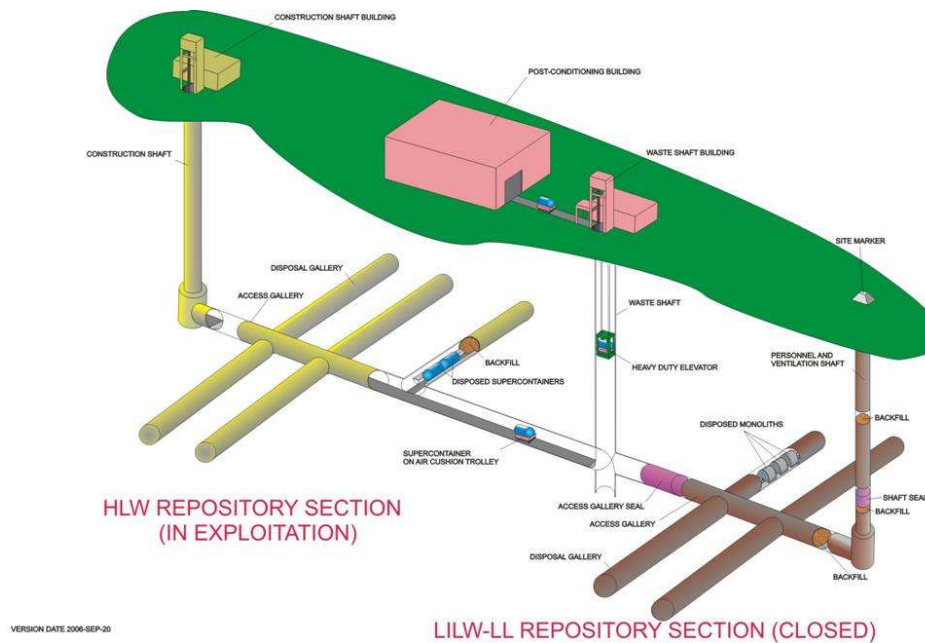


Figure 3.2: Artistic view of the HLW & ILW repository (Belgian reference concept)
[source: ONDRAF/NIRAS]

2.2.2 The buffer

2.2.2.1 Introduction

There are three layers of cementitious components inside the concrete buffer: (i) Phase 1 concrete buffer, (ii) Phase 2 filler, and (iii) Phase 3 concrete end-piece and lid (Figure 3.1b). The discussion of each of the mentioned layers is given below. Before discussing the different concrete phases, a general remark is given. To create favourable conditions from a corrosive point of view, the saturation of the buffer should take place as quickly as possible. Under saturated conditions, transport of any oxidizing and/or aggressive species will be diffusion controlled. In case of a fully saturated buffer, reached by a curing and storage under water, the presence of the envelope has no detrimental influence on the chemical environment around the overpack. Once the liner is perforated, the transport of species through the buffer is controlled by diffusion. If the buffer is not completely saturated, the presence of the envelope will retard the transport of aggressive species but once perforated, those species could very soon reach the overpack due to capillary suction.

2.2.2.2 Phase 1 concrete buffer

A concrete buffer (Phase 1) will be fabricated within the envelope. The two reference compositions that are considered for the buffer will be defined and tested experimentally, respectively in Chapter 5 and Chapter 6: a Self-Compacting Concrete

(SCC) and a Traditional Vibrated Concrete (TVC). The concrete composition includes a Portland cement CEM I that has not been interground with materials other than gypsum, contains no slag and has an SO₃ content preferably not exceeding 2 %. Coarse and fine limestone aggregates are specified and contain not more than 2 % of magnesium, silicium and aluminium (as oxides) (Chapter 5).

The concrete buffer has two major functions:

- To create a favourable alkaline environment with high pH around the carbon steel overpack, during the thermal phase of the Supercontainer (Chapter 1, HEATING 1 and HEATING 2). The highly alkaline concrete passivates the carbon steel of the overpack and reduces the corrosion rate [Crawford et al., 2004]. Also a sufficiently low hydraulic conductivity to retard the migration of aggressive species originating from the clayey Host Rock is desired.
- To provide radiological protection during the transportation of the Supercontainer to the underground disposal galleries. The dose rates at the outer surface of the Supercontainer must be as low as reasonable achievable (ALARA, Chapter 2). Possibly, the containers must be handled without using shielding equipment. This will simplify underground operations.

2.2.2.3 Phase 2 filler

Once the Phase 1 concrete buffer is cast into the stainless steel envelope and hardened sufficiently, the vitrified HLW canister or the SF assemblies in its overpack will be inserted into the created opening. The remaining annular gap between the Phase 1 buffer and the overpack will be filled by means of the Phase 2 filler. The inner cylindrical cavity must be large enough to permit insertion of the overpack (the largest aggregates used in the concrete can have a diameter up to 20 mm). The principal function of the filler is to fill the void space at the overpack surface, thereby ensuring a good contact between the overpack, the buffer and the filler itself. This is to contribute to the minimisation of the overpack's local corrosion and to allow heat transfer deriving from the overpack.

Three types of Phase 2 filler materials have been proposed. They are preferably compatible with the proposed composition of the Phase 1 concrete buffer, they should provide a high pH environment, minimise overpack corrosion and they should have beneficial behaviour towards emplacement in the annular gap. The three considered materials are:

- A fluid mortar (grout).
- A concrete mixture, preferably with a composition derived from the previously mentioned SCC composition (Chapter 5). Also the use of expansive additives is being considered to improve the contact between the buffer, the overpack and the filler [Areias, 2009].
- A powder (e.g. portlandite powder).

Advantages regarding the corrosion aspects state that the use of a cementitious grout or a concrete is more appropriate because they should guarantee a better quality (stronger

bond strength, lower porosity, higher homogeneity) of the interface with the steel than a powder. It is also more likely for a grout or a concrete to have a more uniform and constant thermal conductivity in comparison to a powder, in a way that preferential pathways for heat transfer are avoided.

Considering the placement under hot cell conditions, grout or SCC seems to be the most appropriate material, because it does not need the use of external and additional vibration energy. The use of powder will produce a considerably larger amount of dust compared with grout or SCC. Also the emplacement itself will be easier with a fluid mortar or concrete than with a powder. On the other hand, the (hardening) behaviour of fresh grout or fresh concrete in contact with the hot surface of the overpack is still unknown and further research needs to be provided in the nearby future to overcome this potential disadvantage.

A concrete mixture based on the SCC composition is chemically more compatible with the buffer composition of the Phase 1 concrete and also provides a higher pH environment, which minimises overpack corrosion in a larger extent, compared to the cementitious grout. The grout even can induce additional danger for the expansive Alkali Aggregate Reaction (AAR), in case siliceous sand is used in the mix. Even a portlandite powder would create a better chemical environment. The proposed wet mixtures could be replaced by dry powders: dry emplacement does not have the adverse property of introducing additional complexity relating to the behaviour of the water near the hot overpack. Also the use of plasticizers to facilitate the pouring of the wet mixtures is not needed. Finally, a dry powder can be preferential because of its ability to penetrate into small cracks and its elimination of macroscopic void spaces at the overpack surface. Table 3.2 summarizes the advantages and the disadvantages of the use of the three proposed Phase 2 filler materials. Nevertheless, additional research is needed and is ongoing to investigate the compactation methods, the emplacement methods and the quality control.

Table 3.2: Advantages and disadvantages of the use of wet mortar, wet concrete or dry powder for the Phase 2 filler

	Grout	Concrete	Powder
Compatibility with buffer	+	++	-
Compatibility with Host Rock	+	+	++
Corrosion protection	+	++	++
Emplacement	++	++	+
Behaviour near hot surface	-	-	++

2.2.2.4 Phase 3 concrete end-piece and lid

The main functions of the Phase 3 concrete are the same as for the Phase 1 concrete. Therefore it is preferable that it has the same concrete composition as the Phase 1 concrete buffer. The end-piece and the lid must prevent the rapid passage of external fluids to the surface of the overpack. Therefore, a good bond between the Phase 1 and Phase 3 materials is desirable.

Problems might occur with casting of fresh concrete in hot cell. Out of the limited experience level (nuclear sector, oil industry) available concerning the casting of concrete under elevated temperatures, the same conclusions can be drawn: it is a very complex process with a considerable amount of fabrication problems occurring and with the undesirable demand of organic plasticizers that can occur. More information on this topic can be found in Chapter 4.

The comparison between a precast lid and a freshly cast lid must be made from the 'contact' point of view. Freshly cast concrete to close the Supercontainer is slightly preferred (better contact between the Phase 1 and Phase 2 concrete, but a complex process of casting in hot cell appears). The water in the poured Phase 3 concrete is heated by the heat-emitted radioactive waste, causing migration to the Phase 1 concrete and the Phase 2 filler by means of the capillary forces and the thermal gradient. The principal advantage of a precast Phase 3 lid is that the need to cast concrete close to the hot overpack would be eliminated. The precast solution on the other hand, can only assure a good contact by means of a stepped configuration (Figure 3.3a). This could potentially create preferential transport pathways for aggressive species originating from the Host Rock. There remains an uncertainty concerning the quality of the bond between the Phase 1 concrete and the Phase 3 concrete. The mechanism for the closure of the Supercontainer has not been finalised, but various possible mechanisms are being examined [Villers, 2008].

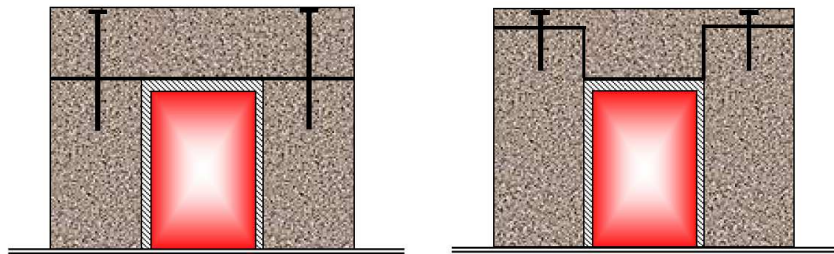
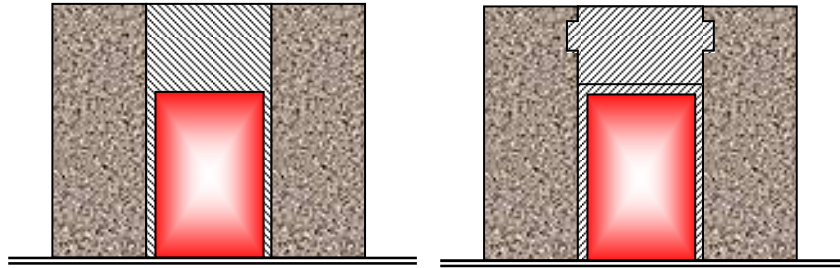


Figure 3.3a: The precast lid as Phase 3 concrete
[source: Tractebel Engineering]

The precast lid as the solution has the benefit of a simple placement by bolting and a good quality control. The disadvantage of casting fresh concrete on a hot overpack is not applicable. Corrosion of the bolts and the higher permeability in the contact zone can be seen as a possible disadvantage (Figure 3.3a).

Freshly cast concrete on top of the overpack provides a better contact buffer/plug and an improved tightness. There is no need for additional metallic objects that can be seen as a source of corrosion. Disadvantages of the freshly cast lid are: fresh concrete can experience early-age cracking behaviour risk due to shrinkage and hydration heat and there is a minimal level of experience concerning the pouring of fresh concrete on a heat source and in hot cell (Figure 3.3b). The need of vibration and other operations inside hot cell environment is complicated, but can be prevented by using self-compacting compositions.



*Figure 3.3b: The freshly cast lid as Phase 3 concrete
[source: Tractebel Engineering]*

The combining solutions provide a better contact with the Phase 1 concrete buffer in comparison with the precast lid. A concrete precast piece will play the role of thermal isolator, limiting the temperature when pouring the final plug. The disadvantage of pouring on a heat source is counteracted by using a smaller lid on top of the hot overpack. The use of additional bolts is not needed (Figure 3.3c). This extra lid also provides radiological protection (shielding) in case of transfer of the Supercontainer outside the hot cell. This option seems to be very promising and needs to be further evaluated.

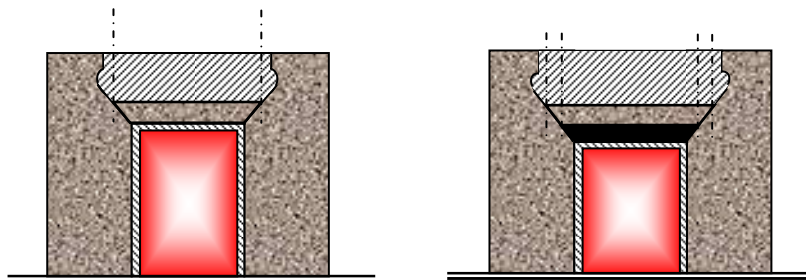


*Figure 3.3c: The mixed solution lid as Phase 3 concrete
[source: Tractebel Engineering]*

A good contact between the Phase 3 concrete and the steel envelope is also essential. Even the welding of the steel liner lid can be a source of additional concrete damage.

The use of bolts or screwing a top plate on top of the envelope can be seen as a valuable solution for this problem with the already mentioned disadvantage of possible corrosion.

2.2.2.5 Main roles of the buffer

Conclusions concerning the feasibility to construct the Supercontainer are given by means of the main roles and constraints of the buffer:

- Long-term safety: create a favourable environment to optimize the lifetime of overpack (corrosion). The integrity of the overpack must be guaranteed during the thermal phase.
- Operational safety: provide permanent shielding for workers during the handling of the waste packages.
- Provide efficient heat dissipation.
- Provide sufficient mechanical strength (handling, gallery support, accidental fall, retrievability).
- Limit chemical disturbances with the clayey Host Rock.

Therefore an Ordinary Portland Cement (OPC) with high pH, and carbonate aggregates to eliminate AAR, are chosen. Also the selection and the limitation of superplasticizers is being discussed in Chapter 5. The feasibility program has to take into account the specific safety related constraints when developing the concrete buffer composition, the preparation and the emplacement methods [Van Humbeeck, 2009].

2.2.3 The envelope

The outermost part of the Supercontainer is a cylinder made from a stainless steel sheet with a thickness of about 6 mm with a solid welded bottom and a lid that fits on the concrete buffer at the end of the fabrication process. Currently, the stainless steel envelope is considered in the reference design. The advantages of the envelope are (i) to serve as a mould to allow the casting of the concrete buffer, thus no additional chemical agent is needed for demoulding, and (ii) to provide sufficient mechanical strength and confinement during transportation and handling (= must have). Moreover it presents the advantages to facilitate reversibility and to prevent water ingress from the Host Rock (= nice to have) [Crawford et al., 2004]. For long-term radiological safety, the envelope is not taken into account for calculations due to the most probable risk of local corrosion processes such as pitting.

Whether the use of the outer stainless steel envelope is desired or whether or not the use of vents is appropriate, is still under consideration. Vents would reduce the risk of internal gas pressurisation, but would allow the ingress of water from the surroundings. The explanation can be found in the degradation mechanisms discussed in Chapter 4. There will be a considerable amount of gas production inside the concrete buffer due to corrosion (highest share), due to radiolysis of the pore water under irradiation, due to water vapour creation caused by the heat of the HLW and the SF and due to microbial activity. If a closed design is chosen, with the outer envelope surrounding the concrete buffer, an internal pressure build-up due to the above mentioned gas producing

mechanisms is expected and a risk for internal crack formation occurs if the tensile strength of the concrete buffer is exceeded. In this case, an open design (without the outer stainless steel envelope) can be desired, where the produced gasses can escape and the risen internal pressure build-up remains acceptable. Downside in case of an open design however, is the inflow of groundwater originating from the geological clay layers.

Regarding the protection of the overpack, a stainless steel envelope contributes as an additional barrier against the transport of aggressive species towards the overpack. On the other side, once the envelope (in case of a closed system) is perforated, aggressive species from outside the Supercontainer begin to migrate through the concrete buffer towards the overpack surface. This can initiate corrosion. The large uncertainties related to the lifetime of the envelope and the pitting corrosion process evolution do not allow to take into account the potential contribution of the envelope in the safety assessments.

On the level of the mechanical support of the Supercontainer inside the disposal gallery (Figure 3.1c), stress corrosion cracking of the envelope can originate. Also there is a risk of crevice corrosion and pitting corrosion if the ingress of the groundwater reaches the envelope and it contains a considerable high amount of aggressive chlorides, bicarbonates, sulphates and sulphides, but still lower compared to the case of a Supercontainer without the confining envelope.

From a technological point of view, advantages and disadvantages of the use of the envelope are identified. Advantages: (i) the envelope can be used as a lost formwork excluding the need of additional chemical demoulding agents. (ii) In case of fall of the Supercontainer in horizontal position during transportation, the envelope can ensure a coherence between the concrete pieces. In case of transportation in vertical position in the shaft of the disposal gallery, the envelope will not insure guarantee for the buffer integrity. The envelope also has beneficial effects towards the decontamination aspects of aggressive species originating from the Host Rock.

Disadvantages: (i) in case of a fall of the Supercontainer without breaking of the envelope, it will not be possible to visualise the general damage and the presence of cracking in the concrete buffer. (ii) A perfect contact between the envelope and the buffer is necessary but not easy to guarantee. (iii) Placing the stainless steel closing piece will not be easy and welding of the lid of the envelope could negatively influence the vicinity of the concrete buffer. Caution is wanted during the welding of the liner during construction and during closure to prevent early-age concrete cracking and to avoid corrosion. (iv) The use of an envelope will also increase significantly the unit price of a Supercontainer.

The decision about the removal of the stainless steel envelope in the Supercontainer reference design is still to be verified. The presence of an envelope for the Supercontainer is considered as the reference design for our studies.

2.3 The Host Rock formation

Scientific programs give increasing confidence in clay as a natural barrier. Clay is a suitable Host Rock for the Belgian reference disposal concept for its diverse variety of properties:

- It is present as a thick, homogenous layer over a large area.
- It is a stable geological layer at a suitable depth.
- It is plastic and thus has a strong capacity and ability for self-sealing following physical disturbances (for example after the excavation of gallery shafts). The creation of an excavation disturbed or damaged zone (EDZ) is expected for all geological formations showing macrofracturing, microfracturing and rearrangement of rock structures resulting in significant increase of permeability to flow. Experimental data show a clear tendency for self-sealing processes in disturbed Boom Clay layers [SELFRACT Final Report, 2007].
- It has a very low permeability so that the groundwater in the clay is practically immobile and all transport is limited to a slow diffusion process and not an advective transport were particles, such as radionuclides, are displaced due to a ground water flow.
- It has favourable geochemical characteristics and a strong capacity to retain most of the long-lived radionuclides, leading to a very low mobility of these radionuclides.
- It does not contain preferential pathways for fast radionuclide migration.

The underground laboratory HADES (High Activity Disposal Experimental Site) is the pre-eminent instrument available for research into the potential for disposing of highly radioactive and long-lived waste in deep clay layers. In the heart of the clay foundation in Boom, numerous experiments are being carried out 225 meters below ground level over an area of 200 meters (Figure 3.4). HADES is an underground scientific and technological research facility that investigates the feasibility of constructing, operating and sealing a waste repository in a deep clay layer. The research activities aim at gaining proper understanding of the processes that are important in evaluating the safety and feasibility of deep disposal on a representative scale in time and space. It must be clear that no radioactive waste is or will ever be disposed of at HADES and that 25 years of research and experience is gained. Valuable information can be derived from this underground facility. The practicability of the step-by-step process of the construction and excavation of the shafts and galleries supplies a wide range of information, confidence and experience. It confirms that it is technologically and economically feasible to construct shafts and galleries in the Boom Clay in a reasonable time and that disturbances within the host clay formation are limited.

Vitrified HLW and SF assemblies generate heat over a long period of time (hundreds to thousands of years). The effect of this heat on the Boom Clay is being studied via the PRACLAY Heater Experiment. The combined thermal and excavation induced disturbances of the Boom Clay are the main focus of the experiment, essential to determine the extent to which these temporary or permanent changes could affect the

containment and isolation capacity of the potential Host Rock. These tests will start in 2010 and are planned to last for ten years.

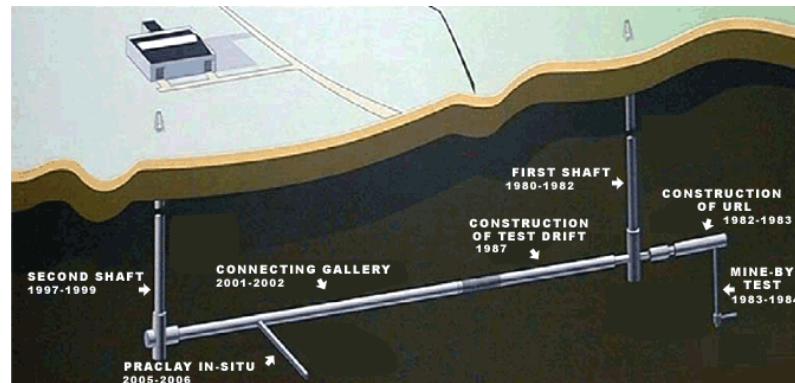


Figure 3.4: Step-by-step progress of the HADES project [source: website ESV EURIDICE]

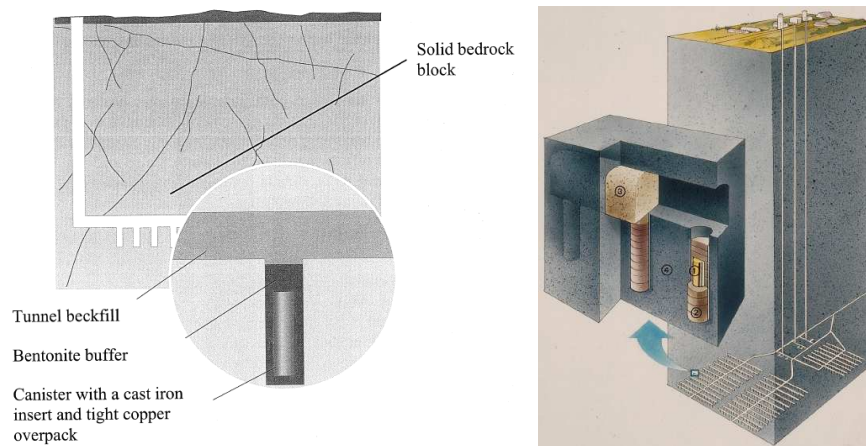


Figure 3.5: Example of hard rock as Host Rock: the Finnish reference concept (left) [Tanskanen, 2007] and the Swedish reference concept (right) [Pedersen, 1999]

3 International policy on geological disposal

For HLW and long-lived radioactive waste, the international consensus is that deep disposal is the best option currently available or likely to be available in the foreseeable future. There are mainly 3 types of Host Rock formations allowing deep disposal of HLW and SF assemblies. The rock formations mostly studied for deep disposal depend on the availability of these formations in the country and are listed below:

- Sediments: clays, marls, volcanic sediments, shales.
- Hard crystalline rocks: granite, gneiss, tuffs, metamorphic basement.
- Evaporites: salt domes, bedded salts, anhydrites.

These rock formations have different advantages and constraints but it seems difficult to claim that one is better than the other (Table 3.3). There is no unique solution. The Host Rock preferably must provide a stable deep environment: low groundwater flow rates and volumes around the EBS, stable hydrochemistry for the EBS, stable stress regime, not susceptible to tectonic events (seismic, volcanic), well buffered from dynamic surface processes caused by changed climate, etc. The overall aim is to find environments where conditions at depth evolve slowly, allowing the EBS to act and evolve as envisaged. Different environments have been considered by different countries (Table 3.4). Preference goes to simple structures with a low geological complexity.

To conclude this chapter, some examples of the international policy on the disposal of radioactive waste are given. The Finnish reference design concept is based on hard crystalline rock (granite) as the Host Rock on the island Olkiluoto, and will be operational in 2020. The SF is placed in a copper canister and is surrounded by a bentonite buffer. Bentonite is a smectite-rich clay that easily absorbs water and swells. It is a very impermeable material and retards the radionuclides via ion-exchange and surface adsorption. It is also permeable to gas. After completion, the EBS is transported and placed inside the disposal galleries (500 m depth). The remaining gap is backfilled with a sandy bentonite mixture (Figure 3.5). In comparison with the Belgian reference concept, a considerably smaller amount of concrete is being used: during the excavation of the underground galleries, the faces are covered with a concrete (shotcrete) to insure sufficient mechanical strength to prevent collapse. Just before the backfill is placed, the shotcrete is removed. Possible crack formation in the EDZ is being filled with a cementitious grout to reduce the possible groundwater ingress. Partial inflow of groundwater is desired to induce swelling of the bentonite backfill and to assure a good contact and seal between the EBS and the crystalline Host Rock [Tanskanen, 2007]. The Swedish repository has a similar design as the Finnish reference concept. The galleries located in Forsmark, in stable hard rock, are about 500 meters below ground surface and will be operational in 2024. The copper canisters are placed inside the vertical shafts of the gallery, backfilled with bentonite blocks and afterwards, the galleries are also backfilled with bentonite (Figure 3.5). The bentonite prevents groundwater flow around the canisters and contains the radionuclides in case of failure of the canisters. The Host Rock itself provides a durable mechanical and chemical environment [Pedersen, 1999].

Table 3.3: Requirements and Host Rock performances [Chapman, 2008]

	Hard Rocks (e.g. granite)	Sediments (e.g. clay)	Evaporites (e.g. salt)
Heat conduction	good	variable	extremely good
Hydraulic conductivity	good	very good	extremely good
Stable near-field hydrochemistry	variable	very good	extremely good
Low-flux geological environment	variable	extremely good	extremely good
Intrusion potential	good	variable	poor
Construction flexibility	extremely good	variable	good
Gas dispersability	extremely good	variable to poor	low relevance

Table 3.4: Considered environments for radioactive waste disposal [Chapman, 2008]

Host Rock	Countries
Crystalline basement	Sweden, Finland, Canada
Non-basement crystalline rock	Spain, UK, Korea, Japan
Agrillaceous sediments	Belgium, Switzerland, France, Spain, Germany, Italy
Salt domes	Germany, USA, Denmark, Netherlands
Tuffs and volcanic sediments	Japan, USA
Basalts	USA
Below small islands	UK
Very deep boreholes	USA, Sweden, Switzerland, UK
Under sea bed	UK, Japan

The Swiss reference design sees the use of Opalinus Clay as a suitable Host Rock. The buffer around the HLW consist of a bentonite material clearly compatible with the Host Rock. For LL-ILW (long-lived), the waste is emplaced inside a concrete matrix [Palmu, 2008].

The reference repository design in USA (Yucca Mountain, Nevada) intends to dispose SF and HLW in tuff and volcanic sediments, 300 meters below ground surface and 300 meters above the groundwater table via a horizontal emplacement in open drift (currently no backfill). The high heat load leads to initial drying of the tuff, delaying onset of corrosion and preventing aqueous releases of radionuclides. Available groundwater flows around the drifts and an additional drip shield above the waste package (surrounding the waste package itself), is provided to prevent water from contact with the waste (Figure 3.6) [Apted, 2008]. First, the canisters of waste, sealed in special casks, are shipped to the site by truck or train. The shipping casks are removed, and the inner tube with the waste is placed in a steel, multilayered storage container. An automated system sends storage containers underground to the tunnels. Finally, containers are stored along the tunnels, on their side (Figure 3.6). The Yucca Mountain site has already been studied since 1987, and the controversial permit for exploitation is submitted in 2008.

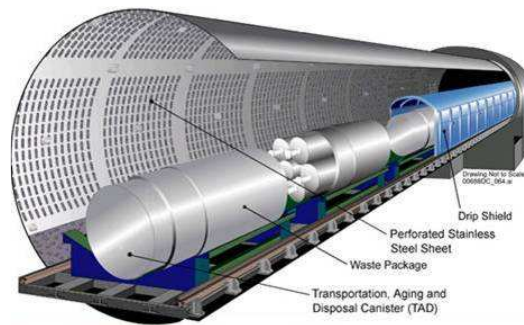


Figure 3.6: Example of volcanic sediments as Host Rock: USA reference design at Yucca Mountain [Apted, 2008]

In Germany, it is planned to dispose of radioactive waste in a repository in deep geological formations several hundred meters below the surface in salt mines. This mineral layers posses particularly good isolating properties for radioactive, heat-generating wastes. The investigations of repository sites in Germany thus concentrate chiefly on rock salt formations as a Host Rock (for example in the Morsleben repository or Project Gorleben). The concrete, considered for the backfilling and sealing of the repository contains crushed salt instead of natural aggregates, as the material should be as similar as possible to the salt rock (compatibility). The filling of the opening with salt concrete, mixed in a plant above ground and pumped underground, corresponds to massive concrete structures with high requirements regarding low heat of hydration and little or no cracking potential [Gutsch et al., 2009].

References

Apted M. (2008), *Design Concepts for Repositories and Underground Storage*, Geological Disposal of High-Level Waste, ITC School International Course, Las Vegas, USA.

Areias L. (2009), *Supercontainer research and experimental program: Reduced Scale Tests on filler component with Type 1 cells*, LA-SC/rs/09, SCK-CEN.

Bel J., Van Cotthem A., De Bock C. (2005), *Construction, operation and closure of the Belgian repository for long-lived radioactive waste*, Proceedings of the 10th International Conference on Environmental Remediation and Radioactive Waste Management, ICEM05, Glasgow, Scotland, 7p.

Chapman N. (2008), *The Concept of Geological Disposal and Geological Environments investigated worldwide*, Geological Disposal of High-Level Waste, ITC School International Course, Las Vegas, USA.

De Belie N. (2007), *Durability of Concrete*, Faculty of Engineering, Ghent University.

Crawford M.B., Wickham S.M., Galson D.A. (2004), *Workshop on the Evolution of OPC Buffer and Steel Corrosion in the Belgian Supercontainer Design for HLW Disposal*, Stamford, UK.

Galson Sciences (2005), *Belgian Supercontainer Design for HLW and Spent Fuel Disposal: Evaluation of the Reference Design*, Galson Sciences Report 0460-5, Version 1, 2005.

Gutsch A.-W., Preuss J., Mauke R. (2009), *Experimental results on salt concrete and results of calculations of restraint stresses of barrier elements made of salt concrete in a repository for radioactive waste in salt mine*, Proceedings of the International workshop on the Long Term Performance of Cementitious Barriers and Reinforced Concrete in Nuclear Power Plants and Waste Management, NUCPERF09, Cadarache, France.

International Atomic Energy Agency (1994), *Classification of Radioactive Waste: a Safety Guide*, IAEA Safety Series No. 111-G-1.1, Vienna, Austria.

ONDRAF/NIRAS (2004), *A review of corrosion and material selection issues pertinent to underground disposal of highly active nuclear waste in Belgium*, report 2004-02.

Palmu M. (2008), *International HLW examples*, Cement and Cementitious Materials in the geological disposal of radioactive waste, ITC School International Course, Eurojoki, Finland.

Pedersen K. (1999), *Subterranean microorganisms and radioactive waste disposal in Sweden*, Engineering Geology 52, 163-176.

Rahman A. (2008), *Decommissioning and Radioactive Waste Management*, Whittles Publishing, Scotland, UK.

SELFRAC Final Report (2007), *Fractures and self-healing within the excavation disturbed zone in clays*, ESV Euridice GIE.

Tanskanen J. (2007), *Posiva Facility Description 2006*, Working Report 2007-21.

Van Humbeeck H. (2009), *Feasibility related aspects of cementitious materials for final disposal of radioactive waste*, 13th Exchange Meeting ESV Euridice GIE, The role of cementitious materials for deep disposal of high-level waste in Boom Clay, Mol, Belgium.

Villers L. (2008), *Supercontainers: components-choice and tests*, ONDRAF/NIRAS meeting 190308.

CHAPTER 4:

PARAMETERS AFFECTING THE BUFFER

During fabrication of the Supercontainer, the three concrete layers (buffer, filler, lid) come into contact with the heat-emitting overpack containing highly active waste. Therefore it seems interesting to take a look at the effect of temperature and radiation on the most relevant thermo-mechanical properties of the concrete considered for this research study. Afterwards, when finished, the Supercontainer will be transported into the disposal galleries of the Host Rock. Other effects, such as corrosion processes, microbial activity and concrete degradation, then will play a significant role in the durability of the Supercontainer. An overview of these processes seems interesting to be aware of the parameters that affect the Supercontainer, however further analysis lies out of the scope of this early-age study. For this research study, only the short-term effect of elevated temperature and gamma radiation on the concrete buffer, will be evaluated and considered in the following paragraphs.

1 Temperature effects

1.1 Fundamentals of heat transfer

There are three models of energy (heat) transfer: conduction, convection and radiation. All heat transfer processes involve one or more of these discussed models [Welty et al., 2000].

1.1.1 Conduction

Energy transfer by conduction is accomplished in two ways:

- Molecular interaction: the greater motion of a molecule at a higher energy level (temperature) imparts energy to adjacent molecules at lower energy levels. This type of interaction occurs in all systems in which a temperature gradient exists and in which molecules of a solid, liquid or gas are present.
- The second mechanism of conductive heat transfer is by means of free electrons: this is primarily significant in pure metallic solids. The concentrations of free electrons varies considerably for alloys and becomes

very low for non-metallic solids. Pure metals are the best heat conductors as they possess a high concentration of free electrons.

The general equation describing the molecular heat conduction phenomenon is stated by Fourier's first law in the form (4.1) and expresses the heat flux as proportional to the temperature gradient, with the thermal conductivity k as the proportionality constant. The negative sign in equation (4.1) indicates that heat flow is in the direction of a negative temperature gradient, going from a high energy level to a lower energy level. The thermal conductivity k is assumed to be primarily a function of temperature and is independent of the direction, thus equation (4.1) applies for an isotropic medium. Common values of k are given in Table 4.1. The thermal conductivity measures the capacity of a material to conduct heat.

$$\frac{q_{x,y,z}}{A} = -k \cdot \nabla T \quad (4.1)$$

where: $q_{x,y,z}$ = the heat transfer rate in the x-y-z direction (W)
 A = the area normal to the direction of the heat flow (m^2)
 k = the thermal conductivity ($W/(m \cdot ^\circ C)$)
 ∇T = the temperature gradient ($^\circ C/m$)

The thermal conductivity of concrete is affected by several factors of which the proportions of the concrete components, the mineralogical composition of the aggregates and the saturation degree are the most important ones [Kaplan, 1986]:

- The cement paste has lower thermal conductivity than the majority of aggregates. At ambient temperatures, an OPC based paste has a thermal conductivity of about $1.1 \text{ W}/(m \cdot ^\circ C)$ to $1.6 \text{ W}/(m \cdot ^\circ C)$. Therefore, if the amount of aggregates inside the concrete increases, the k -value increases.
- The mineralogical nature of the aggregates strongly affect the thermal conductivity of the concrete. For calcareous granules, the thermal conductivity is about $2.3 \text{ W}/(m \cdot ^\circ C)$ to $2.8 \text{ W}/(m \cdot ^\circ C)$, which is translated into a k -value between $1.9 \text{ W}/(m \cdot ^\circ C)$ to $2.8 \text{ W}/(m \cdot ^\circ C)$ for calcareous concrete.
- A saturated concrete has a greater tendency to conduct heat better than an unsaturated concrete due to the higher thermal conductivity of water in comparison to air (Table 4.1). A dry concrete has a mean k -value of $1.85 \text{ W}/(m \cdot ^\circ C)$ where a more humid concrete has a mean k -value of $2.2 \text{ W}/(m \cdot ^\circ C)$.

1.1.2 Convection

Heat transfer due to convection involves the energy exchange between a surface and an adjacent fluid. Two types of convection need to be taken into account:

- Forced convection: a fluid is made to flow past a solid surface by an external agent such as a fan or a pump.

- Free or natural convection: warmer (or cooler) fluid next to the solid boundary causes circulation because of the density difference resulting from the temperature variation throughout a region of the fluid.

The rate equation for convective heat transfer is better known as the Newton rate equation or Newton's law of cooling.

$$\frac{q}{A} = h_c \cdot \Delta T \quad (4.2)$$

where: q = the rate of convective heat transfer (W)
 A = the area normal to the direction of the heat flow (m^2)
 h_c = the convective heat transfer coefficient ($W/(m^2 \cdot ^\circ C)$)
 ΔT = the temperature difference between surface and fluid ($^\circ C$)

Equation (4.2) is not a law but a definition of the coefficient h_c . This convective heat transfer coefficient is thus a function of the geometry of the system, of the fluid and flow properties, and of the magnitude of the temperature difference. Approximate values are given in Table 4.2.

1.1.3 Radiation

Radiant heat transfer between surfaces differs from conduction and convection in a way that no medium is required for its propagation. The energy transfer by radiation is maximal when two surfaces, which are exchanging energy, are separated by a perfect vacuum. The rate of energy emission of a perfect black body is given by

$$\frac{q}{A} = \sigma \cdot T^4 \quad (4.3)$$

where: q = the rate of radiant energy (W)
 A = the area of the emitting surface (m^2)
 T = the absolute temperature ($^\circ C$)
 σ = the Stefan-Boltzmann constant ($= 5.676 \times 10^{-8} W/(m^2 \cdot ^\circ C^4)$)

Both the amount of radiation and the quality of the radiation depend on the temperature. Radiation of a hot object will be different in quality than radiation originating from a body at lower temperature. Also the colour of the objects has an influence on the radiation behaviour.

Radiation travels at the speed of light, having both wave properties and particle-like properties. The radiation between wavelengths of 0.1 and 100 microns is termed thermal radiation. The thermal band of the spectrum includes a portion of the ultraviolet and all of the infrared regions.

Table 4.1: Approximate values of the thermal conductivity [Welty et al., 2000]

Material	k W/(m·°C)		
	20 °C	100 °C	300 °C
<u>Metals</u>			
Aluminium	229	229	230
Copper	386	379	369
Iron	73	68	54
Stainless steel alloy	16	17	23
<u>Non Metals</u>			
Concrete	1.21	-	-
Glass (Pyrex)	1.09	1.16	1.45
Wood	0.3	-	-
<u>Air</u>	0.00241	0.00317	0.00450
<u>Water</u>	0.56	0.68	0.56

Table 4.2: Approximate values of the convective heat transfer coefficient [Welty et al., 2000]

Mechanism	h_c W/(m ² ·°C)
Free convection (air)	5 – 50
Forced convection (air)	25 – 250
Forced convection (water)	250 – 15 000
Boiling water	2500 – 25 000
Condensing water vapor	5000 – 100 000

1.1.4 Combined mechanisms of heat transfer

It is rare, in actual situations, that one of the three previously discussed models of heat transfer is the only mechanism involved in an energy transfer system. In most cases heat transfer is accomplished by a combination of these mechanisms.

Considering a composite wall as given in Figure 4.1, constructed of i material layers and with its surfaces held at constant temperatures. The steady state heat transfer rate per unit area between a hot gas at temperature T_1 on the left side of the wall and a cool gas at temperature T_r on the right side, can be determined by application of equations (4.1) and (4.2). Each temperature difference is expressed in terms of q_x and is given by equations (4.4a) to (4.4d).

$$T_1 - T_1 = q_x \cdot \left(\frac{1}{h_{c,l} \cdot A} \right) \quad (4.4a)$$

$$T_1 - T_2 = q_x \cdot \left(\frac{t_1}{k_1 \cdot A} \right) \quad (4.4b)$$

...

$$T_{i-1} - T_i = q_x \cdot \left(\frac{t_i}{k_i \cdot A} \right) \quad (4.4c)$$

$$T_i - T_r = q_x \cdot \left(\frac{1}{h_{c,r} \cdot A} \right) \quad (4.4d)$$

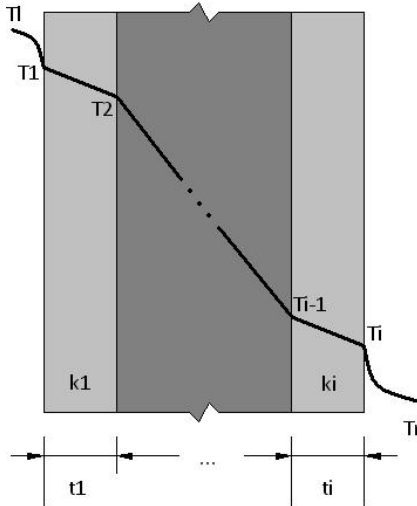


Figure 4.1: Steady-state heat transfer through a composite wall, thermal resistance due to conduction and convection

Combining equations (4.4a) to (4.4d) and solving for q_x , leads to equation (4.5).

$$q_x = \frac{T_i - T_r}{\left(\frac{1}{h_{c,l} \cdot A} + \frac{L_1}{k_1 \cdot A} + \dots + \frac{L_i}{k_i \cdot A} + \frac{1}{h_{c,r} \cdot A} \right)} = \frac{\Delta T}{\sum_i R_{thermal}} \quad (4.5)$$

This relation can be applied to steady state heat transfer systems of other geometries as well. The thermal resistance term, $R_{thermal}$, will change in form for cylindrical or spherical systems, but once determined, it can be utilized in equation (4.5). The thermal resistance of a cylindrical conductor with inner radius r_i and outer radius r_o and length L , is given as an example in equation (4.6).

$$R_{thermal} = \frac{\ln\left(\frac{r_o}{r_i}\right)}{2\pi \cdot k \cdot L} \quad (4.6)$$

1.2 Thermal analysis of the Supercontainer concept

To avoid boiling of pore water fluids within the concrete buffer, it has been suggested that the temperature of the buffer may never exceed 100 °C [Wickham et al., 2005]. The maximum temperature attained during the fabrication of the Supercontainer depends on the thermal power of the vitrified HLW or SF assemblies. Most of the time, irradiation goes along with an increase of temperature of the elements in the nearby environment of the radioactive source. Conduction and convection of heat, thermal radiation and heat originating from the absorption of gamma photons and neutrons give cause to elevated temperatures. In case of the Supercontainer concept, two temperature related problems can occur: the difference in thermal expansion of the different construction parts of the Supercontainer can lead to micro- and macrocracking of the concrete buffer [Madigan et al., 1997]. Therefore it is meaningful to carefully choose the different components of the Supercontainer and to reduce the thermal gradients inside the Supercontainer. Concrete elements with a good thermal conductivity are preferable.

Preliminary studies concerning the temperature evolution inside the Supercontainer due to heat-emitting vitrified HLW and SF indicate that the maximum temperature is already achieved a couple of years after emplacement of the canisters inside the concrete buffer (Figure 4.2) [Wickham et al., 2004]. This temperature increase depends on a cooling period of 50 to 70 years of the radioactive waste preceding the emplacement. Also the thermal conductivity of the concrete, the saturation degree of the concrete buffer and the thermal conductivity of the surrounding Host Rock affect the temperature. Finally, the choice of an appropriate concrete composition with its specific hydration heat production rate has an influence on the presented results. A sensitivity study indicates that the thermal conductivity of the buffer influences only

temperatures of the overpack and the buffer itself, while the thermal conductivity of the host formation (estimated $k_{\text{Boom Clay}} = 1.69 \text{ W/(m}\cdot\text{°C)}$ for undisturbed and saturated Boom Clay) has a large influence on the entire temperature field and the temperature rise in the concrete buffer due to the heat-emitting waste canister. This is why the thermal conductivity of the clayey Host Rock must be determined very accurately.

Taking into account the heat output from the decay of HLW and SF, it is necessary to investigate the effects of this thermal source on the EBS and the first meters of the host formation. Therefore, SCK-CEN performed 2D axisymmetrical thermal scoping calculations for the near field, in order to determine the maximum temperatures to which the overpack and buffer materials are exposed to and to determine which parameters can be changed by design choice having a considerable influence on the results [Weetjens and Sillen, 2006]. The peak temperature in the concrete buffer is attained between 5 and 10 years after waste emplacement. For vitrified HLW, the maximum temperatures at the buffer-overpack interface surface reach 111 °C, 92 °C and 77 °C for pre-cooling periods of 50, 60 and 70 years respectively after approximately 5 years. For SF, these values are slightly higher and occur later (after 10 – 12 years): 111 °C, 99 °C and 89 °C (Figure 4.3). The initial temperature in the disposal zone and the clayey Host Rock is assumed to be 15.7 °C. Also the additional temperature increase due to the heat-emitting waste in the neighboring gallery is taken into account. This effect is negligible in case of SF, where the gallery spacing is considered to be 120 meters. These temperature evolution data will be used to simulate the effect of an outer heat source on the stress development due to the thermal gradient inside the Supercontainer concrete buffer (Chapter 8).

When the annular gap between the disposal gallery and the Supercontainer is backfilled, only conduction plays a role. On the other hand, an evaluation of the heat transport in an unbackfilled annular gap around the Supercontainer revealed that the contribution of the different processes (conduction, convection and radiation) depends substantially on the emissivity value of the stainless steel envelope. However, it seems that radiation is the largest contributor to the overall heat transfer in case of an annular unbackfilled gap.

1.3 Thermal power of vitrified HLW and SF assemblies

The heat generated by vitrified HLW and SF can be estimated by using the formula derived by Put [Put et al., 1992]. It can be written as:

$$Q_{TP} = \sum_i A_i \cdot e^{-\lambda_i \cdot t} \quad (4.7)$$

where: Q_{TP} = the thermal output (W/tHM, Watts per ton of Heavy Metal equivalent)
 A_i, λ_i = coefficients described in [Put et al., 1992]

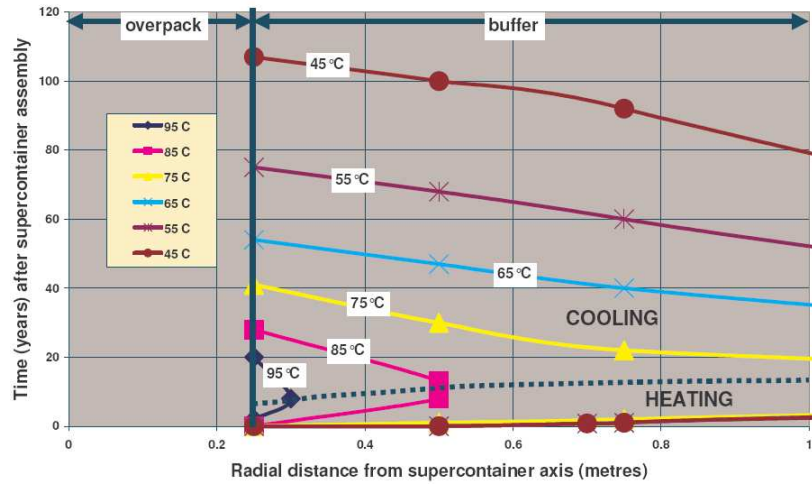


Figure 4.2: Thermal evolution inside the Supercontainer for vitrified HLW. OPC based concrete (with limestone aggregate) is chosen for the buffer, diameter is 2028 mm, k equals $1.7 \text{ W}/(\text{m}\cdot^\circ\text{C})$ and a cooling period of 50 years is being considered [Wickham et al., 2004]

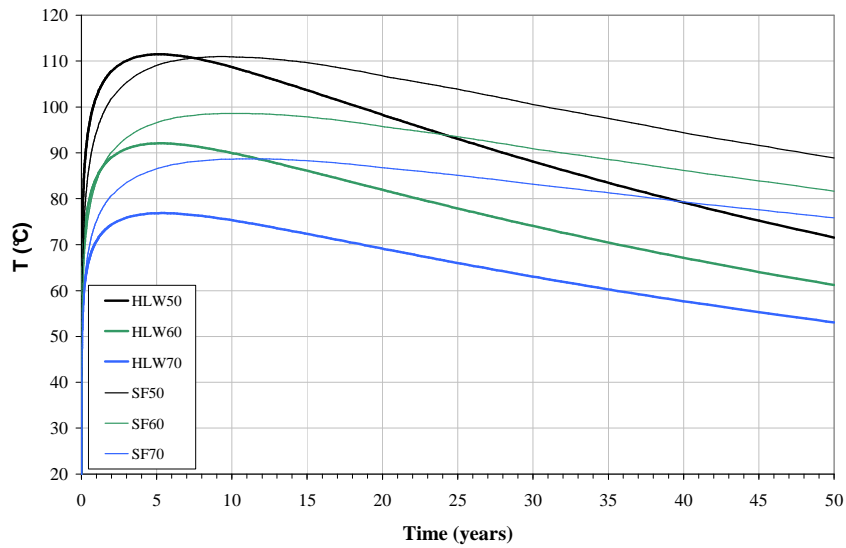


Figure 4.3: Temperature evolution at the buffer-overpack interface for vitrified HLW and SF assemblies after cooling periods of 50 – 60 – 70 years [Weetjens and Sillen, 2006]

The variation of the power output of the waste with time is given in Figure 4.4 and Figure 4.5.

Put's formula for HLW is in good agreement with calculations made using the ORIGEN code and independent data from NAGRA and JNC (Figure 4.4). Each canister contains approximately 1.333 tons of heavy metals and there are two canisters in one Supercontainer totalizing a length of roughly 2.8 meters. Taking into account a pre-cooling period of 50 years, the heat emission of the HLW canisters can be determined and converted into (W/m): 360 W/m. Pre-cooling periods of 60 and 70 years will lead to a thermal output of respectively 285 W/m and 240 W/m.

In the scoping calculations according to [Weetjens and Sillen, 2006] only the spent fuel type UNE with a burn-up of 55 GWd/tHM is considered, because this type of fuel has the largest heat output per assembly. UNE55 fuel originates from the Doel3 and Tihange2 nuclear power reactors. A higher thermal output over an extended period of time is noticed for SF (Figure 4.5).

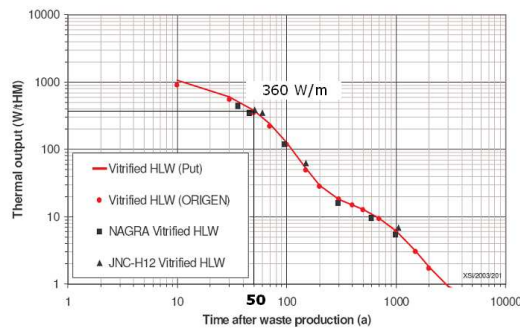


Figure 4.4: Thermal power output of vitrified HLW [Put et al., 1992]

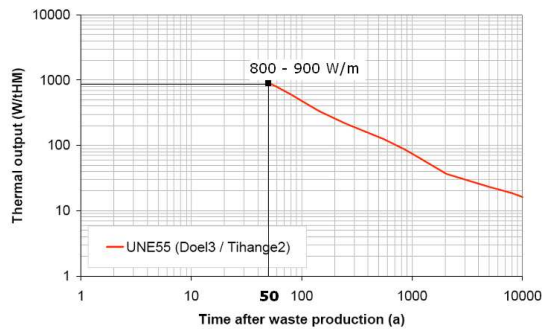


Figure 4.5: Thermal power output of UNE55 SF [Weetjens and Sillen, 2006]

1.4 Effect of temperature on mechanical properties

Usually, concrete can resist temperatures in the environment of 200 °C to 300 °C. A decomposition of the main components of the concrete matrix, such as CSH and portlandite $\text{Ca}(\text{OH})_2$ can occur though and lead to a deterioration of the concrete properties. The effect of high temperatures on the mechanical properties depends strongly on the nature of the aggregates, the cement type, the W/C ratio, the conservation conditions (humidity) and the duration of exposure. The heating rate, the temperature peak, the phase transformation (gas-liquid-vapor) and the incompatibility between aggregates and cement influences the concrete behaviour at elevated temperatures [Piasta et al., 1984, Chang et al., 1999]. Therefore it is quite hard to generalize the observations and to make a global conclusion. A summary is given below.

Eurocode 2 (NBN EN 1992-1-2) defines a formula to calculate the reduction of the characteristic compressive resistance of concrete in function of the temperature and in case of a fire.

$$f_{ck}(T) = k_c(T) \cdot f_{ck}(20^\circ\text{C}) \quad (4.8)$$

where: $f_{ck}(T)$ = the characteristic compressive strength at temperature T (MPa)
 $k_c(T)$ = a temperature dependent coefficient (-) :

- $k_c(T) = 1$ if $T = 20 - 100$ °C
- $k_c(T) = (1600 - T/1500)$ if $T = 100 - 400$ °C
- $k_c(T) = (900 - T/625)$ if $T = 400 - 900$ °C
- $k_c(T) = 0$ if $T = 900 - 1200$ °C

Other expressions are found in literature using a residual resistance factor β_T : the ratio of the compressive strength of heated concrete at temperature T to the compressive strength of unheated concrete. Different authors give different formula's of β_T . These equations only apply in case of exposure to fire (Figure 4.6a and Figure 4.6b).

Malhotra (1982):

$$\beta_T = 1 - \frac{T}{600} \quad \text{if } T = 20 - 300 \text{ }^\circ\text{C} \quad (4.9a)$$

$$\beta_T = 0.95 - \frac{T - 300}{588} \quad \text{if } T = 300 - 800 \text{ }^\circ\text{C} \quad (4.9b)$$

Bhal and Jain (1999):

$$\beta_T = e^{-0.005316 \left(\frac{T}{100}\right)^{3.0295}} \quad \text{for concrete tested warm} \quad (4.10a)$$

$$\beta_T = e^{-0.04665 \left(\frac{T}{100}\right)^{1.6274}} \quad \text{for concrete tested cold} \quad (4.10b)$$

Figure 4.6a and Figure 4.6b give the comparison of the strength reduction of concrete of the previously given equations. In case of elevated temperatures up to 800 °C, a compressive strength reduction of 75 % – 95 % is noticed. Concrete exposed to an elevated temperature of 100 °C due to fire leads to a maximal reduction of 5 % (Table 4.3). In case of fire exposure of concrete with resulting temperature elevation less than 100 °C a strength reduction up to 1 % to 8 % is noticed, depending on the considered equation.

According to Kaplan (1987) the compressive strength reduction of different types of concrete, under elevated temperatures during a longer period of time, varies between 10 % and 35 % for a temperature near 100 °C (Figure 4.7). This reduction can be caused by an internal microcracking due to the hindered deformation at the interface of the aggregates and the cement paste during heating. A decrease of 15 % is observed for concrete with calcareous aggregates exposed to elevated temperatures for periods varying from 1 to 8 months [Neville, 2000]. The loss in strength is higher for concrete with W/C ratio of 0.6 in comparison with a W/C ratio of 0.45. The highest strength loss occurs in the first two hours of exposure to elevated temperature. The duration of heating has no significant effect on the strength results [Neville, 2000].

Vodák et al. (2004) determined a compressive strength loss of 15 % due to an increase of temperature from 25 °C up to 100 °C. Further increase of temperature (up to 285 °C) has a beneficial effect on the compressive strength. Also an increase of porosity is noticed. The test samples are based on a rapid hardening cement with small addition of fly ash and slag.

The compressive strength of an OPC based concrete reduces with a temperature increment from 100 °C up to 600 °C (75 % reduction) [Saad et al., 1996]. By adding silica fume, a smaller reduction is noticed, leading to a 20 % reduction of compressive strength at 600 °C. Also the tensile strength reduces with temperature. The porosity and the water absorption increase with higher temperature.

Arios (2007) tested OPC based concrete with limestone aggregates or river gravel on temperature effects. The results indicate a weight loss with increasing temperature. This loss becomes significant at 800 °C. The W/C ratio and the type of aggregates have a smaller influence on the test results. Also a strength reduction is recorded, which is higher in case of river gravel used as aggregates. The concrete is totally deteriorated at 1200 °C (Figure 4.8).

Table 4.3: Values of the residual resistance factor at $T = 100\text{ }^{\circ}\text{C}$

Formula	β_T
Eurocode 2 (1992)	1.000
Malhorta (1982)	0.983
Bhal & Jain (1999) tested cold	0.954
Bhal & Jain (1999) tested hot	0.995

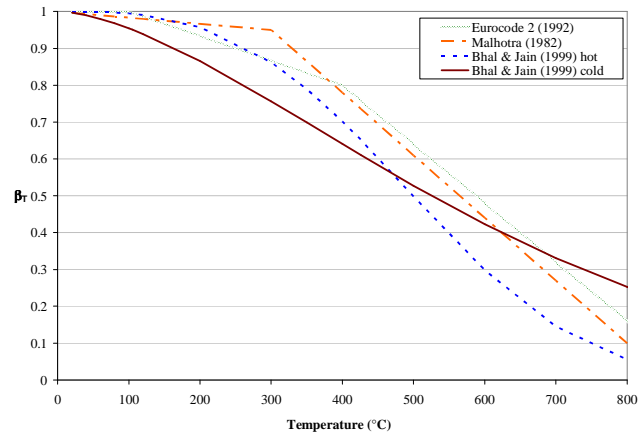


Figure 4.6a: Effect of the temperature (up to $800\text{ }^{\circ}\text{C}$) on the compressive strength of concrete

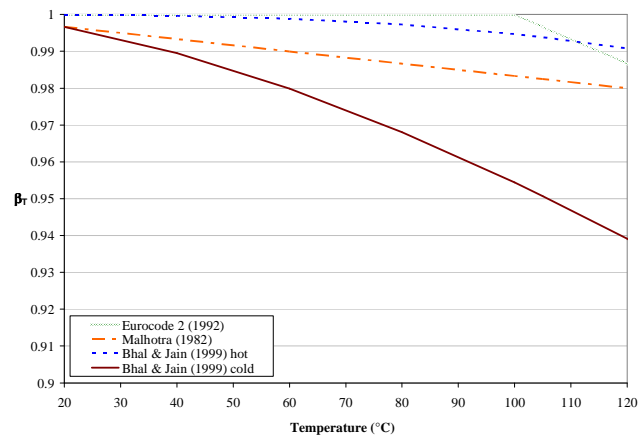


Figure 4.6b: Effect of the temperature (up to $120\text{ }^{\circ}\text{C}$) on the compressive strength of concrete

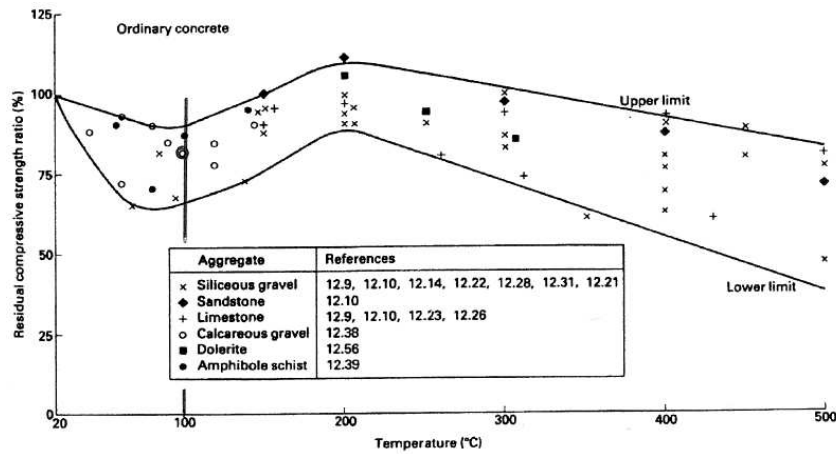


Figure 4.7: Influence of elevated temperatures on the compressive strength of different types of concrete [Kaplan, 1987]

The compressive strength and the modulus of elasticity of two types of concrete (one based on limestone aggregates and one on siliceous aggregates, both with CEM I 42.5 N as OPC) are affected differently due to heating [Savva et al., 2005]. No superplasticizer is being used. During the first 28 days of hardening, the test samples are kept under climatic conditions (20 °C, 90 % Relative Humidity). Afterwards they are stored in an environment with 60 % RH and 20 °C for 3 years. Afterwards and after exposure to elevated temperatures (100 °C – 300 °C – 600 °C – 750 °C) the compressive strength and the modulus of elasticity are determined. The results show a slight increase of compressive strength in case of temperatures lower than 300 °C (Figure 4.9a). Temperatures up to 600 °C induce a portlandite decomposition and simultaneous strength reduction. Further temperature increase leads to the deterioration of the test samples and dehydration of the CSH (600 °C: 50 % strength reduction, 750 °C: 75% reduction). Young’s modulus is more affected by increased temperature due to a progressive destruction of the cement matrix (Figure 4.9b). Overall, the strength reduction is higher in case limestone aggregates are being used.

The modulus of elasticity strongly affects the behaviour of concrete structures, and this parameter has a non-negligible temperature influence. A progressive reduction is noticed with elevated temperatures between 50 °C and 800 °C [Neville, 2000]. This reduction depends on the cement amount and the type of aggregates used in the concrete mixture, but are less pronounced in case of quartz or porphyry as chosen aggregates in comparison with limestone [Maréchal, 1970]. Certain authors indicate a reduction of the modulus of elasticity up to 15 % to 30 % for temperatures near 100 °C for concrete based on limestone aggregates [Kaplan, 1989].

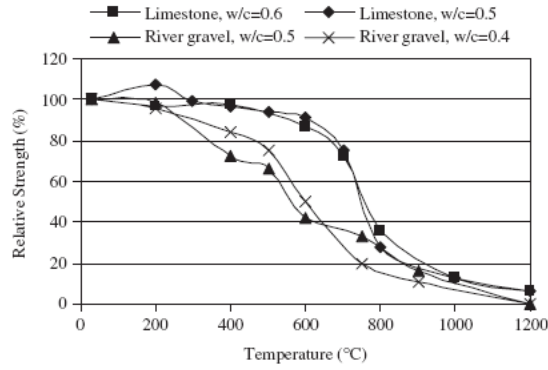


Figure 4.8: Relative concrete strength of limestone and river gravel concrete [Arioz, 2007]

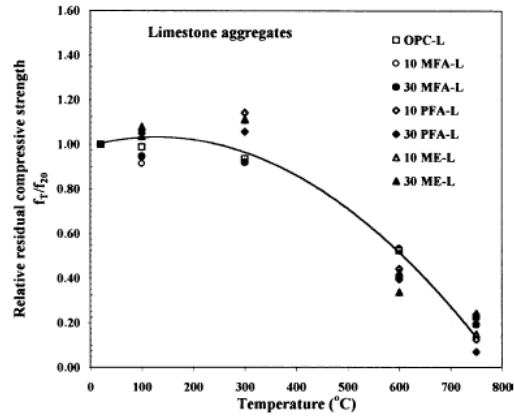


Figure 4.9a: Relative residual compressive strength of limestone concrete at elevated temperatures [Savva et al., 2005]

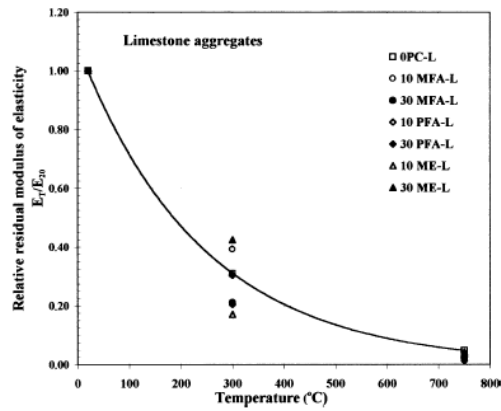


Figure 4.9b: Relative residual elasticity modulus of limestone concrete at elevated temperatures [Savva et al., 2005]

Also Poisson's ratio shows a temperature dependency. A small increase around 50 °C is noticed followed by a 15 % reduction at a temperature level of 100 °C (absolute value of 0.25 at 100 °C) for concrete samples subjected to an uniaxial load [Maréchal, 1970].

The influence of high temperature on OPC based SCC with limestone used as filler and as aggregate is studied by Liu et al. (2006). Up to 100 °C a weight loss is noticed due to evaporation of the capillary pore water (free water), but little significant influence on the mechanical properties is shown. Moving on to temperatures up to 400 °C and higher, decomposition of the portlandite is observed.

Overall, it can be concluded that the exposure of concrete compositions to elevated temperature up to 100 °C affects the mechanical properties and can induce a strength reduction varying from 15 % up to 35 %. The type of aggregate and the cement type used in the concrete mixture considerably affect the test results. Further examination of the effect of elevated temperatures on the strength of limestone based SCC and TVC will be made (Chapter 7).

1.5 Effect of temperature on thermal properties

1.5.1 Specific heat

A mean value of 1000 J/(kg·°C) is common for the specific heat of a concrete in a temperature range of 0 °C up to 100 °C [Taerwe, 1997]. The specific heat strongly depends on the water amount of the concrete, mainly because the specific heat of water is somewhat higher than that of concrete: 4190 J/(kg·°C). The specific heat of a saturated fresh concrete is 1.2 – 1.5 times higher than of a dry concrete.

The specific heat of concrete increases with temperature. Eurocode 4 (ENV 1994-1-2) defines the specific heat c_c of dry concrete in function of the temperature:

$$c_c = 900 + 80 \cdot \left(\frac{T}{120} \right) - 4 \cdot \left(\frac{T}{120} \right)^2 \quad (4.11)$$

where: $T =$ the temperature of the concrete, $20 \text{ °C} \leq T \leq 1200 \text{ °C}$

A 20 % rise is noticed for calcareous concretes at a temperature of 100 °C [Mounajed and Obeid, 2001]. Vodák et al. (1997) measured the thermal properties of High Performance Concrete (HPC) based on siliceous aggregates and calcareous filler for the construction of a nuclear centre at Penly, France. A weak variation of the specific heat of the HPC is noticed at temperatures lower than 100 °C (Figure 4.10). An increasing tendency in the whole temperature range from -30 °C to 1000 °C is identified. No hysteresis is observed in going up and down with temperature.

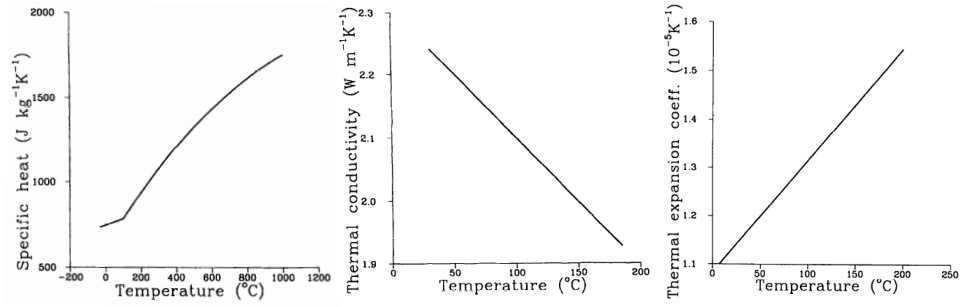


Figure 4.10: Thermal properties of HPC at elevated temperatures [Vodák et al., 1997]

1.5.2 Thermal conductivity

The thermal conductivity k (equation (4.1)) of dry concrete (HPC) samples decreases with increasing temperature, and this tendency appears for the whole temperature range up to 200 °C (Figure 4.10) [Vodák et al., 1997].

The thermal conductivity of concrete decreases with temperature according to Eurocode 4 (ENV 1994-1-2) following the polynomial equation (4.12):

$$k = 2 - 0.24 \cdot \left(\frac{T}{120}\right) + 0.012 \cdot \left(\frac{T}{120}\right)^2 \quad (4.12)$$

where: T = the temperature of the concrete, $20 \text{ °C} \leq T \leq 1200$

An explanation of the reducing effect of temperature can be found in the lower water content of saturated concrete samples with water driven out due to the elevated temperatures. Saturated concrete has a higher thermal conductivity than dry concrete. In case of partially saturated concrete, the effect of temperature becomes more complex. The thermal conductivity of calcareous concrete even rises with 15 % between 50 °C and 90 °C, because of the augmentation of k of the water with temperature (Table 4.1) [Mounajed and Obeid, 2000].

A comparison of thermal conductivity values of various siliceous concretes is given in Table 4.4.

Table 4.4: Comparison of thermal conductivity of various siliceous concretes ($W/(m \cdot ^\circ C)$)
[Vodák et al., 1997]

	50 °C	100 °C	150 °C
Vodák et al. [1997]	2.20	2.10	2.00
Harwathy [1970]	2.50	2.39	2.22
Abe et al. [1972]	2.53	2.26	2.03

1.5.3 Coefficient of thermal expansion (CTE)

The dependency of the CTE of HPC on temperature is shown in Figure 4.10 according to Vodák et al. (1997). A rise of 15 % at a temperature of 100 °C is noticed in comparison with the CTE factor at ambient temperature (20 °C). To compare the CTE of an ordinary concrete and a HPC, Table 4.5 is given.

Table 4.5: Comparison of CTE of ordinary concrete and HPC ($10^{-6}/^\circ C$)
[Mounajed and Obeid, 2000]

	20 – 50 °C	50 – 90 °C	90 – 200 °C
Ordinary concrete	11.0	12.0	13.0
HPC	14.1	14.6	16.6

2 Irradiation Effects

2.1 Radiation originating from the waste canisters

The concrete buffer of the Supercontainer will be subjected to a radiation flux, owing to proximity to the vitrified HLW and the SF assemblies. The radiological dose rates in the concrete layers of the Supercontainer will be at a maximum level immediately after waste emplacement and during the thermal HEATING phase (Chapter 1). Dose rates will decrease over time as a result of radioactive decay [Wickham et al., 2005].

A recent study determined the radioactive dose and the dose rates originating from the waste canisters at the interface of the concrete buffer and the overpack and inside the buffer [Poyet, 2007]. This radiological inventor only considers the fissile materials and actinides placed inside the concrete buffer after a cooling period of at least 50 years. Concerning the type of radiation, only gamma rays are considered: alpha and beta particles are stopped by the carbon steel layers of the overpack surrounding the canisters, and the flux of neutrons is insignificantly low. Moreover, the shielding provided by the overpack results in concrete experiencing a relatively low dose rate. According to the calculations, the gamma irradiation dose in the buffer, averaged over the entire concrete buffer, is 1.635×10^{-4} Gy/s or 0.589 Gy/h. The values are obtained via the TRIPOLI-IV code using the Boltzmann equations [Both et al., 2003]. Approximately 99 % of this dose derives from the combined decay of ^{137}Cs and its metastable decay product $^{137\text{m}}\text{Ba}$. At the overpack surface, and closer to the radioactive source, the dose rate has a higher value of 6.387×10^{-3} Gy/s or 22.993 Gy/h. The dose rate is higher than the average value close to the overpack and lower further away. From the given values of the time dependent dose rates, the doses, absorbed by the buffer during the first 300 years after waste emplacement, can be calculated. The evolution of the dose and of the dose rate in time during the first 300 years is given in Figure 4.11. The absorbed dose converges to an asymptotical value: 8.86 MGy at the interface of the buffer and the overpack, and 0.23 MGy in the middle of the buffer. Initially the dose rate at the interface has a value of approximately 23 Gy/h. After 300 years it is decreased with a factor 1000 to 0.025 Gy/h (Table 4.6).

2.2 Irradiation-induced physical degradation

The knowledge and research on the effect of irradiation on concrete behaviour and its properties is inevitable for this study. The most important effect of the irradiation is the contribution to the gas production in the concrete buffer due to radiolysis of the concrete pore water [Bouniol, 2004]. However, there are no significant influences to be expected for the cementitious matrix (ONDRAF/NIRAS and CEA statement). On the other hand, the hardening of freshly cast concrete under the presence of an irradiation field (for example during the casting of the lid of the Supercontainer in hot cell) can occur with some unneglectable and unforeseen difficulties. Rather small amounts of useful information concerning the effect of irradiation on concrete behaviour and properties are available in literature.

Table 4.6: Values of the dose (D) and the dose rate (Dr) at the interface (IF) buffer-overpack and in the middle (M) of the buffer (according to [Poyet, 2007])

Time years	IF canister-buffer		M buffer	
	D MGy	Dr Gy/h	D MGy	Dr Gy/h
0	0.00	22.99	0.00	0.59
5	0.95	20.52	0.02	0.53
10	1.80	18.32	0.05	0.47
25	3.84	13.03	0.10	0.34
50	6.02	7.38	0.16	0.19
100	7.95	2.37	0.21	0.06
300	8.86	0.03	0.23	0.00

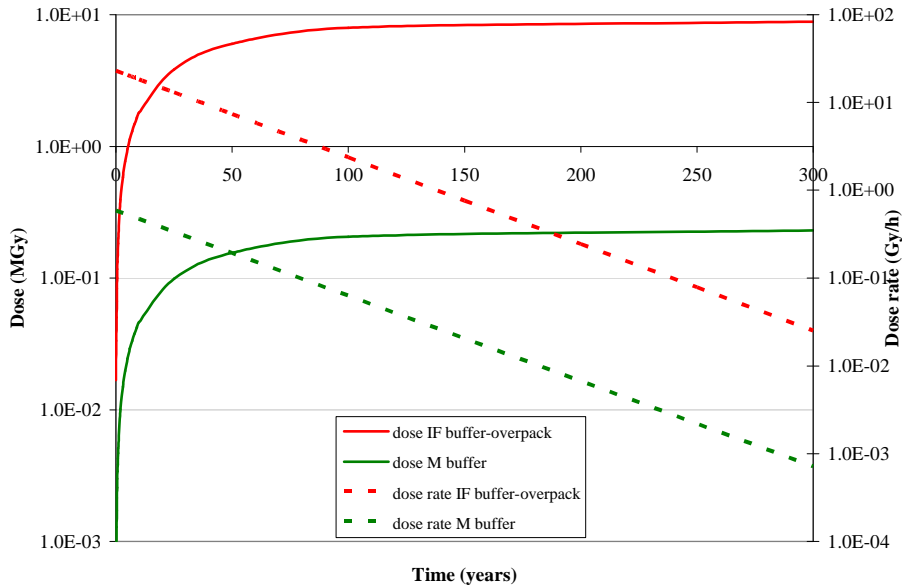


Figure 4.11: Evolution of the dose and the dose rate at the interface (IF) buffer-overpack and in the middle (M) of the buffer (according to [Poyet, 2007])

Gamma radiation has a non-negligible effect on the concrete mechanical properties according to Vodák et al. (2005). In this study, concrete used for the nuclear facilities in NPP's, is exposed to doses up to 0.35 MGy in a time span of 40 years. Compressive strength reduction (up to 10 %), reduction of pore space and an increase of the amount of calcite CaCO_3 (irradiation carbonation) are noticed. The concrete samples, after 90 days of hardening, are exposed to an irradiation field with different doses during 90 days, all smaller than 1 MGy and significant dose rates varying from 130 Gy/h up to 260 Gy/h. The tested concrete contains siliceous aggregates, is based on CEM I 42.5R as cement and has a W/C ratio of 0.43. Figure 4.12 shows a compressive strength reduction with increasing dose. A dose of 0.5 MGy gives a 10 % compressive strength reduction (compressive strength of unirradiated samples: 69.4 MPa after 180 days). The same dose lowers the tensile strength with 5 %. Conclusions are drawn saying that the interaction of gamma rays with concrete induces pore water radiolysis and ends by formation of calcite, which leads to a reduction of the pore space and a strength reduction is caused. This amount of calcite rises with the radiation dose, a phenomenon called 'irradiation carbonation'.

These results are not supported by the findings indicating that the mechanical properties of concrete are not influenced by doses up to 100 MGy according to Pachner (1998).

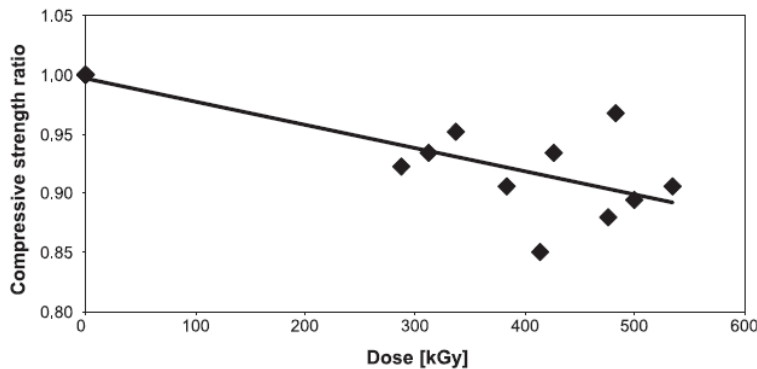


Figure 4.12 : Influence of gamma exposure on the compressive strength ratio [Vodák et al., 2005]

Richardson et al. (1990) examined the microstructural changes of BFSC/OPC mixes, consisting of Blast Furnace Slag (75 %) and Ordinary Portland Cement (25 %), under gamma irradiation with a total exposure dose of 80 MGy obtained over a time span of 2 years, environmental temperature of 50 °C. This high dose given over a short time period, leading to high dose rates, are used to imitate the behaviour of Intermediate Level Waste (ILW). Some of the exposed samples show an additional ettringite formation. The degree of hydration and the CSH products are not influenced by the gamma rays and the CSH gel remains unchanged in both composition and morphology.

A smaller amount of Ca(OH)_2 in the irradiated test samples indicates a portlandite reduction as a consequence of the irradiation.

Other studies show the negligible effect of gamma irradiation with doses up to 10 000 MGy [Kelly and Davidson, 1969, Elluch et al., 1972]. On the other hand, the exposure of the concrete to a neutron flux higher than 10^{19} n/cm² can lead to deterioration caused by the relative expansion of the aggregates and the induced shrinkage of the cement paste due to the neutrons. The related reduction in tensile strength is higher than in compressive behaviour.

Morigana (1997) suggests an increased reduction of the concrete resistance by nuclear irradiation with higher amount of SiO_2 in the aggregates, which indicates an irradiation enhanced Alkali Aggregate Reaction (AAR). The same behaviour was found by Ichikawa et al. (2002), who identified the critical dose that leads to this type of AAR ($1 - 5 \times 10^{19}$ neutrons/cm², $0.5 - 5 \times 10^5$ MGy). The use of limestone can be seen as an additional safety towards irradiation induced AAR.

A dose rate of 2275 Gy/h leading to an integral dose of 10 MGy shows the effect of gamma irradiation on the transport properties of immobilized Sr and Cs ions in cementitious pastes, based on OPC with W/C ratios of 0.3 up to 0.6 [Bar-Nes et al., 2008]. An increased depth of carbonation was found in case of the irradiated samples related to the marked decrease in the leached fraction of Sr ions. The enhanced carbonation is associated with the dehydration due to radiolysis of pore water in the paste. A small increase of Cs ions, on the other hand, was found on irradiated samples, associated with the formation of microcracks. Irradiation can degrade cementitious materials via two main mechanisms:

- The relocation of atoms from their sites, mainly due to the recoil of energy of the radionuclides (mainly beta and gamma), resulting in a micro-structural change in the immobilizing material.
- The most important mechanism is the radiolysis of pore water and interstitial water, leading towards internal overpressure and accumulation of explosive hydrogen gas (see further).

Irradiation would not change usually the macroscopic properties of the material [Bar-Nes et al., 2008].

For the doses expected in the concrete buffer of the Supercontainer, no degradation of the concrete mechanical properties is expected (ONDRAF/NIRAS and CEA statement). Most of the cement matrices and grouts used for the containment of radioactive waste, do not show significant deterioration due to gamma irradiation. They have a good mechanical resistance towards physical degradation due to irradiation. The behaviour though, depends on the type of grout and on the encapsulated waste [Wilding et al., 1989].

Overall, it is hard to come to a consensus about the possible effect of gamma radiation on the mechanical properties of concrete. Moreover, in case of the Supercontainer, the applied doses and dose rates (doses up to 9 MGy after 300 years and a maximum dose rate of 23 Gy/h) are generally much lower than the doses and dose rates applied in the previously discussed studies (doses up to 100 000 MGy and dose rates up to 2275 Gy/h). Nevertheless, some preliminary irradiation tests will be conducted on SCC based mortars, with more significant dose rates up to 10 Gy/h applied by means of a ^{60}Co source, to study the effect of gamma radiation on the compressive strength and the porosity of hardening mortar (Chapter 7).

2.3 Radiolytic Gas Generation

2.3.1 Introduction and Definition

Concrete, mortar and other cementitious materials are often used for nuclear applications such as nuclear reactor vessels, nuclear waste containment facilities and other disposal media. Due to the ionizing effect of the radioactive radiation originating from the radioactive materials, the residual pore water of the cementitious materials can decompose. Radiolysis, a radio-chemical mechanism, is the dissociation of molecules due to irradiation and can give cause to an internal gas production [Bouniol and Aspart, 1998]. According to Burns et al. (2003) every chemical process occurring in an irradiation field, can be seen as radiolysis. Ionizing radiation has a considerable effect on other chemical processes affecting the radioactive containment medium such as corrosion, radionuclide absorption, organic material deterioration, etc. On the other hand, cementitious materials, especially in the absence of organic components, give prove of a good resistance towards physical degradation due to irradiation [Burns et al., 2003].

The intensity of the radiolysis process depends on the irradiation dose, the type of irradiation and on the initial composition and pH of the pore water. Only 2 % of the total deposited irradiation energy is used for radiolysis, the remaining 98 % is converted into heat. Radiolysis leads to internal gas production, that can lead to internal cracking due to over-pressure. Also an accumulation of extremely explosive hydrogen gas H_2 is determined. Initially and after hardening of the cement matrix, residual gasses (N_2 , O_2) are present in the pore volume of cementitious materials, such as concrete. Due to radiolysis H_2 and additional O_2 are also formed. Water vapor can be formed due to the heat-emitting waste. A model is designed to predict the concrete pore water behaviour under influence of irradiation in function of the dose rate, the saturation degree of the irradiated material and the initial H_2 amount: CHEMSIMUL [Kirkegaard and Bjergbakke, 2005]. The radiolysis simulations discussed below, using the CHEMSIMUL code, consider the effect of the radiation dose on the concrete pore water. Only the effect of gamma radiation will be considered, as the alpha and beta radiation is prevented by the overpack and the flux of neutrons is insignificantly low.

A hardening cementitious material undergoes specific changes due to gamma radiation [Bouniol and Aspart, 1998]:

- i. Hydrogen peroxide H_2O_2 is formed due to the hydrolysis of the molecular water.
- ii. H_2O_2 reacts with portlandite $Ca(OH)_2$ and the octahydrate $CaO_2 \cdot 8H_2O$ is formed in case of a minimal dose rate of 0.1 Gy/s. This reaction consumes O_2 .
- iii. The octahydrate is meta stable, little dissoluble and disappears if H_2O_2 is no longer present, and again converts into CaO_2 and peroxide H_2O_2 .
- iv. Next CaO_2 reacts with the pore water to form portlandite and oxygen according to equation (4.13).



- v. Eventually the portlandite reacts with the CO_2 present in the air of the pore volume: calcite is formed. The process characterized by equation (4.14) is better known as 'irradiation carbonation'.



The interaction of gamma radiation with concrete leads to an increase of the calcite amount and a clogging of the pore volume of the material.

The CHEMSIMUL model determines the kinetics of the chemical reactions of a system in a homogeneous environment and the behaviour of a material under influence of radiolysis. The most important input data are listed below:

- The material properties of the concrete: the cement, the pore water composition, the hydration reaction and hydration degree (Powers' model) and the pore size distribution.
- The properties of the radioactive source: the initial dose (TRIPOLI-IV code using the Boltzmann equation [Both et al., 2003]), the type of radiation, the evolution of the dose rate and the half-life of the radionuclides.
- The homogeneous radiolysis phenomena: the primary and secondary reactions.
- The heterogeneous radiolysis phenomena: the gas transport by diffusion (Fick), the gas transport by permeability (Darcy), the considered system (open or closed) and the phase shift.

2.3.2 Primary and secondary radiolysis reactions

The pore water of a concrete material consists of 3 types:

- The liquid water in the capillary spaces and in the pores between the CSH layers (H_2O).
- The molecular water, for example present in gypsum ($CaSO_4 \cdot 2H_2O$).

- The water in the form of OH⁻ ions, for example present in portlandite Ca(OH)₂.

About 10⁻⁷ to 10⁻⁶ s after the gamma rays have entered the concrete material, the decomposition of the pore water (with high initial pH) starts and eight primary substances are formed and scattered uniformly in the solution: four stable molecules H₂, H₂O₂, OH⁻, H₃O⁺ and four unstable radicals e⁻_{aq}, H, OH, HO₂ (Figure 4.13). These primary reactions are the motor behind the radiolysis mechanisms of pore water. A certain amount of heat Q is produced. Especially the liquid water is affected by the radiolysis. However, the amount of available water has no influence on the primary reactions whatsoever.

The efficiency of these primary reactions is expressed by means of the amount of molecules or radicals formed due to 100 eV absorbed irradiation energy [Bouniol, 2004]. It is influenced by the type of radiation and the dose rate, the homogeneity of the concrete material, the pH of the pore water and the temperature.

After the created molecules and radicals are diffused throughout the entire pore volume, they react with the H₂O solution and its most active substance OH⁻ via seven acid alkaline equilibrium reactions. The eight created primary substances also can interact between themselves by means of approximately sixty reactions [Bouniol and Bjergbakke, 2008]. These secondary reactions lead to the secondary production of molecules and radicals. Besides these radicals, also newly formed products are found, such as O₂ and O₃. A change of phase is induced and leads to convective and diffuse gas transport. Also the precipitation of the octahydrate CaO₂·8H₂O, which consumes oxygen, is a secondary reaction. The temperature, the pH and the dissolved particles (carbonates, nitrates, chlorides and iron particles) have a considerable effect on the secondary reactions. The presence of carbonates deranges the radiolysis [Cai et al., 2001], the nitrates and iron particles slow down the H₂ production [Möckel and Köster, 1982].

2.3.3 Gas transport mechanisms

The resistance a gas experiences during the flow through a material depends on the molecular properties of the gas, the interaction with the material and its pore structure, the size of the molecules and the nearby presence of a liquid in the pore volume. There are different mechanisms to explain the gas transport through a material, depending on the interaction of the gas with the material [Boel, 2006]. For each transport mechanism, equation (4.15) can be used.

$$N_i = -D_i^e \cdot F_i \quad (4.15)$$

where: F_i = the local force behind the mass transport (pressure, concentration, etc.)
 D_i^e = the correspondent effective mass transport coefficient (m²/s)

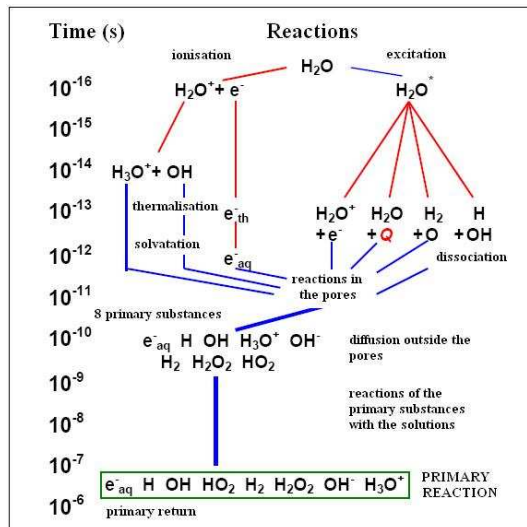


Figure 4.13 : Chronology of the primary hydrolysis reactions [Bouniol, 2004]

The different transport mechanisms have diverse driving forces leading the movement. Diffusion, permeability, capillarity and migration are driven by a difference in respectively concentration, pressure, capillary under-pressure and an electric field.

Diffusion is a spontaneous, non-directional spread of free molecules or ions leading to a uniform distribution of the matter. The flow goes from regions with higher concentrations to the regions with lower concentrations [Boel, 2006]. Diffusion is a very slow process that can be expressed by using Fick's law.

Permeability is the flow of a gas or liquid due to an enforced pressure gradient and it can be determined experimentally. The permeability can be expressed by means of Darcy's law.

Capillary suction arises from the surface tension present in the pores of a porous material such as concrete.

Transport of ions through a material due to an outer electric field, is better known as migration. The positive ions move towards the negative anode, the negative ions go to the positive cathode.

2.3.4 Design concept assumptions

The concrete buffer of the Supercontainer will be subjected to a radiation flux, owing to proximity to the vitrified HLW or the SF assemblies [Bouniol, 2004]. The radiolysis calculations and statements, discussed below, have been attained for three possible cases.

All three calculation cases are made at 25 °C, considering the encapsulation of vitrified HLW and using OPC based concrete, and differ in the following aspects:

- An open system (vented envelope) and an unsaturated concrete buffer.
- A closed system (sealed envelope) and an unsaturated concrete buffer.
- A closed system with a saturated concrete buffer.

A fully saturated system can be seen as a closed system for gas transport. Only the effect of gamma irradiation will be considered, as the buffer is shielded from the alpha and beta radiation by the canister and the overpack. The Bouniol calculations take into account the input data listed in Table 4.7.

2.3.5 Internal pressure build-up due to radiolysis

An open system

In the open system, hydrogen gas generated by the radiolysis can easily escape by diffusion and therefore essentially no change in the total pressure of the system is noticed. The maximum rate of release of H₂ gas from the Supercontainer is around 9.3 cm³/day at about 5 years and the cumulative amount of H₂ released from the system is 152 litres after 100 years. An open system has typical differences in comparison with a closed system. First of all, the total pressure build-up is especially related to the increment of N₂, which has a greater contribution to the internal pressure than the H₂ amount (Figure 4.14). The H₂ gas can easily escape via diffusion. Secondly, the total internal pressure is higher in case of an open system with the same radiation conditions as a closed system. Four years after fabrication and placement of the Supercontainer in the disposal galleries, an internal pressure maximum of 0.23 MPa is reached. Afterwards, this pressure evolves towards an equilibrium of 0.12 MPa. These values are much lower than the tensile strength of the concrete considered for the buffer (Chapter 6) and only apply in case of a decreasing dose rate. The higher the initial dose rate, the higher the pressure peak, the sooner the peak occurs and the greater the contribution of H₂ to the total pressure. It can be concluded that the H₂ production due to the primary reactions is ventilated fast by means of diffusive gas transport. The saturation degree plays an important role.

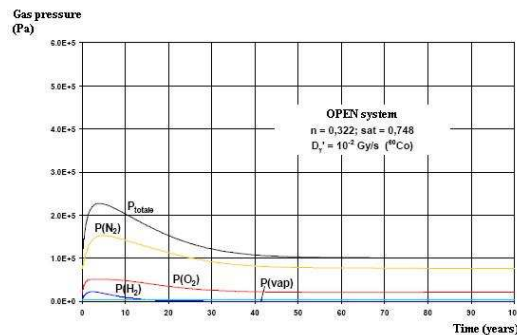


Figure 4.14 : Pressure build-up in an open system [Bouniol, 2004]

Table 4.7: Input data for the Bouniol calculations [Bouniol, 2004]

Input data	
Cement matrix	
Cement type	OPC CEM I
W/C	0.36
$\alpha_{h,max}$	0.857
Total porosity (P)	0.322
Saturation degree (S)	75 %
Pore water pH	13.25
Environmental temperature	25 °C
Radioactive source	
Isotopes	^{60}Co
Dose rate	10^{-2} Gy/s
Type	gamma
Radiation duration	100 years
Initial internal pressure	
P_i (O ₂)	20 562 Pa
P_i (N ₂)	76 647 Pa
P_i (H ₂)	0.05 Pa
P_i (vapour)	3166 Pa

A closed system

The precipitation of the octahydrate $\text{CaO}_2 \cdot 8\text{H}_2\text{O}$ affects the pressure build-up inside a closed system. This mineral regulates the O_2 and H_2 production in a system. Not taking into account this regulator will lead to greater pressures inside the closed system. The pressure due to N_2 and the water vapor remains constant in both the cases (Figure 4.15). As hydrogen and oxygen gases are generated by radiolysis, and they cannot escape the closed system, the gas pressure increases (Figure 4.15).

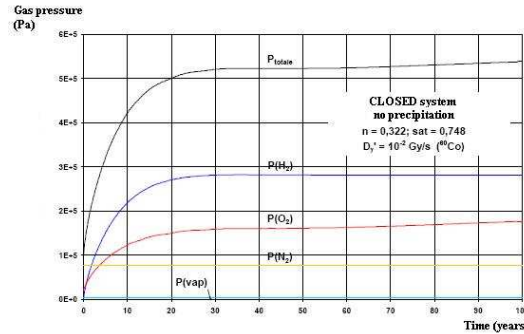


Figure 4.15 : Pressure build-up in a closed system [Bouniol, 2004]

The total pressure in the system is greater than 0.5 MPa in case precipitation is not taken into account. Otherwise, the total pressure is around 0.2 MPa. These values are valid for a decreasing dose rate.

The combination of a closed system with a constant dose rate leads towards a linear increment of total pressure with time. Pressure due to N_2 , O_2 and water vapor remains constant. The higher the dose rate, the higher the H_2 pressure.

It can be concluded that the irradiation (by means of gamma rays) of a closed system causes an O_2 and H_2 production (proportion 1:2) until an equilibrium is reached.

2.3.6 Parameters influencing the radiolysis process

Little experimental results can be found concerning radiolysis of cementitious materials. However, a considerable amount of parameters influence the radiolysis processes [Bouniol, 2004]: the dose rate, the radiation type, the duration of irradiation, the concrete composition, the type of cement, the W/C ratio, the saturation degree, the type of waste, the geometry of the structure, the temperature, etc.

Type of radiation

The energy of heavy alpha particles is dissipated very fast and on short distance, making the alpha radiation differ fundamentally from the beta and gamma radiation [Schorr et al., 1979]. The total gas pressure due to hydrolysis of gamma radiation (^{60}Co

source) of cementitious materials, evolves slowly to a constant value, with magnitude depending on the dose rate of the irradiation. In case alpha irradiation (^{244}Cm) is included in the calculations, the gas pressure does not converge, but rises continuously with time and can cause a problematic gas pressure build-up.

Alpha radiation gives cause to the formation of molecules whereas beta and gamma radiation especially creates radicals in the primary radiolysis reactions. In case of the Supercontainer concept, alpha particles are blocked by the carbon steel overpack and thus can be kept out of consideration.

Temperature

The evolution of the total gas pressure is also influenced by a temperature rise, for example caused by the heat-emitting waste. Taking into account a temperature rise up to 100 °C, the total pressure can be twice as high as the case where the temperature is kept constant (25 °C, closed and unsaturated system) [Bouniol, 2004]. This is mainly caused by the creation of water vapor due to the boiling of the water in the pores. The pressure due to the water vapor has a large contribution to the total pressure, in case high temperatures are considered. The production of O_2 and H_2 is little affected by the temperature.

Dose rate

The total pressure inside an open system rises with increasing dose rate (Figure 4.16). Approximately 5 years after the gamma irradiation initiates, a pressure peak occurs. The higher the dose rate, the greater the peak. Afterwards, the pressure drops, slower in case of higher dose rate. Also the H_2 ventilation is higher for higher dose rate (Table 4.8). The higher the dose rate, the higher the proportion of the convective gas transport [Bouniol, 2004].

For a closed system, the pressure evolves to a constant value, independent of the dose rate. A higher dose rate only leads towards an earlier pressure build-up.

Table 4.7: Maximum total pressure and H_2 ventilation for an open system [Bouniol,2004]

Dose rate γ (Gy/s)	$P_{\text{tot,max}}$ (MPa)	H_2 ventilation (cm^3/d)
0.001	0.125	19
0.01	0.227	132
0.1	0.276	369
1	0.288	472

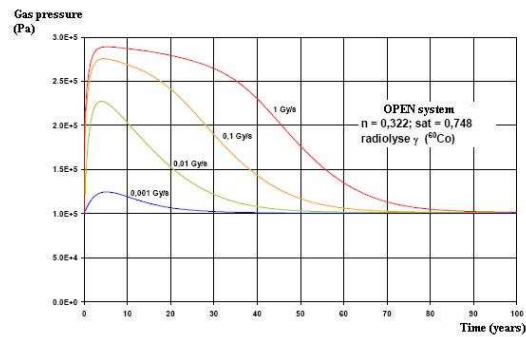


Figure 4.16 : Influence of the dose rate on total pressure of an open system [Bouniol, 2004]

Saturation degree

The gas transport through a cementitious matrix strongly depends on the saturation degree of the matrix. In case of a fully saturated matrix (closed system) the gas is enclosed by the water and transport becomes more difficult. The displacement pressure of the water can have the same order of magnitude as the tensile strength of a concrete. In case of alpha irradiation of a saturated concrete, the gas pressure build-up will exceed the tensile strength of the concrete [Madic and Koehly, 1986]. The hydrogen gas can migrate through the water via diffusion, an extremely slow transport process. So a higher saturation degree leads to a reduced H₂ ventilation. The energy deposit of gamma rays is much more uniform due to the destruction of H₂ by means of the produced radicals. The slow diffusive migration of hydrogen gas gives sufficient time for the gamma photons to attack the H₂ [Bouniol, 2004].

The use of organic additives and the applied W/C ratio

In a saturated environment, the presence of strongly reducing organic additives can induce a quick reduction of oxygenous products. Therefore, the H₂ is not touched and can accumulate if the dose rate is higher than 0.1 Gy/s [Bouniol, 2004]. Due to this disadvantageous effect, organic additives are often refused as a concrete component. On the other hand, organic additives, such as superplasticizers, can be added to improve the rheological properties of fresh concrete.

Adding 1 % of superplasticizer (in comparison with the cement mass), considerably influences the radiolysis processes. Naphthalene Sulphonate (NFS), containing two aromatic chains, has an excellent behaviour towards irradiation: it gives a radio-resistance to the molecules and partially prevents decomposing of the pore water due to radiolysis. In comparison to concrete without NFS, the H₂ gas generation and gas pressure build-up is lower (Figure 4.17) [Bouniol, 2004]. Another type of superplasticizer, based on Melamine Sulphonate (MFS) has the similar beneficial behaviour.

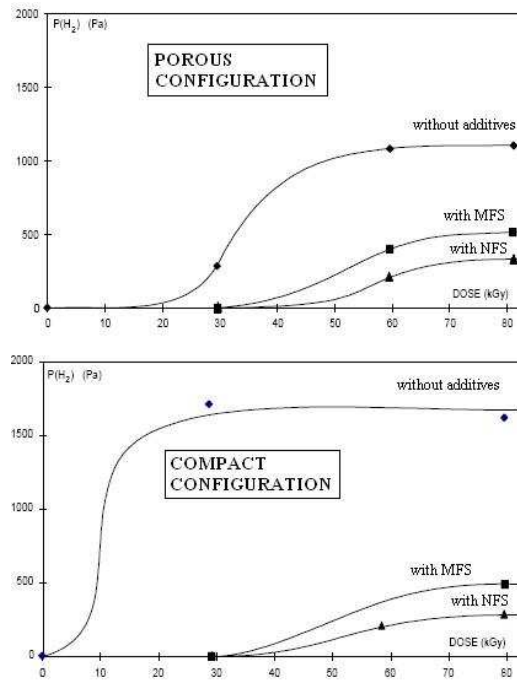


Figure 4.17 : Influence of NFS and MFS on H₂ pressure build up, radiation dose rate 41.8 Gy/h [Bouniol, 2004]

A lower water content, thus a more compact configuration, experiences a higher pressure build-up (Figure 4.17). The radiation passed on to the pore water rises with the solid to water proportion. The efficiency of the primary hydrolysis reactions and thus the gas production is higher in case of a lower water content (Compton effect). This is why the H₂ pressure is higher in case of a more dense concrete, where the opposite behaviour is expected (higher water content gives more available pore water for radiolysis).

Polycarboxylate based plasticizers (such as Glenium, with no aromatic chains) also create the discussed beneficial effect of decreasing H₂ pressure build-up, but in a smaller extent. Other studies confirm those statements [Lewis and Warren, 1990, Palmer and Fairhall, 1993]. Finally, the use of additives such as sodium nitrate (NaNO₃) and sodium periodate (NaIO₄) also leads to a reduced H₂ production.

The use of calcium carbonate

The radiolysis is little changed by adding CaCO₃. The calcite provides a clogging of the pores, creating a more uniform gas distribution and spreading inside the concrete pore volume [Bouniol, 2004].

3 Gas production and gas transport due to corrosion

3.1 Introduction

As seen as in Chapter 3, the Belgian Supercontainer concept consists of a carbon steel overpack, surrounding the waste canisters and encircled by a concrete buffer, creating a favourable alkaline geochemical environment. This buffer is enclosed by a stainless steel envelope, to facilitate the construction and the handling of the Supercontainer (Chapter 3). The Supercontainer, after emplacement in the waste galleries (concrete blocks, thickness 30 cm), is embedded with a cementitious backfill. A review was undertaken to evaluate the corrosion processes and the associated gas generation that might occur during the lifetime of the Supercontainer. This gas production of the overpack and the outer envelope can only occur from the moment water is in contact with these metallic objects. Three corrosion cases exist during the evolution of the Supercontainer [Gens et al., 2006]:

- Corrosion of the outer surface of the carbon steel overpack and the inner surface of the outer envelope due to the water present in the concrete buffer. This corrosion exists under aerobic and anaerobic conditions and starts before penetration of external fluids originating from the Host Rock.
- Corrosion of the outer surface of the stainless steel envelope, due to the groundwater deriving from the clayey Host Rock (external fluids).
- Corrosion of the overpack by water from the Host Rock (external fluids).

Several potentially aggressive species can be introduced by ingress of ground water and can give cause to corrosion of the steel envelope and the overpack: chlorides, bicarbonates, thiosulphates and sulphides. The concentrations of these ions can be estimated from their concentrations present in the pore water of the Host Rock.

3.2 Corrosion before penetration of external fluids

Corrosion under oxidizing conditions (aerobic) and corrosion under more reducing conditions (anaerobic) are being considered [Gens et al., 2006]. Especially the gas generation and the linked gas pressure build-up inside the buffer is very interesting.

Aerobic corrosion

The oxidizing agents present in the Supercontainer are oxygen from entrapped air in the concrete of the Supercontainer, and the oxygen and other oxidizing radicals produced by radiolysis. It is quite hard to estimate the duration of the oxidizing conditions in the underground disposal site. Estimations range from 0.5 years up to 900 years depending on the diffusion capacity of the air through the concrete buffer. Near the overpack, the reducing conditions will develop more rapidly because the oxygen will be consumed fast due to corrosion, so reducing conditions can be expected after about 1 year. This value is probably valid for saturated concrete.

Oxide layers, passivating the surfaces of stainless steel and carbon steel, provide a protection from corrosion, in case good quality concrete is present. The rate of metal corrosion is related to the thickness and the nature of this passivating film, and can be determined by means of electrochemical tests (with residual passivating current). Carbon steel, when passivated (due to the formation of ferric oxide Fe_2O_3), will corrode at a rate of $0.25 \mu\text{m/y}$, whereas the protection capacity of the oxide film of passivated stainless steel is even better: less than $0.01 \mu\text{m/y}$ [Wickham et al., 2005].

Anaerobic corrosion

At a certain period of time, the amount of enclosed air will be depleted. In this case, the carbon steel will form a stable magnetite layer, and this relatively rapidly. Long term corrosion in this case is rather low, with a rate typically smaller than $0.1 \mu\text{m/y}$. Experiments performed by AEA Technology (2004) with carbon steel corrosion in high pH and anaerobic conditions, with temperatures higher than 90°C also indicate that the carbon steel and the stainless steel will repassivate under these conditions: the protective film will repair itself and reform. In repositories, the corrosion potential is expected to decrease during the transition from oxic to anoxic conditions, and this has a definite influence on the initiation and propagation of localized corrosion [Pourbaix and L'Hostis, 2006].

Effect of irradiation on corrosion

In absence of radiation, the anaerobic corrosion rate of carbon steel is around $0.1 \mu\text{m/year}$ at 30°C and smaller than $1 \mu\text{m/y}$ at 80°C . For stainless steel the corrosion rate is $0.01 \mu\text{m/y}$ [Chambers et al., 1995]. Irradiation, in combination with elevated temperatures will have an effect on the corrosion process: increasing reactivity, making brittle, irradiation induced damage positions [Byalobzheskii, 1970]. Shoesmith et al. (1992) indicated a rise of the uniform corrosion rate of steel and iron with elevated dose rates (up to $3 - 10 \text{ Gy/h}$). According to Marsh et al. (1983) the corrosion rate in seawater, with an elevated temperature of 90°C , slightly rises up to $15 \mu\text{m/y}$ at a dose rate of 3 Gy/h . The uniform corrosion rate of a carbon steel container enclosing HLW is $1 \mu\text{m/y}$ at a dose rate of 3 Gy/h according to Gray and Doherty (1988). In alkaline and ventilated environments, such as concrete, and in absence of chloride ions, carbon steel gives proof of a very good corrosion resistance and can be seen as a passivated material. In the presence of large concentrations of chloride ions, there is a chance pitting will occur until all the oxygen is consumed, anaerobic conditions settle in, and pitting initiation and even propagation will disappear [Pourbaix and L'Hostis, 2006]. Localized corrosion of stainless steel under influence of gamma radiation can increase or decrease [Gray and Doherty, 1988].

Gas generation

A considerable amount of gas is produced inside the Supercontainer due to a variety of mechanisms: the corrosion of metals, organic degradation (production of carbon dioxide and methane), radiolysis, steam and water vapor production due to the heat-

emitting radioactive waste and the production of radioactive gasses [Ortiz et al., 2002]. The contribution of corrosion to the H₂ gas generation is assumed to be bigger than the contribution of the gas generation due to the radiolysis of the water. This postulate is determined for LLW and ILW, but can also be accepted for HLW. According to Biddle et al. (1987) approximately 2×10^5 m³ is created due to corrosion in a time span of 10 years. Due to radiolysis this amount is estimated at 3 m³.

The hydrogen, produced by the corrosion of steel, is generated at a rate equivalent to the corrosion rate (expressed in $\mu\text{m/y}$). This calculated amount of gas can be converted into the pressures (expressed in MPa) that would arise within the Supercontainer, in case of a closed configuration (a closed, non-perforated envelope). Pressure relief due to reactions between gasses and solids, and the possibility of the appearance of additional porosity (due to microcracking), are kept out of consideration. The following remarks can be mentioned [Wickham et al., 2005]:

- The higher the amount of initially unfilled porosity, the lower the calculated gas pressures. A drier concrete (more porous) might experience lower gas pressure than a wetter concrete.
- Approximately 800 years after emplacement of the Supercontainer in the galleries, thus assuming 300 years of oxidizing conditions followed by 500 years of anaerobic conditions, a total gas pressure of 2.6 MPa is calculated for a concrete with saturation degree of 40 %. A value of 4.2 MPa is noticed for a saturation degree of 75 %. This is in the same order of magnitude as the tensile strength of the considered concrete compositions for the buffer.
- The calculation results consider that any local H₂ pressure build-up would be negligible because the gas can diffuse away at a rate comparable to its production rate. In case the envelope becomes perforated, resaturation of the buffer will occur quickly. The rate of diffusive removal of hydrogen will exceed the gas production rate, and therefore no free gas phase or pressure build-up will occur in the Host Rock. An open envelope gives cause to a pressure relief: the produced gasses can escape through the buffer and the envelope.

3.3 Corrosion after penetration of external fluids

In case a dry concrete is being used for the buffer, pore water originating from the Host Rock can come in contact with the stainless steel envelope after migration through the concrete gallery blocks and the backfill. After penetrating the corroded steel envelope and after transport through the concrete buffer of the Supercontainer, the pore water reaches the carbon steel overpack. Therefore, a considerable time span is needed. This water will have a similar composition as the ground water but with a higher pH due to the high pH of the concrete buffer and filler.

Corrosion of the envelope depends on the rate of supply of potentially corrosive species to the envelope and the electrochemical potential of the envelope itself. Once the envelope is perforated, several potentially aggressive species can be introduced by

ingression of groundwater and give cause to further corrosion of the steel envelope and migration via diffusion of the aggressive species towards the overpack that can induce corrosion of the overpack: chlorides, bicarbonates, thiosulphates and sulphides. The concentrations of these ions can be estimated from their concentrations present in the pore water of the Host Rock.

Chloride

Chlorides can cause a break down of the passivating layer, and this can be a reason of corrosion of steel (deep pitting). Also different concentrations of chlorides among the length of a metallic surface can lead towards corrosion. Corrosion of stainless steel in alkaline environment is not expected though with chloride concentration between 25 mg/l and 400 mg/l determined in the pore water of the potential Boom Clay Host Rock. There is little to no risk of localised corrosion of the stainless steel envelope due to chloride attack because of the low chloride concentrations and because of the oxygen consumption leading to a drop in potential of the stainless steel which makes localised corrosion impossible ('near-perfect protection', [Wickham et al., 2005]).

The level of acceptable chloride concentrations is 10 times higher for stainless steel in comparison to carbon steel [Nürnberg, 1996]. The effect of chloride on the corrosion of carbon steel in concrete has been studied extensively previously (structures, roads, buildings in saline and marine environments). Experience suggests chloride levels exceeding 500 mg/l as a minimal chloride dose to initiate corrosion, a value much higher than the expected chloride concentrations in the pore water of the Supercontainer due to Boom Clay pore water infiltration.

Bicarbonate

Bicarbonate can react with cement and reduce the pH in the vicinity of the overpack. This carbonation process leads to a decrease in the amount of free lime Ca(OH)_2 and thus lowers the pH value:



If the carbonated zone reaches the metallic surfaces, the passivating layer is no longer stable and the steel becomes susceptible to corrosion. Calculations based on the amount of bicarbonate present in the Boom Clay pore water, on the diffusion coefficient of bicarbonate in concrete and based on the initial concrete composition, suggest that the pH of the buffer near the overpack will remain higher than 12.4 for several thousands of years at 25 °C and higher than 11 at 100 °C [Wang et al., 2004]. Stainless steel exhibits low corrosion rates because it has the ability to develop a passive layer even in neutral environments.

Sulphide

Three possible sources of sulphide can appear in the case of Boom Clay considered as the Host Rock for disposal: pyrite, microbial production of sulphide by sulphate reducing bacteria (SRB) and the possible reduction of thiosulphate by corroding iron. Boom Clay, that can be seen as a plastic self-sealing clay material, is expected to have insufficient available space in which significant active microbial populations could develop [Pedersen et al., 2000]. In addition, SRB activity may be suppressed if pore water sulphide concentrations rise far above 400 mg/l and SRB are also too large to be transported through pores of the Boom Clay.

A general good experience with stainless steel use in the oil and gas industry is available. The amount of sulphide at the overpack is expected to be very low due to the long period following the perforation of the envelope and transport by diffusion. However, there is currently not enough data to determine the possible effects of sulphide concerning the envelope corrosion and the corrosion of the overpack. Further studies are justified.

4 Water content and transport

The initial water content of the concrete buffer of the Supercontainer is an important parameter which has a considerable effect on the transport through the buffer. In case a relative dry concrete buffer is considered, a retardation effect of the migration of water through the buffer is expected. Calculations indicate that it will take several of hundreds to thousands of years for the harmful specimens to migrate through the concrete by means of diffusion [Wang et al., 2004]. CEA (Commissariat à l'Énergie Atomique) indicated a duration of 300 years for 90 % of the damaging substances deriving from the Host Rock to migrate through a cementitious layer of 10 cm by means of diffusion.

On the other hand, transport by means of capillarity can also occur. This type of transport has a much higher velocity. The influence of the different saturation degrees on the properties of the concrete buffer, is further explained in Chapter 5.

5 Redox and pH

5.1 Redox

Redox is an electrons exchanging reaction between molecules and/or ions, and in which atoms have their oxidation state changed. Redox is a contraction of reduction and oxidation:

- Oxidation describes the loss of electrons.
- Reduction describes the gain of electrons.

The reaction can take place in case an electrolyte is available for the transport of ions.

For the Supercontainer, the initial redox conditions are oxidizing (aerobe phase) after fabrication of the Supercontainer and emplacement in the galleries and closure with a backfill. Due to the consumption of O₂ in the disposal galleries (mainly due to the corrosion processes), anaerobic conditions will gradually settle in depending on the corrosion rate and the initial water content of the Supercontainer: the higher the water content, the higher the corrosion rate, thus the earlier the anaerobe (reducing) conditions start. Experience deriving from the Chunnel (the Channel Tunnel connecting France and Great Britain) show that the aerobe conditions last for about 10 to 15 years in water saturated systems. The analogy with the Supercontainer is only partly true. Nirex (1995) calculations indicate a fast development of the reducing anaerobe conditions for concrete containers surrounded by concrete backfills. Taking into account the corrosion and leaving out of consideration the radiolysis of the pore water due to irradiation, the estimations lead to a value of 10 years for the anaerobic state to settle in. The Supercontainer concept for HLW and SF, considering the corrosion processes and the radiolysis, maintains longer oxidizing circumstances: the radiolyse process produces hydrogen, oxygen and other oxidizing radicals. Concrete materials such as hematite and nitrite also can prolong the aerobe phase.

5.2 pH

The acidity of an aqueous solution can be expressed by means of the pH. Neutral solutions have a value of 7 at room temperature. Acid solutions have a lower pH, alkaline solutions have a higher pH.

The Supercontainer, with a composition chosen to create a favourable alkaline environment, will have a pH initially higher than 13. The portlandite Ca(OH)₂ is the main factor creating this highly alkaline conditions and thus acts as a pH buffer. At 25 °C the pH will have a value of approximately 12.4 and this value will be sustained for thousands of years after ingress of pore water originating from the Host Rock [Wang et al., 2004]. At elevated temperatures up to 100 °C, the pH buffered by the portlandite can drop to 11, due to changes in the solubility of the portlandite and the change in the water activity product with temperature.

6 Mechanical processes

The early-age behaviour of massive concrete structures has become increasingly important, and is the main scope of this research study. Massive hardening concrete elements are very prone to early-age thermal cracking due to the heat of hydration and early-age shrinkage (autogenous shrinkage) (Chapter 5). Concrete, characterized by a low tensile strength, can often not withstand the stresses created inside the massive structure. The service life of the concrete element, can be severely reduced by the presence of even small cracks [De Schutter, 2002]. Stresses leading towards cracking can be the result of different actions [Van Nieuwenburg, 1986]:

- Direct loading of structural elements.
- Restrained plastic shrinkage or settlement.
- Restrained deformation due to a thermal gradient or due to shrinkage (autogenous, drying, etc.).
- Forced displacement due to differential settlement of structural elements.
- Expansive forces inside the concrete due to corrosion, AAR, ettringite formation, etc.

During fabrication, transport and emplacement of the Supercontainer, the risk of cracking is existing and must be examined. Especially early-age cracking of the massive concrete buffer, during fabrication and due to the heat of hydration and the autogenous shrinkage of the cementitious material, is a topic worth considering. The heat-emitting canisters create a thermal gradient into the Supercontainer and thus thermal stresses appear into the concrete of the buffer (Phase 1 buffer, Phase 2 filler, Phase 3 lid). During transportation and emplacement of the Supercontainer in the disposal galleries, undesired circumstances can occur: horizontal fall, vertical fall in the shaft. This can also have a detrimental effect on the Supercontainer but lies out of the scope of this study. Microcracking of concrete is inevitable and therefore accepted. On the other hand, macrocracking, which will considerably ease the transport mechanisms inside the Supercontainer (especially in radial and axial direction), must be prevented at all times. Preferential paths for water inflow and radionuclides are not desired.

Lab tests, macro-scale tests and simulations are executed to predict the early-age behaviour of the concrete buffer of the Supercontainer during construction [Craeye et al., 2009]. The need of reinforcement to limit or better prevent early-age cracking must be evaluated. Preference is given to a massive concrete buffer without the use of additional reinforcement or steel fibers which can induce additional corrosion processes and linked gas pressure build-up. In case decent measures are taken, early-age cracking (macrocracks) of the concrete buffer is not expected during construction, even without the use of additional reinforcement. The subsequent chapters give a good overview of the performed tests (Chapter 6, Chapter 7, Chapter 9) and simulations (Chapter 8) to support the non-cracking postulate. After emplacement of the Supercontainer on the mechanical supports inside the disposal galleries, stresses will occur due to the weight of the Supercontainer and the backfill. At the support location, stress induced corrosion of the stainless steel envelope can appear.

7 Microbial activity

Assuming the nearby environment of a disposal site prevents the formation or the survival of microbial organisms is wrong. Several types of microbes have the ability to resist high radiation doses [Space Studies Board], and high pH environments and redox fronts are well known locations where microbial activity is significant [West et al., 1982, Mayfield and Barker, 1982, West and McKinley, 1985]. Their activity can be limited by a lack of available nutrients. Evaluations of the consequences of microbial activity on nuclear disposal galleries are available [McKinley et al., 1997]: in case of a simplified homogeneous disposal site for HLW, microbial activity can be neglected. According to a more complex model, that takes into account the alkaline plume and the redox fronts, the micro-organisms consume steel or produced H_2 (due to earlier corrosion or radiolysis) as an energy source. The presence of hydrogen gas is one requirement for the existence and survival of active microbial life.

Experimental proof is given of the natural presence of three types of bacteria into Boom Clay layers: methane forming bacteria (4.17a), sulphate reducing bacteria (SRB) (4.17b) and thiosulphate reducing bacteria (4.17c) [Ortiz et al., 2002]. These bacteria consume H_2 according to the following reactions [Madigan et al., 1997]:



A hydrogen source is necessary for the survival and the development of the micro-organisms. Micro-organisms can reduce important components of the ground water, and they can produce and consume gasses (Figure 4.18).

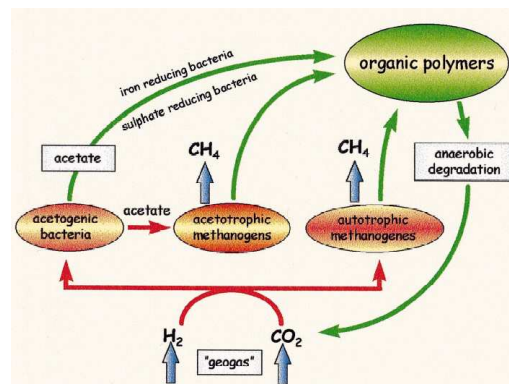


Figure 4.18: The underground biosphere in granite stone. H_2 and CO_2 are consumed as energy source [Pedersen, 1999]

Microbial activity has to be considered in the design of a disposal site for HLW and SF assemblies. The concrete buffer is expected to be fairly sterile initially, but will normally contain a few per cent sulphur of SO_3 , which can be assimilated by SRB. High concentrations of SRB have been observed in the Swiss Mont Terri research program. In repository environment, SRB may be one of the principal causes of the introduction of the reducing conditions [Wickham et al., 2005]. Some of the bacteria survive at high pH levels and reactions, such as the oxidation of H_2S to H_2SO_4 , and the reaction even is accelerated due to the high alkalinity [De Belie, 2007]. The presence of H_2S and H_2SO_4 (very low pH values may occur locally) can lead towards a significant deterioration of the concrete, the carbon steel overpack and the outer stainless steel envelope. Elevated temperatures have a beneficial effect on the sulphuric acid production. Ventilation can be required to release the H_2S and prevent H_2SO_4 production during the aerobic phase. Otherwise, the production of sulphuric acid is limited when the anaerobic conditions are initiated.

Herbert (2002) reviewed the potential microbial activity in the nearby environment of the Supercontainer and its disposal galleries with Boom Clay considered as the Host Rock. Three factors suggest that microbial activity within the Supercontainer will be negligible:

- The lack of sufficient nutrients for the microbes in the EBS give cause to a limited activity of the microbes, even though the microbes are known to persist at high pH.
- A considerable amount of time after placement of the Supercontainer, the temperature in the buffer will easily exceed values of 80 °C. At this temperature level, most of the thermophilic microbes are killed.
- The radiation inside the Supercontainer (average dose rates between 23 Gy/h and 0.1 Gy/h) also tend to kill or suppress the activity of any microbes present in the buffer.

8 Concrete mineralogy and degradation mechanisms

8.1 Concrete mineralogy

The basic constituents of most structural concretes are cement, water, coarse and fine aggregates, and some additives (superplasticizer, filler, fly ash, silica fume, etc.). Portland cement (OPC) is made primarily from a combination of calcareous material (limestone, chalk) and of silica and alumina found as clay or shale [De Belie, 2007]. Four minerals are regarded as the major constituents of OPC: the calcium silicates C_2S and C_3S (abbreviations: C = CaO, S = SiO₂, A = Al₂O₃, F = Fe₂O₃), the calcium aluminate C_3A and the tetracalcium alumino ferrite C_3AF .

The calcium silicates (70 % – 80 % of OPC) contribute most to the binding power and strength of concrete. The overall hydration reaction of both silicates leads to the formation of a calcium silicate hydrate gel, CSH, which is the main binding agent of the cement paste, and of crystalline calcium hydroxide Ca(OH)₂, contributing to the high pH of concrete and most easily leached from OPC in case of chemical attack. The CSH gel is metastable at lower temperatures and has a life span of thousands of years. At elevated temperatures, the gel transforms into a more stable, crystalline phase that leads towards an increased porosity of the concrete and thus more available space for any internally produced gasses [Wickham et al., 2005]. Portlandite resists temperatures up to 100 °C and its solubility diminishes with increasing temperatures [Wickham et al., 2005].

The reaction of C_3A with water is very rapid, leads to a quick evolution and considerable amount of heat is produced without the addition of gypsum. A high sulphate tricalcium sulphoaluminate, or ettringite, is formed. This component has little effect on the ultimate physical properties of concrete but is at most vulnerable to attack by sulphate solutions. Sulphate resisting OPC, called HSR (High Sulphate Resistance), has a low C_3A content (below 3 %), whereas normal OPC has an amount of about 8 % – 11 % of C_3A .

The C_4AF reacts at a slower rate and contributes little to the strength of the cement. In the reaction process Ca(OH)₂ is consumed.

8.2 Degradation mechanisms

Different types of concrete degradation can be distinguished [De Belie, 2007]:

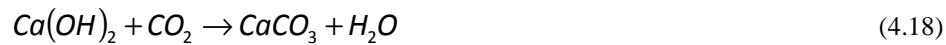
- According to the affected material: degradation of the concrete or degradation of the metallic elements in the concrete (indirect degradation)
- According to the cause: external cause (aggressive substances from the environment) or internal cause (impurities in the concrete itself)

- According to the reaction process: production of soluble salts leading towards decomposition of CSH or disruption due to swelling reactions caused by the formation of products with greater volume than the reactant material.

The vulnerability of concrete depends on its permeability, alkalinity and reactivity. The rate and the extent of attack are influenced by a variety of factors: the strength of the attacking medium, the pH, the physical state of the attacking medium, the temperature, the availability and replenishment of the aggressive medium, the pressure, the wetting conditions, etc. The transport properties (e.g. permeability) also have a decisive influence on the degradation mechanisms of concrete. Due to the large number of parameters influencing the transport properties, it is hard to fully understand and analyze the results and come to general conclusions. The W/C ratio, the degree of hydration and the type and amount of mineral addition strongly affect the transport mechanisms. Self-compacting mixes (e.g. SCC, Chapter 5) generally have a lower oxygen permeability coefficient and water sorptivity, depending on the used cement and filler type. The refined pore structure and the denser interfacial transition zone between the aggregates and the cement paste are the main contributors to the enhanced fluid transport resistance of SCC compared to a Traditional Vibrated Concrete (TVC) [RILEM Technical Committee, 2008].

Carbonation

The carbonation of concrete, influenced by the diffusion velocity and the presence of CO₂, leads to a decrease in the amount of portlandite and thus a decrease in pH:



The proceeding of this process depends on the amount of available materials susceptible to carbonation: the more CSH and Ca(OH)₂ present in the concrete (especially present in SCC), the lower the carbonation depth. If the carbonation zone reaches the metals imbedded in the concrete, the passivating layer on top of the metals becomes unstable and the metal becomes susceptible to corrosion. In general it seems that the carbonation rate of SCC is comparable to that of a Traditional Vibrated Concrete (TVC) [Audenaert, 2006]. The denser pore structure, often found in SCC due to the larger amount of fine particles, leads to a reduction of the carbonation depth. The smaller the porosity, the lower the diffusion velocity. A slightly higher vulnerability can be noticed with SCC containing limestone filler.

Acid attack

Acidic substances attacking concrete, being an alkaline material, cause leaching of the portlandite Ca(OH)₂ to restore the equilibrium. The porosity of the concrete increases and the pH drops. The hydrates of the hardened cement paste decompose and the concrete loses its strength and disintegrates. The rate of degradation by acid attack depends on the preceding carbonation process. The produced CaCO₃ is relatively

insoluble and may block the concrete pores, slowing down the degradation processes due to acid attack (the infiltration of the acid is slowed down). It must be noticed that even water, having a smaller pH than concrete, can be seen as an acid towards concrete degradation.

Attack by salts

The salts of Mg^{2+} , NH_4^+ , NO_3^- and Cl^- (salt attack) react with the free lime of the concrete (portlandite) and produce a quite soluble calcium salt, which can be leached. $Mg(OH)_2$ is a solid blocking the pores and slowing down further attack and causing a decrease of the pH in the pore solution, making the CSH unstable creating magnesium silicate hydrates with no binding capacity.

Ammonium salts are even more detrimental to concrete than magnesium salts because pore blocking is no longer possible. These reactions will not come to an equilibrium unless one of the reacting elements (the portlandite or the salt) is completely used.

The effect of chlorides on the concrete itself is not often discussed. Known consequences are the production of unstable water soluble compounds when reacting with portlandite, the formation of expansive Friedel salts due to the reaction with C_3A or the production of calcium oxychlorides [De Belie, 2007]. The increased risk of corrosion of embedded metals, however, is the best known effect of chlorides when present in concrete. Chloride ions can break down the passivating layer of the metals by forming the soluble $FeCl_3$. SCC containing a higher volume of powder and an additional amount of admixtures has an altered chloride binding behaviour towards chloride attack than TVC due to the different pore volumes and the different ionic compositions. The chloride diffusivity is highly dependent on the type of cement and the additional powder added to the mixture.

Sulphates can cause the formation of the soluble $CaSO_4$ salts which can be leached or react with C_3A to form ettringite, leading to expansive internal concrete forces (cracks), due to the high water consumption ability of the ettringite. Physical resistance to sulphate attack is especially important, as it may be seen as one of the main factors which differentiates SCC from TVC [RILEM Technical Committee, 2008]. Factors influencing the sulphate attack are once again the type and the amount of added fillers, the type of cement and the composition of the sulphate solution. The denser microstructure of SCC prolongs the initiation time for sulphate attack in SCC. On the other hand, the higher the amount of used limestone, the more vulnerable the SCC is to the thaumasite form of sulphate attack (TSA) [RILEM Technical Committee, 2008]. Sulphate concentrations between 700 mg/l and 1400 mg/l $MgSO_4$ promote TSA in approximately five years. The use of sulphate resisting cement makes the degree of attack smaller and the rate slower, in case TSA is expected. Addition of pozzolanic material (fly ash, silica fume, blast furnace slag) to the mixture, to reduce the pore size and densify the microstructure, can lead towards TSA due to the reactive components (Si, Al) present in these materials.

Sugars (retarding effect on the hardening of the cement paste), fats, tars and oils can also attack a concrete material.

Alkali aggregate reaction

If alkali metal hydroxides, reactive siliceous aggregates and water are present in a concrete mixture, a chemical reaction can occur, at which the alkali metal hydroxides in the pore water of the cement paste attack the reactive silica to give a gel of alkali silicates. The alkali aggregate reaction (AAR), also known as the alkali silica reaction (ASR), is an expansive reaction that occurs between certain types of reactive aggregates and alkali metal hydroxides available in the cement clinkers. The reaction products have the ability to absorb water, grow in volume and cause swelling pressure within concrete. Therefore, a careful and well considered selection of the main constituents of the concrete mixture can avoid AAR.

Frost and thaw

Saturated concrete is vulnerable to frost because of the expansion of water during freezing [De Belie, 2007]. These expansive forces can induce an internal pressure inside the saturated concrete exceeding the tensile strength values and this can cause cracking of the concrete. High quality concrete and concrete with small porosity are quite resistant to frost because of the lowered freezing point of water in small concrete pores. The addition of an air entrainment agent can overcome the frost and thaw cracking risk.

Degradation of concrete in saturated environment

Several studies are conducted by CEA, dealing with the degradation of concrete in water saturated environments. Different types of water are considered:

- De-ionized water
- Water containing bicarbonate
- Water containing sulphates

The leached Ca^{2+} and OH^- ions are measured and the concrete is being analyzed three months after immersion. Higher temperatures lead to higher leaching rates, an increase of pH counteracts the degradation of the concrete.

Under influence of de-ionized water, the eroded outer surface of the concrete has a zone rich in aluminum and silicates, a zone of CSH and a zone of CSH with ettringite. The porosity increases in the degraded zones.

In the presence of bicarbonate, as in the case of the Boom Clay pore water (composition of NaHCO_3), the concrete will create a calcareous crust on top of a dense layer of calcite (CaCO_3) and CSH. The calcite precipitates in the pores and creates a

stoppage. In some cases, in aggressive environments such as heated Boom Clay, CO_2 is found in the pore water, hindering the formation of the protective calcite layer.

Sulphates create a potential risk of cracking (perpendicular to the outer surface) and spalling (parallel to the outer surface), in case reactive cements (high C_3A content) are used. Clay, and for example Boom Clay, has a rather low sulphate content and OPC with high sulphate resistance (HSR) is being considered in practice, in which case cracking is not expected.

References

Abe H., Kawahara T., Ito T., Haraguchi A. (1972), *Concrete for Nuclear Reactors*, ACI Speciam Publ. No 34, Vol. 2, Paper SP34-40, p. 847, American Concrete institute, Detroit.

AEA Technology (2004), *The anaerobic corrosion of carbon and stainless steels in simulated cementitious repository environments: a summary review of Nirex Research*, AEA Technology Report No. AEAT/ERRA-0313.

Arioz O. (2007), *Effects of elevated temperatures on properties of concrete*, Fire safety Journal 42 516-522.

Audenaert K. (2006), *Transport mechanisms in Self-Compacting Concrete in relation with carbonation and chloride penetration*, doctoral thesis (in Dutch), Ghent University, Magnel Laboratory for Concrete Research, Belgium.

Bar-Nes G., Katz A., Peled Y., Zeiri Y. (2008), *The combined effect of radiation and carbonation on the immobilization of Sr and Cs ions in cementitious pastes*, Materials and Structures 41, 1563-1570.

Biddle P., McGahan D., Rees J.H., Rushbrook P.E. (1987), *Gas generation in Repositories*, UKAEA Report AERE-R, 12291.

Boel V. (2006), *Microstructure of a Self-Compacting Concrete in relation to gaspermeability and durability aspects*, Ghent University, Magnel Laboratory for Concrete Research, Belgium.

Both J.P., Mazzolo A., Penelieu Y., Petit O., Roesslinger B. (2003), *Notice d' utilisation du code TRIPOLI-4, version 4.3 : code de transport de particules par la méthode de Monte Carlo*, Rapport CEA, R-6043.

Bouniol P., Aspart A. (1998), *Disappearance of oxygen in concrete under irradiation: the role of peroxides in radiolysis*, Cement and Concrete Research, Vol. 28, No. 11, pp. 1669-1681.

Bouniol P., Bjerbakke E. (2008), *A comprehensive model to describe radiolytic processes in cement medium*, Journal of nuclear materials, 372 1-15.

Bouniol P. (2004), *État des connaissances sur la radiolyse de l'eau dans les colis de déchets cimentés et son approche par simulation*, Rapport CEA, R-6069.

Burns W.G., Henshaw J., Walters W.S., Williams S.J. (2003), *Possible effects of radiolysis in the near field*, AEA Technology report AEAT/R/ENV/0239.

Byalobzheskii A.V. (1970), *Radiation Corrosion*, Nauka, Moscow, AEC-tr 7096.

Cai Z., Li X., Katsumura Y., Urabe O. (2001), *Radiolysis of bicarbonate and carbonate aqueous solutions: product analysis and simulation of radiolytic processes*, Nuclear Technology 136, 231-240.

Chambers A.V., Williams S.J., Wisbey S.J. (1995), *Nirex near-field research: report on current status in 1994*, Nirex Science Report S/95/011.

Chang Y.N., Peng G.F., Anson M. (1999), *Residual strength and pore structure of high strength concrete and normal strength concrete after exposure to high temperatures*, Cement & Concrete Composites, 21-23.

Craeye B., De Schutter G., Van Humbeeck H., Van Cotthem A. (2009), *Early age behaviour of concrete supercontainers for radioactive waste disposal*, Nuclear Engineering and Design 239, 23-35.

De Belie N. (2007), *Durability of Concrete*, Magel Laboratory for Concrete Research, Ghent University.

De Schutter G. (2002), *Finite element simulation of thermal cracking in massive hardening concrete elements using degree of hydration based material laws*, Computers & Structures 80, 2035-2042.

Elluch L.F., Dubois F., Rappeneau J. (1972), A Concrete Institute Special Publication 34, p.1071.

Gens R., Bel J., Pourbaix A., Hélie M., Wickhal S., Bennett D. (2006), *Corrosion processes and the expected evolution of the BSC-1 Supercontainer design for disposal of Belgian HLW and spent fuel*, NUCPERF 2006 – EFC Event 284.

Gray W.J., Doherty A.L. (1988), *Assessment of the significance of gamma radiolysis on uniform corrosion of container materials: salt repository project*, Pacific Northwest Laboratory Report PNL/SRP-6663.

Harwathy T.Z. (1970), ASTM J. of Materials 5, 47.

Herbert B.N. (2002), *The potential for microbial activity affecting the integrity of buried high level radioactive waste in the Boom Clay at Mol, Belgium*, Unpublished ONDRAF/NIRAS Report.

Ichikawa T., Koizumi H. (2002), *Possibility of radiation-induced degradation of concrete by alkali-silica reaction of aggregates*, Journal of Nuclear Science and Technology, Vol. 39, No. 8, p. 880-884.

Kaplan M.F. (1987), *Concrete Radiation Shielding – Nuclear Physics, Concrete Properties, Design and Construction*, Longman Scientific & Technical, England, 457pp.

Kelly B.T., Davidson I. (1969), 2nd Conference on Prestressed Concrete Pressure Vessels and Their Insulation, p. 237, London.

Kirkegaard P., Bjergbakke E. (2005), *CHEMISUL: a simulator for chemical kinetics*, Report Risoe-R-1085 (Ed.2) (EN), Risoe National Laboratory.

Lewis M.A., Warren D.W. (1990), *The use of additives for reducing hydrogen yield in mortar containing slag and chloride salts*, Scientific Basis for Nuclear Waste Management XIII, 53-60.

Liu X. (2006), *Microstructural investigation of Self-Compacting Concrete and High-Performance Concrete during hydration and after exposure to high temperatures*, Doctoral thesis, Magnel Laboratory for Concrete Research, Ghent University, Belgium.

Madigan M.T., Martinko K.M., Parker J. (1997), *Biology of Micro-organisms: Prentice-Hall*, Englewood Cliffs.

Madic C., Koehly G. (1986), *Comportement à long terme des matrices d'enrobage contaminées en émetteurs alpha : étude de phénomène de rupture d'éprouvettes constituées de liants hydrauliques contaminés en plutonium 238 et curium 244 au cours de leur lixiviation*, Rapport interne CEA DGR/134.

Maréchal J.-C. (1970), *Contribution à l'étude des propriétés thermiques et mécaniques du béton en fonction de la température*, Annales de L'Institut Technique du Bâtiment et des Travaux Publics, N°274, pp. 122-147.

Marsh G.P., Bland I.D., Desport J.A., Naish C., Westcott C., Taylor K.J. (1983), *Corrosion assessment of metal overpacks for radioactive waste disposal*, European Applied Res. Reports – Nuclear Science Technology 5, 223-252.

Mayfield C.I., Barker J.F. (1982), *An evaluation of microbiological activities and possible consequences in a fuel waste disposal vault – literature review*, Atomic Energy of Canada Ltd. Report TR-139, Chalk River.

McKinley I.G., Hagenlocher I., Alexander W.R., Schwyn B. (1997), *Microbiology in nuclear waste disposal: interfaces and reaction fronts*, FEMS Microbiology Reviews 20, 545-556.

Möckel H.J., Köster R.H. (1982), *Gas formation during the gamma radiolysis of cemented low an intermediate level waste products*, Nuclear Technology 59, 494-497.

Morigani S. (1997), Preprint East Asia Alkali-Aggregate Reaction Seminar, p.101, Tottori, Japan.

Mounajed G., Obeid W. (2001), *Modélisation du comportement thermo-hygro-mécanique des bétons à haute température*, Rapport d'Etude BHP 2000, CSTB, 55 pp.

Nirex. (1995), *The evolution of the Eh in the pore water of a radioactive waste repository*, Nirex report NSS/R374.

Nürnberg U. (1996), *Stainless steel in concrete*, State of the Art Report, Institute of Materials, EFC no. 18, London.

Ortiz L., Volckaert G., Mallants D. (2002), *Gas generation and migration in Boom Clay, a potential host rock formation for nuclear waste storage*, Engineering geology 64, 287-296.

Pachner J. (1998), IAEA-TECDOC-1025, IAEA, Vienna.

Palmer J.D., Fairhall G.A. (1993), *The radiation stability of ground granulated blast furnace slag / ordinary Portland cement grouts containing organic admixtures*, Scientific Basis for Nuclear Waste Management XVI, 285-290.

Pedersen K. (1999), *Subterranean microorganisms and radioactive waste disposal in Sweden*, Engineering Geology 52, 163-176.

Pedersen K., Motamedi M., Karnland O., Sanden T. (2000), *Mixing and sulphate-reducing activity of bacteria in swelling compacted bentonite clay under high-level radioactive waste repository conditions*, J. Appl. Microbiol. 89, 1038-1047.

Piasta J., Sawicz Z., Rudzinski L. (1984), *Changes in structure of hardened cement paste due to high temperature*, Material Constructions 17100, 291-6.

Pourbaix A., L'Hostis V. (2006), *Passivation, localised corrosion and general corrosion of steel in concrete and bentonite. Theory and experimental*, NUCPERF 2006 – EFC Event 284.

Poyet S. (2007), *Design of the ONDRAF Supercontainer concept for vitrified HLW disposal in Belgium: study of the thermo-hydrological behaviour of the concrete buffer*, Rapport CEA, RT DPC/SCCME/07-741-7.

Put M., Henrion P. (1992), *Modelling of radionuclide migration and heat transport from an HLW-repository in Boom Clay*, EC, Nuclear Science and Technology, Luxembourg, EUR 14156.

Richardson I.G., Groves G.W., Wilding C.R. (1990), *Effect of γ -irradiation on the microstructure and microchemistry of ggbs/OPC cement blends*, Proceedings of the Materials Research Society Symposium, Vol. 176.

RILEM Technical Committee. (2008), *Final report of RILEM TC 205-DSC: durability of self-compacting concrete*, Materials and Structures 41, 225-233.

Saad M., Abo-El Enein S.A., Hanna G.B., Kotkata M.F. (1996), *Effect of temperature on physical and mechanical properties of concrete containing silica fume*, Cement and Concrete Research 26, 669-675.

Savva A., Manita P., Sideris K.K. (2005), *Influence of elevated temperatures on the mechanical properties of blended cement concretes prepared with limestone and siliceous aggregates*, Cement & Concrete Composites 27, 239-248.

Schorr V.W., Duschner H., Starke K. (1979), *The generation of radiolysis gases from low and medium level radioactive waste solidification products*, Atomkernenergie 33, 265-269.

Shoesmith D.W., Ikeda B.M., King F. (1992), *Effect of radiation on the corrosion of candidate materials for nuclear waste containers*, Scientific Basis for Nuclear Waste Management XV, 407-414.

Space Studies Board, *Biological Contamination of Mars. Issues and Recommendations, Chapter 4, Limits of Life on Earth: Expansion of the Microbial World and Detection of Life*, National Academy of Sciences.

Taerwe L. (1997), *Concrete Technology*, Course material (in Dutch), Ghent University, Mangel Laboratory for Concrete Research, Belgium.

Van Nieuwenburg D. (1986), *Influence of cracking and the purpose of the concrete cover*, Faculty of Engineering, Ghent University.

Vodák F., Cerny R., Drchalova J., Kapicková O., Hosková S., Michalko O., Semerak P., Toman J. (1997), *Thermophysical properties of concrete for nuclear safety related structures*, Cement and Concrete Research 27, 415-426.

Vodák F., Trík K., Kapicková O., Hosková S., Demo P. (2004), *The effect of temperature on strength porosity relationship for concrete*, Construction and Building Materials 18, 529-534.

Vodák F., Trík K., Sopko V., Kapicková O., Demo P. (2005), *Effect of γ irradiation on strength of concrete for nuclear-safety structures*, Cement and Concrete Research 35, 1447-1451.

Wang L., Volckaert G., De Canière P. (2004), *A scoping calculation on the evolution of pH within the supercontainer*, Summary produced for ONDRAF/NIRAS workshop, SCK-CEN.

Weetjens E., Sillen X. (2006), *Thermal analysis of the Supercontainer concept 2D axisymmetrical heat transport calculations*, SCK-CEN report, Belgium.

Welty J.R., Wicks C.E., Wilson R.E., Rorrer G.L. (2000), *Fundamentals of Momentum, Heat and Mass Transfer*, John Wiley & Sons Inc., New York, Fourth Edition, 201-224.

West J.M., McKinley I.G. (1985), *The geomicrobiology of nuclear waste disposal*, Science Basis Nuclear Waste Management VII, 487-494.

West J.M., McKinley I.G., Chapman N.A. (1982), *Microbes in deep geological systems and their possible influence on radioactive waste disposal*, Radioactive Waste Management Nuclear Fuel Cycle 3,1-15.

Wickham S.M., Bennett D.G., Crawford M.B., Pourbaix A. (2004), *Supercontainer Conceptual Model. Information to support a workshop on the evolution of OPC Buffer and steel corrosion in the Belgian Supercontainer Design for HLW/Spent Fuel Disposal*, Galson Sciences Limited, Report no 0427.

Wickham S.M., Bennett D.G., Galson D.A. (2005), *Belgian Supercontainer Design for HLW and Spent Fuel Disposal. Evaluation of the Reference Design*, Galson Sciences Limited, Report no 0460-5.

Wilding C.R., Phillips D., Lyon C.E. (1989), *The effects of Radiation on Intermediate Level Wasteforms*, Scientific Basis for Nuclear Waste Management XII, Pittsburgh, 513-578.

CHAPTER 5:

REFERENCE CONCRETE COMPOSITIONS

Two types of concrete are considered for the cementitious buffer around the overpack of the Supercontainer: a Self-Compacting Concrete (SCC) [De Schutter et al., 2008] and a Traditional Vibrated Concrete (TVC). This buffer must provide sufficient radiological attenuation and protection against gamma photons. Other requirements are the creation of a favourable chemical environment (high pH, long term safety) and the guaranty of operational safety during transportation. Preference is given to the use of SCC because it will ease considerably the precast process and complies with all other requirements regarding compressive strength, long term durability, chemical interactions, etc.

In this chapter, the process of choosing a reference composition for the SCC and TVC will be explained, taking into account the early-age behaviour of massive concrete structures and the restrictions the compositions are exposed to. The formulated requirements differ, at least for some points, significantly from those frequently used in classical structures. Consequently, an appropriate choice for cement, aggregates and superplasticizer results from these requirements.

1 Early-age behaviour of massive concrete

1.1 Introduction

The early-age behaviour of massive concrete structures has become increasingly important. Massive hardening concrete elements are very prone to early-age thermal cracking especially due to the heat of hydration. The service life of the concrete element can be severely reduced by the presence of even small thermal cracks [De Schutter, 2002]. Cracks can be seen as preferential pathways for water, acids, salts and other aggressive species that can be introduced into the concrete element and (negatively) affect the durability of the concrete (Chapter 4).

1.2 Properties of young concrete

Initially, when water comes into contact with the cement grains of a concrete mixture, there is no significant activity. This period is better known as the induction period or the dormant phase. The concrete specimen remains plastic and is easily processable but has no strength or stiffness. After a certain time, the dormant phase has passed, and the concrete mixture gains additional stiffness and gradually loses its processability. This is the start of the setting. Afterwards the stiffness increases and the mixture develops into a solid body with an initial strength. This is the end of setting. Now the concrete mixture starts to harden and the strength of the concrete increases. It is desirable that the dormant phase is long enough to handle the fresh concrete for placement into the formwork (good workability). On the other hand, the final setting time may not occur too late in order to reduce the casting time and reduce the time of completion. The strength and stiffness development of a hardening concrete, the ultimate strain and deformation capacity are important properties of a young and developing concrete [De Schutter, 1996].

Development of strength

The strength development of a hardening concrete can be related to time or even better to the maturity of the concrete, giving the linked effect of time and temperature. Alternatively, the strength development can be expressed as a function of the degree of hydration. The degree of hydration can be defined as the relative amount of cement that has already reacted with the added water [De Schutter, 2002]. It ranges between zero at the very beginning of the reaction (when the water and the cement are initially brought together), and one when all cement in the concrete has reacted: an ideal situation that never occurs in real concrete structures. For real concrete, an ultimate degree of hydration is taken into account, with a value lower than one.

The compressive strength f_c increases with increasing hydration degree, and this in a linear way (Figure 5.1). The strength development starts after the induction period is over. In case of a lower W/C ratio, less water is available for the cement grains to hydrate, but also a more dense configuration of these grains is obtained. The distance between the cement grains is smaller, leading to a reduced dormant period and thus a quicker start of the hydration reaction. A less porous structure with higher strength is obtained in case of a lower W/C ratio. On the other hand a lower ultimate degree of hydration is received.

Similar conclusions can be drawn for the tensile strength f_{ct} development, this time with a more parabolic progress of the tensile strength with the hydration degree. Normally, the development of tensile strength is a slightly faster in comparison to the compressive strength development [De Schutter, 1996].

Development of stiffness

The development of the modulus of elasticity E_c goes in a more non-linear way (Figure 5.1). The stiffness develops faster than the compressive strength. At a young age, considerable stresses can arise in concrete structures due to thermal effects or shrinkage, which can lead to a noticeable cracking risk.

The stiffness and the tensile strength of concrete develop with time. At early age, they have a rather small value. The modulus of elasticity develops faster than the tensile strength, giving cause to a critical phase where the induced stresses can exceed the tensile strength and can cause cracking. The development of strength and stiffness starts once the induction period is over (Figure 5.1), and the setting time is reached (time zero). A synonym of this induction period or dormant phase is the ‘percolation threshold’ (Chapter 6).

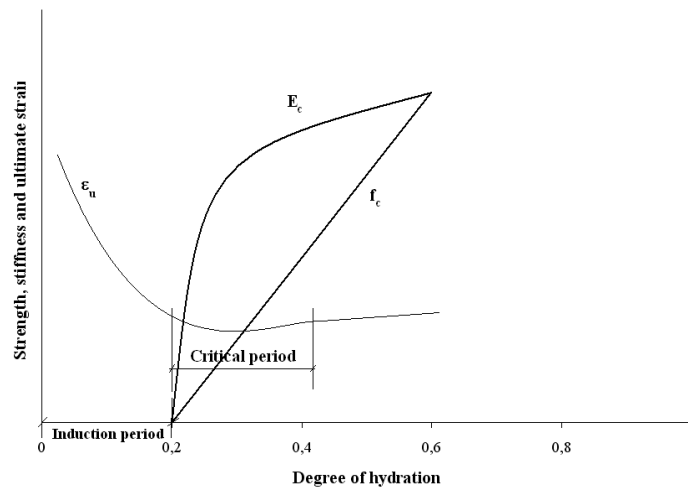


Figure 5.1: Development of strength and stiffness of concrete [De Schutter, 1996]

Ultimate strain

As mentioned previously: the strength and stiffness of concrete increase with time, while the deformation capacity decreases (Figure 5.1). The ultimate strain ϵ_u reaches its minimum after approximately 2 hours to 20 hours. In this critical period, the concrete is very prone to crack formation, and special concern needs to be given to the curing of the freshly cast concrete. When the critical period is over, the increasing strength and the increasing ultimate strain lead towards a diminishing cracking risk.

It must be noted that young concrete has great plastic and creep deformation possibilities and shows notable stress relaxation, giving a considerable stress relief compared to elastic simulations [De Schutter, 1996].

1.3 Crack creating actions

1.3.1 *Situation*

The relatively low tensile strength of concrete causes the high early-age cracking risk of young developing concrete. In general, stresses leading towards crack formation can be caused by several crack creating actions [Van Nieuwenburg, 1986]:

- Prevented plastic deformation (setting, swelling or shrinkage) of fresh concrete.
- Prevented deformation due to thermal gradients or shrinkage.
- Forced deformations due to differential setting of structural elements.
- Direct loading of structural elements.
- Internal pressure due to the expansion of corroded reinforcement, or due to the ASR gels that can be internally formed inside the concrete and create considerable internal stresses.

In the Supercontainer case, no additional reinforcement inside the concrete buffer is desired, due to the additional corrosion risk (Chapter 4). Cracks due to shrinkage, setting and swelling of the concrete and cracks due to thermal stresses have a significant effect on the early-age behaviour of a concrete buffer and therefore will be discussed subsequently.

1.3.2 *Shrinkage of concrete*

Shrinkage can be seen as a volume reduction caused by the evaporation of water and in a smaller extent caused by the hydration reaction and even the carbonation reaction of concrete. Too much shrinkage can severely compromise the concrete's durability by increasing the concrete's cracking risk. Five types of shrinkage can be distinguished, with a different nature but with a cumulative effect [De Schutter, 2005]:

- Plastic shrinkage due to evaporation of water out of the plastic fresh concrete. A couple of hours after casting, plastic cracking can occur. If the amount of evaporated water exceeds the amount of bleeding water, capillary forces are induced. If the decrease of volume is prevented by the environment of the surface of a structure or due to the internal restraint, tensile forces and irregular cracks appear.
- Drying shrinkage of hardened concrete caused by evaporation of water due to differences in relative humidity between the concrete and its environment. This leads towards the evaporation of the free capillary water due to the development of internal capillary under-pressure. This causes a minor shrinkage. Afterwards (after a longer period of time, mostly for hardened concrete), a difference in relative humidity exists inside the concrete, and the physically bond water will disappear and lead to higher deformations. This shrinkage has a slight irreversible character.
- Autogenous shrinkage due to the self-desiccation of the fresh concrete (there is a lack of water during the cement hydration) and due to the smaller volume of hydrated cement and the formed reaction products compared to the original volume of the unreacted cement and the water at younger age [Craeye, 2006].

Autogenous shrinkage is a macroscopic volume change occurring with no moisture transferred to the exterior surrounding environment and is a result of the internal volume reduction linked with the hydration of cement particles, i.e. chemical shrinkage [Holt and Leivo, 2004]. The processes of self-desiccation and chemical shrinkage should not be interchanged: self-desiccation causes long-term autogenous shrinkage due to differences in internal relative humidity during hydration where chemical shrinkage is due to the hydration products consuming less space than the initial products.

- Shrinkage due to the carbonation of hardened concrete. The formed products, such as calcite, have a smaller volume than the concrete not yet affected by carbonation.
- Thermal shrinkage due to the thermal gradients inside the concrete (see further).

Another way to distinguish the shrinkage of concrete is by looking at its appearing stage: early and later age [Holt and Leivo, 2004]. The early age is defined as the first day, while the concrete is setting and starts to harden. Three types of shrinkage can be noticed at this early age: (i) autogenous, (ii) drying and (iii) thermal shrinkage. The later ages refer to an age of 24 hours and beyond, and the same three types of shrinkage can occur with addition of a fourth type of shrinkage: carbonation shrinkage (Figure 5.2).

The drying shrinkage especially is affected by the surrounding environmental conditions (temperature, relative humidity and wind velocity). An increase of evaporation of free water of the fresh and hardening concrete goes along with an increase in magnitude of early-age drying shrinkage.

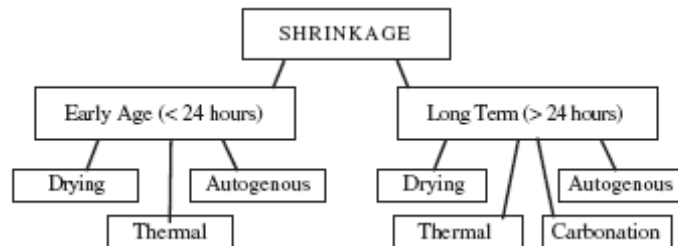


Figure 5.2: Shrinkage types and stages according to [Holt and Leivo, 2004]

Therefore, in practice, it is very important to optimize the curing conditions in such a way that evaporation and drying shrinkage can be totally eliminated. Suggested measures are listed below.

These curing measures must be taken as soon as possible [Holt and Leivo, 2004]:

- The use of evaporation retarders.
- Curing of concrete under water.
- Maintenance of high humidity by applying a fog spray or covering by means of plastic or humid sand.
- Lowering the wind speed by using wind breaking advices.
- In warm conditions: keep the concrete cool to encourage condensation.
- In cold conditions: keep the concrete warm to accelerate setting.
- The overdose use of superplasticizers will retard the setting.

In case decent curing measures are taken, preferably under water curing, only the autogenous shrinkage has to be taken into account for the early-age behaviour of the concrete buffer of the Supercontainer. In case excellent evaporation limiting techniques are used, the only shrinkage stresses at early age will be attributed to autogenous deformations. In that case, mainly the material properties affect the shrinkage [Craeye, 2006, Holt and Leivo, 2004, Igarashi et al., 2000]. The main parameters are the amount of water and the amount and the type of cement and admixtures in the mixture. Some findings concerning the autogenous shrinkage are listed below:

- The increased use of superplasticizers, and thus a lower W/C ratio, will increase the autogenous shrinkage and will delay the setting time of the concrete. Also the dispersion of the cement is improved and therefore provides a quicker chemical reaction.
- A lower W/C ratio and the use of silica fume and other pore refining admixtures will create finer pores. These finer pores experience a higher internal capillary pressure resulting in a greater autogenous shrinkage.
- Mixtures made with a rapid hardening cement, or with a high C_3A content, have autogenous shrinkage with faster development and with greater magnitude. Therefore, it is better to use slower hydrating cements that have lower chemical shrinkage.
- Aggregates restrain the autogenous shrinkage, so the amount of aggregates should be maximized to reduce the cracking risk.
- Bleeding is acceptable as the expansive deformation can act as antipole for the autogenous shrinkage.

Overall it can be concluded that the total shrinkage increases with increasing W/C ratio (higher drying shrinkage) and increasing cement amount for a given W/C ratio. For autogenous shrinkage, it is the other way around: the lower the W/C ratio, the higher the autogenous shrinkage [Craeye, 2006].

Holt and Leivo (2004) have defined various scenarios for early-age drying and autogenous shrinkage. If a W/C ratio in excess of 0.45 is used, no cracking is expected in case of a good and early curing and in case of high bleeding. In case the setting time is delayed (for example by using a considerable amount of superplasticizer), the cracking risk remains low. A poor curing scenario with high evaporation obviously increases the cracking risk.

1.3.3 Creep of concrete

Creep is the increasing deformation in time due to an applied constant load. An additional amount of physically bond water can be driven out of the hydrating layers (seepage) due to the application of a compressive load. Also a distinction can be made between autogenous or basic creep and drying creep [Vuylsteke, 2003].

1.3.4 Plastic settlement of fresh concrete

Finally, plastic setting of the aggregates in a very liquid concrete due to gravity can be disturbed by reinforcement or formwork. Gravity attracts the heaviest concrete particles in the fresh concrete and the water will rise in the direction of the top surface (bleeding). This can also lead to the formation of cracks if this deformation is prevented by the formwork or by the reinforcement.

1.3.5 Thermal stresses

Thermal stresses are mainly caused by the exothermal behaviour of the hydration of the cement present in concrete after contact with water. At the edges and the outer surface of a massive concrete structure, heat energy can easily be exchanged with the environment. On the other hand, the temperature inside the concrete structure increases. Taking into account the rather small heat conduction capacity of concrete, the concrete in the core of a massive element obtains a higher temperature in comparison with the concrete near the outer surface of the element (convective heat transfer). This induces a thermal gradient, leading to a tendency of the core to expand more than the outer surface. This effect is strengthened by the fact that the hydration reaction goes faster at elevated temperatures. This can cause a rather large thermal expansion. Due to the coherence of the concrete, this differential deformation partly is prevented, giving cause to a stress build-up: compressive stresses in the core and tensile stresses near the outer surface (Figure 5.3). The concrete is in an insufficient state of hardening and has a large deformation capacity and relaxation, which reduces the created stresses. This relaxation leads to a smaller cracking risk at the outer surface of massive concrete elements during the hydration heating phase, although cracking can occur. Cooling down of the concrete can also create cracks. At that time, the concrete has a proper hardening state with a minimal plastic deformation capacity. Also Young's modulus has increased and the relaxation is diminished. The core of the concrete undergoes a greater temperature drop compared to the outer surfaces, wants to shrink more, creating tensile stresses in the core and compressive stresses at the edges of the element (Figure 5.1, Figure 5.3) [De Schutter, 1996, Hamfler, 1988].

1.4 Early-age cracking of concrete

Concrete is characterized by a low tensile strength. Especially young concrete is very sensitive to crack formation. During the early hours, thus immediately after casting, concrete has the lowest strain capacity (Figure 5.1) and is most sensitive to internal stresses. Is the tensile strength, at any time, greater than the tensile stress, then no cracking is expected.

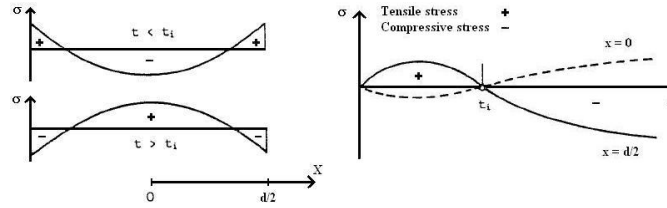


Figure 5.3: Stress development in concrete section, t_i is the time between heating and cooling (core: $x = 0$, outer surface: $x = d/2$) [De Schutter, 1996]

In that case, the thermal stresses remain in the concrete element as eigenstresses. In case the tensile stress exceeds the tensile strength, cracks will occur (Figure 5.4). This crack formation can occur in two cases: (i) during the heating of the concrete, the tensile stresses at the outer surface locally can exceed the tensile strength. The resulting cracks are visibly noticeable. The type of formwork and a judicious demoulding of the element can prevent crack formation. (ii) It is very hard, or even impossible to observe internal cracks created in the core of the concrete element during cooling. In this case, numerical simulations are needed to bring clearance. The compressive stresses, caused by the cooling down of the structure, can close the created cracks created during heating. Stresses that lead to cracks in concrete can be caused by different actions such as direct loading, prevented shrinkage and swelling, differential settings, etc. The thermal gradient between the core and the outer surface of the concrete can be seen as a very important parameter on behalf of the early-age behaviour of hardening concrete [De Schutter, 1996]. If movement is prevented by the environment of the surface of a structure, tensile forces are induced and cracks can appear.

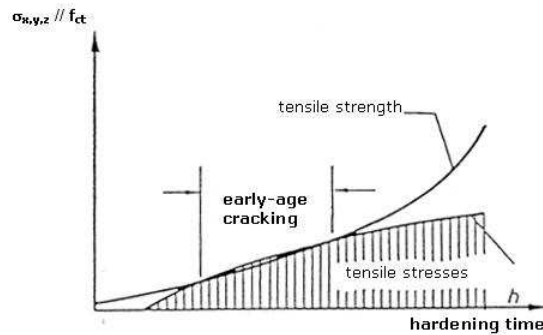


Figure 5.4: Young concrete is very prone to early-age cracking [De Schutter, 1996]

The main technological problem related to the production of the concrete buffer of the Supercontainer, is the effect of the heat of hydration during hardening of the fresh concrete. On the other hand, the early-age shrinkage, such as autogenous shrinkage, must also be taken into account. Finally creep, defined as the time dependent increase of deformation under sustained load, affects the deformation of structural elements and

the stress distribution. All these effects should be taken into account in design, construction and maintenance of radioactive waste repositories. Cracks inside the concrete buffer can be seen as preferential transport pathways for aggressive species and groundwater once placed inside the underground disposal galleries, and therefore should be eliminated.

Compared to a traditional vibrated concrete (TVC), Self-Compacting concrete (SCC) is a very fluid concrete showing several advantages on an environmental, human, technological and economical level. However, because of the particular composition, often resulting in a higher fines content and a higher paste volume, SCC could be more sensitive to cracking than TVC [Rozière et al, 2007].

1.5 Crack reducing or crack preventing measures

A side from the earlier mentioned measures in order to reduce the early-age shrinkage, several other measures can be taken in order to reduce, prevent or eliminate early-age cracking of massive concrete structures [Vuylsteke, 2003]:

- Reinforcing concrete can limit crack formation in concrete, but is not desired inside the Supercontainer during the thermal phase due to the corrosion risks and the related H₂ gas pressure build-up (Chapter 4).
- The cement type choice is very important. The less cement used, the smaller the amount of heat of hydration and the smaller the differential heating and cooling. Therefore, LH cement (Low Heat) or BFSC can be considered, because of their low heat production rate. For corrosion protection purposes (low pH) and irradiation influences (additional ettringite formation, Chapter 4), BFSC is not acceptable. LH cement not only reduces the hydration heat production, it also reduces drying shrinkage and the permeability is reduced as well.
- Massive concrete structures have a thermal gradient between the core and the edges. Therefore it is often useful to cast the structure in separate parts with reduced volumes. The smaller the element, the less massive it becomes: this reduces the cracking risks. The time between casting of the different parts must be well considered.
- Insulating the concrete element, which can raise the outside temperature near the outer surface and reduce the temperature gradient between the core and the edges, can prevent cracking. In this case, the time of demoulding is very important.
- The temperature of the concrete can be lowered by using a cooling system: (i) using ice instead of water, (ii) using cooled or wetted aggregates, (iii) using nitrogen as an external cooling agent, or (iv) using a cooling circuit with tubes connected to the reinforcement conducting a cooling fluid.
- A hot circuit with tubes conducting a hot fluid can also reduce the temperature gradient. Afterwards, when the hydration peak is passed, the tubes are filled with a cement paste. In case of the Supercontainer, it is desirable to reduce the amount of metallic parts inside the buffer. Therefore the use of circuits is not advised as a crack reducing action.

2 SCC: a comparison with TVC

2.1 Origin and background of Self-Compacting Concrete

Self-Compacting concrete (SCC) is an innovative concrete that does not require vibration for placing and compaction. It is able to flow and completely fill a formwork, under influence of its own weight [RILEM Technical Committee, 2008]. The use of SCC originates from construction applications where compactation was physically impossible. Examples can be found in underwater concrete constructions, foundation works using large diameter concrete piling, deep concrete diaphragm walling, etc. In Japan, SCC has been used for large office buildings and also for advanced types of extruded tunnels in combination with steel fibers. Mixes used for such applications had to be self-compacting. Admixtures, such as plasticizers, were used to help in the production of these highly specialized mixtures.

The stream of development of modern SCC originates from Japan, due to the high postwar demand of buildings. To meet this call, a concrete was developed with such a workability that compactation of the fresh concrete mix was no longer needed. This also led to an improvement of the concrete durability: the postwar reconstruction of Japan in the 1950s and 1960s created a building boom where speedy project delivery obscured the importance of quality. The creation of durable concrete structures requires adequate compactation by skilled workers. However, the gradual reduction in the number of skilled workers in Japan's reconstruction industry has led to a similar reduction in the quality of construction work [Ouchi et al., 2003]. Within several years, many reinforced structures started to deteriorate caused by the poor and insufficient compactation of the fresh concrete mixes. Afterwards, full-scale trials and demonstrations were carried out to prove the feasibility of SCC. The new, modern SCC enabled an important step towards the improvement of the quality of concrete in general and of its durability in particular [De Schutter et al., 2008].

In modern civil engineering applications, the demand of high quality and durable solutions is highly asked for. Also the productivity and the time dependency of a project is a main goal. The quality, durability and even the visual aspect of reinforced concrete are very dependent on the workability of fresh concrete. High concentrations of reinforcement, complex formworks and attractive construction forms hamper the casting process of concrete and increase the needed man power. In case of an insufficient care during casting and compacting of fresh concrete, the concrete element can suffer from inferior quality [Poppe, 2004]. Once again, the use of SCC is imposed. Nowadays, special interest in a wide range of structural practice goes to the use of SCC. The advantages of durability, homogeneity and work force independency are the main reasons of the increasing interest towards SCC.

Nowadays, SCC has developed in different directions in the various national construction markets. In some cases, the main focus is found in using SCC as a high-performance concrete for very demanding structures, in others development targets

mainstream concrete for conventional applications. SCC is used for in situ applications as well as for precast production. With increasing knowledge and experience, an improving track record has increased confidence in the market, leading to the development of production plants and equipment specifically adapted to SCC [De Schutter et al., 2008].

Researches worldwide are conducted on a wide variety of concrete topics: thermal properties, mechanical behaviour, rheological properties, casting conditions, influence of the different components (filler amount, type of filler, amount of superplasticizer, etc.) of SCC on properties, microstructure, early-age behaviour, creep and shrinkage, etc.

The increasingly widespread availability of superplasticizers in the 1970s also led to the introduction and use of flowing concrete, with a beneficial advantage towards different production situations. Thus, the development of SCC can also be seen as a logical step in the exploitation of superplasticizer technology.

2.2 Characterization of Self-Compacting Concrete

2.2.1 *The definition of Self-Compacting Concrete*

The definition of SCC appears to be quite simple and obvious regarding its name. It refers to the behaviour of the concrete mix in its fresh state and it separates fresh concrete mixes which are self-compacting from those which are not. SCC has the ability to flow under its own weight and fill the required space or formwork without the need of compaction in such a way that an adequately homogenous material is formed. In comparison with a Traditional Vibrated Concrete (TVC), SCC possesses a very high workability, it completely resist segregation and it maintains its stable composition throughout transport and placing [De Schutter et al., 2008].

Self-Compacting Concrete is defined according to De Schutter et al. (2008): ‘a kind of concrete which needs to possess sufficient fluidity in order to be able to fill a formwork completely (filling ability) without the aid of other forces than gravity, even when having to flow through narrow gaps (passing ability), but also showing a sufficient resistance to segregation, during flow and in stationary conditions (stability).’ First of all, SCC is a concrete and therefore must comply with all demands given to a traditional concrete: cement content, W/C ratio, air content, strength development, durability, pore structure, etc. Producing SCC is like finding a compromise between the fluidity and the stability: a very fluid material is wanted in order to have sufficient filling and passing ability, but the needed stability conditions require almost the opposite [Feys, 2009].

2.2.2 *The properties of fresh Self-Compacting Concrete*

Different durability aspects can occur for SCC due to the different mix design in comparison with TVC. The main difference between SCC and TVC lies in their fresh

state properties (rheology), and the absence of vibration energy needed in case of SCC. A low yield stress, in combination with a sufficiently high viscosity forms the base of a good SCC [Poppe, 2004]. SCC with sufficient flowing ability is able to flow under its own weight, completely filling the formwork and achieving full compaction, even in the presence of a dense reinforced network. Successful SCC needs a combination of three key distinct properties:

- Filling ability: the ability to flow into and completely fill all spaces within the formwork under its own weight. This property is a combination of total flow capacity and flow rate.
- Passing ability: the ability to flow through and around confined spaces between steel reinforcing bars without segregation or blocking.
- Segregation resistance: the ability to remain homogenous both during transport and placing (under dynamic conditions) and after placing (under static conditions).

In rheological terms the first and the third properties require a combination of low yield stress and a moderate plastic viscosity. Different levels and combinations of these properties are required for different applications [De Schutter et al., 2008]. These rheological properties strongly affect the flowing behaviour of a fresh concrete [Feys, 2009]. A yield stress that is too high leads towards a very stiff material that does not flow under its own weight. If the dynamic viscosity of the cement paste is significantly low the risk of segregation of the concrete raises, which can lead to blocking of the aggregates and of the concrete flow near narrow openings and zones with dense reinforcement configuration. On the other hand, if the yield stress is too low, the risk of segregation increases. The casting of the concrete can be slowed down and the fluent concrete flow can be stopped if the viscosity is too high. A suitable area for SCC can be defined according to Figure 5.5.

The early development of SCC in Japan established the essential criteria for achieving the three key properties [Okamura et al., 1995]:

- A low W/C (or Water/Powder, W/P) ratio with high doses of superplasticizer to achieve high flow capacity without instability or bleeding. It must be noticed that SCC with higher W/C ratio also is possible.
- A paste content sufficient to overfill all the voids in the aggregate skeleton to the extent that each particle is surrounded by an adequate lubricating layer of paste, thus reducing the frequency of contact and collision between the aggregate particles during flow.
- A sufficiently low content of coarse aggregates to avoid particle bridging and hence blocking of flow when the concrete passes through confined spaces.

The determination of rheological properties such as dynamic viscosity and yield stress is hard to establish in practice. A rheometer can be used to determine whether the dynamic viscosity and the yield stress are situated in the acceptable zone for SCC, according to Figure 5.5.

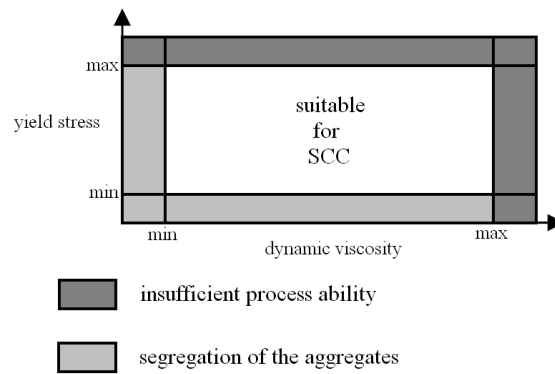


Figure 5.5: Definition of the suitable area for SCC

Alternative test methods are set up to characterize the fresh properties of SCC such as the filling and passing ability, the segregation resistance and the viscosity of the SCC (Chapter 6): the slump flow, V-funnel, L-box, sieve stability test, etc.

2.2.3 The constituent materials of Self-Compacting Concrete

SCC can be made from any of the constituent materials that are normally used for structural concrete: cement and additions, aggregates, sand, admixtures, fibres and water. However, SCC mixes are less tolerant to variations in material supply than TVC, and so uniformity and consistency of supply throughout the production of the concrete are essential.

For a concrete, to be considered as SCC, the use of superplasticizers is recommended to increase the flow ability of the concrete without adding an additional amount of water. In comparison with TVC, SCC also has a larger need of additives to increase the viscosity: fly ash, limestone powder, silica fume, etc. A well balanced grain size distribution of fine and coarse aggregates controls the viscosity of the fresh SCC.

SCC requires a high powder content due to the application of fillers and a low W/P ratio. Additions of all types can be considered in a blend with the cement and this has its own specific influence on the fresh and hardened properties of the concrete mixtures: inert material (limestone powder), pozzolanic (fly ash, silica fume), or latent hydraulic (BFS). These additions lead to a heat production reduction, a strength control, a reduced AAR risk, improved rheological behaviour and improved stability.

A well-distributed overall grading of aggregates in SCC is desirable. For most applications, the maximum aggregate size is lower than 20 mm, while for TVC coarser aggregates can be used (Figure 5.6). Fine aggregates are most suitable for SCC. The amount of very fine material is of particular importance. A sufficiently low content of coarse aggregates is demanded to avoid blocking during casting.

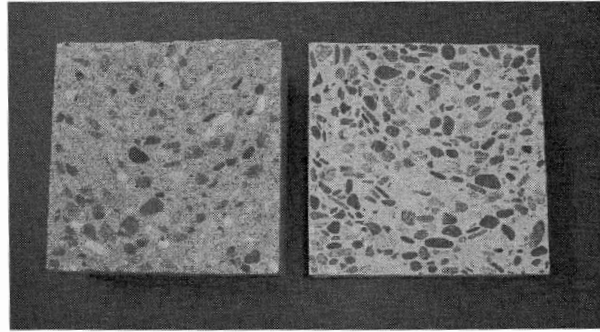


Figure 5.6: SCC has a lower content of coarse aggregates in comparison with TVC

Worldwide, there is a wide range of mix proportions that can produce SCC successfully. Expressed in volumetric terms, a number of key composition factors fall within limiting values [RILEM Technical Committee, 2008]:

- A paste volume of 34 % to 40 % of the concrete volume.
- A W/P ratio of 0.8 to 1.2 (by volume), with the use of a viscosity agent in case of values near the upper value.
- A fine aggregate volume of 40 % to 50 % of the mortar volume.
- A coarse aggregate volume of 30 % to 34 % of the concrete volume, whereas typical values of normal concrete are between 40 % and 45 %.
- A water content of 150 l/m³ to 175 l/m³ in case no viscosity agent is used, otherwise up to about 200 l/m³.

These ranges are equivalent to a weight of 750 – 920 kg/m³ coarse aggregates, 710 – 900 kg/m³ fine aggregates, 450 – 600 kg/m³ powder and 150 – 200 kg/m³ water. The microstructure of SCC significantly differs from those of TVC due to the application of fillers, the higher amount of superplasticizers and the absence of vibration. The hydration process of SCC is altered, depending on the type of used fillers and especially when limestone filler is applied. In that case three phenomena occur: (i) a considerable shortening of the dormant stage, thus a quicker start of the hydration reaction, (ii) an acceleration of the hydration reactions after the dormant stage, and (iii) in some cases the appearance of a third peak in the heat production rate (Chapter 6). When an additional amount of filler is used at constant cement content, there will be an improvement on hydration and structure formation because of the lower proportion of water compared to the total amount of solid powder material [RILEM Technical Committee, 2008].

To summarize, the three main properties are given with the specifications towards the concrete materials to obtain a Self-Compacting Concrete:

- Filling ability: the ability to flow into and completely fill all spaces within the formwork is possible if the amount of the largest aggregates and the maximum grain sizes are limited. It is desirable to increase the dynamic segregation

resistance during flow, made possible by implementing a sufficiently low water to powder ratio (W/P ratio) and by using a viscosity increasing admixture.

- Passing ability: this can be improved by using superplasticizers and filler materials. Reducing the internal friction of the concrete materials can be obtained by reducing the amount of coarse aggregates and by replacing them by filler materials.
- Segregation resistance: the stability of the concrete must be assured by reducing the volume of aggregates and by reducing the largest grain sizes. The cohesion and the viscosity of the concrete can be improved by using a viscosity increasing admixture or by realizing a sufficiently low W/P ratio. To diminish the bleeding effect, the following measurements can be taken: reducing the total water amount, obtaining a low W/P ratio, using a filler with high specific surface and using a viscosity increasing admixture.

Taking into consideration the indicated recommendations, it is possible to design and prepare a well flowing, segregation resisting SCC (Figure 5.7). A good reason for introducing SCC is the avoidance of durability problems linked to the possible bad vibration conditions. On the other hand, little information is available on the intrinsic durability of the material itself (i.e. the durability paradox [RILEM Technical Committee, 2008]).



Figure 5.7: Casting of SCC with a good flowing ability

2.2.4 *The advantages and disadvantages of Self-Compacting Concrete*

Advantages

- Excess in vibration can lead to segregation of TVC. The exclusion of vibration with SCC can lead towards the avoidance of segregation related issues [Boel, 2006]: precipitation of coarse aggregates, (micro) bleeding in the cement paste, large concrete density variations, etc.
- The lack of vibration also leads to a reduced working force, working costs and energy cost and a reduced dependency of the concrete properties on the skills of the workmen on site. Using SCC has great productivity advantages: the production speed can be increased leading to a decreased construction time.
- In case of SCC, the casting can practically occur in one layer, if the formwork can withstand the occurring pressure.
- SCC has an improved homogeneity which beneficially affects the concrete's durability.
- As SCC does not need any form of compactation, it can be pumped from the bottom of the formwork instead of from the top: the height of the structure can be increased and the risk of segregation or large air inclusions due to fall of concrete from a certain height can be avoided [Feys, 2009].
- One of the aims of the development of SCC is to avoid the use of external vibration and thus reducing previously occurring health problems such as 'white finger syndrome', reduced sense of hearing and other physical complaints of workers due to the use of vibration needles [RILEM Technical Committee, 2008].
- A reduction of environmental problems, caused by the noise of vibration, can be achieved [RILEM Technical Committee, 2008].
- Due to the good flowing ability of SCC in complex geometries, the architectural aesthetics can be improved. The designers can increase their creativity and have a greater freedom in styling the concrete structure.

Disadvantages

- One of the most important disadvantages of SCC, standing in the way of a more frequent use of SCC in comparison to TVC, is the higher material cost: in SCC, higher amounts of more expensive binders (cement and other powders) and admixtures (superplasticizers) are needed in order to make the concrete self-compacting. On the other hand, the use of SCC strongly reduces the working labor and the construction time and improves the productivity.
- The properties of fresh SCC are much more sensitive to alterations in one of its constitutive materials than TVC. Especially the moisture content of the aggregates can lead towards important changes in the flow ability of the fresh SCC. A good quality control, and an accurate determination of the water content of the applied aggregates is one of the roughest issues SCC has to deal with in the concrete industry.
- A complete tightness of the formwork used for SCC is needed and the formwork needs to withstand high pressures.

3 Special Protection Concrete

3.1 Definition of Special Protection Concrete

In the nuclear industry, Special Protection Concrete (SPC) is often used because of its beneficial ability and behaviour towards attenuating, mitigating and blocking irradiation of a radioactive nature. SPC is a concrete and complies with other types of concrete (same type of cement, same architecture, etc.), except for the addition of specific components [Bouniol, 1998]. Three types of SPC are given:

- Heavy Concrete: has a high volumetric mass and is used for the protection against gamma radiation.
- Neutrophage Concrete: a large proportion of light elements is used to provide protection against neutrons attack and to realize absorption of neutrons.
- Hybrid Concrete: a well-considered combination of heavy and light elements which provides protection against electromagnetic waves and photons (gamma rays and X-rays) and against neutrons attack.

An additional reinforcement is often provided inside these concrete types to assure sufficient mechanical strength. Due to the increasing use of additives, these concrete types become more and more compact. This introduces an improved resistance towards aggressive environments and additional mechanical strength.

3.2 Formulating the composition of SPC

To optimize the concrete composition, efforts must be made to formulate efficiently the aggregate skeleton: the type of aggregates (radiological, mechanical and thermal requirements), the grain size (requirements concerning the density and casting conditions of the concrete) and the grain size distribution are of major importance. Next, a compatible cement matrix must be chosen which can fill the annular gaps between the aggregates. This matrix also must comply with specific requirements: type of cement (thermal, chemical and mechanical properties to sustain the environment's aggressiveness), amount of cement, W/C ratio (consistency, durability and strength) and the amount of filler and/or additives to realize a consistent and processable concrete mix.

To mitigate the present gamma rays, heavy elements such as haematite, magnetite and limonite aggregates are used in combination with cement with limited hydration heat to reduce the thermal cracking risk. At high temperatures, exceeding 50 °C, aggregates with limited thermal deformation capacities and elevated conductivity are preferred. Ordinary Portland Cement (OPC) or Aluminate Cement (AC), with its typical beneficial resistance to heat and sulphate attack, are highly recommended [Madigan et al., 1997]. The use of BFS is discouraged due to the appearance of additional ettringite formation under the influence of radioactive gamma beams [Richardson et al., 1990]. Colemanite aggregates and AC behaves beneficial in a concrete mixture towards

neutrons attack. In general, a concrete layer with a thickness bigger than 0.5 meters, based on a CEM I 42.5 (OPC) and with good heat conducting aggregates, is very suitable for protection against gamma rays and neutrons in environmental temperatures between 20 °C and 100 °C [Bouniol, 1998]. Table 5.1 summarizes three types of SPC used for different nuclear applications.

3.3 Properties of SPC

The most important property of SPC is the ability to attenuate radioactive radiation. Attenuation of electromagnetic waves is the decrease of the total amount of photons with a specific energy level E due to the traversing of a bundle of the electromagnetic waves through an absorbing medium. For a certain given thickness of a concrete element, the attenuation of the radiation depends on the chemical composition of the irradiated element and can be determined by means of μ , the attenuation coefficient:

$$\mu(E_p) = \sum_i \left[f_i \cdot \left(\frac{\mu}{\rho} \right)_i(E_p) \right] \cdot \rho_c \quad (5.1)$$

where: $\mu(E_p)$ = the attenuation coefficient of the concrete element (1/cm)
 f_i = the mass fraction of component i in the concrete element (-)
 $(\mu/\rho)_i(E_p)$ = the absorption coefficient towards photons of component i in the concrete element (cm²/g)
 ρ_c = the volumetric mass of the concrete element (kg/m³)

Consider an initial amount N_0 of a bundle of energetic photons with energy level E_p that invades a layer of an attenuating material with a certain thickness a. Due to the attenuation, the amount of photons that reaches a certain depth x of the irradiated material is given by:

$$N(x) = N_0 \cdot e^{-\mu \cdot x} \quad (5.2)$$

where: N_0 = amount of energetic photons at depth $x = 0$ (-)
 μ = attenuation coefficient of the absorbing material according to (5.1) (1/cm)
 x = depth inside the absorbing material (cm)

By means of the equations (5.1) and (5.2) it is possible to calculate the necessary thickness of the SPC to prevent electromagnetic waves to get through a protecting material.

The thickness of an absorbing medium necessary to reduce the initial amount of energetic photons to its half, is called the halving thickness HT of an absorbing medium. To calculate HT equation (5.3) is used.

$$HT = \frac{\ln 2}{\mu} \quad (5.3)$$

where: μ = attenuation coefficient of the absorbing material according to (5.1) (1/cm)

According to Bouniol (1998), the attenuation coefficient, for photons with a constant energy level of 1 MeV, of the Standard concrete and the Haematite concrete (Table 5.1) equals respectively 0.1527 cm^{-1} and 0.2494 cm^{-1} . For variable photon energy levels, the use of graphs is necessary to acquire the attenuation coefficient and thickness necessary to reduce the radiation intensity (Figure 5.8). For example: a Standard concrete needs a thickness of 150 cm to reduce a photon radiation field with energy level of 1 MeV to 10^{-8} of its initial value whereas the heavy Haematite concrete only needs a thickness of 90 cm. Standard concrete with thickness of 250 cm can reduce a photon radiation field, with high energy level of 10 MeV, to maximum 10^{-6} of its initial value. Only 175 cm of Haematite concrete is needed to reduce the same photon bundle to 10^{-8} of its initial value.

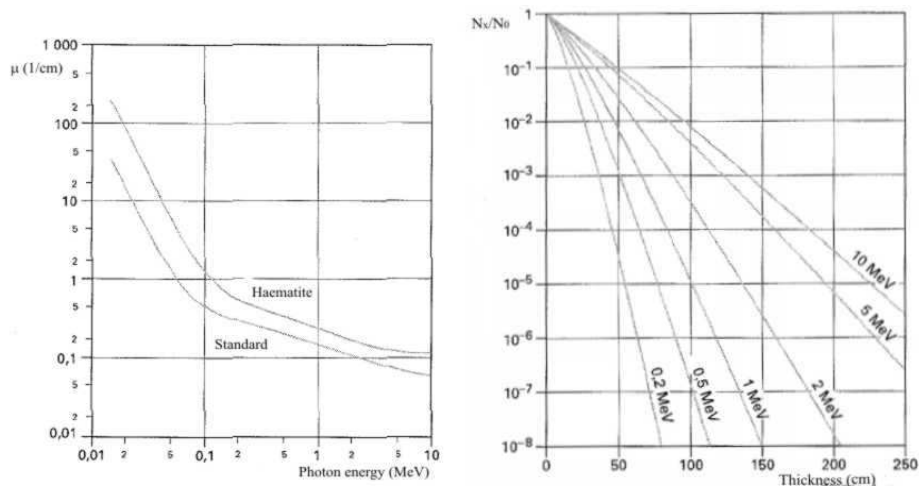


Figure 5.8: Evolution of the attenuation coefficient of Standard and Haematite concrete (left)
Determination of the attenuation thickness for Standard concrete (right)
[Bouniol, 1998]

Table 5.1: Concrete compositions of three different types of SPC (according to [Bouniol, 1998])

Components	Haematite concrete	Magnetite concrete	Standard concrete	
Cement	AC 400	CC 350	OPC 350	kg/m ³
Water	140	175	150	kg/m ³
Superplasticizer	4.25	5.25	1.75	kg/m ³
Sand 1	990 (0/1)	200 (0/1)	750 (0/4)	kg/m ³
Sand 2	920 (0/6)	1100 (0/5)	420 (4/12)	kg/m ³
Aggregates	1680 (6/20)	1800 (5/20)	780 (8/20)	kg/m ³
W/C	0.35	0.5	0.43	-
ρ_c	4075	3500	2380	kg/m ³
k	6.23	3.37	2.26	W/(m·°C)
α_T	8.5×10^{-6}	8.9×10^{-6}	10.0×10^{-6}	1/°C
$\epsilon_f(28d)$	140	300	175	$\mu\text{m/m}$
$f_c(28d)$	76	44	63	MPa
$f_{ct}(28d)$	5.0	3.5	4.4	MPa
$E_c(28d)$	81	42	44	GPa
Utilization	Concrete plug for radioactive disposal site	Armour-plating cores	Deep disposal of fission products	
	AC Aluminate Cement			
	OPC Ordinary Portland Cement			
	CC Composite Cement			

4 Engineered Cementitious Composites

Engineered Cementitious Composites (ECC), an ultra ductile concrete, is a unique type of high performance fibre reinforced cementitious composites. To counteract the negative effects on the durability and the mechanical behaviour of cracks in concrete, ECC's are introduced. The cracks inside these cementitious materials have the ability to seal themselves, slowing down the water transport through the cracked concrete.

This self-healing ability of ECC is founded on five main mechanisms of autogenous healing:

- The further hydration of non-reacted cement.
- The expansion of the concrete in the crack flanks due to swelling of CSH.
- Crystallization (calcium carbonate).
- Crack closure by impurities in water.
- Crack closure by loose concrete particles resulting from crack spalling

Most of the precedent research indicate crystallization of calcium carbonate as the main mechanism behind self-healing of mature concrete [Yang et al., 2009]. The growth of calcite inside the tight cracks is found. More studies are ongoing to indicate whether this growth is the main mechanism behind the self-healing ability of ECC. Crack width, water pressure, pH, temperature, water hardness, water chloride concentration and the concrete properties are affecting parameters of self-healing. Crack width is the dominating factor so that the control of the crack width is very much desirable. The microstructure of ECC before and after self-healing, with the typical white residue present along the crack lines after wet-dry conditioning cycles, are shown in Figure 5.9. EDX (Energy Dispersive X-rays) analysis results indicate that the majority of the self-healed products are characteristics of calcium carbonate crystals.

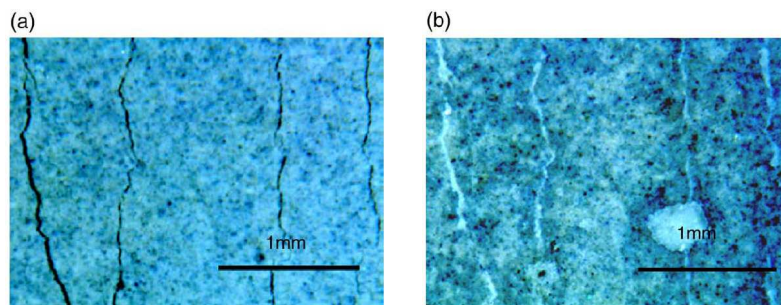


Figure 5.9: Microcracks in ECC before self-healing (a) and after self-healing (b) [Yang et al., 2009]

ECC features high tensile ductility and tensile strain capacity: the capability to deform over 3 % under load, while maintaining a crack width of about 20 μm to 60 μm up to failure (Figure 5.10). This steady state crack state can be seen as an inherent material

property of ECC. Even with a large number of surface cracks, ECC may behave like sound concrete with no cracks, by virtue of its tight crack width control (typically less than 60 μm).

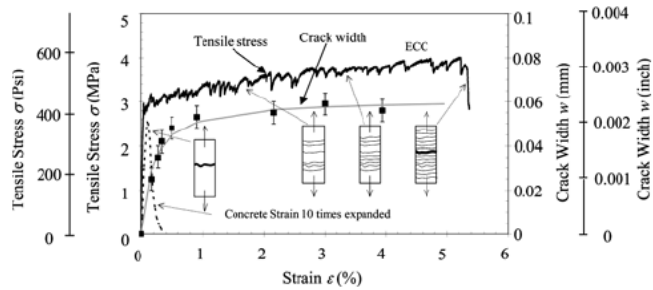


Figure 5.10: A typical tensile stress-strain crack curve of ECC [Li et al., 2001]

A number of other specific conclusions towards self-healing can be drawn:

- In order to obtain noticeable self-healing, the crack widths within the cementitious materials must be controlled below 150 μm , preferably below 60 μm .
- Four to five wet-dry cycles are necessary to induce a full recovery and attain a full benefit of self-healing.
- Self-healing can distinctly enhance the stiffness of cracked ECC (i.e. mechanical healing).
- An increase of ultimate strength and a light decrease of tensile strain capacity of self-healed ECC is found with increased temperatures.
- A recovery of 76 % to 100 % is found in specimens subjected to a tensile strain of respectively 3 % and 0.3 %.
- The tensile ductility characteristics of ECC are retained due to self-healing of pre-loaded specimens.
- The tensile strain capacity of ECC is approximately 500 times higher than that of normal concrete.

The establishment of self-healing and the use of ECC seems to improve the long-term durability of the concrete material after cracking. However, further discussion on behalf of the Supercontainer concept, remains out of the scope of this study.

5 Concrete Buffer Composition

5.1 Introduction and restrictions

In Chapter 3, the main functions of the concrete buffer of the Supercontainer are given (long-term safety and operational safety). Considering these functions and taking into account the predefined limitations, a reference concrete composition (Table 5.3, Figure 5.12) for the buffer of the Supercontainer is determined.

Two types of concrete are considered for the cementitious buffer around the overpack: a Self-Compacting Concrete SCC and a Traditional Vibrated Concrete TVC. As mentioned before, preference is given to the use of SCC because it will ease considerably the precast process and complies with all other requirements regarding compressive strength, long term durability, chemical interactions, etc.

There are certain restrictions to the different components of the buffer. It is recommended that CEM I (OPC), with limited hydration heat production to avoid or limit thermal cracking, is used to prevent portlandite consumption (with additional pH drop), with additional restriction that the cement has a low SO_3 and C_3A content. This avoids formation of dense hydrogarnet with resulting increase of porosity and permeability. The concrete must have high sulphate attack resistance to better resist to sulphur species potentially present in the clayey Host Rock pore water. It is also recommended that both fine and coarse aggregates should be limestone (calcium, calcite) containing not more than 2 % each of magnesium, silicon and aluminium (as oxides). This limits the risk on AAR resulting in expansion and cracking. No other organic additives are acceptable except, as low quantity as possible, a small amount of superplasticizer.

Other wanted properties are listed below:

- Good workability (preferably pumpable).
- Sufficient tensile and compressive strength in order to resist to normal and accidental loads.
- Microcracks are allowed (and cannot be avoided) but tangential and axial, through-going cracks, that might jeopardize the radiological shielding capacity and ease the transport mechanisms through the buffer, should be avoided.
- Good quality, homogeneous and dense concrete is desired (no quantitative values imposed).
- A reasonable thermal conductivity k to sufficiently convey the heat originating from the exothermal hydration processes and from the heat-emitting waste.

These considerable number of functions are being looked at and discussed in the following paragraphs.

5.2 The pH of the concrete buffer

One of the major functions of the concrete buffer is the creation of a favourable chemical environment with high pH in order to prevent corrosion of the canister during the thermal phase (long-term safety, Chapter 3). Preferably, a pH of 13 is realized by means of the concrete buffer composition. This highly alkaline environment intends to passivate the carbon steel overpack, resulting in a reduction of the corrosion rate. The potential for significant lowering of the pH values is reduced by using only OPC and by not permitting blending agents, such as FA, SF or BFS, which will cause a significant drop in pH, into the concrete composition.

5.3 Compatibility with the Host Rock

Scientific programs give increasing confidence in a clayey Host Rock as the natural barrier (for example: Boom Clay). Clay is a suitable Host Rock for the Belgian reference disposal concept for its diverse variety of properties (Chapter 3). Whether the clay and its retention capacity is vulnerable to high pH, needs to be further examined. Recent studies indicate that concrete types with lower pH values (< 11) and low hydration heat show a greater compatibility with a clayey environment [Cau Dit Caumes et al., 2006]. Clay properties may be degraded by high pH conditions and a high temperature rise can induce microcracking of the material. Therefore different types of concrete with low alkali amount, low hydration heat and high strength were examined. Therefore, a part of the cement of OPC based reference samples are replaced by silica fume (SF) and/or fly ash (FA). By addition of these additives, the amount of produced portlandite $\text{Ca}(\text{OH})_2$, mostly responsible for the high pH of concrete, is reduced. In case blends of 60 % OPC + 40 % SF or 37.5 % OPC + 32.5 % SF + 30 % FA are used, good processable and high strength concrete with pH lower than 11 was obtained.

According to Alexander (2008) the use of high pH concrete for deep disposal will induce an alkaline plume (Figure 5.11) in the Host Rock in the presence of groundwater flow. The Host Rock behaviour will be influenced by this highly alkaline environment. The hydration of the cement based materials in the underground disposal facilities by means of groundwater induces an initial state of hyper alkalinity (pH ≈ 13.5) due to the formed alkali hydroxides and due to the portlandite buffer [Atkinson, 1985, Berner, 1987]. In case of an escape of the hyper alkaline pore water to the surrounding Host Rock, interaction with and deterioration of this soil can occur with a detrimental effect its retention capacity [Haworth et al., 1987].

Whether a lower pH is desirable in the Belgian case needs to be discussed. One of the major functions of the concrete buffer is the provision of a highly alkaline environment to slow down the corrosion rate of the overpack. The clay layers near the disposal galleries, thus close to the underground repository, will experience the influence of the alkaline plume in case of a groundwater flow. However, going further away from the repository, the effect becomes negligible. Preservation of hyper alkaline conditions over an extended period of time induces a reduction of the retention capacity of the

Host Rock, but an improved sorption of the radionuclides via the cement [Hodgekinson et al., 1987]. Further discussion lies out of the scope of this doctoral thesis.

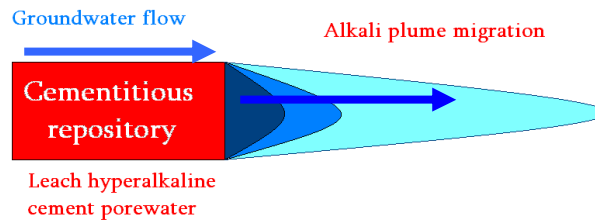


Figure 5.11: The alkaline plume has an impact on the Host Rock [Alexander, 2008]

5.4 Limitation of the hydration heat

Massive hardening concrete elements are very prone to thermal cracking at younger age due to the exothermal hydration reaction of the cement. Concrete, with its low tensile strength, hardly sustains the created stresses developed inside the structure attributed to the rather small heat conduction capacity of concrete, leading to thermal gradients inside a massive structure and giving cause to differential thermal deformations.

To avoid thermal cracking, the choice of a cement with limited hydration heat (LH) is recommended. Reducing the total amount of cement used, is also possible but could negatively affect the mechanical strength and the permeability of the concrete.

5.5 Sufficient mechanical strength

Microcracking is inevitable in massive concrete structures and therefore sustained and acceptable. Through-going tangential or axial macrocracks, on the other hand, have to be prevented at all times. This will facilitate the possibility to get preferential pathways for water inflow, for straightway flows and for gamma rays and radionuclide preferential paths [Craeye et al., 2009, Benats et al., 2005]. Previous studies have indicated that a characteristic tensile strength of 2 MPa is necessary. Finite element calculations show that the tensile stress due to the hydration heat can be close to 2 MPa near the outer surface of the concrete buffer in some cases (Chapter 8).

Also the compressive strength should be sufficient to withstand normal and possible accidental mechanical loads such as a horizontal fall from a certain height. Cracking could take place when tilting, independent of the presence of reinforcement or the stainless steel envelope. Further research is necessary to evaluate the robustness of the Supercontainer in case of an accidental load (out of the scope of this research).

Finally, after the Supercontainer is placed inside the disposal gallery and the repository tunneling is closed, the concrete buffer must have sufficient strength.

5.6 Ettringite formation and sulphate attack

For the cement, an additional restraint on the amount of SO_3 ($< 2\%$) and the amount of C_3A ($< 5\%$), which is very vulnerable to sulphate attack, is demanded. The ettringite formation is a very expansive process and can deteriorate hardened concrete structures. A scattered and branched network of cracks is formed in that case. The cement also must have a high sulphate resistance (HSR) to resist the sulphate attack of the groundwater (Chapter 4).

5.7 Permeability, water content and desired degree of saturation

The heat production due to hydration inside the concrete buffer can be prevented by means of reducing the total cement amount. Lowering the cement amount results in an increasing permeability which can increase the diffusivity of water and gas through the buffer. This is disadvantageous towards the corrosion protection of the carbon steel overpack around the waste canisters but advantageous towards gas production inside the buffer due to heating and/or radiolysis of the pore water (Chapter 4). This leads to another discussion: the water content inside the concrete buffer.

A low water content could lead to a reduced gas production due to heating and radiolysis of the pore water, but an equilibrium pressure of H_2 cannot be established (Chapter 4). An increased permeability can lead to the necessity of ventilation of the buffer to release the produced gasses. This reopens the discussion whether the use of an outer stainless steel liner is desired (Chapter 3). A part of the water used during mixing of the concrete of the buffer, will be chemically bound to the cement during hardening. There also must be a sufficient amount of water available during mixing to insure a desirable plasticity. A part of the water is still available after hardening and hydration of the cement, present as free pore water. The porosity of the concrete increases with increasing water amount and W/C ratio. If these pores interconnect, the permeability of the concrete will increase. The excess of water can be reduced by heating the concrete in such a way that the pore water is driven out of the concrete. The advantages of pre-heating the concrete lies in the fact that gas production due to radiolysis is reduced and the resistance of the concrete increases towards heating related changes. A dry concrete shall induce a lower gas pressure build-up, has lower thermal conductivity and does not have the same shielding effects towards radiation as saturated concrete [Galson Sciences, 2005].

Finally, the degree of saturation S of the concrete is considered. This has an influence on the properties of the concrete. Two limit states occur: dry concrete previously dried at 60°C and wet concrete after curing in water at 20°C with their specific (dis-) advantages (Table 5.2) [Crawford et al., 2004]. The water inside the wet concrete buffer will redistribute through the buffer under influence of the thermal gradient by

inserting the heat-emitting canisters. Dry concrete undergoes a drying process that leads to a stabilized water content and probably a strength reduction and an increased porosity. A wet concrete will have a higher water permeability than a dry concrete, leading to a higher migration rate of pore water (originating from the Host Rock) through the buffer towards the radioactive waste containing canisters.

5.8 Choice of cement

One of the main technological issues of the concrete buffer is the creation of thermal stresses due to the heat of hydration of the cement. Therefore, the choice of a blast furnace slag cement (BFSC), which produces less hydration heat and thus creates less internal stresses than OPC, occurs. This idea is being dismissed for different reasons:

- The use of OPC is stimulated due to its relative simple chemical properties in normal and elevated temperatures during the thermal phase of the Supercontainer. Concrete using BFSC, with a lower Ca/Si ratio, has a more complex mineralogy in case silica aggregates are being used.
- In a first phase, the Portland clinker inside BFSC reacts with the available water and forms portlandite Ca(OH)_2 . This portlandite subsequently reacts with the blast furnace slag present in BFSC. This process consumes portlandite, leading towards a pH reduction. A pH of 13 cannot be achieved by using a BFSC. This high pH is a desired property of the concrete buffer to prevent corrosion of the canister's overpack.
- BFSC has a considerable lower amount of C_3S , which leads to a lower strength development of the young concrete in comparison to OPC based concretes and to a later setting time and a slower stiffness development.
- Richardson et al. (1990) indicate that in case of BFSC/OPC mixes, containing 75 % BFSC and 25 % OPC, additional ettringite formation is noticed in the irradiated test pieces. Also the amount of Ca(OH)_2 was reduced, indicating a portlandite consumption due to irradiation and leading to a decrease of pH.
- Concretes using BFSC show higher shrinkage after 6 days than OPC according to Lura et al. (2001). The phenomenon could be related to the supposed denser structure of the BFSC paste, which shows smaller pores that can induce higher capillary forces during the self-desiccation process and increasing the autogenous shrinkage.

The reduced heat production and the increased sulphate resistance (due to higher amount of present C_3A) can be seen as the advantages of using BFSC.

This leads to the choice of an OPC, with low alkali amount (LA), to reduce the risk of AAR and corrosive effects of the alkali's on the carbon steel overpack. The cement has a limited hydration heat (LH) and high sulphate resistance (HSR). The use of silica fume and/or fly ash is rejected to avoid a drop in pH.

5.9 Choice of aggregates

Nuclear irradiation can considerably increase the AAR reactivity of silica rich aggregates (either crystalline quartz as amorphous quartz), even if those aggregates were chosen for their ability to resist AAR (Ichikawa et al., 2002).

Limestone (CaCO_3 , calcite) containing not more than 2 % of magnesium, silicon and aluminium (as oxides), should be used as filler, fine aggregates and coarse aggregates. This limits AAR resulting in expansion and cracking, increases the pH of the concrete and does not unnecessarily make the mineralogy more complex. Dolomite is best prevented because it can induce magnesium into the system, which can react with the silicon present in the concrete. The radiolysis is little changed by adding CaCO_3 . The calcite provides a clogging of the pores, creating a more uniform gas distribution and spreading inside the concrete pore volume (Chapter 4). The addition of limestone powder can also lead to an increased viscosity and stability of the concrete [De Schutter et al., 2008].

Out of safety consideration, it can be necessary to broaden the thickness of the buffer to provide better radiological protection and operational safety. This can lead to additional fabrication and transportation problems. To overcome this problem, it can be useful to replace a part of the limestone aggregates by an equal volume of a heavier aggregates, such as haematite. Concrete containing haematite has improved thermal conductivity and attenuating properties [Bouniol, 1998, Wickham et al., 2004].

Finally, the type of aggregates also has an considerable influence on the behaviour of concrete submitted to high temperatures: the aggregates thermal expansion is partly opposed to the drying and the autogenous shrinkage of the cement paste. Limestone aggregates, whose thermal coefficient of expansion is lower than that of siliceous aggregates is more favourable to the behaviour at high temperature of concrete [Bouniol, 1998].

5.10 Choice of admixtures

Organic admixtures, such as superplasticizers, are often added to improve the rheological properties of fresh concrete, especially in case of SCC. The adding of 1 % of superplasticizer (in comparison with the cement mass) has a considerable effect on the radiolysis (Chapter 4). In a saturated and irradiated environment, the presence of organic substances (highly reducing) can accomplish a fast reduction of the oxygenous products. Therefore, the H_2 present in the concrete buffer (due to corrosion, hydrolysis, heating), shall not be deteriorated and can cause accumulation of gas pressure if the dose rate is higher than 0.1 Gy/s [Bouniol, 2004].

Table 5.2: Advantages (+) and disadvantages (-) of wet concrete (high S) and dry concrete (low S)

	Wet concrete / High S	Dry concrete / Low S	
+/-	Low gas permeability	High gas permeability	+/-
-	High water permeability	Low water permeability	+
+	High protection capacity towards irradiation	Lower protection capacity towards irradiation	-
+	High thermal conductivity	Lower thermal conductivity	-
+	Good bond between the different concrete interlayers	Bond between the different concrete interlayers is worse due to dehydration shrinkage	-
-	Higher gas production due to corrosion/radiolysis/heating	Lower gas production due to corrosion/radiolysis/heating	+
-	Risk of steam formation	No risk of steam formation	+
-	Need of curing after casting, to limit evaporation	The fabrication process needs to take into account a drying stage	-
+	Reduced capillary sorption of groundwater	Increased capillary sorption of groundwater	-

The use of additives is often rejected. NFS (naphthalene formaldehyde sulphonate), MFS (melamine formaldehyde sulphonate) and polycarboxylate superplasticizers (such as Glenium) can have a beneficial effect under irradiated conditions towards H₂ production (Chapter 4). It is recommended to limit the amount of organic admixtures inside the concrete buffer composition except, as low quantity as possible, a small amount of superplasticizer (polycarboxylate based) to increase the processability, flowability and workability of the fresh concrete. It must also be noticed that the addition of superplasticizers can increase the early-age shrinkage behaviour and can retard the setting time [Holt and Leivo, 2004].

5.11 Reference concrete compositions of the concrete buffer

Based on this extensive range of requirements, the following concrete compositions for SCC and TVC are determined (Table 5.3, Figure 5.12). A laboratory characterization program is performed to obtain to most important thermal, mechanical and maturity-related properties, and will be discussed in Chapter 6.

Table 5.3: Reference concrete buffer composition of SCC and TVC

Component		SCC	TVC
Cement CEM I/42.5N HSR LA LH	kg/m ³	350	350
Limestone filler	kg/m ³	100	50
Limestone 0/4	kg/m ³	840	708
Limestone 2/6	kg/m ³	327	414
Limestone 6/14	kg/m ³	559	191
Limestone 6/20	kg/m ³	0	465
Superplasticizer Glenium 27/20	kg/m ³	10-14	4-5
Water	kg/m ³	175	175

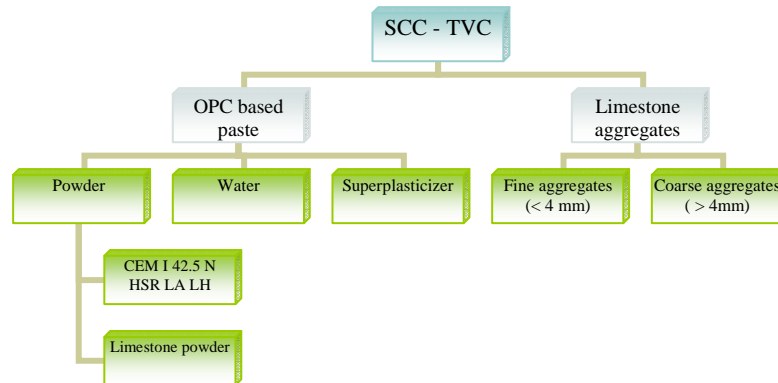


Figure 5.12: Constituent components of SCC and TVC

References

Alexander W.R. (2008), *Jordan natural cement analogues*, Cement and Cementitious Materials in the geological disposal of radioactive waste, ITC School International Course, Eurajoki, Finland.

Atkinson A. (1985), *The time-dependence of pH within a repository for radioactive waste disposal*, UKAEA Technical Report AERE-R11777, Harwell, Oxon, UK.

Audenaert K. (2006), *Transport mechanisms in Self-Compacting Concrete in relation with carbonation and chloride penetration*, Doctoral thesis (in Dutch), Ghent University, Magnel Laboratory for Concrete Research, Belgium.

Benats V., de Marneffe L. (2005), *Demonstration of the Supercontainer design for S.P.W.D.: Preliminary study if the Supercontainer – first stage concreting and waste thermal effects*, Tractebel Engineering Technical Report TIERSDI/4NT5406, 000/00050829.

Berner U. (1987), *Modelling porewater chemistry in hydrated cement*, Material Research Symposium, Proc. 84, p 319.

Boel V. (2006), *Microstructure of Self-Compacting Concrete in relation with gas permeability and durability aspects*, Doctoral thesis (in Dutch), Ghent University, Magnel Laboratory for Concrete Research, Belgium.

Bouniol P. (1998), *Bétons spéciaux de protection*, Rapport CEA BN 3 740, France.

Bouniol P. (2004), *État des connaissances sur la radiolyse de l'eau dans les colis de déchets cimentés et son approche par simulation*, Rapport CEA-R-6069.

Cau Dit Caumes C., Courtois S., Nectoux D., Leclercq S., Bourbon X. (2006), *Formulating a low-alkalinity, high resistance and low-heat concrete for radioactive waste repositories*, Cement and Concrete Research 36, 2152-2163.

Craeye B. (2006), *Mitigation of autogenous shrinkage by means of internal curing*, Master thesis (in Dutch), Ghent University, Magnel Laboratory for Concrete Research, Belgium.

Craeye B., De Schutter G., Van Humbeeck H., Van Cotthem A. (2009), *Early age behaviour of concrete supercontainers for radioactive waste disposal*, Nuclear Engineering and Design 239, 23-35.

Crawford M.B., Wickham S.M., Galson D.A. (2004), *Workshop on the Evolution of OPC Buffer and Steel Corrosion in the Belgian Supercontainer Design for HLW Disposal*, Stamford, UK.

De Schutter G. (1996), *Fundamental and practical study on thermal stresses in massive hardening concrete elements*, Doctoral thesis (in Dutch), Ghent University, Magnel Laboratory for Concrete Research, Belgium.

De Schutter G. (2002), *Finite element simulation of thermal cracking in massive hardening concrete elements using degree of hydration based material laws*, Computers & Structures 80, 2035-2042.

De Schutter G. (2005), *Beheersing van krimp bij jong beton: eindverslag van activiteiten Laboratorium Magnel voor Betononderzoek*, Ghent University, Magnel Laboratory for Concrete Research, Belgium.

De Schutter G., Bartos P., Domone P., Gibbs J. (2008), *Self-Compacting Concrete*, Whittles Publishing, Caithness, UK, pp. 296.

Feys D. (2009), *Interaction between Rheological Properties and Pumping of Self-Compacting Concrete*, Doctoral thesis, Ghent University, Magnel Laboratory for Concrete Research, Belgium.

Galson Sciences (2005), *Belgian Supercontainer Design for HLW and Spent Fuel Disposal: Evaluation of the Reference Design*, Galson Sciences Report 0460-5, Version 1, 2005.

Hamfler H. (1988), *Berechnung von Temperatur-, Feuchte- und Verschiebungsfeldern in erhärtenden Betonbauteilen nach der Methode der finiten Elementen*, Deutscher Ausschuss für Stahlbeton, Beuth Verlag, Heft 395, Berlin, Germany.

Haworth A., Sharland S.M., Tasker P.W., Tweed C.J. (1987), *Evolution of the groundwater chemistry around a nuclear waste repository*, Science Basis Nuclear Waste Management. XI, 645-651.

Hodgekinson D.P., Robinson P.C. (1987), *Nirex near-surface repository project. Preliminary radiological assessment: Summary*, NSS/RE100, Nirex, Harwel, UK.

Holt E., Leivo M. (2004), *Cracking risks associated with early age shrinkage*, Cement & Concrete Composites 26, 521-530.

Ichikawa T., Koizumi H. (2002), *Possibility of radiation-induced degradation of concrete by alkali-silica reaction of aggregates*, Journal of Nuclear Science and Technology, Vol 39, No 8, p 880-884.

Igarashi S.I., Bentur A., Kovler K.. (2000), *Autogenous shrinkage and induced restraining stresses in high-strength concretes*, Cement and Concrete Research 30, 1701-1707.

Li V.C., Wang S., Wu C. (2001), *Tensile strain-hardening behaviour of polyvinyl alcohol engineered cementitious composite (PVA-ECC)*, ACI Materials Journal 98, 483-492.

Lura P., Van Breugel K., Maruyama I. (2001), *Effect of curing temperature and type of cement on early-age shrinkage of high-performance concrete*, Cement and Concrete Research 31, 1867-1872.

Madigan M.T., Martinko K.M., Parker J. (1997), *Biology of micro-organisms*, Prentice-Hall, Englewood Cliffs.

Persson B. (2001), *A comparison between mechanical properties of self-compacting concrete and the corresponding properties of normal concrete*, Cement and Concrete Research 31, 193-198.

Okamura H., Ozawa K. (1995), *Mix design method for self-compacting concrete*, Concrete Library of Japan Society of Civil Engineers No 25, pp 107-120.

Ouchi M., Okamura H. (2003), *Self-Compacting Concrete*, Journal of Advanced Concrete Technology, Vol 1, No 1, 5-15.

Poppe A.M. (2004), *Influence of additives on hydration and properties of Self-Compacting Concrete*, Doctoral thesis (in Dutch), Ghent University, Magnel Laboratory for Concrete Research, Belgium.

Richardson I.G., Groves G.W., Wilding C.R. (1990), *Effect of gamma irradiation on the microstructure and microchemistry of ggbfs/OPC cement blends*, Proceedings of the Material Research Society Symposium, Vol 176.

Rozière E., Granger S., Turcry Ph., Loukili A. (2007), *Influence of paste volume on shrinkage cracking and fracture properties of self-compacting concrete*, Cement & Concrete Composites 29, 626-636.

RILEM Technical Committee. (2008), *Final report of RILEM TC 205-DSC: durability of self-compacting concrete*, Materials and Structures 41, 225-233.

Van Nieuwenburg D. (1986), *Invloed van scheurvorming en belang van betondekking*, Ghent University, Magnel Laboratory for Concrete Research, Belgium.

Vuylsteke M. (2003), *Betontechnologische studie van opvatting en uitvoering van een ongewapende massieve kaaimuur*, Master thesis (in Dutch), Ghent University, Magnel Laboratory for Concrete Research, Belgium.

Wickham S.M., Bennett D.G., Crawford M.B., Pourbaix A. (2004), *Supercontainer Conceptuel Model. Information to support a workshop on the evolution of OPC Buffer and steel corrosion in the Belgian Supercontainer Design for HLW/Spent Fuel Disposal*, Galson Sciences Limited, Report no 0427.

Yang Y., Lepech M.D., Yang E.-H., Li V.C. (2009), *Autogenous healing of engineered cementitious composites under wet-dry cycles*, Cement and Concrete Research 39, 382-390.

CHAPTER 6:

THERMO-MECHANICAL AND FRESH PROPERTIES

An extensive laboratory characterization program is conducted to determine the concrete properties of SCC and TVC. Several thermo-mechanical tests and maturity-related tests are performed to examine the differences between the two considered concrete compositions. The applied test methods and an overview of previously conducted tests are also mentioned to give a brief overview and to compare SCC and TVC by means of results obtained in literature.

1 Goal and methodology

The determination of the concrete properties of a Self-Compacting Concrete (SCC) and a Traditional Vibrated Concrete (TVC), with compositions described in Chapter 5, is part of an intensive laboratory characterization program. Several phenomena must be taken into account to examine the early-age behaviour of massive concrete structures, hence leading towards a considerable complexity [Benboudjema and Torrenti, 2008]:

- The evolution of the hydration processes and the evolution of the temperature including the release of heat due to the hydration reaction.
- The evolution of autogenous and thermal strains.
- The evolution of the modulus of elasticity and the tensile strength.
- The description of cracking in tension.
- Basic creep.
- Drying shrinkage and drying creep can be neglected for the early-age behaviour because the drying process for massive structures is 1000 – 10 000 times slower than the thermal one. Therefore, drying of the concrete and moisture transport is kept out of consideration in this study.

Therefore, thermal, mechanical and maturity-related tests are performed to predict the behaviour and the differences between SCC and TVC (Figure 6.1).

The obtained data will be implemented in the material database of the finite element program HEAT/MLS [Van Beek et al., 2001, Vuylsteke and De Schutter, 2004, Craeye

et al., 2009]. The material database can be subdivided into three categories: (i) thermal properties, (ii) maturity-related properties and (iii) mechanical properties. By means of the implemented concrete properties, the early-age thermo-mechanical behaviour of the concrete buffer of the Supercontainer during construction and fabrication can be predicted (Chapter 8). Also the fresh properties and the volumetric weight of the hardened concrete are determined.

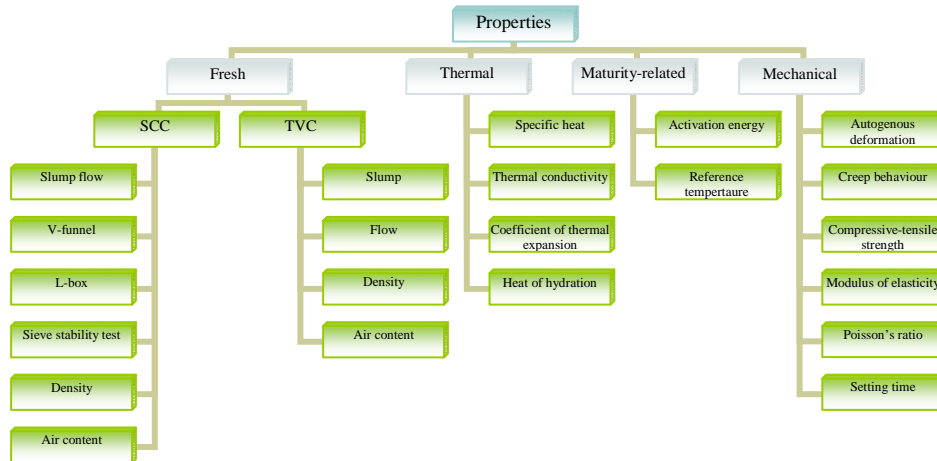


Figure 6.1: Fresh, thermal, maturity-related and mechanical properties of SCC and TVC

2 Principles, test procedures and previous studies

2.1 Concrete compositions and mixing procedure

Within the experimental research program to determine the early-age behaviour of the concrete buffer of the Supercontainer, a Self-Compacting Concrete (SCC) and a Traditional Vibrated Concrete (TVC) are proposed (Chapter 5).

Mix design and fresh properties of TVC are well known. The principal differences in the mix proportions of TVC compared to SCC are higher coarse aggregates contents, lower powder contents, higher W/P ratio and a significantly lower superplasticizer content. The need to obtain a number of distinct fresh properties and the potential combinations of materials of SCC, means that mix design procedures are more complicated for SCC (Chapter 5). Combining the constituent materials in the optimum proportions to give concrete with required combination of fresh and hardened properties for a particular application, is an essential part of the SCC production process. For SCC, three key parameters are needed for the composition to be successful [De Schutter et al., 2008]: (i) filling ability, (ii) passing ability and (iii) segregation resistance in dynamic and static conditions (Chapter 5). In rheological terms, the first and the last recommendation can be translated into the need of a combination of low yield stress and moderate plastic viscosity. Also some general considerations concerning the mix proportioning must be taken into account [Okamura and Ozawa, 1995]:

- To achieve a high flow ability without stability loss or bleeding, a sufficiently low W/C ratio is needed with high doses of superplasticizer.
- A sufficient paste content is necessary to overfill all the voids in the aggregate skeleton in such a way that the contact and collision between the aggregates during the flow is reduced.
- To avoid particle bridging and blocking of the flow, a sufficiently low coarse aggregate content is desired.

A sufficient stability at high W/P ratios can be achieved by applying a viscosity modifying agent (VMA). VMA can be used to improve the robustness of the mix in a way that variations in material supply such as the grading or the moisture content of the (fine) aggregates are tolerated. However, in the Supercontainer concept, the amount of superplasticizers should be limited in the concrete buffer composition (Chapter 5). SCC without the use of VMA is also known as a powder-type mix. Medians and ranges of key proportions of SCC mixes can be found in literature [De Schutter et al., 2008]. It must be noted that there is no unique mix of a given set of materials to give a particular set of fresh and hardened properties. Ranges of key mix proportions of SCC and TVC are shown in Table 6.1 [EFNARC, 2005, Domone, 2006].

*Table 6.1: Typical ranges of key proportions of SCC and TVC mixes
 (*TVC with cube strength 40 MPa, 75 mm slump, CEM I, 20 mm aggregates and typical superplasticizer dose)*

		Typical ranges SCC	Typical mid-range TVC*
Coarse aggregates	% by vol	27 – 36	46
Fine aggregates	% by vol	23 – 40	25
	% by wt total aggr	48 – 55	35
Paste (water + powder)	% by vol	30 – 38	29
Powder	kg/m ³	380 – 600	355
Free water	kg/m ³	150 – 210	160
W/P ratio	by wt	0.28 – 0.42	0.45
	by vol	0.85 – 1.10	1.41

Both the compositions of SCC and TVC (Table 6.2, Table 6.3) have a W/C ratio of 0.50, using 350 kg/m³ cement and 175 kg/m³ water. The superplasticizer is a polycarboxylic ether. It must be noted that the amount of superplasticizer varies between 10 kg/m³ and 14 kg/m³ for SCC (2 % – 3 % by mass of powder) and between 3 kg/m³ and 5 kg/m³ for TVC (0.75 % – 1.25 % by mass of powder).

Limestone aggregates are chosen, having a particle size mainly varying between 2 mm and 14 mm for SCC and a maximum diameter of 20 mm for TVC. The amount of fine aggregates in SCC is 840 kg/m³, and 708 kg/m³ for TVC. A higher amount of coarse aggregates is used for TVC: 1070 kg/m³ in comparison with 886 kg/m³ for SCC. SCC also has a higher amount of limestone filler: 100 kg/m³ in comparison with 50 kg/m³ for TVC. The W/P ratio is 0.39 for SCC and 0.44 for TVC.

Table 6.2: Proportions of SCC

SCC	[kg/ 1 m ³]	[m ³ / 1 m ³]
Cement CEM I/42,5 N	350	0.113
Limestone filler	100	0.038
Limestone (fine)	840	0.317
Limestone (coarse)	886	0.334
Superplasticizer	12	0.011
Water	175	0.175
Powder	450	0.151
Paste	625	0.326
Mortar	1465	0.643
W/C	0.50	1.55
W/P	0.39	1.16
C/P	0.78	0.75

Table 6.3: Proportions of TVC

TVC	[kg/ 1 m ³]	[m ³ / 1 m ³]
Cement CEM I/42,5 N	350	0.113
Limestone filler	50	0.019
Limestone (fine)	708	0.267
Limestone (coarse)	1070	0.404
Superplasticizer	4	0.004
Water	175	0.175
Powder	400	0.132
Paste	575	0.307
Mortar	1283	0.574
W/C	0.50	1.55
W/P	0.44	1.33
C/P	0.88	0.86

For SCC, the proportions given in Table 6.2 fit the typical ranges of the key proportions for a Self-Compacting Concrete (Table 6.1), except for the W/P ratio (by vol %). In order to fit this value, an additional amount of powder is needed: approximately 25 kg/m³ extra limestone filler or cement is enough to fit the proposed W/P ratio. Comparison of the TVC composition given in Table 6.3 with a typical mid-range TVC (Table 6.1, TVC with cube strength 40 MPa, 75 mm slump, CEM I, 20 mm aggregates and typical superplasticizer dose) shows a lower amount of coarse aggregates and a higher amount of fine aggregates and powder used in the TVC composition expressed in Table 6.3, but still the proposed proportions are acceptable for a normally vibrated mix.

During the laboratory characterization program and for the different tests, nineteen SCC mixes and seventeen TVC mixes are made in different proportions, varying from 0.03 m³/mix to 1 m³/mix, at three different locations: (i) BASF, Antwerp (design mix of 0.05 m³ for SCC and TVC), (ii) SOCEA, Ranst (3 x 1 m³ for SCC and TVC in order to obtain thermal and mechanical properties of the mixes) and (iii) Magnel Laboratory for Concrete Research, Ghent (mixes varying from 0.03 m³ to 0.15 m³ for the determination of thermal and mechanical properties). For the Half-Scale Tests for the validation of the simulation results (Chapter 9), two test mixes SCC of 2 m³ and seven final mixes SCC of 2 m³ are made at Kesteleyn, Ghent, and will be discussed later.

At the Magnel Laboratory for Concrete Research, two mixers are available with cross current mixing principle (Figure 6.2) and with a capacity of 0.05 m³ and 0.2 m³. The mixing procedure is the same for SCC and TVC: first the fine and coarse aggregates are placed in the mixer and mingled for 15 seconds. Afterwards the powder (first the limestone filler, then the cement) is added and once more mixed for 15 seconds. Then the water is poured, and the mixing continues for another 120 seconds. Finally, the superplasticizer is added and the composition is mixed once more, for 180 seconds, totalizing a mixing time of 5.5 minutes.

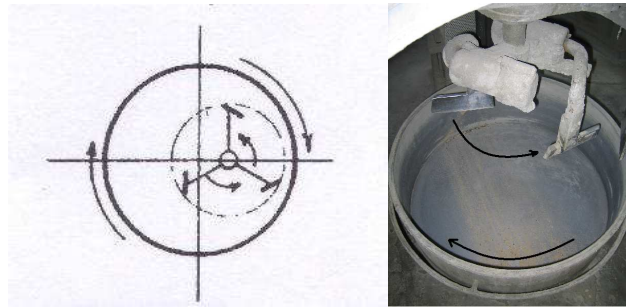


Figure 6.2: Cross current mixing principle (left) and mixer with capacity of 50 liters (right)

2.2 Fresh concrete properties

2.2.1 Fresh properties of SCC

The fresh properties of the SCC can be evaluated by means of standard tests. Only the tests applied in this study will be briefly discussed. Also the density and the air content of the SCC needs to be determined: the description of the method is the same as for TVC (see further). However, for SCC no external vibration is needed to fill the container with a known volume of 0.008 m³.

Slump flow (EN 12350-8)

The slump flow test (Figure 6.3) is very similar to the slump test performed on traditional concrete, using an Abrams-cone (diameter 200 mm at the bottom and 100 mm at the top, the height is 300 mm). The cone is filled with SCC in one movement without compactation and is lifted vertically upwards by which the SCC spreads out on a base plate. The average diameter of the SCC spread-out is taken as the slump flow test value. Slump flow values describe the flow ability of a fresh mix in unconfined conditions. The higher the slump flow spread, the greater the filling ability of the fresh mix. SCC mostly requires a slump flow value larger than 600 mm to achieve an adequate filling ability [De Schutter et al. 2008], while SCC with a value of 900 mm shows a significant segregation risk [Feys, 2009]. Even minimal values of 650 mm and 700 mm are often recommended in practice for a concrete to be defined as self-compacting [Boel, 2006]. Visual inspection of the distribution of the coarse aggregates inside the SCC cake can give a first indication of horizontal segregation occurring.

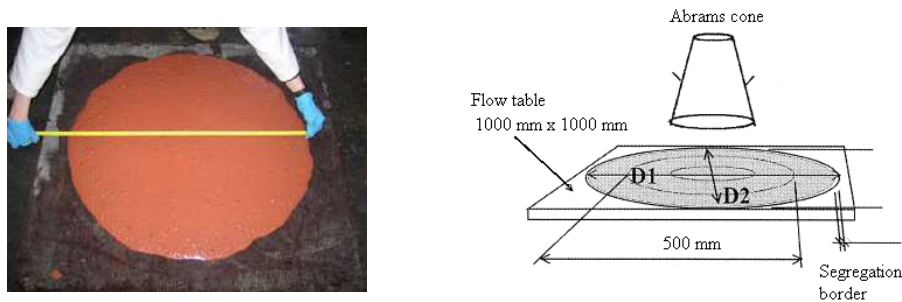


Figure 6.3: Slump flow test

V-funnel (EN 12350-9)

A V-shaped container is completely filled with SCC. Afterwards, the valve at the end of the V-funnel is opened. The time SCC needs to empty the V-funnel through the narrow opening at the bottom, is known as the V-funnel time (Figure 6.4). The V-funnel values characterize the viscosity of the SCC: long flow times indicate that the

SCC is quite stiff and is not easily deformable due to high internal friction or high viscosity of the paste. Blocking due to a lack of cohesion of the mortar and thus coagulation and arching of coarse aggregates near the opening can slow down the flow. On the other hand, low V-funnel values are the result of a very fluid SCC with an increasing risk for segregation.

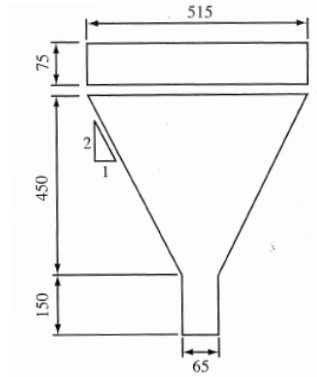


Figure 6.4: V-funnel test (dimensions in mm)

L-box (EN 12350-10)

To evaluate the passing ability of the SCC, the L-box apparatus can be used. The L-box (Figure 6.5) consists of a vertical rectangular reservoir connected to a horizontal part, hence the L form. The two parts are separated by means of a valve and 3 reinforcement bars are placed in this transition zone. Once the vertical reservoir is filled with SCC and a resting time of 2 minutes is respected, the valve is opened and the SCC flows into the horizontal part, trying to level. The ratio of the concrete height at the end of the horizontal part H_2 to the concrete height in the vertical reservoir H_1 is preferably higher than 0.8. In that case the SCC is supposed to be sufficiently self-compacting. If the SCC segregates or blocking near the bars occurs, a value H_2/H_1 lower than 0.8 will be obtained. In case of a low flow ability, it is hard for the SCC to flow through the opening in between the rebars. In case of SCC with very high flow ability, segregation can occur near the bars and the flow can be stopped due to blocking.

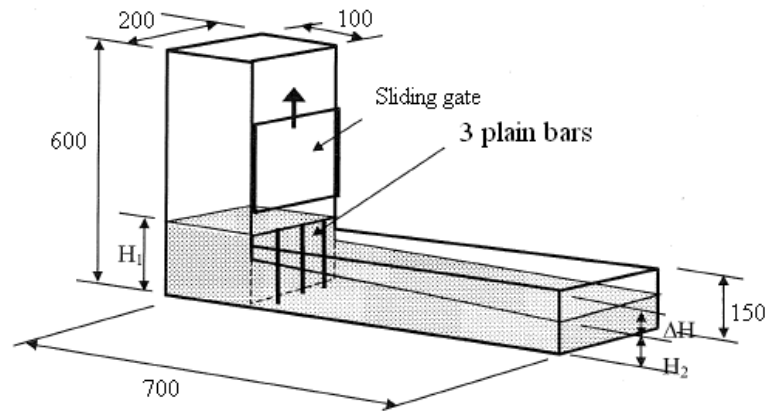


Figure 6.5: L-box apparatus (dimensions in mm)

Sieve stability test (EN 12350-11)

The segregation resistance of SCC is evaluated by means of the sieve stability test. After pouring 5 ± 0.2 kg of SCC on a sieve (mesh size of 5 mm, pouring height: 0.50 m) immediately (no initial resting period of 5 minutes is applied according to [Feys, 2009]), waiting for 2 minutes (rest period), the amount of cement mortar which has fallen through the sieve is weighted (Figure 6.6). The ratio of this percolated material to the total amount of poured concrete is called the sieve stability value. The lower this value, the more stable the SCC. A value smaller than 15 % is recommended for the SCC to avoid segregation.



Figure 6.5: Sieve stability test: pouring of the SCC (left) and the amount of mortar fallen through the sieve (right)

Classification of SCC

There is no direct association between the rheological parameters (yield stress and viscosity) and the fresh concrete properties (slump flow, V-funnel time, L-box ratio, segregation percentage). Therefore, the tests have to be combined in order to determine whether a concrete can be categorized as self-compacting. Different types of classifications of applications of SCC with different properties can be found in literature [Walraeven, 2003, EFNARC, 2005]. One possible classification, produced by EFNARC, is illustrated in Table 6.4. The SCC can be subdivided into different classes for each fresh property.

Table 6.4: SCC classes proposed by EFNARC (2005)

Slump flow		Viscosity		Passing ability		Segregation resistance	
Class	Slump flow [mm]	Class	V-funnel [s]	Class	L-box [-]	Class	Sieve segregation [%]
SF1	550 – 650	VF1	≤ 8	PA1	≥ 0.80 (2 bars)	SR1	≤ 20
SF2	660 – 750	VF2	9 – 25	PA2	≥ 0.80 (3 bars)	SR2	≤ 15
SF3	760 – 850						

An analysis of 68 case studies of SCC worldwide in the period 1993 – 2003 [Domone, 2006] showed that nearly 50 % of SCC has a slump flow value in the range 650 mm – 700 mm, with nearly 90 % in the range 600 mm – 750 mm. V-funnel times varied from 3 s to 15 s. All L-box values are higher than 0.80. In order to get a slump flow value higher than 650 mm, ACI (2007) recommends a minimal powder content of 445 kg/m³.

2.2.2 Fresh properties of TVC

The fresh concrete properties and thus the consistency of the concrete mixture TVC can be determined by means of the slump test (Figure 6.7) and the flow test respectively according to the Belgian Code NBN EN 12350-2 and NBN EN 12350-5. Also the density of the fresh concrete can be easily determined by measuring the net weight of a reservoir with a known volume (0.008 m³) filled with compacted TVC. Afterwards, the air content can be determined by means of the pressure method. These tests are described in and performed according to the Belgian Code NBN EN 12350-7.

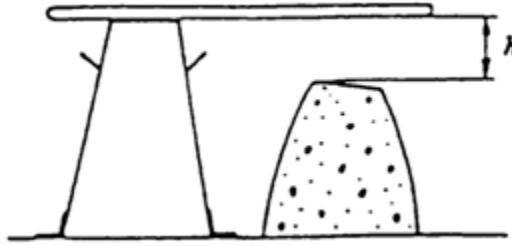


Figure 6.7: Slump test

2.2.3 Previous studies

The fresh TVC composition shows a higher robustness than the SCC composition. Therefore only previous studies on fresh properties of SCC are briefly investigated.

A previous study was conducted at the Magnel Laboratory for Concrete Research [Poppe, 2004], to determine the influence of the amount of superplasticizer (SP) and filler on the consistency of the fresh SCC. The total powder content has an amount up to 600 kg/m^3 . Some conclusions were drawn:

- It was proved that an increasing amount of SP leads to a small increase of slump flow and a small decrease of V-funnel time. Moreover, a reduction of the efficiency is noticed. By adding more SP, especially the risk of segregation of the concrete mixture increases.
- The influence of the C/P ratio on the slump flow values are insignificant. An increase of the powder content leads towards a small decrease in V-funnel time.
- Also the type of filler and the cement type affect the fresh properties of the SCC. No clear correlation is found however. The grain size distribution, the form and the surface type of the powder grains play a role in the process ability of fresh concrete.

A mix design is needed to realize and optimize an SCC composition that fits the demanded requirements concerning fresh properties (process ability, flow ability and viscosity) and hardened properties (strength and durability). An example of a previously proposed design method is given by Okamura and Ozawa (1995), including several steps that must be depicted in order to obtain a self-compacting composition: air content, quantity of coarse and fine aggregates (40 % of the total mortar volume is the goal), dose of SP, W/P ratio, aid of VMA. Overall, the ideal proportion of all the components of the SCC must be found via a trial and error process [Poppe, 2004]. Therefore, the production of a considerable amount of trial batches is inevitable. The values of the tests on fresh SCC can be used as a guideline in order to optimize the self-compacting composition.

Sonebi (2004) quoted that statistical models can simplify the test protocol required to optimise a given SCC mix by reducing the number of trial batches needed to achieve a balance among mix variables. Polynomial regression can identify those primary factors

(such as filler content, W/P ratio, cement and SP amount) and their interactions on the measured fresh and hardened properties. These models provide a design approach that is valid for a wide range of mix proportioning and clearly state the influence of the key variables on the SCC properties. W/P had the most significant effect on the slump flow and the segregation followed by limestone powder and cement amount for slump flow, and cement and limestone powder amount for segregation. An increase in W/P ratio and in SP amount led to an increase in segregation and separation of the constituents of the mix resulting in non-uniform distribution, due to the increase in free water and the decrease in viscosity of the matrix.

For example [Sui et al., 2009], Figure 6.8 indicates the trade-off between the W/P ratio and the dosage of SP on the slump flow and the compressive strength at 28 days for mixes with 340 kg/m³ cement and 75 kg/m³ (left) or 120 kg/m³ (right) limestone powder. If a minimal slump flow of 700 mm is desired in combination with f_{c28d} of 45 MPa, the required W/P and SP amount respectively has an approximate value of 0.55 and 0.80 % in case 75 kg/m³ limestone powder is added. In case 120 kg/m³ limestone powder is added, and to achieve the same strength and slump flow, only 0.50 as the W/P ratio and 0.60 % SP is necessary. If we add more SP in this case of 120 kg/m³ limestone powder addition, for example 0.80 % SP, an increase of strength and slump flow is established, hence indicating the beneficial effect on fresh and hardened concrete properties of addition of limestone powder.

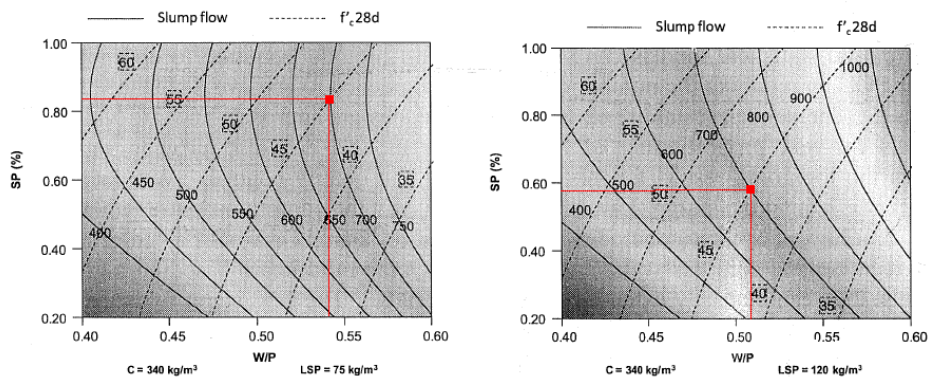


Figure 6.8: Isoresponses of slump flow and f_{c28d} with W/P and SP for two dosages of added limestone powder [Sui et al., 2009]

2.3 Thermal properties

2.3.1 Specific heat

Principle

The specific heat gives the quantity of heat necessary to produce a unit change of temperature (1 °C) in a unit of mass (1 kg) of a substance and is expressed in J/(kg·°C). Therefore, it represents the capacity of the material to store heat.

The heat capacity of a material is the amount of heat that can be held by that material. It is linked to the specific heat by means of the volumetric weight of the material, using equation (6.1):

$$c_T = c_p \cdot \rho_c \quad (6.1)$$

where: c_T = the heat capacity of the material (J/(m³·°C))
 c_p = the specific heat of the material (J/(kg·°C))
 ρ_c = the volumetric weight of the material (kg/m³)

Testing procedure

The heat capacity of SCC and TVC is not determined experimentally. This parameter has a negligible influence on the prediction of stresses and the early-age cracking behaviour of concrete elements according to Briffaut et al. (2009). Therefore, the use of a reasonable approximate value is sufficient and can be determined by using equation (6.1). The volumetric weight of the concrete can be determined experimentally by dividing the mass of a concrete sample by its volume according to the Belgian Code NBN EN 12390-1. A constant mean value of 1000 J/(kg·°C) for the specific heat is considered and seems to be common for a concrete in a temperature range between 0 °C and 100 °C [Taerwe, 1997].

Previous studies

Data on the evolution of specific heat during hardening are scarce. The most common trend indicates that the specific heat decreases (linearly) with time. A minor decrease, from 1180 J/(kg·°C) after 3 days to 1160 J/(kg·°C) after 10 days, was found for cement mortar by Löfqvist (1946). Brown and Javaid (1970) declare a higher decrease of 20 % of hardening concrete with time. A renewed test method by Hansen et al. (1982) took into account the heat of hydration production: a linear decline from 1920 J/(kg·°C) after 1.5 h to 1650 J/(kg·°C) after 120 h was found. This decrease behaves in a linear way with the logarithm of time. This test method was improved by De Schutter and Taerwe (1995), and a linear decrease in function of the degree of hydration was reported. Overall, there seems to be no agreement concerning the magnitude of decrease of the specific heat of a hardening concrete. This decrease varies from 1 % to 20 % depending

on different parameters such as cement type, W/C ratio, aggregate type, humidity, temperature, etc. The effect of the temperature and the saturation degree on the specific heat is expressed previously (Chapter 4).

2.3.2 Thermal conductivity

Principle

In physics, the thermal conductivity k , is the property of a material that indicates its ability to conduct heat. The thermal conductivity depends on the type of concrete, the type of aggregates, the saturation degree, etc. Also the environmental temperature affects the thermal conductivity (Chapter 4).

Testing procedure

Even though previous studies indicate that the conductivity has a negligible influence on the prediction of stresses and the early-age cracking behaviour of concrete elements [Briffaut et al., 2009], the characteristic value of k for SCC and TVC is determined by ESV Euridice (2007). It must be noted that the concrete buffer of the Supercontainer has an important role in efficiently conducting the heat originating from the radioactive waste towards the Host Rock in order to reduce the thermal gradients in the buffer..

A probe, measuring the thermal conductivity (type Hukseflux FTN01, range: 0.1 W/(m·°C) to 6.0 W/(m·°C)), is placed in the middle of a vertically cast prismatic column with side 600 mm and height 6000 mm (SOCEA), after 28 days of hardening. The measurement method is based on the so called non steady-state probe (NSSP) technique, which uses a probe (also called thermal properties sensor or thermal needle) in which both a heating wire and a temperature sensor are incorporated. The probe is inserted into the concrete. From the response to a heating step, the thermal resistivity (or the inverse value: the conductivity) of the concrete can be calculated. In general a NSSP consists of a heating wire, representing a perfect line source, and a temperature sensor capable of measuring the temperature at this source.

Table 6.5: Influence of the type of aggregate on the thermal conductivity of concrete

Aggregate type	k-value W/(m·°C)
Siliceous rocks (quartzite, sandstone)	2.4 – 3.6
Igneous crystalline (granites and gneisses)	1.9 – 2.8
Sedimentary carbonate (limestone, dolomite)	1.9 – 2.8
Igneous amorphous (basalts, dolerites)	1.0 – 1.6

The NSSP principle relies on a unique property of a line source: after a transient period (approximately three weeks after the column is cast) the temperature rise ΔT , only depends on the heater power Q of the test equipment, and on the medium thermal conductivity k of the tested material. By measuring the heater power, and tracing the temperature in time (typically during 300 seconds), k can be calculated. Equation (6.2) can be used to determine the thermal conductivity k of the tested material.

$$T = \frac{Q}{4 \cdot \pi \cdot k} \cdot [\ln(t) + B] \quad (6.2)$$

where: T = the measured temperature ($^{\circ}\text{C}$)
 Q = the heat source with constant power (W/m)
 k = the thermal conductivity ($\text{W}/(\text{m}\cdot^{\circ}\text{C})$)
 t = the time (s)
 B = a constant value

Previous studies

The dependency of the thermal conductivity of concrete on the proportions of the concrete components, the mineralogical composition of the aggregates and the saturation degree according to Kaplan (1989) is already discussed in Chapter 4. The thermal conductivity of different aggregate types is given in Table 6.5.

Also the volumetric weight and the environmental temperature have a significant influence. The thermal conductivity drops if the temperature rises, mainly due to the evaporation of the water and the replacement by air, that has lower thermal conductivity than water (Chapter 4). According to Neville (2000), the thermal conductivity of a saturated concrete is situated between $1.4 \text{ W}/(\text{m}\cdot^{\circ}\text{C})$ and $3.6 \text{ W}/(\text{m}\cdot^{\circ}\text{C})$. The volumetric weight does not have a significant influence on the thermal conductivity of a normal concrete, but on the other hand, the thermal conductivity of light concrete is strongly affected by its volumetric weight due to the poor thermal conductivity of the encapsulated air trapped into the pores.

Finally, a reduction of 28 % of the thermal conductivity is noticed during the first period of hydration of concrete (6 hours until 7 days) [Bergstrom and Byfors, 1979].

2.3.3 Coefficient of thermal expansion

Principle

The coefficient of thermal expansion (CTE) α_T gives the thermal deformation, expressed in $\mu\text{m}/(\text{m}\cdot^{\circ}\text{C})$ or $10^{-6}/^{\circ}\text{C}$, due to a variation in temperature and is given by equation (6.3) in case of a linear deformation.

$$\alpha_T = \frac{\Delta l}{l_0 \cdot \Delta T} = \frac{\varepsilon_T}{\Delta T} \quad (6.3)$$

where: Δl = the length change of the material due to variation in temperature (μm)
 l_0 = the initial length of the material (m)
 ΔT = the temperature change ($^{\circ}C$)
 ε_T = the thermal deformation ($\mu m/m$)

The thermal strains are directly linked to the temperature evolution by means of the CTE. This parameter tends rapidly to a constant value which only depends on the concrete mix [Loukili et al., 2000]. The lower the CTE, the lower the deformation of the material under an external thermal load.

Testing procedure

The CTE for SCC and TVC is determined by BBRI (2007). Six concrete prisms (cured at 20 $^{\circ}C$ and 90 % RH) with side 70 mm and length 280 mm are cast and after a hardening time of 28 days subjected to a temperature cycle, varying from 10 $^{\circ}C$ to 60 $^{\circ}C$. The deformation during the cycle is measured and plotted: thermal deformation ε_T on y-axis, temperature on x-axis. The slope of the plotted curve is the CTE (Figure 6.9).

The reference temperature is 20 $^{\circ}C$. Evaporation is limited by sealing the test samples with an adhesive aluminum foil. The water mass loss is smaller than 0.05 %.

Previous studies

For concrete, the CTE strongly depends on the nature of the aggregates and the volumetric fraction of the aggregates in the concrete [Kaplan, 1989]. The cement paste has a higher CTE than the aggregates in the concrete. The thermal dilation coefficient has an influence on the maximal strain value in a concrete structure [Briffaut et al., 2009]. A porphyry based concrete has a CTE of $10.0 \times 10^{-6}/^{\circ}C$, a calcareous concrete has a CTE of $8.0 \times 10^{-6}/^{\circ}C$. The saturation degree has an impact.

According to Kaplan (1989), mean values for the CTE of a calcareous concrete are reported:

- $6.1 \times 10^{-6}/^{\circ}C$ for concrete submerged in water (100 % RH) during 3 months at 18 $^{\circ}C$.
- $7.4 \times 10^{-6}/^{\circ}C$ for concrete stored at 65 % RH during 3 months at 18 $^{\circ}C$.

Fully saturated and empty (dry) pore systems give much lower CTE values than partly saturated pore systems, mainly due to some kind of additional hygrothermal effect (redistribution of pore water and change in capillary tension) [Neville, 2000].

Not much data is given in literature concerning the evolution of the CTE during hardening. The value of CTE is highly elevated at young age and reduces progressively the first 24 hours of hydration [Bergstrom and Byfors, 1979]. The evolution of the CTE at young age is given in Figure 6.10. The general finding is that the CTE starts at a high value of about $70 \times 10^{-6}/^{\circ}\text{C}$ before concrete has set, and drops to about $10 \times 10^{-6}/^{\circ}\text{C}$ during the setting process.

High values of CTE during the fresh state are attributed to the dominance of the water phase that has high CTE compared to solids. Some relative time dependency of the CTE during hardening is given in Table 6.6. These values are given for conventional gravel concrete, but can also be used for other types of concrete as well [De Schutter, 1996].

The dependency of the CTE of concrete on temperature is discussed in Chapter 4. A rise of 15 % is noticed at an elevated temperature of 100°C [Vodák et al., 1996].

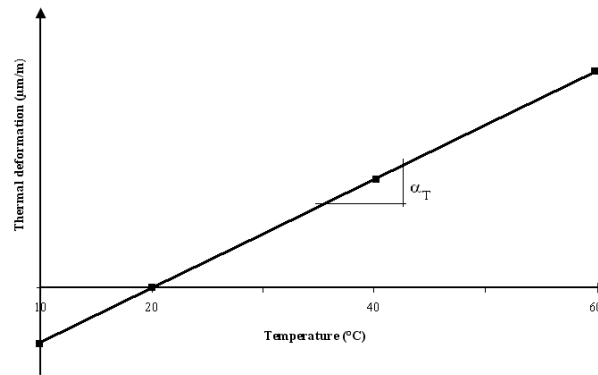


Figure 6.9: Determination of the linear CTE

Table 6.6: Relative values of CTE during hardening [De Schutter, 2002]

Fresh concrete	8 h - 24 h	24 h - 144 h	Hardened concrete
1.82	1.36	1.09	1.00

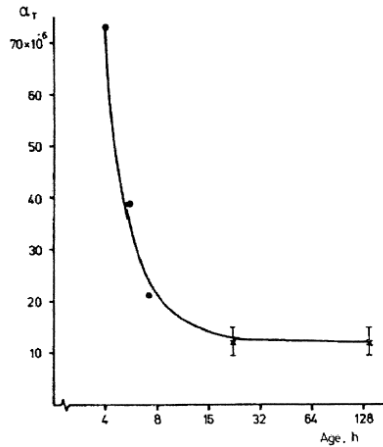


Figure 6.10: Time dependent evolution of CTE [Bergstrom and Byfors, 1979]

2.3.4 Heat production

Principle

Immediately after contact of water with cement, the hydration process of concrete begins and the different minerals of the cement react with the water and new combinations or hydration products are formed who eventually determine the properties, the strength and the stiffness of the concrete. The main components of OPC reacting with water are C_3S , C_2S , C_3A and C_4AF (the abbreviations of CaO (C), SiO_2 (S), Al_2O_3 (A) and Fe_2O_3 (F) as the oxides of an OPC are commonly used). After reaction of C_3S and C_2S with water (standard abbreviation H), CSH as the most important component is formed. In this reaction also CH (calcium hydroxide) is formed, which has an important influence, especially on the highly alkaline character of concrete.

Not only material transformations occur, also energy changes occur. The hydration of cement is an exothermal reaction: during hardening of the concrete, heat is produced, due to the heat of hydration of the concrete [Taerwe, 1997]. The heat production inside a pure hydrating OPC paste is measured via the conduction method according to the Belgian Code NBN B12-213 and starts with an early flash set and a very high peak in the heat production rate curve occurs, only lasting for a couple of minutes (Figure 6.11). This peak has a negligible contribution on the total heat of hydration Q_{max} , and thus will be kept out of consideration. In practice, this peak will not induce significant stresses into the concrete structure due to the time needed between mixing, transport and casting of the concrete. After this first peak, a period of about 2 hours with more or less no hydration activity is noticed, also known as the induction period of the hydration process. About 5 to 15 hours after water is added, a second hydration peak appears, mainly devoted to the hydration of C_3S . In some case, especially when there is a high amount of C_3A in the cement, a third hydration peak occurs. Bensted (1987)

indicates a minimal amount of 12 % of the C_3A content in the cement for the third peak to appear. Generally, for OPC based concretes, this peak most of the time can not be distinguished. On the other hand, BFSC based concrete usually exhibits a third hydration peak due to the hydration of the slag and after Portland activation: the slag reacts with the CH formed earlier during the reaction of C_2S and C_3S . It can be noticed that the total amount of heat is not released at once. Overall, the heat development is very fast in the beginning of binding and during the first hours of hydration and slowly decreases afterwards (Figure 6.11).

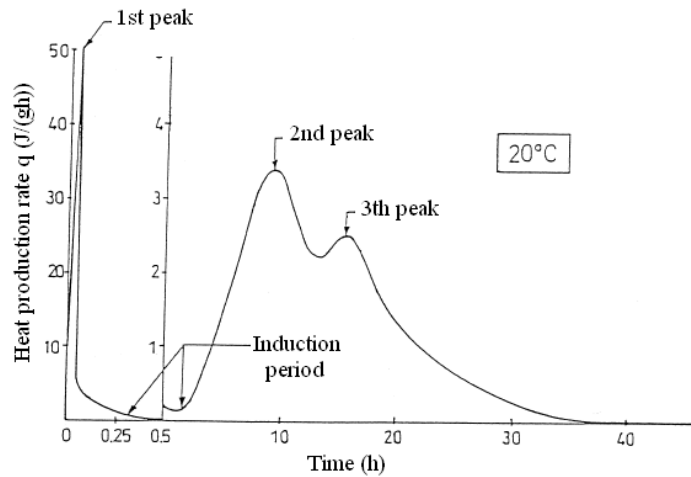


Figure 6.11: Heat production rate of concrete during an isothermal hydration test [Taerwe, 1997]

The total amount of hydration heat can be determined by using the hydration heat of the minerals composing the cement (C_3S , C_2S , C_3A and C_4AF) and making a superposition of the full hydration of each mineral individually [Taerwe, 1997].

In order to investigate the early-age behaviour of massive concrete elements, it is better to determine the heat of hydration and the heat production rate experimentally by means of two types of tests that are commonly used: (i) the adiabatic hydration test and (ii) the isothermal hydration test. The adiabatic hydration tests on concrete will be discussed as a part of the thermal properties. The principles of the isothermal hydration tests of cement pastes are part of the determination of the maturity-related properties, such as the apparent activation energy E , determined under isothermal conditions.

Testing procedure

The total heat production Q , and the heat production rate q of SCC and TVC can be determined by using the adiabatic hydration test according to De Schutter and Taerwe (1995). Therefore, the temperature rise of a perfectly insulated concrete is measured as a function of time (Figure 6.12). A cylindrical concrete specimen (diameter of 280 mm, height 400 mm) is surrounded by a temperature controlled water bath. An electrical heating element connected with an automated steering equipment keeps the water at the same temperature of the concrete, hence creating an adiabatic environment. Insulation between concrete and water is created by using an air-ring. By means of this test set-up, the adiabatic hydration curve can be obtained for SCC and TVC, and the immediate hydration heat production rate can be derived from this curve.

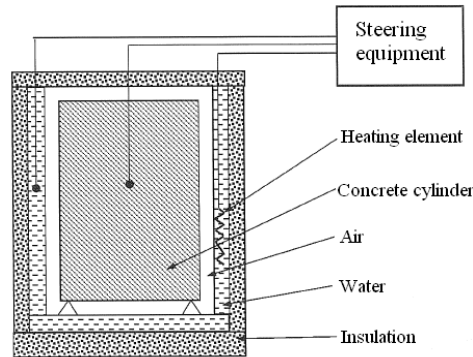


Figure 6.12: The adiabatic hydration test [De Schutter and Taerwe, 1995]

From the adiabatic curves, more detailed results can be obtained by using an expression of the heat of hydration per unit weight of cement. The adiabatic temperature curve can be translated into a heat production curve, according to equation (6.4):

$$Q(t) = c_p \cdot \frac{\rho_c}{C} \cdot [\theta(t) - \theta_0] \quad (6.4)$$

where:

- Q = the cumulated heat of hydration (J/g_{cement})
- t = the time (h)
- c_p = the specific heat of the material ($J/(kg \cdot ^\circ C)$)
- ρ_c = the density of the concrete (kg/m^3)
- C = the cement content (kg/m^3)
- θ = the temperature ($^\circ C$)
- θ_0 = the starting temperature ($^\circ C$)

In case the total heat production $Q(t)$ is calculated out of the adiabatic temperature evolution $\theta(t)$ via equation (6.4), the heat production rate $q(t)$ in adiabatic conditions can be calculated:

$$q(t) = \frac{dQ(t)}{dt} \quad (6.5)$$

where: Q = the cumulated heat of hydration (J/g_{cement})
 q = the heat production rate ($J/(g_{\text{cement}} \cdot h)$)

For further analysis of the hydration process of SCC in comparison with TVC, and in order to obtain a good comparison between the different concrete compositions, $q(t)$ can be further transformed into $q_{20^\circ\text{C}}(r)$, with $q_{20^\circ\text{C}}(r)$ as the heat production rate at 20 °C and r defined as the degree of the hydration reaction. For completeness, the degree of hydration α_h is also defined in equation (6.6b):

$$r(t) = \frac{Q(t)}{Q_{\max}} = \frac{\int q(t) \cdot dt}{Q_{\max}} \quad (6.6a)$$

$$\alpha_h(t) = \frac{Q(t)}{Q_{\text{tot}}} = \frac{\int q(t) \cdot dt}{Q_{\text{tot}}} \quad (6.6b)$$

where: Q_{\max} = the maximal cumulated heat of hydration at end of reaction (J/g_{cement})
 Q_{tot} = the total cumulated heat of hydration after full hydration (J/g_{cement})

This transformation can be done by using the most accurate temperature function, namely the Arrhenius function, according to equation (6.8) and after the determination of E/R , where E is the apparent activation energy of the cement paste (see further) [De Schutter, 1996].

$$q(t) = q_{20^\circ\text{C}}(t) \cdot g(\theta, t) \quad (6.7)$$

where: $g(\theta, t)$ = the temperature dependency function, according to equation (6.8)

$$g(\theta, t) = \exp \left[\frac{E}{R} \cdot \left(\frac{1}{293} - \frac{1}{273 + \theta(t)} \right) \right] \quad (6.8)$$

where: E = the apparent activation energy (kJ/mol)
 R = the universal gas constant ($= 0.0831 \text{ kJ}/(\text{mol} \cdot \text{K})$)

Previous studies

Poppe (2004) investigated the effect of limestone filler in combination with OPC by performing adiabatic hydration tests and isothermal hydration tests. Although this filler material is often considered to be inert, experimental results show that it does influence the hydration process.

Considerable amounts of filler contents must be added to a concrete composition in order to make it self-compacting. The reason for this addition is to avoid problems with excessive heat development during hardening of the concrete by reducing the total cement content for a constant powder content, thus by replacing cement by (inert) filler material. The most important data of this research program dealing with the adiabatic hydration of Self-Compacting Concrete and traditional concrete are recited by Poppe and De Schutter (2005). Four compositions are considered: two self-compacting compositions and two traditional compositions (Table 6.7). The cement type is the varying parameter. In comparison with SCC, no limestone filler is added into the TVC (different with the Belgian reference program of the Supercontainer) and more coarse aggregates and less fine aggregates are added to the mixture.

Table 6.7: Compositions of the mixes (according to [Poppe and De Schutter, 2005])

Component		SCC1	SCC2	TVC1	TVC2
CEM I 42.5 R	kg/m ³	360	-	300	-
CEM I 52.5	kg/m ³	-	360	-	300
Limestone filler	kg/m ³	240	240	-	-
Sand 0/4	kg/m ³	853	853	670	670
Gravel 4/14	kg/m ³	698	698	1280	1280
Water	kg/m ³	165	165	150	150
Superplasticizer	l/m ³	2.3	2.2	-	-

The experimentally obtained temperature curves are given in Figure 6.13. It can be seen that the maximum temperature rise is systematically higher for SCC. It must be noted that a different amount of cement is used for SCC and TVC. Going more into detail, by expressing the heat production rate at 20 °C per unit weight of cement (by using equations (6.4) to (6.8)), an alteration in the hydration mechanism is found when limestone filler is added to the mix. Especially for OPC the heat of hydration of the cement in SCC seems to be different from the heat of hydration developed in TVC. The hydration reaction is significantly influenced by the presence of the limestone powder in SCC. After 40 hours, the adiabatic temperature is about 10 % higher for SCC.

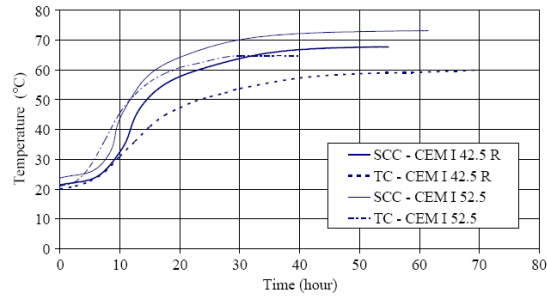


Figure 6.13: Results of the adiabatic hydration test using two types of cement [Pope and De Schutter (2005)]

The hydration models developed for TVC show some discrepancy with the experimental results when applied to the case of SCC (Figure 6.14). Also a second hydration peak is noticed. Isothermal hydration tests on pure cement and on cement and limestone filler mixes are carried out and the results and a more detailed explanation of the effect of limestone filler on the hydration process will be discussed further on.

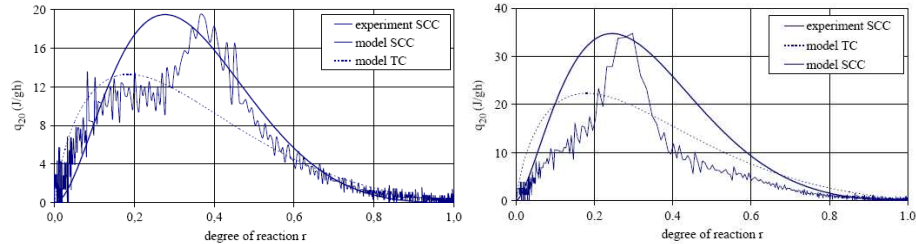


Figure 6.14: Adiabatic test for SCC1 (left, CEM I 42.5 R) and SCC2 (right, CEM I 52.5) [Pope and De Schutter, 2005]

2.4 Maturity-related properties

Principle

As mentioned before, immediately after water comes into contact with cement, the hydration process begins and the different minerals are formed. This process is an exothermal process, and heat is produced due to this reaction at a rate q (Figure 6.11). Two types of tests are commonly used to determine the heat production rate q of a concrete or cement paste: (i) the adiabatic hydration test and (ii) the isothermal hydration test. The adiabatic hydration tests on concrete is discussed previously. The isothermal hydration tests of cement pastes will be used for the determination of the maturity-related properties, such as the activation energy E of the cement paste, under isothermal conditions.

The most important maturity-related property is the activation energy E . By varying the cement/powder ratio, the effect of the filler on the hydration reaction can be determined and E can be derived by the method described in Poppe (2004).

The activation energy (expressed in kJ/mol) is a term that was first introduced by Arrhenius, who initially investigated the temperature dependency of the reactions of sugar in water. It can be defined as the minimal energy that is required in order for a reaction to occur. This activation concept can be used on a wide variety of chemical and physical processes, for example the complex reaction of water and cement. Cement consists of different components and the grains have different sizes. Therefore the activation concept is based on a weighted average of the temperature susceptibility of the simultaneous small partial reactions of the different components of the cement. For that reason, the activation energy for the hydration reaction of cement is also called 'apparent' activation energy [Poppe, 2004]. The activation energy represents the sensitivity of the concrete mixture to temperature: the higher E is, the more sensitive the concrete mix is to a change in temperature. The activation energy is depending on parameters that affect the hydration kinetics, such as mix design (W/C ratio, type of cement, fineness of the cement, mineral additions, etc.) and physical variables such as temperature.

Testing procedure

To evaluate the heat generation in isothermal conditions, an eight-channel heat conduction calorimeter (TAM AIR) is used. All eight channels form a calorimeter block housed in a temperature controlled air thermostat. Each calorimetric channel is constructed in a twin configuration with one side for the tested sample and the other side for a static reference. Each calorimeter operates using the heat flow principle: the heat created due to the hydration reactions of the cement in a sample flows rapidly to its surroundings. The heat flow is measured by two heat flow sensors: one under the sample and one under the reference. The flow of heat of the tested sample, caused by the temperature gradient across the sensor, generates a voltage signal proportional to the heat flow and is compared directly with the heat flow of the inert reference. The voltage difference gives a quantitative expression of the overall rate of the heat production in the sample. This comparison enhances the stability and limits the noise within the system [Gruyaert et al., 2008].

To investigate and compare the hydration process of the SCC and the TVC composition, isothermal hydration tests are performed on pure cement samples and on samples of mixes of cement and filler in different proportions. Each sample contains 14 gram paste (a mix of OPC, limestone filler and water). The tested cement is an OPC, the same cement as used in the reference composition of SCC and TVC: CEM I 42.5 N HSR LA LH. Limestone filler is being used as the filler material. Thus, the influence of any aggregates is excluded.

Table 6.8 gives the different powder mixtures. Four different compositions are tested at three considered temperatures. The isothermal calorimetric measurements are

performed at different temperature: 10 °C, 20 °C (reference temperature) and 35 °C. The W/C ratio, C/P ratio and W/P ratio are also given in Table 6.8 and for SCC and TVC these values are equal to the values listed in Table 6.2 for SCC and Table 6.3 for TVC. The W/C ratio is kept constant. The powder content is the sum of both the cement and the limestone filler.

The mixing procedure is performed manually and outside the calorimeter. First the cement and the filler are placed into the ampoule and blended manually, and afterwards the water is added. Since mixing takes place outside the calorimeter, the first hydration peak (Figure 6.11) could not be entirely registered. This 'wetting' peak only amounted to a few percent of the total heat liberated and will therefore not be considered in the further analysis.

Table 6.8: Compositions of the powder mixes for the isothermal hydration tests

Component		REF	TVC	SCC	SCC'
Cement	g	9.33	8.52	7.84	6.35
Limestone filler	g	-	1.22	2.24	4.47
Water	g	4.67	4.26	3.92	3.18
W/C	-	0.50	0.50	0.50	0.50
W/P	-	0.50	0.44	0.39	0.29
C/P	-	1.00	0.87	0.78	0.59

In this research program, the isothermal hydration heat of four types of compositions with the same type of cement and filler in different proportions are tested to investigate the effect of limestone filler in combination with OPC and to determine the apparent activation energy E. De Schutter (1996) gives a value of 33.5 kJ/mol for the hydration reaction of OPC. After determination of the maximal heat production rates of the compositions at the different temperatures ($q_{\max,10^\circ\text{C}}$, $q_{\max,20^\circ\text{C}}$, $q_{\max,30^\circ\text{C}}$) derived from the isothermal hydration tests and assuming a reference temperature of 20 °C, the value of E of each composition and the mean value of E can be derived using the least squares method [Poppe, 2004]. Equation (6.9) must be reduced to a value that is as low as possible (near zero) by adjusting the value E. Equation (6.8), the most adequate Arrhenius equation, is used for the expression of $g(\theta)$.

$$\sum_{\theta=10-20-35^\circ\text{C}} \left(\frac{q_{\max,\theta^\circ\text{C}}}{q_{\max,20^\circ\text{C}}} - g(\theta) \right)^2 \quad (6.9)$$

where: $q_{\max,\theta^\circ\text{C}}$ = the maximal heat production rate ($\theta=10-20-35^\circ\text{C}$) ($\text{J}/(\text{g}_{\text{cement}} \cdot \text{h})$)
 $q_{\max,20^\circ\text{C}}$ = the maximal heat production rate ($\theta_{\text{ref}} = 20^\circ\text{C}$) ($\text{J}/(\text{g}_{\text{cement}} \cdot \text{h})$)

Previous studies

The previously discussed testing procedure is based on a previous study conducted by Poppe (2004). In this study the effect of the different ratios (W/C, W/P, C/P) on the hydration reaction of cement pastes is being looked at. The reaction rate is influenced due to a modified nucleation possibility and, in some cases, the reaction mechanisms are altered resulting in a new hydration peak. The induction period (Figure 6.11) can be reduced and the hydration process within the first hours is accelerated. The C/P ratio seems to be an important parameter for the cement-filler systems.

Conduction calorimetry is used for the evaluation of the heat generation of small samples of cement paste (pure cement as well a cement and filler mixtures) in isothermal conditions according to the Belgian Code NBN B12-213. The combination of two types of filler (a limestone filler and a quartzite filler) and three types of OPC (CEM I 42.5 R, CEM I 52.5, CEM I 52.5 HSR LA) is being looked at. The combinations of the powder mixes used in the isothermal tests, are given in Table 6.9.

Table 6.9: Compositions of the powder mixes for the isothermal hydration tests (according to [Poppe and De Schutter, 2005])

Component		Mix 1	Mix 2	Mix 3	Mix 4
Cement	g	7.5	4.5	4.5	2.5
Limestone filler	g	-	3	3	5
Water	g	3.75	2.25	3.75	3.75
W/C	-	0.50	0.50	0.83	1.50
W/P	-	0.50	0.30	0.50	0.50
C/P	-	1.00	0.60	0.60	0.33

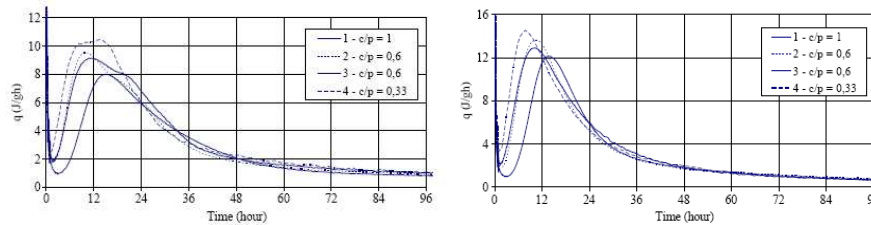


Figure 6.14: Heat production rate for mixtures with CEM I 42.5 R (left) and with CEM I 52.5 HSR LA (right) with limestone filler at 20 °C [Poppe and De Schutter, 2005]

The heat production rate q as a function of time, is obtained for all mixes, using different combinations of the three types of cement and the two types of filler. In Figure 6.15 the heat production rate for mixtures with CEM I 42.5 R and with CEM I 52.5 HSR LA with limestone filler at 20 °C are given. Similar curves can be obtained using quartzite filler and/or CEM I 52.5. The use of quartzite filler is of less interest to this study and thus will be kept out of consideration.

From Figure 6.14 it can be clearly seen that the reaction mechanism of the hydrating cement is altered by the presence of the filler. Several observations are noticed and some conclusions are drawn:

- The more limestone filler is added, the higher the heat production rate and the more cumulative heat is released. The rise in cumulative heat can be explained by the varying W/C ratios of the different mixes. Also the environmental temperature influences the results. The higher the outside temperature, the more pronounced the hydration peak is and the earlier this peak occurs. In first approximation, a linear dependency of the maximal heat production rate on the C/P ratio can be accepted (Figure 6.15).
- Due to the addition of limestone filler (decreasing C/P ratio), the induction period is shortened.
- In case of CEM I 42.5 R is used in combination with limestone filler, an extra hydration peak is noticed. In case of Mix 4 (with very high limestone filler amount), the second hydration peak is even higher than the first peak. This behaviour is not noticed in case CEM I 52.5 HSR LA is used.

The reduction of the dormant phase and the acceleration of the hydration process are well known consequences of the influence of added limestone filler on the hydration of cement, and are previously found in literature [Billberg, 2001, Sharma and Pandey, 1999].

Different hypotheses can be listed to explain the occurrence of the extra hydration peak appearing in the mixes with a combination of CEM I 42.5 R and limestone filler:

- It might be related to the C_3A content in the cement. Bensted (1987) indicates a minimal amount of 12 % of the C_3A content in the cement needed for a visible third hydration peak to appear. This hydration peak is related to the transformation of ettringite into monosulphate, which can be activated by the presence of limestone filler. Proof is given in Figure 6.14: a decreasing C/P ratio, thus a higher filler content, leads to a higher third hydration peak in case of CEM I 42.5 R. OPC with high sulphate resistance (HSR) has a very low content of C_3A (lower than 3 %), which demonstrates the absence of the third peak in case of CEM I 52.5 HSR LA.
- Another approach starts from the viewpoint of a non-inert behaviour of the limestone filler. The limestone filler actually takes part in the hydration reactions and modifies these reactions resulting in a possible delayed ettringite formation, but in case of CEM I 52.5 HSR LA, this is not expected. A more detailed discussion can be found in the literature [Bonavetti et al., 2001].

Finally, the apparent activation energy E is also calculated using the least squares method and is listed in Table 6.10. These values differ from the value proposed by De Schutter (1996) who gives a value of 33.5 kJ/mol for activation of the hydration reaction of pure OPC. The addition of the limestone filler can be seen as the reason for this alteration. It must be noted that the energy needed for the extra (third) hydration peak is quite high and only is found for CEM I 42.5 R.

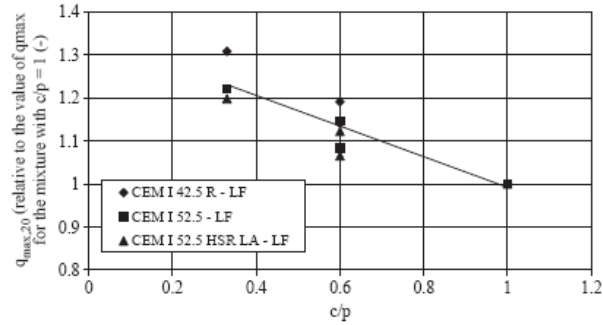


Figure 6.15: Maximal heat production at 20°C, $q_{max,20^\circ C}$ [Poppe and De Schutter, 2005]

Table 6.10: Activation energy of three types of OPC in combination with limestone filler (according to [Poppe and De Schutter, 2005])

		CEM I 42.5 R	CEM I 52.5	CEM I 52.5 HSR LA
E_1	kJ/mol	43.1	38.6	32.5
E_2	kJ/mol	81.8	-	-

2.5 Mechanical properties

2.5.1 Autogenous deformation

Principle

The total deformation of a concrete is the sum of different components (Chapter 5). Overall, the origin of the deformation behaviour lies in the paste phase of the concrete, with especially the properties of the hydration products and the microstructure of the paste influencing the behaviour. In case moisture exchange with the environment is prohibited, for example in case decent curing measures are taken, only the autogenous deformation must be considered for the early-age shrinkage of the concrete. Autogenous shrinkage is defined as the external macroscopical (bulk) dimensional reduction (volume or linear) of the cementitious system, which occurs under sealed isothermal unrestrained conditions [Kovler and Jensen, 2007]. Autogenous shrinkage

of hardening concrete remains subject of various researches entirely devoted to the subject. In case the free autogenous shrinkage of a concrete structure is prevented, internal stresses are introduced into the concrete at early ages, which can exceed the strength of the structure. As a result, premature cracks can be created, making the concrete more vulnerable to the ingress of potentially aggressive species and thus severely reducing the durability of the concrete.

The main parameters affecting the autogenous shrinkage are the amount of water and the amount and type of cement and admixtures in the mixture [Craeye, 2006]. Some findings concerning the autogenous shrinkage are listed below [De Schutter, 2005, Piérard et al., 2005]:

- The increased use of superplasticizers, and thus a lowered W/C ratio, can increase the autogenous shrinkage and can delay the setting time of the concrete. Also the dispersion of the cement is improved and therefore provides a quicker chemical reaction.
- A lower W/C ratio and the use of silica fume and other pore refining admixtures will create finer pores. These finer pores experience a higher internal capillary pressure resulting in a greater autogenous shrinkage.
- Mixtures made with a rapid hardening cement or with a high C₃A content have autogenous shrinkage with faster development and with greater magnitude. The use of slower hydrating cements that have lower chemical shrinkage is suggested.
- Aggregates restrain the autogenous shrinkage, so the amount of aggregates should be maximized to reduce the autogenous shrinkage and the related cracking risk.
- Bleeding of the fresh concrete is acceptable to some extent, as this expansive behaviour can act as antipole for the autogenous shrinkage.

Overall it can be concluded that the total shrinkage increases with increasing W/C ratio (higher drying shrinkage) and increasing cement amount for a given W/C ratio. For autogenous shrinkage, it's the other way around: the lower the W/C ratio, the higher the autogenous shrinkage

Especially HPC, with a low W/C ratio, experiences a high early-age autogenous deformation due to the hydration of cement and water, which consumes less space than the initial products, and due to the self-desiccation of the concrete matrix during hydration [Craeye, 2006]. In literature, little information can be found concerning the autogenous deformation of SCC. The contradicting data makes it hard to come to a general conclusion [Poppe, 2004]. According to Hu and Barcelo (1998) the shrinkage behaviour is higher for the self-compacting compositions in comparison with traditional vibrated ones. On the other hand, Bui and Montgomery (1999) found a reducing effect of limestone filler with an adequate chosen grain size distribution on the shrinkage. Therefore it seems interesting to determine experimentally the short-term and the long-term autogenous behaviour of both the considered compositions SCC and TVC (Table 6.2, Table 6.3).

Testing procedure

Autogenous shrinkage has a strong influence on the early-age crack prediction simulation results [Briffaut et al., 2009]. Therefore, this parameter has to be determined accurately. At the Magnel Laboratory for Concrete Research, a vertical dilatometer for concrete has been developed to determine the autogenous deformation at early age, directly after mixing and continuously during the first 6 days (Figure 6.16) [Craeye, 2006]. The fresh concrete is cast into a vertical cylindrical Teflon tube, and compacted on a vibrating table in case of TVC. The length of the tube is 30 cm and the tube has an internal diameter of 6 cm. Additional Teflon foil is provided in between to reduce friction between the concrete and the mould. Linear vertical shrinkage measurements can start immediately after casting, by means of LVDT's placed on top of a Teflon lid, that follows the shrinkage behaviour of the concrete by means of a bolt. Shrinkage measurements are performed on two identical specimens in parallel. At the same time, temperature measurements are performed on a third specimen, in order to take into account the effect of the heat of hydration on the autogenous shrinkage results. The tests are performed inside a climate room (20 °C, 60 % RH). Evaporation is eliminated by using plastic foil around the concrete and by using Teflon with a low absorbing coefficient as the formwork material.

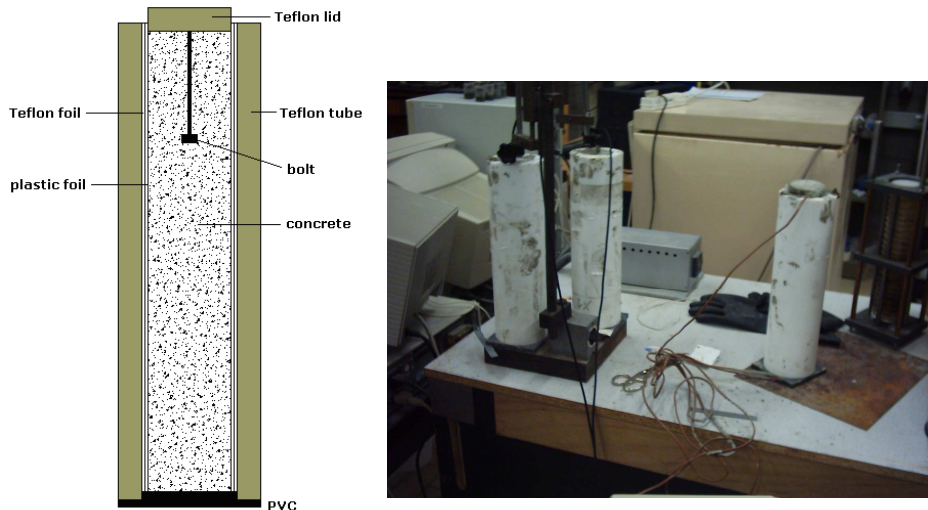


*Figure 6.16: Linear vertical dilatometer for concrete
(On the picture - left : two specimens for deformation measurements - right : one specimen for temperature measurements)
[Craeye, 2006]*

To determine the long-term autogenous shrinkage of SCC and TVC, two prismatic test pieces with a cross section of 150 mm x 150 mm and 500 mm in height are cast

according to the Belgian Code NBN B15-228. After mixing, the test pieces are placed in a climate room (20 °C, 90 % RH) for 24 hours. After demoulding, these specimens are covered with an adhesive aluminium foil to prevent drying and each plane of the prisms is provided with four measurement bases (initial length of 200 mm) in the middle of each plane. The prisms are placed in a climate room (20 °C and 60 % RH). The autogenous deformation is determined mechanically with a deformation meter on the two test pieces: the measurements start after 1 day of hardening until the age of 917 days for SCC and 910 days for TVC. Shrinkage is taken negative.

Previous studies

The previous research study conducted by Poppe (2004), investigated the difference in long-term autogenous shrinkage behaviour of traditional concrete and Self-Compacting Concrete with a comparable strength. The same testing procedure is being used according to the Belgian Code NBN B15-228. The main conclusion is that similar results are found and identical behaviour can be expected for the two types of concrete SCC and TVC. It must be noted that next to the W/C ratio, the C/P ratio also has a considerable effect on the autogenous shrinkage, especially for SCC. The most important findings of the study are briefly discussed:

- By gradually replacing the filler content by an additional amount of cement at constant powder content (C/P ratio increases, the W/C ratio drops), the (autogenous) shrinkage increases. After 100 days, the autogenous shrinkage of a concrete with C/P ratio of 0.75 is approximately 60 % higher compared to a concrete with C/P ratio of 0.5. After approximately 1000 days, the difference is smaller (25 %).
- An increase in W/C ratio of a concrete causes a decrease in autogenous shrinkage. By increasing the W/C ratio from 0.41 to 0.47, the autogenous shrinkage decreases with 20 % after 100 days and with 25 % after 1000 days.
- The use of CEM I 52.5 instead of CEM I 42.5 R or the use of a more fine limestone filler, does not have a significant influence on the results.

It can be concluded, that shrinkage of SCC is of a magnitude entirely comparable with that of TVC [De Schutter et al., 2008]. Estimations of the (autogenous) shrinkage by using design and model codes derived for TVC, can be used for SCC if the cement content and W/C ratio is moderate. However, the use of models and the discussion of these models are not discussed in this work and reference is made to literature [Poppe, 2004]. To predict the early-age behaviour and the early-age autogenous shrinkage of the concrete buffer of the Supercontainer, experimental results are used.

2.5.2 Creep behaviour

Principle

Creep of concrete, resulting from the action of a sustained stress, is a gradual increase in strain with time. It can be of the same order of magnitude as the drying shrinkage.

As defined, creep does not include any immediate elastic strains caused by loading or any shrinkage or swelling caused by moisture changes [Feldman, 1969].

The effects of creep may be harmful, for example the loss of prestress due to creep is well known and accounted for the failure of early attempts at prestressing. Overall, creep, unlike shrinkage, is beneficial in relieving stress concentrations (Chapter 5).

If moisture exchange with the environment is prohibited, only the basic creep deformation needs to be considered. Otherwise, drying creep must be taken into account. It is useful to define the specific basic creep compliance (expressed in $\mu\text{m}/\text{m}/\text{MPa}$), which is obtained by dividing the basic creep by the applied compressive stress, and thus this quantity is independent of the stress level.

According to Taerwe (1997) the basic creep compliance increases with:

- Increasing W/C ratio.
- Decreasing relative humidity. This is especially important for the drying creep, not for the basic creep.
- Decreasing amount of coarse aggregates in the concrete.
- Higher amount of cement for a given W/C ratio.
- Decreasing age at loading.

Several factors influence the creep behaviour. The same factors which govern the rate of development and magnitude of creep of hardened TVC apply to SCC. Concrete that exhibits high shrinkage generally shows a high creep. Also the strength of concrete has a considerable influence on creep and within a wide range creep is inversely proportional to the strength of concrete at the time of application of load [Feldman, 1969]. Experiments have shown that creep continues for a very long time, even as long as 30 years. However, the rate decreases and develops towards a limiting value.

If the sustained load is removed (Figure 6.17), the strain decreases immediately by an amount equal to the elastic strain at the given age. This value ϵ_{cor} is generally lower than the elastic strain on loading ϵ_{c0} since the modulus of elasticity has increased in the intervening period (t_1-t_0). This instantaneous recovery is followed by a gradual decrease in strain, called creep recovery, mainly due to the presence of the aggregates, who are not susceptible to creep and thus act as rigid enclosures taking a part of the stress at loading and slowly spring back at relief [Taerwe, 1997]. This recovery is not complete because creep is not simply a reversible phenomenon, and a non-recoverable creep remains.

Testing procedure

Creep strains can be significant at early age and should be taken into account [Benboudjema and Torrenti, 2008]. In order to determine and compare the basic creep (compliance) behaviour of SCC and TVC, a prismatic test piece with a cross section of 150 mm x 150 mm and 500 mm in height is tested according to the Belgian Code NBN B15-228. Similar to the preparation method used for the determination of the long-term

autogenous deformation, the test piece is chronologically cast, placed in a climate room (20 °C, 90 % RH) for 24 hours, covered with an adhesive aluminium foil to avoid moisture exchange with the environment, and a measurement base (initial length of 200 mm) in the middle of each plane is provided.

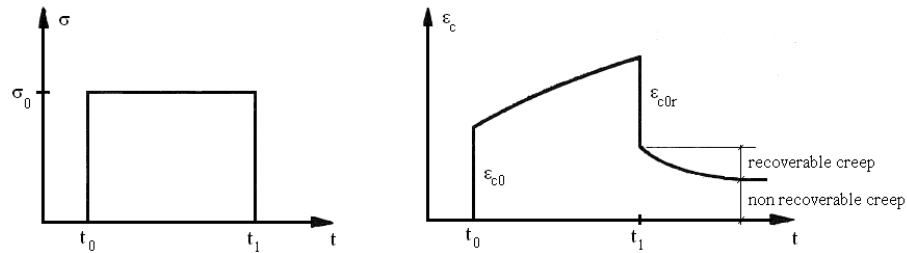


Figure 6.17: Creep deformation due to an applied constant load σ_0 during a time interval $[t_0, t_1]$ [Taerwe, 1997]

At the age of 2 days, 7 days, 14 days and 28 days, the test specimen is placed into a creep apparatus (Figure 6.18) and uni-axially loaded immediately under compression. It is supposed that the creep behaviour is identical in compression and traction. The loading is 30 % of the momentaneous strength of the test pieces ($0.3 \cdot f_{c,prism}$). The total deformation is being measured using a mechanical deformation meter during a long period of time (up to 900 days). Strains are measured before loading and immediately after loading and repeatedly afterwards. By subtracting the instantaneous deformation (when loading is placed on the test specimen) and the value of the autogenous shrinkage from the total deformation, the basic creep value is obtained. The basic creep tests are performed in a conditioned environment with an overall temperature of 20 °C and a relative humidity of 60 %. Conventionally, shrinkage is taken negative.

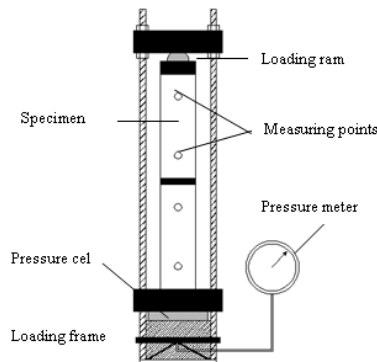


Figure 6.18: A schematic view of the creep apparatus [Craeye et al., 2009]

Previous studies

The previous research study conducted by Poppe (2004), also investigated the difference in creep behaviour, both basic as drying creep, of the same traditional concrete and Self-Compacting Concrete as discussed for the autogenous shrinkage determination. The same testing procedure is being used. It seems that several parameters have an influence on the creep behaviour:

- The C/P ratio has a role in the creep behaviour of concrete, but no clear correlation can be found in the effect of this ratio on the basic creep.
- The W/C ratio: an increasing ratio leads towards higher total creep deformation mainly due to the evaporation of free water, but also no clear relation can be found for the basic creep.
- The type of filler and the type of cement have an insignificant influence on the total creep behaviour, but in case CEM I 52.5 is used instead of CEM I 42.5 R, the basic creep is significantly lower (approximately 25 % after 100 days and 40 % after 1000 days). According to De Schutter et al. (2008) the cement type does have an influence on the total creep. Also the fineness of the additions does not affect the total creep, but a finer filler leads towards a higher basic creep, especially after later ages (> 100 days).

Generally, the magnitude of creep of TVC and SCC tends to be similar. Estimations of the creep by using design and model codes derived for TVC, can be used for SCC if the cement content and W/C ratio is moderate. However, the use of models and the discussion of these models are not discussed in this work and reference is made to literature [Poppe, 2004]. To predict the early-age behaviour of the concrete Supercontainer, experimental results are used to simulate and evaluate the basic creep behaviour of SCC and TVC.

2.5.3 *Compressive strength*

Principle

The strength of the concrete, both in compressive as in tensile nature, considered for the concrete buffer of the Supercontainer, is undoubtedly one of the most important properties of this practical study. Strength gives an overall picture of the quality of concrete because it is directly related to the structure of the hydrated cement paste and is linked with other very important properties such as durability and permeability [Neville, 1963]. The strength of the concrete, self-compacting or traditionally vibrated, is inevitably linked with the quality of the concrete.

The compressive strength of concrete can be expressed via a wide range of formulations (Feret, Abrams, Bolomey, Dutron, Lambotte, expressed in [Taerwe, 1997]), where the W/C ratio is the most important parameter. The compressive strength decreases with increasing W/C ratio (Figure 6.19). The basic relationships between compressive strength and W/C ratio apply equally to SCC as to TVC. In case a higher W/C ratio is applied, thus due to the addition of more water, initially the distance

between the cement grains in the mix will be higher. Therefore, it will take more time for a percolating structure to be formed (see further). Moreover, the hardened concrete will have a greater porosity in case of a higher W/C ratio, which negatively affects the strength and durability issues.

Other parameters affect the compressive strength such as the type and strength of the cement (also the fineness), the type of aggregates (form, grain size distribution, maximal diameter), the cement to aggregate ratio, the compactation degree, the age, the curing conditions (temperature, relative humidity), the form or shape of the samples, etc.

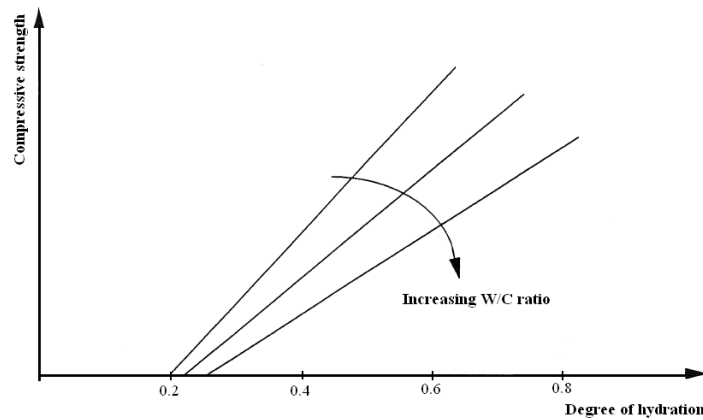


Figure 6.19: The evolution of the compressive strength with varying W/C ratio [De Schutter, 1996]

Looking at the different components of a traditional concrete, the strength of concrete depends on (i) the strength of the mortar and the cement paste, (ii) the bond between the mortar and the aggregates and (iii) the strength of the aggregates. The hardened cement paste consists of three components: (i) hydrated cement, which is the most important component responsible for the created strength, (ii) non-hydrated cement, acting as a filler material and slightly contributing to the strength of the concrete and (iii) the pores, the weaknesses in the matrix. The fact that non-hydrated particles partly contribute to the resistance of concrete is of great importance for the strength of SCC. A typical SCC contains a high proportion of fine additions, which will densify the microstructure of the hardened matrix. Some of these filler materials may actively take part in the hydration process and this may tend to an increased compressive strength (up to 10 % at 28 days compared to TVC with comparable W/C ratio [De Schutter et al., 2008]). Therefore it is often hard to create an SCC with a low strength. The strength of SCC is not necessarily of a high-performant nature: SCC can have a strength varying from very low to very high, which is comparable to TVC [De Schutter et al., 2008]. To conclude, SCC with the same cement and water content as TVC, tends to have the same or greater concrete strength [De Schutter et al., 2008].

Testing procedure

To determine the compressive strength of SCC and TVC, tests are performed at different ages (1 day, 2 days, 3 days, 7 days, 14 days and 28 days) on cubic samples with a side of 150 mm. The samples are placed inside a climate room (20 °C, 90 % RH) during 28 days and are demoulded after 1 day. At each age, uni-axial tests are performed on three samples at the Magnel Laboratory for Concrete Research and at BBRI (2007) according to the Belgian Code NBN EN 12390-3. The compressive strength at the different ages can be found by dividing the maximal load at rupture by the surface of the sample on which the load is applied:

$$f_{ccub150} = \frac{F_c}{A_c} \quad (6.10)$$

where: $f_{ccub150}$ = the compressive strength of a cubic sample (side 150 mm) (MPa)
 F_c = the maximal load at rupture (N)
 A_c = the surface of the sample on which the load is applied (mm²)

In some cases, different curing conditions (curing under water at 20 °C or preservation at the test site) are employed or tests are conducted on smaller cubic samples with a side of 100 mm. The Belgian Code NBN B15-220 foresees empirical conversion factors to take into account the size of the samples:

$$\frac{f_{ccub150}}{f_{ccub100}} = 0.94 \quad (6.11)$$

where: $f_{ccub100}$ = the compressive strength of a cubic sample (side 100 mm) (MPa)

These factors must be handled with the requested care. Samples with the same shape give higher results for compressive strength in case they are smaller. The greater the volume, the higher the risk of imperfections in the sample. In general, the compressive strength of concrete is expressed by means of f_c , determined on cylinders with a diameter of 150 mm and a height of 300 mm. This value forms the base for most of the calculations in concrete structures.

The cylinder to cube (of different sizes) conversion factors are listed below:

$$\frac{f_c}{f_{ccub200}} = 0.83 \quad // \quad \frac{f_c}{f_{ccub150}} = 0.79 \quad // \quad \frac{f_c}{f_{ccub100}} = 0.74 \quad (6.12)$$

where: f_c = the compressive strength of a cylindrical sample (diameter 150 mm, height of 300 mm) (MPa)

Previous studies

Data from more than seventy recent studies, spread over more than a decade, on the hardened mechanical properties of SCC have been analyzed and compared with properties of equivalent strength traditional concrete by Domone (2006). The 28 day strength values of SCC ranged from 20 MPa to nearly 100 MPa, with about 80 % of the mixes having strengths in excess of 40 MPa. This shows it is possible to produce SCC with strengths to suit nearly all normal concreting situations. The strengths are controlled mainly by the binder composition, and not with water/binder ratio as in conventional workability concrete. It is also shown that a significant increase in compressive strength is observed across a wide range of limestone powder contents inside concrete for all ages up to 28 days. On the other hand, if the aggregates in the concrete are more coarse or crushed (and all other concrete parameters are kept constant), a higher compressive strength can be achieved. The difference of strength between mixes with crushed and uncrushed coarse aggregates is lower for SCC than for TVC. Another interesting finding is the existence of a significant difference between the cylinder to cube strength ratio, originally applicable for TVC but also obtained for SCC. Especially for SCC with high strength, this value is almost equal to 1 in case of SCC with a compressive strength of 90 MPa, compared to a value of 0.80 for TVC.

In the pilot project by Poppe (2004) the evolution of the compressive strength of SCC is investigated on cubic samples with a side of 150 mm. Two series of SCC are prepared with different amounts of powder (500 kg/m³ and 600 kg/m³). The amount of water and aggregates is kept constant, only the C/P ratio is varied. CEM I 42.5 R is used as cement. By increasing the C/P ratio at a constant powder content, the development of the compressive strength is faster and $f_{ccub150}$ at 28 days is higher in both the considered cases: $f_{ccub150}$ of SCC (C/P ratio of 0.75) is 30 % higher compared to $f_{ccub150}$ of SCC (C/P ratio of 0.50) in case 500 kg/m³ powder is used. In case 600 kg/m³ is added, this difference is still 20 %. The use of filler material in SCC has an effect on the strength development: it provides a better dispersion of the cement and so the average pore size decreases. Also the addition of superplasticizer can have a beneficial effect on the strength of concrete. The superplasticizer also provides a better dispersion of the cement grains and a higher ultimate degree of hydration is achieved, which can lead towards a higher strength. Finally, the addition of superplasticizer can have an influence on the setting time or on the percolation threshold.

2.5.4 Tensile strength

Principle

In contrast to the widespread knowledge on compressive strength, there is relatively little information available on tensile strength of concrete, especially on the effect of changes in SCC on the tensile behaviour. The behaviour of concrete in traction is mainly determined by its internal structure and by the present imperfections and holes that can initiate or propagate cracking under tensile stress. The tensile strength strongly depends on the size of the tested sample: the greater the volume, the lower the tensile

strength statistically will be due to the greater chance of the presence of imperfections in the concrete [Taerwe, 1997]. The type of aggregates (crushed or uncrushed) also has an influence on the tensile strength: concrete with crushed aggregates generally has a better bonding between the aggregates and the cement paste and thus will have a greater tensile strength. The tensile strength also decreases with increasing W/C ratio (Figure 6.20). The basic relationships between tensile strength and W/C ratio moreover apply equally to SCC as to TVC. The tensile strength development is slightly faster than the compressive strength development, but overall the behaviour is similar.

There are three known types of tensile strength of concrete, depending on the applied test method: (i) the pure tensile strength, (ii) the splitting tensile strength and (iii) the bending tensile strength. Only the first two types are being considered in the testing procedure for SCC and TVC.

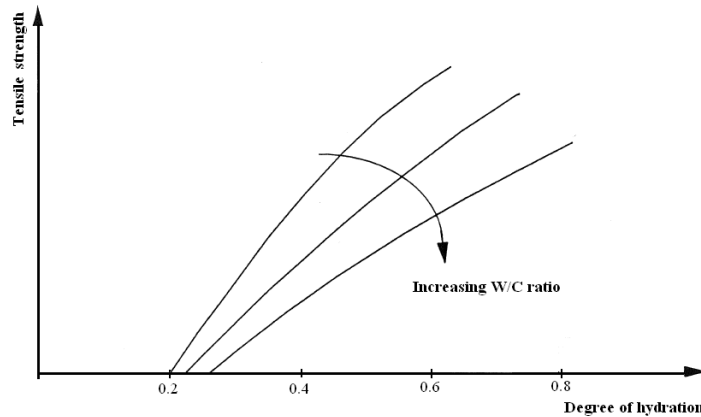


Figure 6.20: The evolution of the tensile strength with varying W/C ratio [De Schutter, 1996]

Testing procedure

To determine the pure tensile strength of SCC and TVC, tests are performed on cores drilled out of a vertically cast prismatic concrete column (SOCEA) with side 600 mm and height 6000 mm [BBRI, 2007]. The cylindrical samples have a diameter of 80 mm and a height of 140 mm. After 56 days, tests are performed on nine samples (three on each level) according to the Belgian Code NBN B15-211. A simple uniform tensile stress is created in the cores: on each end surface of the sample, a metal plate is glued on top of it, provided with a ball joint to prevent the effect of possible eccentric placement of the sample in the test apparatus (Figure 6.21).

The pure tensile strength can be found by dividing the maximal load at failure by the section of occurrence of rupture:

$$f_{ct} = \frac{F_{ct}}{A_{ct}} \quad (6.13)$$

where: f_{ct} = the pure tensile strength of the drilled core (MPa)
 F_{ct} = the maximal load at rupture (N)
 A_{ct} = the section of occurrence of rupture (mm²)

The splitting tensile test is based on the assessment that in case a flat element in an elastic material is subjected to two equal line loads, situated in the same plane and seized perpendicular to the outer surfaces, a uniform tensile stress distribution is created in the material according to Figure 6.22 [Taerwe, 1997]. The tested sample will split according to this plane when the tensile strength is exceeded by the internal stress σ_t . After 42 days and 119 days, the splitting tests are performed on three cubic samples (side 100 mm) after the following curing procedure is followed: first 24 hours at 20 °C and 90 % RH, secondly and until the age of 28 days cured under water, and finally (until the age of 42 days and the age of 119 days) placed in an environment of 20 °C and 60 % RH. The splitting tensile strength tests are performed according to the Belgian Code NBN B15-218.

The splitting tensile strength can be found according to equation (6.14):

$$f_{ctsp} = \frac{2 \cdot F_{ctsp}}{\pi \cdot l \cdot d} \quad (6.14)$$

where: f_{ctsp} = the splitting tensile strength of the cubic sample (MPa)
 F_{ctsp} = the maximal load at rupture (N)
 l = the length of the splitting plane (mm)
 d = the height of the splitting plane (mm)

In case a pure tensile strength test is conducted, failure (or rupture) shall occur in the weakest surface along the total length of the sample. On the other hand, the plane of failure is fixed in case of a splitting tensile strength test, which is not necessarily the weakest zone. Therefore, the splitting tensile strength test statistically gives higher results than the pure tensile strength tests [Taerwe, 1997]. Equation (6.15) is approximately correct.

$$f_{ct} = 0.9 f_{ctsp} \quad (6.15)$$

Previous studies

Most of the available data regarding tensile strength are expressed as the splitting tensile strength, mostly performed on cylindrical specimens.



Figure 6.21: The test set-up to determine the pure tensile strength [BBRI, 2007]

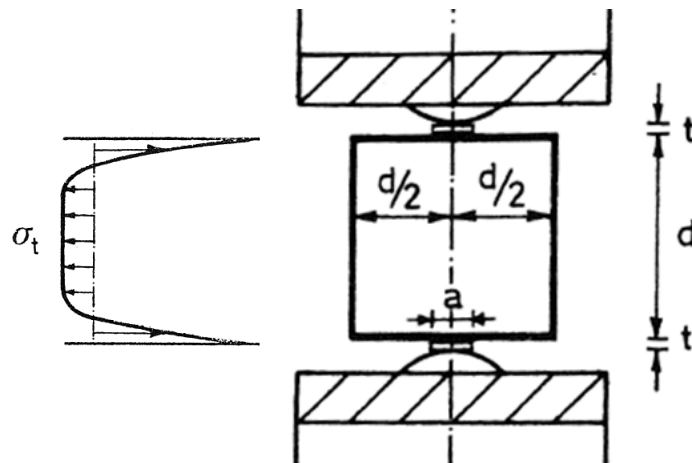


Figure 6.22: The principle of the splitting tensile strength test on a cubic sample [Taerwe, 1997]

Domone (2007) quotes that the ratio of tensile to compressive strength for SCC is similar to that for TVC (about 0.1), where the ratio tends to be within the upper half (Figure 6.23). Other available data slightly tend to indicate a better value of the tensile strength for SCC compared to TVC [De Schutter et al., 2008].

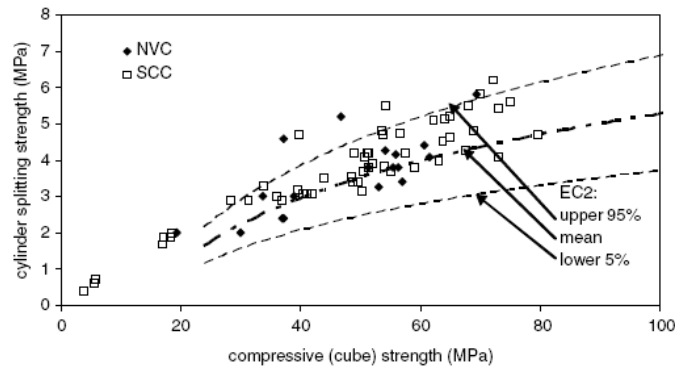


Figure 6.23: Cylindrical splitting tensile strength versus compressive strength of SCC and TVC (=NVC) [Domone, 2007]

2.5.5 Modulus of elasticity

Principle

In solid mechanics, the modulus of elasticity (also known as Young's modulus) is a measurement of the stiffness of an isotropic elastic material. It is defined as the ratio of the uni-axial stress σ , caused by an external loading, over the uni-axial strain ϵ , along the loading direction, in the range of stress in which Hooke's law holds. Two types can be distinguished: (i) the secant modulus of elasticity and (ii) the tangent modulus of elasticity in the origin of the stress-deformation curve and corresponding to the dynamic modulus for elasticity for the analysis of dynamic phenomena (it can be determined via measurements of the resonant frequency of a concrete sample). The secant modulus can be experimentally determined from the slope of a stress-strain curve created during tensile or compressive tests conducted on a test sample of the material.

The development of the modulus of elasticity E_c with time goes in a more non-linear way than the development of the compressive and tensile strength (Chapter 5). The modulus of elasticity develops faster than the (tensile) strength, giving cause to a critical phase where the induced stresses can exceed the tensile strength and can cause cracking (Chapter 5). At a young age, considerable stresses can arise in concrete structures due to thermal effects or shrinkage, which can lead to a noticeable cracking risk. The development of stiffness starts after the induction period is over, and the setting time starts (time zero, see further).

Testing procedure

The modulus of elasticity has a strong influence on the early-age crack prediction simulation results of massive concrete structures [Briffaut et al., 2009]. Therefore, this parameter has to be determined accurately for SCC and TVC. The secant modulus of elasticity is determined by BBRI (2007) according to the Belgian Code NBN B15-203, by measuring the deformation under pressure in a longitudinal way. The tests are performed after 28 days on nine cores drilled out of the vertically cast prismatic concrete column (SOCEA) as discussed previously. The cylindrical samples have a diameter of 113 mm and a height of 226 mm (ratio height/diameter equals 2).

The static secant modulus of elasticity is determined under compression. The stress inside the test sample is increased stepwise by a load that creates a stress increase in the sample inferior to 0.5 MPa until failure of the concrete occurs. After each load step, the longitudinal deformation is measured via a mechanical deformation meter (Figure 6.24). The modulus of elasticity E_c can be calculated by means of equation (6.16), derived from Hooke's law:

$$E_c = \frac{\Delta\sigma}{\Delta\varepsilon_l} \quad (6.16)$$

where: E_c = the secant modulus of elasticity of the concrete sample (GPa)
 $\Delta\sigma$ = the stress gradient applied by the test apparatus (MPa)
 $\Delta\varepsilon_l$ = the longitudinal deformation of the test sample under uni-axial compression ($\mu\text{m}/\text{m}$)



Figure 6.24: Determination of the modulus of elasticity (left) and Poisson's ratio (right) [BBRI, 2007]

Previous studies

A survey conducted by Domone (2007) indicates that the modulus of elasticity of most SCC mixes is lower than that of TVC with a comparable compressive strength. The difference is greater for lower compressive strengths (Figure 6.25): the elastic modulus can be up to 40 % lower than TVC at low compressive strength (< 20 MPa), but the difference reduces to less than 5 % at high strengths (90 MPa – 100 MPa). This behaviour is consistent with the lower coarse aggregate quantities in SCC. Considering hardened concrete as a composite, with coarse aggregates being the principle component contributing to the modulus of elasticity, the reduction of the content of coarse aggregates for SCC in comparison to TVC can explain the lowering of the value of the modulus for SCC [Domone, 2007].

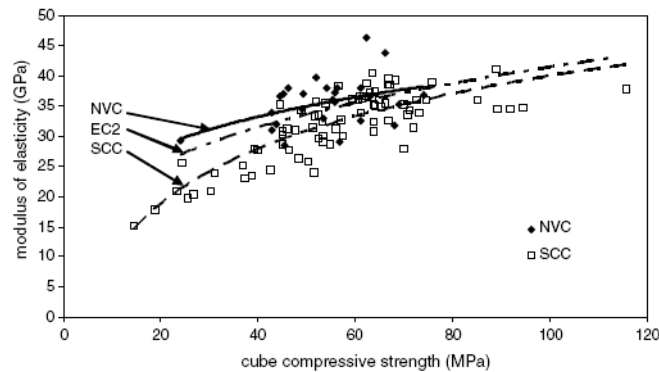


Figure 6.25: Modulus of elasticity versus compressive strength of SCC and TVC (=NVC) [Domone, 2007]

The evolution of the modulus of elasticity of SCC is investigated on cylindrical samples (diameter 150 mm, height 300 mm), stored for 28 days in a conditioned environment (20 °C, 90 % RH) [Poppe, 2004]. As well as the test conducted to determine the compressive strength, two series of SCC are prepared: different amounts of powder is being used (500 kg/m³ and 600 kg/m³), CEM I 42.5 R is used as cement and the amount of water and aggregates is kept constant. By increasing the C/P ratio at a constant powder content, the development of Young's modulus is faster and E_c at 28 days is higher in both the considered cases: E_c of SCC (C/P ratio of 0.75) is 12 % higher compared to E_c of SCC (C/P ratio of 0.50) in case 600 kg/m³ powder is added. In case 500 kg/m³ is added, this difference is less than 3 %. By comparing the results of SCC and TVC, the same relationship between the modulus of elasticity and the compressive strength can be found and also the development of the Young's modulus is faster than the strength development for SCC and TVC.

Sideris et al. (2004) mentioned that an increase of compressive strength goes along with an increase of modulus of elasticity. Several formulations can be expressed to indicate the relationship between those two quantities (Pauw, Parrott, Irvani, Klink,

etc.) where the volumetric weight and the aggregate type are the influencing parameters. Concrete based on limestone aggregates show a reduction of approximately 10 % in modulus of elasticity compared to quartzite aggregates based concrete [Taerwe, 1997].

2.5.6 Poisson's ratio

Principle

The Poisson's ratio is the ratio of the transversal deformation (perpendicular to the applied force) and the longitudinal deformation (in the direction of the applied force). Thus, in case a compressive force is applied on a concrete sample, Poisson's ratio can be found by dividing the transversal expansion by the longitudinal shortening.

Testing procedure

Briffaut et al. (2009) have indicated that the concrete Poisson's ratio has no significant influence on numerical simulation results of concrete strains and stresses in massive structures as long as reasonable values are used. Anyhow, the values of Poisson's ratio of SCC and TVC are determined by BBRI (2007). Poisson's ratio is determined during the same test performed to determine the modulus of elasticity and according to the Belgian Code NBN B15-203. By measuring the deformation under pressure in the transversal way (via LVDT's) and in the longitudinal way (Figure 6.24), Poisson's ratio can be found according to equation (6.17). The tests are performed after 28 days on nine cores (diameter 113 mm, height 226 mm) drilled out of the previously discussed vertically cast prismatic concrete column (SOCEA).

$$\nu_c = \frac{\Delta \varepsilon_t}{\Delta \varepsilon_l} \quad (6.17)$$

where: ν_c = Poisson's ratio of the concrete sample (-)

$\Delta \varepsilon_t$ = the transversal deformation of the test sample under axial compression ($\mu\text{m/m}$)

$\Delta \varepsilon_l$ = the longitudinal deformation of the test sample under axial compression ($\mu\text{m/m}$)

Previous studies

For linear elastic and isotropic materials, Poisson's ratio is constant, but in the case of concrete a value in between of 0.15 and 0.20 is reasonable and is in fact time dependent. In case this quantity is determined by measuring the deformation during a compression test, the general value of 0.15 to 0.22 is most likely to appear in case the deformation of the concrete lies in the linear zone ($\sigma_c < 0.5 \cdot f_c$) and this behaviour is similar in traction and compression. It is also possible to determine the Poisson's ratio dynamically (via ultrasonic tests) by measuring the speed and the resonant frequency of

a longitudinal vibrating pulse through a concrete sample. In this case the measured mean value will be slightly higher, around 0.24 [Neville, 2000].

According to the Belgian Code NBN EN 1992-1, it is preferable to consider a time dependent behaviour for the Poisson's ratio, according to (6.18). On the other hand, for calculation measurements, a relative value of 0.20 for uncracked concrete is also acceptable. In case the concrete is cracked, Poisson's ratio is zero.

$$\begin{cases} \nu_c = 0.5 & [t \leq t_0] \\ \nu_c = -0.0375 \cdot t + 0.65 & [t_0 < t \leq 12 \text{ h}] \\ \nu_c = 0.2 & [t \geq 12 \text{ h}] \end{cases} \quad (6.18)$$

where: $t_0 =$ the time zero (see further) (h)

Klink (1985) indicates that Poisson's ratio is little or not influenced by the chemical composition of the cement or by the mineralogical composition of the aggregates. An actual Poisson's ratio is defined in the middle of the concrete, dependent on the compressive strength and the volumetric weight of the concrete, and elevated values (up to 50 %) are found in comparison to the values found with the standard test methods.

$$\nu_c = 2 \cdot 10^{-9} \cdot (\rho_c^{1.75} \cdot \sqrt{f_c}) \quad (6.19)$$

where: $\rho_c =$ the volumetric weight of the concrete (kg/m^3)
 $f_c =$ the compressive strength of the concrete (kPa)

For HPC ($f_c > 50$ MPa), Iravani (1996) shows values varying between 0.15 and 0.20 depending on the compressive strength, with a mean value of 0.17 if f_c is smaller than 55 MPa and 0.20 if f_c is in between of 55 MPa and 125 MPa.

2.5.7 Time zero

Principle

The microstructure of concrete determines its material properties, such as strength and stiffness. Hardening concrete has a continuously changing microstructure and thus continuously changing thermal and mechanical properties. It is important to know from what time on the changing microstructure is vulnerable to internal stresses. Time zero t_0 is the moment when the imposed deformations give cause to an internal stress build-up in concrete in case free deformation is prevented: it is the moment when the strength and the stiffness of the hardening concrete start to develop. Translating this into the hydration concept (see equation (6.6b), the hydration degree at a certain time can also be seen as the relation of the amount of cement that already is hydrated to the initial

amount of cement), this moment is also known as the percolation threshold α_0 , the hydration degree when a percolating microstructure originates during hydration of the cement [De Schutter, 1996]. Therefore, it is useful to examine the phenomenological effect during hydration more into detail. Considering one cement particle in contact with water: the particle starts to grow hydration products inwards and outwards of its original grain boundary during hydration. Inside the concrete, a numerous amount of cement particles comes into contact with water and show the same behaviour as one particle and undergoes a material transformation: hydrating products are formed around the cement particles (Figure 6.26). If these hydration products do not come in contact with each other (there is still water separating them), the material has no strength or stiffness yet. At a certain moment in time t_0 , or at a certain hydration degree α_0 , these hydration products interconnect and an internal percolating structure is formed. The induction period is over. The plastic and processable specie has developed into a stiff and non-workable paste. From now on, the strength and the stiffness start to develop (Figure 6.19, Figure 6.20). Overall, three periods can be distinguished (Figure 6.26): (i) the induction period, (ii) the start of the setting and (iii) the end of the setting or the beginning of the hardening of the concrete. Time zero coincides with the initial setting time.

The W/C ratio of the concrete mixture has a considerable influence on this percolation threshold: the higher the ratio, the further away the cement particles are from each other initially, thus the longer it takes for them to form an interconnecting percolating structure. On the other hand, more water is available for the cement to form hydration products, thus a higher ultimate degree of hydration is achieved (Figure 6.19, Figure 6.20). As mentioned before: a higher W/C ratio also leads towards a higher porosity [De Schutter, 1996, Poppe, 2004]. The onset of the percolating structure formation is also influenced by the filler amount, the fineness and the type of filler due to a possible effect of the filler on the cement hydration. For example: limestone filler accelerates the hydration process and reduces time zero, while this is not the case when using quartzite filler [Poppe, 2004].

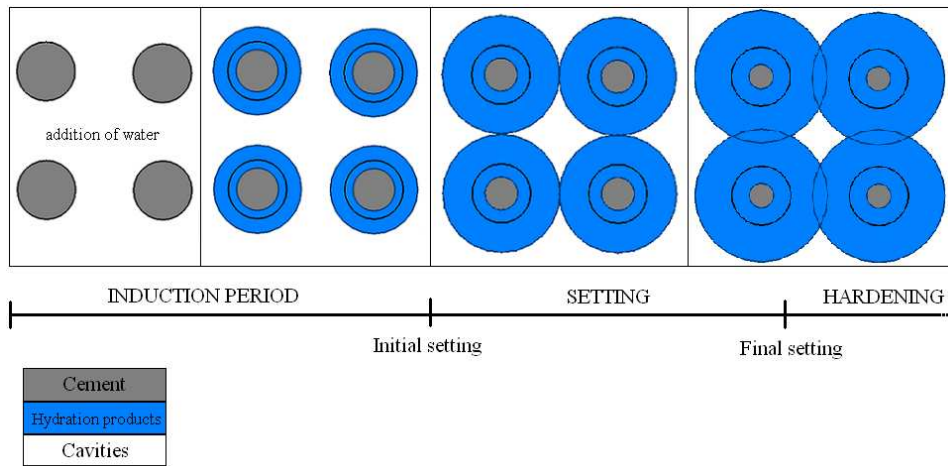


Figure 6.26: The hydration of cement (according to [De Schutter, 1996])

Testing procedure

To come to a reasonable value of time zero of SCC and TVC, estimations can be made based on the results of the compressive strength tests [Craeye, 2006]:

- The development of the compressive strength has a linear connection with the logarithm of time. By plotting the test results of the compressive strength tests at different ages (from 1 day up to 28 days), and by performing a linear regression, time zero (the time where the compressive strength starts to develop) can be estimated. The same analysis can be done by plotting the relative strength (relative to the strength at 28 days) in function of the logarithm of time and by performing the linear regression method. The determination via these methods is not very accurate due to the absence of results of compressive strength at very young age (< 12 hours) and due to the scatter on the obtained compressive strength results.
- The estimation of time zero can be done by using the hydration concept. The (relative) compressive strength can be plotted in function of the hydration degree (time can be translated into hydration degree by using the adiabatic hydration test results and equation (6.6b)). By performing linear regression, the percolation threshold α_0 can be found (Figure 6.27) and back translated into time zero t_0 .

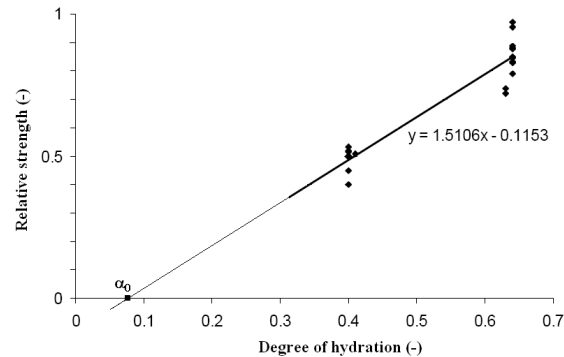


Figure 6.27: Using linear regression and the hydration concept for the determination of α_0 [Craeye, 2006]

By means of this method, Craeye (2006) found a time zero of approximately 2 hours (first method) to 6 hours (second method) for HPC, using CEM I 52.5 R and a W/C ratio of 0.32. Only the first method is applied for the determination of time zero of SCC.

Other methods to determine the onset of cluster formation of the hydration products are traditional ones such as the apparatus of Vicat (according to the Belgian Code NBN EN 196-3) or the Proctor needle test (according to ASTM C403). Unfortunately these methods can only be used on cement pastes (Vicat) or on mortar (Proctor). Therefore they are kept out of consideration for further discussion.

Non-destructive ultrasonic transmission measurements tests, performed by the FreshCon system, allow the continuous monitoring of the setting of both mortar and concrete samples, and thus give a more complete picture of the binding of the concrete [Robeyst et al., 2008]. The compression waves (p-waves) used in this test method provide a more accurate determination of the velocity through fresh concrete because of the high signal-to-noise ratio. These waves can propagate through fluids which clearly indicates the advantage of p-waves compared to other waves, such as shear waves. The change that the velocity of an ultrasonic p-wave undergoes with time during setting and hardening of concrete is registered and the three periods discussed in Figure 6.26 can be clearly distinguished (Figure 6.28): the first part is the induction period, characterized by a constant low velocity. Afterwards, the velocity increases more rapidly at first and finally more gradually to reach an asymptotic value. The very early increase in velocity is devoted to the formation of ettringite and thus has no influence on the stiffening process and does not contribute to the strength development of the fresh concrete. Thereafter, starting from the inflection point (Figure 6.28), the actual setting takes place. The end of the setting corresponds with the third stage of the velocity curve: the slow increase of velocity towards the constant value.

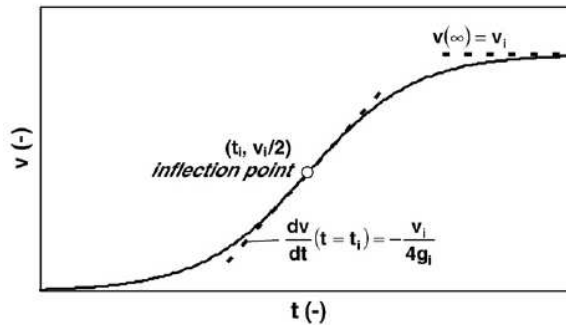


Figure 6.28: Demonstration of ultrasonic measurements on concrete samples [Robeyst et al., 2008]

By means of this method, Robeyst et al. (2008) found that the start of the setting of concrete with CEM I 42.5 and CEM I 52.5, without any other additions and with a W/C ratio of 0.5 is between 4 hours and 6 hours. The first hours before the inflection point is reached, the velocity in the concrete and the equivalent mortar mixture (same type of cement, sand and W/C ratio) changes analogously in time. Thus, the influence of the larger aggregates is rather small as long as the setting (start of binding) has not occurred. Therefore an equivalent time zero for SCC and TVC can be assumed. Finally, the addition of BFSC delays the start of the setting and the hardening.

3 Results and Discussion

3.1 Fresh concrete properties

3.1.1 Fresh properties of SCC

As mentioned before, nineteen SCC mixes are tested at three locations during the laboratory characterization program to determine the fresh properties of the SCC composition discussed in (Table 6.2): the slump flow, the V-funnel time, the L-box value, the sieve stability percentage, the density and the air content. The results are listed in Table 6.11 and Table 6.13. There is a rather large dispersion on the fresh test results of the SCC.

The slump flow value varies between a wide range of 575 mm and 800 mm, respectively translated into the lower class SF1 and the upper class SF3 according to Table 6.4, and a mean value of approximately 690 mm (class SF2). A rather good flow ability and no horizontal segregation is found in the mixes. No segregation is found in the mixes: the sieve stability test results are at all times smaller than the recommended limit value of 15 %.

Also the two V-funnel classes (VF1 and VF2) are represented for SCC, the mean value is 16.0 s, with a standard deviation of 12.5 s, hence demonstrating the wide spread on the results. Even V-funnel times in excess of 25 s are found. These high flow times indicate that the SCC can be quite stiff and is not easily deformable due to high internal friction and high viscosity of the mix. A high V-funnel time can also be caused due to clogging of the coarse aggregates near the opening of the test apparatus.

The L-box value is often smaller than the recommended value of 0.80, and blocking near the reinforcement bars is found in those cases. The SCC has a poor passing ability, but in case of casting of the concrete buffer and the lid of the Supercontainer, this is not fully required.

The mean density of the fresh SCC is 2405 kg/m³ and the average air content is 1.5 %. The only varying parameter in the SCC compositions is the superplasticizer content with a value in between 10 kg/m³ and 14 kg/m³. The mean superplasticizer content is 11.8 kg/m³, with a standard deviation of 1.3 kg/m³.

There is hardly no correlation to be noticed between the slump flow and the superplasticizer content except for a small increase of slump flow value with increased superplasticizer content (Figure 6.29). Also no correlation can be found in case of the V-funnel time. By adding more SP, especially the risk of segregation of the concrete mixture increases [Poppe, 2004].

Previously, typical ranges of key proportions of an SCC composition are discussed in Table 6.1. Although the proportions of SCC fit the proposed ranges, some fresh test results (V-funnel and L-box) do not give acceptable results. The W/P ratio (1.16 by vol

%) of the discussed SCC is higher than the highest value given in Table 6.1 (i.e. 1.10). Therefore, it can be recommended to adjust the amount of limestone filler to increase the powder content at a constant cement content and thus lower the W/P ratio to comply with the recommended value of 1.10 (by vol %). Tests are performed at the Magnel Laboratory for Concrete Research to determine the fresh properties of SCC with the same composition as given in Table 6.2, but with an additional amount of 50 kg/m³ of limestone filler, replacing 50 kg/m³ of coarse limestone aggregates with size 6/14. In this mix, 11.8 kg/m³ superplasticizer is added. Next to a similar slump flow value of 690 mm, a tolerable V-funnel time of 10.3 s and an acceptable L-box value of 0.84 is registered for the SCC with a density of 2390 kg/m³ and an air content of 1.7 %. Thus, the addition of limestone powder leads to more satisfying fresh tests results and the compressive strength at 28 days (of cubes with a side of 150 mm) is 54.6 MPa. In case 50 kg/m³ of the coarse aggregates (6/14) is replaced by the same amount of fine aggregates (0/4) and once again 11.8 kg/m³ of superplasticizer is added, the following fresh properties are found: a slump flow of 650 mm, a V-funnel time of 14.2 s. The result of the L-box has an intolerable value of 0.62. The density of the fresh concrete is 2390 kg/m³, the air content is 1.8 % and the compressive strength at 28 days is 51.0 MPa. Thus, in order to get more acceptable fresh properties for the SCC, it is recommended to replace 50 kg/m³ coarse aggregates by 50 kg/m³ limestone filler better than to replace the coarse aggregates by 50 kg/m³ fine aggregates (0/4).

3.1.2 *Fresh properties of TVC*

Apart from the nineteen SCC mixes, also seventeen TVC mixes are tested at the three locations during the laboratory characterization program to determine the fresh properties of the TVC composition given in Table 6.3: the slump, the flow, the density and the air content. The results are listed in Table 6.12 and Table 6.14. The mean superplasticizer content added is 4.0 kg/m³ (s = 0.4 kg/m³, s is the standard deviation on the mean value). The standard deviations on the fresh test results of TVC are much smaller compared with those of SCC.

The mean slump value of TVC is 225 mm, the mean flow value is 760 mm, making this an extremely good flow able traditional concrete, categorized in the upper consistency classes S5 for the slump value and F6 for the flow value according to the Belgian Code NBN EN 12350. Compared to SCC, TVC has a higher mean density of 2440 kg/m³ and a lower air content after vibration (1.0 %). The common tendency is that a higher air content leads towards a lower density of the fresh concrete mix (Figure 6.30).

External vibration energy is needed to overcome the internal friction and the cohesion forces between the different concrete constituents and the possible capillary forces in the fresh specie. The flow ability of fresh TVC is not sufficiently high enough to drive away the air bubbles by itself and under influence of the gravity, as in the case of SCC.

Table 6.11: Characteristic values of the fresh properties of SCC

SCC properties		max	min	mean	s	#
Slump flow	mm	800	575	690	50	19
V-funnel	s	41.0	5.0	16.0	12.5	17
L-box	-	0.84	0.40	0.69	0.16	8
Sieve stability	%	13.5	2.7	6.8	3.5	8
Density	kg/m ³	2435	2350	2405	25	15
Air content	%	2.4	0.9	1.5	0.5	9

Table 6.12: Characteristic values of the fresh properties of TVC

TVC properties		max	min	mean	s	#
Slump	mm	250	175	225	20	17
Flow	mm	800	705	760	40	5
Density	kg/m ³	2470	2400	2440	20	14
Air content	%	1.6	0.5	1.0	0.4	11

Table 6.15: Characteristic values of the volumetric weight (in kg/m³) of hardened SCC and TVC at different ages

SCC				TVC			
	mean	s	#		mean	s	#
1 day	2415	30	7	1 day	2415	15	5
2 days	2400	10	10	2 days	2415	15	7
3 days	2390	15	4	3 days	2415	20	7
7 days	2390	15	9	7 days	2415	15	10
14 days	2380	20	7	14 days	2410	5	4
28 days	2390	20	11	28 days	2410	25	11

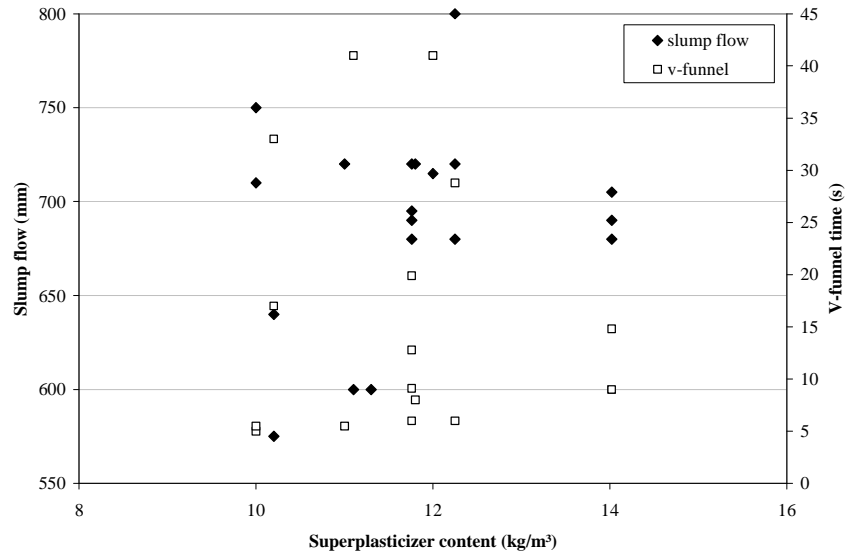


Figure 6.29: Slump flow and V-funnel time in function of the superplasticizer content

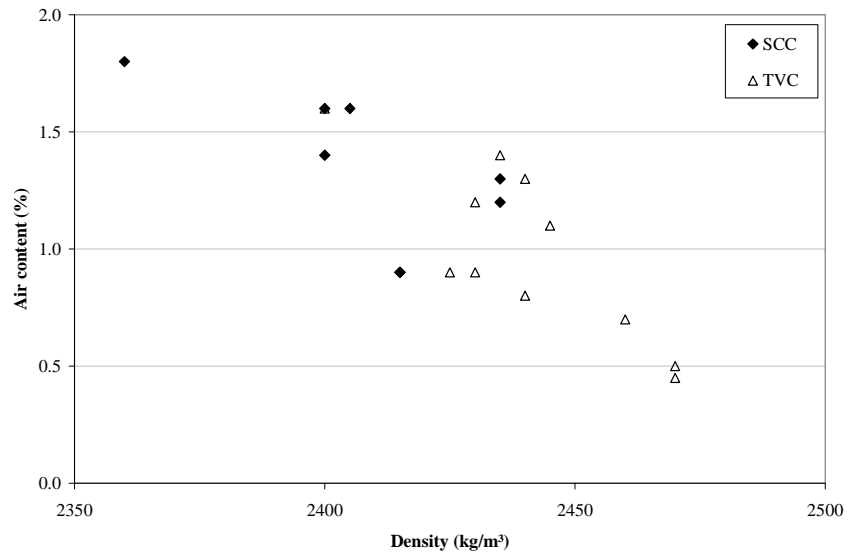


Figure 6.30: The air content versus the density of fresh SCC and TVC

Table 6.13: Fresh properties of 19 SCC mixes

		SCC	SCCm1	SCCm2	SCCm3	PSCC1	PSCC2	PSCC3	PSCC4	DSCC1	DSCC2
Date		31/08/06	7/11/06	7/11/06	7/11/06	5/12/06	5/12/06	3/01/07	3/01/07	23/01/07	23/01/07
Location		BASF	SOCEA	SOCEA	SOCEA	MAGNEL	MAGNEL	MAGNEL	MAGNEL	MAGNEL	MAGNEL
Superplasticizer	kg/m ³	14.0	11.0	10.0	10.0	11.8	11.8	14.0	14.0	11.8	11.78
Mix quantity	m ³	-	1	1	1	0.04	0.04	0.05	0.05	0.15	0.15
Fresh results											
Slump flow	mm	680	720	710	750	720	695	705	690	690	680
V-funnel	s	9.0	5.5	5.0	5.5	9.1	-	19.9	14.8	9.0	12.8
L-box	-	-	0.77	0.84	0.78	0.50	0.72	0.81	0.67	-	-
Sieve stability	%	-	2.7	3.1	5.3	8.1	8.1	5.6	7.8	-	-
Density	kg/m ³	2360	2405	2425	2405	2405	-	2435	2435	2400	-
Air content	%	1.8	-	-	-	1.6	-	1.2	1.3	1.6	-

		SCC ad	NSCC1	NSCC2	SCC AK	SCC1	SCC2	SCC3	SCC4a	SCC4b
Date		15/05/07	31/07/07	31/07/07	31/10/07	3/03/09	10/03/09	24/03/09	7/04/09	21/04/09
Location		MAGNEL	MAGNEL	MAGNEL	MAGNEL	MAGNEL	MAGNEL	MAGNEL	MAGNEL	MAGNEL
Superplasticizer	kg/m ³	11.8	12.3	12.3	12.3	10.2	10.2	12	11.1	11.3
Mix quantity	m ³	0.055	0.15	0.15	0.03	0.05	0.05	0.05	0.05	0.05
Fresh results										
Slump flow	mm	720	720	800	680	640	575	715	600	600
V-funnel	s	6.0	8.0	28.8	-	6.0	17.0	33.0	41.0	41.0
L-box	-	-	0.40	-	-	-	-	-	-	-
Sieve stability	%	-	13.5	-	-	-	-	-	-	-
Density	kg/m ³	2400	2415	-	2415	2350	2405	2405	-	2395
Air content	%	1.4	0.9	-	0.9	-	-	-	-	2.4

Table 6.14: Fresh properties of 17 TVC mixes

		TVC	TVCm1	TVCm2	TVCm3	PTVC1	PTVC2	DTVC1	DTVC2
Date		31/08/06	14/11/06	14/11/06	14/11/06	5/12/06	5/12/06	30/01/07	30/01/07
Location		BASF	SOCEA	SOCEA	SOCEA	MAGNEL	MAGNEL	MAGNEL	MAGNEL
Superplasticizer	kg/m ³	4.8	4.4	4.4	4.4	3.6	3.6	3.6	3.6
Mix quantity	m ³	0.05	1.05	1.05	1.05	0.04	0.04	0.15	0.15
Fresh results									
Slump	mm	225	245	245	250	225	225	225	225
Flow	mm	-	745	-	745	705	-	-	-
Density	kg/m ³	2400	2470	2425	2430	2430	-	2460	-
Air content	%	1.6	0.5	0.9	0.9	1.2	-	0.7	-

		TVC ad	NTVC1	NTVC2	TVC AK	TVC1	TVC2	TVC3	TVC4a	TVC4b
Date		29/05/07	7/08/07	7/08/07	7/11/07	5/03/09	12/03/09	26/03/09	5/05/09	26/05/09
Location		MAGNEL	MAGNEL	MAGNEL	MAGNEL	MAGNEL	MAGNEL	MAGNEL	MAGNEL	MAGNEL
Superplasticizer	kg/m ³	3.6	3.6	3.6	3.6	6.0	4.0	4.0	4.1	4.1
Mix quantity	m ³	0.055	0.15	0.15	0.03	0.05	0.05	0.05	0.05	0.05
Fresh results										
Slump	mm	250	205	215	245	55	175	205	205	215
Flow	mm	800	800	-	-	-	-	-	-	-
Density	kg/m ³	2470	2440	-	2445	2425	2440	2450	2435	2440
Air content	%	0.5	0.8	-	1.1	-	-	-	1.4	1.3

3.2 Thermal properties

3.2.1 Specific heat

Considering a mean value of 1000 J/(kg·°C) for the specific heat of concrete based on OPC according to Taerwe (1997), the heat capacity of SCC and TVC can be determined according to equation (6.1). Note that the specific heat of a saturated fresh concrete is 1.2 – 1.5 times higher than a dry concrete. The specific heat strongly depends on the water amount of the concrete, mainly because the specific heat of water is much higher than that of concrete: 4190 J/(kg·°C). However this will be kept out of consideration and a constant value is maintained during hardening.

To determine the heat capacity, the volumetric weight of SCC and TVC needs to be determined at different ages, and on cubic samples with a side of 150 mm, cured at a temperature of 20 °C and a relative humidity of 90 % until the age of testing. The mean values with the standard deviation are given in Table 6.15. In comparison to the density of fresh concrete, the volumetric weight of hardened concrete is significantly lower, mainly due to the evaporation of unbound free water available in the pores (drying). Also a slight tendency to decrease of the volumetric weight of the hardening SCC and TVC is noticed. Overall, the volumetric weight of TVC is, at all times, higher than that of SCC.

For further calculations (Chapter 8 and Chapter 9), a reasonable constant value of respectively 2390 kJ/(kg·°C) and 2410 kJ/(kg·°C) will be considered for the heat capacity of SCC and TVC, based on the volumetric weight after 28 days and equation (6.1).

3.2.2 Thermal conductivity

As a result of the probe measuring technique, with a probe embedded in a 6 meter high cast column (SOCEA), the thermal conductivity of SCC and TVC can be determined. Once a minimal temperature variation in the concrete (smaller than 0.02 °C) sets in, approximately 3 weeks after casting (then the heat production rate due to hydration is significantly small), the determination of the thermal conductivity is performed. Minimal variation is necessary because the slightest external temperature gradient during the measurements will disturb the results. At a certain amount of time, the temperature increase T (order of magnitude smaller than 1 °C) due to a constant heat source Q shows a linear behaviour and is registered.

Plotting the temperature rise in function of a logarithmic function of time, $Q/(4 \cdot \pi \cdot k)$ can be extracted out of equation (6.2) as the slope of the straight line through the registered points. Another way is to plot $(4 \cdot \pi \cdot T)/Q$ in function of time and then the thermal conductivity can be found as the inverse of the slope of the straight line and according to equation (6.2) (Figure 6.31a, Figure 6.31b).

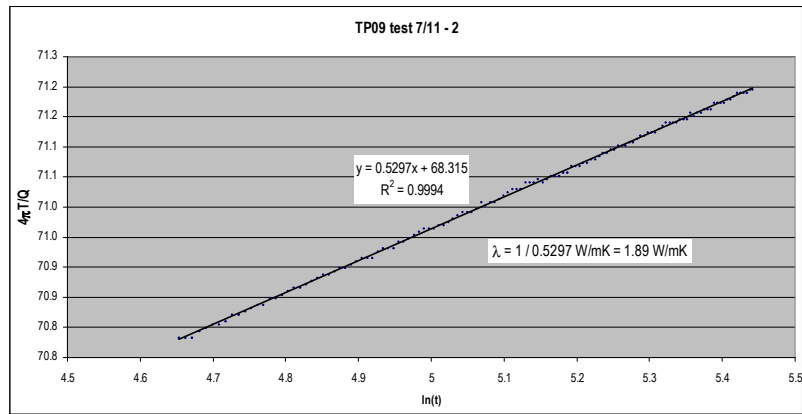


Figure 6.31a: Determination of the thermal conductivity of SCC by means of linear regression [ESV Euridice, 2007]

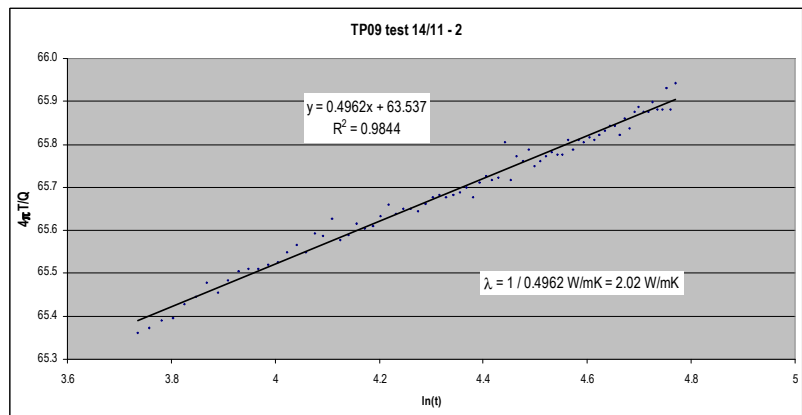


Figure 6.31b: Determination of the thermal conductivity of TVC by means of linear regression [ESV Euridice, 2007]

$$\frac{4 \cdot \pi \cdot T}{Q} = \frac{1}{k} \cdot [\ln(t) + B] \quad (6.2b)$$

where: T = the measured temperature ($^{\circ}\text{C}$)
 Q = the heat source with constant power (W/m)
 k = the thermal conductivity (W/(m \cdot $^{\circ}\text{C}$))
 t = the time (s)
 B = a constant value

In this way, the thermal conductivity of SCC (1.89 W/(m·°C)) is slightly lower compared to the thermal conductivity of TVC (2.02 W/(m·°C)). These values correspond to the values of concrete with limestone aggregates according to Table 6.5 and a constant value will be considered for further computations. The ability of SCC to conduct heat is smaller than that of TVC: SCC acts more like an insulator compared to TVC.

3.2.3 Coefficient of thermal expansion

The deformation of six hardened prismatic concrete samples of SCC and TVC under influence of a temperature cycle (10 °C – 20 °C – 40 °C – 60 °C) is measured. The temperature in the samples is measured by means of thermocouples placed in the middle of the sample, the deformations are measured at the top of the samples.

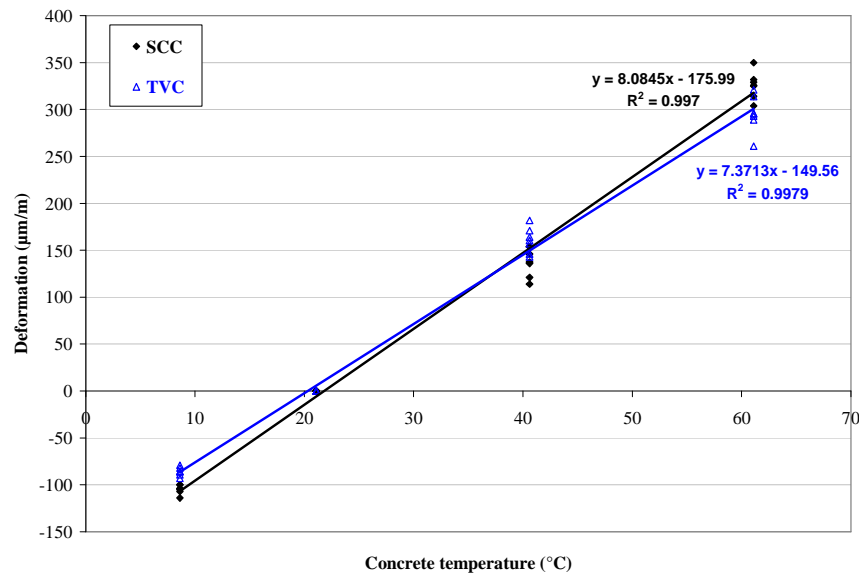


Figure 6.32: Determination of the CTE of SCC and TVC by means of linear regression [BBRI, 2007]

By plotting the registered deformation in function of the temperature inside the concrete, the coefficient of thermal expansion (CTE) is determined as the slope of the straight line found after linear regression through the plotted points (Figure 6.32) and according to equation (6.3). For SCC the CTE is approximately $8.1 \times 10^{-6}/^{\circ}\text{C}$, and is higher than the CTE of TVC ($7.4 \times 10^{-6}/^{\circ}\text{C}$). These values correspond very well with the values of the CTE of calcareous concrete found in literature: $8.0 \times 10^{-6}/^{\circ}\text{C}$.

SCC has the tendency to deform more under influence of a temperature variation compared to TVC. For further calculations, time dependent values will be considered

according to Table 6.6 [De Schutter, 2002]. The general finding is that the CTE starts at a very high value (82 % higher than the CTE of hardened concrete) and drops during the setting and hardening process. Therefore the values given in Table 6.16 will be used further on.

	Fresh	6 h – 24 h	24 h – 144 h	Hard	
SCC	14.7×10^{-6}	11.0×10^{-6}	8.8×10^{-6}	8.1×10^{-6}	/°C
TVC	13.5×10^{-6}	10.1×10^{-6}	8.1×10^{-6}	7.4×10^{-6}	/°C

Table 6.16: The time dependent CTE of SCC and TVC

3.2.4 Heat production

The adiabatic heat production of SCC and TVC is determined by using the adiabatic hydration test according to De Schutter and Taerwe (1995). By using equation (6.4) the cumulated heat of hydration Q can be derived, using the values of the density of hardened SCC (2390 kg/m^3) and TVC (2410 kg/m^3) according to Table 6.15 and the approximated value of $1000 \text{ J/(kg}\cdot\text{°C)}$ for the specific heat. Knowing the cumulated heat production Q at a time t , the heat production rate q in adiabatic conditions and the heat production rate $q_{20^\circ\text{C}}$ at 20 °C can be calculated according to equation (6.5), (6.7) and (6.8). The influence of the temperature is modelled by means of the Arrhenius function with the activation energy E determined further on: 37.3 kJ/mol for SCC and 38.0 kJ/mol for TVC (Table 6.18).

For SCC and TVC the adiabatic temperature development and the cumulated heat of hydration development with time is shown in Figure 6.33 and Figure 6.34. Clearly, a more rapid development in TVC is noticed, but the temperature T and cumulated heat Q after 72 hours is higher in case of SCC, respectively 1.3 % and 4.1 %. This behaviour is also found by Poppe in case of CEM I 52.5 (Figure 6.13).

After processing these results, the heat production rate q is given and the peak of hydration heat occurs approximately 3 hours earlier and is about 9 % higher in case of TVC (Figure 6.34, Table 6.17).

Finally the comparison at 20 °C between SCC and TVC is made in Figure 6.35, with the reaction degree determined via equation (6.6a). The hydration peak is slightly higher in case of TVC (7 %) but the time of appearance of the maximum is quite similar.

It is clear that for SCC and TVC no second hydration peak appears, mainly due to the very low content of C_3A present in the cement.

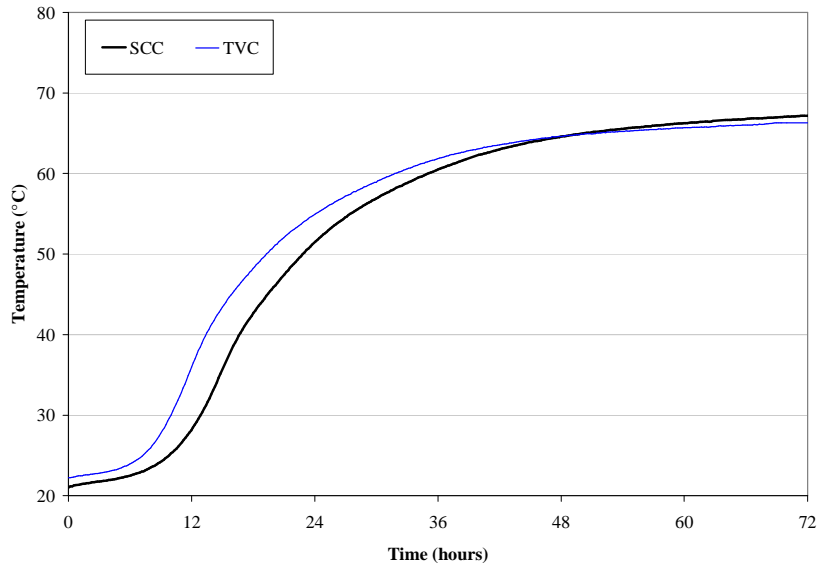


Figure 6.33: The adiabatic temperature development of SCC and TVC

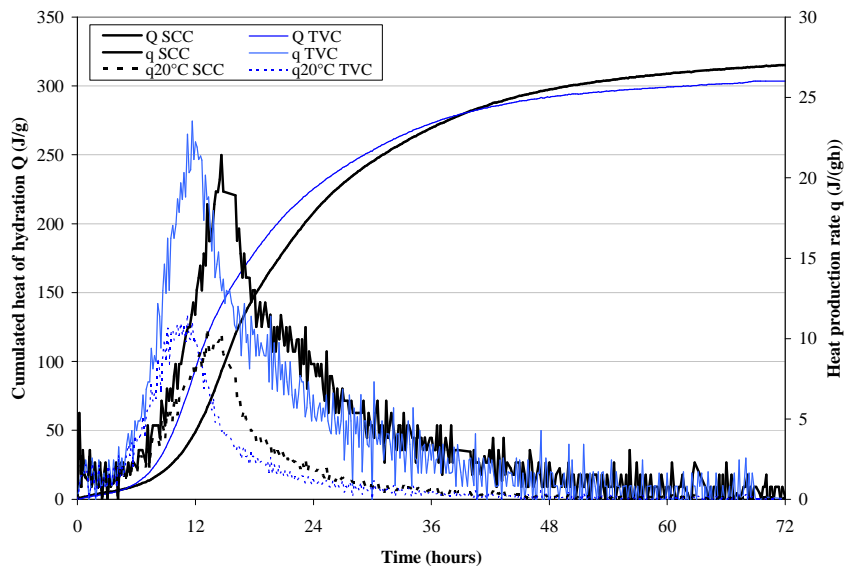


Figure 6.34: The cumulated heat of hydration Q and the heat production rates q and $q_{20^\circ\text{C}}$ of SCC and TVC

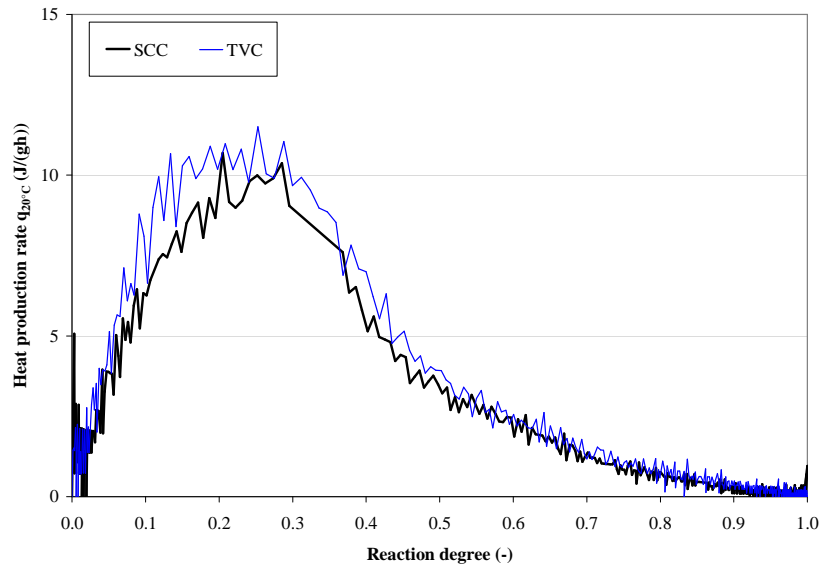


Figure 6.35: The heat production rates $q_{20^{\circ}\text{C}}$ of SCC and TVC in function of the reaction degree

Table 6.17: Values derived from the adiabatic hydration test performed on SCC and on TVC

	SCC	TVC	
$T_{72\text{h}}$	67.2	66.3	$^{\circ}\text{C}$
$Q_{72\text{h}}$	316.6	303.5	J/g
q_{max}	21.4	23.5	J/(g·h)
$t_{q_{\text{max}}}$	14.6	11.7	h
$q_{\text{max},20^{\circ}\text{C}}$	10.7	11.5	J/(g·h)
$t_{q_{\text{max},20^{\circ}\text{C}}}$	13.2	11.2	h
$r_{q_{\text{max},20^{\circ}\text{C}}}$	0.20	0.25	-

3.3 Maturity-related properties

As a result of the isothermal hydration tests, the heat production rate, expressed in $\text{J}/(\text{g}_{\text{cement}} \cdot \text{h})$, is received in function of time. In Figure 6.36, the heat generation in isothermal conduction with different environmental temperature conditions (10°C , 20°C and 35°C) of the four mixes, with different C/P ratio (Table 6.8), is plotted. For the further analysis of these results, 20°C is taken as the reference temperature T_{ref} . These results can be used for the evaluation and the determination of the activation energy E

(Table 6.18) by minimizing equation (6.9). Also the effect of the filler on the hydration reaction will be briefly discussed. The reaction mechanism of the OPC is clearly influenced by the addition of limestone filler. The most important conclusions are listed below:

- At each temperature, the replacement of the cement by limestone filler, and thus the decrease of C/P ratio induces a higher heat production rate per amount of cement, expressed in $J/(g_{\text{cement}} \cdot h)$ (Figure 6.37). This decrease is more pronounced in case of higher environmental temperature. Also the induction period shortens if C/P decreases (Figure 6.36).
- If the environmental temperature is increased, the heat production rate is higher (Figure 6.36, Figure 6.37) and the hydration peak occurs earlier, thus the induction period is shortened by elevating the surrounding temperature (Figure 6.36).
- In all cases, and neglecting the previously discussed wetting peak, only one hydration peak is noticed (Figure 6.36). Due to the prescribed small amount of C_3A present in the OPC to create a high sulphate resistance (Chapter 5), the possibility of occurrence of a third hydration peak is overcome.
- In case of 20 °C, the heat production rate development of SCC and TVC show quite a good similarity with the curve obtained via the adiabatic hydration test (Figure 6.34). In both cases, the peak appears after approximately 12 hours, but the isothermal hydration test indicates a higher heat production rate $q_{\text{max},20^\circ\text{C}}$ in case of SCC while the adiabatic hydration tests indicate it is the other way around.

The reduction of the dormant phase and the acceleration of the hydration process are well known consequences of the influence of added limestone filler and CaCO_3 on the hydration reaction of the cement [Poppe, 2004]. Further discussion lies out of the scope of this study.

From the values derived from the isothermal hydration tests at the different temperatures, the activation energy E for each of the four mixes can be derived (Table 6.18). A mean value of 38.4 kJ/mol is found, which is 13 % higher than the value obtained by De Schutter (1996) and equal to the value found by Poppe (2004). Comparing the obtained values of SCC and TVC (note that these mixes have the same W/C, C/P, W/P ratio as the concrete mixes given in Table 6.2 and Table 6.3), the activation energy E of TVC (38.0 kJ/mol) is about 2 % higher than E of SCC (37.3 kJ/mol), meaning TVC is more sensitive to temperature changes than SCC.

Finally the temperature dependency of the different mixes is presented in Figure 6.38 and also the values obtained with the Arrhenius equation (6.8) with the calculated mean value of E (38.4 kJ/mol) are shown, indicating a good resemblance.

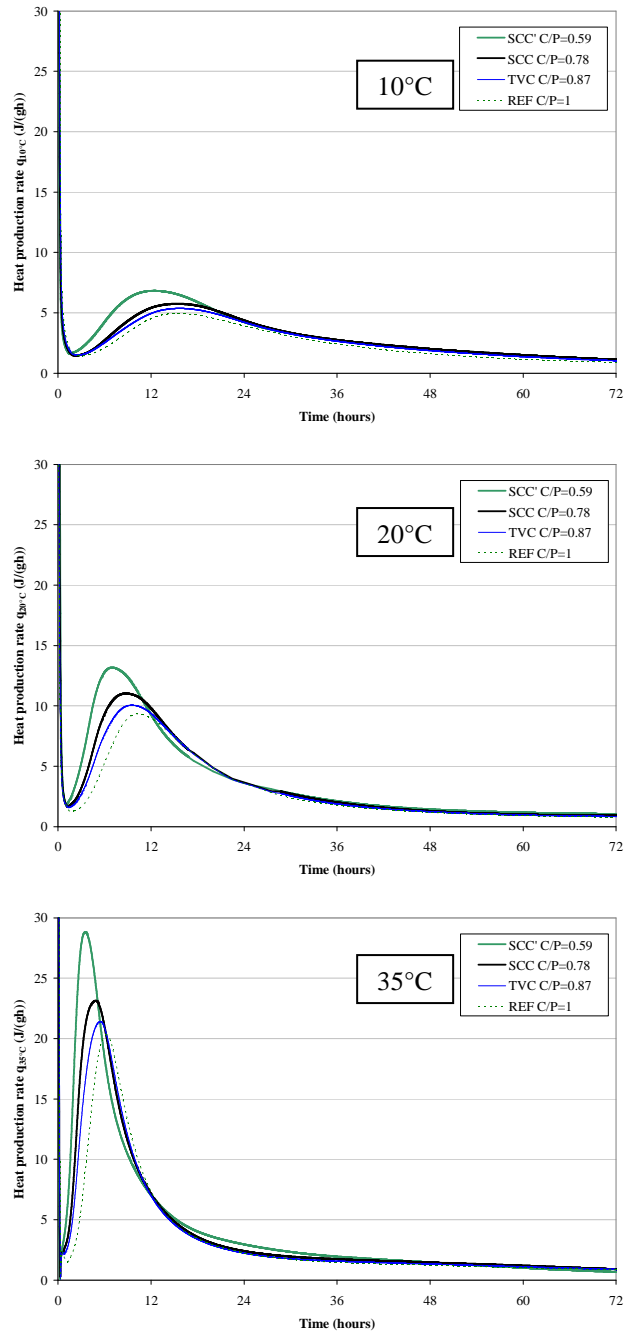


Figure 6.36: The isothermal heat production rates q of the 4 mixes at 10 °C, 20 °C and 35 °C

Table 6.18: Values derived from the isothermal hydration tests and the determination of the activation energy E of the four mixes with different C/P ratio

	SCC'	SCC	TVC	REF	
c/p	0.59	0.78	0.88	1	
$q_{\max,10^{\circ}\text{C}}$	6.823	5.754	5.373	4.945	J/(g·h)
$q_{\max,20^{\circ}\text{C}}$	13.176	11.031	10.059	9.333	J/(g·h)
$q_{\max,35^{\circ}\text{C}}$	28.849	23.139	21.420	20.327	J/(g·h)
$q_{\max,10^{\circ}\text{C}}/q_{\max,20^{\circ}\text{C}}$	0.518	0.522	0.534	0.530	-
$q_{\max,20^{\circ}\text{C}}/q_{\max,20^{\circ}\text{C}}$	1.000	1.000	1.000	1.000	-
$q_{\max,35^{\circ}\text{C}}/q_{\max,20^{\circ}\text{C}}$	2.190	2.098	2.129	2.178	-
$g(\theta = 10^{\circ}\text{C})$	0.565	0.582	0.576	0.567	-
$g(\theta = 20^{\circ}\text{C})$	1.000	1.000	1.000	1.000	-
$g(\theta = 35^{\circ}\text{C})$	2.198	2.110	2.138	2.185	-
$(q_{\max,10^{\circ}\text{C}}/q_{\max,20^{\circ}\text{C}} - g(\theta = 10^{\circ}\text{C}))^2$	0.002	0.004	0.002	0.001	-
$(q_{\max,20^{\circ}\text{C}}/q_{\max,20^{\circ}\text{C}} - g(\theta = 20^{\circ}\text{C}))^2$	0.000	0.000	0.000	0.000	-
$(q_{\max,35^{\circ}\text{C}}/q_{\max,20^{\circ}\text{C}} - g(\theta = 35^{\circ}\text{C}))^2$	0.000	0.000	0.000	0.000	-
Σ	0.002	0.004	0.002	0.001	-
E	39.4	37.3	38.0	39.1	kJ/mol
E/R	4739	4491	4570	4703	K
E_{mean}	38.4 kJ/mol				

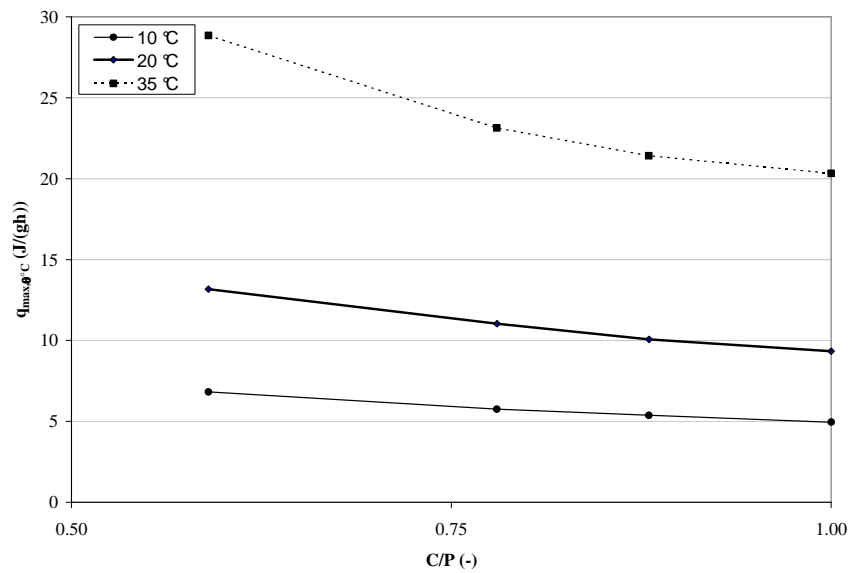


Figure 6.37: The influence of temperature and C/P on the heat production rate

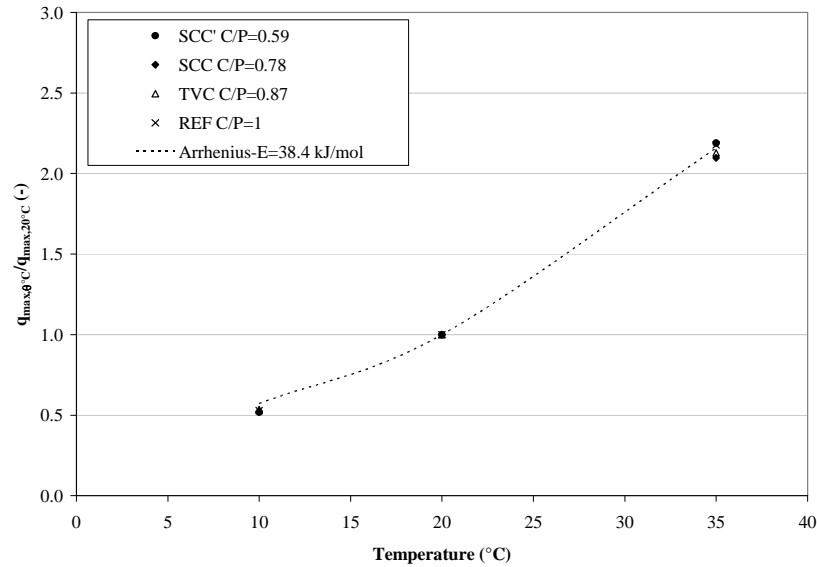


Figure 6.38: Isothermal hydration test results and results obtained via the Arrhenius equation

3.4 Mechanical properties

3.4.1 Autogenous deformation

The resulting early-age autogenous deformations of SCC and TVC, measured by means of the vertical dilatometer at 20 °C, are shown in Figure 6.39. It is clear that SCC experiences a higher autogenous shrinkage compared to TVC.

The behaviour of SCC and TVC is quite similar. The autogenous deformations are zeroed at a concrete age of 6 hours (time zero). Before 6 hours, some deviating results are obtained, most probably due to the effect of some bleeding water. For real concrete structures, shrinkage deformations become important as soon as stresses can be built up. On the material level, this requires a percolating structure of hydration products, giving strength and stiffness to the cementitious material (Figure 6.26).

Once time zero has passed, a swelling peak ϵ_p occurs at a time t_p of approximately 16 hours for TVC (value of 62 $\mu\text{m}/\text{m}$) and 18 hours for SCC (value of 70 $\mu\text{m}/\text{m}$). This phenomenon of early-age swelling is well known in literature and different reasons can be mentioned to explain this expansive nature: (i) the reabsorption of bleeding water on the cement and the filler surface and the resulting disjoining pressure [Bjøntegaard, 1999, Poppe, 2004], (ii) the growth of further hydration reaction products inside the network that generates an internal pressure causing a moderate swelling of the system [Bazant and Whittman, 1982], (iii) the ettringite formation [Teizuka et al., 1986] and

(iv) the growth of $\text{Ca}(\text{OH})_2$ crystals especially when the cement has a low aluminate content [Baroghel-Bouny et al., 2006]. This swelling peak can be influenced by the fineness and the nature of the filler and there can be an interaction of the superplasticizer. When the swelling peak is over, the autogenous shrinkage starts developing. A final value ϵ_f of $-14 \mu\text{m/m}$ (TVC) and $-26 \mu\text{m/m}$ (SCC) is registered. An average autogenous shrinkage value $\epsilon_p - \epsilon_f$ of $-76 \mu\text{m/m}$ (TVC) and $-96 \mu\text{m/m}$ (SCC) is noticed after 144 hours, measured from the top of the swelling peak until the end of the test period. Thus, the early-age autogenous shrinkage is approximately 20 % higher for SCC after 144 hours.

The long-term evolution of the autogenous deformation is given in Figure 6.40. At an age of approximately 900 days, the autogenous shrinkage is $-136 \mu\text{m/m}$ and $-106 \mu\text{m/m}$ for respectively SCC and TVC. Thus the long-term autogenous shrinkage is approximately 22 % higher for SCC after 910 days. The increased use of superplasticizer and the use of 50 kg/m^3 more fine limestone filler in case of SCC, and the use of larger aggregates in case of TVC can be an explanation for the higher autogenous shrinkage in case of SCC.

3.4.2 Creep behaviour

At the age of 2 days, 7 days, 14 days and 28 days of hardening, the covered test specimens are placed in the creep apparatus and loaded immediately to determine the basic creep behaviour of SCC and TVC. The loading is 30 % of the momentaneous strength of the test pieces. The basic creep can be extracted by measuring the total deformation and by using the autogenous shrinkage results. It can be seen that the basic creep of SCC and TVC increases steeply up to 1 to 2 months after placement of loading, and then increases smoothly with age (Figure 6.41, Figure 6.42). It is shown that SCC has the tendency to have a larger basic creep compared to TVC, especially at ages under 364 days. At that time the basic creep is approximately 10 % higher for SCC when loading is placed after 2 days: $-280 \mu\text{m/m}$ for SCC compared to $-253 \mu\text{m/m}$ for TVC. In case loading is placed later (increasing age at loading), the basic creep strain is higher, but the difference in basic creep between SCC and TVC becomes smaller. For example after 350 days (and placement of loading after 28 days), the basic creep is $-378 \mu\text{m/m}$ for SCC and $-361 \mu\text{m/m}$ for TVC, a difference of approximately 5 %. In case the loading is placed on the specimen before the age of one week (7 days), the basic creep of SCC is at all times higher than that of TVC (Figure 6.41). However, after 561 days (time of load placement: 14 days) and 383 days (time of load placement: 28 days), the basic creep of TVC becomes higher than the basic creep of SCC (Figure 6.42). Although literature suggests the opposite [Taerwe, 1997], the basic creep is higher in case the time of placement of loading is 14 days compared to placement after 28 days (Figure 6.42). After approximately 720 days, the opposite is found: the basic creep becomes higher in case the time of placement of loading is 28 days. The 'final' basic creep values of SCC and TVC are listed in Table 6.19.

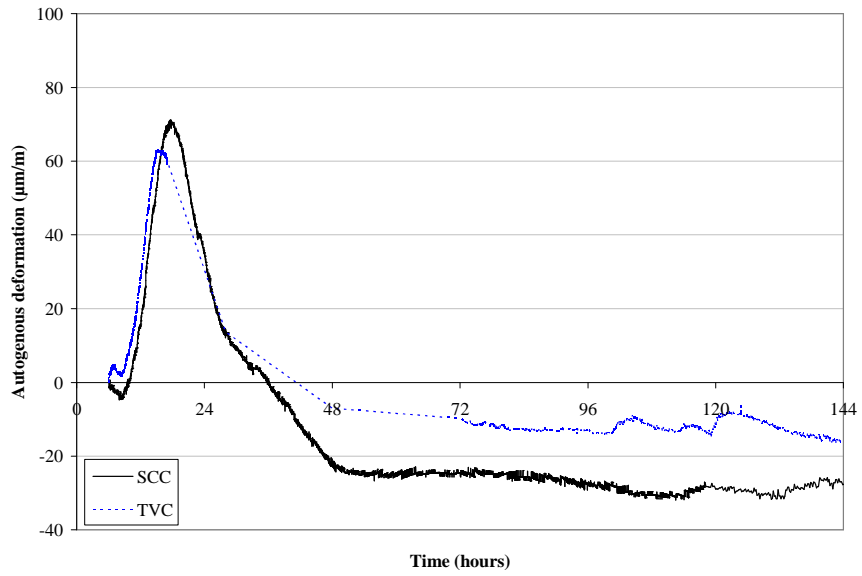


Figure 6.39: The autogenous shrinkage at early age of SCC and TVC

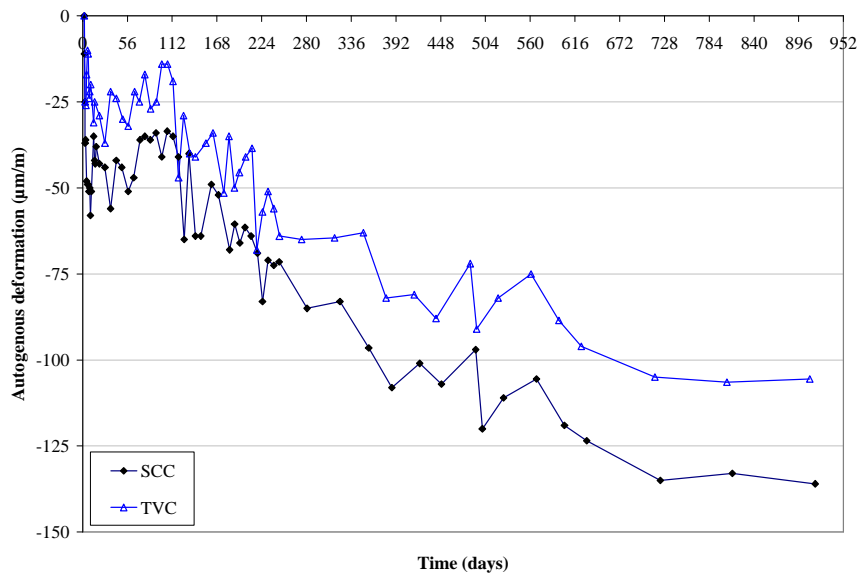


Figure 6.40: The long-term autogenous shrinkage of SCC and TVC

It can be more useful to plot the stress independent specific basic creep compliance (expressed in $\mu\text{m}/\text{m}/\text{MPa}$), which is obtained by dividing the basic creep by the applied compressive stress level imposed by the creep apparatus and created in the test specimen. In this case the trends are more clear:

- The basic creep compliance of SCC and TVC also increases steeply up to 1 to 2 months after placement of loading, and then increases smoothly with age.
- Compared to TVC, SCC has a higher basic creep compliance if the concrete age is smaller than 364 days (Figure 6.43)
- The basic creep compliance of SCC and TVC increases with decreasing time of placement of loading (Figure 6.43).
- The fact that SCC has a higher basic creep and basic creep compliance, especially at an age younger than 364 days and in case time of placement of loading is smaller than 7 days, can be explained by the smaller amount of coarse aggregates present in SCC [Taerwe, 1997].
- After 561 days (time of placement of loading: 14 days) and after 383 days (time of placement of loading: 28 days) the basic creep compliance of TVC becomes higher than that of SCC (Figure 6.44).

The 'final' basic creep compliance values of SCC and TVC are listed in Table 6.19.

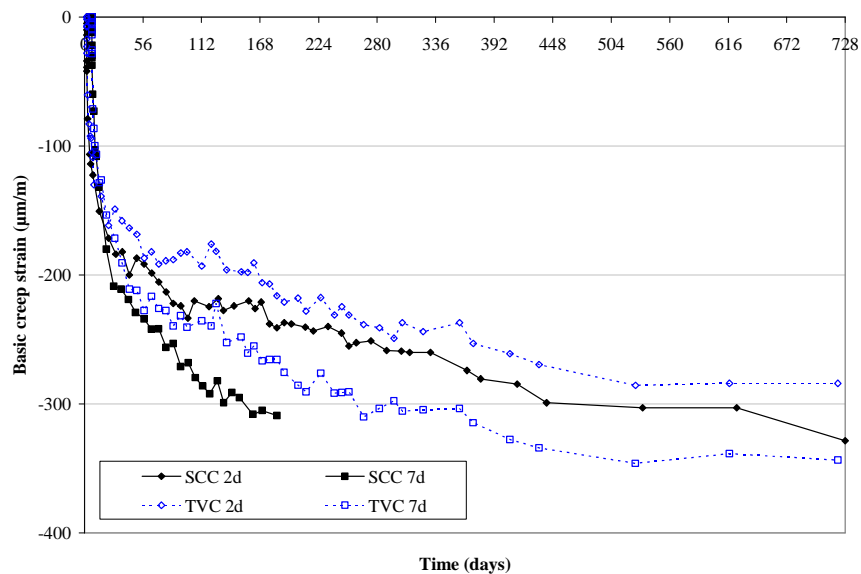


Figure 6.41: The basic creep strain due to loading at 2 days and 7 days of SCC and TVC

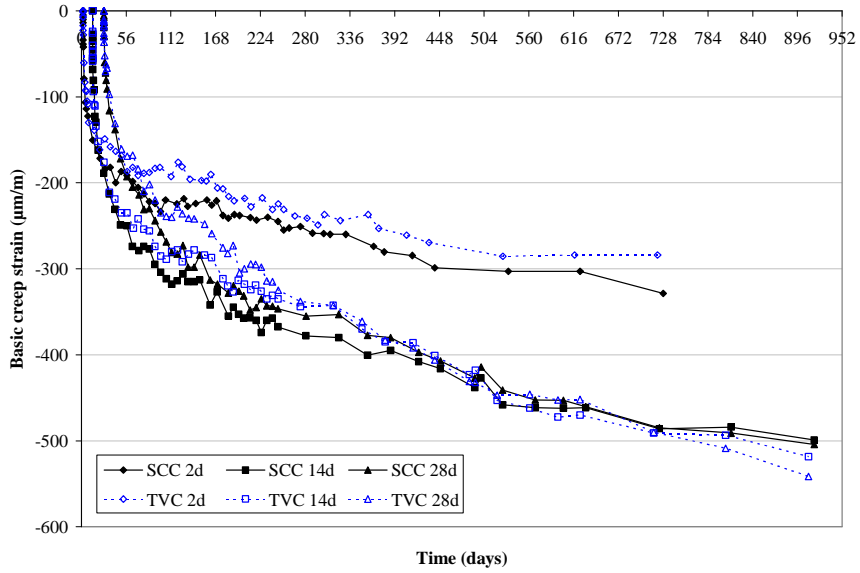


Figure 6.42: The basic creep strain due to loading at 2 days, 14 days and 28 days of SCC and TVC

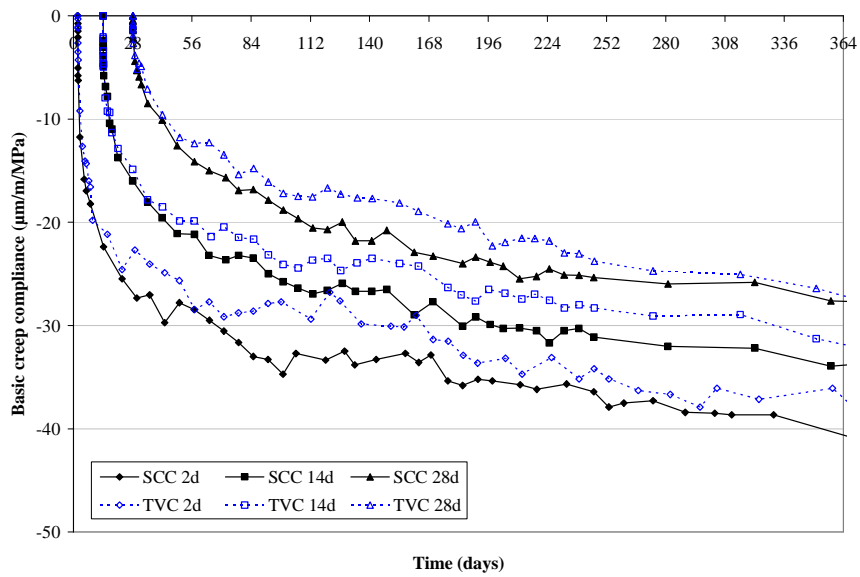


Figure 6.43: The basic creep compliance due to loading at 2 days, 14 days and 28 days of SCC and TVC (< 364 days)

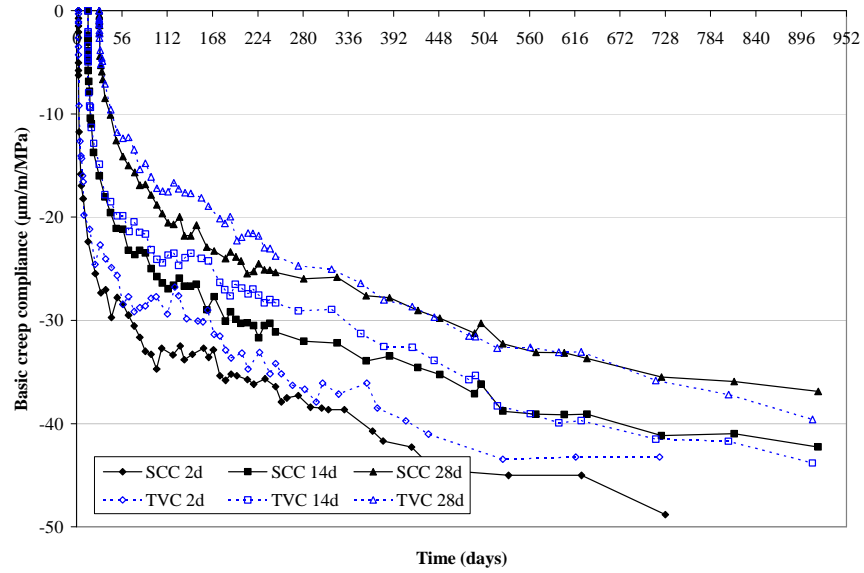


Figure 6.44: The basic creep compliance due to loading at 2 days, 14 days and 28 days of SCC and TVC (< 1000 days)

Table 6.19: Values of basic creep and basic creep compliance at different ages and different times of placement of loading of SCC and TVC

Time of placement of loading		SCC	TVC
2 days	µm/m	-328 (728 d)	-284 (721 d)
7 days	µm/m	-309 (184 d)	-343 (721 d)
14 days	µm/m	-499 (917 d)	-514 (910 d)
28 days	µm/m	-504 (917 d)	-542 (910 d)
2 days	µm/m/MPa	-41 (366 d)	-36 (358 d)
14 days	µm/m/MPa	-34 (358 d)	-31 (351 d)
28 days	µm/m/MPa	-28 (358 d)	-26 (351 d)
2 days	µm/m/MPa	-49 (728 d)	-43 (721 d)
14 days	µm/m/MPa	-42 (917 d)	-44 (910 d)
28 days	µm/m/MPa	-37 (917 d)	-40 (910 d)

3.4.3 Compressive strength

The evolution of the compressive strength (and the standard deviation s) of SCC and TVC is given in Figure 6.45 and the values are listed in Table 6.20. These values are obtained on cubes with a side of 150 mm at different ages varying from 1 day until 28 days. It can be seen that, although the compressive strength development of TVC is slightly faster than SCC the first 48 hours, the compressive strength after 28 days is 6 % higher in case of SCC.

The additional use of limestone filler (50 kg/m³ more compared to TVC) in case of SCC can be seen as the main reason for the higher compressive strength value after 28 days. As mentioned before by Poppe (2004), the use of filler material in SCC has an effect on the strength development: due to a better dispersion of the cement and the decrease of the average pore size (by adding additional filler) in case of SCC, a beneficial effect on the strength is obtained.

3.4.4 Tensile strength

The pure tensile strength of SCC and TVC, determined after 56 days on cores drilled out of a massive concrete column (SOCEA), is 26 % higher in case of SCC [BBRI, 2007]. A mean value of 4.4 MPa ($s = 0.5$ MPa) is obtained for SCC compared to a mean value of 3.3 MPa for TVC ($s = 0.4$ MPa).

The splitting tensile strength tests performed on three cubic samples (side 100 mm) at an age of 42 days result in a 5 % higher tensile splitting strength value for TVC compared to SCC: f_{ctsp} equals 4.0 MPa ($s = 0.4$ MPa) for TVC and 3.8 MPa ($s = 0.3$ MPa) for SCC. It must be noted that the compressive strength determined on cubes (side 100 mm) $f_{ccub100}$ made with concrete of the same mix is about 24 % higher in case of TVC, which make these splitting tensile strength results disputable.

Cubes from another batch are tested after 117 days and more acceptable values are found: f_{ctsp} is 18 % higher for SCC. In this case a mean value of 5.8 MPa ($s = 0.4$ MPa) is obtained for SCC compared to a mean value of 4.8 MPa for TVC ($s = 0.3$ MPa) for the splitting tensile strength. The compressive strength of the cubes (side 100 mm) $f_{ccub100}$ made with concrete of the same batch is also higher for SCC (approximately 4 %).

3.4.5 Modulus of elasticity

Out of 9 cores drilled out of a massive concrete column (SOCEA) after 28 days of hardening, the static secant modulus of elasticity is determined [BBRI, 2007]. This has a value of 36.1 GPa ($s = 2.9$ GPa) for SCC and 32.4 GPa ($s = 2.1$ GPa) for TVC. Thus, by replacing 184 kg/m³ coarse limestone aggregates of the TVC composition (size 2/6, 6/14, 6/20) by an additional amount of 132 kg/m³ of fine limestone sand (size 0/4) and 50 kg/m³ limestone filler, in order to obtain the self-compacting composition SCC, the secant modulus of elasticity increases with 10 %.

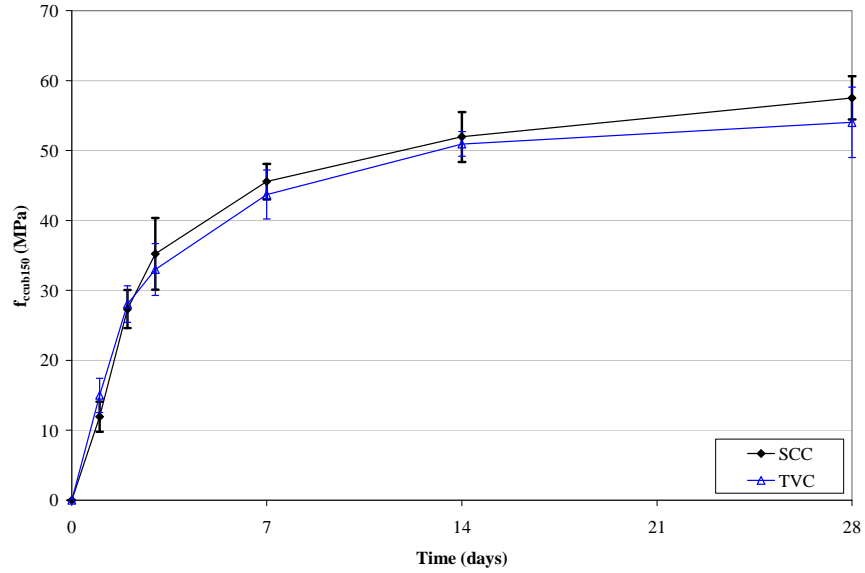


Figure 6.45: The compressive strength of SCC and TVC at different ages (error bars: $\pm s$ around mean value)

Table 6.20: Values of the compressive strength at different ages of SCC and TVC

Age		SCC			TVC		
		$f_{ccub150}$	s	#	$f_{ccub150}$	s	#
1 day	MPa	11.9	2.1	7	15.0	2.5	6
2 days	MPa	27.3	2.7	6	28.0	2.6	5
3 days	MPa	35.2	5.1	2	33.0	3.7	3
7 days	MPa	45.6	2.6	8	43.7	3.5	8
14 days	MPa	52.0	3.6	5	51.0	1.8	4
28 days	MPa	57.5	3.1	9	54.0	5.0	10

3.4.6 Poisson's ratio

The values of Poisson's ratio of SCC and TVC are determined by BBRI (2007). For SCC a value of 0.39 ($s = 0.08$) is found compared to a value of 0.16 ($s = 0.04$) for TVC. Especially the obtained value for SCC differs significantly from the results discussed in literature, that define a relative value of 0.20 for uncracked concrete as acceptable. Due to Briffaut et al. (2009), who have indicated that the concrete Poisson's ratio has no

significant influence on numerical simulation results of concrete strains and stresses in massive structures as long as reasonable values are used, the linear time dependent values listed in the Belgian Code NBN EN 1992-1 will be used for Poisson's ratio of SCC and TVC with a value varying from 0.5 before time zero and 0.2 afterwards.

3.4.7 Time zero

To estimate time zero, the compressive strength and the relative compressive strength are plotted in function of the logarithm of time (Figure 6.46). A linear correlation is found, and by performing linear regression, time zero can be extrapolated. Values of 7.2 hours and 4.7 hours for respectively SCC and TVC are found by plotting the compressive strength versus $\log t$. A time zero of 7.0 hours and 5.0 hours is found in case of the relative compressive strength (Equation (6.20), Figure 6.46).

$$t_{0,SCC} = 24 \cdot e^{\left(\frac{-0.2822}{0.23}\right)} = 7.0 \text{ h} \quad (6.20)$$

$$t_{0,TVC} = 24 \cdot e^{\left(\frac{-0.3311}{0.2102}\right)} = 5.0 \text{ h}$$

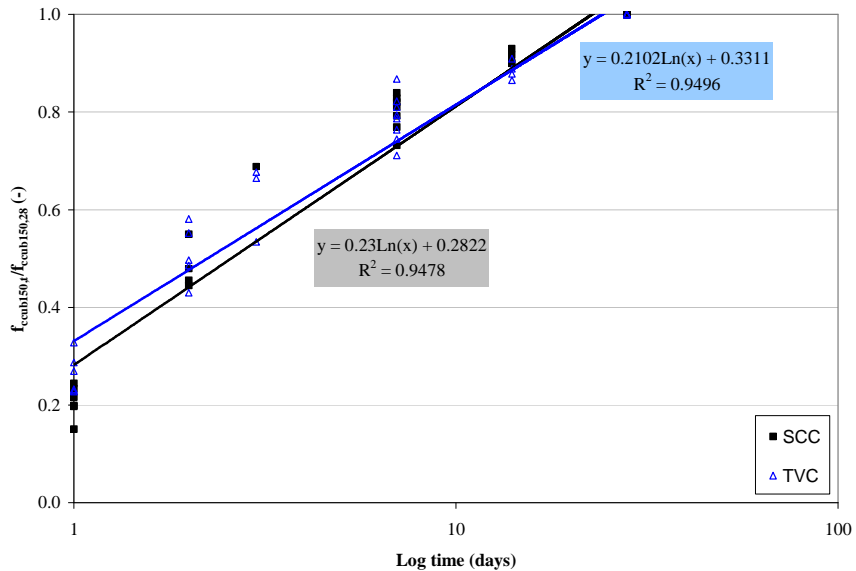


Figure 6.46: Relative compressive strength development in function of $\log t$

Another way to determine time zero is by using non-destructive ultrasonic measurements (by mean of the FreshCon system). In Figure 6.47, the inflection point in the velocity versus time curve appears after approximately 5 hours for TVC in

correspondence with equation (6.20). Time zero of SCC could not be determined accurately due to an inexplicable electronic hitch.

Due to the addition of limestone filler, it can be expected for the binding to occur earlier due to the accelerating effect of limestone filler on the hydration process [Poppe, 2004]. Following this argumentation, time zero of SCC should occur earlier compared to TVC due to the addition of 50 kg/m³ extra limestone filler, which is not the fact according to Figure 6.46. On the other hand, more superplasticizer is used in the SCC composition, which can also induce a retardation effect concerning time zero [Winnefeld et al., 2007]. Overall, considering the experimentally obtained values and taking into account the values for time zero found by Robeyst et al. (2008), an equivalent time t_0 of 6 hours for SCC and TVC seems reasonable for the setting of the concrete (with W/C ratio of 0.5) to take place.

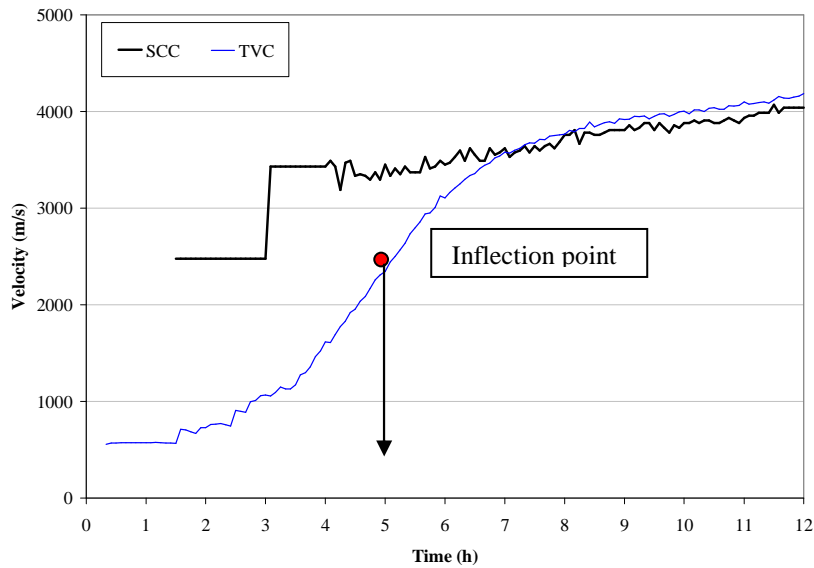


Figure 6.47: Results of the ultrasonic determination of time zero

4 Conclusion

In order for the SCC composition to be self-compacting, additional amounts of limestone filler and superplasticizer are added to the mixture (compared to the traditional TCV composition). Via a laboratory characterization program, the most important thermal, mechanical and maturity-related concrete properties are determined, according to Figure 6.48. It is shown that TVC has slightly better thermal properties, whereas SCC has its benefits towards strength related properties. The properties are implemented in the material database of the finite element program HEAT/MLS for the prediction of the early-age behaviour of the concrete Supercontainer. A short summary of the obtained results is listed in Chapter 8.

Overall, it can be concluded that there is a good similarity with the previously obtained results via the literature study.

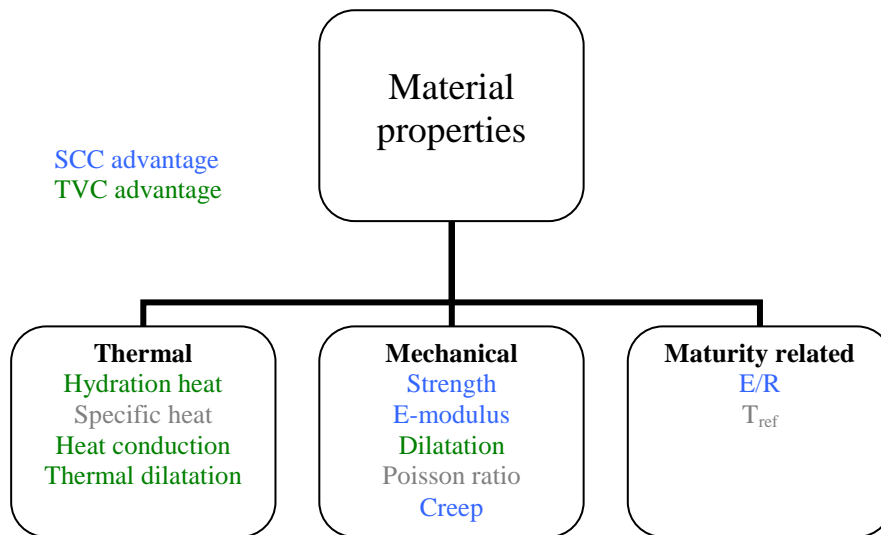


Figure 6.48: Comparison between the concrete properties of SCC and TVC

References

ACI Committee 237. (2007), *Self-Consolidating Concrete*, ACI Report 237R-07, American Concrete Institute, Detroit, USA.

Baroghel-Bouny V., Mounanga P., Khelidj A., Loukili A., Rafai N. (2006), *Autogenous deformation of cement pastes. Part II. W/C effects, micro-macro correlations, and threshold values*, Cement and Concrete Research 36, 122-136.

Bazant Z.P., Whittman F.H. (1982), *Creep and Shrinkage in Concrete Structures*, Wiley New York.

BBRI (Belgian Building Research Institute). (2007), *Rapport d'essais*, BBRI Report DE 611XB050.

Benboudjema F., Torrenti J.M. (2008), *Early age behaviour of concrete nuclear containments*, Nuclear Engineering and Design 238, 2495-2506.

Bensted J. (1987), *Some applications of conduction calorimetry to cement hydration*, Advanced Cement Research 1, 35-44.

Bergstrom S.G., Byfors J. (1979), *Properties of concrete at early ages*, Report of technical committees, 32nd meeting of RILEM Permanent Committee, pp 265-278.

Billberg P. (2001), *Influence of filler characteristics on SCC rheology and early hydration*, Proceedings of the Second International RILEM Symposium on Self-Compacting Concrete, Tokyo, Japan.

Bjøntegaard Ø. (1999), *Thermal dilation and autogenous deformation as driving forces to self-induced stresses in high-performance concrete*, PhD thesis, Norwegian University of Science and Technology, Trondheim, Norway.

Boel V. (2006), *Microstructure of Self-Compacting Concrete in relation with gas permeability and durability aspects*, Doctoral thesis (in Dutch), Ghent University, Magnel Laboratory for Concrete Research, Belgium.

Bonavetti V.L., Rahhal V.F., Irassar E.F. (2001), *Studies on the carboaluminate formation in limestone filler-blended cements*, Cement and Concrete Research 31, 853-859.

Briffaut M., Benboudjema F., Torrenti J.-M., Nahas G. (2009), *A new analysis of the restrained ring shrinkage test*, Proceedings of the International RILEM Conference NUCPERF09, Cadarache, France.

Brown T.D., Javaid M.Y. (1970), *The thermal conductivity of fresh concrete*, Material Constructions 3, 411-416.

Bui V., Montgomery D. (1999), *Drying shrinkage of self-compacting concrete containing milled limestone*, Proceeding of the First International RILEM Symposium on Self-Compacting Concrete, Stockholm, Sweden.

Craeye B. (2006), *Reduction of autogenous shrinkage of concrete by means of internal curing*, Master thesis (in Dutch), Magnel Laboratory for Concrete Research, Ghent University, Belgium.

Craeye B., De Schutter G., Van Humbeeck H., Van Cotthem A. (2009), *Early age behaviour of concrete supercontainers for radioactive waste disposal*, Nuclear Engineering and Design 239, 23-35.

De Schutter G. (1996), *Fundamental and practical study on thermal stresses in massive hardening concrete elements*, Doctoral thesis (in Dutch), Ghent University, Magnel Laboratory for Concrete Research, Belgium.

De Schutter G. (2002), *Thermal properties*, Report of RILEM Technical Committee 181-EAS on Early Age Cracking in Cementitious Systems, pp 121-125.

De Schutter G. (2005), *Early age shrinkage control of concrete: Final Report*, Research Rapport (in Dutch), Ghent University, Magnel Laboratory for Concrete Research.

De Schutter G., Bartos P., Domone P., Gibbs J. (2008), *Self-Compacting Concrete*, Whittles Publishing, Caithness, UK, pp. 296.

De Schutter G., Taerwe L. (1995), *General hydration model for portland cement and blast furnace slag cement*, Cement and Concrete Research 25, 593-604.

De Schutter G., Taerwe L. (1995), *Specific heat and thermal diffusivity of hardening concrete*, Mag. Concrete Research 47, 203-208.

De Schutter G., Vuylsteke M. (2004), *Minimisation of early age thermal cracking in J-shaped non-reinforced massive concrete quay wall*, Engineering Structures 26, 801-808.

Domone P.L. (2006), *Self-compacting concrete: an analysis of 11 years of case studies*, Cement and Concrete Composites 28, 197-208.

Domone P.L. (2006), *A review of the hardened mechanical properties of self-compacting concrete*, Cement and Concrete Composites 29, 1-12.

EFNARC European Project Group. (2005), *The European guidelines for Self-compacting concrete: specification, production and use*.

ESV Euridice. (2007), *Meetresultaten voor verticale balk*, EURIDICE/JVe/06-xxx.

Feldman R.F. (1969), *Volume Change and Creep of Concrete*, Canadian Building Digest, CBD-119.

Feys D. (2009), *Interaction between Rheological Properties and Pumping of Self-Compacting Concrete*, Doctoral thesis, Ghent University, Magnel Laboratory for Concrete Research, Belgium.

Gruyaert E., Robeyst N., De Belie N. (2008), *Modelling the hydration heat of Portland cement blended with blast-furnace slag*, Proceedings of the conference on Non-traditional cement and concrete III, Brno, Czech Republic.

Hansen P.F., Hansen J.F., Kjaer V., Pedersen E.J. (1982), *Thermal properties of hardening cement paste*, Proceedings of the International RILEM Conference on Concrete at Early Ages, Paris, France.

Hu C., Barcelo L. (1998), *Investigation of the shrinkage of self-compacting concrete for building construction*, Proceedings of the international workshop on self-compacting concrete, Kochi, Japan.

Iravani S. (1996), *Mechanical properties of High-Performance Concrete*, ACI Journal, pp 1-11.

Kaplan M.F. (1989), *Concrete Radiation Shielding: Nuclear Physics, Concrete Properties, Design and Construction*, Longman Scientific & Technical, England pp 457.

Klink S.A. (1985), *Actual Poisson's Ratio of Concrete*, ACI Journal, pp. 813-817.

Kovler K., Jensen O.M. (2007), *Internal Curing of Concrete*, State-of-the-art report of RILEM Technical Committee 196-ICC, RILEM Report 41, RILEM Publications S.A.R.L., ISBN 978-2-35158-009-7, pp.140.

Löfquist. (1981), *Properties of set concrete at early ages*, Materials & Constructions 14, 399-450.

Loukili A., Chopin D., Abdelhafid K., Le Touzo J.-Y. (2000), *A new approach to determine autogenous shrinkage of mortar at an early age considering temperature history*, Cement and Concrete Research 30, 915-922.

Neville A. (1963), *Properties of concrete*, Pitman Publishing Cie., London, United Kingdom.

Neville A. (2000), *Propriétés des bétons*, Editions Eyrolles, pp 860.

Okamura H., Ozawa K. (1995), *Mix design method for self-compacting concrete*, Concrete Library of Japan Society of Civil Engineers No 25, pp 107-120.

Piérard J., Pollet V., Cauberg N. (2005), *Mitigation of autogenous shrinkage in HPC by internal curing using superabsorbent polymers*, Belgian Building Research Institute.

Poppe A.M. (2004), *Influence of fillers on hydration and properties of Self-Compacting Concrete*, Doctoral thesis (in Dutch), Ghent University, Magnel Laboratory for Concrete Research, Belgium.

Poppe A.M., De Schutter G. (2005), *Cement hydration in the presence of high filler contents*, Cement and Concrete Research 35, 2290-2299.

Robeyst N., Gruyaert E., Grosse C.U., De Belie N. (2008), *Monitoring the setting of concrete containing blast furnace slag by measuring the ultrasonic p-wave velocity*, Cement and Concrete Research 38, 1169-1176.

Sharma R.L., Pandey S.P. (1999), *Influence of mineral additives on the hydration characteristics of ordinary Portland cement*, Cement and Concrete Research 29, 1525-1529.

Sideris K.K., Manita P., Sideris K. (2004), *Estimation of ultimate modulus of elasticity and Poisson ratio of normal concrete*, Cement & Concrete Composites 26, 623-631.

Sonebi M. (2004), *Medium strength self-compacting concrete containing fly ash: Modelling using factorial experimental plans*, Cement and Concrete Research 34, 1199-1208.

Sui C., Sonebi M., Gupta A., Taylor S. (2009), *Development of Self-Compacting Concrete to produce precast cladding panels*, Proceedings of the 2nd International RILEM Conference on Design, Performance and Use of Self-Consolidating Concrete SCC '09, Beijing, China.

Taerwe L. (1997), *Concrete Technology*, Course material (in Dutch), Ghent University, Magnel Laboratory for Concrete Research, Belgium.

Tezuka Y., Djanikan J.G., Uchikawa H., Uchida S. (1986), *Hydration characteristics and properties of mixtures of cement and high content of calcium*, Proceedings of the Symposium on Chemistry of Cement, Rio de Janeiro, Brazil.

Van Beek A., Schlangen E., Baetens B.E.J. (2001), *Numerical model for prediction of cracks in concrete structures*, Proceedings of the International RILEM Conference on Early Age Cracking in Cementitious Systems EAC '01, Haifa, Israel.

Vodák F., Cerny R., Drchalova J., Kapicková O., Hosková S., Michalko O., Semerak P., Toman J. (1997), *Thermophysical properties of concrete for nuclear safety related structures*, Cement and Concrete Research 27, 415-426.

Walraeven J. (2003), *Structural applications of self compacting concrete*, Proceedings of the Third RILEM International Symposium on Self-compacting Concrete, Reykjavik, Iceland.

Winnefeld F., Zingg A., Holzer L., Fifi R., Pakusch J., Becker S. (2007), *Interaction of polycarboxylate-based superplasticizer and cement: influence of polymer structure and C₃A-content of cement*, Proceedings of the 12th International Congress on the Chemistry of Cement, Montréal, Canada.

CHAPTER 7:

EFFECT OF RADWASTE ON STRENGTH OF THE SUPERCONTAINER

The concrete applied for the Supercontainer, i.e. the concrete buffer, the filler and the lid, will be exposed to heat-emitting radioactive waste (surrounded by the overpack) during hardening and in its hardened state. It seems interesting to investigate the effect of heat (temperatures up to 100 °C [Weetjens and Sillen, 2007]) and gamma radiation (alpha radiation, beta radiation are blocked by the carbon steel overpack, the impact of the neutrons can be neglected [Wickham et al., 2005]) on the strength of the concrete used for the Supercontainer in order to evaluate the possibility of early-age cracking of the concrete during the fabrication of the Supercontainer.

1 Goal and methodology

Two main questions need to be answered in this chapter:

- What is the effect of gamma radiation on the strength of the concrete Supercontainer, especially during hardening? Therefore, an SCC based mortar composition will be irradiated by means of a ^{60}Co source during hardening. Afterwards (after 28 days of hardening under gamma irradiation) the effect of the radiation on the compressive strength will be examined.
- What is the effect of elevated temperatures (between 20 °C and 105 °C) on the strength of the Supercontainer? After hardening, the TVC and the SCC will be subjected to an external heat source, creating an environmental temperature up to 105°C. The effect of heat on the strength, both in tensile and in compressive behaviour, will be discussed.

Afterwards, thin sections of the concrete or mortar samples are made to investigate the effect of heat and gamma radiation on a microscopic level. The intensity of the fluorescence of the thin sections viewed through the eyepiece of a microscope is a function of the capillary porosity and can give an indication or an explanation for a possible strength loss [Braeckman, 2007].

2 Previous results and testing procedure

2.1 Effect of gamma irradiation on strength of concrete

2.1.1 Previous results

As mentioned before (Chapter 4), the most important effect of gamma irradiation of concrete is the hydrolysis (radiolysis of the concrete pore water) and the gas production which can lead to a detrimental gas pressure build-up [Bouniol, 2004]. Moreover, it is interesting to investigate the effect of gamma radiation on the strength of irradiated hardened concrete samples. The most important observations and conclusions concerning strength losses due to gamma irradiation are listed in Table 7.1.

Table 7.1: Summary of the effect of gamma irradiation on concrete

Reference	Dose (MGy)	Strength loss (%)	Observations
Vodák et al. (2005)	0.5	10	Irradiation enhanced carbonation
Bar-Nes et al. (2008)	10	-	*Altered transport properties and increased carbonation depth *No change of macroscopic properties of the irradiated material
Richardson et al. (1990)	80	-	Additional ettringite formation in case BFS is used
Pachner (1998)	100	0	Mechanical properties are not influenced
Kelly&Davidson (1969)	10 000	0	Negligible effect of gamma irradiation
Ichikawa et al. (2002)	500 000	-	Irradiation enhanced AAR. Use of limestone is preferred
Morigani (1997)	-	-	Irradiation enhanced AAR in case high amounts of SiO ₂ aggregates are added to the mix

Only the study according to Vodák et al. (2005) indicates a strength loss of about 10 %. The mechanism leading to the eventual deterioration of the mechanical properties of the concrete is explained: 'Interaction of concrete with gamma irradiation generates the

succession of chemical reactions in the material, starting with radiolysis of water and terminating in formation of calcite, crystals who decrease both the size of the pore space and also the strength of the material'. It must be noted that the applied dose rate, in order to get to a total dose of 0.5 MGy in 90 days, is about 230 Gy/h, which is rather high compared to the dose rates applied in the Supercontainer concept.

Poyet (2007) determined the radioactive dose and the dose rate originating from the heat-emitting radioactive waste at the interface of the overpack and the buffer and in the middle of the buffer for the Supercontainer concept (Chapter 4). Taking into account a cooling period of 50 years, the total dose subjected to the buffer at the interface evolves to an asymptotic value of 8.86 MGy with an initial dose rate of 22.99 Gy/h, and a dose rate of 0.03 Gy/h after 300 years. In the middle of the buffer the calculated dose is 0.23 MGy after 300 years with a decreasing dose rate of 0.59 Gy/h (initially) to 0 Gy/h. For those doses, no degradation of the concrete mechanical properties of the Supercontainer is expected. Most of the cement matrices give proof of a good mechanical resistance towards physical degradation due to gamma irradiation (ONDRAF/NIRAS and CEA statement). However, it seems interesting to examine the effect of gamma irradiation (with a significant dose rate) on freshly cast mortar (for example: the filler comes into direct contact with the overpack containing radwaste and emitting gamma radiation during hardening in hot cell). Therefore, an SCC based mortar composition is used, determined via the MBE method ('Mortier de Béton Equivalent').

2.1.2 MBE method

Out of the SCC composition used for the buffer of the Supercontainer (Chapter 6), it is possible to define a related mortar composition using the MBE method. The aggregates (not the sand!) of the SCC will be replaced by a certain amount of sand with an equal specific surface as the replaced coarse aggregates, in order to get an SCC based mortar. The main principle is based on the rheological properties of the concrete and the mortar: the flow ability of the SCC can be correlated to the flow ability of the SCC based mortar [Schwartzentruber and Catherine, 2000]. The aim for defining this SCC based mortar is given:

- The general aim of defining an SCC based mortar is to reduce the amount of concrete batches (material consuming).
- In order to get a more or less uniform distribution of the applied dose rates (see further), the irradiated samples must be sufficiently small. A mortar, with sand as the only aggregate, is found more suitable for those small prismatic samples (dimensions 40 mm x 40 mm x 30 mm).
- The samples will be irradiated outside the Magnel Laboratory for Concrete Research. To be able to mix the fresh SCC mortar and irradiate it during hardening, a mixer must be present at the institute that irradiates the samples. Therefore a small transportable mortar mixer is more appropriate than a cumbersome concrete mixer.
- The effect of gamma irradiation on hardening cement based compositions will be examined. In the Supercontainer concept, the buffer will be in a

particular state of hardening when the radioactive waste is inserted. On the other hand, in hot cell, the filler will be freshly cast around the overpack, and thus will be in direct contact with the overpack emitting gamma radiation during hardening. It is more appropriate to use an SCC based mortar as the filler material, compared to an ordinary SCC.

In order to define the SCC mortar and to find the amount of sand needed to replace the aggregates, several parameters of the sand and the aggregates need to be determined: the amount G , the grain size distribution in order to calculate the specific surface S_s and the absorption coefficient A_a . These parameters of limestone 0/4, limestone 2/6 and limestone 6/14 are determined at the Magnel Laboratory for Concrete Research and are given in Table 7.2.

Table 7.2: Amount G , specific surface S_s and absorption coefficient A_a of limestone

	G (kg/m³)	S_s (m²/kg)	A_a (%)
limestone 0/4	840	3.94	1.25
limestone 2/6	327	0.48	1.25
limestone 6/14	559	0.19	0.80

The amount of additional limestone sand 0/4 needed to replace the limestone aggregates 2/6 and 6/14, can be calculated by using equation (7.1):

$$\Delta G_{0/4} = \frac{G_{2/6} \cdot S_{s,2/6} + G_{6/14} \cdot S_{s,6/14}}{S_{s,0/4}} \quad (7.1)$$

where: G_i = the amount of limestone aggregates (kg/m³)
 $S_{s,i}$ = the specific surface of the limestone aggregates (m²/kg)

Substituting the values of Table 4.2 in equation (7.1), it can be found that approximately 67 kg/m³ of limestone 0/4 is needed to replace the aggregates (2/6 and 6/14). Finally, the difference in absorption between the sand and the aggregates needs to be evaluated in order to correct the amount of water that needs to be added to the SCC based mortar composition. By using equation (7.2), a total amount of approximately 167 kg/m³ water needs to be added to the SCC mortar. Finally the SCC mortar composition is given in Table 7.3.

$$W_{MBE} = W_{SCC} - G_{2/6} \cdot A_{a,2/6} - G_{6/14} \cdot A_{a,6/14} + G_{0/4} \cdot A_{a,0/4} \quad (7.2)$$

where: W_{MBE} = the amount of water added to the SCC mortar composition (kg/m³)
 W_{SCC} = the amount of water added to the SCC composition (kg/m³)
 $A_{a,i}$ = the absorption coefficient of the limestone aggregates (%)

Table 7.3: The composition of the SCC based mortar

Component	MBE kg/mix	MBE kg/m ³
Cement CEM I/42,5N HSR LA LH	350	512
Limestone filler	100	146
Limestone 0/4	907	1327
Limestone 2/6	0	0
Limestone 6/14	0	0
Limestone 6/20	0	0
Superplasticizer glenium 27/20	10	14
Water	167	245

2.1.3 Testing procedure

In order to evaluate the effect of gamma irradiation on the SCC based mortar (Table 7.3), different types of tests are conducted. First approximately 1 dm³ of mortar is mixed and the fresh mortar is characterized by means of a slump flow value. In total 3 x 4 prisms with size 40 mm x 40 mm x 30 mm are prepared and gamma irradiated (at different dose rates) during 28 days of hardening. Afterwards the compressive strength of the mortar samples is determined, and the volumetric weight is measured. Thin sections are made to investigate the effect the gamma radiation on a microscopic level and to quantify the capillary porosity of the mortar samples.

Mixing procedure and fresh mortar properties

At ISIB (Institut Supérieur des Ingénieurs de Bruxelles), two batches of 1 dm³ of SCC mortar (mix 1, mix 2), composition according to Table 7.3, are made by using a Hobart mixer (Figure 7.1).

First the cement, the limestone filler and the limestone sand 0/4 are added to the mixer and mixed with a rotational speed of 140 rpm for 30 seconds. Subsequently, the water is added to the blended dry components and the mixing continues for another 60 seconds at a speed of 140 rpm. Finally, the superplasticizer is added and an additional 60 seconds of mixing time, at a rotational speed of 285 rpm, is supplied. To evaluate the fresh properties of the SCC mortar, the slump flow is measured by using the Mini-cone (Figure 7.1). Finally 3 x 4 prisms (batch 1) and 4 x 4 prisms (batch 2) are cast, without the need of external vibration, with size 40 mm x 40 mm x 30 mm.

Irradiation scheme

Once the mix is executed and the mortar prisms cast, and after 24 hours of hardening, eight samples will be placed under a radiotherapy ⁶⁰Co irradiator (Barzetti, type Jupiter C: energy between 1.17 MeV and 1.33 MeV, activity = 2 TBq) at two different levels

(four at the Top-level and four at the Low-level, Figure 7.2). The irradiated surface is 40 mm x 40 mm. The thickness of the samples is 30 mm. For each mix, four samples remain unirradiated as a reference, but are conserved at the same temperature and humidity conditions as the irradiated samples (the samples have the same maturity).

To quantify the applied dose rate at the two levels, and to perform the dose measurements, a radio chromic film (Gafchromic EBT) is being used (dosimeter). In order to take into account the shielding effect of the sample thickness (30 mm), a gafchromic film is placed on top of the samples at position 1 and position 3 (Figure 7.2) and at the bottom of the samples at position 2 and position 4 (Figure 7.2). Four different dose rates are measured at different distances (d_s) from the source. In Table 7.4 the obtained dose rates are listed.

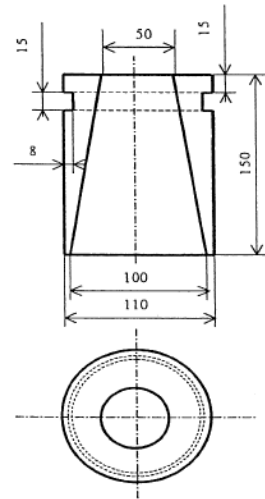


Figure 7.1: The Hobart mixer (left)
The Mini-cone to evaluate the slump flow of the fresh SCC mortar (dimension in mm) (right)

Table 7.4: Obtained dose rates at the four different positions

Position	d_s (cm)	Dr (Gy/h)
1	18	9.34
2	21	6.33
3	43	2.16
4	46	1.87

For dose rates that have a rather low value (< 20 Gy/h) and for small mortar samples, a uniform dose rate distribution can be accepted over the height of the irradiated samples (ISIB statement). Therefore, a mean constant dose rate of 7.84 Gy/h (Top-level) and 2.02 Gy/h (Low-level) can be considered for the applied dose rates.

Finally, to obtain the total dose received by the irradiated mortar samples, the dose rate must be multiplied by the total amount of irradiation time. For mix 1 and after 1 day of hardening in an unirradiated environment, the four Top-level samples (Top 1) and the four Low-level (Low 1) samples are placed under the ^{60}Co source and irradiated for approximately 27 days with the dose rates and irradiation times recited in Table 7.5, giving a total received dose of respectively 5076 Gy and 1302 Gy (Table 7.5). For mix 2 the Low-level (Low 2) samples also undergo the same procedure and received a total dose of 1301 Gy after 28 days of hardening (Table 7.5).

In order to evaluate the effect of different dose rates on the strength of the mortar samples, four samples (Top 2a) are placed on the Top-level and irradiated for 165.7 hours (also after 1 day of hardening without gamma irradiation) until a total dose of approximately 1300 Gy is reached, which is comparable to the dose the samples at the Low-level receive. Afterwards, these four samples are replaced by four samples of the same mix (Top 2b), that did not receive any irradiation yet and so far hardened in unirradiated conditions. The irradiation of these four samples continues until the mortar reaches an age of 28 days. The total dose received for these samples is 3759 Gy (Table 7.5).

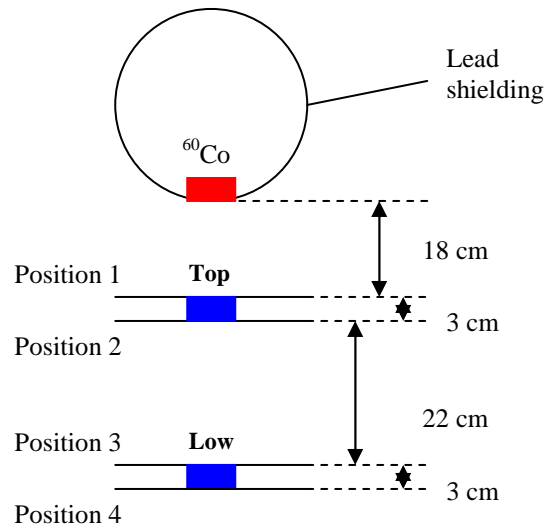


Figure 7.2: The irradiation scheme at ISIB for gamma irradiation (red = irradiation source, blue = mortar sample)

Table 7.4: Applied dose rates and absorbed doses of the mortar prisms

Name	Mix	Dr (Gy/h)	Irradiation time (h)	D (Gy)	Irradiation start age (h)
Ref 1	1	0	0	0	-
Top 1	1	7.84	647.8	5076	24.0
Low 1	1	2.02	647.8	1302	24.0
Ref 2	2	0	0	0	-
Top 2a	2	7.84	165.7	1298	24.0
Top 2b	2	7.84	479.8	3759	165.7
Low 2	2	2.02	645.5	1301	24.0

Compressive strength tests

After 28 days of hardening, the compressive strength of the samples, both the reference and the irradiated ones, is determined to evaluate the effect of gamma irradiation on the strength of the hardening SCC mortar. Therefore, the samples are placed inside an Amsler compression testing machine (capacity 200 kN), with the casting surface placed in a way that it faces the exterior. Thus, the loaded surface A_m has a size of 40 mm x 30 mm. The compressive strength can be found by dividing the maximal load at rupture by the surface of the sample on which the load is applied:

$$f_{m,irr/ref} = \frac{F_m}{A_m} \quad (7.3)$$

where: $f_{m,irr/ref}$ = the compressive strength of the mortar samples, irradiated or reference (MPa)

F_m = the maximal load at rupture (N)

A_m = the surface of the sample on which the load is applied (mm²)

However, the most interesting parameter is the relative strength loss of the irradiated samples. This can be found by using equation (7.4).

$$\frac{f_{m,irr}}{f_{m,ref}} \quad (7.4)$$

where: $f_{m,irr}$ = the compressive strength of the irradiated mortar samples (MPa)

$f_{m,ref}$ = the compressive strength of the reference mortar samples (MPa)

Also the volumetric weight of the hardened mortar samples can be easily determined by dividing the net weight of the samples by the three dimensions of the mortar samples.

Fluorescence microscopy

Out of one of the four mortar samples at each level, a thin section is made to investigate the effect of gamma irradiation on the SCC mortar on a microscopic level. Thin sections of concrete or mortar samples are micrometer thin specimens (size 30 mm x 40 mm) that can be viewed under an optical microscope. During the preparation of the thin sections, the capillary pores in the cement paste are filled with a fluorescent epoxy by impregnating the specimen in vacuum [Braeckman, 2007]. The thin sections are fabricated conform the principles described in the Nordtest Method (1991) and can be analysed under a microscope in fluorescent mode.

For the analysis, a monochromatic light source is needed to generate the fluorescence in the thin section. Monochromatic light is generated by normal light going through a blue filter (Figure 7.3): only ultraviolet (UV) light goes through. This UV light excites the fluorescent pigment in the thin section and a yellow filter eliminates the superfluous UV light. The resulting image presented in the ocular (or eyepiece) of the microscope originates exclusively from the fluorescent pigment in the thin section.

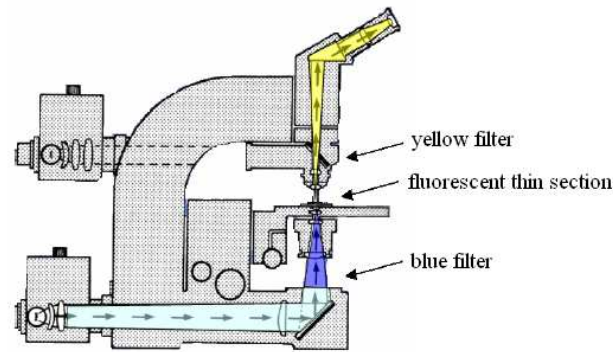
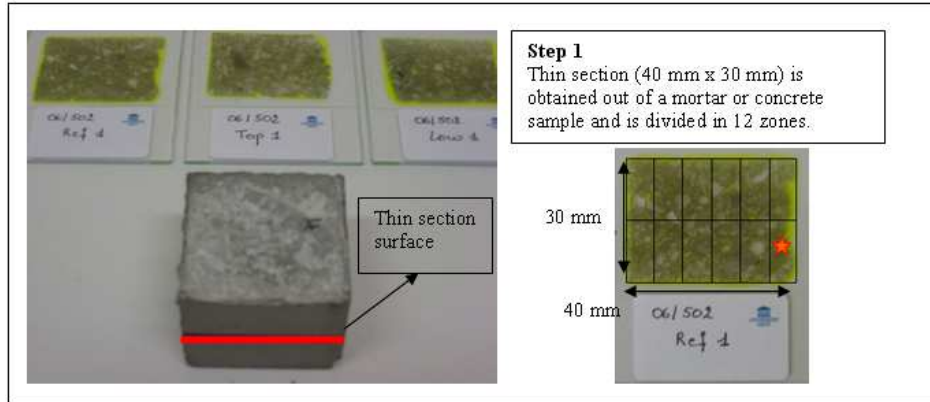


Figure 7.3: Fluorescence microscopy according to Jakobsen (2003)

According to Braeckman (2007), there exists a linear correlation between the intensity of the fluorescence of the cement paste in a thin section and the capillary porosity of the concrete or mortar. In other words, the higher the green tone of the mortar paste, the higher the capillary porosity of the mortar will be.

On the other hand, there is also a relationship between the W/C ratio and the capillary porosity of a concrete or mortar sample: the higher the W/C ratio, the higher the capillary porosity will be [Powers and Brownyard, 1946-1947]. It is well known that an increase in W/C ratio leads towards a decrease in compressive strength [De Schutter,

1996]. By summarizing the previous recited postulates, it can be concluded that an increase in fluorescence of the cement paste leads towards a decrease of the compressive strength. In this way it is possible to give an indication or an explanation for a possible strength variation of mortar samples due to gamma irradiation. To obtain the mean fluorescence of each thin section, a four step chronology must be followed, as explained below. The fluorescence of the thin section of the reference prism (Ref1, unirradiated) of mix 1 is determined as an example. The pictures presented in Figure 7.4b and Figure 7.4c originate from zone number 12.



*Figure 7.4a: First step of the determination of the fluorescence of the thin section
Preparation of the thin section and division of the thin section in twelve zones
(zone number 12 is presented in the figure by means of a star shape)*

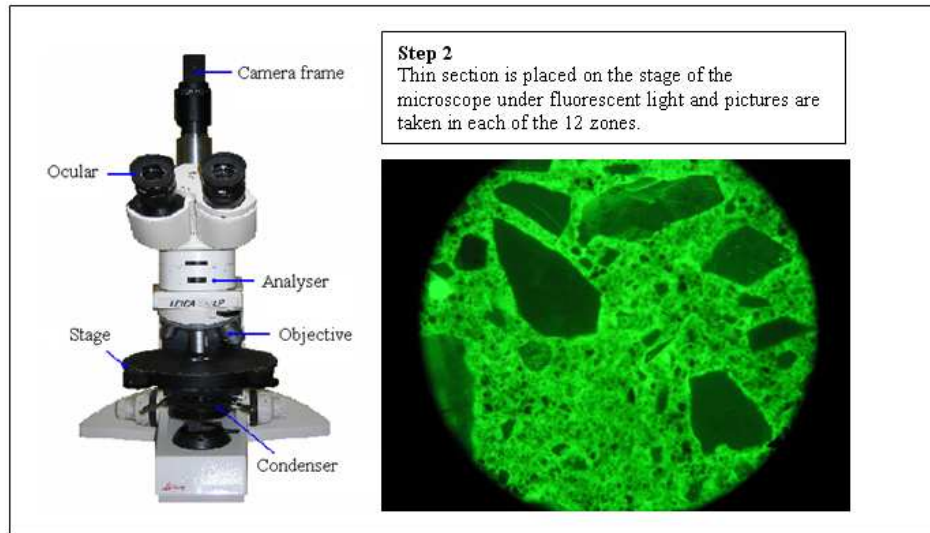


*Figure 7.4b: Second step of the determination of the fluorescence of the thin section
Making images of the thin section in each of the twelve zones
(image taken from zone number 12)*

For each mix, and for each level of irradiation of the mortar (Top, Low, Ref), one prism is available to obtain a thin section. The surface of the thin section is located at mid-height (15 mm) of the mortar prism, as presented in Figure 7.4a. Each thin section is divided into twelve imaginary zones.

In a second step (Figure 7.4b), the thin section is placed on top of the stage of the microscope and in each predefined zone a picture is taken with a digital camera mounted on the microscope by means of a camera frame. The enlargement reached with the microscope is 100:1. The enlargement ratio of the microscope and the settings of the camera must be equal during the capturing of the pictures in order to have a relevant comparison between the fluorescence of the different thin sections.

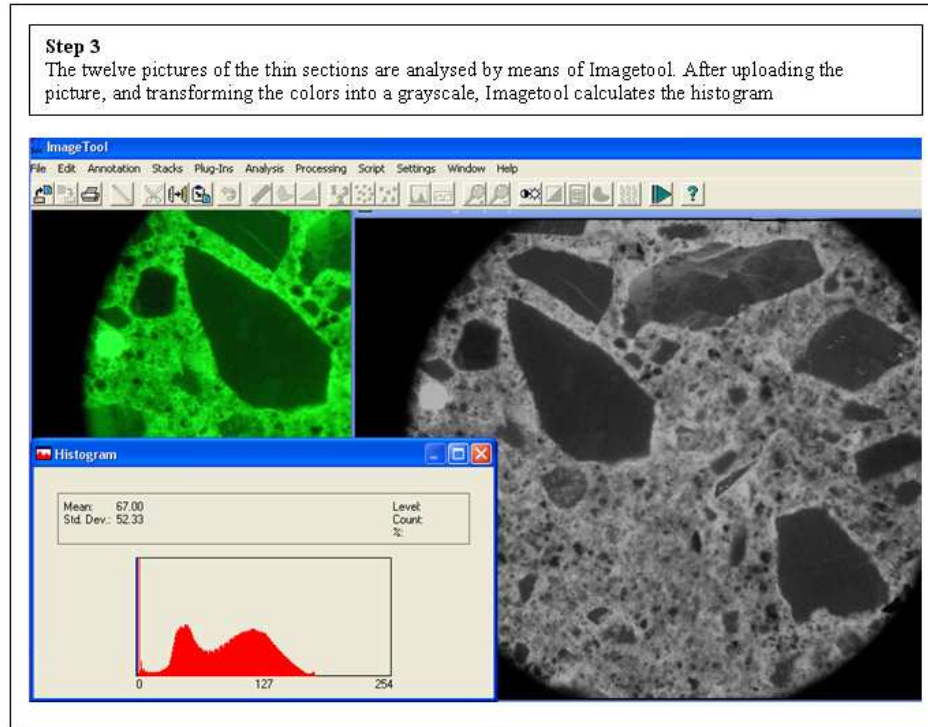


*Figure 7.4c: Third step of the determination of the fluorescence of the thin section
Analysis of the images to obtain the histogram
(image taken from zone number 12)*

In a third step (Figure 7.4c), the twelve images taken from the thin section are analysed by means of the operator independent image analysis tool UTHSCSA Imagetool (semi-automatic method): the program transforms the images to a histogram that expresses the amount of the different colours. A disadvantage of this tool is the fact that only histograms of images in gray tones can be obtained. Therefore, the pictures taken in the fluorescent mode need to be converted into gray tones.

Step 4

The histograms of the 12 pictures of the thin section are placed together. First the lowest threshold T_1 (aggregates) and the highest threshold T_h (air voids) are determined and eliminated, and finally the mean gray tone of the zone in between the thresholds is determined by using equation (7.5) to characterize the fluorescence of the cement paste.

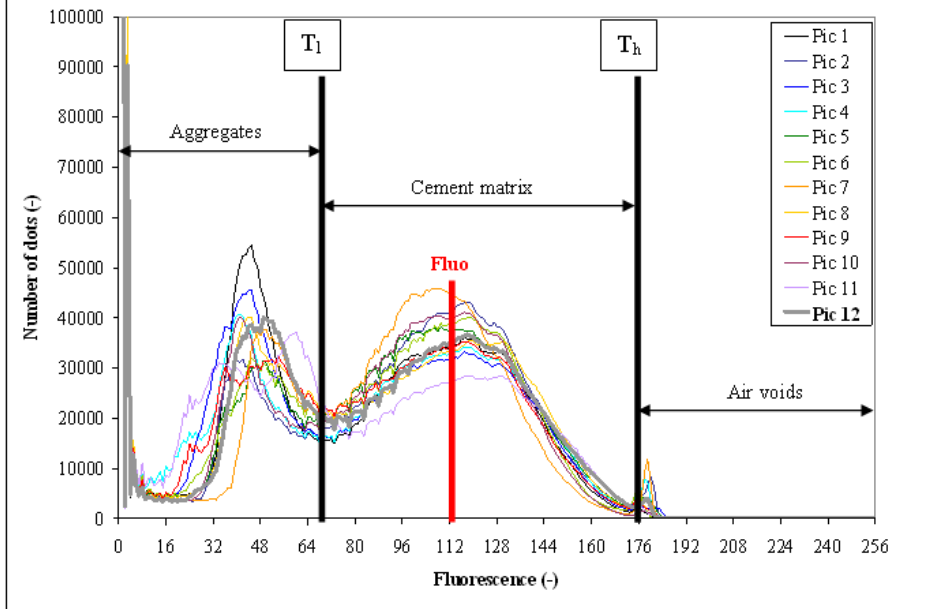


Figure 7.4d: Fourth step of the determination of the fluorescence of the thin section
Determination of the thresholds and the mean gray tone
(the histogram of the picture taken from zone number 12 is marked in bold)

In a fourth step (Figure 7.4d), the mean gray tone is measured in the twelve zones. For each thin section, the mean gray tone of the cement paste and the dispersion of the green tone is calculated: first, all histograms of the twelve images are placed together and then the lowest thresholds of the aggregates T_1 (dark gray and black) and highest threshold T_h of the air voids (very light gray) are determined. The zone in between those two limit values represents the cement matrix. The zones representing the aggregates and the zones representing the air voids need to be eliminated. To calculate the mean fluorescence of the cement paste, equation (7.5) is used to determine the fluorescence of each valuable zone of the thin section.

Finally, the mean value of the fluorescence is calculated out of the obtained value of each of the twelve zones. This mean value is representative for the fluorescence of the whole thin section, while the dispersion gives an indication of the homogeneity of the cement paste of the thin section.

$$Fluo = \frac{\sum_{i \in [T_l, T_h]} x_i \cdot y_i}{\sum_{i \in [T_l, T_h]} y_i} \quad (7.5)$$

where: x_i = the fluorescence in each point within the zone of the two thresholds (-)
 y_i = the number of dots with a specific fluorescence (-)

2.2 Effect of heat on strength of concrete

2.2.1 Previous results

Aside from the gamma radiation originating from the vitrified HLW and the SF assemblies present inside the Supercontainer, there is also a considerable amount of heat originating from the radioactive waste, hence the term ‘heat-emitting’ waste. Irradiation mostly goes hand in hand with an increase of temperature of the elements in the nearby environment of the radioactive source. This amount of heat depends on the thermal power of the vitrified HLW and SF assemblies (Chapter 4).

Preliminary studies concerning the temperature evolution inside the Supercontainer due to heat-emitting vitrified HLW and SF assemblies indicate that the maximum temperature at the interface of the buffer and the overpack is already achieved a couple of years after emplacement of the canisters inside the concrete buffer (Chapter 4) [Wickham et al., 2004]. To avoid boiling of pore water fluids within the concrete buffer, it has been suggested that the temperature of the buffer may never exceed 100 °C [Wickham et al., 2005]. This temperature increase depends on a cooling period of 50 to 70 years of the radioactive waste preceding the emplacement into the Supercontainer. A 2D axisymmetrical thermal scoping study performed by Weetjens and Sillen (2006) indicates that the peak temperature in the concrete buffer is attained between 5 and 10 years after waste emplacement. For vitrified HLW, the maximum temperatures at the buffer-overpack interface surface reach 111 °C, 92 °C and 77 °C for pre-cooling periods of 50, 60 and 70 years respectively after approximately 5 years. For SF, these values are slightly higher and occur later (after 10 – 12 years): 111 °C, 99 °C and 89 °C (Chapter 4). The initial temperature is assumed to be 15.7 °C.

According to Bazant and Kaplan (1996), the most important effects of elevated temperature on concrete are: dehydration of the cement paste, porosity increase, modification in moisture content, thermal expansion, alteration of pore pressure, thermal cracking due to incompatibility (cement matrix – aggregates), transient thermal creep and thermal spalling. Only the effect of elevated temperatures (up to a relevant temperature of approximately 100 °C) on the strength of the heated concrete samples is examined. A literature review on behalf of that subject is conducted previously (Chapter 4).

Table 7.5: Summary of the effect of elevated temperatures on concrete strength

Reference	Temperature (°C)	Strength loss (%)	Observations
Vodák et al. (2004)	100	15	Increase of porosity
Kaplan (1987)	100	10 – 35	Internal microcracking due to hindered deformation at the interface aggregates-cement. For concrete with calcareous aggregates the strength loss is 15 %
Savva et al. (2005)	100	+ 5	Obtained for concrete based on limestone aggregates
Liu et al. (2006)	100	-	Weight loss due to evaporation of capillary pore water
Castillo & Durrani (1990)	100 – 200	15 – 20	-
Noumowé et al. (2009)	110	0 – 5	No significant deterioration of the mechanical properties of the concrete with limestone aggregates
Noumowé et al. (1996)	120	-	No significant change in porosity
Noumowé (2003)	200	18 – 38	The use of PP fibers did not improve the behaviour under elevated temperatures

The most important and relevant observations and conclusions concerning the strength loss of concrete due to an external heat source are listed in Table 7.5. A strength reduction between 0 % and 35 % is observed in case of exposure to elevated temperatures up to 100 °C, mainly caused by an internal microcracking behaviour or an increase in porosity. This coarsening of the pore structure of the concrete can be seen as the main reason influencing the decrease of mechanical properties at elevated temperature attack [Janotka and Nürnbergerová, 2005]. Several parameters affect the test results: the type of cement, the type of aggregates, the W/C ratio, the duration of exposure, etc. Therefore it remains hard to come to any general conclusions (Chapter 4). Tests are conducted at the Magnel Laboratory for Concrete Research on concrete samples (SCC and TVC), subjected to elevated temperatures between 20 °C and 105 °C to investigate the effect on the mechanical strength of the concrete.

2.2.2 Testing procedure

In these experiments, to evaluate the effect of elevated temperatures on the strength of SCC and TVC, different types of tests are conducted: fresh concrete tests, compressive strength and splitting tensile strength tests and fluorescence microscopy tests to investigate the effect of heat on a microscopic level and to quantify the capillary porosity of the concrete samples.

Mixing procedure and fresh concrete properties

In total, four mixes of SCC and four mixes of TVC (50 liters each, using the cross current mixing principle) are made and the fresh mix is characterized by its slump flow value (EN 12350-8), the V-funnel time (EN 12350-9) and the density of the fresh mix. For each mix, thirty cubes with size 100 mm are prepared, placed inside a climate room (20 °C, 90 % RH) for 24 hours, demoulded and placed under water (20 °C) until the age of 28 days is reached. Afterwards, the samples are placed in ovens with different temperatures (40 °C – 60 °C – 80 °C – 105 °C), in some cases covered with an adhesive aluminium foil (to limit the evaporation of capillary pore water), for an extended period of time, as indicated in Table 7.6. The reference temperature is 20 °C. Afterwards, the samples are tested to determine the compressive strength, the splitting tensile strength and the weight loss.

Table 7.6: Conservation conditions of the SCC and TVC cubes

Name	Time in oven	Age at testing	Covered?
SCC0 - TVC0	14 days	42 days	no
SCC1 - TVC1	14 days	42 days	no
SCC2 - TVC2	14 days	42 days	yes
SCC3 - TVC3	91 days	119 days	no

Compressive strength tests and splitting tensile tests and weight loss

When the heating time is over, the samples are taken out of the oven and tested immediately. Three cubes are needed to determine the compressive strength $f_{ccub100}$ according to the Belgian Code NBN EN 12390-3. Also splitting tensile strength tests are conducted on the samples according to the Belgian Code NBN B15-218 to determine f_{ctsp} . These tests are also explained in Chapter 6.

The most interesting parameters are the relative strength ratios in compressive (f_{Rc}) and splitting tensile (f_{Rct}) behaviour. These can be found by using equations (7.6a) and (7.6b).

$$f_{Rc} = \frac{f_{ccub100,T}}{f_{ccub100,20^{\circ}C}} \quad (7.6a)$$

$$f_{Rct} = \frac{f_{ctsp,T}}{f_{ctsp,20^{\circ}C}} \quad (7.6b)$$

where: $f_{ccub100,T}$ = the compressive cube strength (side 100 mm) of the heated samples at temperature $T = 20^{\circ}C - 40^{\circ}C - 60^{\circ}C - 80^{\circ}C - 105^{\circ}C$ (MPa)

$f_{ccub100,20^{\circ}C}$ = the compressive cube strength (side 100 mm) of the reference samples at temperature $T = 20^{\circ}C$ (MPa)

$f_{ctsp,T}$ = the splitting tensile strength of the heated samples at temperature $T = 20^{\circ}C - 40^{\circ}C - 60^{\circ}C - 80^{\circ}C - 105^{\circ}C$ (MPa)

$f_{ctsp,20^{\circ}C}$ = the splitting tensile strength of the reference samples at temperature $T = 20^{\circ}C$ (MPa)

In order to quantify the weight loss WL of the concrete samples due to the enforced elevated temperatures, the mass of the samples is measured after 28 days (M_0 , before placing in the oven) and afterwards (M_f), right after the samples are taken out of the oven, thus: just before the strength tests are executed. The weight loss can be found according to equation (7.7):

$$WL = \frac{M_0 - M_f}{M_0} \cdot 100 \% \quad (7.7)$$

Fluorescence microscopy

Out of one sample of the mixes of SCC0 and TVC0, heated to the different temperatures ($20^{\circ}C - 40^{\circ}C - 60^{\circ}C - 80^{\circ}C - 105^{\circ}C$), thin sections are made to perform fluorescence microscopy. In total ten thin sections are made. The mean value of the fluorescence of the cement matrix of each thin section is calculated via the four step method explained previously. As mentioned before, an increase in mean fluorescence of the cement paste, or an increase in capillary porosity, can be an explanation for a decrease in compressive strength. In this way it is possible to give an indication for a possible strength variation of the concrete due to elevated temperatures.

3 Results and discussion

3.1 Effect of gamma radiation on strength of the Supercontainer

The slump flow value of the fresh mortar mixes is 235 mm and 295 mm for mix 1 and mix 2 respectively, determined by means of the Mini-cone (Figure 7.1). Nevertheless, the strength results and the results of the fluorescence microscopy are more important to evaluate the effect of gamma radiation on the strength of the SCC based mortar. These results are presented in Table 7.7 and Figure 7.5.

A certain tendency strikes: with increasing dose of applied gamma radiation, the compressive strength ratio of the mortar samples decreases (Figure 7.5, blue dots and line). It was investigated whether an explanation could be found by means of the fluorescence microscopy of thin sections. Although a very slight increasing trend of fluorescence with increased dose is noticeable (Figure 7.5), this increase is statistically not significant. Therefore, the amount of examined thin sections should be increased or alternative test methods should be considered. According to Bouniol (2004), a redistribution or reorganization of the pores of irradiated hardened paste samples is found by means of mercury porosimetric measurements.

It must be mentioned that these test results are only indications. At this state of research, it is hard to come to exclusive conclusions and further research is inevitable and needed, preferably on an even smaller scale (for example: investigation of the gel pore structure on a nanoscale by means of Scanning Electron Microscopy (SEM)). Nevertheless, some main observations are worth mentioning:

- A tendency is noticed that an increasing gamma radiation dose during hardening of an SCC based mortar leads towards a compressive strength loss, up to 15 %.
- The dose rate does not have a significant effect on the compressive strength ratio. By comparing this ratio of the samples Low 1 and Low 2 (mean dose rate of 2.02 Gy/h) with the ratio of sample Top 2a (mean dose rate 7.84 Gy/h), no significant difference is noticed (Figure 7.5). These samples have received equal gamma radiation doses of approximately 1300 Gy, making the received dose a more important parameter to indicate strength losses compared to the dose rate (valid in case of sufficiently low dose rates, smaller than 20 Gy/h).
- The reference samples, which remain unirradiated, have a higher volumetric weight compared to the irradiated samples.
- The samples of mix 2 compared to the samples of mix 1 have a higher compressive strength f_m . On the other hand, the fluorescence is slightly smaller in case of mix 2, once more demonstrating the inverse proportionality between strength and fluorescence (or capillary porosity).
- The dispersion of the fluorescence of the samples of mix 2 is slightly higher than the dispersion of the samples of mix 1, indicating a smaller homogeneity of the cement matrix of the samples originating from mix 2.

Table 7.7: The received dose, strength, fluorescence and volumetric weight of the different mortar samples

Name	D Gy	f_m MPa	s MPa	$f_{m,irr}/f_{m,ref}$ -	Fluo -	s -	ρ_m kg/m ³
Ref 1	0	33.1	3.7	1.00	114.0	2	2265
Top 1	5076	30.0	3.4	0.91	115.6	1.9	2250
Low 1	1302	28.5	2.5	0.86	114.4	1.9	2250
Ref 2	0	40.8	6.2	1.00	112.2	2.8	2260
Top 2a	1298	34.2	5.3	0.84	115.9	2.1	2235
Top 2b	3759	34.9	5.4	0.86	112.1	2.7	2235
Low 2	1301	34.9	3.5	0.86	112.4	2.3	2245

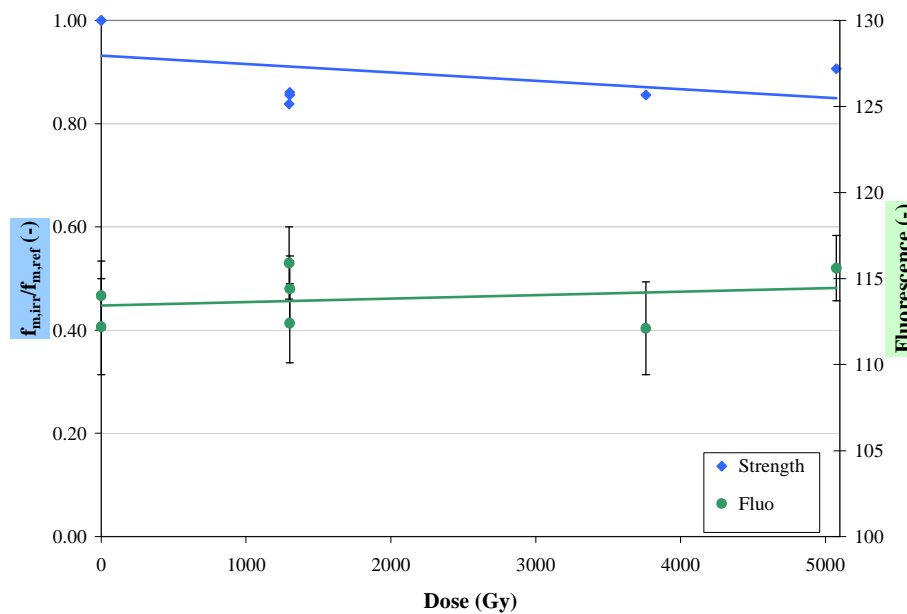


Figure 7.5: Dependency of the compressive strength ratio and the fluorescence of mortar samples on the applied dose of gamma radiation

3.2 Effect of heat on strength of the Supercontainer

Four SCC and TVC mixes are made to investigate the effect of elevated temperatures on the strength properties of the concrete. To characterize the fresh SCC and TVC, tests are performed. For SCC, the slump flow value, the V-funnel time and the density are determined, while for the fresh TVC, the slump and the density of the fresh concrete

are determined. For each mix, 15 + 15 cubes are cast, and after a certain storage period the compressive strength and the splitting tensile strength, and the dependency on the elevated temperatures (40 °C – 60 °C – 80°C – 105 °C, reference: 20 °C) is examined. In order to explain the strength variation, fluorescence microscopy is conducted to quantify the capillary porosity of the concrete samples. Finally, the difference in storage conditions is taken a look at.

Properties of the fresh SCC and TVC

The fresh properties of the SCC and TVC mixes are listed in Table 7.8a and Table 7.8b. Overall, the density of the TVC mixes is slightly higher compared to the density of the fresh SCC. A rather large variation on the slump, slump flow and V-funnel test results is noticed.

Table 7.8a: The fresh properties of the SCC mixes

		SCC0	SCC1	SCC2	SCC3
Superplasticizer	kg/m ³	10.0	10.2	10.2	12.0
Quantity	m ³	0.05	0.05	0.05	0.05
Fresh results					
Slump flow	mm	680	640	575	715
V-funnel	s	8.3	6.0	17.0	33.0
Density	kg/m ³	2400	2350	2405	2405

Table 7.8b: The fresh properties of the TVC mixes

		TVC0	TVC1	TVC2	TVC3
Superplasticizer	kg/m ³	3.6	6.0	4.0	4.0
Quantity	m ³	0.05	0.05	0.05	0.05
Fresh results					
Slump	mm	235	55	175	205
Density	kg/m ³	2420	2425	2440	2450

Compressive and splitting tensile strength

The influence of the temperature variation on the compressive strength ratio f_{Rc} and the splitting tensile strength ratio f_{Rct} of the samples of mixes SCC0 – SCC1 and TVC0 – TVC1 (Table 7.6) is given in Figure 7.6, Table 7.9a and Table 7.9b. In the compressive behaviour of the concrete, an indication of strength loss is noticed, at most at a temperature of 60 °C (Figure 7.6). Compared to TVC, the compressive strength loss of SCC is slightly higher. In the splitting tensile behaviour, it is the other way around: a strength increase is noticed, higher for SCC compared to TVC.

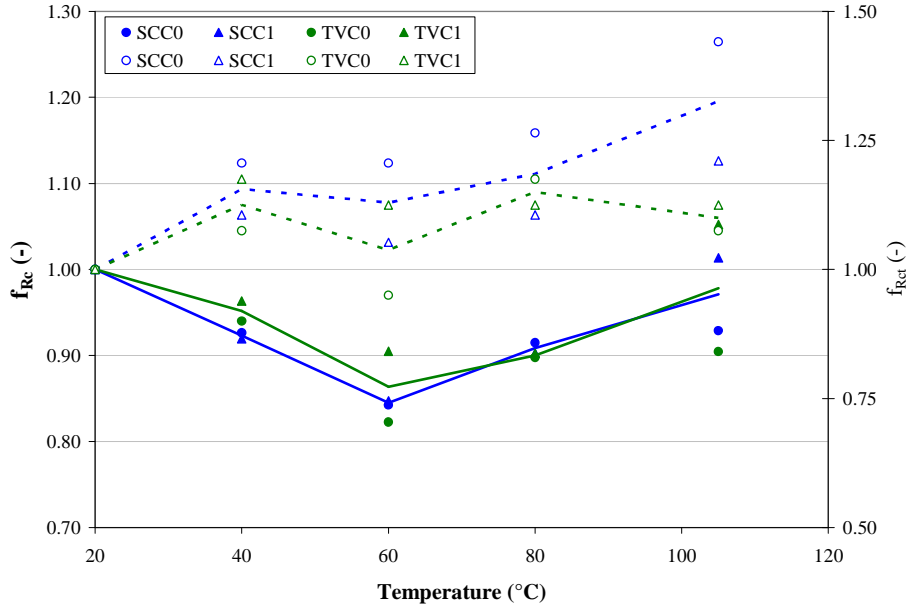


Figure 7.6: Dependency of the compressive strength ratio f_{Rc} (bold line) and the splitting tensile strength ratio f_{Rct} (dotted line) on the temperature variation

Fluorescence microscopy

A compressive strength loss tendency with increasing temperature is noticeable. To further examine this position, fluorescence microscopy is conducted on thin sections made out of one sample originating from the mixes SCC0 and TVC0, and for each of the five forced temperatures. One explanation of the compressive strength loss of the concrete samples with elevated temperatures can be found in the fact that the fluorescence of the thin sections, made of the different samples, indicates a noticeable increasing trend with increasing temperature (Figure 7.7, green dots and lines), although these results are statistically not significant. As mentioned before, an increase in fluorescence, thus an increase in capillary porosity, goes along with a decrease in compressive strength (Figure 7.7, blue dots and lines). The results of TVC and SCC (for mixes TVC0 and SCC0) are more or less similar. On the other hand, the increase in splitting tensile behaviour can not be explained by means of the fluorescence microscopy results.

Taking a closer look at the thin sections of the different samples, cracks through the aggregates are identified in all cases. With increasing temperature, the amount of cracks increases and the crack width enlarges. Microcracking can occur due to the thermal incompatibility of hardened cement paste and the aggregates, which increases the porosity and decreases the strength [Bazant and Kaplan, 1996].

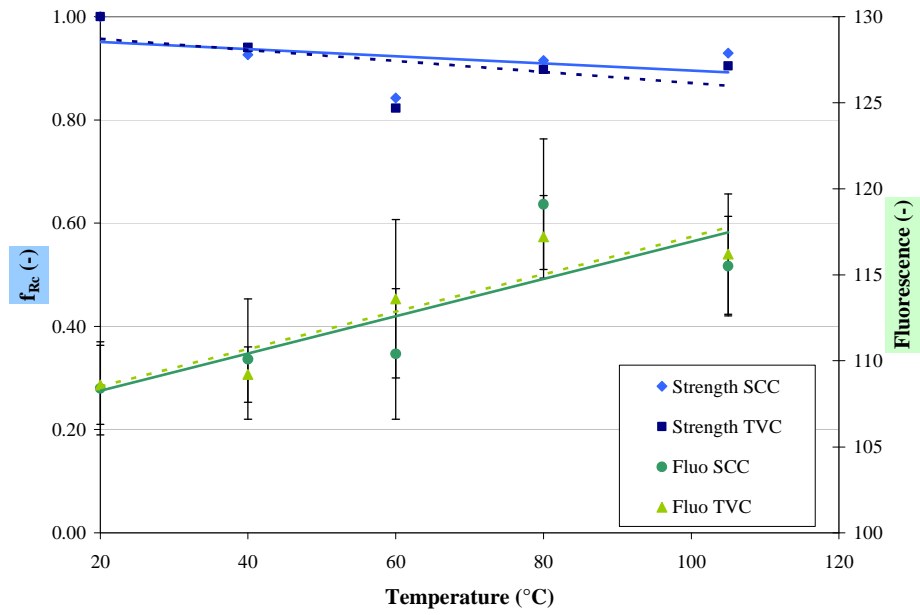


Figure 7.7: Dependency of the compressive strength ratio and the fluorescence of the SCC and the TVC samples on the temperature variation

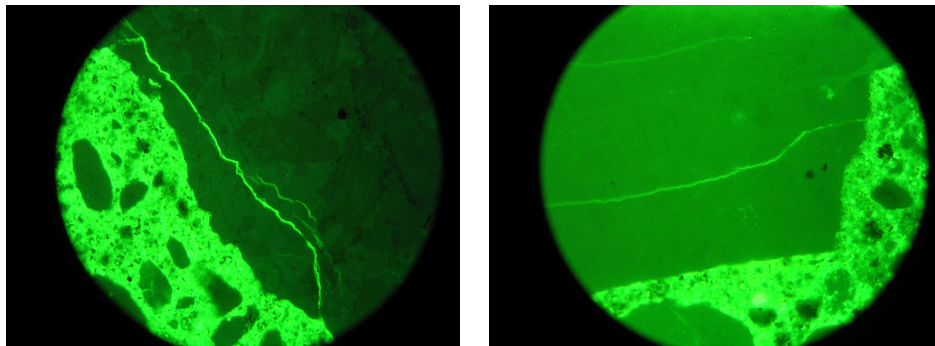


Figure 7.8: Image of cracks in aggregates of the thin section of SCC0 105 (left) and SCC0 20 (right)
Enlargement ratio 200:1

Table 7.9a: The compressive strength and the splitting tensile strength of the SCC samples at different temperatures

Name	T °C	f_{ccub100} MPa	s MPa	f_{RC} -	f_{ctsp} MPa	s MPa	f_{Rct} -
SCC0	20	78.7	2.8	1.00	3.4	0.2	1.00
	40	72.9	0.5	0.93	4.1	0.1	1.21
	60	66.3	1.7	0.84	4.1	0.0	1.21
	80	72.0	1.3	0.91	4.3	0.2	1.26
	105	73.1	2.0	0.93	4.9	0.4	1.44
SCC1	20	59.6	0.6	1.00	3.8	0.3	1.00
	40	54.8	1.2	0.92	4.2	0.2	1.11
	60	50.5	1.3	0.85	4.0	0.4	1.05
	80	53.8	2.5	0.90	4.2	0.4	1.11
	105	60.4	1.3	1.01	4.6	0.1	1.21
SCC2	20	67.0	3.1	1.00	5.0	0.4	1.00
	40	60.5	2.9	0.90	4.7	0.1	0.94
	60	54.9	1.5	0.82	4.7	0.6	0.94
	80	53.6	0.9	0.80	4.1	0.0	0.82
	105	53.5	1.4	0.80	3.6	0.3	0.72
SCC3	20	77.5	1.7	1.00	5.8	0.4	1.00
	40	68.8	1.5	0.89	5.2	0.4	0.90
	60	73.4	1.1	0.95	5.3	0.3	0.91
	80	73.6	3.8	0.95	5.4	0.3	0.93
	105	71.6	0.8	0.92	5.1	0.2	0.88

Table 7.9b: The compressive strength and the splitting tensile strength of the TVC samples at different temperatures

Name	T °C	f_{ccub100} MPa	s MPa	f_{Rc} -	f_{ctsp} MPa	s MPa	f_{Rct} -
TVC0	20	73.3	0.9	1.00	4.0	0.3	1.00
	40	68.9	2.0	0.94	4.3	0.3	1.08
	60	60.3	2.0	0.82	3.8	0.2	0.95
	80	65.8	1.6	0.90	4.7	0.1	1.18
	105	66.3	1.1	0.90	4.3	0.2	1.08
TVC1	20	78.8	0.3	1.00	4.0	0.4	1.00
	40	75.9	1.7	0.96	4.7	0.7	1.18
	60	71.3	1.8	0.90	4.5	0.6	1.13
	80	71.1	2.0	0.90	4.5	0.6	1.13
	105	82.9	1.9	1.05	4.5	0.2	1.13
TVC2	20	64.6	1.9	1.00	5.7	0.1	1.00
	40	63.8	1.2	0.99	5.1	0.2	0.89
	60	58.0	2.0	0.90	4.6	0.4	0.81
	80	56.6	1.2	0.88	4.4	0.3	0.77
	105	54.3	2.3	0.84	3.7	0.4	0.65
TVC3	20	74.6	1.0	1.00	4.8	0.2	1.00
	40	66.0	0.6	0.88	4.4	0.3	0.92
	60	70.6	1.0	0.95	4.8	0.2	1.00
	80	71.5	0.8	0.96	5.1	0.2	1.06
	105	67.5	1.3	0.90	4.9	0.2	1.02

Table 7.9c: The fluorescence and the weight loss of the SCC and the TVC concrete samples at different temperatures

Name	T °C	Fluo -	s -	WL %	s -	Name	T °C	Fluo -	s -	WL %	s -
SCC0	20	108.4	2.7	1.16	0.05	TVC0	20	108.6	2.3	0.97	0.03
	40	110.1	3.5	2.56	0.03		40	109.2	1.6	2.52	0.06
	60	110.4	3.8	4.05	0.13		60	113.6	4.6	4.32	0.14
	80	119.1	3.8	5.33	0.09		80	117.2	2.4	5.43	0.51
	105	115.5	2.9	5.82	0.13		105	116.2	3.5	5.53	0.70
SCC1	20			2.43	0.11	TVC1	20			1.32	0.04
	40			4.16	0.10		40			2.59	0.07
	60			5.90	0.06		60			3.88	0.15
	80			6.66	0.21		80			4.69	0.10
	105			7.59	0.18		105			5.74	0.17
SCC2	20			0.01	0.01	TVC2	20			0.01	0.00
	40			0.14	0.03		40			0.08	0.04
	60			0.35	0.07		60			0.33	0.09
	80			1.09	0.29		80			0.97	0.29
	105			5.25	0.16		105			5.16	0.22
SCC3	20			2.12	0.03	TVC3	20			1.88	0.06
	40			4.34	0.18		40			4.23	0.23
	60			5.27	0.09		60			5.17	0.18
	80			5.60	0.12		80			5.39	0.09
	105			5.93	0.12		105			5.68	0.15

Figure 7.7: Dependency of the compressive strength ratio and the fluorescence of the SCC and TVC samples on the forced elevated temperatures

For example (Figure 7.8), the crack width in the aggregate of the thin section of SCC0 (temperature rise up to 105 °C) is approximately 20 µm, while the crack width in the thin section of the reference sample (20 °C) is smaller than 5 µm. This can also explain the previously found compressive strength losses with increasing temperature.

Weight loss and influence of the storage conditions

Except for the increasing capillary porosity, the increasing amount of cracks and the increment of crack widths as an indication for the compressive strength loss, the weight loss can also have an influence on the strength results.

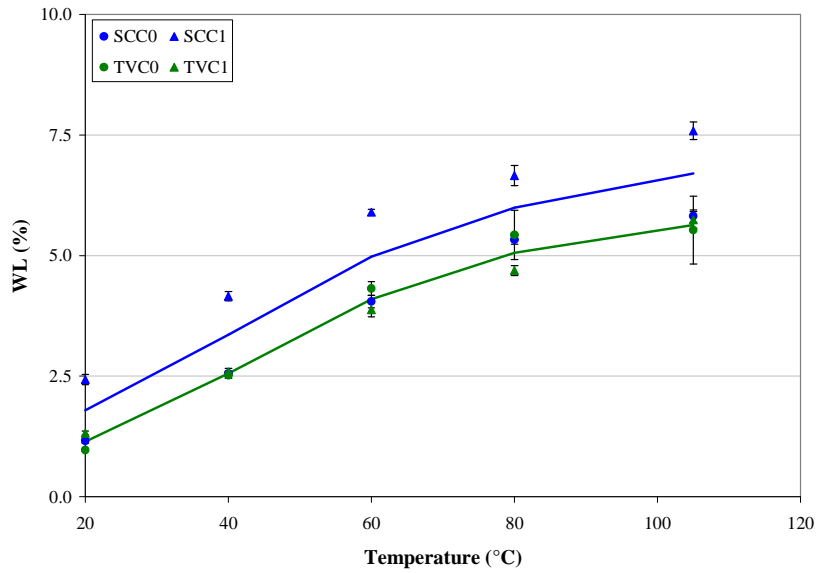


Figure 7.10a: Dependency of the weight loss of the SCC and TVC samples on the forced elevated temperatures

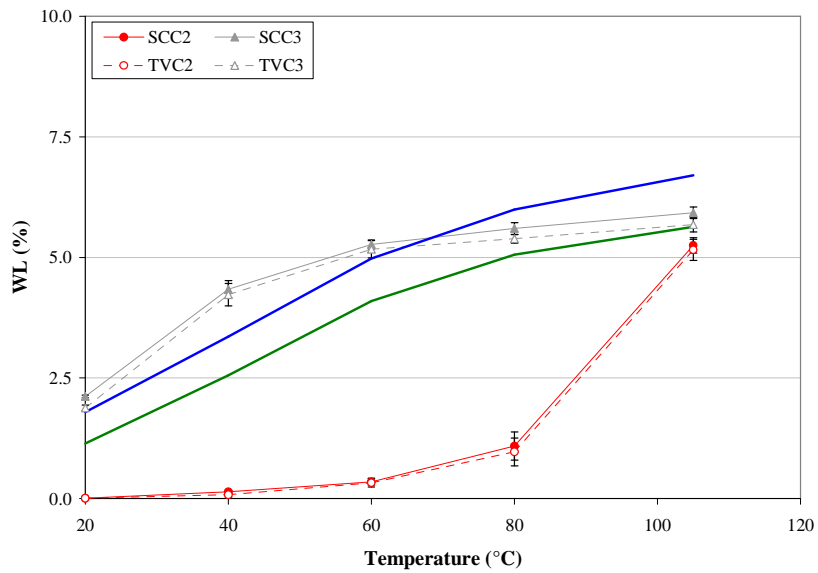


Figure 7.10b: Dependency of the weight loss of the SCC and TVC samples on the forced elevated temperatures with altered conservation procedures

According to Taerwe (1997), three types of water are present in a hydrating cement matrix: (i) the chemically bound water in the CSH hydrates, (ii) the physically adsorbed gel water (attached to the CSH layers) and the interlayer water in between the CSH layers, and (iii) the pore water present in the capillary pores (Figure 7.9). Due to elevated temperatures up to 105 °C, evaporation of the capillary pore water takes place, giving an explanation for the weight loss observed during the laboratory tests. It must be noted that at a temperature of 105 °C evaporation of the gel water occurs [De Schutter, 1996]. For cubic samples of the mixes SCC0 – SCC1 and TVC0 – TVC1, after a hardening period of 28 days under water, and placed inside an oven for 14 days at a specific temperature, the weight loss is measured and depicted in Figure 7.10a. Especially due to the evaporation of the pore water, the weight loss increases with increasing temperature and is higher in case of SCC.

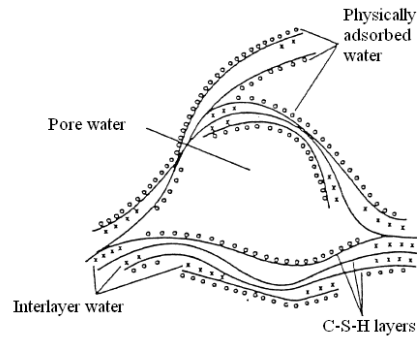


Figure 7.9: Three types of water present in the hydrating cement matrix [Taerwe, 1997]

If the conservation procedure of the samples, after a hardening time of 28 days under water, is altered (according to Table 7.6), the measured weight losses after emplacement in the ovens at different temperatures are changed (Figure 7.10b).

In case an adhesive foil is provided, enclosing the samples (SCC2 and TVC2), the weight loss decreases significantly, especially at temperatures below 80 °C. Total prevention of evaporation is not achieved, mainly due to imperfections in the joining of the adhesive foil, and the weight loss still increases with increasing temperature, but in a smaller extent compared to the unpacked samples. At 105 °C, the weight loss is almost equal as the case of unpacked samples: at those temperatures the glue of the aluminium foil dissolves, making evaporation of the pore water possible. The weight loss is slightly higher in case of SCC, but the difference with the weight loss of TVC is insignificant.

In another conservation procedure (SCC3 and TVC3), the unpacked samples are placed at elevated temperatures for a longer period of time: 91 days compared to 14 days (Figure 7.10b). In case of SCC, up to temperatures of approximately 60 °C, the weight loss is higher if the drying period is longer. For TVC, the weight loss is higher in the total temperature range (20 °C – 105 °C) in case the drying period is longer. Once more, the weight loss is slightly higher in case of SCC.

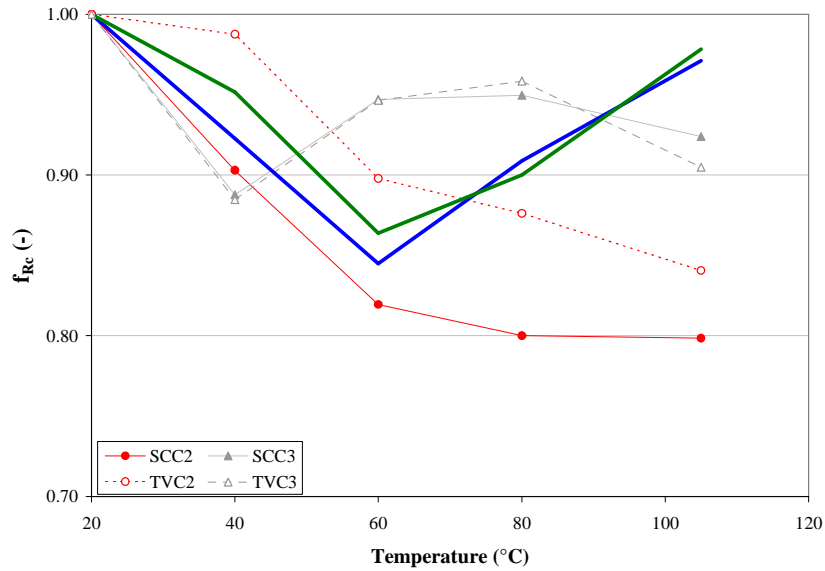


Figure 7.11: Dependency of the compressive strength ratio f_{Rc} on the temperature variation with different drying conditions

The compressive strength loss, in case the evaporation is limited by means of an adhesive foil, increases continuously with increasing temperature and is significantly higher in case of SCC (Figure 7.11, red curves). A decrease of respectively 20 % and 16 % is noticed for SCC and TVC respectively. If the drying period is prolonged up to 91 days (compared to 14 days), there is also an indication of compressive strength loss and a rather good resemblance is obtained between SCC and TVC (Figure 7.11, grey curves). However, no continuous decrease in strength is observed and kinks in the curves are noticed at 40 °C and 80 °C, while in case of heating of unpacked samples during 14 days, only one significant kink is observed at a temperature of 60 °C.

4 Conclusion

Overall, the heat-emitting radioactive waste inserted in the buffer increases the temperature of the concrete (buffer, filler and lid). The effect of these elevated temperatures on the strength of the concrete (SCC and TVC), considered for the Supercontainer concept, is evaluated by means of laboratory tests. It is known that elevated temperatures can result in deterioration of the physico-chemical properties of concrete, and that the concrete porosity plays the main role in affecting the changes of the compressive strength [Vodák et al., 2004].

Out of the tests performed at the MagneL Laboratory for Concrete Research, indications of a possible compressive strength loss of SCC (up to 20 %) and TVC (up to 15 %) due to elevated temperatures are found. The increasing capillary porosity, measured by means of fluorescence microscopy, can be seen as a reasonable explanation for this strength loss. Also greater amounts of cracks and larger crack widths are found in the heated samples, compared to the reference samples (20 °C), hence confirming the previously found microcracking behaviour of concrete under elevated temperatures [Bazant and Kaplan, 1994]. The preservation conditions and the related weight loss of the samples also affect the results.

Gamma radiation is also emitted by the vitrified HLW and SF assemblies in the Supercontainer concept and the concrete inside the Supercontainer absorbs this radiation emitted at dose rates inferior to 20 Gy/h. At the MagneL Laboratory of Concrete Research, in cooperation with ISIB, SCC based mortar samples are irradiated during hardening in order to examine the compressive strength variation. A certain tendency of decreasing strength ratios with increasing dose of gamma radiation appears: the compressive strength of the mortar samples decreases with 15 %.

It must be mentioned that these test results are only indications. At this state of research, it is hard to come to exclusive conclusions and further and repetitive research is inevitable and needed, preferably on an even smaller scale (for example: characterization of the porosity by means of mercury intrusion or investigation of the gel pore structure on a nanoscale by means of Scanning Electron Microscopy (SEM)). For now, although it is not statistically proven, a trend is found that the capillary porosity increases with increasing radiation dose and increasing temperature, as indicated by the fluorescence measurements.

Moreover, the combined effect of gamma radiation and elevated temperature on the mechanical properties (not only the strength) of concrete samples is worth taking a look at in the nearby future. However, this is out of the scope of this doctoral research and is subject for further research.

References

- Bar-Nes G., Katz A., Peled Y., Zeiri Y. (2008), *The combined effect of radiation and carbonation on the immobilization of Sr and Cs ions in cementitious pastes*, Materials and Structures 41, 1563-1570.
- Bazant Z.P., Kaplan M.F. (1996), *Concrete at high temperatures: material properties and mathematical models*, Essex: Longman.
- Bouniol P. (2004), *État des connaissances sur la radiolyse de l'eau dans les colis de déchets cimentés et son approche par simulation*, Rapport CEA, R-6069.
- Braeckman J. (2007), *Control of the water-cement ratio of hardened concrete using fluorescence microscopy*, Master thesis (in Dutch), Magnel Laboratory for Concrete Research, Ghent University, Belgium.
- De Schutter G. (1996), *Fundamental and practical study on thermal stresses in massive hardening concrete elements*, Doctoral thesis (in Dutch), Ghent University, Magnel Laboratory for Concrete Research, Belgium.
- Ichikawa T., Koizumi H. (2002), *Possibility of radiation-induced degradation of concrete by alkali-silica reaction of aggregates*, Journal of Nuclear Science and Technology, Vol. 39, No. 8, 880-884.
- Jakobsen U.H. (2002), *Fluorescence petrography of concrete*, Training Course Concrete Experts International.
- Janotka I., Nürnbergerová T. (2005), *Effect of temperature on structural quality of the cement paste and high-strength concrete with silica fume*, Nuclear Engineering and Design 235, 2019-2032.
- Kaplan M.F. (1987), *Concrete Radiation Shielding – Nuclear Physics, Concrete Properties, Design and Construction*, Longman Scientific & Technical, England, 457pp.
- Kelly B.T., Davidson I. (1969), 2nd Conference on Prestressed Concrete Pressure Vessels and Their Insulation, p. 237, London.
- Liu X. (2006), *Microstructural investigation of Self-Compacting Concrete and High-Performance Concrete during hydration and after exposure to high temperatures*, Doctoral thesis, Magnel Laboratory for Concrete Research, Ghent University, Belgium.
- Morigani S. (1997), Preprint East Asia Alkali-Aggregate Reaction Seminar, p.101, Tottori, Japan.
- Nordtest Method (1991), *Concrete, hardened: Water-cement ratio*, NT Build 361.

Noumowé A.N., Clastres P., Debicki G., Costaz J.L. (1996), *Transient Heating Effects on High Strength Concrete*, Nuclear Engineering and Design 166, 99-108.

Noumowé A.N. (2003), *Temperature distribution and mechanical properties of high-strength silica fume concrete at temperatures up to 200 °C*, ACI Materials Journal 100 (4), 326-330.

Noumowé A.N., Siddique R., Ranc G. (2009), *Thermo-mechanical characteristics of concrete at elevated temperatures*, Nuclear Engineering and Design 239, 470-476.

Pachner J. (1998), IAEA-TECDOC-1025, IAEA, Vienna.

Powers T., Brownyard L. (1946-1947), *Studies of the physical properties of hardened Portland cement paste*, Journal of the American Concrete Institute, Vol. 43.

Poyet S. (2007), *Design of the ONDRAF Supercontainer concept for vitrified HLW disposal in Belgium: study of the thermo-hydrological behaviour of the concrete buffer*, Rapport CEA, RT DPC/SCCME/07-741-7.

Richardson I.G., Groves G.W., Wilding C.R. (1990), *Effect of γ irradiation on the microstructure and microchemistry of ggbfs/OPC cement blends*, Proceedings of the Materials Research Society Symposium, Vol. 176.

Savva A., Manita P., Sideris K.K. (2005), *Influence of elevated temperatures on the mechanical properties of blended cement concretes prepared with limestone and siliceous aggregates*, Cement & Concrete Composites 27, 239-248.

Taerwe L. (1997), *Concrete Technology*, Course material (in Dutch), Ghent University, Magnel Laboratory for Concrete Research, Belgium.

Schwartzentruber A., Catherine C. (2000), *La méthode du mortier de béton équivalent (MBE) : un nouvel outil d' aide à la formulation de bétons adjuvantés*, Materials and Structure 33, 475-482.

Vodák F., Trík K., Kapicková O., Hosková S., Demo P. (2004), *The effect of temperature on strength porosity relationship for concrete*, Construction and Building Materials 18, 529-534.

Vodák F., Trík K., Sopko V., Kapicková O., Demo P. (2005), *Effect of γ irradiation on strength of concrete for nuclear-safety structures*, Cement and Concrete Research 35, 1447-1451.

Weetjens E., Sillen X. (2006), *Thermal analysis of the Supercontainer concept 2D axisymmetric heat transport calculations*, SCK·CEN report, Belgium.

Wickham S.M., Bennett D.G., Crawford M.B., Pourbaix A. (2004), *Supercontainer Conceptuel Model. Information to support a workshop on the evolution of OPC Buffer and steel corrosion in the Belgian Supercontainer Design for HLW/Spent Fuel Disposal*, Galson Sciences Limited, Report no 0427.

Wickham S.M., Bennett D.G., Galson D.A. (2005), *Belgian Supercontainer Design for HLW and Spent Fuel Disposal. Evaluation of the Reference Design*, Galson Sciences Limited, Report no 0460-5.

CHAPTER 8:

THERMO-MECHANICAL BEHAVIOUR OF THE SUPERCONTAINER

For the Belgian reference disposal concept for long-lived, heat-emitting HLW and SF assemblies (Chapter 2) in a clayey Host Rock, an intensive study of the early-age behaviour of the Supercontainer is conducted by the Magnel Laboratory for Concrete Research in cooperation with ONDRAF/NIRAS. This Supercontainer is based on the use of an integrated waste package composed of a carbon steel overpack surrounded by a concrete buffer based on Ordinary Portland Cement (OPC) surrounded by an outer stainless steel envelope (Chapter 1, Chapter 3 and Chapter 4). For the choice of the cementitious buffer, SCC and TVC (Chapter 5) are considered, tested and compared by means of a concrete characterization program in order to obtain the relevant thermal, maturity related and mechanical properties of the two types of concrete (Chapter 6). These obtained data are implemented into the finite element simulation program HEAT/MLS to study the behaviour of the concrete buffer during the different stages of manufacturing of the Supercontainer (Figure 8.1):

- Stage 1: Fabrication of the concrete buffer inside the stainless steel envelope.
- Stage 2: Emplacement of the carbon steel overpack containing the heat-emitting waste canisters inside the concrete buffer.
- Stage 3: Filling of the remaining annular gap with the filler under thermal load.
- Stage 4: Closure by fitting the concrete lid.

1 Goal and methodology

Through-going macrocracks (in tangential and axial direction) in the concrete buffer should, at all times, be avoided for radioprotection reasons but also to prevent transport mechanisms through the buffer and to retain its corrosion protection purposes. Therefore, knowledge and comprehensiveness of the (early-age) behaviour of the hardening SCC and TVC is non-negligible.

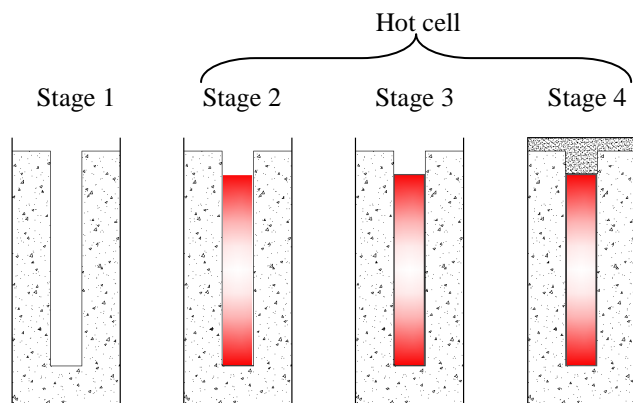


Figure 8.1: Four construction stages of the Supercontainer (stage 2-4 are carried out in hot cell)

For the numerical simulations, the 2D finite element program HEAT/MLS is used, which calculates the stresses and the strength of a concrete structure via a state parameter approach linked by the material database [Van Beek et al., 2001, De Schutter and Vuylsteke, 2004, Craeye et al., 2009]. The early-age behaviour of the concrete of the Supercontainer is widely studied and the potential use of reinforcement is evaluated.

First of all, this research study provides the calculations and the simulations of the first construction stage of the Supercontainer, out of the hot cell. Via a sensitivity analysis, the behaviour of the concrete buffer is investigated and the dependency, of the reference casting situation, on the time dependent concrete parameters (thermal deformation due to the hydration reaction of the cement, shrinkage, creep), on the dimensions of the Supercontainer (geometry: height, diameter and thickness), and on the casting boundary conditions (environmental temperature, wind velocity, insulation type) is taken a closer look at.

In a second step, the construction stages inside hot cell, i.e. the insertion of the heat-emitting waste preceded by the filling of the annular gap and the closure by means of the concrete lid, are combined and simulated. The effect of the elevated temperature on the stresses inside the buffer, the filler and the lid, the determination of the temperature influence, the influence of the insertion time, the effect of the type of inserted waste (vitrified HLW or SF assemblies) and the effect of the cooling period preceding the insertion is investigated. Finally the effect of the expansive behaviour of the overpack (due to the temperature elevation) is being discussed.

The Supercontainer for the disposal of vitrified HLW, with SCC as the reference concrete, is taken as the reference concept for the following analysis. The effect of adjusting dimensions of the container in order to obtain the Supercontainer for the disposal of UOX or MOX (SF assemblies) is studied via the sensitivity analysis.

2 The numerical simulation tool HEAT/MLS

For the numerical simulation of the fabrication of the Supercontainer, the finite element program HEAT/MLS is used. HEAT/MLS enables advanced thermal and mechanical computations particularly focused on the building practice. This state parameter based program is linked to a material database and calculates stresses (due to temperature and humidity effects) and the strength in concrete structures. The values for the input parameters for each material in this database are obtained via an intensive laboratory characterization program (Chapter 6). Most of the material properties of hardening concrete are dependent on the actual state of the hydration process. This can be described with fundamental parameters like degree of hydration, reaction degree, equivalent time or maturity. Thus, HEAT/MLS simulates the hydration process in the concrete structure and calculates the stresses and the strength in the structure. Afterwards the cracking risk is evaluated. Although the simulation tool is two-dimensional, an accurate simulation is possible in case of an axisymmetrical structure and will be less time consuming and cumbersome compared to a three-dimensional finite element method.

The models that are considered by HEAT/MLS, and that are relevant for the determination of cracks in hardening concrete, are outlined below. For the first 28 days of hardening of a structure, the humidity effect is not considered.

First, the actual state parameters are calculated (like the temperature, the degree of hydration or the maturity of the concrete) in each point of the structure at each moment, taking into account the various building phases and the environmental conditions during and after construction. The governing equation for the problem of heat generation and heat diffusion in a hardening concrete is expressed by means of the non-stationary Fourier equation. This partial differential equation (8.1) describes the heat transfer under transient conditions and needs to be combined with the relevant initial boundary conditions (initial temperature of the cast concrete, convection and radiation at the exposed surface).

$$c_T \frac{\partial T}{\partial t} = \frac{\partial}{\partial x} \left(k \frac{\partial T}{\partial x} \right) + \frac{\partial}{\partial y} \left(k \frac{\partial T}{\partial y} \right) + H_T \quad (8.1)$$

where: c_T = the heat capacity of the concrete ($J/(m^2 \cdot ^\circ C)$)
 T = the temperature ($^\circ C$)
 t = the time (s)
 x, y = the coordinates (m)
 k = the thermal conductivity of the concrete ($W/(m \cdot ^\circ C)$)
 H_T = the heat production source (W/m^2)

The heat source H_T is implemented and is determined by means of the adiabatic hydration test according to De Schutter and Taerwe (1995), previously explained in Chapter 6.

In order to calculate and determine the thermo-mechanical properties of the hardening concrete, a maturity-based model is implemented into HEAT/MLS. Most of the material properties of hardening concrete are dependent on the actual state of the hydration process, in this case expressed by means of the maturity. The maturity M is defined by means of equation (8.2) taking into account the influence of the temperature following the Arrhenius equation. Properties such as tensile strength, compressive strength, modulus of elasticity, shrinkage and creep behaviour are maturity related.

$$M(t) = \int_{t_{con}}^t e^{\frac{E}{R} \left(\frac{1}{T_{ref}} - \frac{1}{T} \right)} dt \quad (8.2)$$

where: E = the apparent activation energy (kJ/mol)
 R = the universal gas constant (kJ/(mol·K))
 T = the temperature (K)
 T_{ref} = the reference temperature (K)
 t = the time (s)
 t_{con} = the casting time (s)

The visco-elastic material behaviour (creep) of mass concrete is described by means of a Maxwell model (Figure 8.2) [Bazant, 1986], with E_k the spring stiffness and τ_k the retardation time of the branch k . These material properties are dependent on the maturity.

Due to the developed thermal gradients inside the structure, and taking into account the autogenous shrinkage and the creep effect, the most significant question is whether the created tensile stresses will exceed the tensile strength of the concrete, giving cause to early-age cracking.

No cracking and strain softening behaviour is taken into account in the simulations. It is assumed that in the simulations it is possible to have stresses inside the structure that can exceed the strength of the structure. When analyzing the obtained stress values, a stress based cracking criteria is defined for the estimation of the cracking risk [Rostásy et al., 2002]. Tensile cracking will occur in real structures if the cracking index γ_{cr} , given by equation (8.3), is smaller than 1 (or the stresses S_{ii} inside the structure exceed the actual tensile strength $f_{ct,act}$ of the structure).

$$\gamma_{cr} = \frac{f_{ct,act}}{S_{ii}} \quad (8.3a)$$

The actual tensile strength $f_{ct,act}$ of the structure equals 0.7 times $f_{ct,lab}$, the tensile strength determined in laboratory conditions [Rostásy et al., 2002].

By rearranging equation (8.3a), the non-cracking criteria (8.3b) is obtained:

$$S_{ii} \leq 0.7 \cdot f_{ct,lab} \quad \text{or} \quad \frac{S_{ii}}{0.7 \cdot f_{ct,lab}} \leq 1 \quad (8.3b)$$

If the tensile stress in a concrete structure remains smaller than 0.7 times the tensile strength (determined in laboratory conditions), no cracking will occur. According to Reinhardt and Cornelissen (1985) the safety limit factor 0.7 can be explained by the long-term effect of the tensile strength: $f_{ct,\infty}$ equals 0.7 times f_{ct} .

Conventionally, tensile stresses are taken positive, compressive stresses are taken negative.

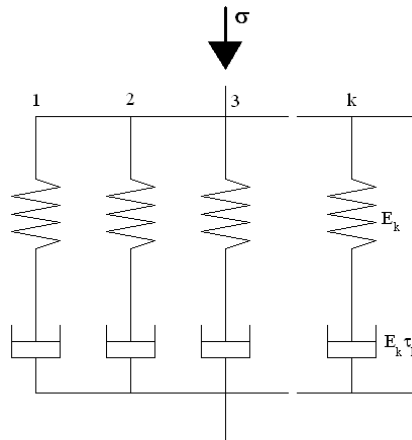


Figure 8.2: Maxwell model for visco-elastic material behaviour of massive concrete

3 Pre-processing

3.1 Implementation of the concrete properties

Several thermal, maturity-related and mechanical property tests are performed to predict the difference between the two compositions considered for the Supercontainer concept: SCC and TVC. The determination of the concrete properties of SCC and TVC is part of an intensive laboratory characterization program (Chapter 6). These properties are implemented in the material database of the finite element program HEAT/MLS. A short summary of the obtained results is listed below. Conventionally, the SCC composition can be seen as the reference concrete composition (ONDRAF/NIRAS statement). The relevant concrete properties of SCC and TVC are listed in Table 8.1.

3.1.1 Thermal properties

The specific heat c_p of the SCC is fixed at $2390 \text{ J}/(\text{m}^3 \cdot ^\circ\text{C})$ while the value for TVC is slightly higher, $2410 \text{ J}/(\text{m}^3 \cdot ^\circ\text{C})$. Also the thermal conductivity k is higher in case of TVC ($2.02 \text{ W}/(\text{m} \cdot ^\circ\text{C})$) in comparison with SCC ($1.89 \text{ W}/(\text{m} \cdot ^\circ\text{C})$). The SCC acts more like an insulator. Although in reality these properties depend on the hydration process, only constant values are considered in HEAT/MLS.

The exothermal heat production due to the hydration reactions is simulated using the results of the adiabatic hydration tests according to De Schutter and Taerwe (1995). The adiabatic temperature development and the cumulated heat of hydration results are time dependent and are shown in Figure 6.33 and Figure 6.34. Clearly, a more rapid development in TVC is noticed, but the temperature rise (and the cumulated heat) after 72 hours is 1.3 % (4.1 %) higher in case of SCC

For the coefficient of thermal expansion (CTE), SCC has the tendency to deform more under influence of a temperature variation compared to TVC. For the calculations, the CTE of the SCC and the TVC in a hardened state is taken respectively $8.1 \times 10^{-6}/^\circ\text{C}$ and $7.4 \times 10^{-6}/^\circ\text{C}$ and it is taken time dependent, with higher values at early age according to Table 6.13.

3.1.2 Maturity-related properties

For the maturity concept, the reference temperature $T_{\text{ref}} = 293 \text{ K}$ ($20 \text{ }^\circ\text{C}$). The ratio E/R , determined via the isothermal hydration tests, is equal to 4491 K and 4570 K for SCC and TVC respectively.

3.1.3 Mechanical properties

Autogenous deformation

The time dependent early-age autogenous deformation evolution of SCC and TVC, measured by means of the vertical dilatometer at $20 \text{ }^\circ\text{C}$, and implemented into the

material database of the simulation tool HEAT/MLS, is given in Figure 8.3. It is clear that SCC experiences a higher autogenous shrinkage compared to TVC.

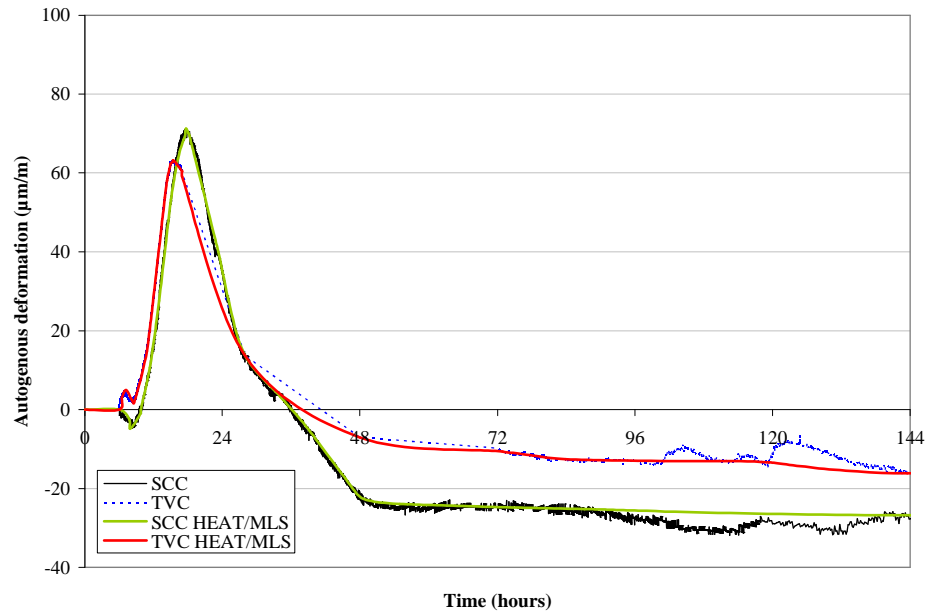


Figure 8.3: The autogenous deformation curve implemented in the material database

Compressive strength and tensile strength

The data for the compressive strength $f_{ccub150}$ of SCC and TVC are based on the obtained results according to Figure 6.45 and Table 6.17. These values vary in time. Although the compressive strength development of TVC is slightly faster, the compressive strength of SCC is 6 % higher after 28 days. In the material database of the simulation tool HEAT/MLS, the (time dependent) values of the compressive strength f_c , determined on cylinders with diameter 150 mm and height 300 mm, must be implemented. Therefore the conversion factor of 0.79 must be taken into account (Chapter 6).

For the tensile strength of the two types of concrete, the implemented data are based on the results obtained via the pure tensile strength tests after 56 days: 4.4 MPa for SCC and 3.3 MPa for TVC. By following the same time evolution as for the compressive strength, the time dependent tensile strength evolution is obtained.

The values introduced in the material database are listed in Table 8.2.

Modulus of elasticity and Poisson's ratio

Although the modulus of elasticity test results after 28 days indicate a higher value for SCC (36.1 GPa compared to 32.4 GPa for TVC), these values are not used for the simulations. Due to the visco-elastic material behaviour (creep) of mass concrete, which is described by means of a Maxwell model (Figure 8.2) [Bazant, 1986], the spring stiffness E_k (represented by the modulus of elasticity) and the retardation time τ_k of each branch k must be adjusted in order to approach the experimentally obtained creep behaviour as well as possible (see further). Therefore, the values introduced in the material database are slightly different (especially for TVC) and are listed in Table 8.2.

Poisson's ratio is taken time dependent with a value equal to 0.5 if the age of the concrete is below 6 hours (time zero) and is equal to 0.2 from the age of 12 hours. It varies linearly between those two values.

Table 8.1: Summary of the thermal, maturity-related and mechanical properties of SCC and TVC

Properties	Time dependent		SCC	TVC
c_p	no	J/(m ³ ·°C)	2390	2410
k	no	W/(m·°C)	1.89	2.02
Q (72 h)	yes	J/g	316.6	303.5
α_T (28days)	yes	$\mu\text{m}/(\text{m}\cdot^\circ\text{C})$	8.1	7.4
E/R	no	K	4491	4570
f_c (28 days)	yes	MPa	45.4	42.7
f_{ct} (28 days)	yes	MPa	4.1	3.1
E_c (28 days)	yes	GPa	36.1	32.4

Table 8.2: The time dependent evolution of the implemented material database values of f_c , f_{ct} and E_c of SCC and TVC (values in MPa)

Age	f_c		f_{ct}		E_c	
	SCC	TVC	SCC	TVC	SCC	TVC
1 day	9.4	11.9	0.9	0.9	-	-
2 days	21.6	22.1	1.9	1.6	27 500	27 500
3 days	27.8	26.1	2.5	1.9	32 000	32 000
7 days	36.0	34.5	3.2	2.5	33 500	35 000
14 days	41.1	40.3	3.7	2.9	35 500	35 500
28 days	45.4	42.7	4.1	3.1	36 000	37 000

Creep behaviour

The visco-elastic behaviour of the concrete is modelled by means of a Maxwell Chain Fitting approach [Bazant, 1986] (Figure 8.2) with E_k as the spring stiffness and τ_k as the retardation time of each branch k . These two chain parameters are determined by means of the obtained results of the compressive creep tests at the age of 2 days, 7 days, 14 days and 28 days. By adjusting the two main parameters E_k and τ_k the total strain, found by the subtraction of the autogenous shrinkage from the total deformation (the immediate elastic strain when the loading is placed on top of the test specimen is included), approaches the test results as well as possible (Figure 8.4).

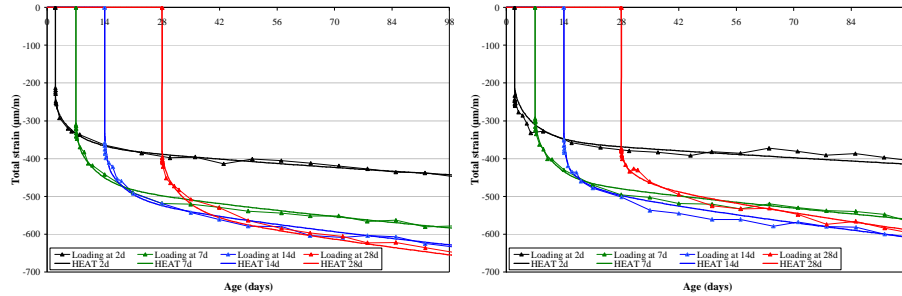


Figure 8.4: The Maxwell fitting of the total strain of SCC (left) and TVC (right) by adjusting the spring stiffness E_k and the retardation time τ_k

3.2 Geometry and boundary conditions

The Supercontainer for the disposal of vitrified HLW is taken as the reference concept. The effect of adjusting the dimensions of the container in order to obtain the Supercontainer for the disposal of UOX or MOX (SF assemblies) is studied via the sensitivity analysis.

An axisymmetrical cross section of the Supercontainer is considered in order to define the geometry of the two-dimensional macro needed to simulate its behaviour (Figure 8.5). The geometry is implemented into HEAT/MLS by defining three concrete layers: the buffer, the filler and the lid. The dimensions of the Supercontainer are given in Chapter 3. The simulations are divided into two parts: out of the hot cell (construction stage 1) and in the hot cell (construction stage 2-3-4). For each simulation part, a mesh of the macro needs to be defined. The macro layers are divided into elements, yielding the mesh given in Figure 8.6. Towards the edges of the Supercontainer, and towards the interfaces of the different concrete layers, the size of the elements is reduced.

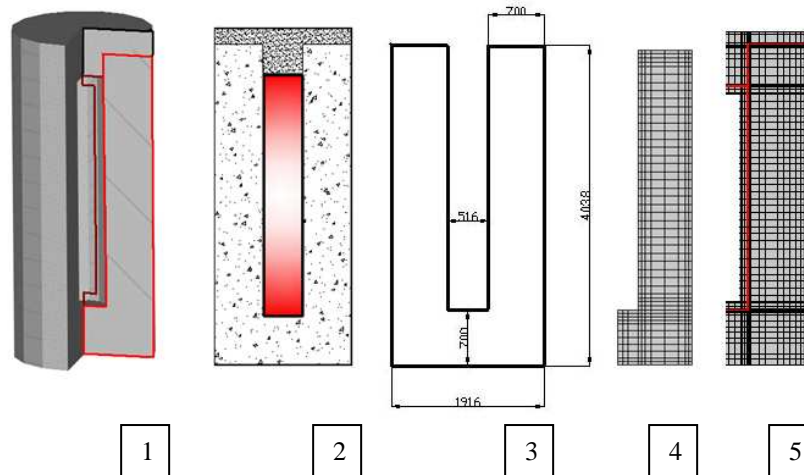


Figure 8.4: The axisymmetrical cross section (1), the scheme (2), the dimensions (in mm) (3), the mesh of stage 1 (4) and the mesh of stage 2-3-4 (5) of the Supercontainer

After defining the geometry and the mesh, some boundary conditions need to be defined. The Supercontainer is supposed to be simply supported by a concrete floor (kinematic boundary condition). For the environmental boundary conditions (physical boundary conditions), the temperature, the wind velocity (climate) with the formwork and insulation type (combined into the convective heat transfer coefficient h_c) are of importance.

For the reference case, the initial temperature of the concrete macro elements is set at 20 °C and the environmental temperature will be kept at a constant value of 20 °C. The inner formwork, made of steel with a thickness of 6 mm, is removed after 72 h. The outside steel envelope (thickness = 6 mm), used as formwork, will not be removed at all. The wind speed W in the reference case has a velocity of 0 m/s, and will at all times be held out of consideration at the inside of the container. HEAT/MLS has a tool that calculates the convection coefficient depending on the material type, thickness, wind speed and covering insulation type. Before releasing of the internal formwork, the convective heat transfer coefficient h_c is 5.59 W/(m²·°C) and after releasing the formwork its value is 5.6 W/(m²·°C). The steel formwork provides almost no insulation: on behalf of the created thermal stresses, the use of a steel envelope or formwork has no significant impact on the simulation results. The convection coefficient is 2.0 W/(m²·°C) at the bottom (massive concrete floor) (Figure 8.6).

For the reference simulation of stage 2-3-4 of manufacturing of the Supercontainer, the insertion of the heat-emitting canisters surrounded by the carbon steel overpack occurs after 240 hours. The same boundary conditions, as discussed previously, are used until the time of emplacement. As a reference, the overpack is inserted after 240 hours,

directly followed by the emplacement of an SCC filler, and the closure of the lid by freshly cast SCC. At the interface of the filler and the heat-emitting overpack ($h_c = 5.59 \text{ W}/(\text{m}^2 \cdot ^\circ\text{C})$), the temperature rise curve according to Weetjens and Sillen (2006) is used (Figure 8.5) and depends on the type of radioactive waste (vitrified HLW or SF assemblies) and the duration of the preceding cooling period. Once the filler and the lid are cast, the convective heat transfer coefficient on top of the Supercontainer equals $5.6 \text{ W}/(\text{m}^2 \cdot ^\circ\text{C})$ (no ambient wind).

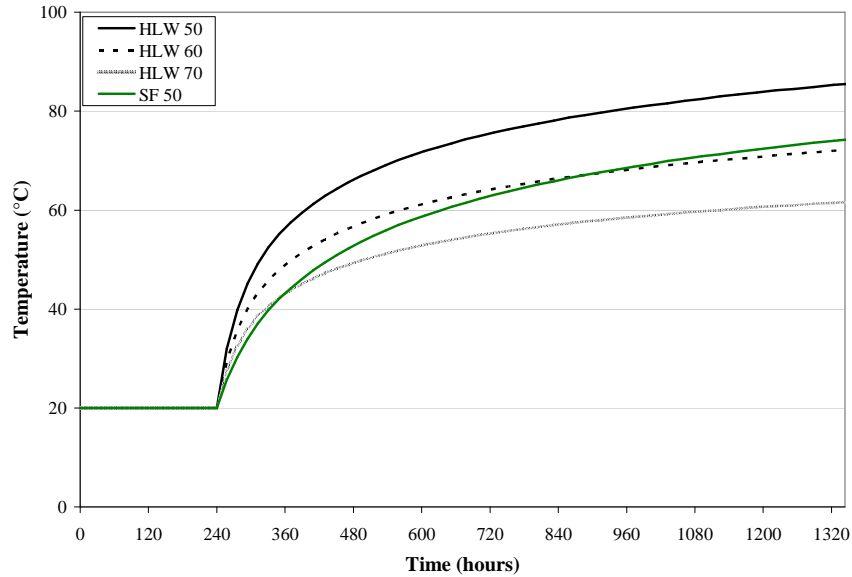


Figure 8.5: Temperature evolution at the buffer-overpack interface for vitrified HLW and SF assemblies after cooling periods of 50 – 60 – 70 years [Weetjens and Sillen, 2006]

Finally, the behaviour of the Supercontainer, during the construction stages in hot cell, is taken a look at in a more thermo-mechanical way: an additional macro layer is inserted in the 2D model for the overpack, with the total area of the overpack macro following the temperature increase according to Figure 8.5. In this way, the expansive behaviour of the overpack is taken into account (due to the temperature elevation), which is not the case for the reference simulations, where the overpack is only considered as an environmental boundary condition. This will have a significant effect on the stress creation in the concrete and the cracking risk of the buffer.

4 Post-processing

4.1 Overview

After the implementation of the concrete properties of SCC and TVC in the material database of the simulation tool HEAT/MLS and after drawing the geometry of the Supercontainer and setting the initial boundary conditions, the simulation of the early-age behaviour of the concrete layers inside the Supercontainer (the buffer, the filler and the lid) can start. HEAT/MLS simulates the hydration process in the layers of the structure and calculates the stresses and the strength inside those layers. The simulations will occur in two phases:

- Phase 1 gives the early-age behaviour of the first stage of the construction of the Supercontainer out of hot cell, i.e. the casting of the buffer inside the stainless steel envelope.
- Phase 2 gives the early-age behaviour of stage 2-3-4 of the construction of the Supercontainer in hot cell, i.e. the insertion of the heat-emitting carbon steel overpack, the placement of the filler inside the annular gap and the closure by fitting the lid.

Cracks in massive concrete structures do not only depend on the material properties. Also the structure itself, with its specific dimensions and the boundary conditions are of a considerable importance towards the early-age cracking behaviour. To evaluate the early-age behaviour of the Supercontainer, different quantities can be regarded:

- The stresses are depicted in a three-dimensional way (x-, y- and z-directions given in Figure 8.6): the normal stresses S_{xx} , S_{yy} and S_{zz} and the shear stress S_{xy} . By means of contourplots at a certain time, the regions with considerable compressive and tensile stresses can be found. The stresses and the evolution of the stresses in time at a certain point will be compared with the concrete strength evolution by means of time graphs. The goal is to evaluate whether the stress to strength ratio $S_{ii}/(0.7 \cdot f_{ct})$ remains smaller than 1 according to equation (8.3b).
- Similar to the stresses, the temperature evolution (T) inside the concrete layers can be evaluated by means of time graphs at a certain point, and the temperature distribution in a region at a certain time can be shown by means of a contourplot. This temperature distribution can give an indication for the internal stresses inside the concrete layers. The thermal gradient ΔT between the middle and the outer surface of the buffer is also investigated, as this parameter has a major impact on the (thermal) stress creation inside the Supercontainer [De Schutter, 1996].
- Also the radial displacement U_x of the concrete layers can be simulated by means of HEAT/MLS. A picture of the deformed mesh at any time, and the displacement evolution in the radial x-direction at a certain point can be given by means of a time graph. In this way, the bond between the buffer and the outer stainless steel liner on one side, and the bond between the filler and the carbon steel overpack on the other site, can be investigated.

For the different construction stages of the Supercontainer (simulation Phase 1 and Phase 2), a sensitivity analysis is conducted to evaluate which parameters have a considerable effect on the obtained results.

The casting of the massive buffer (simulation Phase 1), and the early-age behaviour of the buffer strongly depend on different parameters:

- Concrete parameters: if the deformations due to shrinkage and/or temperature are restrained by the structure, this can lead towards cracking [Van Beek et al., 2001]. Via the sensitivity analysis, the impact of the adiabatic hydration curve (thermal properties), the autogenous shrinkage results and the creep results (mechanical properties) on the simulation results is evaluated. The other thermal properties (specific heat and thermal conductivity) and mechanical properties (Poisson's ratio) have a negligible effect on the stresses and strains in massive concrete structures according to Briffaut et al. (2009). Nevertheless, other types of concrete differ from SCC due to the higher thermal conductivity, specific heat or thermal expansion (e.g. Haematite Concrete), and their effect is briefly discussed.
- Dimensions of the Supercontainer: by adapting the height, the thickness or the diameter of the buffer, the effect on the results is evaluated. The dimensions of the Supercontainer for vitrified HLW differ from the dimensions of the Supercontainer used for the disposal of SF assemblies (UOX/MOX) (Chapter 4). By means of the sensitivity analysis, the effect of adjusting the dimensions is investigated.
- The boundary conditions: especially the effect of a changed climate (environmental and initial concrete temperature, wind velocity), and changed insulation conditions will be evaluated.

In the simulation of Phase 2, the construction stages inside hot cell, the effect of the elevated temperature originating from the heat-emitting waste on the stresses inside the buffer, the filler and the lid, the determination of the maximal sustainable temperature, the influence of the insertion time, the effect of the type of inserted waste (vitrified HLW or SF assemblies), and the effect of the cooling period preceding the insertion will be investigated. Therefore, the presence of the overpack is examined in two ways: (i) by considering the overpack simply as a boundary condition, and (ii) by considering the overpack as a deformable macro layer.

The early-age cracking behaviour of the different concrete layers is studied via the simulations in order to evaluate whether additional reinforcement, to reduce the cracking possibility, is needed. Conventionally, the Supercontainer for vitrified HLW, with the three concrete layers made of SCC, can be seen as the reference concept for the simulations (ONDRAF/NIRAS statement). In the reference simulation, the overall temperature is 20 °C.

Conventionally, tensile stresses are taken positive, compressive stresses are taken negative.

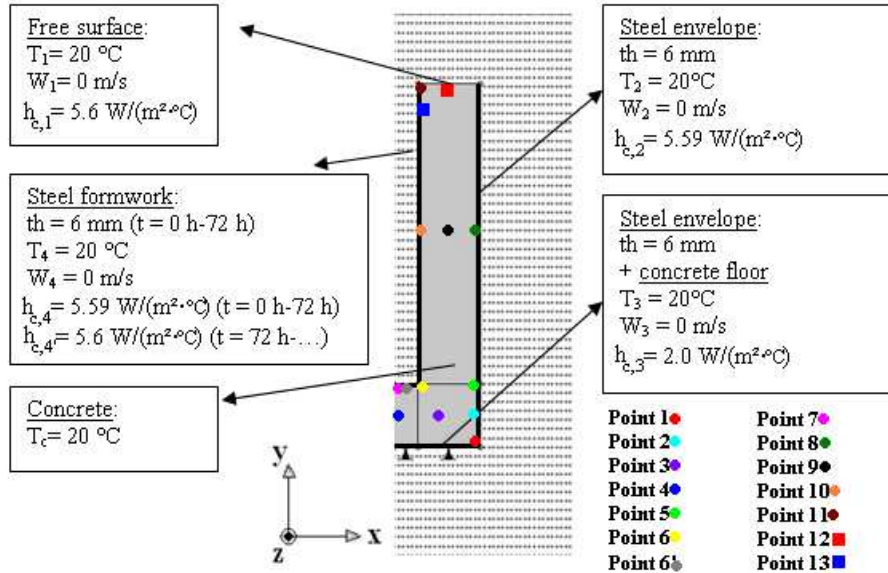


Figure 8.6: Boundary conditions of the reference simulation case (Phase 1)

4.2 Phase 1 of the simulations: casting of the buffer (out of hot cell)

4.2.1 Reference simulation 20 °C with SCC

4.2.1.1 Temperature T

In a first reference simulation, the casting temperature of the concrete and the environmental temperature are equal to 20 °C. The other boundary conditions are given in Figure 8.6.

First, contourplots of the temperature at different times are plotted (Figure 8.7a). These plots give a clear indication where the highest temperatures occur, and at which points time evolution graphs are useful. As expected, the highest temperature rise occurs in the middle of the bottom of the buffer (point 4): 54.54 °C after 41 hours. After 72 hours (the demoulding time), the temperature in this region is still 47.89 °C.

At points 1-4-5-6-7 (location given in Figure 8.6), the time graph of the temperature evolution is plotted (Figure 8.7b). From the start of casting the buffer, a temperature rise is noticed, entirely devoted to the exothermal hydration reaction of the cement in the concrete, until a peak temperature is reached. Comparing the middle of the buffer (e.g. point 4) with the outer border of the buffer (e.g. point 1), the peak temperature is about 35 % higher in the middle, but the peak occurs more or less 10 hours later.

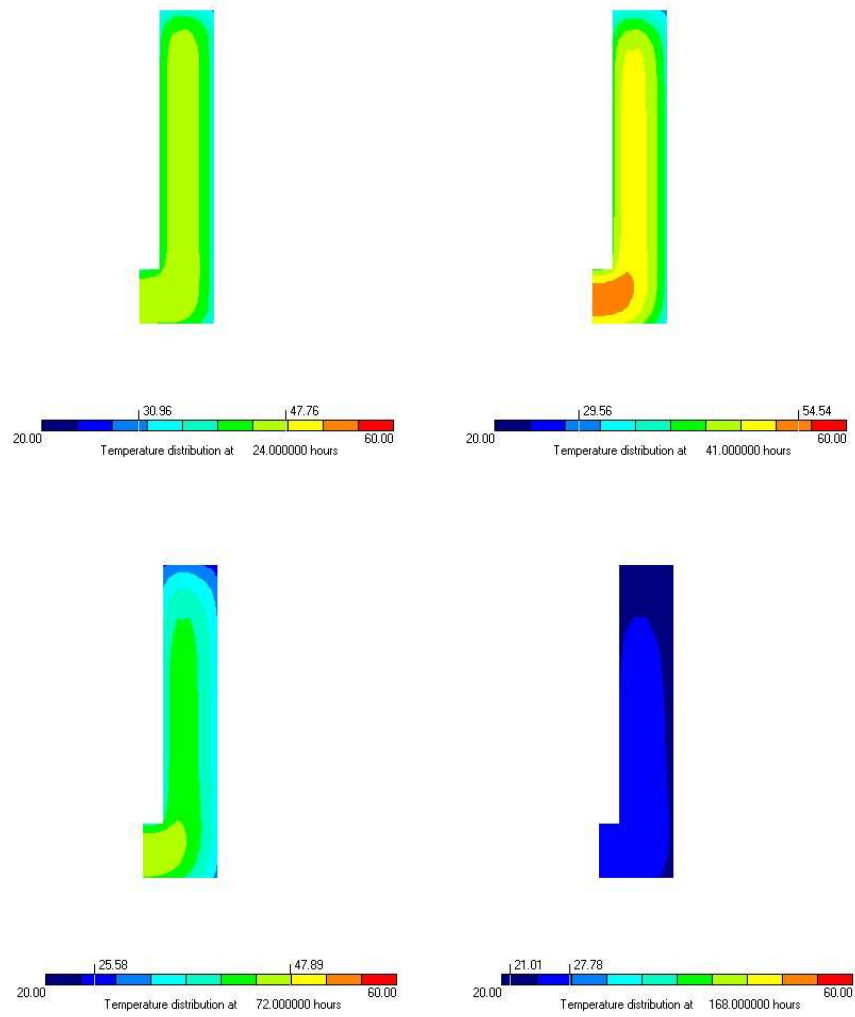


Figure 8.7a: Contourplots of the temperature in the reference simulation 20 °C (SCC-Phase 1) at 24 h, 41 h, 72 h and 168 h

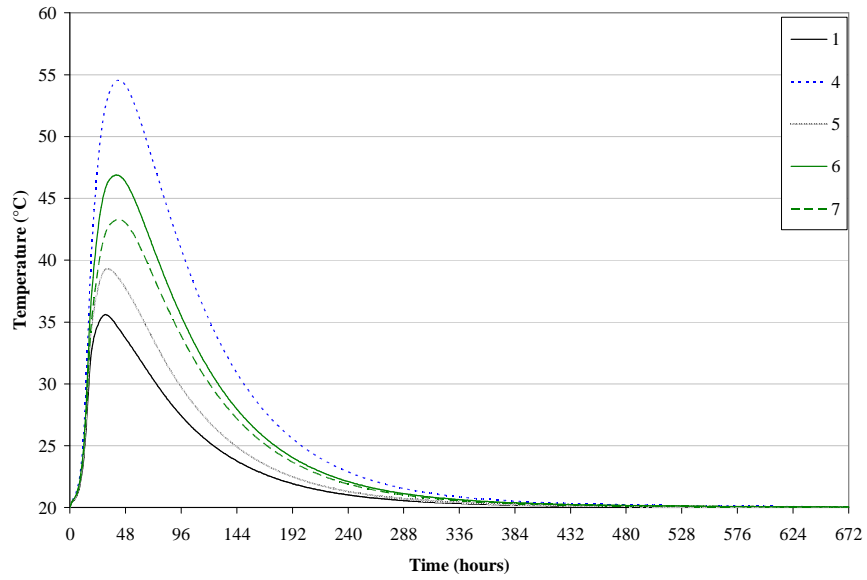


Figure 8.7b: Time graph of the temperature in the reference simulation 20 °C (SCC-Phase 1) at points 1-4-5-6-7

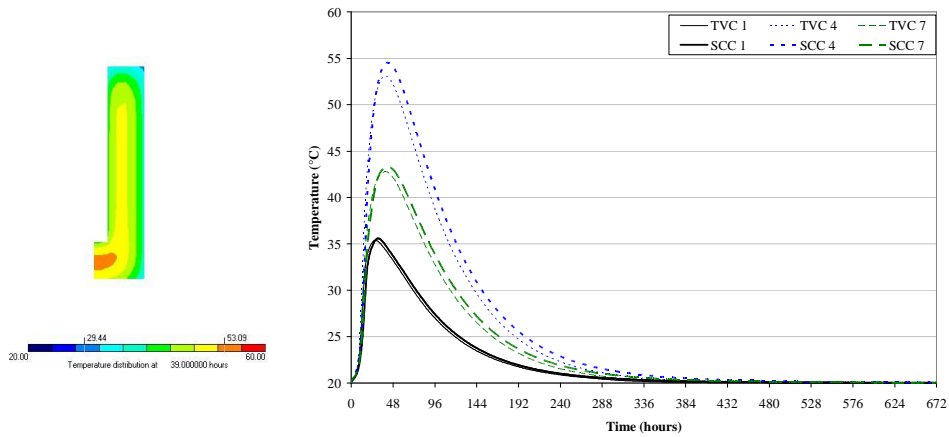


Figure 8.7c: Contourplot of the temperature (TVC-Phase 1) at 39 h (left) and comparing time graph of the temperature in SCC and TVC at points 1-4-7 (right)

When the peak has passed, the temperature drops and returns to the initial environmental value of 20 °C, which is reached after approximately 336 hours. After 240 hours, the temperature in the middle of the buffer is 22.89 °C, and 21.31 °C at the outer border. Near the inner border, represented by points 6-7, the temperature rise is higher compared to the temperature rise near the outer border. The highest temperature gradient ΔT between the core of the buffer (point 4) and the outer border (point 1) is approximately 20.17 °C after 43 hours. According to De Schutter (1996), there is a high cracking risk if ΔT of a massive structure approaches 20 °C due to the hindered internal deformation.

Replacing the SCC by TVC, a decrease of the peak temperature is noticed. In the middle of the TVC buffer, the highest temperature reaches a value of 53.09 °C after 39 hours (Figure 8.7c, left). The temperature peak in TVC is slightly lower (less than 3 %) and occurs 2 hours earlier (Figure 8.7c, right), a result of the obtained adiabatic hydration test results (Chapter 6).

4.2.1.2 Stresses S_{zz} , S_{yy} , S_{xx} , S_{xy}

The normal stresses in the three-dimensional direction (axisymmetrical: x is radial, y is axial, z is tangential) are plotted via contourplots at the time of appearance of maximal stress and via time graphs at points in regions with high stresses and a potential cracking risk. Those regions, with high tensile stresses, that are vulnerable to early-age cracking, are clearly noticeable (Figure 8.8, left): at the bottom of the cavity and the top of the buffer in x-direction and near the outer border in y- and z-direction.

Due to the heat of hydration and taking into account the autogenous deformation and the creep behaviour of the concrete, stresses will be induced into the concrete buffer (Chapter 5). Considering a region in the middle of the buffer (e.g. point 4, blue lines Figure 8.8), due to the heat of hydration, the concrete in this region wants to expand more, but the expansion is prevented by the surrounding concrete, hence creating a compressive stress. When the cooling of the midzone of the buffer settles in (the hydration peak is over), it is the other way around: the midzone wants to shrink more but this movement is prevented, hence creating a tensile stress behaviour in the middle of the buffer. For regions near the outer border (e.g. point 1, black lines Figure 8.8) and the inner border of the buffer (e.g. point 10, green line Figure 8.8), the opposite story applies: tensile stresses before the hydration peak, and compressive stresses afterwards. This behaviour can be found in Figure 8.8 (right) in a radial, axial and tangential way. In compressive behaviour, the highest peak stresses occur in the middle of the buffer, especially near point 4. The maximal compressive stresses of S_{xx} , S_{yy} and S_{zz} are -1.04 MPa, -0.93 MPa and -1.03 MPa after 49 h, 53 h and 51 h respectively. These rather small compressive stresses will not have a detrimental effect on the concrete buffer (after 48 hours the compressive strength f_c is 21.6 MPa at 20 °C curing temperature). The highest radial tensile stress S_{xx} occurs near point 7, with a value of 0.70 MPa after 36 hours. The highest axial tensile stress S_{yy} occurs in the region of point 2-5, with a maximal value of 1.47 MPa after 41 hours. Finally, the highest tangential tensile stress S_{zz} occur near point 1, with a value of 1.37 MPa after 41 hours.

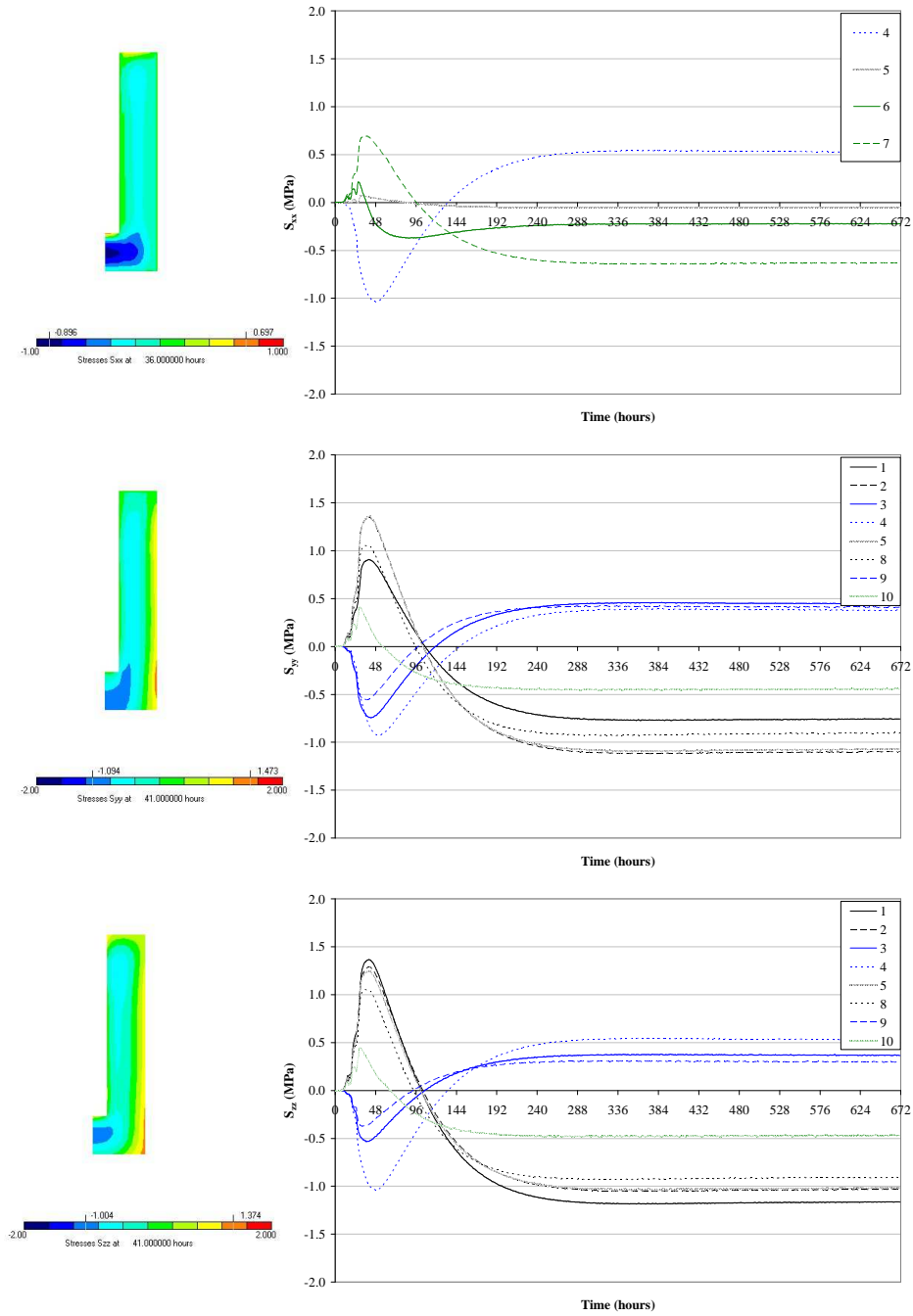


Figure 8.8: Contourplots at 36 h, 41 h and 41 h (left) and time graphs (right) of S_{xx} , S_{yy} and S_{zz} (SCC-Phase 1) at different points

The appearing axial and tangential tensile stresses near the outer border are higher (e.g. points 1-2-5-8, black lines, Figure 8.8) compared to the tensile stresses near the inner border (e.g. point 10, green line, Figure 8.8). In the radial direction, the tensile stresses at the inner border (especially at the bottom of the opening, e.g. point 7) are higher than the tensile stresses near the outer border.

The values of the shear stresses S_{xy} are more or less marginal compared to the axial, tangential and radial stresses (Figure 8.9). Most of the time, the stresses are situated in the interval $]-0.1 \text{ MPa}, 0.1 \text{ MPa}[$, except in the region near point 6 (corner zone) and the right top of the buffer. At point 6, S_{xy} has a maximal value of -0.36 MPa after 51 hours. In the further discussion, shear stresses are kept out of consideration, and roughly the radial, axial and tangential stresses can be considered as principal stresses.

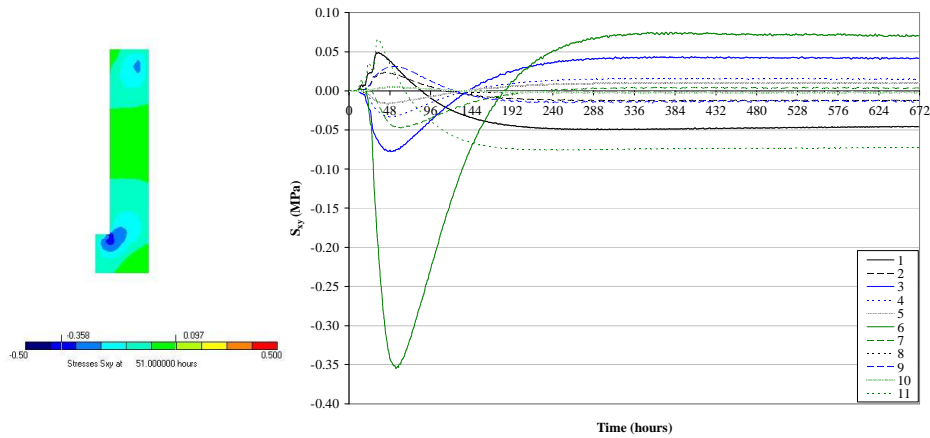


Figure 8.9: Contourplot at 51 h (left) and time graph (right) of the shear stresses S_{xy} in the reference simulation $20 \text{ }^{\circ}\text{C}$ (SCC-Phase 1) at different points

The difference between the stresses S_{xx} , S_{yy} and S_{zz} of SCC and TVC at the most critical regions, are given in Figure 8.10

In case the buffer is cast in TVC, the maximal stresses occur in the same regions as for SCC, but the absolute values of the stress peaks due to the heat of hydration are lower in compressive and tensile behaviour and occur earlier, except in the less critical radial direction. Afterwards the stresses near the inner border and outer border evolve towards a constant value, that is approximately equal for SCC and TVC.

Compared to SCC, the TVC concrete in the midzones of the buffer, experience a lower compressive stress during the hydration peak, but afterwards the TVC stress curve evolves towards a slightly higher tensile stress.

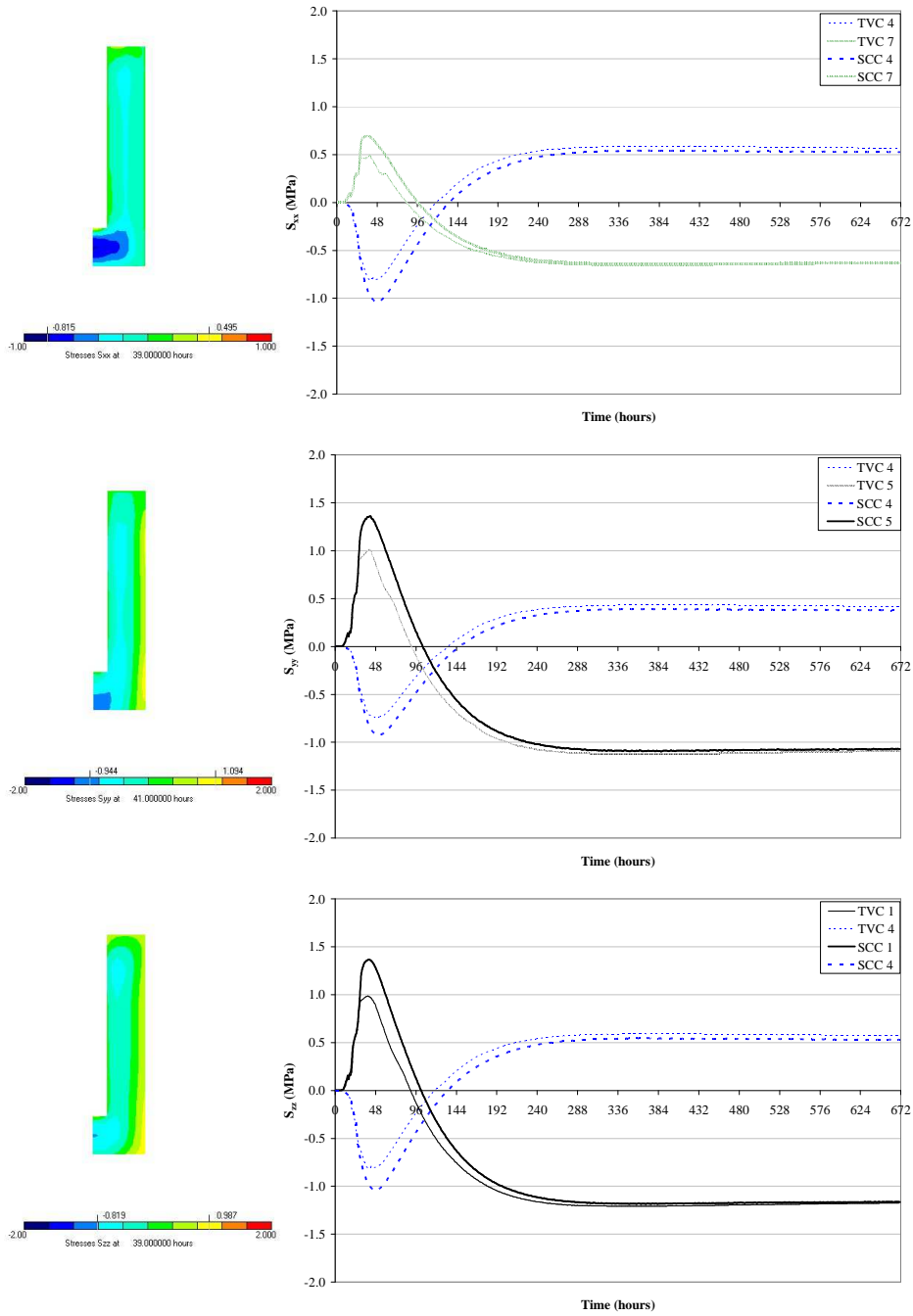


Figure 8.10: Contourplots at 39 h, 41 h and 39 h (left) and comparing time graphs (right) of S_{xx} , S_{yy} and S_{zz} (TVC-Phase 1)

For TVC, the highest tensile stress S_{xx} (point 7) has a value of 0.50 MPa after 39 hours, the highest tensile stress S_{yy} (points 2-5) has a maximal value of 1.10 MPa after 41 hours and the highest tensile stress S_{zz} (point 1) has a value of 0.99 MPa after 39 hours. In compressive behaviour, the highest stresses occur near point 4: the maximal compressive stresses of S_{xx} , S_{yy} and S_{zz} are -0.81 MPa, -0.74 MPa and -0.81 after 40 h, 51 h and 40 h respectively.

Overall, after the hydration peak has passed and the concrete is in a certain state of hardening, the tensile stresses (in the core of the buffer) and compressive stresses (near the surfaces of the buffer) remain present in the buffer as eigenstresses and can counteract the expected stress induction due to the insertion of the heat-emitting waste (Phase 2).

4.2.1.3 Cracking criteria: $S/(0.7 \cdot f_{ct}) < 1$

The most significant question however is whether the tensile stresses in SCC and TVC, due to the developed thermal gradients, the autogenous deformation of the concrete, and taking into account the creep effect, will exceed the tensile strength of the concrete buffer, giving cause to early-age cracking. Therefore time graphs of the stress to strength ratios $S_{ii}/(0.7 \cdot f_{ct})$, according to equation (8.3b), of points characterizing the critical regions (middle of the buffer and the outer and inner border of the buffer) are plotted in Figure 8.11. This ratio must remain smaller than one at all times and in all regions, in order to reduce or eliminate the early-age cracking risk [Craeye et al., 2009].

The results and the graphs (Figure 8.11) show that the stress to strength ratios $S_{xx}/(0.7 \cdot f_{ct})$, $S_{yy}/(0.7 \cdot f_{ct})$ and $S_{zz}/(0.7 \cdot f_{ct})$ remain smaller than 1 at all times. For the reference case (20 °C) early-age cracking of the buffer will not occur out of hot cell, both for the cases of SCC and TVC.

The highest cracking risks occur near the outer border of the concrete buffer: in case of SCC $S_{yy}/(0.7 \cdot f_{ct})$ (point 5) has a maximal value of 0.85 after 32 hours and $S_{zz}/(0.7 \cdot f_{ct})$ (point 1) reaches a value of 0.90 after 32 hours. When TVC is used, these peaks occur earlier and are slightly lower: 0.79 after 30 h in axial direction and 0.83 after 30 h in tangential direction. In radial direction, the cracking risk is smaller (approximately 50 %) in the region near point 7 but is also slightly higher in case of SCC.

These peaks are mainly caused by the exothermal hydration reaction. Once the hydration peak is passed, the concrete in the regions near the borders of the buffer comes under compression and no further cracking is expected. In the tensile behaviour near the borders, the stress to strength ratios are higher in case of SCC, meaning SCC has a slightly higher cracking risk compared to TVC.

The concrete in the middle of the buffer (point 4) experiences compressive stresses during the first 48 hours of hydration. The ratio $S_{ii}/(0.7 \cdot f_{ct})$ is negative and has a higher

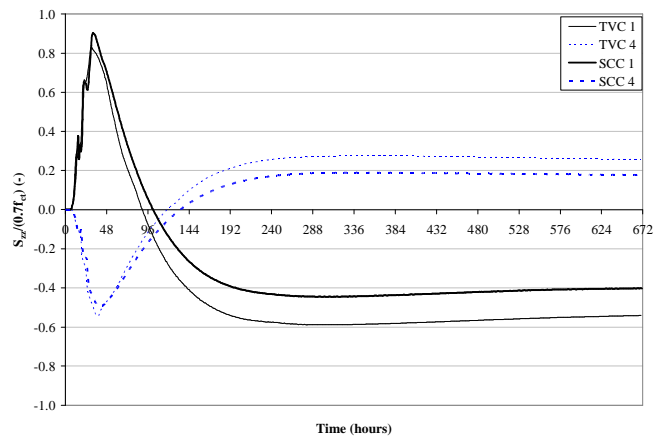
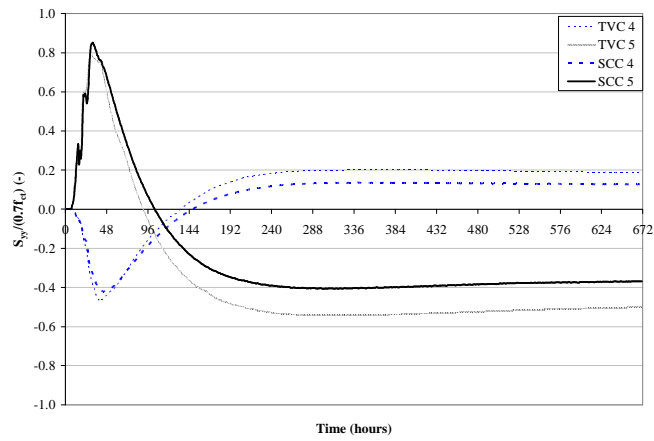
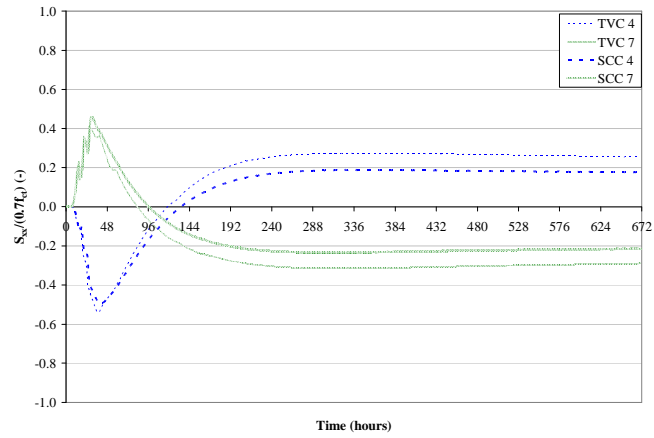


Figure 8.11: Comparing time graphs of $S_{xx}/(0.7 \cdot f_{ct})$, $S_{yy}/(0.7 \cdot f_{ct})$ and $S_{zz}/(0.7 \cdot f_{ct})$ in SCC and TVC at different points of the critical regions

absolute value in case of TVC. Afterwards, when the peak of the hydration reaction is over, the concrete experiences tensile stresses, and the ratio $S_{ii}/(0.7 \cdot f_{ct})$ evolves towards a constant positive value of approximately 0.2, also slightly higher in case of TVC. However, no cracking is expected in the middle of the buffer during the casting out of hot cell at a reference environmental temperature of 20 °C.

4.2.1.4 Displacement U_x

The displacement U_x of the concrete near the outer border, the inner border and the middle of the buffer can be simulated by means of HEAT/MLS. A picture of the deformed mesh after 168 h (Figure 8.12, left) and a contourplot at the time of maximal displacement (Figure 8.12, middle) are given for SCC. The maximal displacement in case of SCC (Figure 8.12, right) is 5 % higher: 0.228 mm after 36 h, compared to 0.217 mm after 32 h for TVC.

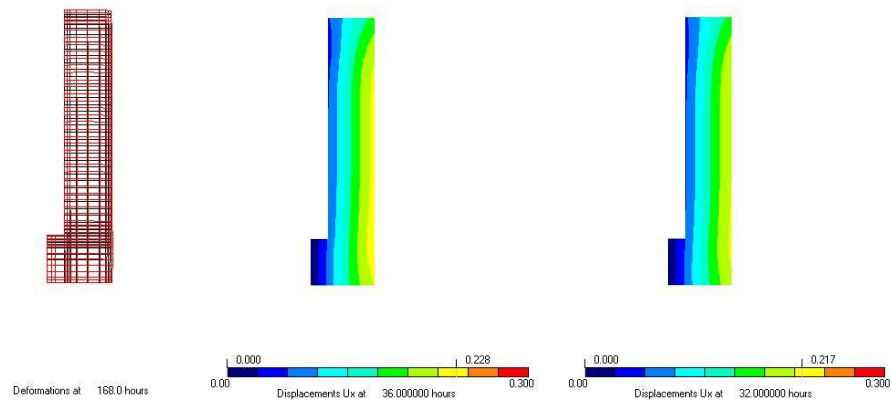


Figure 8.12: Deformed mesh of SCC at 36 hours (left), contourplot of U_x of SCC at 36 hours (middle) and contourplot of U_x of TVC at 32 hours (right)

The buffer expands in the radial direction and in the axial direction (Figure 8.12, left). It is clear that the displacement in the radial direction of the concrete near the outer border, in the middle and near the inner border of the buffer is higher in case of SCC the first 150 hours preceding the casting. Once the displacement peak is over, the concrete returns to its original position. Afterwards, the remaining displacement is higher for TVC (Figure 8.13).

The bond between the buffer and the outer stainless steel envelope on one side can be investigated: due to the expansive nature in a radial way, a good bond can be expected between the concrete buffer and the envelope. The presence of the outer stainless steel envelope around the buffer is accounted for in the simulations by means of a thermal boundary condition (steel formwork), but not as a kinematic boundary condition. In this way, the displacement of the buffer is not hindered by the envelope, thus the displacement will be smaller in reality, but still present and expected due to the

expansive hydration reaction. On the other hand, in case the prevention of the displacement is encountered for, compressive stresses will be induced near the outer concrete border of the buffer, at a time close to the period when the critical tensile stresses occur. Also the steel will experience a certain deformation.

The stainless steel envelope can be seen as an additional safety barrier against early-age cracking of the buffer due to the additional introduced compressive stresses near the outer border, especially at a moment (between 36 h and 48 h) when the displacement and the stresses near the outer border are at their highest values.

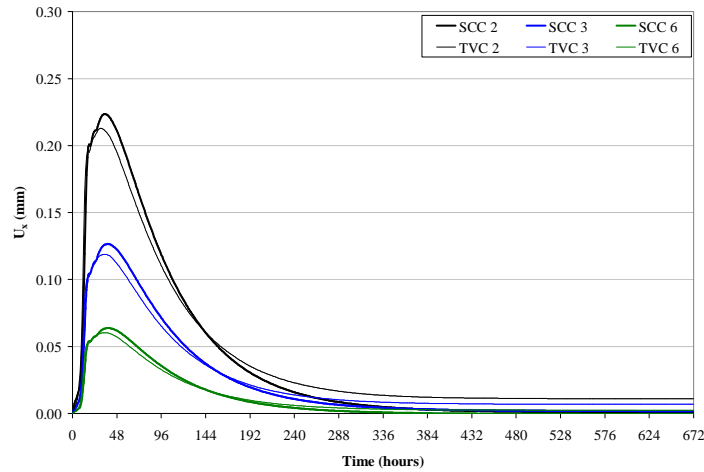


Figure 8.13: Time graph of the deformation U_x of SCC and TVC in the reference simulation

Table 8.3: Summary of the maximal values of temperatures, tensile stresses and displacements inside the SCC and TVC buffer

					t_{\max} (h)	
		SCC	TVC	%	SCC	TVC
T_{\max}	°C	54.54	53.09	2.7	41	39
$S_{xx,\max}$	MPa	0.70	0.50	28.6	36	39
$S_{yy,\max}$	MPa	1.47	1.10	25.2	41	41
$S_{zz,\max}$	MPa	1.37	0.99	27.7	41	39
$S_{xy,\max}$	MPa	0.07	0.04	42.9	34	33
$S_{yy}/(0.7 \cdot f_{ct})$	-	0.85	0.79	7.1	32	30
$S_{zz}/(0.7 \cdot f_{ct})$	-	0.90	0.83	7.8	32	30
$U_{x,\max}$	mm	0.228	0.217	4.8	36	32

4.2.2 Sensitivity analysis: changing the concrete parameters

The first objective of the sensitivity analysis is to study the effect of certain concrete parameters on the stress build-up inside the buffer. SCC is taken as the reference concrete composition because the use of SCC, compared to TVC, will ease considerably the precast process (no external vibration needed, beneficial especially during casting in hot cell) and complies with all other requirements regarding strength (SCC even has higher strength results compared to TVC), long-term durability, chemical interactions, etc. [Craeye et al., 2007], although the cracking risk is slightly lower in case of TVC. Out of the simulation results of the reference case, it seems clear that especially the heat of hydration (implemented by means of an adiabatic hydration test [De Schutter and Taerwe, 1995]) has a major impact on the internal tensile stresses of the massive concrete buffer. Also the autogenous shrinkage and the creep behaviour have a non-negligible effect on the simulation results [Craeye et al., 2009]. To study the effect of the main concrete parameters on the simulation results, SCC cast with 20 °C curing conditions is considered as the reference case. Finally, other types of concrete can be considered for the buffer: Haematite or Magnetite concrete [Bouniol, 1998], or HPC [Craeye, 2006, Geirnaert, 2009] with an alternative concrete composition (other type of cement and aggregates) compared to SCC on behalf of certain concrete parameters (thermal conductivity, density, CTE, etc.).

4.2.2.1 The effect of the autogenous deformation and the creep behaviour

In this scope, the behaviour of the concrete buffer is simulated, first by leaving the autogenous shrinkage (AS) aside, and secondly by looking at the buffer as a linear elastic element (creep effect and AS are not being considered). According to De Schutter (1996), elastic stress calculations overestimate reality and thus are a safe calculation method.

The exclusion of AS and/or creep (mechanical properties) does not affect the temperature rise (due to thermal properties) inside the concrete buffer. Because no thermal properties are adjusted, the temperature inside the buffer, and also the maturity dependent properties (e.g. strength) remain unchanged. Especially the tangential stresses S_{zz} are taken a look at in the midzone region of the buffer (point 4), near the outer border of the buffer (point 1) and near the inner border of the buffer (point 10). On behalf of the previously discussed cracking criteria, the tangential stresses have the largest impact. Also the effect of AS and creep on the displacement evolution U_x is investigated.

Looking at the linear elastic behaviour (no AS and no creep) of the concrete near the outer border (point 1, black lines, Figure 8.14a), compared to the reference case, the tensile stress peak is higher and occurs later: 1.42 MPa after 44 hours. On the other hand, when only the AS is kept out of consideration, the tensile stress peak is smaller: 1.20 MPa after 40 hours. When the hydration peak has passed, and the cooling of the concrete starts, the concrete near the border comes under compression and evolves towards a constant stress. This value is higher in case linear elastic behaviour is

considered (-2.05 MPa after 672 hours). The evolution of the stresses, without AS taken into account, is more or less parallel to the reference case, but also a higher compressive stress is reached after 672 hours (-1.32 MPa compared to -1.16 MPa). For the region in the middle of the buffer (point 4), the stresses are higher, both in the compressive way during hydration and in the tensile way during cooling in case of a linear elastic behaviour (Figure 8.14a, blue lines).

The deflection of the stress curves of the more uniform development the first 30 hours of hardening (e.g. black bolt line, Figure 8.14a) is caused by the autogenous shrinkage behaviour of the concrete. Concerning the cracking risk of the buffer, especially the tensile stress peak due to the heat of hydration is of importance. A conclusion can be drawn: by looking at the concrete buffer as a linear elastic concrete material, the stresses are overestimated and thus a conservative approach is used in case linear elastic behaviour is considered for the analysis of the early-age cracking of the buffer. The notion declared by De Schutter (1996) is hereby confirmed. Taking into account the autogenous shrinkage and the creep behaviour of the hardening concrete for the calculations, the stresses (tensile and compressive) of the concrete buffer will be smaller. Especially the creep behaviour is responsible for a significant stress relaxation.

Figure 8.14b indicates that the displacement near the outer border, in case of linear elastic behaviour, is higher (approximately 10 %) and the expansive peak occurs later, thus also a conservative approach is reached. Due to the autogenous shrinkage and the creep behaviour of the concrete, the displacement of the concrete buffer will be smaller than the linear elastic case.

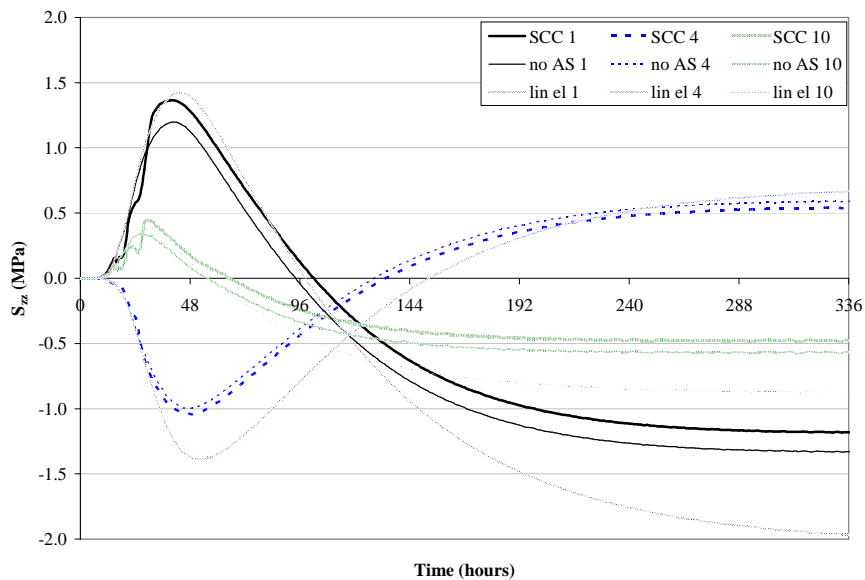


Figure 8.14a: Time graph of the tangential stresses S_{zz} of SCC and the effect of autogenous shrinkage and creep

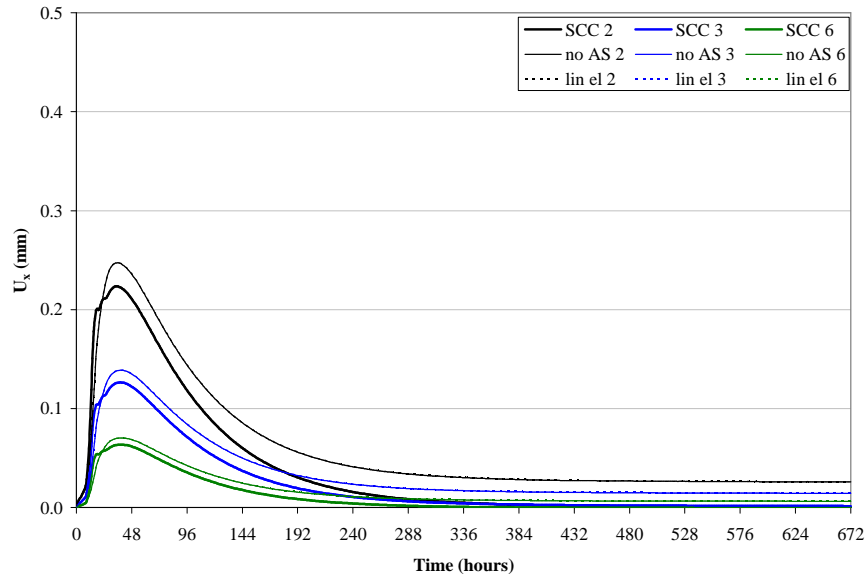


Figure 8.14b: Time graph of the radial displacement U_x of SCC and the effect of autogenous shrinkage and creep

4.2.2.2 The effect of the exothermal hydration reaction

It has been mentioned that the highest tensile stress peaks, found near the outer border of the buffer, are mainly caused by the exothermal hydration reaction and the created internal temperature gradients. It seems useful to investigate the effect of adjusted adiabatic temperature curves (Figure 8.15a) on the temperature development and the internal stresses inside the buffer at the critical regions (e.g. points 1-4-10).

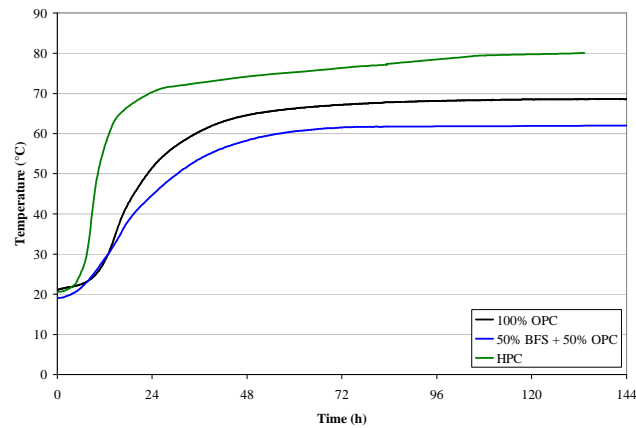


Figure 8.15a: The adiabatic temperature development of SCC, HPC and BFS/OPC

Two other types of concrete, with altered adiabatic temperature curves are considered to investigate the effect of the hydration reaction on the created stresses: HPC according to Craeye (2006) and Geirnaert (2009), and a slag blended cement based concrete (BFSC) containing 50 % BFS and 50 % OPC according to Robeyst et al. (2007). Compared to SCC, HPC has a faster temperature development and the adiabatic temperature after 144 hours is 80.1 °C. The BFSC based concrete has a slower temperature development and the obtained temperature in adiabatic environment is 62.0 °C after 144 hours. In order to exclude the creep effect and the effect of AS, the simulations are made for linear elastic behaving concrete. Only the adiabatic curves are changed, the other thermal and mechanical properties remain unaffected. Note that due to the altered hydration reaction, the maturity and thus the maturity-related strength development is altered.

In case altered adiabatic values are obtained via the method described in [De Schutter and Taerwe, 1995], the temperature rise and the stresses in the concrete buffer will change. The peaks occur earlier and are higher in case of a higher adiabatic curve (HPC), but occur later and are lower in case of a lower curve (BFS) (Figure 8.15b). Translating these temperature variations into the created stresses gives the same story: the tensile and compressive stress peaks occur earlier and are higher in concrete with a HPC based adiabatic curve, and also the stresses once the hydration peak has passed are higher. For BFS, the tensile and compressive stress peaks are lower, afterwards the curves of SCC and BFS evolve to a comparable constant value (Figure 8.15c).

Although it seems that the use of BFSC based concrete seems beneficial towards thermal stress creation inside the buffer, BFSC concrete has lower strength and slower strength development than OPC based concretes, such as SCC [De Belie, 2007]. The use of BFSC only reduces the temperature development inside the concrete buffer but due to the lower strength and lower strength development, the cracking criteria can remain unaltered or can be even worse compared to SCC. Note that BFSC based concrete is not desired for the Supercontainer concept for various reasons recounted in Chapter 5 (lower pH, slower strength development, radiation induced ettringite formation, etc.).

4.2.2.3 *The use of other types of concrete*

According to Bouniol (1998), different types of concrete can be considered in the nuclear industry, especially due to their beneficial effect towards radiation blocking and sulphate attack resistance. For example Haematite concrete can be considered as concrete used for the disposal site and the concrete buffer. Haematite has very high performance for special applications (e.g. on a nuclear level) and is based on the expensive calcium aluminates cements (AC). This type of cement is often used in cases where sulfuric acid generation by bacteria occurs, or where excellent sulphate resistance, resistance to abrasion or resistance to heat is highly needed [De Belie, 2007, Scrivener et al., 1999].

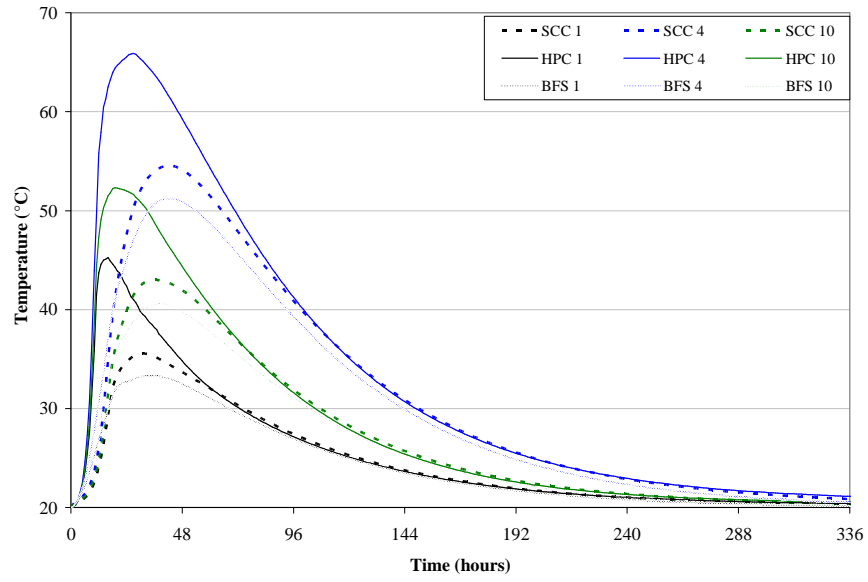


Figure 8.15b: Time graph of the temperature in SCC, HPC and BFS at points 1-4-10

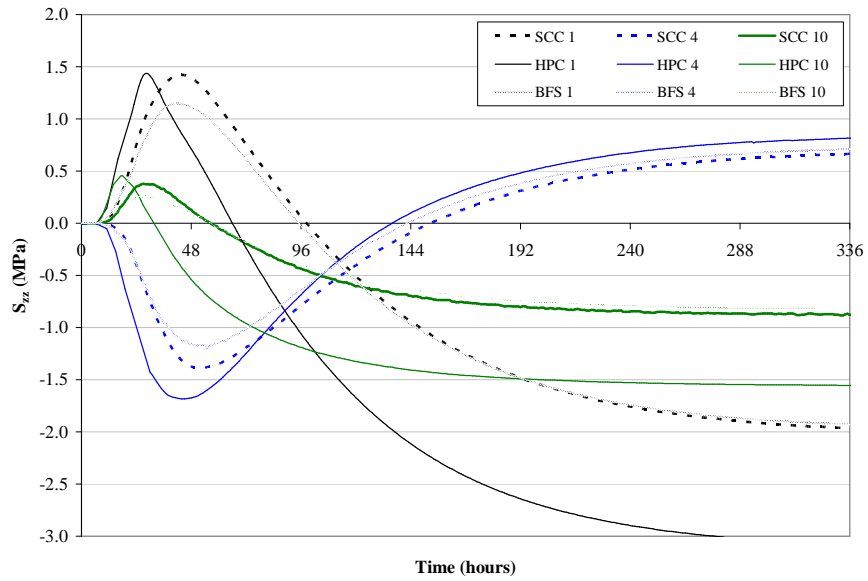


Figure 8.15c: Time graph of the tangential stresses in SCC, HPC and BFS at points 1-4-10

Aside from the higher adiabatic temperature development, and the higher early-age strength and compressive strength (± 75 MPa), compared to SCC, the thermal conductivity k (± 6.25 W/(m \cdot °C)) and the density ρ_c (± 4075 kg/m 3) and consequently the heat capacity according to equation (6.1) of Haematite concrete is much higher [Bouniol, 1999].

The effect of the coefficient of thermal expansion (CTE) α_T also must be considered, as mentioned by previous studies [Briffaut et al., 2009]. Mainly the types of aggregates of the concrete determines the CTE value. For limestone based concrete, α_T equals 8.0×10^{-6} /°C, while for gravel based concrete, it is appropriate to use a value of 12.0×10^{-6} /°C [Taerwe, 1997].

Changing the value of these three parameters (k , ρ_c and α_T) induces alterations of the early-age simulation results. In this case, the temperature and the tangential stresses are observed. As a reminder, the thermal properties of SCC are mentioned: 1.89 W/(m \cdot °C), 2390 kg/m 3 and 8.1×10^{-6} /°C respectively. The comparison is made for linearly elastic behaving SCC. The other thermal and mechanical properties of SCC remain unaffected.

Different values of ρ_c and α_T do not affect the temperature distribution in the concrete buffer (Figure 8.16a). Applying a higher thermal conductivity on the other hand, causes a more uniform temperature distribution and the temperature gradient ΔT between the middle of the buffer (point 4) and the outer border (point 1), which has a major impact on the thermal stress creation, is much lower than ΔT obtained for the limestone based SCC (Figure 8.16b). Due to the higher k -value, the heat escapes more easily from the buffer. As a consequence, the tangential peak stresses are much lower and the stresses after hydration converge more rapidly to a constant value (Figure 8.16c). The stresses remain unchanged with altered volumetric weight. Finally, by using a concrete with higher thermal expansion ability, the stresses will increase significantly both in compressive as in tensile behaviour (Figure 8.16c).

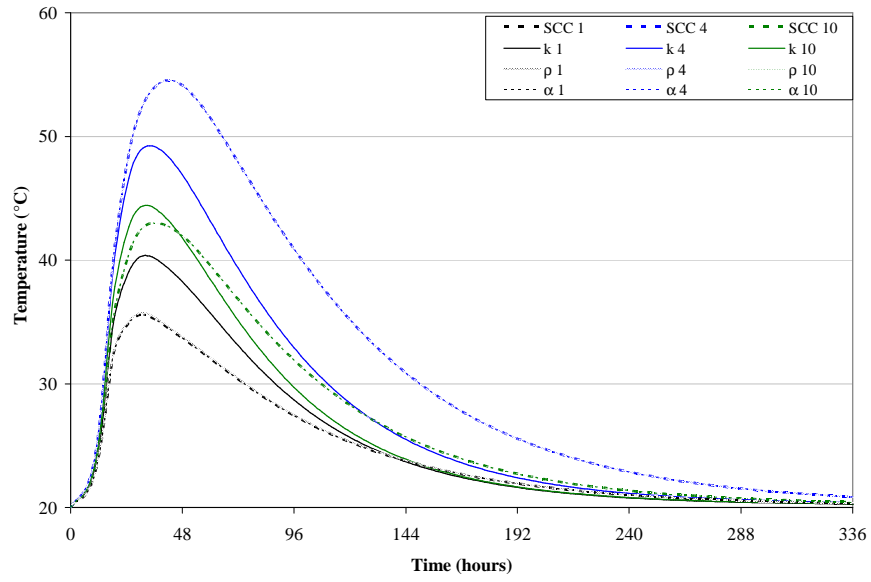


Figure 8.16a: Time graph of the temperature at points 1-4-10 with changed values of k , ρ_c and α_T

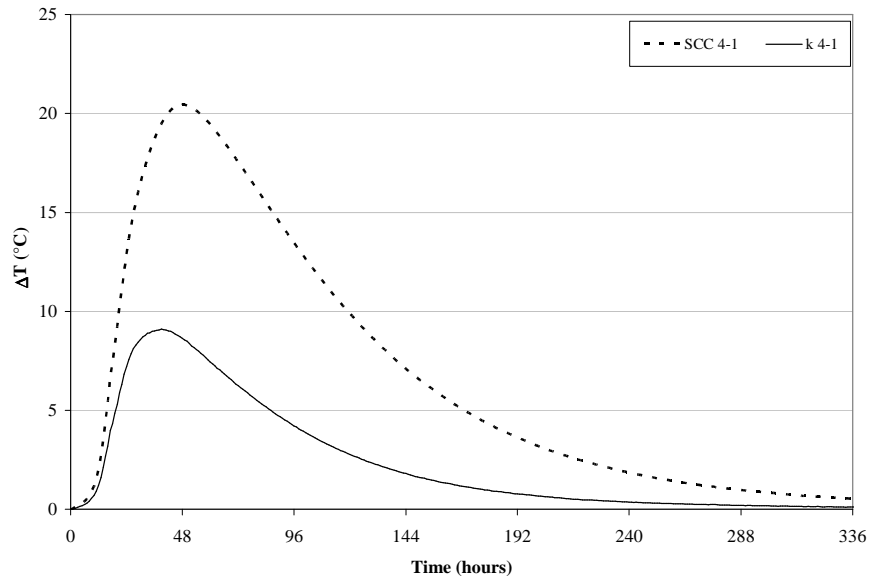


Figure 8.16b: Time graph of the temperature gradient between points 1 and 4 with changed k

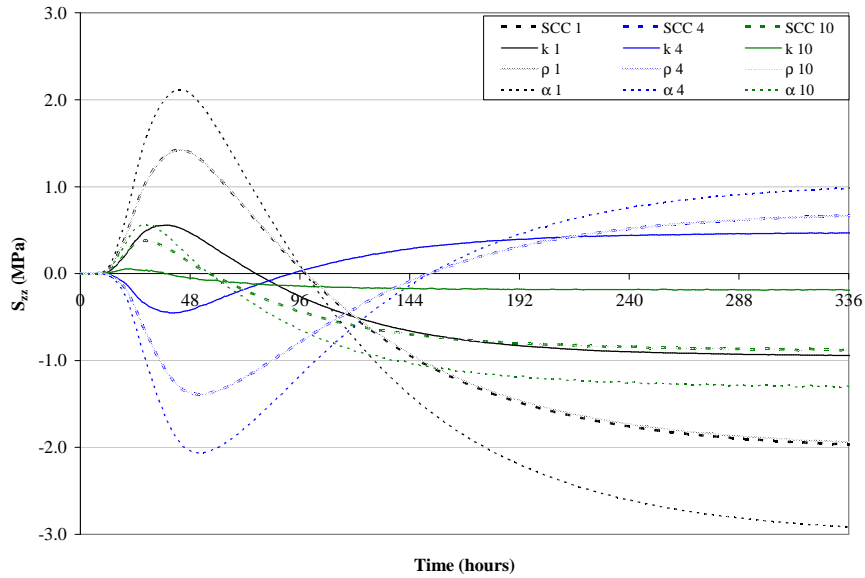


Figure 8.16c: Time graph of the tangential stresses at points 1-4-10 with changed values of k , ρ_c and α_T

4.2.3 Sensitivity analysis: changing the dimensions of the buffer

It is possible that certain dimensions of the Supercontainer must be adapted out of a design point of view (e.g. increasing or decreasing thickness for radiation blocking, expansion of the opening due to changed canister dimensions, adjustment of the diameter to fit the disposal galleries, etc.). Also the dimensions of the Supercontainer depend on the type of waste that needs to be disposed: vitrified HLW or SF assemblies (UOX, MOX). This part of the sensitivity analysis examines the influence of certain dimensions of the Supercontainer in standard environmental conditions (20 °C), with SCC as the reference concrete:

- The height of the buffer (case B, Figure 8.17a): an extension from 4.038 m to 6.038 m.
- The thickness of the buffer (case C, Figure 8.17a): a reduction from 0.7 m to 0.624 m. As a consequence, the diameter of the opening increases to 0.668 m.
- The outer diameter of the buffer (case D, Figure 8.17a): a widening from 1.916 m to 2.092 m. As a consequence, the thickness of the buffer increases to 0.787 m.
- Combining the alteration of those three main dimensions leads towards the dimensions of the buffer of the Supercontainer for the disposal of the SF assemblies (UOX): increased height, reduction of the thickness and expansion of the outer diameter of the buffer. The inner opening has a diameter of 0.844 m (case E, Figure 8.17a).

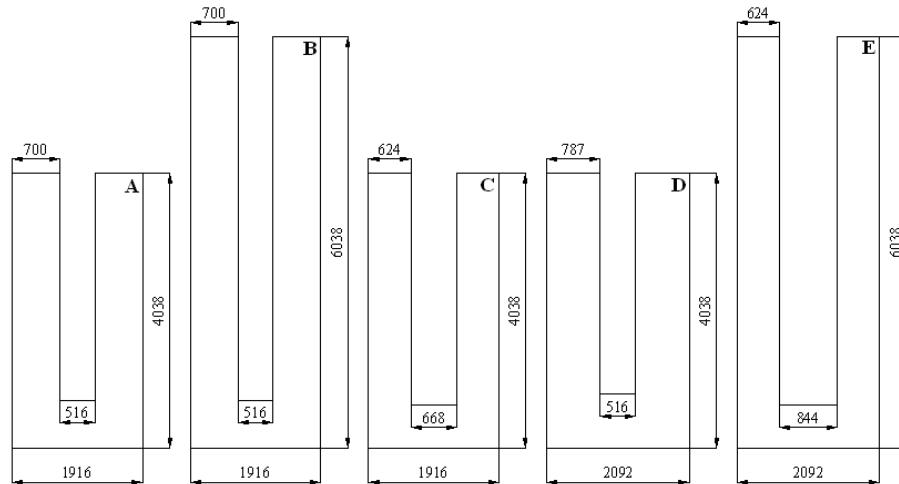


Figure 8.17a: Alteration of the height (B), the thickness (C) and the diameter of the buffer (D)

How those parameters affect the temperature, stresses and displacement of the buffer is discussed below. For the analysis, time graphs are drawn at different point. These points resemble to the previously defined points in Figure 8.6:

- Point 1 lies at the right bottom near the outer border of the buffer.
- Point 2 also lies at the outer border, but 0.35 m higher compared to point 1.
- Point 4 lies in the centre of the massive underside of the buffer.
- Point 10 lies in the opening at midheight of the upright mantle of the buffer.

4.2.3.1 Temperature T

An extension of the height of the mantle of the buffer (case B) does not have an effect on the temperature increase inside the buffer. When the thickness of the buffer decreases (case C), the temperature inside the buffer drops consequently. Higher temperature rises are obtained in case D, when the outer diameter is adjusted (in combination with a greater thickness). The Supercontainer for UOX disposal experiences lower temperatures due to the hydration reaction, compared to the reference Supercontainer for vitrified HLW. Also ΔT between the middle of the buffer (point 4) and the outer border (point 1) is smaller in case of the design for SF assemblies, which can lead towards smaller thermal stresses (Figure 8.17b). Values of the peak temperatures, near point 4, are listed in Table 8.4.

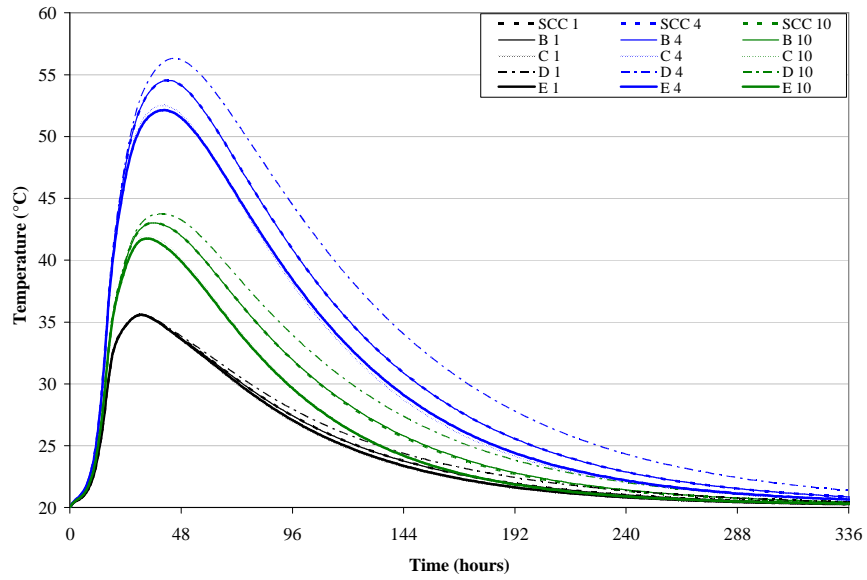


Figure 8.17b: Time graph of the temperature at points 1-4-10 with changed dimensions

As an illustration, two contourplots of the temperature distribution inside the Supercontainer for SF assemblies (UOX) are given after 39 hours (maximal temperature) and after 72 hours (demoulding time).

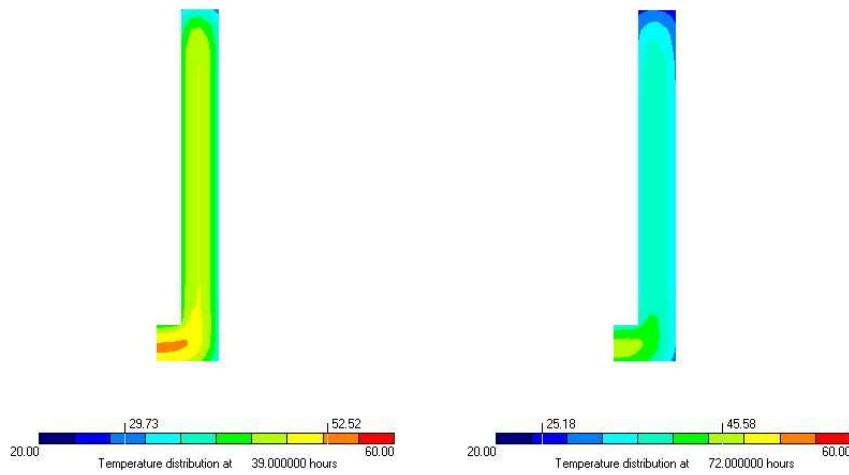


Figure 8.17c: Contourplots of the temperature in the Supercontainer for SF assemblies (UOX) at 39 h and 72 h

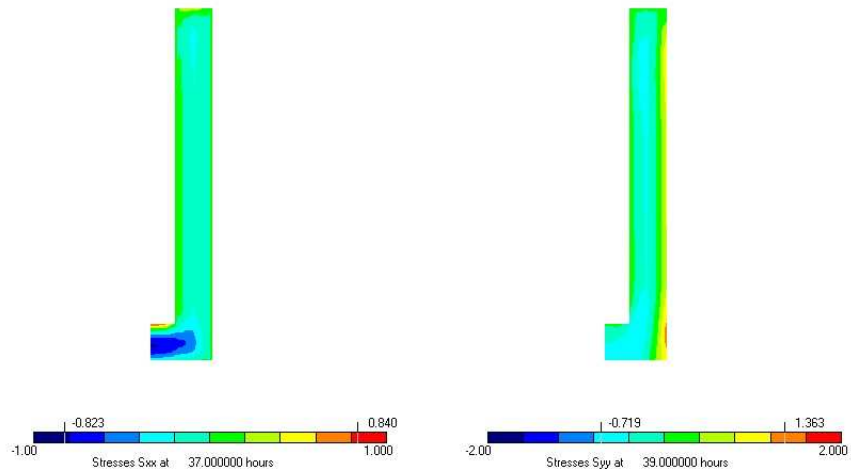


Figure 8.17d: Contourplots of the radial at 37 h (left) and the axial at 39 h (right) stresses in the Supercontainer for SF assemblies (UOX)

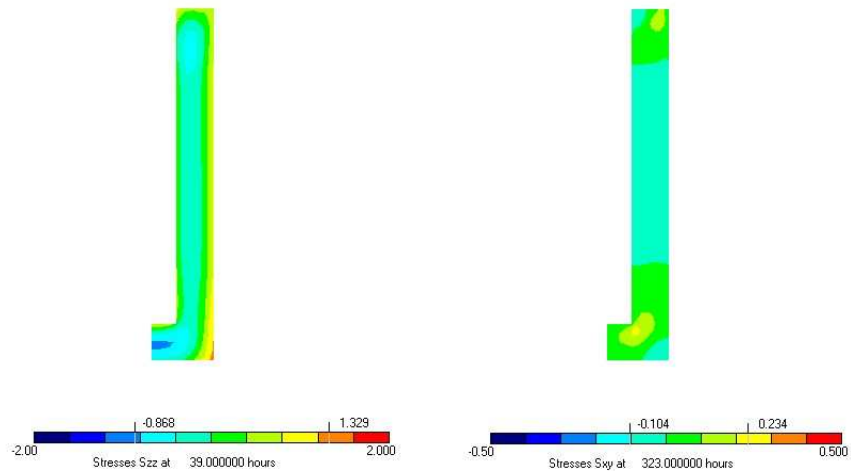


Figure 8.17e: Contourplots of the tangential stresses at 39 h (left) and the shear stresses at 323 h (right) in the Supercontainer for SF assemblies (UOX)

4.2.3.2 Stresses S_{zz}

Although the axial stresses S_{yy} are slightly higher, the most critical stresses on behalf of the cracking risk of the buffer, are the tangential stresses S_{zz} . No significant difference is found in tangential stresses in case the height of the buffer is adjusted (case B). The peak stresses are slightly smaller in case C, the case of a buffer with a smaller mantle thickness. Adjusting the outer diameter of the buffer, in combination with an increased mantle thickness, leads towards higher peak stresses (case D). The maximal stresses due to the hydration peak inside the buffer for UOX disposal are slightly lower compared to the reference buffer (Figure 8.17f, Table 8.4). Afterwards, when the hydration reaction related stress peaks are over, the stresses evolve towards more or less similar constant values.

Note that the radial stresses S_{xx} near the bottom of the opening of the buffer (point 7) are higher in case E (SF assemblies), but these stresses are sufficiently small and cause no concern on behalf of the cracking behaviour of the buffer (Figure 8.17d (left), Table 8.4).

As an illustration, the contourplots of the stress distribution inside the Supercontainer for SF assemblies (UOX) are given at the time of maximal appearance (Figure 8.17d, Figure 8.17e). Once more, the shear stresses are low enough to be neglected.

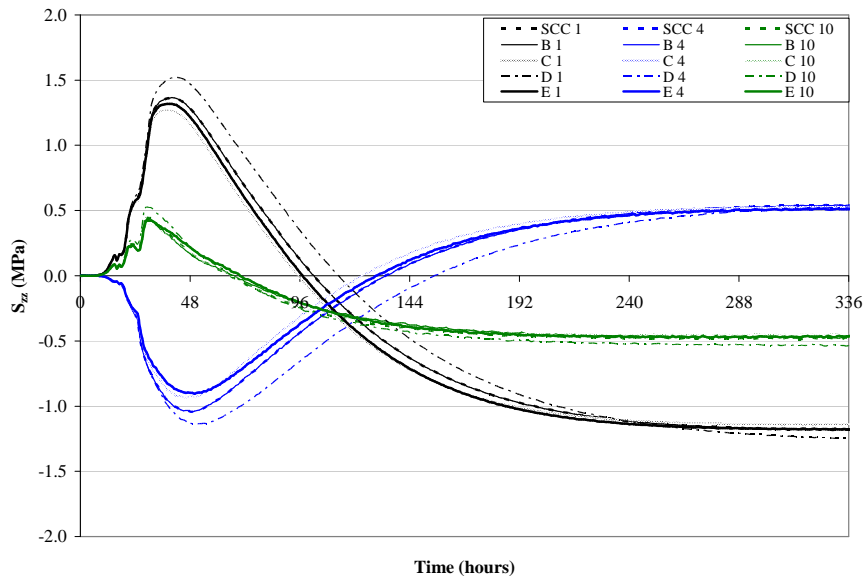


Figure 8.17f: Time graph of the tangential stresses at points 1-4-10 with changed dimensions

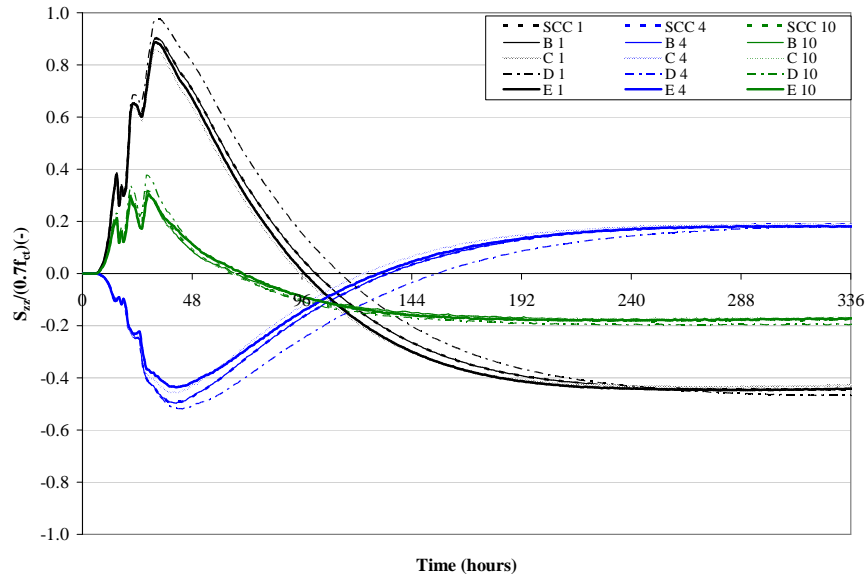


Figure 8.17g: Time graph of $S_{zz}/(0.7 \cdot f_{ct})$ at points 1-4-10 with changed dimensions

4.2.3.3 Cracking criteria: $S_{zz}/(0.7 \cdot f_{ct}) < 1$

As previously mentioned, the most critical case for early-age cracking of the concrete buffer is in tangential direction. By adjusting the dimensions of the buffer, no cracking is expected: the non-cracking criteria is fulfilled at all times in the three directions and for all cases (Figure 8.17g). The most critical case occurs if the outer diameter and the mantle thickness of the buffer are adjusted (case D): $S_{zz}/(0.7 \cdot f_{ct})$ equals 0.98 after 34 hours, compared to a maximal value of 0.90 after 32 hours for the reference case and 0.89 after 32 hours for the buffer intended for SF assemblies disposal. Adjusting the height of the buffer has no influence on the cracking risk, reducing the thickness of the mantle of the buffer has a beneficial effect on the cracking risk.

4.2.3.4 Displacement U_x

The displacement of the concrete near the outer border of the buffer is the highest in case D. The maximal displacement of the SF buffer is higher compared to the reference case of vitrified HLW and evolves faster towards a constant value (Figure 8.17i). If the mantle of the buffer gets thinner, the displacement near the border also decreases.

As an illustration, the contourplot of the displacement of the concrete near the outer border for SF assemblies (UOX) is given at the time of maximal appearance (Figure 8.17h, left) and the deformed mesh after 167 hours is also added.

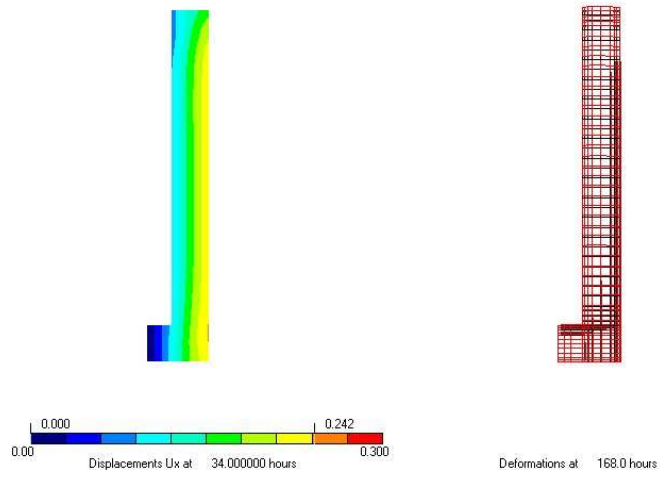


Figure 8.17h: Contourplots of the radial displacement at 34 h (left) and deformed mesh at 168 h (right) of the Supercontainer for SF assemblies (UOX)

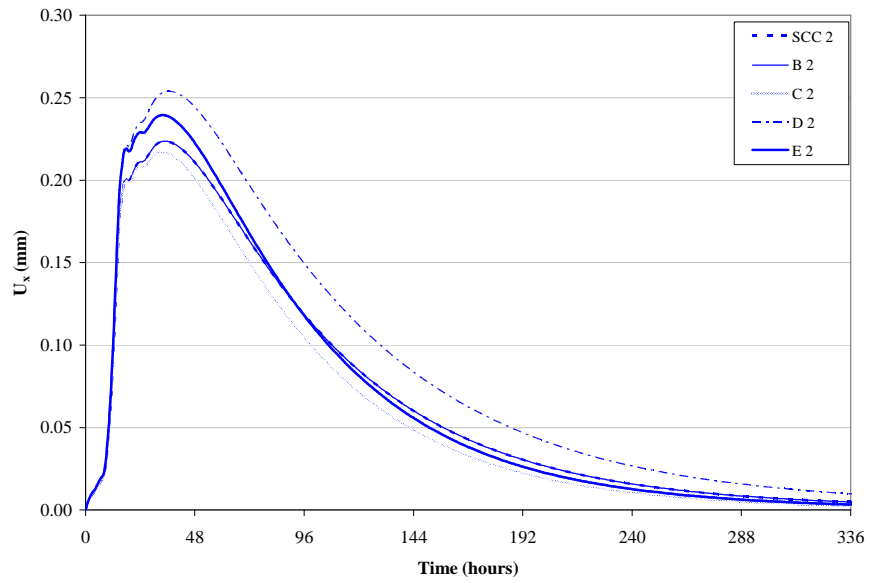


Figure 8.17i: Time graph of U_x at point 2 with changed dimensions

Table 8.4: Summary of the maximal values of temperatures, tensile stresses and displacements for the different cases with altered dimensions

	T_{\max} °C	$S_{xx,\max}$ MPa	$S_{yy,\max}$ MPa	$S_{zz,\max}$ MPa	$U_{x,\max}$ mm
REF (A)	54.54	0.70	1.47	1.37	0.228
B	54.54	0.70	1.47	1.37	0.228
C	52.67	0.76	1.33	1.28	0.220
D	56.32	0.77	1.67	1.53	0.260
E	52.52	0.84	1.36	1.33	0.242
REF (A)	41	36	41	41	36
B	41	36	41	41	36
C	39	37	39	38	33
D	44	33	42	42	37
E	39	37	39	39	34

4.2.4 Sensitivity analysis: changing the environmental conditions

As a final scope of the sensitivity analysis of Phase 1 of the fabrication of the Supercontainer out of hot cell, some boundary conditions are adapted: the environmental temperature and the wind velocity. To study the effect of the boundary conditions on the simulation results, SCC cast with 20 °C curing conditions is considered as the reference case. First, the environmental temperature is adjusted (10 °C and 30 °C), and a realistic temperature curve will be implemented by means of a sine curve varying around 10 °C, amplitude of 3.5 °C and a wavelength of 24 hours. Next, the convective heat transfer coefficients $h_{c,i}$ ($i = 1..2..4$, Figure 8.6) are changed by applying a certain wind velocity near the outer border and in the opening of the buffer. The heat transfer coefficients $h_{c,i}$ in the reference case (no wind) have a value of 5.60 W/(m²·°C) in case of a free surface, and a value of 5.59 W/(m²·°C) in case steel insulation (envelope or formwork) is used. This difference is insignificant: the steel provides no insulation. Once external wind is tolerated (e.g. 1 m/s), the values of $h_{c,i}$ increase towards 9.60 W/(m²·°C) (free surface) and 9.59 W/(m²·°C) (steel coverage). This external wind first is applied only on the outer border, and secondly also on the inner border of the buffer.

The influence of adapted environmental boundary conditions on the simulation results is studied by means of the temperature, the stresses and the displacement of the buffer via time graphs at different points. These points resemble with the previously defined points in Figure 8.6.

4.2.4.1 Temperature T

Figure 8.18a and Figure 8.18b indicate that due to an increase in environmental temperature, up to 30 °C, the temperatures inside the buffer increase and the peak temperatures occur approximately 10 hours earlier. Lowering the environmental temperature to 10 °C, induces a lowering of the temperatures and the appearance of the peak values is delayed with approximately 15 hours. The peak values are listed in Table 8.5. In case a more realistic sine temperature curve is implemented (with daily cycle between 6.5 °C and 13.5 °C), it can be seen that the temperature evolution follows the temperature development of the case with a constant temperature of 10 °C. The fluctuation of the temperature is higher near the outer border and non-existent in the middle of the buffer. More important, concerning the created internal stresses, is the temperature gradient between point 4, situated in the middle of the buffer, and point 1, near the outer border of the buffer: compared to the reference case (20.45 °C after 48 hours), ΔT is higher for 30 °C (21.85 °C after 39 hours) and lower for 10 °C (17.76 °C after 64 hours), which will lead towards higher thermal stresses for the 30 °C case.

The effect of an applied external wind near the outer border (1 m/s), and of an applied wind near the outer border in combination with an applied wind in the opening of the buffer (2 x 1 m/s) gives cause to a temperature decrease near the border (Figure 8.18a).

Even more significant is the increase of ΔT due to the application of external ventilation (Figure 8.18b): 24.00 °C (case 1 m/s) and 22.84 °C (case 2 x 1 m/s) after 46 hours.

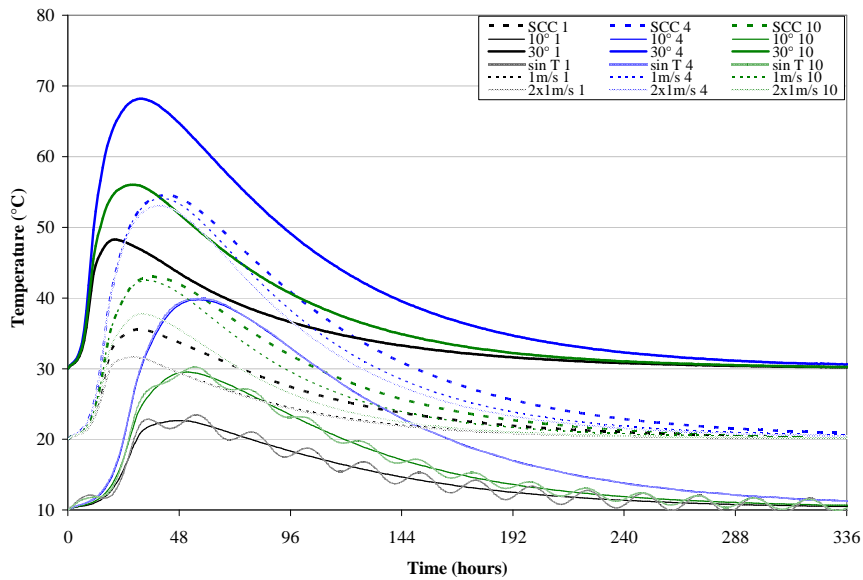


Figure 8.18a: Time graph of the temperature at points 1-4-10 with changed boundary conditions

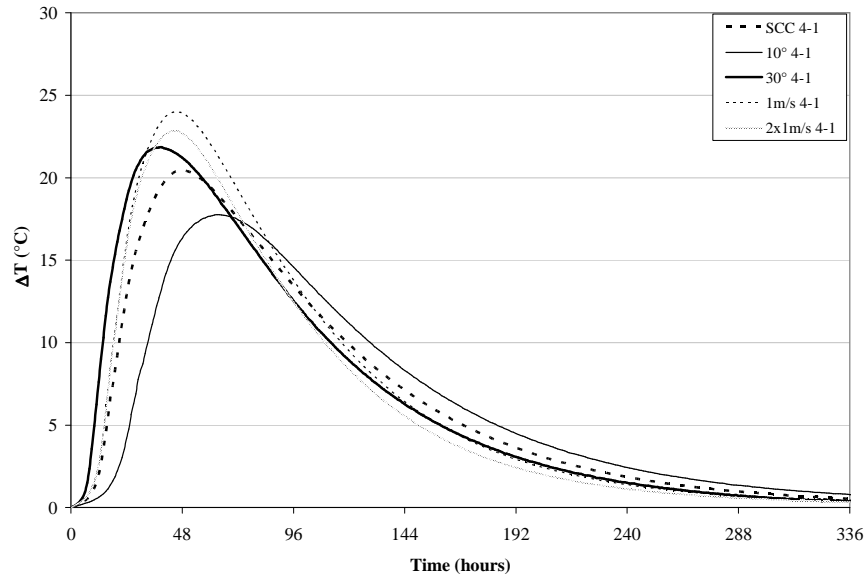


Figure 8.18b: Time graph of the temperature gradient between points 1 and 4 with changed boundary conditions

4.2.4.2 Stresses S_{zz}

The time graphs of S_{zz} (the most critical stresses on behalf of the cracking risk) at points 1-4-10 are given in Figure 8.18c and Figure 8.18d. The results of the peak values of the radial, axial and tangential stresses with their time of appearance are listed in Table 8.5. Due to an increase of the outer temperature with 10 °C, the peak stresses also increase and occur earlier (± 13 hours). Reversely, lowering the temperature lowers the peak stresses and the time of appearance is delayed compared to the reference case (± 15 hours). Also the presence of an external wind on the buffer, induces higher peak stresses that occur approximately 5 hours earlier (Table 8.5). In case of a realistic environmental temperature, the created stresses follow the curve with constant temperature (10 °C). The deflection from the stress curve is 77 % higher in the region near the outer border compared to the middle of the buffer, and 23 % higher compared to the inner border of the buffer (Figure 8.18d). A change of temperature is more sensed near the edged of the buffer than in the middle of the buffer. Note that the radial stresses S_{xx} near the bottom of the opening of the buffer (point 7) are significantly higher in case 2 x 1 m/s compared to the reference case (Table 8.5, Figure 8.18e, left), but these stresses are still sufficiently small and cause no concern.

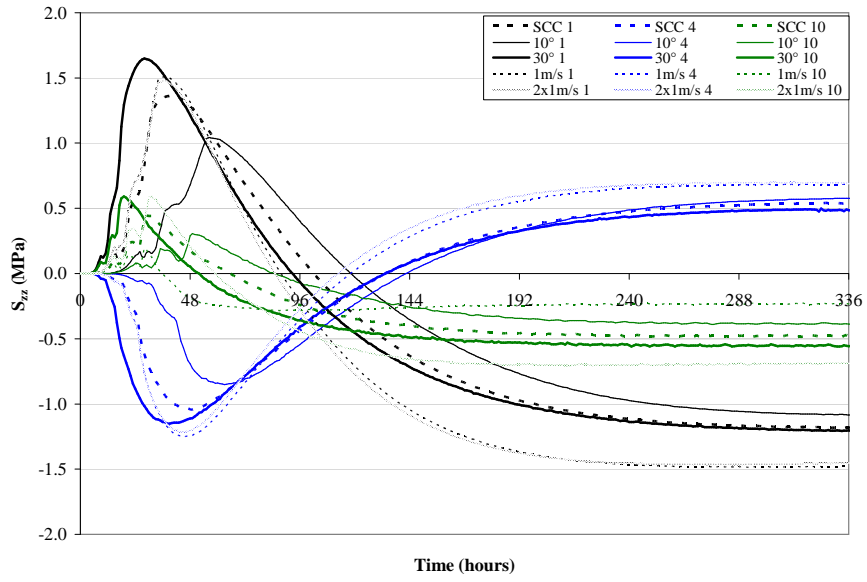


Figure 8.18c: Time graph of the tangential stresses at points 1-4-10 with changed boundary conditions

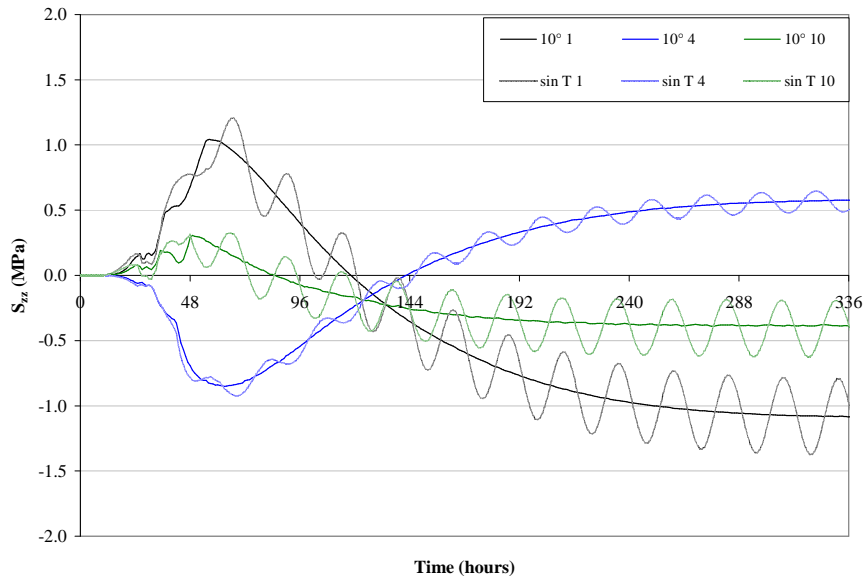


Figure 8.18d: Time graph of the tangential stresses at points 1-4-10 with a realistic temperature curve

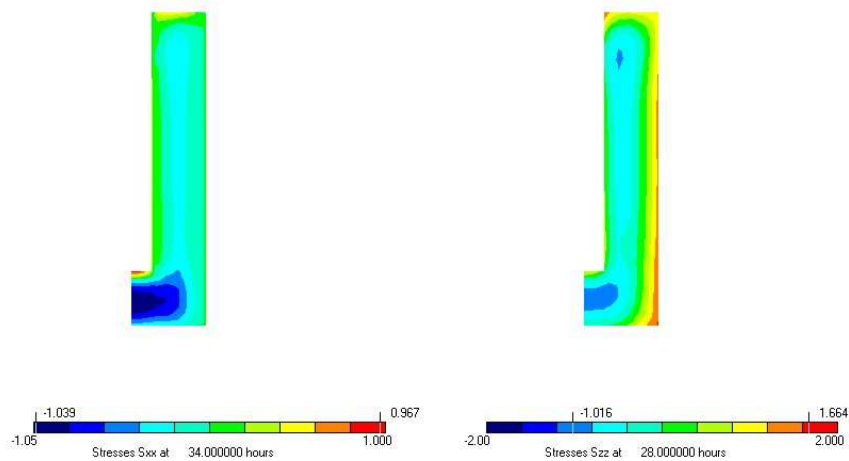


Figure 8.18e: Contourplots of the radial stresses at 34 h (left, case 2 x 1 m/s) and the tangential stresses at 28 h (right, case 30 °C)

4.2.4.3 Cracking criteria: $S_{zz}/(0.7 \cdot f_{ct}) < 1$

The effect of altered boundary conditions on the tensile cracking risk is examined in the most critical case for early-age cracking of the concrete buffer in tangential direction (Figure 8.18f).

The non-cracking criteria is fulfilled in case the environmental temperature increases up to 30 °C, but the maximal $S_{zz}/(0.7 \cdot f_{ct})$ is higher and occurs earlier: 0.94 after 28 hours. A lower temperature (10 °C) provides a lowering of the cracking risk: 0.75 after 56 hours.

By applying an external wind ventilation near the outer border, the non-cracking criteria is no longer fulfilled. $S_{zz}/(0.7 \cdot f_{ct})$ equals 1.08 after 34 hours, which means that a reasonable chance of early-age cracking exists. By applying an additional ventilation into the opening of the buffer, the cracking risk is barely changed: 1.06 after 34 hours. Therefore, in practice, it is advisable to shield the buffer and the casting site from the detrimental wind effect, e.g. by placing a windscreen surrounding the site (Chapter 9).

Although the relevant peak stresses in axial and tangential direction for the case of an increased temperature (30 °C) are higher compared to the cases with an external wind influence (Table 8.5), the cracking risk is higher in latter cases. Explanations can be found in the fact that the temperature gradient middle-border of the buffer is 12 % higher when external wind is applied (Figure 8.18b). Also, the temperature rise is

higher when the environmental temperature is higher, making the hydration process evolve quicker and thus introducing a faster maturity-related strength development.

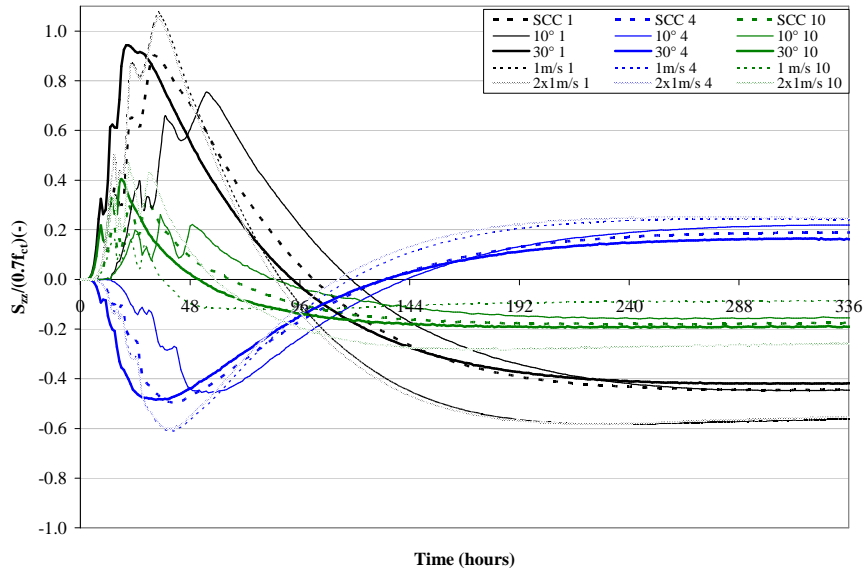


Figure 8.18f: Time graph of $S_{zz} / (0.7 \cdot f_{ct})$ at points 1-10 with changed boundary conditions

4.2.4.4 Displacement U_x

The maximal displacement of the concrete near the outer border of the buffer increases with increasing temperature (12 % for 30 °C) and decreases with decreasing temperature (16 % for 10 °C). The displacement evolves faster towards its original state with higher environmental temperature and with a realistic sine curve for the temperature, the displacement follows the curve of constant temperature (Figure 8.18g). By applying external wind ventilation, the maximal displacement is approximately 9 % lower compared to the reference case (Table 8.5).



Figure 8.19a: Scheme of the reverse cast: standard situation (left) and casting in pit (right)

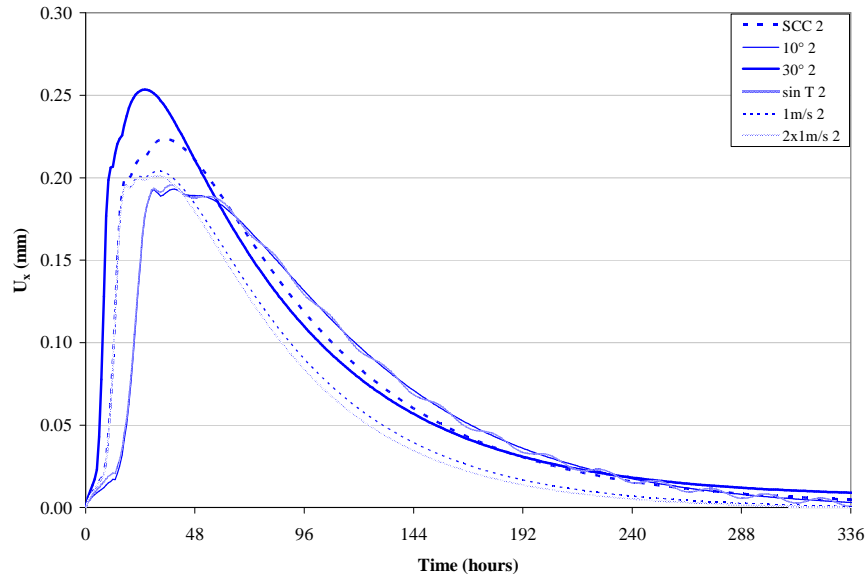


Figure 8.18g: Time graph of U_x at point 2 with changed boundary conditions

Table 8.5: Summary of the maximal values of temperatures, tensile stresses and displacements for the different cases with altered boundary conditions

	T_{\max} °C	$S_{xx,\max}$ MPa	$S_{yy,\max}$ MPa	$S_{zz,\max}$ MPa	$U_{x,\max}$ mm
REF	54.54	0.70	1.47	1.37	0.228
10°	39.79	0.58	1.15	1.05	0.196
30°	68.23	0.81	1.74	1.66	0.259
sin T	39.95	0.65	1.28	1.22	0.200
1 m/s	54.11	0.67	1.66	1.54	0.207
2 x 1 m/s	53.27	0.97	1.60	1.49	0.203
t_{\max} (h)					
REF	41	36	41	41	36
10°	56	53	56	56	39
30°	31	25	28	28	26
sin T	56	66	67	67	38
1 m/s	41	33	36	36	32
2 x 1 m/s	40	34	36	37	32

4.2.5 *Alternative casting condition*

In a final simulation step, an alternative casting way is examined: reverse casting (Tractebel Engineering design). The selected option for the casting of the buffer is in upside-down position. This means that the base of the concrete buffer will be on the upper part during concrete pouring. Two possible situations occur (Figure 8.19a):

- Case RCa: Steel formwork (thickness 6 m) is applied with a hollow steel cone as an inner formwork to create the opening inside the buffer (Figure 8.19a, left). Overall, the convective heat transfer coefficient h_c is $5.6 \text{ W}/(\text{m}^2 \cdot ^\circ\text{C})$ (no external wind is present), except for the lower support part of the buffer (concrete floor: $h_c = 2.0 \text{ W}/(\text{m}^2 \cdot ^\circ\text{C})$).
- Case RCb: The concrete pouring occurs in a pith, so the concrete is not subjected to air flows (Figure 8.19a, right). Overall, the heat transfer coefficient h_c is $2.0 \text{ W}/(\text{m}^2 \cdot ^\circ\text{C})$, except for the upper part of the buffer (free surface: $h_c = 5.6 \text{ W}/(\text{m}^2 \cdot ^\circ\text{C})$).

To compare with the reference case, the environmental temperature is $20 \text{ }^\circ\text{C}$ and SCC is used as concrete material. For the analysis, time graphs are drawn at different points given in Figure 8.6 and contourplots at different times.

4.2.5.1 *Temperature T*

Compared to the upright reference casting case, case RCa experiences lower temperatures inside the buffer (Figure 8.19b), while in case RCb the temperatures are significantly higher. The regions with the highest peak temperatures differ from the reference case as noticed in the contourplots at maximal temperature appearance (Figure 8.19c).

The peak values of the temperature for the two cases are listed in Table 8.6. The temperature gradient ΔT between regions in the middle of the buffer (e.g. point 4) and regions near the outer border of the buffer (e.g. point 1) can give a clear indication for the expected internal thermal stresses. A higher thermal gradient induces higher stresses. Although higher temperatures occur in case RCb, ΔT is smaller as presented in Figure 8.19f and the temperature returns slower to its initial temperature. Due to the lower convective heat transfer coefficients applied in case RCb, the temperature distribution is more uniform. Applying higher insulation around the buffer during casting and thus limiting convective heat transfer near the outer surface, has a beneficial effect on the created temperature gradient between the core and the edges of the buffer.

The temperature gradient ΔT in the upside-down case RCa is higher compared to the upright reference case (Figure 8.19f).

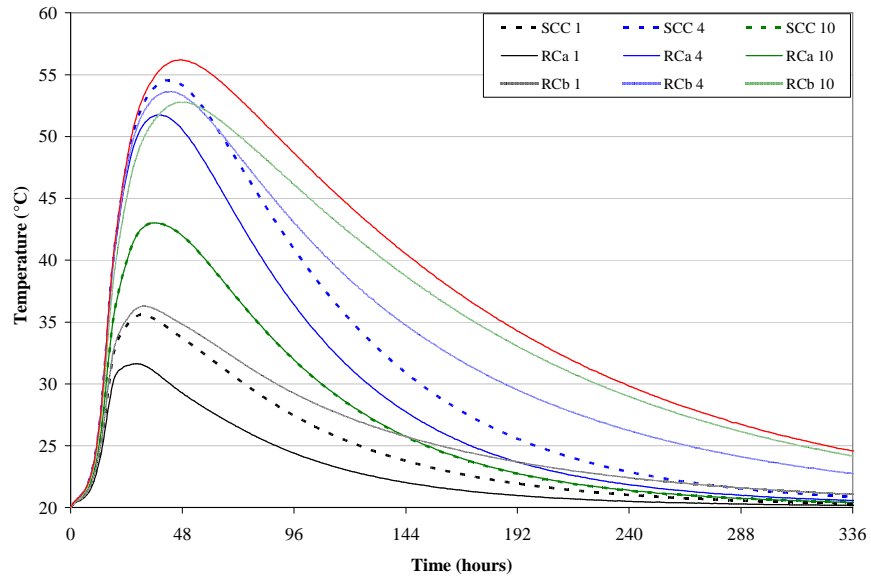


Figure 8.19b: Time graph of the temperature at points 1-10 for reverse casting (red line gives temperature at point 9 for RCb)

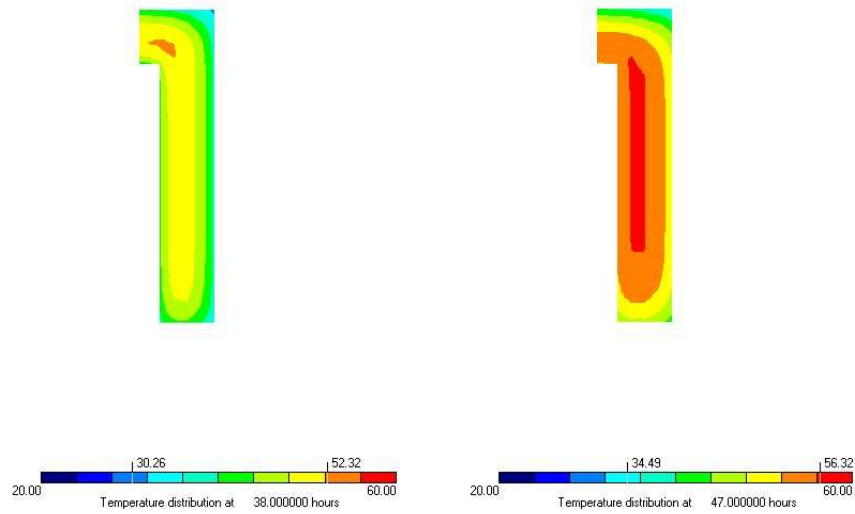


Figure 8.19c: Contourplots of the temperature in RCa at 38 h (left) and RCb at 47 h (right)

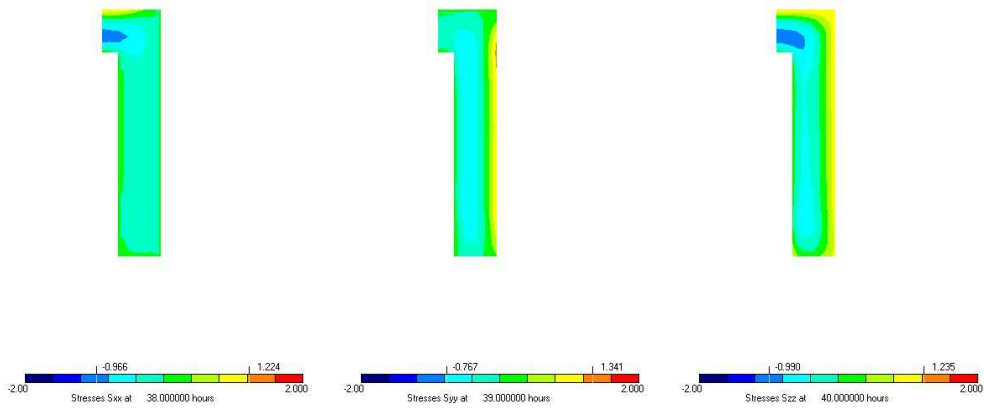


Figure 8.19d: Contourplots of the radial stresses at 38 h (left), the axial stresses 39 h (middle) and the tangential stresses at 40 h (right) in RCa

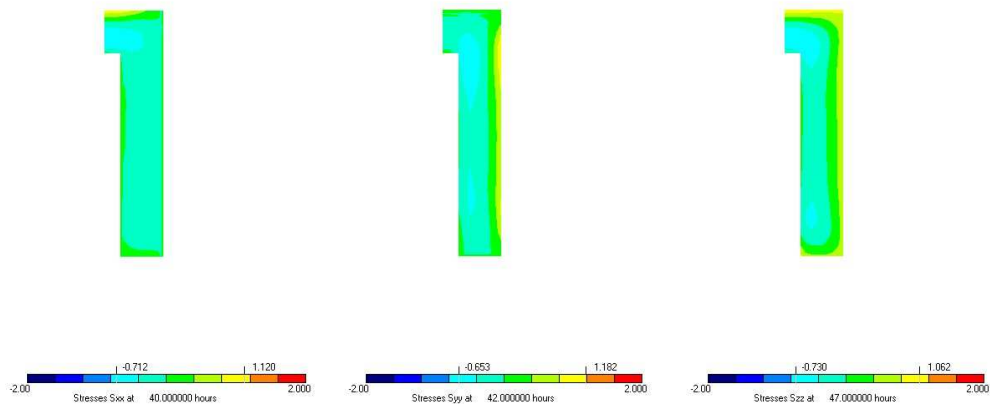


Figure 8.19e: Contourplots of the radial stresses at 40 h (left), the axial stresses at 42 h (middle) and the tangential stresses at 47 h (right) in RCb

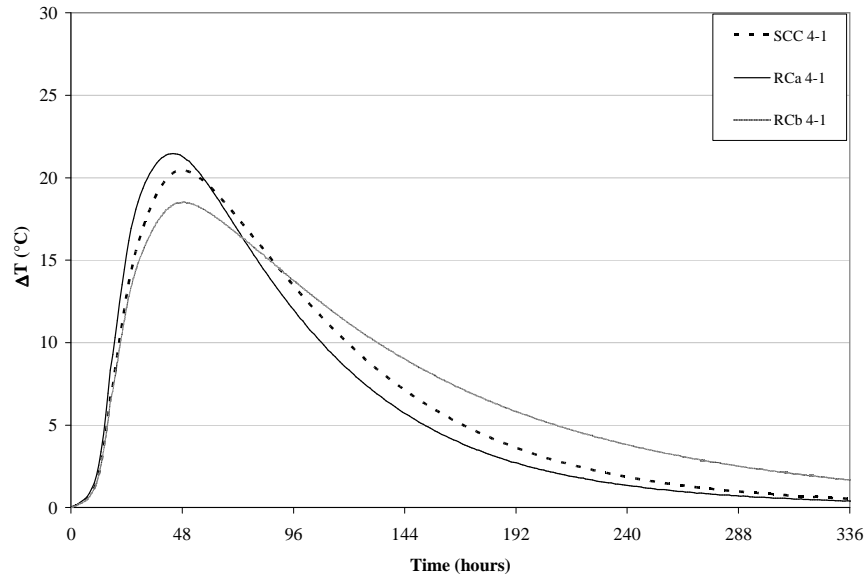


Figure 8.19f: Time graph of the temperature gradient between points 1 and 4 for reverse casting

4.2.5.2 Stresses S_{zz}

Contourplots of the maximal stresses in radial, axial and tangential direction are given in Figure 8.19d (RCa) and Figure 8.19e (RCb). It is clear that the highest stresses occur in case RCa, but overall, reverse casting induces smaller stresses compared to the upright reference case, except in the radial direction. The upper part of the concrete pouring, i.e. the base of the buffer, experiences radial stresses with the same order of magnitude as the axial and tangential stresses in case of reverse casting (Figure 8.19d, Figure 8.19e, Table 8.6). After the stress peaks are passed, the stresses in case RCa evolve to the same values as the reference case. The stresses in case RCb are overall lower, both in tensile as in compressive behaviour, and before and after the hydration peak has passed.

The results of the peak values of the radial, axial and tangential stresses with their time of appearance are listed in Table 8.6. The time dependent development of the tangential stresses is given in Figure 8.19g.

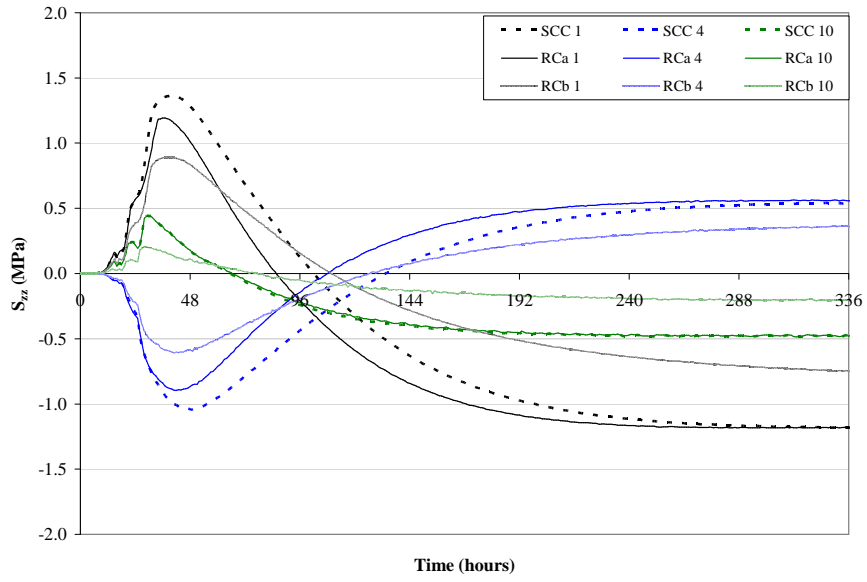


Figure 8.19g: Time graph of the tangential stresses at points 1-4-10 for reverse casting

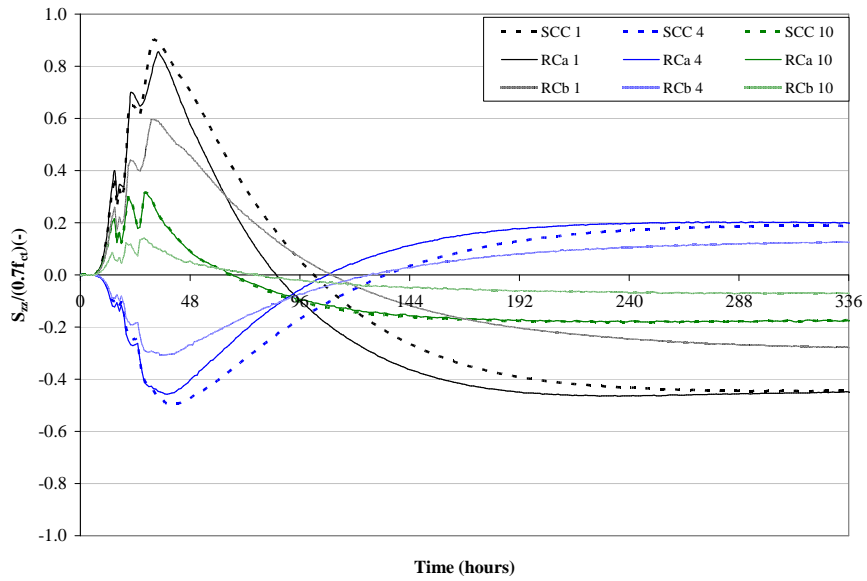


Figure 8.19h: Time graph of $S_{xz}/(0.7 \cdot f_{ct})$ at points 1-4-10 for reverse casting

4.2.5.3 Cracking criteria: $S_{zz}/(0.7 \cdot f_{ct}) < 1$

When reverse casting is applied the cracking risk ratio drops to a value of 0.86 after 34 hours (RCa), and when the cast is performed in a more insulated environment (RCb), such as a deep pith, the cracking risk is even smaller: 0.60 after 32 hours (Figure 8.19 h). Due to the appliance of high insulation, provided by the concrete faces of the pith, the heat cannot easily escape and remains entrapped longer in the buffer leading towards higher temperatures inside the buffer but smaller thermal gradients are obtained. Therefore, the induced stresses are smaller (due to the smaller gradient) and the maturity-related strength development is faster (due to the higher temperatures), thus the cracking risk ratio decreases. Once more, the smaller temperature gradient in the latter case can be seen as the most decisive factor for the stress decrease.

4.2.5.4 Displacement U_x

A higher displacement near the border of the buffer is obtained when the concrete is cast inside a well insulated pith. This deformation is prevented by the surrounding concrete casting hole, leading towards additional compressive stresses near the border, which counteracts the created tensile stresses. Even smaller stresses can be expected as the ones mentioned in Table 8.6. For the other reverse casting case RCa, a smaller displacement is found (Figure 8.19j). As an illustration, the contourplot of the radial displacement of the concrete is given at the time of maximal appearance (Figure 8.17h, left).

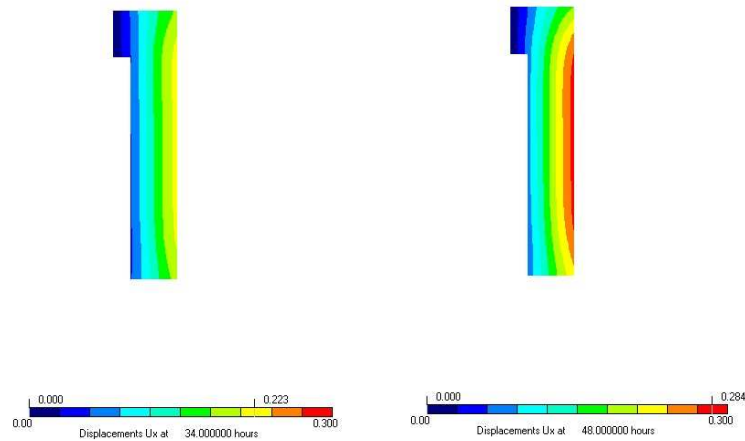


Figure 8.19i: Contourplots of the radial displacement of RCa at 34 h (left) and RCb at 48 h (right)

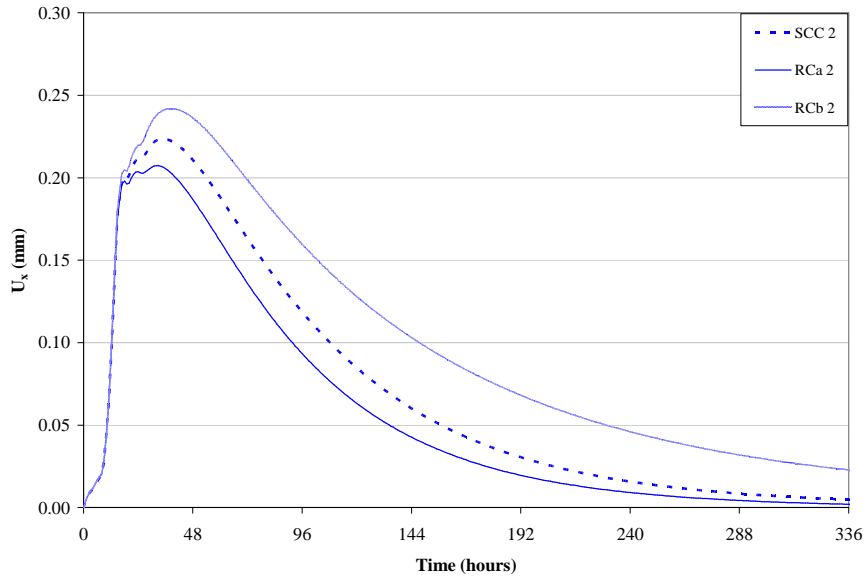


Figure 8.19j: Time graph of U_x at point 2 with changed dimensions

Table 8.5: Summary of the maximal values of temperatures, tensile stresses and displacements for the two reverse casting cases

	T_{\max} °C	$S_{xx,\max}$ MPa	$S_{yy,\max}$ MPa	$S_{zz,\max}$ MPa	$U_{x,\max}$ mm
REF	54.54	0.70	1.47	1.37	0.228
RCa	52.32	1.22	1.34	1.24	0.223
RCb	56.32	1.12	1.18	1.12	0.284
t_{\max} (h)					
REF	41	36	41	41	36
RCa	38	38	39	40	34
RCb	47	40	42	40	48

4.2.6 Casting of the buffer out of hot cell: main conclusions

In the reference casting case, where the initial concrete temperature is 20 °C and the environmental temperature is 20 °C at all times, the casting of the buffer out of hot cell (Phase 1) experiences no cracking risk in case SCC or TVC is considered as the applied concrete composition. Moreover, if cracking of the buffer would occur, measures could be taken out of hot cell, where no radioactivity appears. However, the Half-Scale tests indicate that cracks will not appear during casting and curing of the buffer out of hot cell (Chapter 9). No additional reinforcement is necessary to control cracking.

The maximal values of temperature, stresses and displacement of SCC and TVC are listed in Table 8.3. The main difference between SCC and TVC lies in the compaction method and in the concrete composition: + 50 kg/m³ limestone filler, + 132 kg/m³ sand, - 184 kg/m³ coarse aggregates and + 8 kg/m³ superplasticizer in case of SCC. Therefore, different concrete properties are found leading towards variations in the simulation results of SCC and TVC.

For the reference casting case (20 °C), the maximal temperature inside the midzone of the buffer is 3 % higher when SCC is used, but occurs 2 hours later. The highest tensile stresses inside the buffer occur near the outer border, mainly due to the exothermal and expansive hydration reaction of the cement in the concrete and the created thermal gradients in the buffer (Chapter 5). Due to prevention of the deformation of the concrete, internal stresses are created inside the buffer. Those maximal normal tensile stresses in radial, axial and tangential stresses are higher in case of SCC (29 %, 25 % and 28 % respectively). Applying the cracking criteria by means of equation (8.3b) indicates that the highest cracking risk occurs in tangential direction, with the stress to strength ratio for SCC approximately 8 % higher than for TVC. Shear stresses can be neglected in this study and the normal stresses can be roughly seen as principal stresses. Finally the maximal radial displacement of the buffer is 5 % higher in case of SCC.

In the sensitivity analysis the effect of changed concrete properties, of adjusted dimensions of the buffer and of altered environmental conditions on the temperature, displacement, internal stresses and the cracking risk of the buffer is determined. Therefore, SCC is taken as the reference concrete composition because the use of SCC, compared to TVC, will ease considerably the precast process (no external vibration needed, beneficial especially during casting in hot cell) and complies with all other requirements regarding strength (SCC even has higher strength compared to TVC), long-term durability, chemical interactions, etc. [Craeye et al., 2007], although the cracking risk is slightly lower in case of TVC. The casting with ambient temperature of 20 °C, with no external wind velocity, is taken as reference case for the sensitivity analysis.

The most important findings are listed below:

- Especially the exothermal hydration reaction of the cement and the related thermal gradient lead towards the highest tensile stresses near the outer border of the buffer, but also the autogenous and the creep behaviour of the concrete have a (smaller) effect on the cracking risk. Cement with higher adiabatic temperature curves (in case of unchanged mechanical properties) will inevitably release more heat into the buffer, introduces higher temperatures, induces higher internal stresses, but also contributes to a higher maturity-related (and temperature dependent) strength development. By considering the autogenous shrinkage and the creep behaviour, lower stresses appear compared to the case of a linear elastic material.
- By increasing the thermal conductivity of the concrete, the created heat can circulate more easily through the buffer and can escape faster, hence smaller stresses are found and the cracking risk decreases (Figure 8.20a, only the k -value is changed). Also the time of appearance of the highest cracking risk ratio $S_{zz}/(0.7 \cdot f_{ct})$ decreases with increasing k . The heat capacity of the concrete has no significant effect on the simulation results, but the CTE is important. A higher value of the CTE can induce significantly higher stresses due to the higher tendency of the concrete to deform under influence of elevated temperatures.
- Adjusting the height of the buffer will not lead towards significant differences in the simulation results. Especially the thickness of the buffer is critical: the higher the thickness, the more massive the buffer becomes and thus the higher the cracking risk will be (Figure 8.20b, the thickness and the diameter of the Supercontainer are changed (case D, Figure 8.17a), the insertion opening remains 516 mm). However, the time of appearance is not affected by the changing of the thickness and the diameter. Overall, the cracking risk of the buffer for disposal of SF assemblies is smaller than the cracking risk of the buffer for vitrified HLW disposal.
- Higher environmental temperatures affect the tensile stress creation negatively and reduce the time of appearance of the highest cracking risk. The cracking risk increases with increasing ambient temperature. However, as Figure 8.20c indicates, the $S_{zz}/(0.7 \cdot f_{ct})$ curve remains smaller than one within the considered temperature range (between 5 °C and 50 °C).
- There is a proportionate correlation between the convective heat coefficient h_c (the outer coefficients $h_{c,1}$ and $h_{c,2}$ of Figure 8.6 are changed) and the cracking risk ratio (Figure 8.20d). The coefficient h_c depends on the ambient wind velocity and the type of used formwork (Table 8.6). The presence of wind can have a detrimental effect on the cracking behaviour. There is a high cracking risk if the outer h_c exceeds an approximate value of 7 W/(m²·°C), e.g. in case there is an ambient wind velocity of 0.5 m/s around the steel envelope.
- A side from the adiabatic hydration reactions, especially the two fundamental heat transfer parameters, i.e. the thermal conductivity k and the convective heat transfer coefficient h_c , have a significant effect on the early-age cracking behaviour of the concrete buffer of the Supercontainer.

- Casting of the buffer upside-down is slightly beneficial compared to upright casting, especially when good insulation around the buffer is used, e.g. casting of the buffer in a deep hole.
- The main mechanism behind the early-age cracking of the buffer can be found in the created thermal gradients in the different regions of the buffer: a smaller temperature gradient can be seen as the most decisive factor for a stress decrease.

An ideal casting environment can be created by using formwork material with a high insulation capacity so the heat cannot easily escape and remains entrapped longer in the buffer leading towards higher temperatures inside the buffer but smaller thermal gradients. In this case, the induced stresses are smaller (due to a smaller thermal gradient) and the strength development is faster (due to the higher temperatures and the faster development of maturity-related properties such as the strength), thus the cracking risk ratio is smaller. It has to be remarked however, that an adequate demoulding time has to be chosen in case of an insulating formwork.

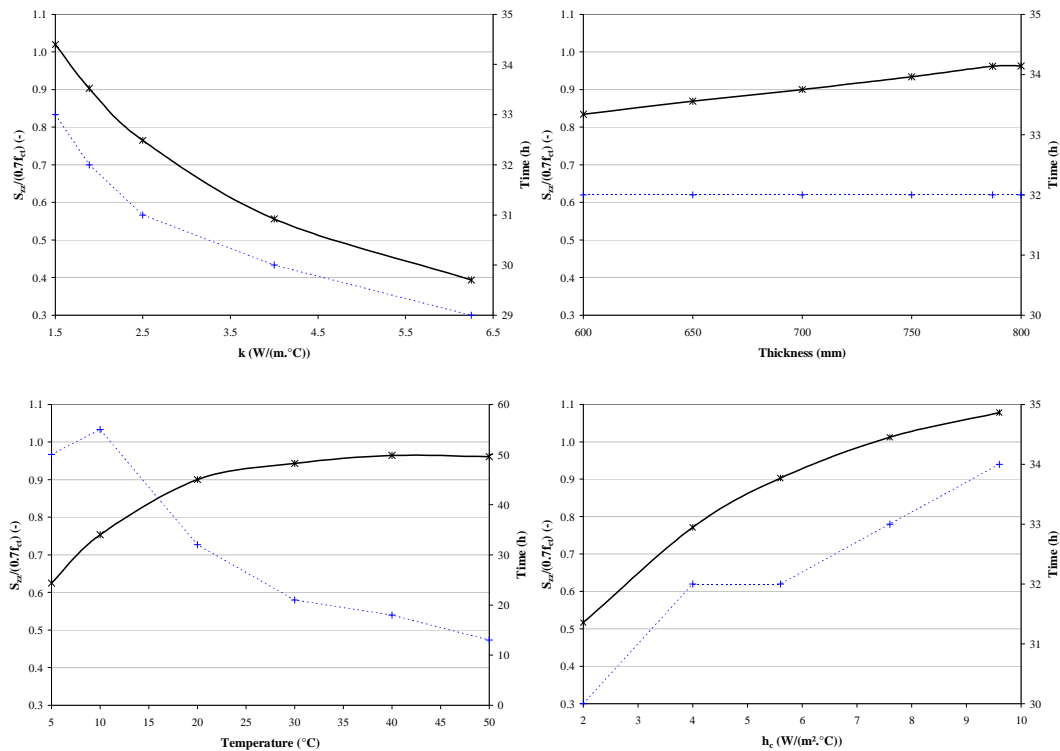


Figure 8.20: Sensitivity analysis – Influence of the altered thermal conductivity of the SCC (a), thickness of the buffer (b), environmental temperature (c), and convective heat transfer coefficient (d) on the cracking risk ratio $S_{zz}/(0.7f_{ct})$ and the time of appearance in point 1

Table 8.6: Insulation type, wind velocity and the convective heat transfer coefficient h_c

Insulation type	W_{1-2} m/s	$h_{c,1-2}$ W/(m ² ·°C)
Concrete – Polystyrene (12 mm)	0	2.0
Wood (30 mm)	0	4.0
Steel (6 mm)	0	5.6
Steel (6 mm)	0.5	7.6
Steel (6 mm)	1	9.6

Using good insulation as formwork material (e.g. concrete, wood or polystyrene surrounding the steel envelope), lowering the environmental temperature during hardening and providing sufficient wind shielding around the casting site are important measures that can be taken, in order to minimize the early-age cracking risk of a cast buffer out of hot cell (Phase 1).

4.3 Phase 2 of the simulations: insertion, filler and lid (in hot cell)

After approximately 240 hours after the casting of the buffer, when the temperature inside the buffer approaches the initial reference temperature of 20 °C, the heat-emitting overpack, containing the vitrified HLW or the SF assemblies, is inserted into the created opening of the buffer and immediately, the remaining annular gap is filled by means of the filler and the Supercontainer is closed by casting and fitting of the lid.

In a first approximation, the presence of the overpack is only taken into account as an environmental boundary condition (no expansion is considered). For the HLW, three different temperature curves can be considered depending on the preceding cooling period (50 years – 60 years – 70 years, Figure 8.5). The Supercontainer, with SCC as the reference concrete material, and considering the same initial boundary and kinematic conditions as mentioned for Phase 1 of the simulations, is taken as the reference case. Aside from the effect of the cooling period, other cases are simulated and discussed below:

- The difference between the insertion of HLW and SF (with cooling period of 50 years).
- The difference between a buffer made of SCC and made a buffer made of TVC.
- The effect of a postponed insertion of the HLW (e.g. after 480 hours instead of 240 hours).
- The effect of the use of a precast lid (PCL) instead of a freshly cast lid.

In a second simulation step, the presence of the overpack is considered via the use of an additional macro layer (Figure 8.21, right), which follows a temperature elevation according to Figure 8.5. Due to the heat creation, the overpack will have the tendency to expand, introducing additional stresses into the buffer. This will have a significant effect on the stress creation in the concrete and the cracking risk of the buffer. Also different cases are considered for these simulations (Table 8.7):

- As a reference, the insertion of a low carbon 316 stainless steel (austenitic) overpack is considered (case $\alpha 16$), with the most relevant properties listed in Table 8.7. A preceding cooling period of 50 years for the waste containing overpack is taken for the reference case.
- In a next step, the CTE of the steel overpack is altered. For example carbon steel (P235) has a CTE of $12 \times 10^{-6}/^{\circ}\text{C}$ (case $\alpha 12$), while 410 stainless steel (ferritic) has a reduced CTE of $9.9 \times 10^{-6}/^{\circ}\text{C}$ (case $\alpha 10$).
- The effect of a prolonged cooling period is examined for a 316 stainless steel overpack, and for a carbon steel overpack, with altered thermal properties (case carbon). Note that the alteration of the thermal conductivity k and the heat capacity c_T of the overpack material does not have an impact on the temperature evolution and the internal stress creation in the buffer.
- Finally, it is examined whether the use of an external top load (case top F) or side load (case side F) has beneficial effects towards crack reduction. This lateral load (2.5 MPa) is introduced after 240 hours on the outer surface of the buffer over its entire height. The top load (2 MPa) is introduced after 336 hours on top of the hardening lid.

Table 8.7: The different simulation cases with the overpack as a macro layer (data is taken from European Standards EN 10028-1 (2001) and EN 10028-2 (2003))

Case	α_T $10^{-6}/^{\circ}\text{C}$	k $\text{W}/(\text{m}\cdot^{\circ}\text{C})$	c_T $\text{kJ}/(\text{m}^3\cdot^{\circ}\text{C})$	cooling years	side load MPa	top load MPa
$\alpha 16$	16	16	3990	50	-	-
$\alpha 12$	12	16	3990	50	-	-
$\alpha 10$	10	16	3990	50	-	-
70y	16	16	3990	70	-	-
carbon	12	76	3780	70	-	-
side F	16	16	3990	50	2.5	-
top F	16	16	3990	50	-	2.0

The early-age behaviour of the buffer, the filler and the lid is discussed separately for the temperature development, the stress development, the cracking risk and the radial displacement, by means of contourplots and time graphs drawn in critical regions and points of the buffer (as given in Figure 8.6), the filler and the lid (as given in Figure 8.21, left). The simulations last until 1344 hours after initial casting of the buffer.

4.3.1 Early-age behaviour of the buffer

4.3.1.1 Temperature T

The temperature inside the three concrete layers is elevated due to two main mechanisms: the hydration reaction of the cast filler and lid, and the heat originating

from the overpack. Contourplots of the temperature at different times are plotted in Figure 8.22a. These plots give a clear indication where the highest temperatures occur, and at which points time evolution graphs are useful.

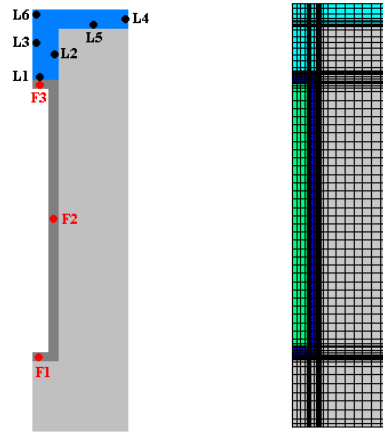


Figure 8.21: Different points in the filler and the lid for the time graphs (left), and the overpack as an additional macro layer in the HEAT/MLS model (right)

Closer to the heat-emitting waste and the freshly cast filler and lid, the temperature rise is higher (Figure 8.22a). Near the inner surface (e.g. point 10), a quick temperature rise occurs, and once the hydration peak of the SCC filler is passed, the temperature drops. Nevertheless, this decrease is counteracted by the heat originating from the HLW (Figure 8.22b). Further away from the heat source (e.g. point 4, point 8), the rise in temperature is lower and the influence of the hydration reaction of the filler and the lid is less sensed. Once the hydration peak of the SCC is over, the temperature development evolves uniformly to an asymptotical value (Figure 8.22a, contourplot after 1344 hours). The temperature after 1344 hours inside the buffer is lower when longer preceding cooling periods of the HLW are maintained. When the Supercontainer for SF is considered (dimensions in Figure 8.17a), the heat-emitting SF, with a cooling period of 50 years, introduces more heat into the buffer and induces higher temperatures compared to the Supercontainer for HLW (Figure 8.22b).

A slightly lower temperature evolution and slightly lower temperatures are found in the TVC buffer case, with a difference that is noticeable near the inner surface but that becomes insignificant near the outer surface (Figure 8.22c). The use of a precast lid (PCL) is not influencing the temperature development inside the buffer, except for the regions that come into direct contact with the lid: in case of a PCL, no hydration reaction occurs, and the heat of hydration is not introduced into the surrounding SCC of the buffer. Finally, a postponement of the insertion time of the heat-emitting waste (e.g. 480 hours instead of 240 hours) causes an elevation of the temperature in regions near

the inner surface, but the temperature in the middle of the buffer and near the outer surface evolves to the same constant value as for the reference case (Figure 8.22c).

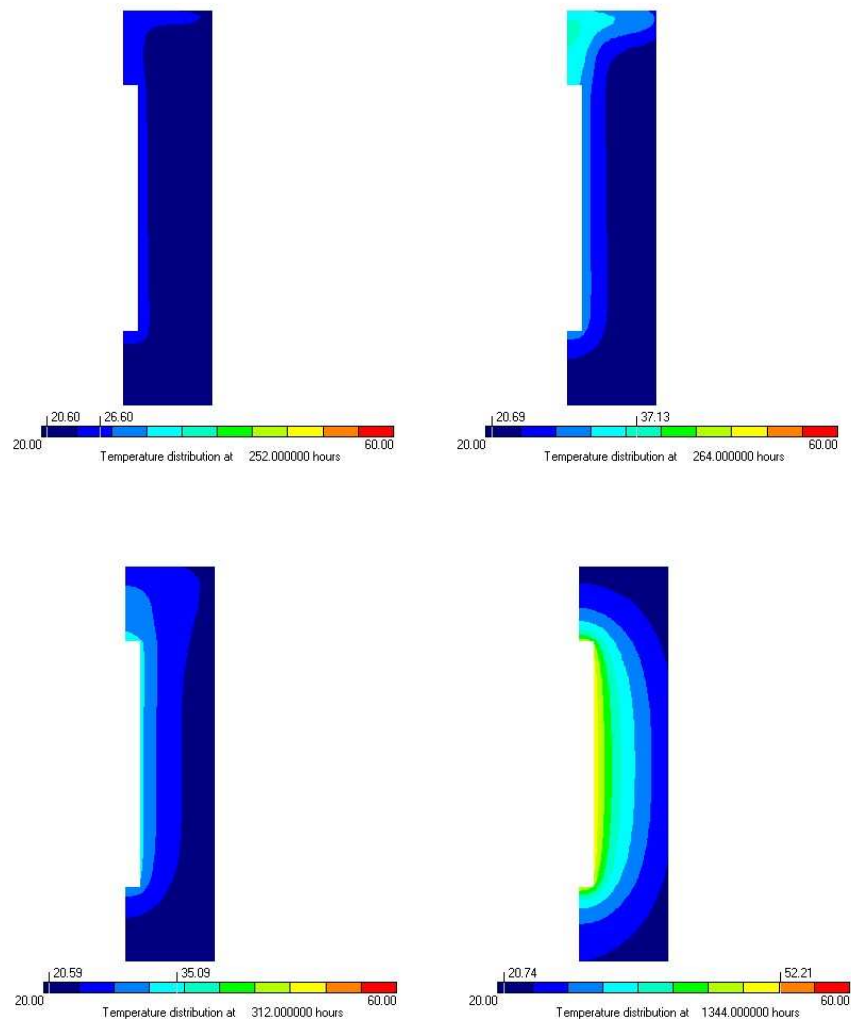


Figure 8.22a: Contourplots of the temperature in the reference simulation 20 °C, after a preceding cooling period of 50 years (SCC-Phase 2) at 252 h, 264 h, 312 h and 1344 h

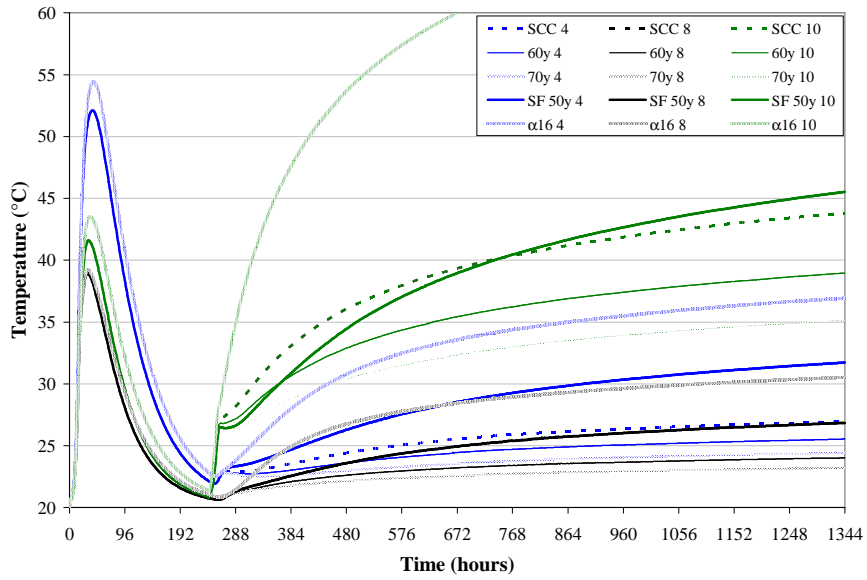


Figure 8.22b: Time graph of the temperature with different cooling periods and types of waste at points 4-8-10

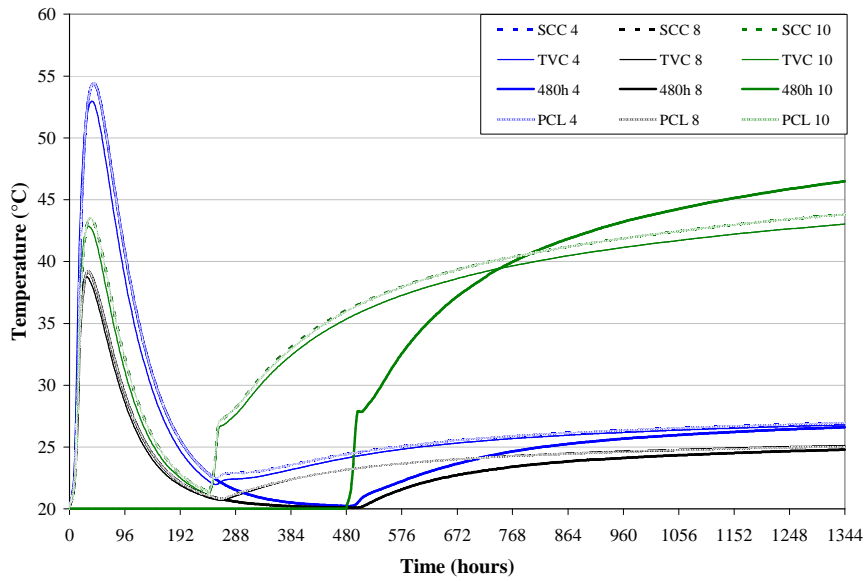


Figure 8.22c: Time graph of the temperature with TVC buffer, postponed insertion and precast lid at points 4-8-10

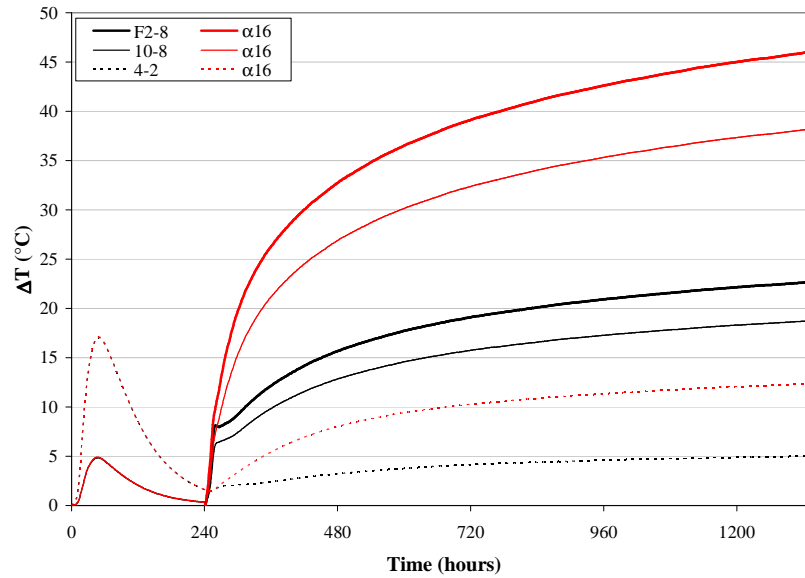


Figure 8.22d: Time graph of the temperature gradient between the outer surface and the inner surface of the filler (F2-8), the inner surface of the buffer (10-8) and the middle of the buffer (4-2) in the reference simulation 20 °C with the overpack as boundary condition (black lines) and as macro layer (red lines), after a preceding cooling period of 50 years (SCC-Phase 2)

Finally, the temperature gradient between the SCC near the inner buffer surface and the outer surface in the reference case, evolves towards 20 °C between the points 10 and 8: a value that is higher than the maximal value due to the hydration of the buffer (Figure 8.22d). The temperature gradient, after insertion of the overpack, remains smaller than 5 °C between the points 4 and 2, but is higher than 20 °C between the points F2 and 8. According to De Schutter (1996), there is a non-negligible cracking risk if ΔT of a massive structure approaches 20 °C due to the hindered internal deformation.

In case the overpack is considered as a macro layer, the temperature rise after insertion of the heat-emitting overpack is significantly higher, and the influence of the hydration reactions of the filler and the lid is no longer noticeable (Figure 8.22b). Also the temperature gradient is significantly higher in this case (Figure 8.22d).

The maximal values of the temperature in the buffer near the overpack after 1344 hours are given in Table 8.8.

4.3.1.2 Stresses S_{zz} , S_{yy} , S_{xx}

The normal stresses in the three-dimensional direction (axisymmetrical: x is radial, y is axial, z is tangential) of the reference casting case are plotted via contourplots at the end of the simulation period (i.e. 1344 hours). Especially at the outer surface of the buffer, tensile stresses are found with values inferior to the expected strength of the SCC. To evaluate the stress development inside the buffer due to the insertion of the overpack and the casting of the filler and the lid, contourplots of the tangential stress are given at different times of appearance, and time graphs are drawn at different points in the most relevant regions: the middle of the buffer (point 4), the outer surface of the buffer (point 8) and the inner surface of the buffer (point 10).

After 240 hours, thus at the time the heat-emitting overpack is inserted and the Supercontainer is closed, eigenstresses are present at the different regions of the buffer (Figure 8.23a, S_{zz} after 240 hours): the middle of the buffer experiences tensile stresses, while the inner and outer edges of the buffer lie under compression.

In case the overpack is considered as a boundary condition, two regions in the time development curve can be depicted (Figure 8.23b): one region governed by the hydration reactions of the filler and the lid the first hours after insertion, and one region governed by the heat-emitting waste.

First, the heat released by the hydration reaction of the freshly cast filler and lid, causes the nearby inner surface to expand more than the middle of the buffer and its outer surface. As a consequence, the expansion of the SCC at the inner surface of the buffer (green line) is prevented, and the SCC comes under additional compression due to the hydration peak. For the surrounding SCC, it is the other way around: due to the heat of hydration, the middle of the buffer (blue line) experiences an additional tensile stress peak, while the compressive stresses at the outer surface of the buffer (black line) counteract the tensile stress build-up due to the hydration reactions of filler and lid. Once the hydration peak is over, and the cooling sets in, tensile stresses are induced near the inner surface, compressive stresses are introduced in the surrounding SCC. From now on, the heat released by the HLW or the SF assemblies sets in. Once more, the SCC near the inner surface wants to expand more than its environment and comes under additional compression. On the other hand, the SCC near the outer surface is forced to expand by the inner surrounding SCC, and experiences tensile stresses. Note that the compressive stresses near the outer surface, due to the cooling down of the buffer before insertion of the waste, act as a buffer which counteracts the tensile stress build-up due to the heat released by the waste. Finally, the stresses in the middle of the buffer evolve towards a safe compressive value.

By prolonging the preceding cooling period of the HLW, the stress peaks due to the hydration reaction of the filler and the lid are not altered. Once these peaks have passed, the tensile stress build-up at the outer surface and the compressive stress build-up near the inner surface of the buffer decrease with increased cooling period.

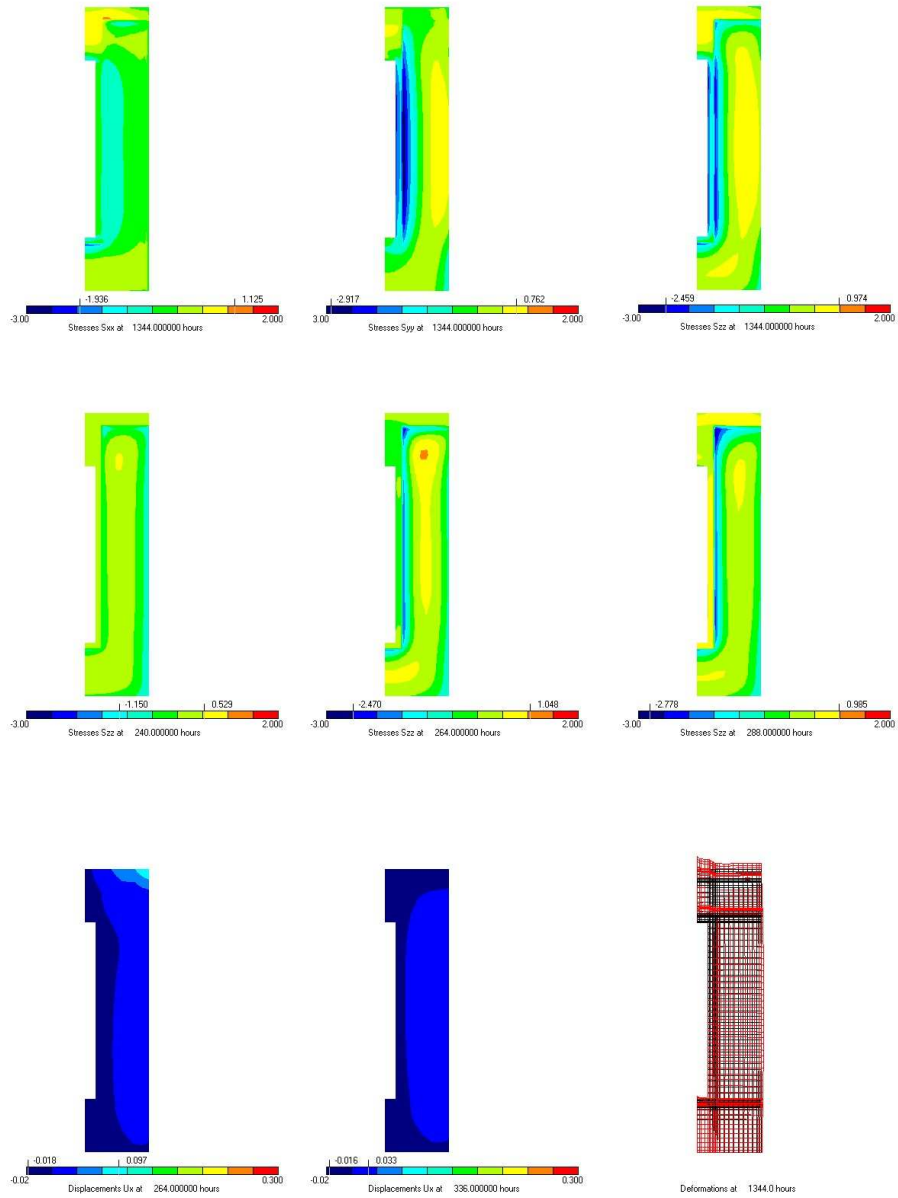


Figure 8.23a: Contourplots of S_{xx} (1344 h), S_{yy} (1344 h), S_{zz} (240 h, 264 h, 288 h and 1344 h), U_x (264 h and 336 h) and the deformation mesh (1344 h) (SCC-Phase 2)

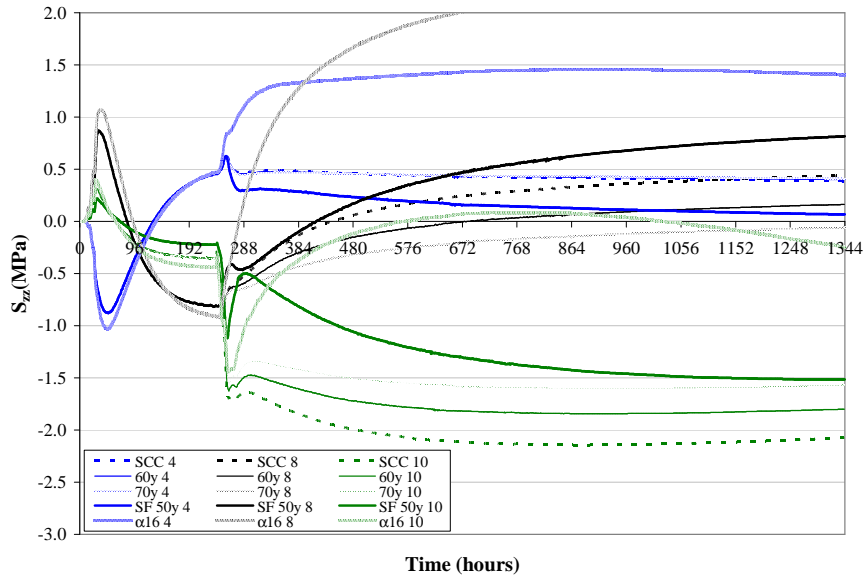


Figure 8.23b: Time graph of S_{zz} with different cooling periods, types of waste and the overpack as macro layer at points 4-8-10

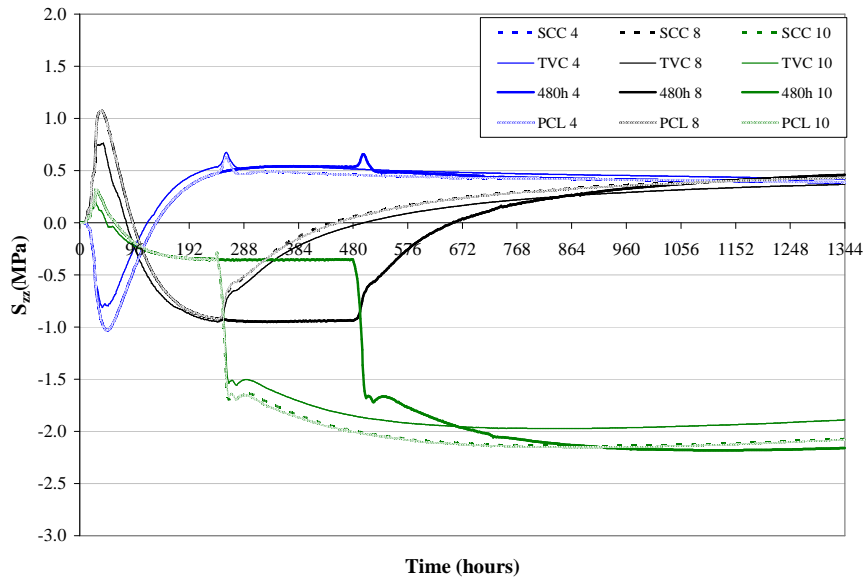


Figure 8.23c: Time graph of S_{zz} with TVC buffer, postponed insertion and precast lid at points 4-8-10

The stresses in the middle of the buffer are not influenced by the preceding cooling period (Figure 8.23b). The buffer, with changed dimensions to be able to insert the SF assemblies, experiences higher tensile stresses in the outer region due to the higher amounts of heat released by the SF compared to the HLW.

Using TVC instead of SCC for the buffer, delaying the insertion time, or considering a precast lid, does not have an effect on the critical tensile stress build-up. In all cases, the outer surface of the buffer experiences tensile stresses with approximate equal values (Figure 8.23c). Also the stresses in the middle of the buffer evolve towards the same comparable value. The compressive stresses near the inner surface, however, are lower in case of a TVC buffer.

Considering the overpack as a macro layer, and not as an environmental boundary condition, higher tangential tensile stresses are noticed in the buffer (Figure 8.23b), especially near the outer surface with a value of 2.2 MPa after 1344 hours. The axial tensile stresses near the outer surface are even higher than the tangential ones (Figure 8.23d), and also a significant difference is noticeable in case the overpack is considered as a boundary layer (Figure 8.23e, grey lines). Due to the expansive behaviour of the overpack, in radial and axial direction (higher deformation in axial direction depicted in Figure 8.23d), the buffer is forced to expand: the overpack comes under compression and the buffer comes under tensile stress, especially in axial direction. Therefore, the differences between the simulation cases (Table 8.7) are being discussed for the axial stresses (Figure 8.23e):

- By decreasing the CTE of the steel overpack, the expansion of the overpack is reduced and the tensile and the compressive internal stress build-up decreases.
- Maintaining a longer preceding cooling period (70 years instead of 50 years) also has a beneficial effect on the stress build-up.
- Using carbon steel instead of stainless steel, in combination with a cooling period of 70 years, causes a tensile stress drop from 4.6 MPa towards 2.2 MPa after 1344 hours.
- Applying a sidewise (tangential) force on the buffer does not have a significant effect on the axial stresses. On the other hand, by applying an axial top force (e.g. 2 MPa after 336 hours), a drop in the tensile stress build-up is noticed and can be very beneficial: a stress drop of 1.9 MPa after 1344 hours is registered in point 8. This additional axial compressive stress can be created e.g. by screwing a top plate on the mantle of the steel envelope. This induces an estimated tensile stress inside the mantle of approximately 190 MPa – 320 MPa, for a thickness of respectively 10 mm and 6 mm. The yield strength of stainless steel is 205 MPa, the tensile strength is 515 MPa according to the European Standards EN 10028-1 (2001) and EN 10028-2 (2003).

To evaluate the cracking behaviour of the buffer of the Supercontainer, the stresses are compared with the strength, especially in tensile behaviour. Therefore and once more, the outer surface of the buffer can be seen as the most critical region towards early-age cracking of the buffer.

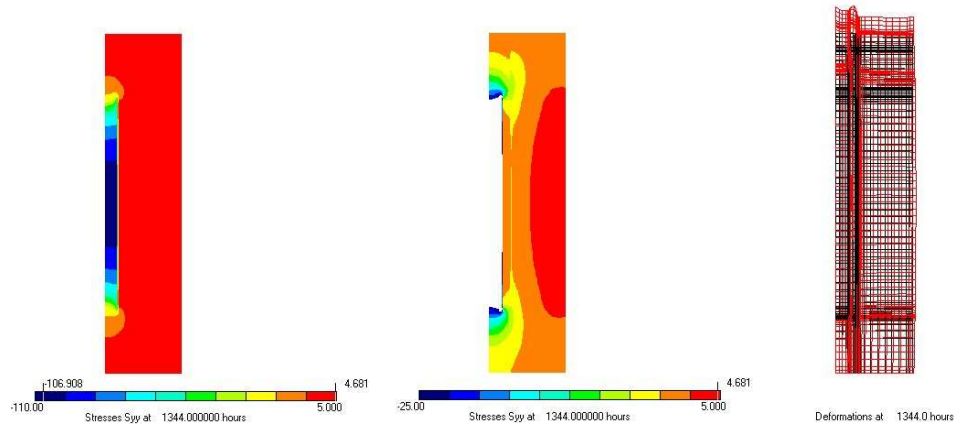


Figure 8.23d: Contourplots of S_{yy} and the deformation mesh at 1344 hours with the overpack considered as macro layer

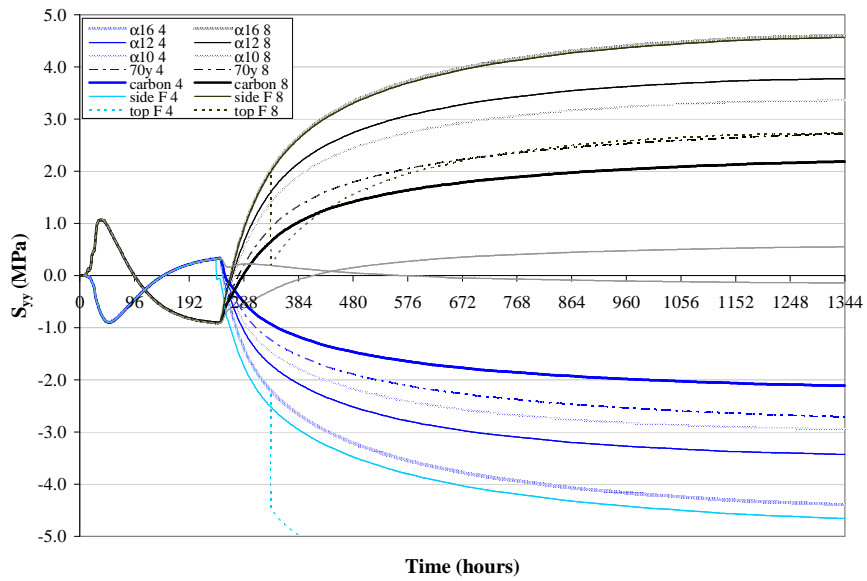


Figure 8.23e: Time graph of S_{yy} in the different simulation cases with the overpack as macro layer at points 4-8

4.3.1.3 Cracking criteria: $S/(0.7 \cdot f_{ct}) < 1$

The maximal stress to strength ratio $S_{zz}/(0.7 \cdot f_{ct})$ is 0.91 (smaller than 1) for the first construction stage of the concrete buffer out of hot cell (Phase 1). The question however is whether the tensile stresses in the buffer, due to the developed thermal gradients (caused by the hydration reaction of the filler and the lid, by the heat originating from the radwaste and by the expandable overpack), the autogenous deformation of the concrete, and taking into account the creep effect, will exceed the tensile strength of the concrete buffer during the fabrication steps in hot cell, giving cause to early-age cracking. Therefore time graphs of the stress to strength ratios $S_{zz}/(0.7 \cdot f_{ct})$ and $S_{yy}/(0.7 \cdot f_{ct})$ are plotted in Figure 8.24a, Figure 8.24b and Figure 8.24c for the different cases (values in Table 8.8). This ratio must remain smaller than one at all times and in all regions, in order to reduce or eliminate the early-age cracking risk [Craeye et al., 2009].

With the overpack as boundary condition, the highest cracking risks in Phase 2 occur near the outer border of the concrete buffer (black lines), due to the thermal gradient between inner and outer surface of the buffer caused by the heat-emitting waste. However, the strength to stress ratio remains much smaller than 1 in all cases, and is higher for the SF cases compared to the HLW cases (Figure 8.24a). Also the cracking risk decreases with increasing preceding cooling period. Moreover, the cracking risk, until the age of 1344 hours, is even higher in the midzone of the buffer (blue line) compared to the outer surface of the buffer, when the cooling period equals 60 years or 70 years (Figure 8.24a). For Phase 2, a slightly higher cracking risk in the middle of the buffer (blue line) is noticed in case a TVC buffer is used (Figure 8.24b). The cracking risk near the outer surface is not changed when the insertion time is postponed, or when a precast lid is considered (Figure 8.24b). After 1344 hours (except for the TVC case in the middle of the buffer), the ratio $S_{zz}/(0.7 \cdot f_{ct})$ has a comparable value in the middle of the buffer and near the outer surface. However, near the outer surface of the buffer, the stresses have the tendency to become more tensile, while the stresses in the middle of the buffer tend to a compressive behaviour.

When the expansive behaviour of the overpack is taken into account, a considerable increase in the tangential cracking ratio $S_{zz}/(0.7 \cdot f_{ct})$ is found (Figure 8.24a), especially near the outer border: a value of 0.71 is found after 1344 hours. However, the stresses in axial direction are even more detrimental for the early-age behaviour of the buffer in hot cell (Figure 8.25c, grey lines give the result with the overpack as boundary condition). In case a stainless steel overpack is inserted, with preceding cooling period of 50 years, there is a high cracking risk of the buffer near the outer surface: $S_{yy}/(0.7 \cdot f_{ct})$ exceeds one after 398 hours and equals 1.49 after 1344 hours. By decreasing the CTE of the steel overpack, the cracking risk also decreases but still the ratio exceeds one (the time of exceeding increases with decreasing CTE): 1.23 if α_T equals $12 \times 10^{-6}/^\circ\text{C}$, and 1.09 if α_T equals $12 \times 10^{-6}/^\circ\text{C}$ after 1344 hours. By prolonging the preceding waste cooling period, up to 70 years, the ratio drops to 0.88 and in combination with a carbon steel overpack even to a value of 0.71. Applying a top axial force, can induce a cracking risk decrease.

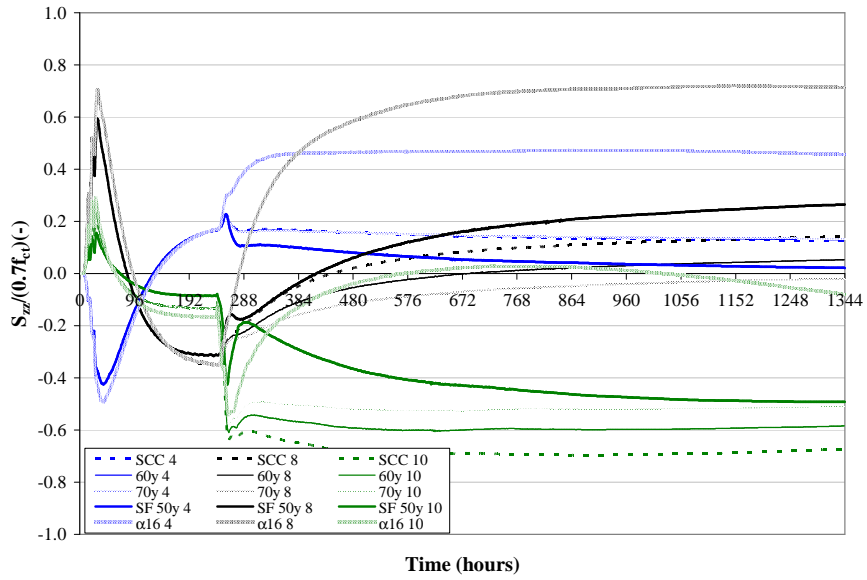


Figure 8.24a: Time graph of $S_{zz}/(0.7 \cdot f_{ct})$ with different cooling periods, types of waste and the overpack as macro layer at points 4-8-10

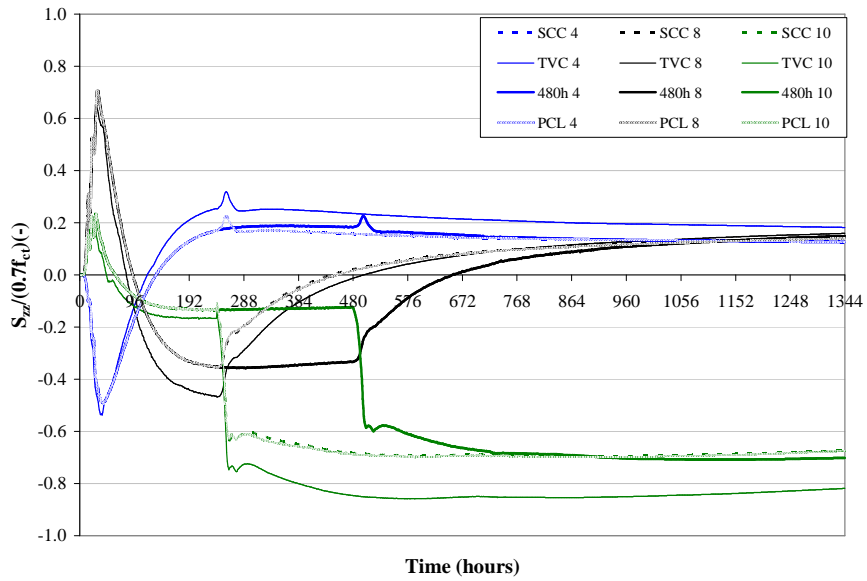


Figure 8.24b: Time graph of $S_{zz}/(0.7 \cdot f_{ct})$ with TVC buffer, postponed insertion and precast lid at points 4-8-10

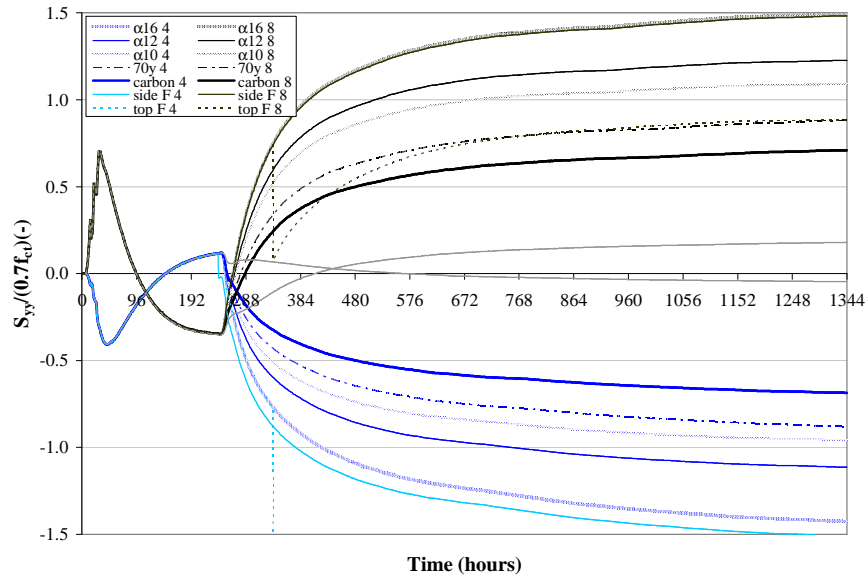


Figure 8.24c: Time graph of $S_{yy}/(0.7 \cdot f_{ct})$ in the different simulation cases with the overpack as macro layer at points 4-8

The eigenstresses that are present in the buffer after Phase 1, the construction stage out of hot cell, counteract the tensile stress build-up in Phase 2, and therefore have a beneficial effect on behalf of the cracking risk.

By considering the overpack simply as an environmental boundary condition, no cracking is expected during the construction stages in hot cell. This will underestimate reality as, due to the temperature elevation caused by the waste, the overpack expands and induces additional stresses (aside from the stresses caused by the heat) into the concrete buffer. In case a stainless steel liner is used, tangential cracks (due to axial stresses) can be expected near the outer surface of the buffer. To overcome early-age cracking, it is advised that carbon steel is used for the overpack, and that the preceding cooling period of the waste is sufficiently long enough (preferably 70 years). Also the appliance of a top force can induce compressive stresses that counteract the tensile stresses in the buffer and reduce the cracking risk. Taking into account the detrimental effect of heat (strength loss up to 20 %) or gamma radiation (strength loss up to 15 %) on the strength of the concrete, as mentioned in Chapter 7, the surplus of strength is high enough to exclude early-age cracking caused by the heat originating from the waste, in case a carbon steel overpack is used in combination with a cooling period of 70 years. In that case $S_{yy}/(0.7 \cdot f_{ct})$ equals 0.71 after 1344 hours, so a surplus of approximately 29 % is available.

After visual inspection of the HC of the Half-Scale Tests (Chapter 9, a seamless carbon steel overpack is used), a criss-cross cracking pattern developed and is identified on the outer surface of the buffer during the heating of the buffer. Especially main tangential macrocracks, caused by the axial stresses, can be distinguished (Figure 8.25), giving confidence in the previously obtained simulation results.



Figure 8.25: A network of cracks appearing in the HC, black lines are the main tangential cracks, blue line is the casting joint (Chapter 9)

4.3.1.4 Displacement U_x

The displacement U_x of the concrete near the outer border and the inner border of the buffer can be simulated by means of HEAT/MLS. A picture of the deformed mesh after 1344 hours and a contourplot at 264 hours and 336 hours are given for the reference casting case (Figure 8.23a, bottom). Once the heat-emitting waste is inserted and the Supercontainer is closed, the buffer expands in radial direction and in axial direction due to the heat originating from the waste. In case the expansion of the overpack is also taken into account, additional radial displacements are registered (Figure 8.26a). In that case, there is also a considerable axial displacement and deformation registered on top of the Supercontainer (Figure 8.23d, right). These axial displacements are considerably higher than the radial displacements.

The radial displacement is higher for the SF case and in case of a shorter preceding cooling period, and is also higher near the outer surface compared to the radial displacement of the inner surface (Figure 8.24a). Using TVC instead of SCC for the

buffer material, leads towards slightly higher radial displacements, especially near the outer surface (Figure 8.24b). The use of a PCL does not affect the expansive nature of the buffer. Finally, by deferring the insertion, the radial displacement evolves towards an identical value after a certain amount of time (Figure 8.24b).

Due to this expansive nature of the concrete buffer, and due to the presence of an outer stainless steel liner, which is not considered as a kinematic boundary condition in the HEAT/MLS simulations, additional compressive stresses will be introduced into the concrete near the outer surface. These compressive stresses counteract the tensile stress build-up and therefore have a beneficial effect towards the early-age cracking risk. For the case where the overpack is considered as an expandable macro layer, additional compressive stresses can be induced into the buffer due to the hindering of the axial expansion by the presence of a screwed top plate. This can lead towards a reduction of the tensile stresses in the buffer and towards a lowering of the cracking risk.

Once more, the stainless steel envelope can be seen as an additional safety barrier against early-age cracking of the buffer due to the additional introduced compressive stresses.

Table 8.8: Summary of the temperature near the inner surface of the buffer (point 10) and of the tensile cracking ratio and the radial displacement near the outer surface of the buffer (point 8) after 1344 hours

	T_{\max} °C	$S_{zz}/(0.7 \cdot f_{ct})$ -	U_x mm
REF 50 y	43.81	0.142	0.085
60 y	38.96	0.053	0.067
70 y	35.14	-0.019	0.053
SF 50 y	45.52	0.265	0.116
TVC 50 y	43.02	0.159	0.087
PCL 50 y	43.81	0.140	0.084
Insert 480 h	42.72	0.149	0.079
	T_{\max} °C	$S_{yy}/(0.7 \cdot f_{ct})$ -	U_x mm
$\alpha 16$	68.77	1.494	0.174
$\alpha 12$	68.77	1.226	0.176
$\alpha 10$	68.77	1.091	0.177
70 y	51.75	0.886	0.112
carbon	51.75	0.710	0.113
side F	68.77	1.483	0.059
top F	68.77	0.885	0.190

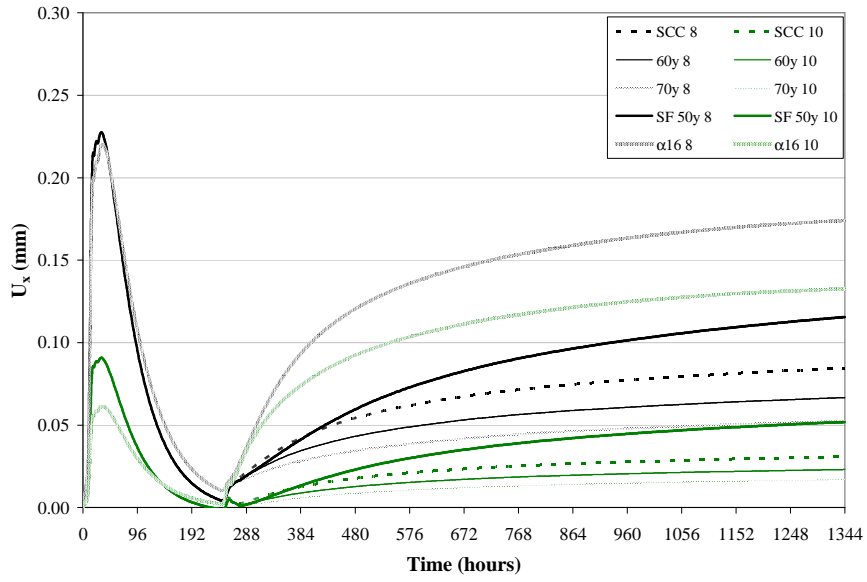


Figure 8.26a: Time graph of U_x with different cooling periods, types of waste and the overpack as macro layer at points 8-10

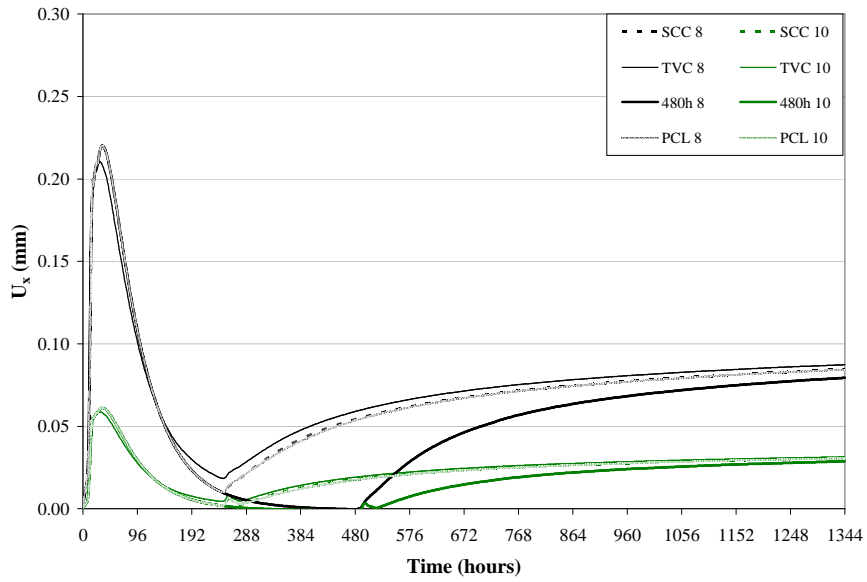


Figure 8.26b: Time graph of U_x with TVC buffer, postponed insertion and precast lid at points 8-10

4.3.2 Early-age behaviour of the filler and the lid

4.3.2.1 Temperature T

By means of time graphs in different points given in Figure 8.21, the temperature development inside the concrete filler and the concrete lid of the Supercontainer is presented (Figure 8.27). A two-step temperature elevation is noticed, devoted to two main mechanisms: the hydration reaction of the freshly cast filler and lid, and the heat originating from the overpack containing the waste.

Due to the hydration reaction of the SCC filler, the temperature in this concrete layer increases. When the hydration peak is over (approximately 24 hours after casting), the preceding drop in the curve is counteracted by a temperature increase due to the heat originating from the heat-emitting waste. After 1344 hours the temperature near point F2 is 47.8 °C (overpack as boundary condition) and will increase further on until the HLW stops spreading its heat to the environment. When the overpack is considered as a macro layer, the temperature increase is much higher in point F2: 76.6 °C after 1344 hours (Figure 8.27). In that case, the temperature peak due to the hydration peak is no longer noticeable.

Also the lid experiences a temperature increase due to the hydration reaction of the hardening SCC with its peak appearing between 256 hours (near the outer border) and 268 hours (in the middle of the lid). Afterwards, a decrease in temperature is registered, followed by an increase in temperature: the heat originating from the waste settles in. The further away from the heat source, the longer it takes for the temperature to increase once more and the smaller the temperature increase will be (e.g. point L1 compared to point L4). When a precast lid is used, no hydration reaction occurs, so the first temperature peak is not appearing (note that the small peak in point PCL1 is due to the hydration reaction of the nearby filler). Nevertheless, the temperature curves of the PCL evolve towards the same values as for a freshly cast lid. In case of a macro layer overpack, the temperature peak due to hydration remains unaltered, but afterwards, the temperature evolves to a higher value: e.g. 35.7 °C (overpack as macro layer) compared to 26.4 °C (overpack as boundary condition) in point L3 (Figure 8.27).

Finally, it is clear that the temperature increase in the filler, in the direct environment of the heat-emitting waste, is significantly higher than the temperature increase in the lid. In case the overpack is implemented into the model as a macro layer, higher temperatures occur.

4.3.2.2 Stresses S_{zz}

After insertion of the overpack and direct filling of the remaining annular gap by means of a fresh SCC filler, the exothermal hydration reaction starts, and the SCC filler has the tendency to expand. However, this movement is prevented by the surrounding buffer, explaining the compressive stress increase in the filler, the first hours after casting (Figure 8.28a): S_{zz} is approximately -0.85 MPa after 256 hours. Once the hydration peak is over, the retrieval of the SCC filler is prevented, and the SCC comes

under tension: S_{zz} is approximately 0.89 MPa after 284 hours. Finally, the heat-emitting waste causes the expansive behaviour of the SCC filler, which is once more prevented by the surrounding buffer: compressive behaviour sets in. Note that the axial and radial stresses give no cracking risk in the filler and the lid.

When the expansion of the overpack is also considered, a comparable behaviour settles in, but with altered values. The first compressive peak in the filler evolves to -1.28 MPa after 255 hours (Figure 8.28b). A higher value is obtained due to the combination of the prevention of the deformation by the surrounding buffer and the expansive nature of the overpack. Afterwards, a tensile stress build-up is noticed with a peak of 2.08 MPa after 615 hours, evolving towards compressive behaviour.

For the freshly cast lid, identical behaviour can be found: (i) compression due to the hydration heat, (ii) tension due to cooling after the hydration peak and (iii) compression when the heat, originating from the overpack, settles in. Except for the middle of the buffer (point L3) and near the filler (point L1) this behaviour is less pronounced for the lid compared to the filler. The first compression peak in point L1 has a value of -0.92 MPa after 256 hours, the tensile stress peak is approximately 1.03 MPa after 408 hours in point L3. In case of a PCL, near the outer border (point PCL4) and the top (PCL6) of the buffer, there is a tensile stress build-up, going towards a value of 0.68 MPa after 1344 hours. In the middle of the PCL and near the filler, a compressive stress development sets in: -1.99 MPa after 1344 hours.

Once more, an identical behaviour of the lid is found in case the overpack's expansion is included. An increasing tensile stress build-up is registered with a value of 2.52 MPa after 1344 hours (stainless steel overpack) in point L6. By using a carbon steel overpack instead, this value drops to 1.20 MPa.

4.3.2.3 Cracking criteria: $S_{zz}/(0.7 \cdot f_{ct}) < 1$

It is evaluated whether the created internal stresses are detrimental and whether the filler and the lid are susceptible to early-age cracking. Therefore, the critical tensile stress to strength ratio $S_{zz}/(0.7 \cdot f_{ct})$ must remain smaller than one at all times, which is the case (Figure 8.29a, Figure 8.29b). No early-age cracking is expected in the filler and the lid of the Supercontainer. The stresses in axial and in radial direction are significantly low enough in tensile nature to be neglected.

The maximal value of $S_{zz}/(0.7 \cdot f_{ct})$ in the filler equals 0.63 after 277 hours near point F1, due to the cooling and the retrieval of the filler after the hydration peak (overpack as boundary condition). Considering the expansion of the overpack leads towards a maximal value 0.69 after 276 hours. There is a sufficient and safe buffer to come to the non-cracking postulate, even keeping in mind the possible strength loss (up to 20 %) due to heat and irradiation effects (Chapter 7). When the heat of the waste reaches the filler layer, the SCC comes under compression, thus no cracking is expected at all from that time on.

The maximal value of $S_{zz}/(0.7 \cdot f_{ct})$ in the freshly cast lid equals 0.48 after 278 hours near point L4, which is also low enough to exclude cracking, even taking into account the possible strength loss (up to 20 %) due to elevated temperatures (Chapter 7). In the PCL, the $S_{zz}/(0.7 \cdot f_{ct})$ ratio increases with time in points PCL4 and PCL6. The maximal value after 1344 hours is 0.24. Including the expansion of the stainless steel overpack causes a continuous increase of the cracking risk: $S_{zz}/(0.7 \cdot f_{ct})$ equals 0.82 in point L6 after 1344 hours. Using carbon steel as the material for the overpack instead, decreases the peak value: 0.39 after 1344 hours (Figure 8.29b).

The cracking risk due to the heat of hydration in the filler and the freshly cast lid is sufficiently small to be able to exclude cracking. However, on a longer term (> 1344 hours), and when the influence of the emitted heat by the waste is sensed by the filler and the lid, there is an increasing tensile cracking risk in case of a PCL and especially in case stainless steel is being used as the overpack's material.

4.3.2.4 Displacement U_x

Except for the expansive radial displacement peak near point L4 (Figure 8.30), which is also noticed in Figure 8.22a (U_x after 264 hours) and with a maximal value of 96 μm after 259 hours, the radial displacement of the filler and the lid of the Supercontainer is sufficiently small enough to be neglected. The PCL experiences a greater expansive radial displacement compared to the freshly cast lid, with values approaching 0 mm after 1344 hours.

When the expansion of the overpack is also taken into account, higher radial (and axial!) displacement are found: 146 μm after 1344 hours in point F2. The displacement in point L4 also evolves towards a higher value once the hydration peak is over and the heat originating from the waste settles in.

4.3.3 Insertion of the radwaste in hot cell: main conclusions

For the simulations of the construction stages of the Supercontainer in hot cell, i.e. insertion of the heat-emitting waste, directly followed by placement of the filler and the lid, two types of simulations are being considered: (i) the overpack is simply seen as an environmental boundary condition with its typical convective heat transfer coefficient (5.59 $\text{W}/(\text{m}^2 \cdot ^\circ\text{C})$) and a temperature curve (according to [Weetjens and Sillen, 2007]) is attached to this boundary, or (ii) the overpack is implemented into the model as an expandable macro layer, with its specific mechanical and thermal properties and with the same temperature curve attached to the macro (not only to the interface with the filler). This explains the obtained higher temperatures via the second simulation method. Two internal stress creating mechanisms are present in the first simulation method: (i) the hydration heat of the hardening filler and the hardening lid, and (ii) the heat originating from the radwaste. For the second simulation method, a third mechanism settles in: (iii) the expansion of the overpack due to the temperature elevation.

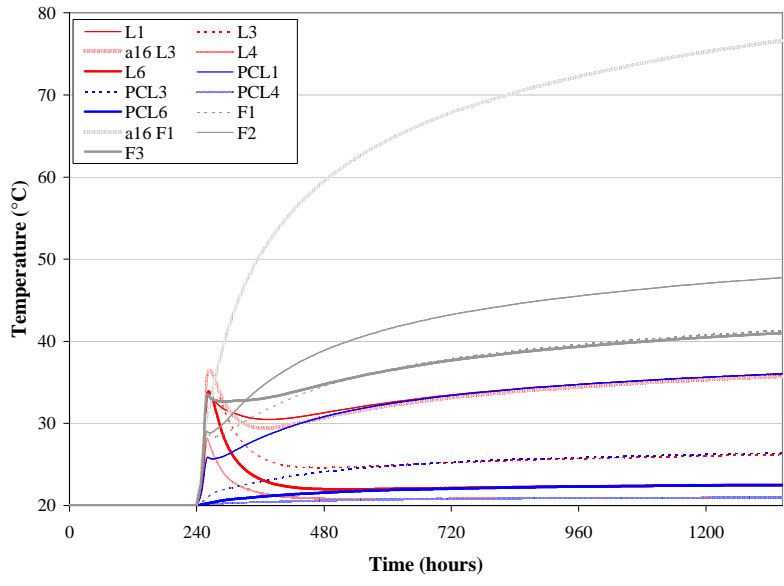


Figure 8.27: Time graph of the temperature in the filler and in the lid

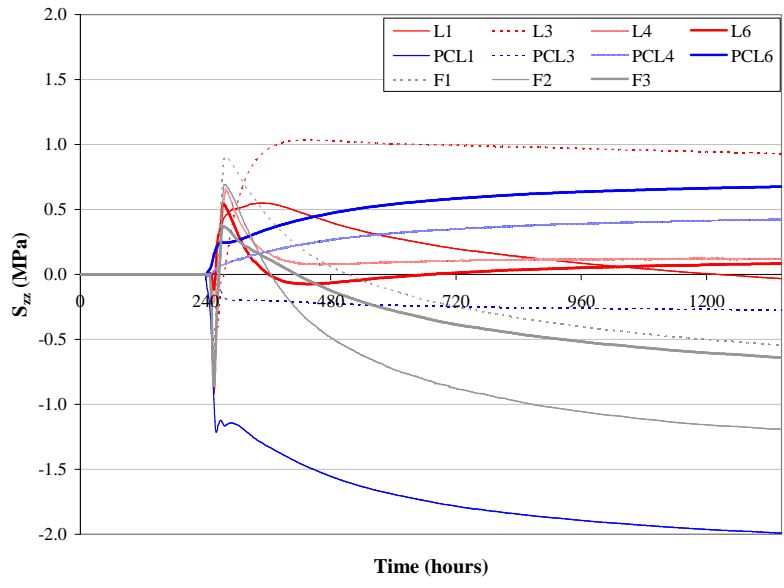


Figure 8.28a: Time graph of S_{zz} in the filler and in the lid (overpack as boundary condition)

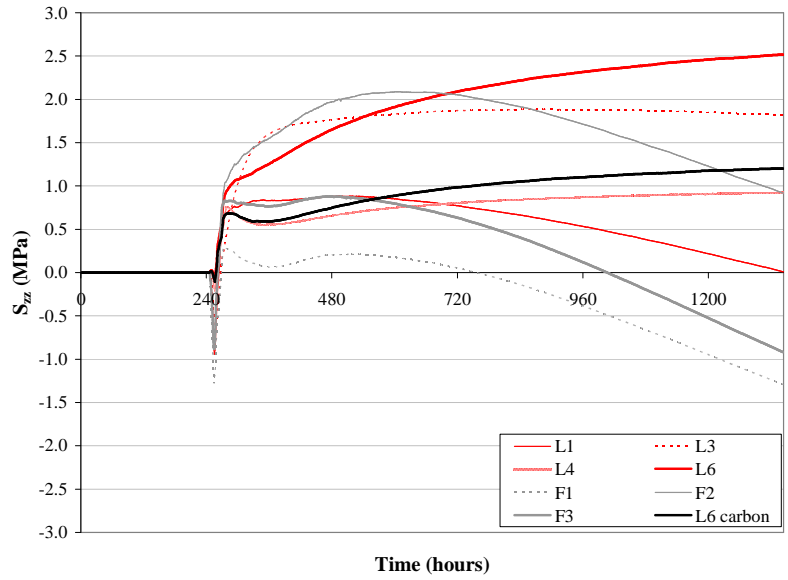


Figure 8.28b: Time graph of S_{zz} in the filler and in the lid (overpack as macro layer)

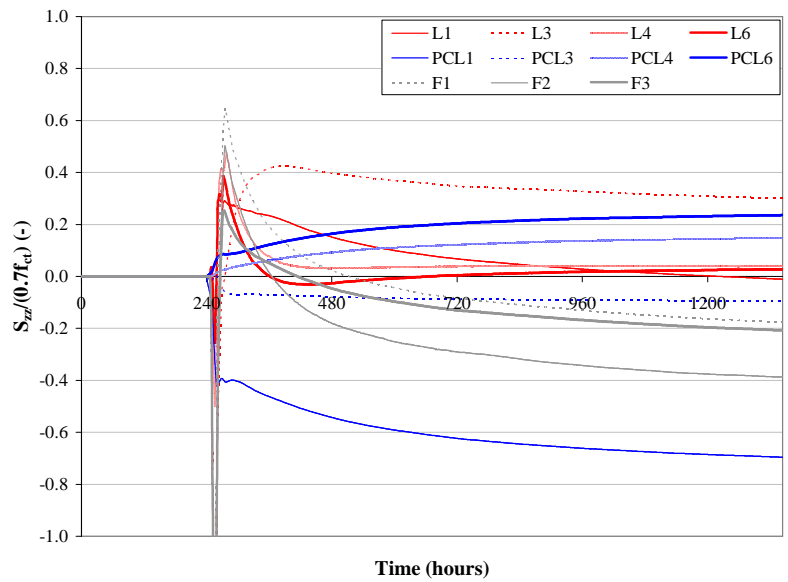


Figure 8.29a: Time graph of $S_{zz}/(0.7f_{ct})$ in the filler and in the lid (overpack as boundary condition)

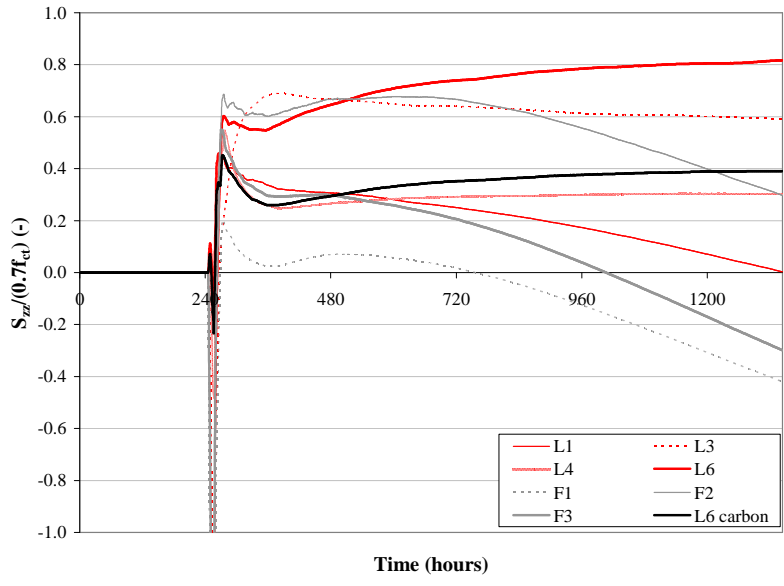


Figure 8.29b: Time graph of $S_{zz}/(0.7f_{ct})$ in the filler and in the lid (overpack as macro layer)

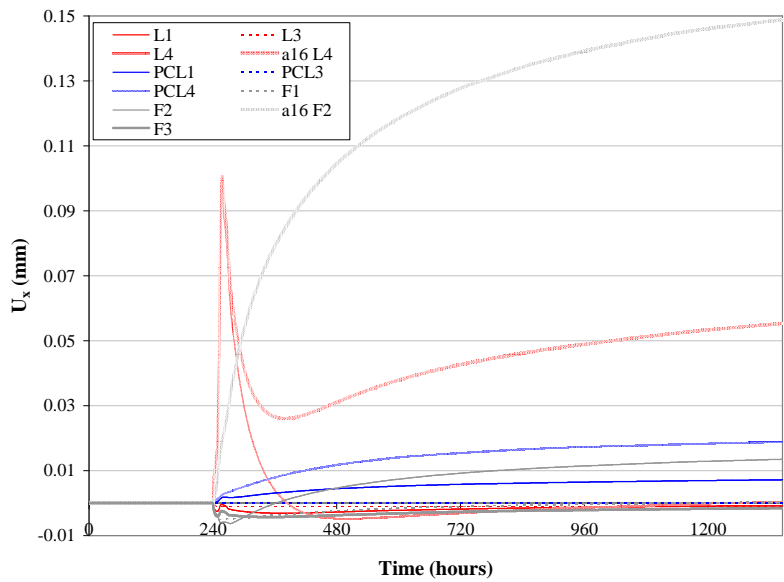


Figure 8.30: Time graph of U_x in the filler and in the lid

Using the first simulation method, and thus leaving the expansive behaviour of the overpack out of consideration (underestimating reality), several conclusions can be drawn:

- The eigenstresses that are present in the buffer after Phase 1, the construction stage out of hot cell, counteract the tensile stress build-up in Phase 2, and therefore have a beneficial effect on behalf of the cracking risk.
- The highest cracking risk is mainly due to the tangential stresses (causing axial cracks) and axial stresses (causing tangential cracks) near the outer border of the buffer. However, no early-age cracking is expected in all cases.
- The cooling period of the HLW or the SF assemblies preceding the insertion into the buffer, has a significant effect on the heat release into the buffer afterwards. The longer the cooling period, the lower the cracking risk will be.
- The cracking risk of the Supercontainer for the disposal of SF assemblies is higher, mainly due to the higher thermal output of the SF.
- Using a TVC buffer instead of SCC, delaying the insertion time or using a PCL instead of a freshly cast lid, does not have an effect on the early-age cracking risk of the buffer.

Simulations indicate that due to the use of an expandable stainless steel overpack, early-age tangential macrocracks appear near the outer surface of the buffer. This expansive nature of the overpack, can be seen as the most detrimental effect, causing early-age cracking of the buffer during the construction stages in hot cell. Several conclusions and experiences can be drawn from the simulations via the second simulation method, with the expansion of the overpack taking into consideration:

- By reducing the CTE of the overpack, the expansive behaviour of the overpack reduces, smaller stresses are induced into the buffer and the cracking risk also reduces significantly. Therefore, on a pure thermo-mechanical matter, it is better to use carbon steel (α_T equals $12 \times 10^{-6}/^{\circ}\text{C}$) instead of stainless steel (α_T equals $16 \times 10^{-6}/^{\circ}\text{C}$).
- Once more, the beneficial effect of a cooling period that is sufficiently long enough is proved and is necessary to reduce the thermal output of the radwaste and to avoid early-age cracking. A smaller thermal output leads towards a smaller thermal expansion of the overpack. A cooling period of 70 years is highly recommended.
- The ideal situation to overcome early-age cracking after insertion of the radwaste is obtained by using a carbon steel overpack in combination with a cooling period of 70 years. In that case, the surplus of strength is high enough to exclude early-age cracking even taking into account the detrimental effect of heat (strength loss up to 20 %) or gamma radiation (strength loss up to 15 %) on the strength of the concrete.
- The filler material does not suffer from an early-age cracking risk. The material is entrapped between the hardened concrete buffer and the expanding overpack, thus comes under compression. In case of a carbon steel overpack, no cracks are expected in the lid. After visual inspection of the HC, using a carbon steel overpack (Chapter 9), no macrocracks are found in the lid.

Finally, a precast lid does not provide additional advantageous compared to a freshly cast lid.

- The beneficial use of the outer stainless steel envelope is once more indicated: due to the internal temperature elevation of the buffer, an axial and a radial displacement is registered. By preventing these deformations, additional beneficial compressive stresses are induced into the buffer, which counteract the tensile stress build-up. For example, by screwing a plate on top of the mantle (for the final closure of the Supercontainer), additional axial compressive stresses can be induced into the concrete layer of the Supercontainer, preferably lower than 2 MPa, in order to avoid exceeding of the yield strength of the stainless steel envelope.
- Finally, it can be advised to propose and investigate another type of filler material, with the ability to take on or counteract the expansion of the overpack, in such a way that the stress build-up transfer towards the outer surface of the buffer is minimized. For example, by reducing the modulus of elasticity of the SCC filler material ($E_{c,filler}$), the cracking risk becomes smaller, with a greater reduction in case of higher CTE values (Figure 8.31). In case the CTE of the overpack is $10 \mu\text{m}/\text{m}/^\circ\text{C}$, a reduction of $E_{c,filler}$ to an approximate value of 18.75 GPa is sufficient for the cracking ratio $S_{yy}/(0.7 \cdot f_{ct})$ to become smaller than one. Advanced analysis is subject for further research.

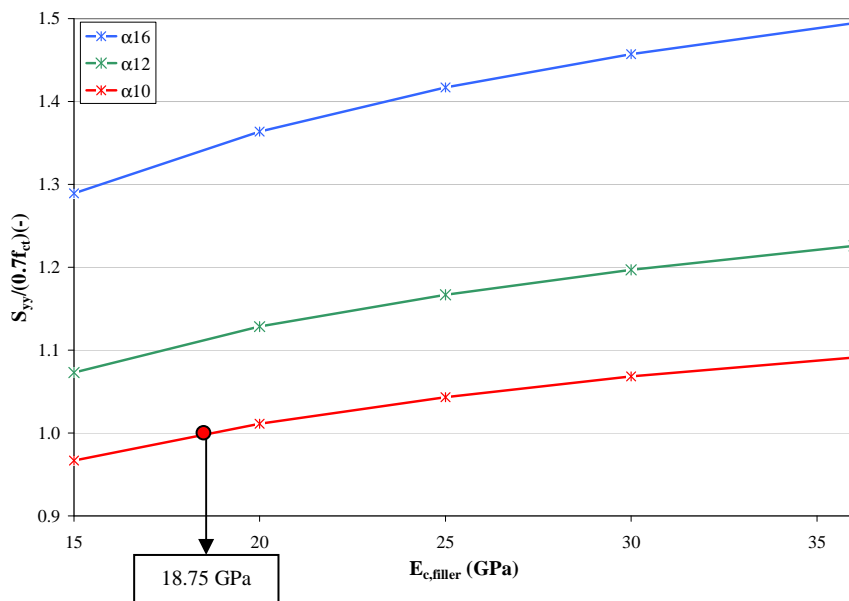


Figure 8.31: Sensitivity analysis – Influence of altered modulus of elasticity of the SCC filler on the cracking risk ratio $S_{yy}/(0.7 \cdot f_{ct})$, with altered CTE, in point 8 after 1344 hours

5 Conclusion

For the reference casting case of the construction step out of hot cell, no early-age macrocracking of the buffer is expected. The thermal gradient between the middle of the buffer and the outer surface of the buffer is the mainspring behind the early-age cracking. By adapting the concrete composition (e.g. concrete with better thermal conductivity), the dimensions of the buffer (e.g. the thickness of the mantle) or the environmental boundary conditions (temperature, wind, e.g. by placing a wind shield or by providing insulation), the cracking risk can be reduced.

Once the hydration peak is over, the created internal stresses remain present in the buffer as eigenstresses, that can counteract the expected stress elevation due to insertion of the radwaste.

During the construction stages in hot cell, a considerable cracking risk exists even taking into account the beneficial behaviour of the eigenstresses present in the buffer. The main crack creating mechanism can be found in the expansive nature of the carbon steel overpack containing the heat-emitting radwaste. However, early-age macrocracking can be prevented in case decent measures are taken:

- The reduction of the thermal expansion coefficient (CTE) of the overpack containing the radwaste.
- The reduction of the heat emitted by the radwaste, by prolonging the preceding cooling period (up to 70 years).
- The reduction of the modulus of elasticity of the filler material.
- The appliance of beneficial stresses by remaining the presence of the stainless steel envelope.

References

- Bouniol P. (1998), *Bétons spéciaux de protection*, Rapport CEA BN 3 740, France.
- Briffaut M., Benboudjema F., Torrenti J.-M., Nahas G. (2009), *A new analysis of the restrained ring shrinkage test*, Proceedings of the International RILEM Conference NUCPERF09, Cadarache, France.
- Craeye B. (2006), *Reduction of autogenous shrinkage of concrete by means of internal curing*, Master thesis (in Dutch), Magnel Laboratory for Concrete Research, Ghent University, Belgium.
- Craeye B., De Schutter G., Bel J., Van Humbeeck H., Van Cotthem A. (2007), *Development of a SCC composition for disposal of heat-emitting, radioactive waste in Belgium*, Proceedings of the International RILEM Conference on Self-Compacting Concrete, SCC2007, Ghent, Belgium.
- Craeye B., De Schutter G., Van Humbeeck H., Van Cotthem A. (2009), *Early age behaviour of concrete supercontainers for radioactive waste disposal*, Nuclear Engineering and Design 239, 23-35.
- De Belie N. (2007), *Durability of Concrete*, Magnel Laboratory for Concrete Research, Ghent University.
- De Schutter G., Taerwe L. (1995), *General hydration model for portland cement and blast furnace slag cement*, Cement and Concrete Research 25, 593-604.
- De Schutter G. (1996), *Fundamental and practical study on thermal stresses in massive hardening concrete elements*, Doctoral thesis (in Dutch), Ghent University, Magnel Laboratory for Concrete Research, Belgium.
- De Schutter G., Vuylsteke M. (2004), *Minimization of early age thermal cracking in J-shaped non-reinforced massive concrete quay wall*, Engineering Structures 26, 801-808.
- Geirnaert M. (2009), *Influence of the internal curing on the mechanical properties and cracking behaviour of high strength concrete by using superabsorbent polymers*, Master thesis (in Dutch), Magnel Laboratory for Concrete Research, Ghent University, Belgium.
- Reinhardt H.W., Cornelissen H.A.W. (1985), *Zeistandzugversuche an Beton*, Baustoffe 85, Bauverslag, Wiesbaden, 162-167.
- Robeyst N., Gruyaert E. and De Belie N. (2007), *Ultrasonic and calorimetric measurements on fresh concrete with blast-furnace slag*, Advances in Construction Materials, Springer, Berlin, 497-504.

Rostásy F.S., Krauss M., Budelmann H. (2002), *Planungswerkzeug zur Kontrolle der frühen Rissbildung in massigen Betonbauteilen*, Bautechnik 79, Ernst & Sohn Verlag.

Scrivener K.L., Cabiron J.L., Letourneux R. (1999), *High-performance concretes from calcium aluminate cements*, Cement and Concrete Research 29, 1215-1223.

Taerwe L. (1997), *Concrete Technology*, Course material (in Dutch), Ghent University, Magnel Laboratory for Concrete Research, Belgium.

Van Beek A., Schlangen E., Baetens B.E.J. (2001), *Numerical model for prediction of cracks in concrete structures*, Proceedings of the International RILEM Conference on Early Age Cracking in Cementitious Systems, EAC01, Haifa, Israel.

Weetjens E., Sillen X. (2006), *Thermal analysis of the Supercontainer concept 2D axisymmetric heat transport calculations*, SCK·CEN report, Belgium.

CHAPTER 9:

HALF-SCALE TESTS: VALIDATION OF THE SIMULATION RESULTS

For the validation of the obtained simulation results of the fabrication of the buffer in a steel envelope (Stage 1) and for the evaluation of the construction feasibility of the buffer of the Supercontainer, Half-Scale Tests are performed. The non-cracking postulate in the first construction stage, as the simulations indicate in Chapter 8, needs to be evaluated.

1 Goal and methodology

Therefore, a Half-Scale Container (HC) is cast, at the Magnel Laboratory for Concrete Research, with a reduced height but with an increased diameter in order to be able to insert a heat-emitting overpack into the created opening (Figure 9.1). The concrete buffer has an outer diameter of 2.11 m and a height of 3.45 m. The inner void space is 0.71 m in diameter and has a height of 2.05 m. Finally, the lid has a diameter of 1.11 m and a height of 0.70 m [Areias, 2009]. Four levels can be depicted (level A to level E) at different heights. Considering the bottom of the buffer as the reference base, level A is situated at 0.35 m, level B at 0.70 m, level C at 1.75 m, level D at 2.75 m and level E at 3.45 m from the base (Figure 9.1, left).

Note that the term ‘Half-Scale’ originates from the original plans of casting a container, identical to the Supercontainer in thickness and in diameter, but with a height that is 50 % of the height of the Supercontainer. Nevertheless, the height is increased, due to the additional tests that are planned and performed on the container: insertion of a heat-emitting overpack, filling of the gap, closure of the lid and quality determination of the interface between the filler, the buffer and the cylindrical metal overpack. The additional tests are not presented in this doctoral research, but are subject for further analysis in the nearby future.

For the Half-Scale Container (HC), Self-Compacting Concrete is considered as the reference concrete. A considerable amount of concrete is needed for the casting of the HC: 10.575 m³ of SCC is needed to cast the buffer. Therefore, the concrete factory NV

Charles Kesteley is asked to deliver the SCC. Kesteley has two concrete mixers with a capacity of 2 m³, and limestone aggregates are available at the site. In total nine batches of 2 m³ are made: two trial batches (TB1 and TB2) of 2 m³, six final batches (FB1) of 2 m³ to cast the buffer, and one remaining batch (FB2) for the filling of the annular gap between the overpack and the buffer and the closure of the HC by means of the lid after the insertion of the heat-emitting overpack (containing no radioactive material).

During mixing and after transport to the Magel Laboratory for Concrete Research, fresh SCC tests are performed in order to evaluate the workability of the fresh mix. Once the buffer is cast, several parameters are measured by means of monitoring equipment [Areias, 2009] during hardening at the different levels in order to validate the simulation results (Table 9.1). Two parameters are very important for the implementation of the boundary conditions in the simulations:

- The environmental temperature T_{in} inside the created opening and the temperature T_{out} around the HC, measured by means of thermocouples (TC).
- The outer wind velocity W_{out} in the vicinity of the buffer, measured by means of two anemometers (ANE). Also the relative humidity (RH) is registered. Inside the opening, the wind velocity is assumed to be non-existent.

Three parameters can be verified by means of the simulations results obtained via HEAT/MLS:

- Temperature measurements at the different levels in the HC (Figure 9.1, left), performed by means of thermocouples.
- Also the displacement (radial and axial) and the deformation (radial, axial and tangential) are registered by means of LVDT's and strain gauges (SG). The displacement and the deformation of the steel envelope, that acts as the formwork, is registered. After demoulding, the displacement and the deformation of the concrete buffer is measured.

Finally, compressive strength tests are performed (on cast cubes and on cores taken out of the HC) to evaluate the strength development.

Table 9.1: Monitoring parameters, instrumentation and location of the Half-Scale Tests [Areias, 2009]

Parameter	Location			Instrumentation
	Ambient	Formwork	Buffer	
Temperature	x		x	Thermocouple
Wind velocity	x			Anemometer
Relative humidity	x			Humidity probe
Displacement		x	x	LVDT
Deformation		x	x	Strain gauge

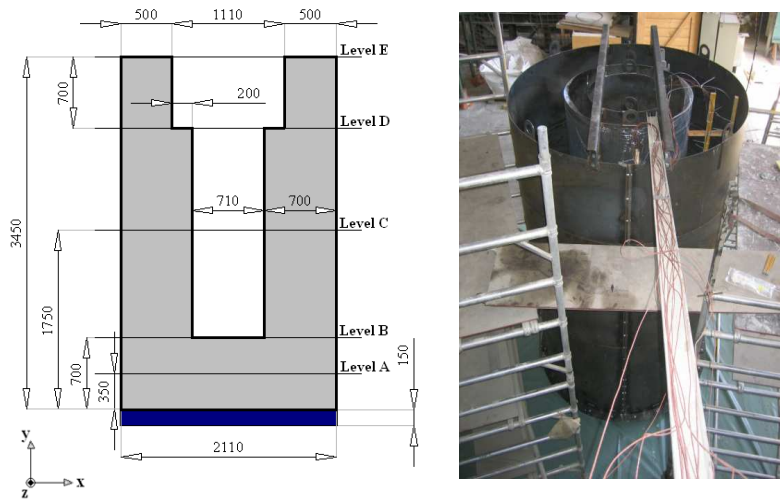


Figure 9.1: The dimensions of the Half-Scale Container (in mm) (left) and set-up of the steel envelope, the inner formwork and the instrumentation (right)

Table 9.2: Time table of the mixing, transport and pumping procedures of the final batch (FB1) (values in hours)

	Mixing		Transport		Pumping	
	Start	End	Depart	Arrival	Start	End
Mix 1	0.00	0.75				
Mix 2	0.80	1.20				
Mix 3	1.30	1.63	1.80	2.13	2.35	2.53
Mix 4	2.01	2.22				
Mix 5	2.27	2.48				
Mix 6	2.53	2.73	3.07	3.48	3.65	3.90

2 Test set-up

2.1 Mixing, casting-pumping and hardening procedure

SCC, with composition previously mentioned in Table 5.3 (Chapter 5), experimentally tested (Chapter 6) and used as reference concrete for the simulations (Chapter 8), is used for the casting of the buffer of the HC. Contrary to the laboratory tests, where mixers with a capacity of 0.05 m³ or 0.2 m³ are used, mixers with a high capacity (up to 2 m³) are needed to be able to deliver the desired amount of fresh SCC for the casting of the HC (10.575 m³ of SCC is needed to cast the buffer).

In order to obtain this amount of fresh SCC, the concrete factory NV Charles Kesteleyn in Ghent is approached.



Figure 9.2: The concrete mixer with a capacity of 2 m³ (left) and the mixing operation tower with the conveyer belt for transportation of the aggregates (right) at the Kesteleyn concrete factory

For each mix of 2 m³, the same procedure is followed according to Figure 9.3:

- First, the limestone aggregates with sizes 0/4 – 2/6 – 6/14, present at the site of Kesteleyn, are transported to the aggregate silos in the mixing operation tower by means of conveyer belts (Figure 9.2, right). Because the aggregates are exposed to the ambient weather conditions, the water content (WC) is determined on a sample ($M_w = \pm 1 - 5$ kg) from the aggregate piles present at

the site. The aggregates are dried in an oven at 105 °C until a constant mass M_d is reached. The water content is found by using equation (9.1).

$$WC = \frac{M_w - M_d}{M_d} \cdot 100 \% \quad (9.1)$$

- The cement used for the SCC composition (CEM I 42.5 N HSR LA LH) is present in a silo of the mixing tower, and also water is available. Because of the lack of an available silo, the limestone filler (LF) needs to be added manually to the concrete mix, as well as the superplasticizer (SP).
- In a second step, the amount of the different components is weighed: first the limestone sand 0/4 is weighed and stored on a weighbridge and secondly the same procedure is followed for the coarse aggregates 2/6 and 6/14. Finally the cement and the water are also weighed separately.
- For the mixing procedure, successively the aggregates, the cement and the water are poured into the concrete mixer (Figure 9.2, left) and the mixing starts. Simultaneously, limestone filler is added manually (eight bags of 25 kg / 2 m³) to the concrete mix. Once the LF adding operation is finished, 20 kg / 2 m³ SP is added to the mix and mixing continuous for another 3 minutes. Afterwards, a slump flow test is performed to define the flow ability of the mix. A minimal SF of 650 mm is desired in order to have a good flow ability. If this value is not achieved, a stepwise procedure is followed: first, an additional amount of 2 kg / 2 m³ SP is added and mixing continues for another 2 minutes, until the SF value is sufficiently high (650 kg/m³) or until a maximal amount of 14 kg/m³ is added to the mix. If in that case, the SF is still unsatisfactory (< 650 mm), additional amounts of water (at each step: 10 kg / 2 m³ is inserted) will be added and an additional mixing time of 60 seconds is followed until the flow ability is sufficiently high.
- Once the flow ability of the SCC is satisfactory and the SF has a minimal value of 650 mm, the batch is dropped into a mobile concrete mixer, and the VF and the SF values are determined once more. Afterwards, the concrete is transported to the Magnel Laboratory for Concrete Research.

For the trial batches (TB1 and TB2), the SCC is cast into a prismatic formwork and tests are applied in order to characterize the fresh SCC composition (Figure 9.4). Cubes are cast in order to characterize the compressive strength and the splitting tensile strength of the SCC mix. For the final batch (FB1), the SCC is made in two portions: first 3 x 2 m³ is mixed, transported and pumped into the steel formwork of the HC. Meanwhile, the remaining SCC amount of 3 x 2 m³ is mixed at Kesteleyn and follows the same transport and transfer procedure (time table given in Table 9.2). Overall, the pumping of the HC is performed in two separate batches of 6 m³ (time between start of the casting: 1.3 hours). During pumping, a flexible hose is lowered to the base of the formwork and lifted upwards during casting of the buffer until the formwork is filled entirely (Figure 9.5).

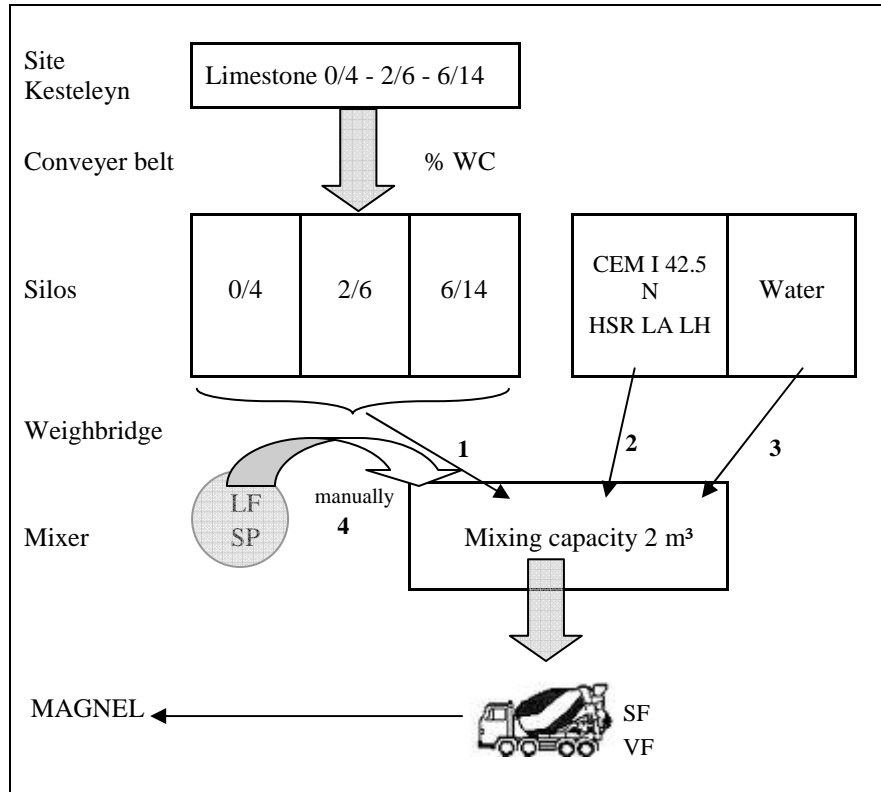


Figure 9.3: The procedure of making an SCC batch of 2 m³

The mould consists of a cylindrical formwork, an inner cylinder and a bottom slab (Figure 9.1, right), and is designed for the use in an upright position to avoid the need to handle the formwork and the buffer, once installed and cast [Areias, 2009]. The cylindrical formwork of the HC is made of stainless steel, consists of two outer-wall sections and has a thickness of 6 mm. Other dimensions are given in Figure 9.1 (left). The steel bottom plate supporting the formwork at its base is also made of stainless steel with a thickness of 12 mm, supported on its side by means of three I-shaped beams resting on a concrete floor (Figure 9.7, left). The beams have a height of approximately 15 cm and are foreseen to facilitate transport of the HC after completion of the tests. The cylindrical formwork is attached to the steel bottom plate by means of twenty-six right angle brackets uniformly placed over the diameter of the cylindrical formwork, on the upper side welded to the formwork and at the bottom side attached to the bottom plate by means of bolts (Figure 9.7, right). In order to create the opening into the buffer of the HC needed to install the heating source and the filler, a stainless steel spill is used, supported by two C-shaped beams, resting on the cylindrical stainless steel formwork (Figure 9.1, right). The spill has a tapered shape to enable removal of the formwork after casting. Also an adhesive plastic foil and demoulding oil

is applied on the spill to facilitate the demoulding operations. Note that a wind shield is placed around the site in order to reduce the detrimental effect of wind on the internal stress creation (Figure 9.5, right), as mentioned in Chapter 8. A plastic sheet (1 mm thickness) covers the free casting top surface of the HC during the first 68 hours (Figure 9.10).



Figure 9.4: Casting SCC in a prismatic formwork (left) and making cubic test samples (right)

Once the casting and pumping is finished, registration of the test set-up starts 4.03 hours after the first mix has started (Table 9.2), by means of monitoring equipment: temperature, wind and RH measurements around and in the buffer (Table 9.1). Note that the first 168 hours after casting, strain gauge deformations of the steel formwork are registered and also the deformation in radial direction of the formwork is determined by means of LVDT's placed on the cylindrical formwork. After approximately 168 hours, the steel spill is lifted and taken out of the created opening (Figure 9.6, left) and SG's and LVDT's are placed on the inner concrete surfaces. The stainless steel formwork is removed after approximately 696 hours (29 days) in order to evaluate whether cracks on the outer surfaces are present or not (Figure 9.6, right). Strain gauges are glued on the inner void space (after 168 hours) and on the top surface of the concrete buffer (after 68 hours) at different levels (see further) and also LVDT's are placed in those regions to register the radial and axial displacement of the concrete buffer of the HC.

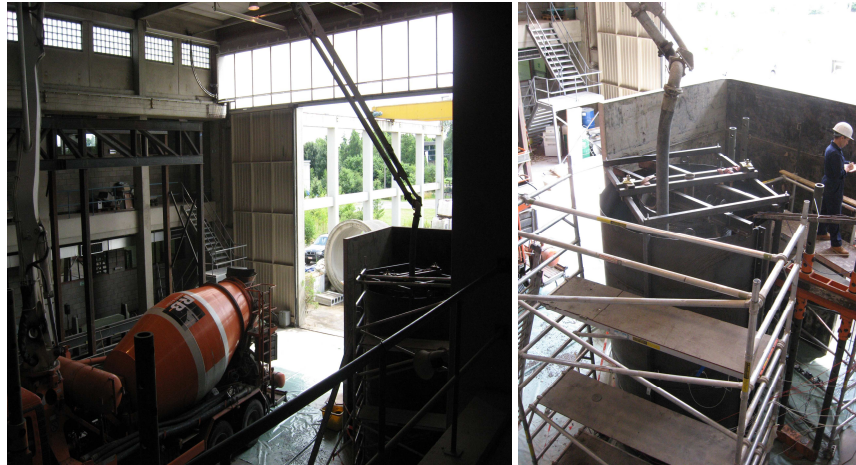


Figure 9.5: Pumping of the buffer of the Half-Scale Container

2.2 Fresh properties of SCC

The fresh properties of SCC of the different batches are evaluated by means of standard tests described in Chapter 6:

- The slump flow (EN 12350-8) can be determined in order to describe the flow ability of the fresh SCC in unconfined conditions.
- The V-funnel time (EN 12350-9) is determined to characterize the viscosity of the SCC.
- The passing ability of the fresh SCC is determined via the L-box apparatus (EN 12350-10).
- Sieve stability tests (EN 12350-11) are conducted to evaluate the segregation resistance of the fresh SCC batches.
- According to the Belgian Code NBN EN 12350-7, the density of the fresh SCC and the air content are determined.

The slump flow, determined at Kesteleyn, is used to decide whether the SCC mix has a sufficient flow ability (> 650 mm) and is ready to be transported.

2.3 Instrumentation test set-up

Once the SCC of the final batch (FB1: 6 x 2 m³) is pumped into the steel formwork, different parameters are registered via monitoring equipment (Table 9.1): temperature, wind velocity, RH, displacement in radial and axial direction and deformation in radial, axial and tangential direction. Therefore, a test set-up using different types of instrumentation is realized to register the time dependent development of these parameters until 672 hours after casting.



Figure 9.6: Uplift of the internal spill in between of the steel framework for the positioning of the LVDT's (left) and removal of the stainless steel formwork (right)

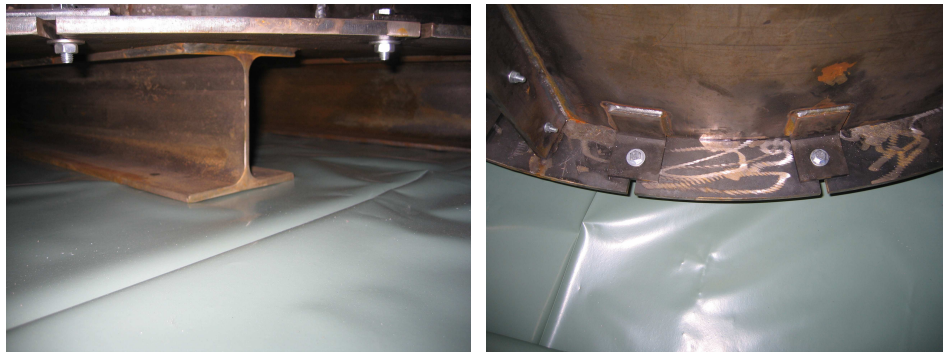


Figure 9.7: The steel bottom is supported by means of three I-shaped beams (left) and the cylindrical formwork is attached to the steel plate via right angle brackets (right)

2.3.1 Temperature, wind velocity and RH instrumentation

In total four thermocouples (custom type T thermocouples) are placed to register the ambient outside temperature T_{out} around the buffer, one thermocouple is placed to register the temperature T_{in} inside the opening of the buffer and fifteen thermocouples are placed in the concrete buffer (Figure 9.8). Notation, for example TCC 1: 'Thermo Couple at level C (Figure 9.1), position 1 (Figure 9.8)'. The L-shaped wind shield placed around the HC is also depicted on Figure 9.8 and can be seen as a reference coordinate system for the positioning of the instrumentation set-up.

The environmental temperature inside the created opening T_{in} (measured by means of TCC 5) and the temperature T_{out} around the HC (four measurements: TCA 1-9 and RHC 1-2) are measured by means of TC's. Note that RHC 1 and RHC 2 are at the same position as TCA 1 and TCA 9 but with a different altitude compared to level A: 60 cm instead of 35 cm. These temperature developments T_{out} and T_{in} at the outer border and the inner border of the HC are implemented as a boundary condition into the HEAT/MLS finite element program.

Finally, and in order to validate the simulation results obtained via HEAT/MLS, the temperature development inside the SCC of the buffer needs to be evaluated. Therefore, fifteen TC's are placed inside the steel formwork at different levels (A, B, C and D, Figure 9.1) and positions by means of a wooden frame (Figure 9.8): seven at level A, one at level B, six at level C and one at level D, or TCA 2-8, TCA 3-7, TCA 4-6, TCA 5, TCB 1, TCC 1-9, TCC 2-8, TCC 3-7 and TCD 1. Because some TC's are situated at the same position of the axisymmetrical cross section of the buffer of the HC (e.g. TCA 2-8), the mean value of the two registrations is determined and plotted.

Also the outer wind velocity W_{out} in the vicinity of the buffer is a very important boundary condition to evaluate the convective heat transfer coefficient h_c , and therefore is measured by means of two anemometers (ANE) placed at the same position of TCA 1 and TCA 9 but with a different altitude compared to level A: 70 cm instead of 35 cm. At the same two positions, but 10 cm lower, the relative humidity (RH 1 and RH 2) is measured by means of humidity probes, but these values are of no importance for this study as drying shrinkage, due to a possible gradient in RH, is kept out of consideration in this research.

2.3.2 Radial and axial displacement

By means of HEAT/MLS, the displacement in radial direction U_x and the displacement in axial direction U_y of the buffer can be simulated. Therefore, displacement registrations are performed by means of LVDT's.

The first 168 hours, the radial displacement of the formwork is obtained at level A and at level C via LVA 1-2-3-4 and LVC 1-2-3-4. Notation, for example LVA 1: 'Linear Variable Displacement Transducer at level A (Figure 9.1), position 1 (Figure 9.8)'. The LVDT's are positioned on the formwork by means of a steel framework (Figure 9.6) placed around the HC. This is to create a base for the displacement measurements which is independent of the movement of the HC itself.

To remove the spill (after 168 hours), the steel frame also needs to be moved and the LVDT measurements on the steel formwork stop. Once the spill is lifted, the steel frame is replaced and the outer radial displacement measurements on level A and on level C of the SCC can start once again. From now on, on level C' (60 cm higher than level C), also the radial displacement inside the opening is measured: LVC 5-6-7-8 (Figure 9.8).

Finally the axial displacement of the SCC is also registered: on top of the HC, starting after 68 hours of hardening (when the plastic covering sheet is removed) by means of LVD 1-2, and at the bottom of the created opening by means of LVB 1 (Figure 9.8) once the internal spill is lifted.

The mean registered value of the LVDT's that are situated at the same position of the axisymmetrical cross section of the buffer (e.g. LVA 1-2-3-4), will be calculated and plotted.

2.3.3 Radial, axial and tangential deformation

The first 168 hours the tangential (H) and axial (V) deformation of the formwork is obtained at level A and at level C via sixteen SG's: SGAH (or V) 1-2-3-4 and SGCH (or V) 1-2-3-4. Notation, for example SGAH 1: 'Strain Gauge at level A (Figure 9.1), Horizontally glued (measurement in tangential direction ϵ_z), position 1 (Figure 9.8)'. Vertically glued SG's measure the axial deformation ϵ_y of the formwork.

Once the spill is lifted, and the inner concrete surfaces are liberated, new SG's are glued on the surfaces of the created inner void space of the SCC of the HC at level C' (60 cm higher than level C). On level C' the four horizontally glued (H) SG's measure the tangential deformation ϵ_z of the SCC, the four vertically glued (V) SG's measure the axial deformation ϵ_y : SGCH (or V) 5-6-7-8.

On the other hand, on level B (bottom surface of the created opening in the HC) and on level E (top surface of the HC), the two horizontally glued SG's measure the tangential deformation ϵ_z , while the two vertically glued SG's measure the radial deformation ϵ_x : SGBH (or V) 1-2 and SGEH (or V) 1-2.

These registrations of the deformation of the SCC of the HC start after approximately 188 hours after casting of the buffer. The registrations of the deformation of the formwork continues until the formwork itself is removed (after 696 hours). Mean values are plotted for data obtained at equal points of the axisymmetrical cross section.

2.4 Strength tests

In total nine batches of 2 m³ are made at Kesteleyn: one batch TB1, one batch TB2, six batches FB1 and one batch FB2. Each batch is characterized by its compressive strength development. At different ages (varying between 1 day – 2 days – 3 days – 7 days – 14 days and 28 days), the compressive strength $f_{c_{cub150}}$ is determined on three cubes with a side of 150 mm, by means of uni-axial loading tests according to the Belgian Code NBN EN 12390-3. These test samples hardened under ideal environmental conditions (20 °C, 90 % RH). Also the splitting tensile strength f_{ctsp} is determined on different ages for TB1, according to the Belgian Code NBN B15-218. Therefore, cubes with a side of 100 mm are cast.

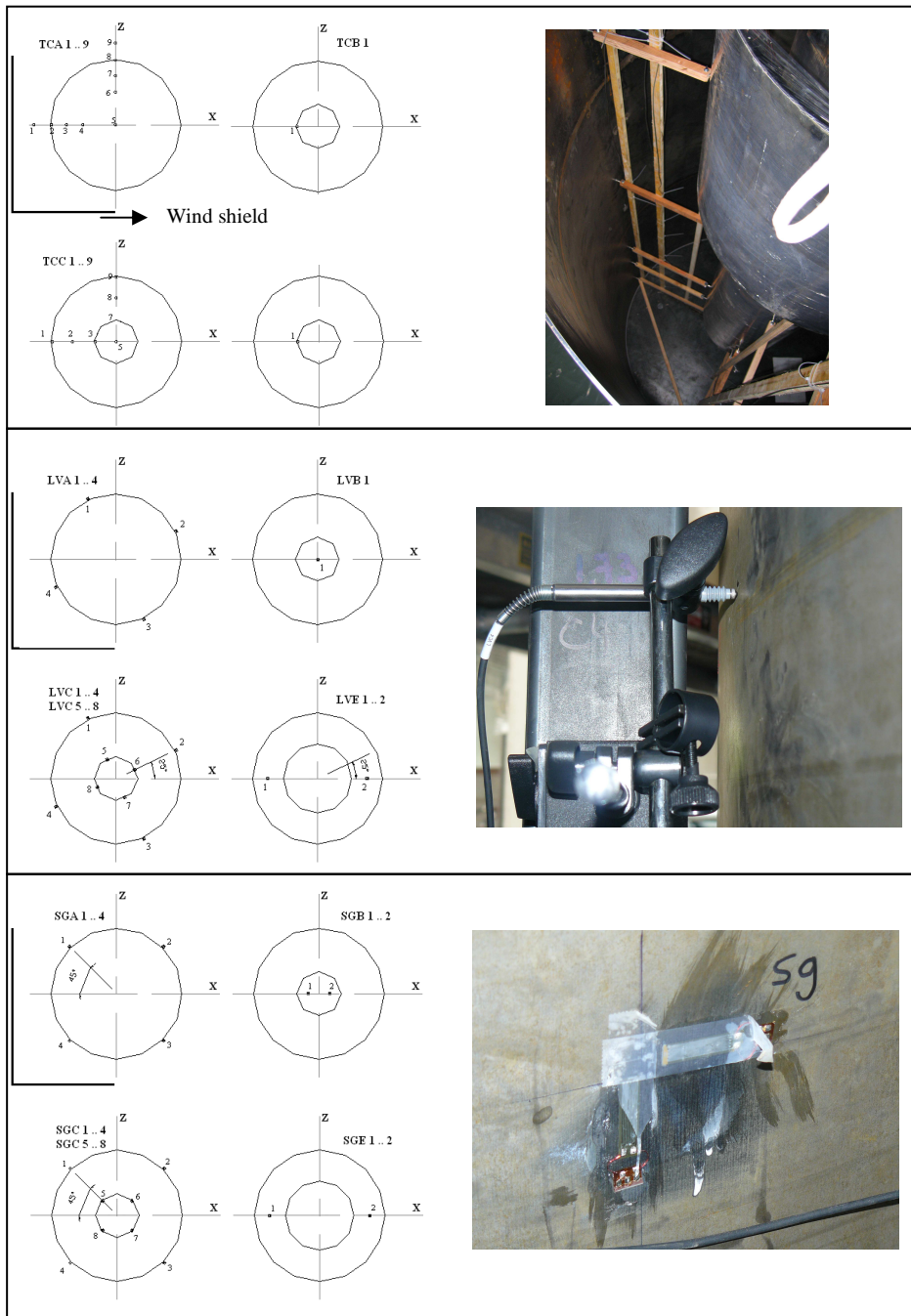


Figure 9.8: Instrumentation set-up of the thermocouples, LVDT's and strain gauges

For the SCC of FB1, used for the casting of the HC, two cores are taken out of the buffer (diameter 113 mm, height 100 mm) after 42 days and uni-axially loaded to determine the compressive strength (Figure 9.9). For the coring activities, two levels can be defined: one sample is taken out of the buffer at height 85 cm, the other core at height 260 cm.

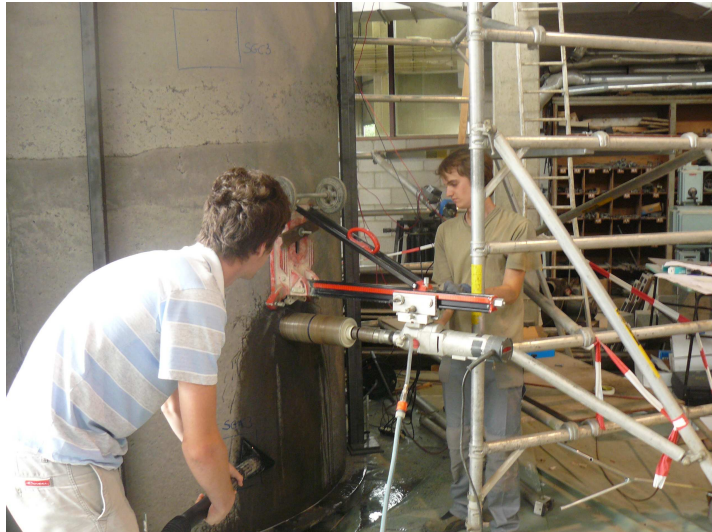


Figure 9.9: Taking cores out of the Half-Scale Container, at height 85 cm



Figure 9.10: The first 68 hours after casting, a plastic sheet covers the Half-Scale Container

3 Results and discussion

3.1 Fresh properties of SCC

The fresh properties of the different SCC batches, made at the Kesteleyn concrete factory, are listed in Table 9.3.

First the amount of added components is discussed. Depending on the water present in the limestone aggregates, expressed by means of the WC, the amount of aggregates and the amount of effectively added water W varies. The amount of cement is approximately 350 kg/m^3 in all cases, the amount of SP varies between 10 kg/m^3 and 17 kg/m^3 in order to obtain the desired SF value of 650 mm. Nevertheless, in case of TB1, FB1 and FB1', the SF value is smaller than 650 mm, although high amounts of SP are added ($> 14 \text{ kg/m}^3$). In case of FB1 and FB1', W_{tot} (= sum of W and the estimated amount of water present in the aggregates) is higher than 175 kg/m^3 , but the desired SF value is not reached.

Looking at the fresh properties of the different batches some general conclusions can be drawn:

- At the Kesteleyn concrete factory, only in case of TB2 and FB2 the desired SF value of 650 mm is reached. Even by adding more water and SP to the mixes, this value is not reached for TB1 and FB1'. Once the batch is released into the mobile mixer and transported to the Magnel Laboratory for Concrete Research, the SF value increases in case of the trial batches but decreases in case of the final batches.
- The VF values are only determined at Kesteleyn in case of the trial batches. Once transported, the VF value decreases and a shorter flowing time is registered. Overall, the VF values in all of the batches are smaller than 8 s.
- A good segregation resistance is obtained, determined by means of the SS test: all values are smaller than 15 %.
- Once more, no good PA is reached for all mixes, with values lower than the desired 0.80 in all cases and blocking of the flow near the rebars. In case of casting the buffer of the HC, a good passing ability is not really desired, because there are no restrictions concerning flowing through the opening of rebars in this casting case.
- A rather low density of the fresh concrete mix is obtained, compared to the mean value mentioned in Chapter 6. Note that a higher air content can be an explanation for the lower values of the density (Figure 6.30), and can be caused by the high amounts of SP added to the batches. Air voids can have an adverse effect on the compressive strength of concrete: f_c decreases with 5 % with an increasing air amount of 1 % according to Taerwe (1997).
- Also the VW after 28 days, determined on cubes, is significantly lower in case of the SCC batches made at Kesteleyn. The presence of air bubbles due to the higher air content can be seen as a reason for this decrement.

Table 9.3: Components and fresh properties of the SCC batches made at Kesteleyn

		TB1	TB2	FB1	FB1'	FB2	SCC
Date		18/05/09	25/06/09	6/07/09	6/07/09	5/10/09	-
Location		KESTELEYN	KESTELEYN	KESTELEYN	KESTELEYN	KESTELEYN	CHAPTER 6
C	kg/m ³	354	353	350	351	350	350
Limestone 0/4	kg/m ³	915	845	873	872	865	840
WC _{0/4}	%	6.50	0.75	1.00	1.00	1.48	0
Limestone 2/6	kg/m ³	335	325	325	328	335	327
WC _{2/6}	%	2.40	0.75	0.34	0.34	1.43	0
Limestone 6/14	kg/m ³	570	570	560	560	560	559
WC _{6/14}	%	1.00	0.75	0.19	0.19	0.40	0
W	kg/m ³	107	162	185	185	156	175
W _{tot}	kg/m ³	175	175	195	195	175	175
Superplasticizer	kg/m ³	17	12	15	15	10	10 – 14
Quantity	m ³	2	2	3x2	3x2	2	variable
Fresh results							
SF Kesteleyn	mm	530	700	600	625	675	-
SF Magnel	mm	570	715	530	560	625	690
VF Kesteleyn	s	8.9	3.6	-	-	-	-
VF Magnel	s	5.2	2.3	4.9	3.1	7.9	16
PA	-	0.60	0.73	0.34	0.49	0.60	0.69
SS	%	-	1.7	4.2	5.1	14.6	6.8
Density	kg/m ³	2330	2250	2310	2340	2375	2405
Air content	%	4.6	5.6	3.4	2.7	2.8	1.5
VW (28 days)	kg/m ³	-	2265	-	2285	2290	2390

Overall, it can be concluded that the SCC batches of 2 m³ have an acceptable flow ability, a good segregation resistance, a good viscosity but a poor passing ability (which might not be critical for the casting of the Supercontainer). The concrete made at Kesteleyn can be classified as Self-Compacting. High air contents are determined leading towards a decrease in density of the fresh mix and the hardened concrete samples. Finally, it must be mentioned that there is a considerable uncertainty on the amount of water present in the aggregates. To determine the WC of the aggregates, small samples are taken from huge stacks exposed to the ambient weather conditions. Questions rise whether this small sample is representative for the huge stack present at the Kesteleyn site and whether the determination of the WC is correct. This can be seen as the most important reason for the rather large dispersion on the obtained fresh SCC properties.

3.2 Validation of the simulation results

3.2.1 Pre-processing: geometry, boundary conditions and concrete properties

In order to validate the simulation results, a comparison is made between the simulations performed by HEAT/MLS and the registered data of temperature inside the buffer, the displacement of the steel formwork in radial direction and the displacement of the HC in axial direction by means of the testing equipment, and this during the first 168 hours after casting. Also the deformation of the formwork and the SCC is registered, but these values cannot be evaluated by means of HEAT/MLS. Finally, the simulations give an identification of the stress development inside the buffer, and a strength and cracking verification is made to evaluate whether the first stage of the fabrication of the Supercontainer is susceptible to early-age cracking.

The dimensions of the HC, given in Figure 9.1 (left), are used for the definition of an axisymmetrical cross section of the model used in HEAT/MLS. A drawing of the applied mesh, with reduced element size towards the outer surfaces, is given in Figure 9.11 (left). The early-age behaviour of the HC is simulated during the first 168 hours after casting, by means of HEAT/MLS.

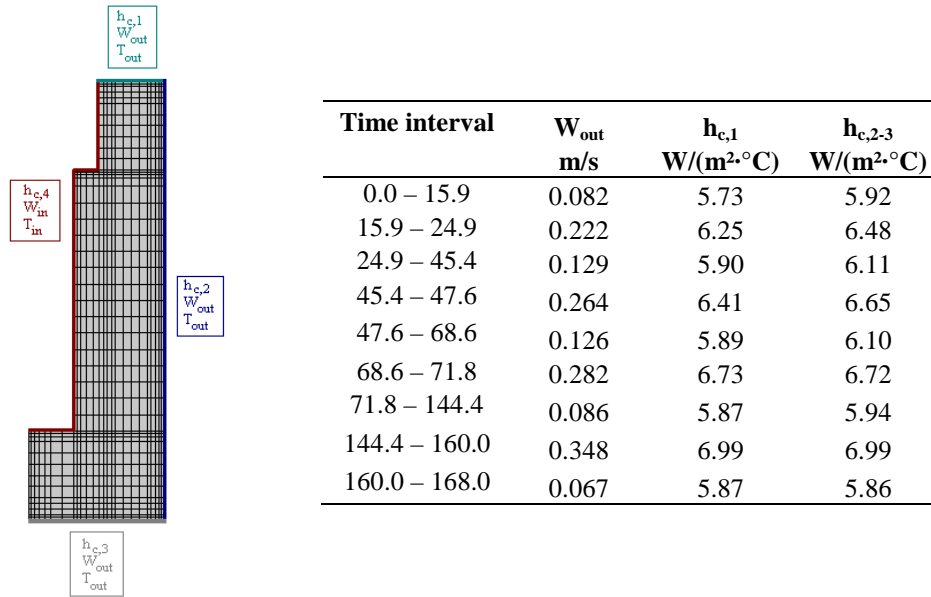


Figure 9.11: The mesh of stage 1 of casting the HC (left) with the applied boundary conditions (right)

Once the geometry and the mesh are defined, the most important boundary conditions need to be assigned to the edges of the axisymmetrical cross section: the temperature (T_{out} and T_{in}) and the wind velocity (W_{out} and W_{in}). The combination of the wind velocity and the type of formwork, is translated into the convective heat transfer coefficient h_c .

The internal temperature T_{in} is registered by means of TCC 5 and is approached by means of the red line given in Figure 9.12. The ambient temperature T_{out} is registered by means of four thermocouples (TCA 1-9 and RHC 1-2), and the mean value is approximated by means of the blue line in Figure 9.12. The average environmental temperature during the first 168 hours equals 24.7 °C, while the average internal temperature equals 32.7 °C. Due to the plastic foil covering the opening of the HC, the heat produced due to the hydration reactions remains entrapped inside the created hole. Once the plastic sheet is removed (after 68 hours), the heat can escape and an internal temperature drop of approximately 7.7 °C is registered in a time span of 1.75 hours (Figure 9.12).

The ambient wind velocity W_{out} in the vicinity of the HC is measured by means of two anemometers (ANE 1 and ANE 2), and the mean value is approximated by means of the stepwise blue line in Figure 9.13. A maximal value of 0.348 m/s and a minimal of 0.082 m/s is found. The presence of the wind shield reduces the wind speed. The internal wind velocity W_{in} is assumed to be non-existent (0 m/s). The spill (steel with thickness 6 mm) acts as internal formwork of the HC to create an internal opening, and is present during the entire simulation time (168 hours). Therefore $h_{c,4}$ equals 5.59 W/(m²·°C). A plastic foil (thickness 1 mm) covers the top surface of the HC during the first 68 hours after casting (Figure 9.10), the outer surface is surrounded by the steel formwork (thickness 6 mm) and the bottom surface rests on a thick steel plate with a thickness of 12 mm. The time dependent values of the convective heat transfer coefficients $h_{c,1}$, $h_{c,2}$ and $h_{c,3}$ are listed in Figure 9.11 (right).

The time dependent values of temperature, wind velocity and convective heat transfer are implemented into the model considered in HEAT/MLS. The SCC material, implemented into the database, corresponds to the material implemented for the simulations in Chapter 8. The initial concrete temperature is 27.0 °C.

As an illustration, the registered values of the RH in the environment of the HC are given in Figure 9.14. The mean value during the first 168 hours after casting is 52.2 %. As mentioned before, these values are of no importance for the early-age cracking behaviour of the HC, as drying shrinkage (which results from a gradient in RH) is not taken into account.

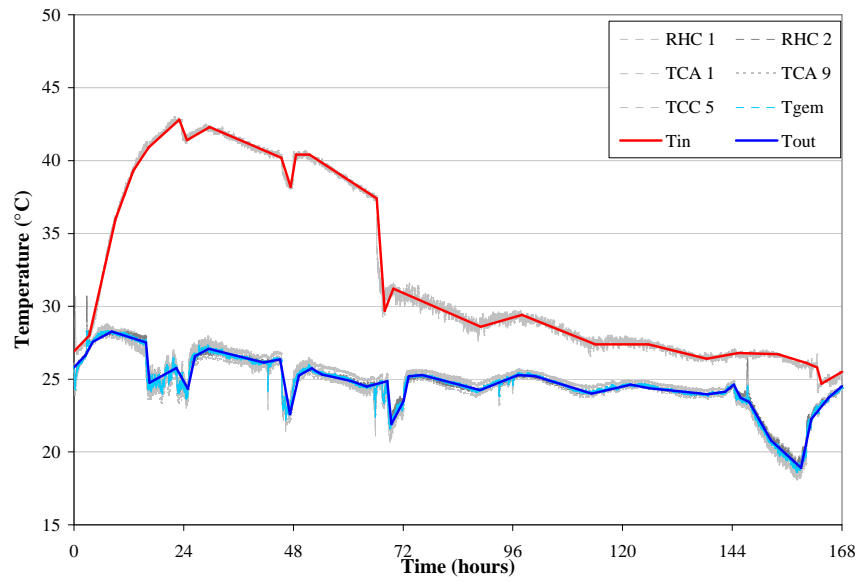


Figure 9.12: The internal and ambient temperature development as a boundary condition

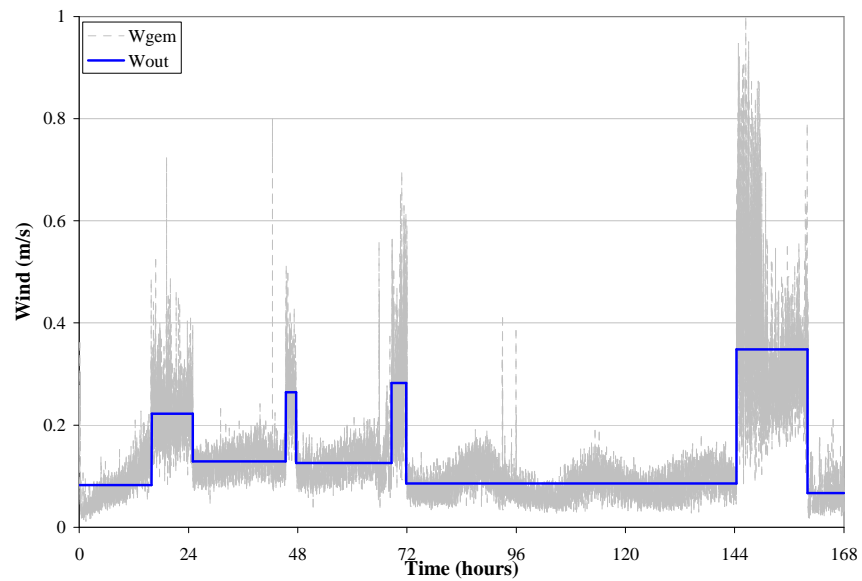


Figure 9.13: The ambient wind velocity as a boundary condition

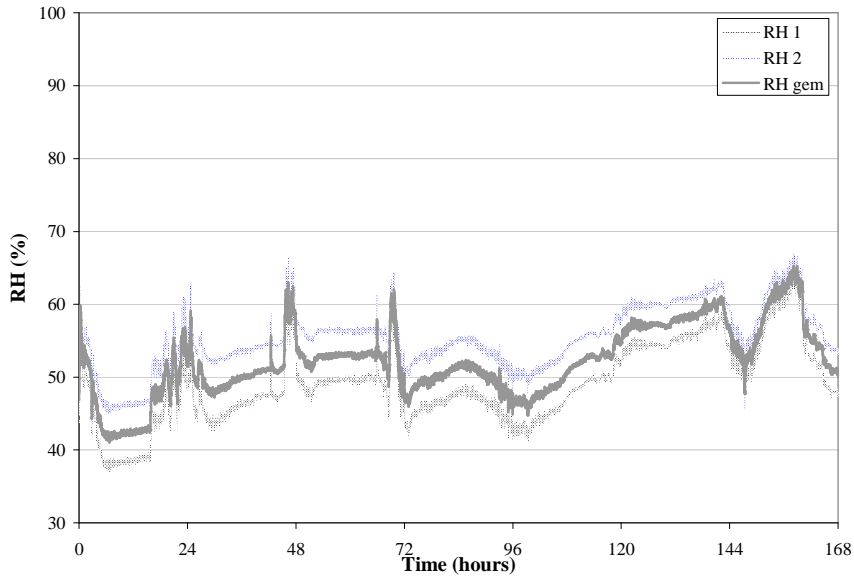


Figure 9.14: An illustration of the development of the ambient relative humidity

3.2.2 Validation of the temperature development

The validation of the temperature development inside the buffer of the HC is performed by comparing the registered data of the TC's and the obtained simulated data by means of HEAT/MLS, at the different positions at each levels (A, B, C and D), as depicted in Figure 9.1 (left).

The registration of the temperature development by means of the TC's starts after approximately 4.03 hours (origin is the start of mix 1 of TB1). However, the concrete mixing started earlier (Table 9.1). Therefore, the origin of the registration data is shifted: 2.73 hours ($= 4.03 - 1.3$) for the first batch (TB1) and 1.5 hours ($= 4.03 - 2.53$) for the second batch (TB1'). The start of the last mix of each batch is taken as the time origin of the beginning of temperature development.

Figure 9.15a (level A), Figure 9.15b (level C) and Figure 9.15c (level B and level D) give the comparison between the measured data (bold line) and the simulated data (thin line). A rather good correspondence is obtained. For level A, the simulation results give higher values, the measured temperatures are lower in reality. The simulations give a conservative and safe approach. Especially near the outer surface (TCA 2-8) and in the middle of the bottom of the buffer (TCA 5), a good similarity is found. These values are important for the thermal gradient ΔT present inside the HC, which has a decisive effect on the thermal stress creation in the buffer [De Schutter, 1996]. Also the deviations of the temperature curves due to the removal of the plastic sheet (at the inner

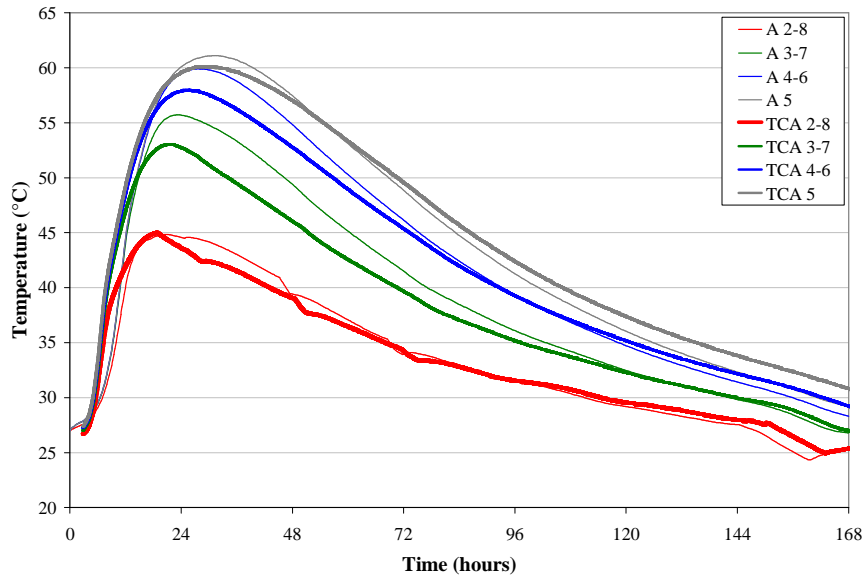


Figure 9.15a: Validation of the temperature development at level A

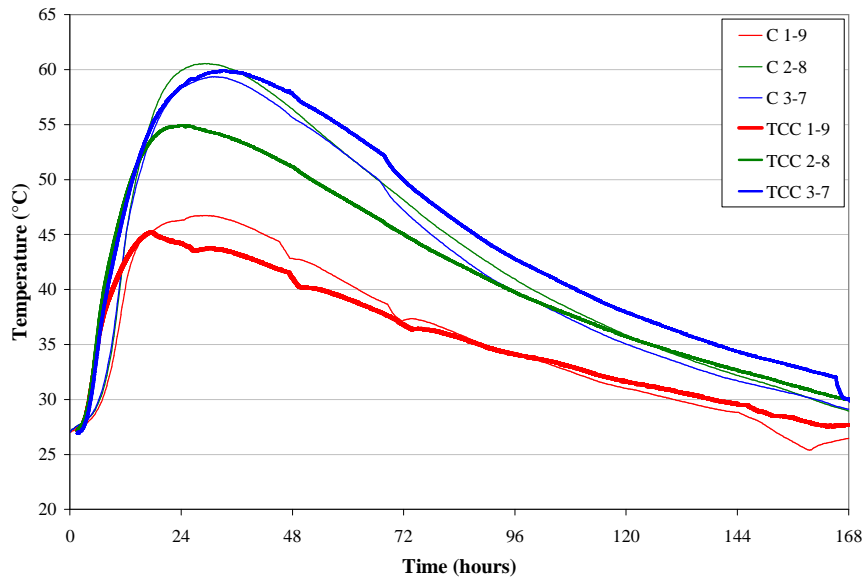


Figure 9.15b: Validation of the temperature development at level C

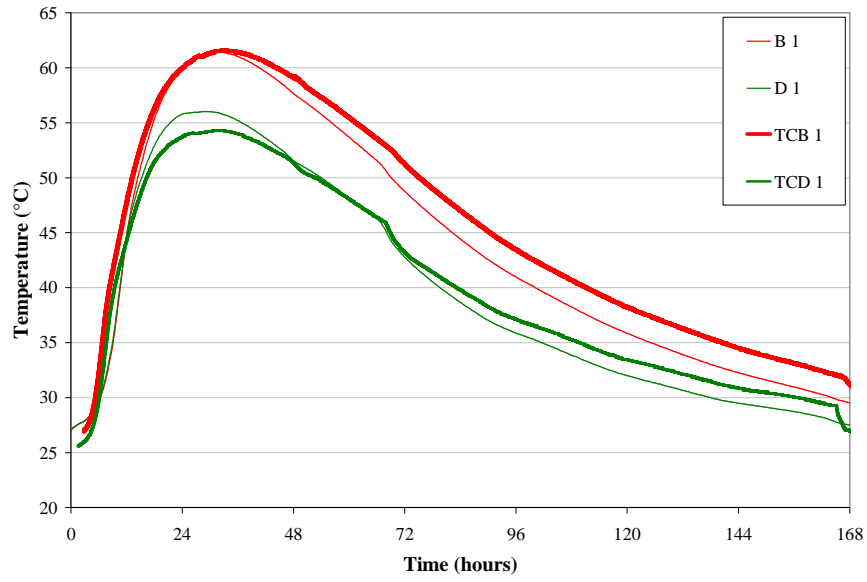


Figure 9.15c: Validation of the temperature development at level B and level D

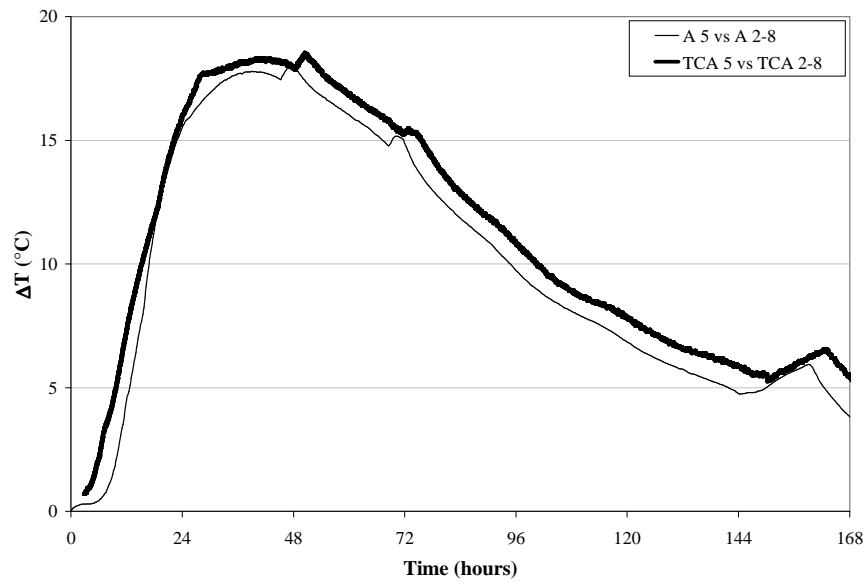


Figure 9.15d: Validation of the temperature gradient at level A

surface and the change in ambient wind velocity at the outer surface are noticeable in the simulations and the registered data. On the level C of the HC, good similarities are found for TCC 1-9 (the simulations overestimate the reality) and for TCC 3-7 (the simulations underestimate the reality). A larger spread is found on the data of TCC 2-8 (Figure 9.15b), but as the simulation results overestimate the reality, this causes no problem in interpreting the drawn conclusions. Moreover, very good similarity is found on level B and level D (Figure 9.15c), located near the inner surface of the HC.

For the evolution of the thermal gradient, higher values of the registered data are obtained and their appearance is delayed, so the simulations slightly underestimate the realistic casting situation. The time shift can be explained by the difficulty of estimating the beginning of the registration: each batch consists of 3 mixes of 2 m³, starting at different times (Table 9.1). Nevertheless, good similarity between the two curves indicate that the simulations by means of HEAT/MLS give a realistic approach, and the used material database can be approved for the simulations. The temperature difference (at maximum temperature) between the simulated and the registered data remains smaller than approximately 5 %, except for level C, position 2-8 (Table 9.4). The contourplot of the temperature distribution, obtained via HEAT/MLS is given as an illustration in Figure 9.16.

After 168 hours, the internal steel spill is removed and the registration of the temperature continues until 672 hours after casting. Especially the first 168 hours are important (due to the hydration reaction peak) for the analysis of the internal stress development and of the cracking risk of the massive SCC buffer.

Table 9.4: Maximum temperature, time of appearance of maximum temperature and temperature difference (TD) of the simulated and the registered data

Position	HEAT/MLS		TC		TD (%)
	T _{max} (°C)	t _{max} (h)	T _{max} (°C)	t _{max} (h)	
A 5	61.1	32.0	60.1	30.5	1.6 %
A 4-6	59.9	28.5	57.9	26.5	3.5 %
A 3-7	55.7	23.8	53.0	22.1	5.1 %
A 2-8	44.8	21.5	44.8	19.5	0.0 %
C 3-7	59.3	32.0	59.9	33.9	-1.0 %
C 2-8	60.5	30.3	54.9	24.7	10.2 %
C 1-9	46.7	30.3	45.0	18.3	3.8 %
B1	56.0	29.8	54.3	32.7	3.1 %
D1	61.4	32.5	61.5	34.3	-0.2 %
ΔT	18.0	48.0	18.4	51.2	-2.2 %

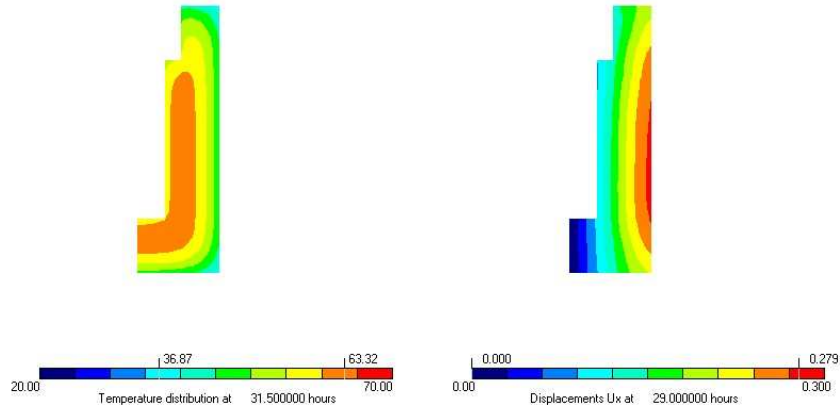


Figure 9.16: Contourplots of the temperature at 31.5 h (left) and the radial displacement at 29 h (right) of the HC

An illustration of the temperature registration after 168 hours at the different positions is given in Figure 9.17. These values fluctuate, due to the day and night cycle, around a mean value of approximately 25 °C. Near the outer surface these temperature fluctuations of the SCC are higher than the temperature fluctuations deeper in the SCC of the buffer.

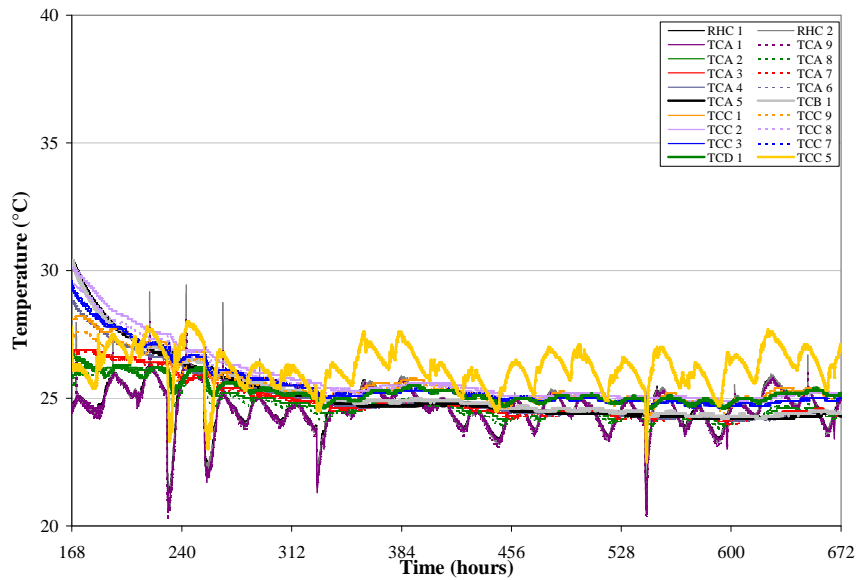


Figure 9.17: Registered temperature development after 168 hours

3.2.3 Validation of the displacement

The radial displacement U_x of the steel formwork due to the expansion of the concrete (mainly due to the hydration reaction) is registered by means of eight LVDT's, four at level A and four at level C, starting immediately after casting. Also the radial displacement U_y of the concrete buffer is registered at level E, by means of two LVDT's, starting after approximately 68 hours, when a sufficient hardening state of the concrete is reached. By simulating the displacement in radial and axial direction, the obtained data can be validated. Conventionally, radial displacements U_x are taken positive in expansive behaviour, while the axial displacement U_y is taken positive in shrinkage behaviour.

Table 9.5: Maximal displacement, appearance of maximal displacement and displacement difference (DD) of the simulated and the registered data

Position	HEAT/MLS		LVDT		DD (%)
	U_{\max} (μm)	t_{\max} (h)	U_{\max} (μm)	t_{\max} (h)	
A 1-2-3-4	247	26.0	59	28.6	418.6 %
C 1-2-3-4	276	30.0	184	28.1	50.0 %
E 1-2	418	147.5	320	147.5	30.6 %

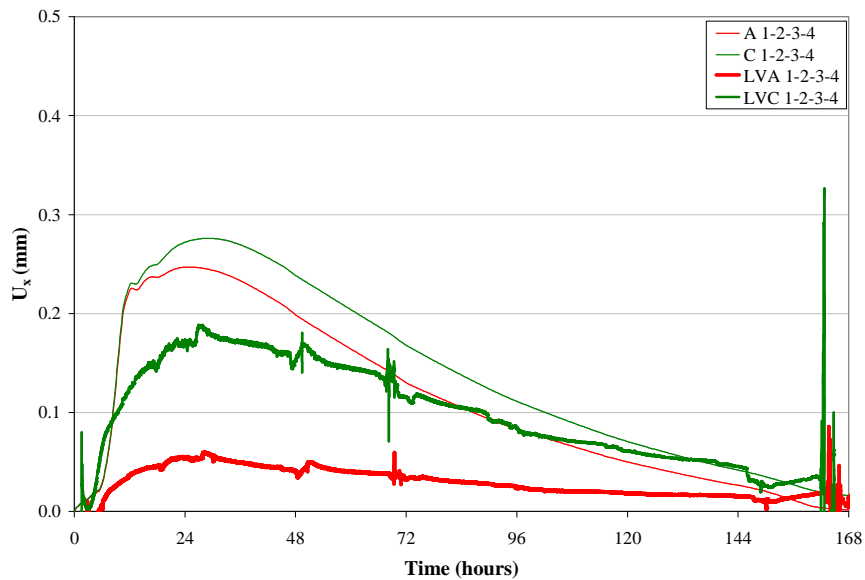


Figure 9.18a: Validation of the radial displacement at level A and level C

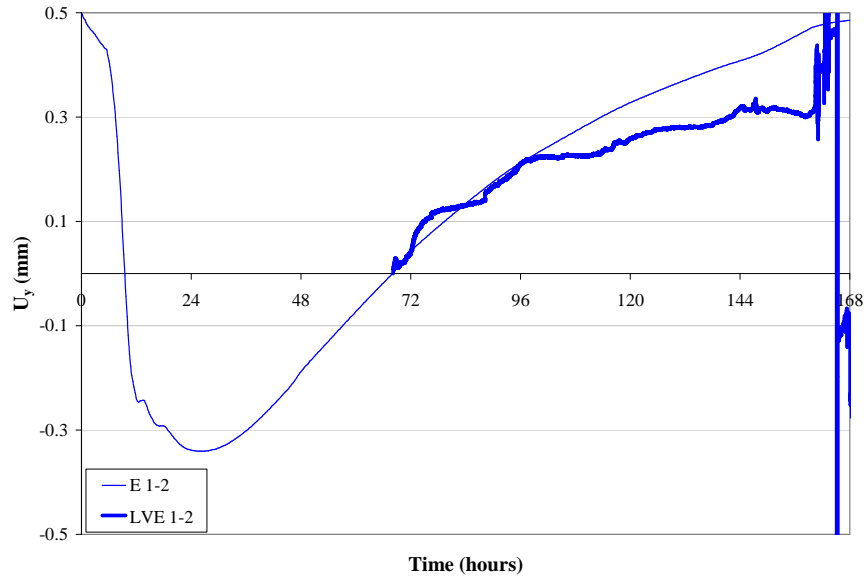


Figure 9.18b: Validation of the axial displacement at level E

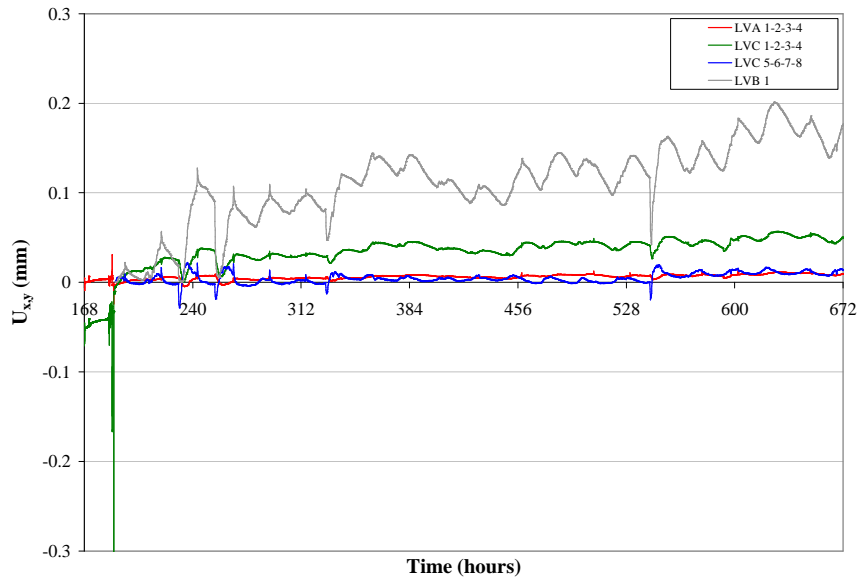


Figure 9.18c: Registered radial and axial displacements after 168 hours

A rather high deviation of the simulation results from the registered data is found. At level A, the simulated radial displacement is significantly higher (four times!) than the registered ones. This difference is smaller at level C: 50 % (Table 9.5). Concluding the simulations seriously overestimate the reality is wrong. In the simulations, the outer stainless steel formwork can only be considered as an environmental boundary condition, not as a kinematic boundary condition. The free displacement of the concrete is simulated, with a contourplot given in Figure 9.16 (right). Actually, the free radial deformation of the concrete is hindered by the stainless steel liner, and due to the expansive nature of the SCC during hydration, the steel formwork will expand. This radial deformation of the formwork is registered by means of the LVDT's. The expansion will be higher at level C than at level A, as found by the data (Figure 9.18a), because the bottom of the steel formwork is attached to the bottom steel plate by means of right angle brackets, as shown in Figure 9.7 (right). The time of maximal displacement is worth taking a look at: a rather good resemblance is found at both the levels A en C (Table 9.5).

The axial displacement at level E is registered starting from 68 hours after casting, when the SCC has sufficiently hardened to place the LVDT's (Figure 9.18b). A shrinkage behaviour is noticed, with a good resemblance between registration and simulation the first 30 hours. Afterwards, the simulation results tend to overestimate the shrinkage behaviour: after 147.5 hours the simulated U_y is 30.6 % higher than the registered U_y . Once more, the presence of the outer steel formwork influences the obtained data. The shrinkage behaviour of the SCC is limited due to the friction between the SCC and the formwork, which is not included in the simulations, leading towards higher simulated shrinkage values.

As an illustration, the displacement curves at level A, level C, level C' and level B (B and C': on SCC in the opening of the HC), after removal of the internal spill, is given in Figure 9.18c. The deformation at level A, level C and level C' remains more or less unaltered, while a shrinkage behaviour, up to 200 μm , at the bottom of the opening in the buffer is registered. This shrinkage behaviour is not expected, especially not after 168 hours, because at that time, simulations indicate that the buffer has already returned to its original position (Figure 9.18d).

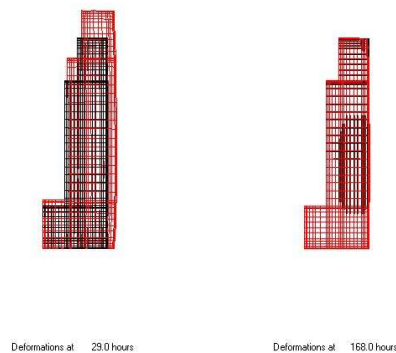


Figure 9.18d: Contourplots of the deformation mesh at 29 h and 168 h

3.2.4 The deformation of the steel formwork and the HC

Next to the displacement of the steel formwork, also the deformation in axial (ϵ_y , blue) and tangential (ϵ_z , green) direction of the steel formwork is registered the first 168 hours after casting (Figure 9.19a). Horizontally (H) glued SG's on the formwork register ϵ_z while vertically glued (V) SG's register ϵ_y . Conventionally, expansion is taken positive. Unfortunately, the strain evolution in time of the steel line cannot be generated by HEAT/MLS. By means of Hooke's law (equation (9.2)), thus by assuming linear elastic behaviour of the steel, the tangential stress S_{zz} and the axial stresses S_{yy} can be calculated, assuming the modulus of elasticity of steel E_s equals 200 GPa [Taerwe, 2004].

$$S_{ij} = E_s \cdot \epsilon \quad (9.2)$$

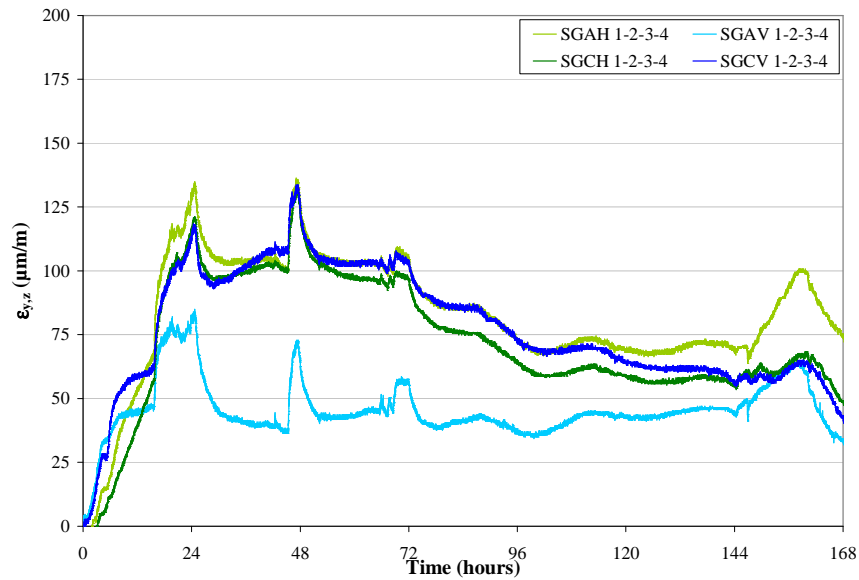


Figure 9.19a: Registered axial and tangential deformation of the formwork the first 168 hours

The deformation in axial and in tangential direction is quite similar for level A and level C, except for the axial deformation on level A, which is significantly lower (Figure 9.19a). Overall, the first 24 hours after casting, an expansion is noticed, mainly due to the formwork pressure caused by hardening and expanding SCC. The steel experiences tensile stresses. Then, in between 24 hours and 72 hours, the deformation remains more or less constant (except for the deformation peaks after 24 hours, 48 hours and 72 hours, devoted to the change in ambient wind velocity and temperature). Afterwards, the shrinkage of the SCC starts to develop and the steel cylindrical

formwork slowly returns to its initial state, causing the deformation and the steel stress to decrease. The maximal deformation, and the maximal stress after 48 hours (calculated by means of equation (9.2)) inside the formwork is given in Table 9.6. The stresses remain far below the linear elastic proportionality limit of steel (approximately 200 MPa according to Taerwe (2004)).

Table 9.6: Maximal deformation and calculated stress in the steel formwork, after 48 hours

Position	$\epsilon_{y,z}$ ($\mu\text{m/m}$)	$\sigma_{y,z}$ (MPa)
AH 1-2-3-4	136.3	27.3
AV 1-2-3-4	72.1	14.4
CH 1-2-3-4	131.0	26.2
CV 1-2-3-4	133.7	26.7

From 168 hours to 360 hours after the casting, once more a slight increase in axial deformation (+ 22 $\mu\text{m/m}$) and tangential deformation (+ 37 $\mu\text{m/m}$) of the steel formwork is noticed on level A. On level C, the deformation remains more or less constant (Figure 9.19b).

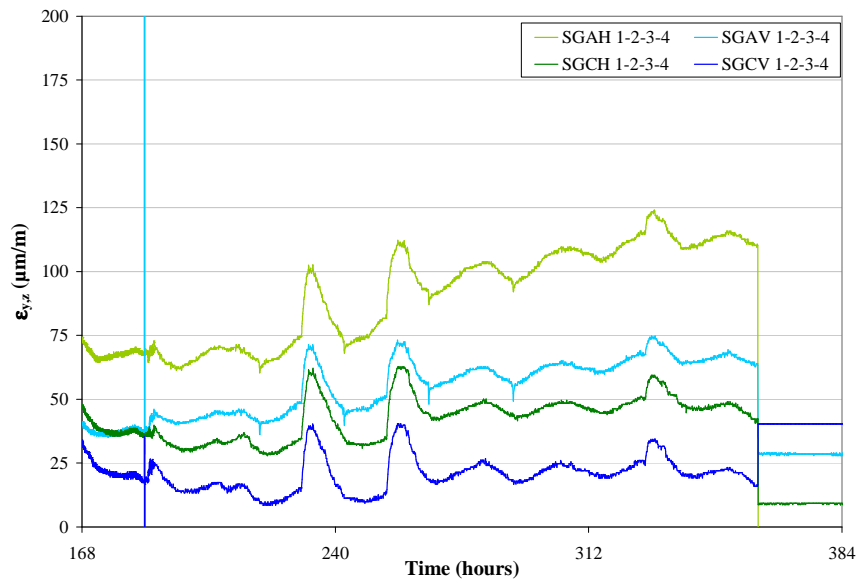


Figure 9.19b: Registered *axial* and *tangential* deformation of the formwork from 168 hours until 360 hours

Once the inner steel spill is removed after 168 hours, SG's are glued on the concrete faces to register the radial deformation (ϵ_x , red), the axial deformation (ϵ_y , blue) and the tangential deformation (ϵ_z , green), starting from 188 hours until 360 hours after the casting. The SG's are glued on level B (bottom of the created opening), on level C' (upright surface of the opening) and on level E (top surface of the HC). On level B and level E ϵ_x and ϵ_z are measured, while on level C' ϵ_y and ϵ_z are registered (Figure 9.19c). Conventionally, expansion is taken positive and shrinkage is taken negative.

The deformations registered on level C and on level B undergo a very small expansion, but the absolute values after 360 hours remain smaller than 10 $\mu\text{m}/\text{m}$. On level E, on the other hand, a shrinkage behaviour is noticed: from 188 hours until 360 hours after casting, the deformation goes from 0 $\mu\text{m}/\text{m}$ to -63 $\mu\text{m}/\text{m}$ in radial direction, and from 0 $\mu\text{m}/\text{m}$ to -76 $\mu\text{m}/\text{m}$ in tangential direction (Figure 9.19c).

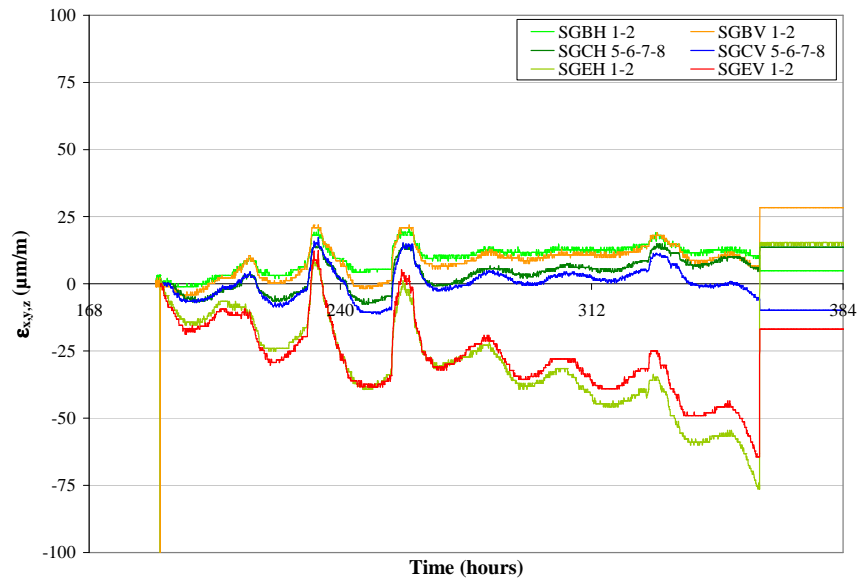


Figure 9.19c: Registered *radial*, *axial* and *tangential* deformation of the SCC from 168 hours until 360 hours

A rather good similarity is obtained between the radial and tangential deformation of the concrete at level B and level E, and between the axial and tangential deformation at level C' of the inner surface of the HC (Figure 9.19c). This equivalence between the axial and the tangential deformation of the formwork is also noticed at level A and level C at the outer surface of the HC (Figure 9.19a and Figure 9.19b). Transforming this finding on a stress level, an explanation can be given on the more or less similar stress creation behaviour in axial (y) direction and tangential (z) direction, as mentioned earlier in Chapter 8. This concludes the registrations of the Half-Scale Tests of the first construction stage of the Supercontainer, i.e. the casting of the buffer.

Finally, the cracking risk of the HC is evaluated by means of the stress simulations, the strength tests and a visualization of the HC after demoulding after 696 hours.

3.2.5 Stress calculation in the HC

Via the finite element tool HEAT/MLS, contourplots can be drawn of the normal stresses in radial (x), axial (y) and tangential (z) direction, and of the shear stresses S_{xy} at the time of maximal value appearance (Figure 8.20). The maximal values of the stresses and their time of appearance are listed in Table 9.7.

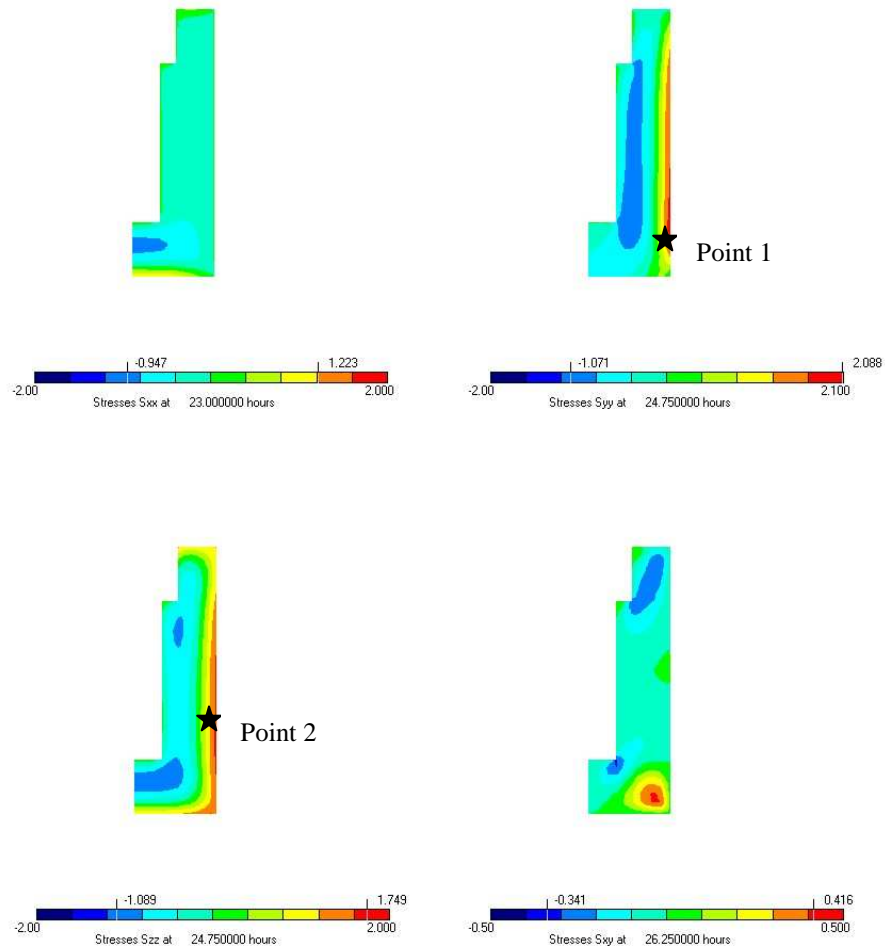


Figure 9.20: Contourplots of the radial stress S_{xx} , the axial stress S_{yy} , the tangential stress S_{zz} and the shear stress S_{xy} of the HPC at 23 h, 24.75 h, 24.75 h and 26.25 h

Table 9.7: Summary of the maximal values of the stresses, the difference between the reference situation (Chapter 8) and their time of appearance

		Value	%	t_{\max} (h)
$S_{xx,\max}$	MPa	1.22	42.6	23.00
$S_{yy,\max}$	MPa	2.09	30.0	24.75
$S_{zz,\max}$	MPa	1.75	21.7	24.75
$S_{xy,\max}$	MPa	0.42	83.3	26.25

Compared to the reference casting situation with SCC at an ambient temperature of 20 °C (Chapter 8), the obtained stresses inside the HC are significantly higher (Table 9.7). Their time of appearance is also slightly earlier, devoted to the higher environmental temperature during casting (up to approximately 28 °C), which accelerates the hydration reactions. Also the altered dimensions (increased diameter) of the buffer have an impact on the stress creation.

The critical tensile stress zones can be easily selected (Figure 9.20) for the derivation of the time evolution of the stresses at the positions near the critical zones: near the outer surface for the axial and tangential stresses, near the top surface and the bottom for the radial stresses, and right below for the shear stresses. The time graphs are given in Figure 9.21a, Figure 9.21b, Figure 9.21c and Figure 9.22d. The different positions resemble with the positions of the TC's, given in Figure 9.8.

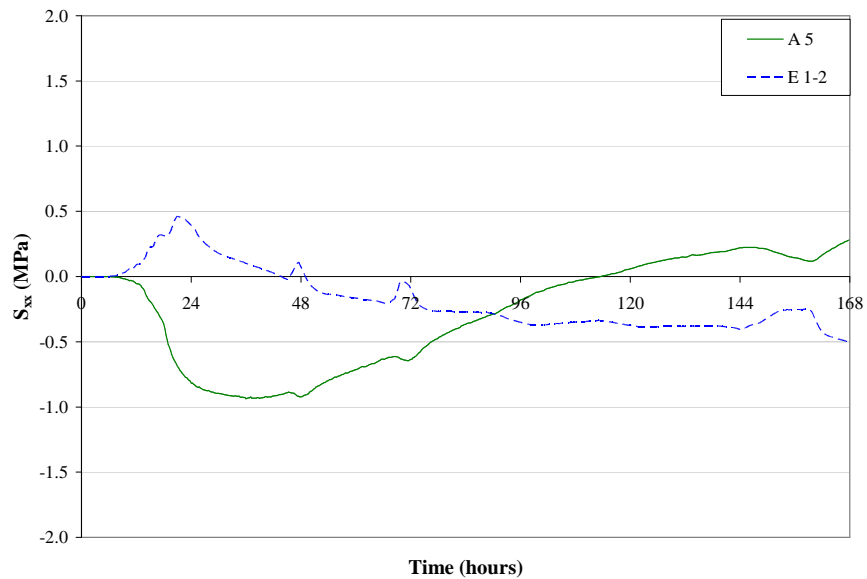


Figure 9.21: Time graph of S_{xx} at different positions

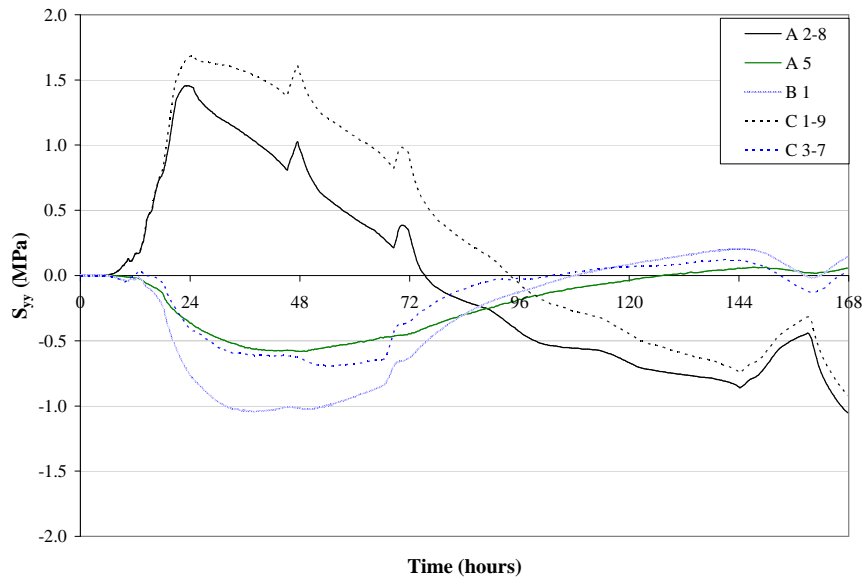


Figure 9.21b: Time graph of S_{yy} at different positions

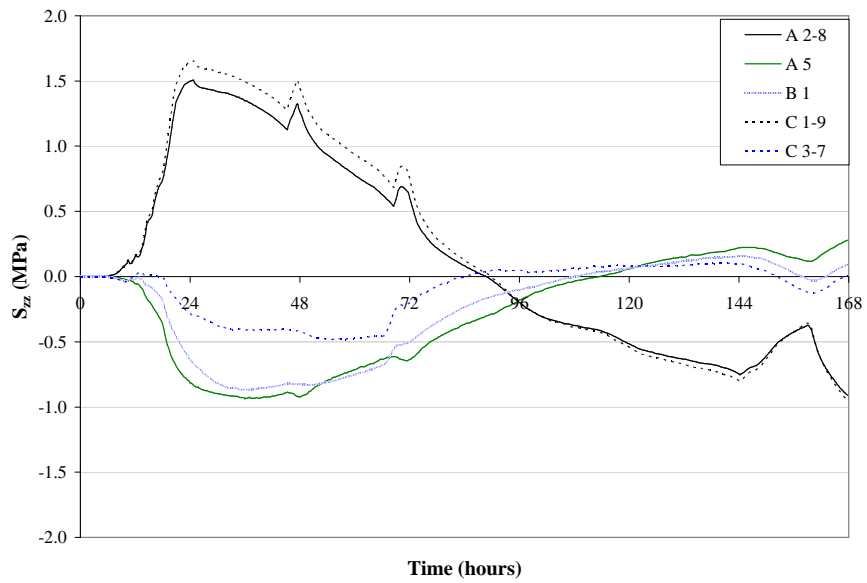


Figure 9.21c: Time graph of S_{zz} at different positions

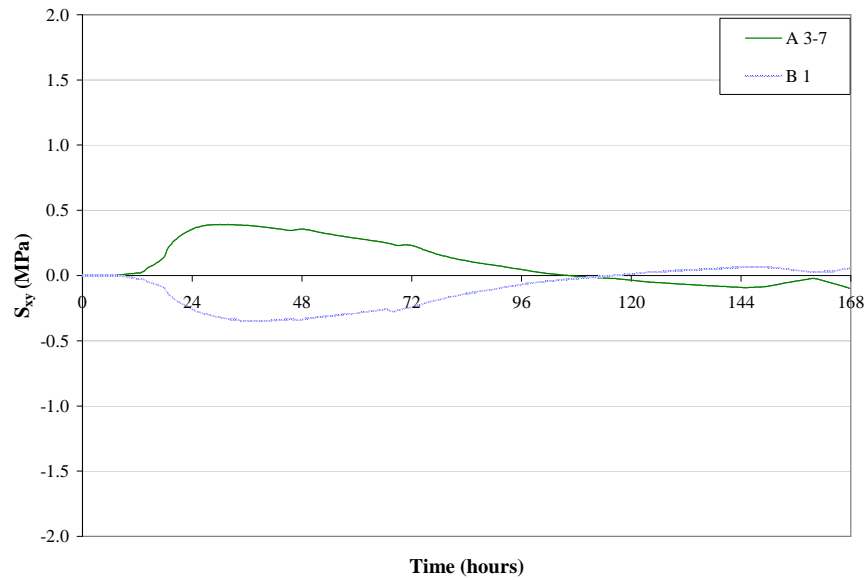


Figure 9.21c: Time graph of S_{xy} at different positions

Some general remarks are given:

- The axial and tangential stress are considerable higher than the radial stresses and the shear stresses. Also the development of S_{yy} and S_{zz} shows considerable similarities.
- Near the outer surface of the HC, tensile stresses occur during the hydration peak reaction, and afterwards, these regions come under compression. For points in the middle of the buffer, it is the other way around: tensile stresses occur, once the hydration peak has passed.
- The inner surface of the HC acts like the regions in the midzone of the buffer: first compression and tension afterwards. An explanation can be found in the presence of the plastic sheet the first 68 hours, covering the opening of the buffer. Because of this sheet, the produced heat, due to the hydration reaction, remains entrapped, and the temperature in the inner void (T_{in} in Figure 9.12) increases and is much higher than the ambient environmental temperature. The temperature at the inner surface (C 3-7 in Figure 9.15b) develops towards values comparable with the temperature inside the middle of the buffer (approximately 60 °C).
- The axial and the tangential tensile stresses near the outer surface are higher at level C compared to level A.
- Once more, the shear stresses are low enough to be neglected, and the normal stresses can be considered as principal stresses.
- The deviations of the stress curves at approximately 24 hours, 48 hours, 72 hours and 144 hours is due to the change in h_c , devoted to the rise in ambient wind velocity, and due to T_{out} . Once more, the non-negligible effect of the

wind and the ambient temperature on the early-age behaviour on massive hardening concrete is presented.

3.2.6 Strength development of the SCC

The compressive strength $f_{ccub150}$ of the different batches is determined at different ages (varying between 1 day – 2 days – 3 days – 7 days – 14 days and 28 days) as a mean value of three uni-axial tests at each age. The cubes of TB1 and TB2 hardened under ideal environmental conditions (20 °C, 90 % RH). For FB1 and FB2 the cubes hardened at the casting site. To examine the influence of the curing regime on the strength development, some cubes of FB1 also hardened under ideal environmental conditions (20 °C, 90 % RH). The strength results are given in Figure 9.22 and Table 9.8.

The obtained compressive strength test results indicate a significant strength loss compared to SCC characterized by means of the laboratory tests (Chapter 6): 14 % for TB1, 33 % for TB2, 30 % for FB1 and 20 % for FB2. The increase in air content of the SCC batches (Table 9.3) could be a reason of the strength loss, but the main reason of this strength loss can be found in the uncertainty of the WC of the aggregates added to the concrete mixes. In laboratory environment, the aggregates added to the mix are totally dry. In case of the mixes at Kesteleyn, the aggregates have a certain WC, that must be estimated. In case this parameter is underestimated, higher total amounts of water W_{tot} than prescribed (175 kg/m³) will be added to the mix, with a disadvantageous effect on the concrete strength. In case of FB1 approximately 10 % more W_{tot} is added (195 kg/m³, Table 9.3) to come to the prescribed SF value (\pm 650 mm). As a consequence, the compressive strength loss of 30 % is obtained.

The concrete samples cured at the site (FB1 Site, Figure 9.22) have higher strength at younger age and a faster strength development due to the ambient temperature that is higher than 20 °C (higher maturity), compared to the samples cured in idealistic curing conditions of 20 °C (FB1, Figure 9.22). After 28 days of hardening, $f_{ccub150}$ is similar for both curing conditions.

The results of the coring activities after 42 days and the corresponding compressive strength test results are also given. At an altitude of 85 cm, the compressive strength of the core (diameter 113.2 mm, height 99.0 mm) is 40.6 MPa and a density of 2265 kg/m³ is measured. For the core at height 260 cm (diameter 113.3 mm, height 99.8 mm), the strength is 38.7 MPa and the density is 2245 kg/m³.

Also the splitting tensile strength f_{ctsp} is determined on different ages for TB1 on cubes with a side of 100 mm. Equation (6.15) is used for the transformation of the splitting tensile strength into the pure tensile strength f_{ct} , which is plotted in Figure 9.23. Note that although $f_{ccub150}$ at 28 days of TB1 is 14 % lower than SCC, f_{ct} after 28 days is 1 % higher.

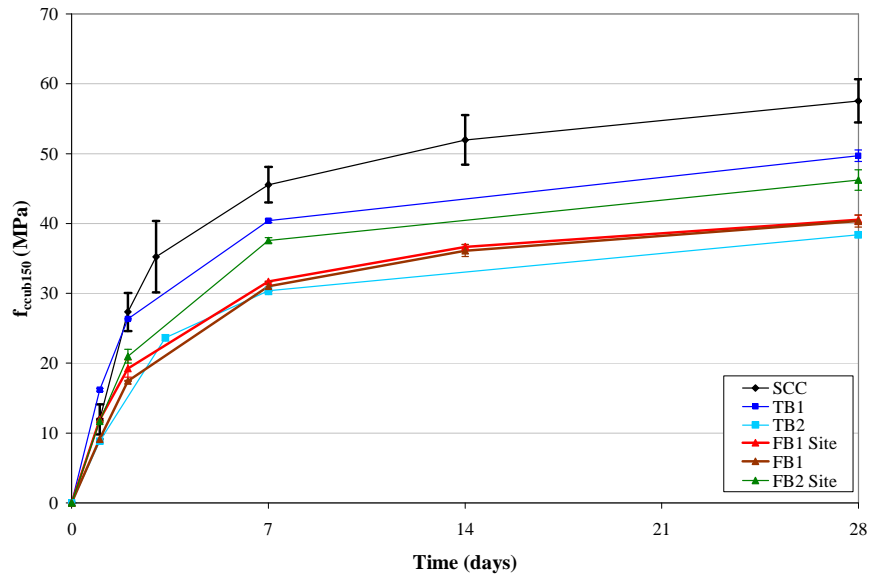


Figure 9.22: The compressive strength test results of TB1, TB2, FB1 and FB2

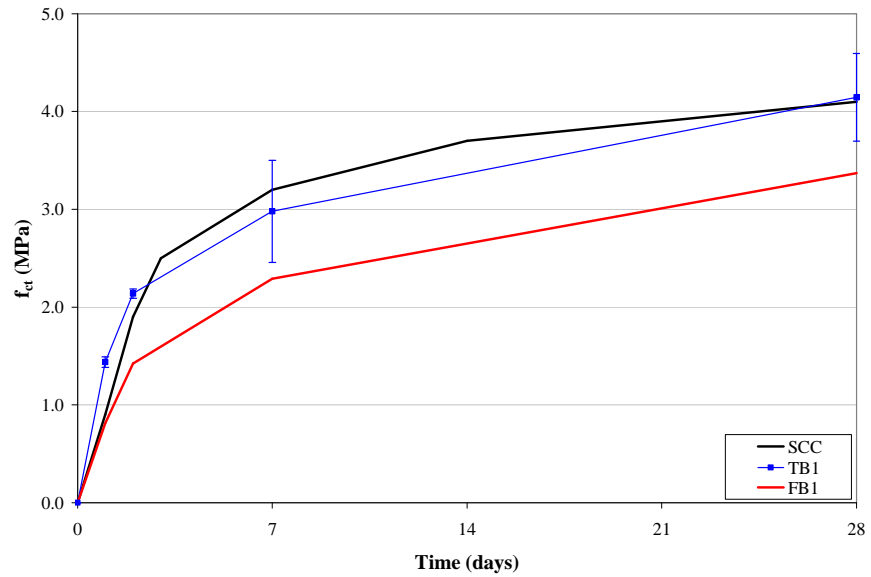


Figure 9.23: The obtained tensile strength of TB1 and the estimated tensile strength of SCC and FB1 at different ages

Table 9.8: The compressive strength test results of TB1, TB2, FB1 and FB2 at different ages

Time	TB1		TB2		FB1 Site		FB2 Site	
	$f_{ccub150}$	s	$f_{ccub150}$	s	$f_{ccub150}$	s	$f_{ccub150}$	s
1 day	16.2	0.2	8.8	0.3	11.9	0.2	11.7	0.1
2 days	26.3	0.1	-	-	19.2	1.2	21.0	1.0
3.3 days	-	-	23.6	0.5	-	-	-	-
7 days	40.4	0.3	30.4	0.5	31.7	0.1	37.6	0.4
14 days	-	-	-	-	36.7	0.3	-	-
28 days	49.7	0.8	38.4	0.4	40.5	0.7	46.2	1.5

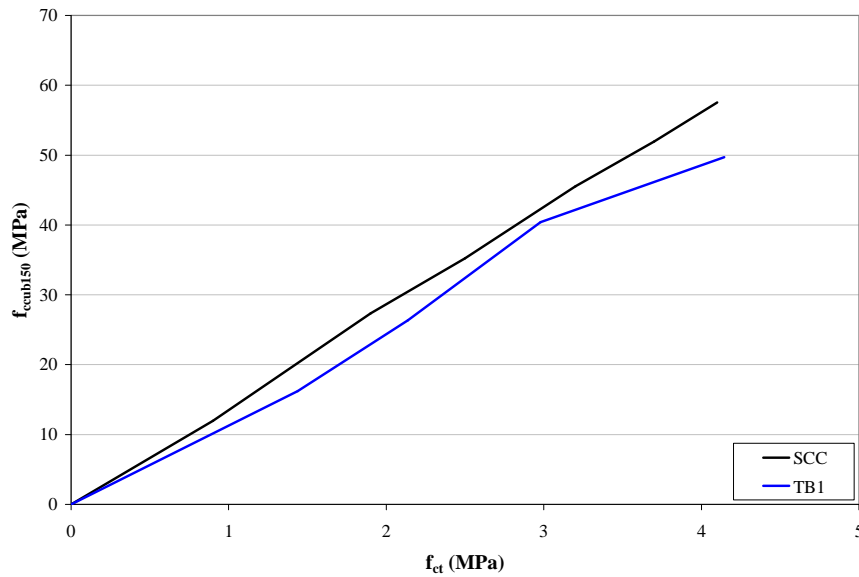


Figure 9.24: The tensile strength f_{ct} versus the compressive strength $f_{ccub150}$ of TB1 and SCC

Also the tensile strength after 24 hours and 48 hours is higher in case of TB1 (Figure 9.23). This has a major impact on the cracking risk due to the expansive hydration reactions. To evaluate the development of compressive strength in comparison with the tensile strength, Figure 9.24 is given. For the simulations in Chapter 8, it is assumed that the tensile strength development is directly proportional to the compressive strength development (Figure 9.24, black line). Nevertheless, the strength tests performed on the concrete of TB1 indicate that the tensile strength evolves faster than

the compressive strength (Figure 9.24, blue line), especially the first 48 hours of hardening. This phenomenon is also mentioned by De Schutter (1996). Thus, the values of f_{ct} used in Chapter 8 slightly underestimate reality, which can be seen as a conservative and safe approach used for the HEAT/MLS simulations. In addition to this argumentation, an additional discourse is held: (i) the tensile strength of TB1 and SCC is more or less equal after 28 days (Figure 9.23). (ii) The compressive strength of SCC is significantly higher than that of TB1. (iii) The values of f_{ct} of SCC used in Chapter 8 are extrapolated from pure tensile strength test results performed on cores drilled out of a massive SCC column after 56 days and based on the compressive strength results. Therefore, it is possible that the tensile strength of SCC used in the simulations is underestimated, confirming once again the safe approach of the simulations.

3.2.7 Cracking behaviour of the HC

After approximately 696 hours the two steel sections of the cylindrical steel formwork are removed (Figure 9.6, right) to evaluate whether early-age cracks are visible. After a visual inspection of the buffer of the HC, no macrocracks in tangential direction (due to the axial stresses S_{yy}) or in axial direction (due to the tangential stresses S_{zz}) are noticed at the inner surface, the outer surface and the top surface of the non-instrumented regions. On the outer surface of the buffer, axial and radial cracks are clearly noticeable, in regions where the wooden framework is inserted for the positioning of the TC's, inducing stress concentrations (Figure 9.25, right). A seam appears on the surface of the buffer, at the position where the two formwork sections meet (Figure 9.25, left, blue line).

As mentioned before, the buffer of the HC is cast with two SCC batches of 6 m³ with a considerable time spam in between the pumping activities. Between the time of ending the pumping of the first batch (FB1) and the start of pumping of the second batch (FB1') a time interval of 1.12 hour exists (Table 9.2). After demoulding the formwork, a casting joint appears at the height corresponding to the pumping time-break (Figure 9.25, left, red line). This 'self-created crack' in tangential direction clearly is a preferential pathway for potentially present aggressive species, is not desired and must be prevented at all times.

Therefore, it is advised to cast and pump the buffer in one fluent movement, without stopping the pumping activities. In that case, the challenge can be found in the necessity of the total amount of concrete, needed for the buffer (10.575 m³), being available at the same time at the casting site.

Overall, visual inspection indicates, that due to the thermal gradient and the thermal stress creation (taking into account autogenous shrinkage and the creep behaviour), no early-age cracking is expected during the fabrication of the buffer (Stage 1).

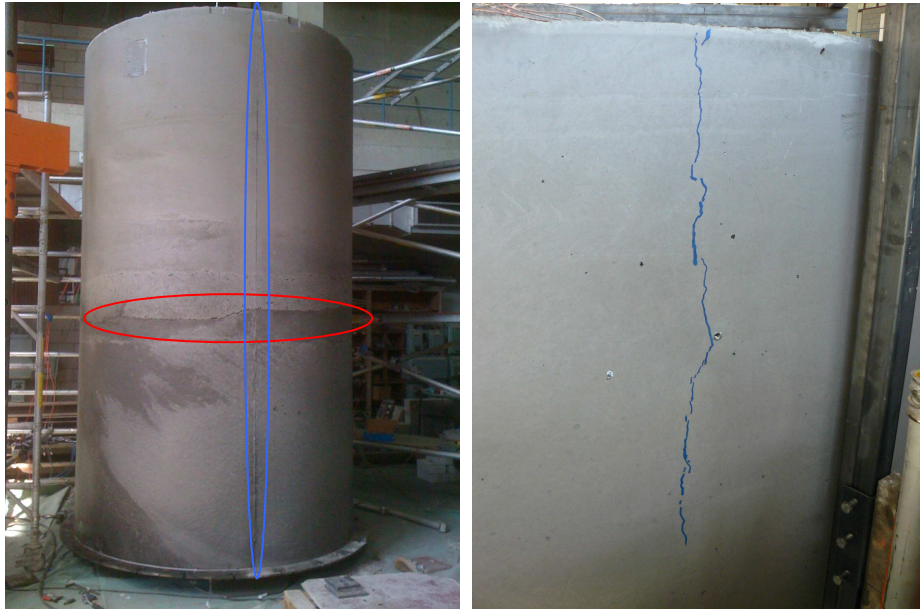


Figure 9.25: Cracks in the casting joint (left) and due to the instrumentation framework (right)

In a final step, simulations are made to confirm this non-cracking postulate. Therefore, the most important and maximal axial and tangential stresses (Figure 9.20, point 1 and point 2) are compared to the tensile strength of the FB1 concrete, as shown in Figure 9.23. The values of the tensile strength of FB1 are estimated out of the tensile strength development of TB1 and the differences in compressive strength between TB1 and FB1 (for the samples preserved in ideal curing conditions).

The axial stress S_{yy} and the tangential stress S_{zz} exceed the assumed tensile strength f_{ct} of FB1, in the time interval 20 hours – 39 hours and 20 hours – 29 hours respectively (Figure 9.26a, Figure 9.26b). By multiplying f_{ct} by 1.12, the tangential stress S_{zz} does not longer exceed the new tensile strength value (Figure 9.26b). For S_{yy} to remain smaller than the tensile strength, f_{ct} needs to be multiplied by 1.34 (Figure 9.26a). However, in reality, no cracks are observed, so it can be assumed that the drawn conclusions, on behalf of the early-age cracking risk, are safe.

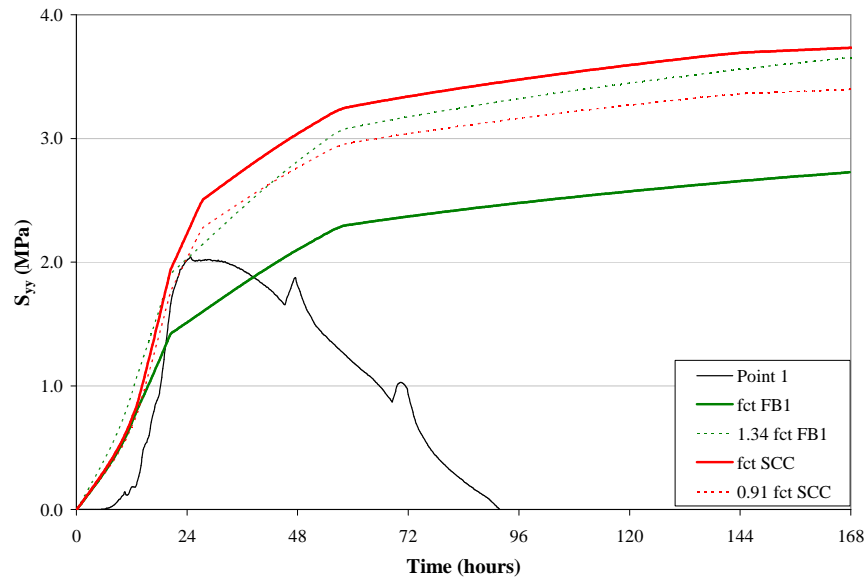


Figure 9.26a: Comparison of S_{yy} with the tensile strength of SCC and FB1

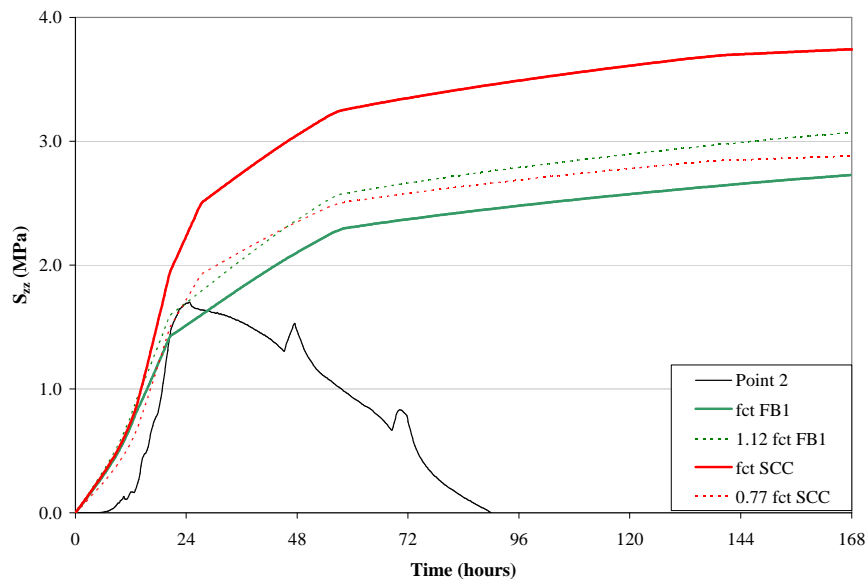


Figure 9.26b: Comparison of S_{zz} with the tensile strength of SCC and FB1

Assuming the estimation of the tensile strength of FB1 is incorrect, S_{yy} and S_{zz} are compared with the tensile strength f_{ct} of SCC. The stresses remain smaller than f_{ct} at all times. The tangential stress S_{zz} does not exceed 0.77 times f_{ct} of SCC (Figure 9.26b), while the axial stress S_{yy} does not exceed 0.91 times f_{ct} (Figure 9.26a).

Compared to the estimated tensile strength of FB1, the tensile stresses exceed the strength barrier, while compared to the estimated tensile strength of SCC, the tensile stresses do not exceed the strength barrier. As the buffer does not suffer from early-age cracking, as the visual inspection indicates, it can be assumed that the actual tensile strength development of FB1 lies in between the two estimated tensile strength curves. Note that also the presence of the outer steel formwork can be seen as an additional safety barrier, as compressive stresses are induced in the critical outer surface regions of the buffer, due to the hindered expansive deformation tendency of the concrete during the first 168 hours after casting.

4 Conclusion

The simulations of the early-age behaviour of the fabrication of the buffer of the Supercontainer inside the steel envelope (Stage 1), indicate that in standardized environment, the buffer does not suffer from early-age cracking behaviour. To enforce this findings, Half-Scale Tests are performed. Therefore, a Half-Scale Container (HC) is made by pumping two batches of approximately 6 m³ into a steel cylindrical formwork. At the Kesteleyn concrete factory, trial mixes and final mixes are made to provide the SCC needed for the casting of the HC. The formwork is provided with test equipment to register the temperature development in the buffer of the HC and to follow the displacement and the deformation of the formwork and of the buffer itself. By means of the finite element tool HEAT/MLS, the registered data are compared with the obtained simulation results in order to come to a validation of the drawn conclusions. The most important remarks and finding that occurred during the first phase of the Half-Scale Tests are listed below:

- The fresh SCC test results show a rather large dispersion. This is mainly devoted to the difficulty linked to the estimation of the water content (and the representativeness of this parameter) of the aggregates used for the concrete mixes. The reduced compressive strength test results can be seen as a proof of the possible underestimation of the water content of the aggregates. In case of an underestimation, a surplus of water is added to the mix, which is not prescribed. Therefore, for the mixing procedure, it is advised that the water content of the aggregates is determined adequately, or even better: that the aggregates are totally dry. Also the placement of the different components into the concrete mixer should be automatized. Finally, a significantly higher air content is found for the batches, which can be a result of the high amount of added superplasticizer and this can induce a strength loss of the SCC.
- The comparison between the registered data and the simulated ones, is rather good. Especially the similarity between registration and simulation of the thermal gradient, which is a very important parameter leading towards thermal cracking, is striking. Also the expansive behaviour of the concrete buffer during the first 168 hours proceeding the casting is found by the registration of the test equipment. The presence of the cylindrical formwork prevents free deformation of the buffer. As a consequence, compressive stresses are induced near the outer surface, which is beneficial and counteracts the tensile stress creation in those regions during the first 48 hours proceeding the casting of the buffer.
- The visual inspection after the removal of the steel formwork indicates that no tangential or axial macrocracks are created due to the thermo-mechanical behaviour of the buffer. Nevertheless, stress and strength simulations indicate that there is a reasonable cracking risk. Thus, the finite element program HEAT/MLS might overestimate the created stresses or underestimate the tensile strength development, which is a conservative and safe approach.
- In case preparatory enactments are taken (e.g. placement of wind shielding equipment, manipulating the ambient temperature, etc.), no thermal cracks are

expected during the first stage of fabrication of the buffer. Especially the impact of a high ambient wind velocity is considerable.

- The only cracks that are found during the visual inspection are tangential cracks at the level of the casting joint between the two SCC batches. Therefore, for the next tests or in practice, it is advised to perform the pumping activities of the buffer in one fluent movement, without stopping in between the delivery of the two SCC batches. In that case, the challenge can be found in the necessity of the total amount of concrete, needed for the buffer (10.575 m³), being available at the same time at the casting site. Also vertical cracks are found, devoted to the framework for positioning of the TC's.

In a second step, once the buffer is hardened sufficiently, a heat-emitting overpack will be inserted into the created opening of the HC (Figure 9.27), the remaining annular gap is filled and the lid is cast immediately after insertion of the heat source to close the HC. Once more, temperature, displacement and deformation of the buffer are registered during the warming up of the HC and the possible appearance of cracks will be determined via visual inspection. Research of the bond between the filler and the buffer, and between the filler and the overpack will be performed, by means of tomographical methods, velocity measurements and coring activities. Afterwards the heat source is disconnected, and the changes during cooling are also registered. The analysis of these discussed activities lies out of the scope of this doctoral study and is subject for research in the nearby future.

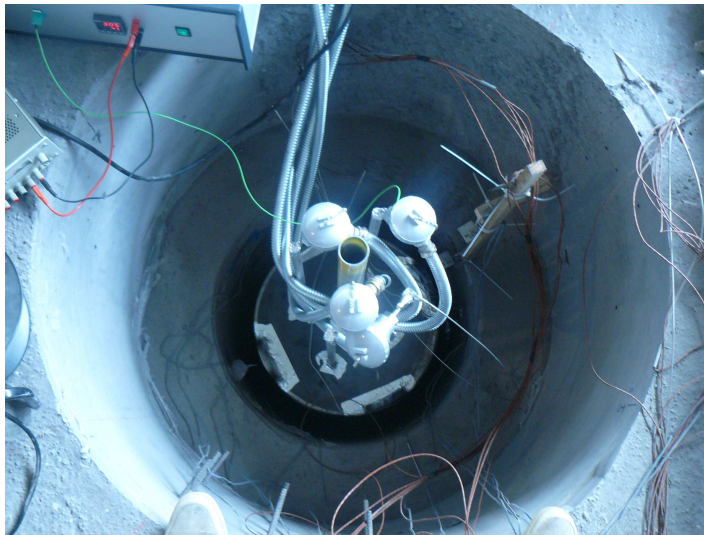


Figure 9.27: Insertion of the heat-emitting element into the Half-Scale Container

References

Areias L. (2009), *1/2 Scale Tests: Description*, SCK·CEN report, Belgium.

De Schutter G. (1996), *Fundamental and practical study on thermal stresses in massive hardening concrete elements*, Doctoral thesis (in Dutch), Ghent University, Magnel Laboratory for Concrete Research, Belgium.

Taerwe L. (1997), *Concrete Technology*, Course material (in Dutch), Ghent University, Magnel Laboratory for Concrete Research, Belgium.

Taerwe L. (2004), *Reinforced concrete: analysis, modelling and design (Part I)*, Course material (in Dutch), Ghent University, Magnel Laboratory for Concrete Research, Belgium.

CHAPTER 10:

CONCLUSIONS AND FUTURE RESEARCH

1 Conclusions and discussion

1.1 Objective of the doctoral research

The final objective of this research study is to examine the early-age behaviour of the concrete buffer of the Supercontainer during the different construction stages, out of hot cell and in hot cell and to evaluate the possible risk of early-age cracking (macrocracking). Via thermal, mechanical and maturity-related laboratory tests, via simulations by means of the finite element tool HEAT/MLS and via a realistic casting situation (Half-Scale Tests), the behaviour of the concrete buffer is analysed in a fundamental way.

1.2 The studied concrete compositions

The buffer of the Supercontainer is made of concrete, to provide a favourable chemical environment around the overpack to slow down corrosion (a high pH passivates the carbon steel overpack), to provide sufficient radiological attenuation of the gamma photons and to facilitate transport operations towards the underground disposal galleries. Therefore, the different components of the selected and designed concrete composition must comply with certain specific requirements. An Ordinary Portland Cement is used (strength class 42.5 N/mm²) which hydrates at a normal rate (N), with limited hydration heat (LH) to avoid thermal cracking, low alkali amount (LA) and sufficient sulphate attack resistance (HSR). The aggregates are preferably of a calcareous nature (e.g. limestone) and limestone filler material is selected. No other organic additives are acceptable except, as low quantity as possible, a small amount of superplasticizer. Finally, good quality and homogeneity, sufficient mechanical strength and good workability (preferably pumpable) are prescribed. As a consequence, two types of concrete are selected for the cementitious buffer and are characterized by means of extensive laboratory tests: SCC (Self-Compacting Concrete) and TVC (Traditional Vibrated Concrete). Preference is given to SCC, because it facilitates the precast processes and complies with all other requirements regarding strength,

durability, chemical interactions, etc. In order for the SCC composition to be self-compacting, a sufficient filling ability, passing ability and segregation resistance is required. Therefore, higher amounts of fine materials (sand, filler) and more superplasticizer are added to the SCC mixes and no external vibration is needed.

1.3 Conclusions of the laboratory characterization program

The thermo-mechanical and fresh properties of the SCC and the TVC are determined via an extensive laboratory characterization program and the comparison between the two compositions is made (SCC vs. TVC). The fresh properties of SCC show a higher dispersion of the results compared to TVC. The density of the fresh mix (2405 kg/m^3 vs. 2440 kg/m^3) and the hardened concrete (2390 kg/m^3 vs. 2410 kg/m^3) is lower in case of SCC. Moreover, in some cases, segregation of the fresh SCC mix is obtained and the passing ability is unsatisfactory in most cases. When an additional amount of 50 kg/m^3 of limestone filler is added (replacing 50 kg/m^3 coarse aggregates, size 6/14), an improvement of the fresh properties of the SCC is achieved, while the compressive strength remains more or less unaltered.

Concerning the thermal properties, and compared to TVC, SCC has a lower heat capacity ($2390 \text{ kJ/(kg}\cdot\text{°C)}$ vs. $2410 \text{ kJ/(kg}\cdot\text{°C)}$) and acts more like an insulator due to the lower value for thermal conductivity ($1.89 \text{ W/(m}\cdot\text{°C)}$ vs. $2.02 \text{ W/(m}\cdot\text{°C)}$). The cumulated adiabatic hydration heat production of SCC has a higher value after 72 hours (316.6 J/g vs. 303.5 J/g), but the heat production rate peak is slightly higher ($21.4 \text{ J/(g}\cdot\text{h)}$ vs. $23.5 \text{ J/(g}\cdot\text{h)}$) and occurs 3 hours earlier for TVC, with a value of the activation energy that is also slightly higher (37.3 kJ/mol vs. 38.0 kJ/mol). Finally, the CTE is higher for SCC, thus SCC will expand more under influence of a temperature increase ($8.1 \text{ }\mu\text{m/(m}\cdot\text{°C)}$ vs. $7.4 \text{ }\mu\text{m/(m}\cdot\text{°C)}$).

The mechanical strength properties, such as the compressive strength (57.5 MPa vs. 54.0 MPa), the pure tensile strength (4.4 MPa vs. 3.3 MPa) and the modulus of elasticity (36.1 GPa vs. 32.4 GPa), are higher for SCC. Also the autogenous shrinkage (on short term and on long term) and the basic creep compliance is higher in case of SCC. The higher amount of fine materials, such as limestone filler, added to SCC in order to make it self-compacting, can be seen as an explanation for the obtained property differences between SCC and TVC. Finally, time zero, i.e. the moment when the imposed deformations give cause to an internal stress build-up, is taken equally for SCC and TVC: 6 hours.

Due to the vitrified, heat-emitting radioactive waste, that will be inserted into the opening of the concrete buffer, the concrete comes into direct contact with elevated temperatures up to 100 °C and with gamma radiation (with dose rates up to 23 Gy/h) during hardening (filler and/or lid) or in a hardened state (buffer).

Out of compressive strength tests performed on hardened concrete samples subjected to elevated temperatures (between 20 °C and 105 °C), a strength loss of 20 % for SCC and a strength loss of 15 % for TVC is found. The increasing capillary porosity (measured by means of fluorescence microscopy: no statistical significance found),

increased microcracking, and the weight loss can be seen as a reasonable explanation for the decrease in mechanical strength.

Also compressive strength loss indications (up to 15 %) of hardening SCC based mortar samples subjected to gamma irradiation during the first 28 days of hardening are found, with the increase in capillary porosity as possible mechanism behind the mechanical strength degradation. However, no statistical significance is found for this postulate.

1.4 Conclusions of the simulation results and the Half-Scale Tests

By means of the finite element simulation tool HEAT/MLS, and after implementation of the most relevant thermal, mechanical and maturity-related properties of SCC and TVC into the material database of the program, the early-age behaviour of the concrete buffer during construction is simulated. The results are subdivided into two parts: the construction stage out of hot cell (i.e. the casting of the buffer in the steel envelope), and the construction stages in hot cell (i.e. the insertion of the waste overpack, the filling of the remaining annular gap and the closure of the Supercontainer by fitting the lid).

Due to the exothermal hydration reaction of the cement, compressive stresses are created in the middle of the buffer and tensile stresses appear near the outer surface. The main mechanism behind the early-age cracking of the buffer can be found in the created thermal gradient between the middle of the buffer and the outer surface, and the prevention of free deformation of the concrete. However, for the first part, and in ideal reference casting conditions (ambient temperature of 20 °C and no ambient wind velocity), the created internal stresses are higher in case of SCC and a higher cracking ratio $S_{ii}/(0.7 \cdot f_{ct})$ is obtained, but this parameter is inferior to one at all times, thus no early-age cracking out of hot cell is expected in case SCC or TVC.

The sensitivity analysis indicates the detrimental effect of ambient wind. An increase of the convective heat transfer coefficient, obtained via poor insulating materials in combination with high wind speed, significantly increases the cracking risk. The use of a surrounding wind shield is advised. In case the environmental temperature increases, the cracking risk also increases, and although the simulations indicate that the cracking ratio $S_{zz}/(0.7 \cdot f_{ct})$ remains smaller than one in all cases, measures can be considered in case the environmental temperature is higher than 30 °C (e.g. by means of a cooling system). In case the dimensions of the buffer need to be adjusted, note that especially an increased thickness of the buffer increases the early-age cracking risk, but even with a thickness of 800 mm, no early-age cracking is expected. Casting the buffer in upside-down behaviour inside a deep hole (with a high insulation capacity and no external wind), reduces the thermal gradient present in the buffer and increases the strength development. To create ideal casting conditions, the appliance of good insulation (e.g. concrete, wood or polystyrene, with a well considered demoulding time) around the steel envelope and the use of wind shielding equipment, and thus a lowering of the convective heat transfer coefficient, is advised.

The validation of the first construction stage of the buffer is obtained by means of Half-Scale Tests: a concrete buffer with volume 10.575 m³ is cast by means of two SCC batches of 6 m³ mixed at a concrete factory and pumped into an instrumented steel cylindrical formwork. These tests once more indicate that no early-age cracking is expected in the first stage. A good similarity is obtained between the registered data (temperature inside the buffer and displacement of the formwork and the buffer) and the simulated data. Especially a good resemblance of the thermal gradient appears. Also the expansive nature of the concrete buffer during the first 168 hours after casting is found by means of the test equipment. Due to this radial expansion, and the prevention of this behaviour due to the presence of the steel formwork (envelope), beneficial compressive stresses are introduced into the buffer which counteract the detrimental internal stress build-up. Overall, HEAT/MLS slightly overestimates the created stresses and underestimates the tensile strength development: a conservative and safe approach.

Concerning the construction feasibility of casting the Half-Scale Container, important experience is acquired and improvements can be suggested for additional tests in the nearby future. Especially the estimation of the water content of the aggregates should be more adequate, or even better: totally dry aggregates should be added to the mix. Rather high dispersion of the obtained fresh test results, and a decrease in compressive strength due to a possible underestimation of the water content, are potential consequences of the insufficient knowledge on behalf of the actual water content of the aggregates added to the mix. Also the addition of the limestone filler and the superplasticizer into the concrete mixer should be automated. Finally, the visual inspection of the concrete buffer indicates a large tangential crack opening at the level of the casting joint in between the two SCC batches. This 'self-made' crack is not desired as it can be seen as a preferential pathway for potentially present aggressive species in the Host Rock (and its pore water) of the disposal galleries. The durability of the concrete inside the Supercontainer can be negatively affected, and processes such as corrosion, microbial activity, sulphate attack, etc. can be accelerated due to the presence of these macrocracks. Therefore, it is highly recommended to perform the casting and the pumping activities in one fluent movement (without stopping), starting from the bottom of the formwork and slowly lifting the pumping tube until the formwork is entirely filled. Therefore, it is necessary that the total amount of concrete, needed for the buffer, is entirely available at the casting site.

Once the temperature inside the buffer approaches the ambient temperature and the buffer is in a certain state of hardening (240 hours is taken as a reference), the heat-emitting waste is inserted into the created internal opening, the remaining gap is filled and the lid is placed to close the Supercontainer. Three mechanisms occur which create an internal stress build-up in the buffer of the Supercontainer: (i) the hydration heat due to the hardening filler and lid, (ii) the heat originating from the heat-emitting radioactive waste, and (iii) the expansive behaviour of the overpack containing the radwaste. In case the effect of the overpack is only implemented as a boundary condition (via the convective heat transfer coefficient), thus only the first two mechanisms are considered, no cracking of the buffer is expected. This is in fact an

underestimation of the reality. Via this simulation method, the effect of altered situations is investigated: a prolongation of the preceding cooling period of the radwaste has a beneficial effect, the insertion of SF assemblies instead of HLW affects the cracking risk negatively, the use of a TVC buffer or a precast lid does not have an influence on the internal stress build-up inside the buffer, and delaying the insertion time also does not have a considerable effect on the early-age behaviour of the buffer. The internal eigenstresses, present in the buffer after the first construction stage out of hot cell, counteract the stress creation due to the three previously mentioned stress creating mechanisms. However, by also considering the expansive behaviour of the overpack, obtained via implementing the overpack as a macro layer (the second simulation type), a considerable cracking risk near the outer surface of the buffer must be taken into account, depending on the coefficient of thermal expansion of the overpack. Especially tangential cracks (due to the axial stresses) can appear, which is confirmed by the Half-Scale Tests. Therefore, the use of a carbon steel overpack (with a lowered coefficient of thermal expansion) instead of a stainless steel overpack is preferential for thermo-mechanical purposes (but also for corrosion related aspects), in combination with a cooling period of 70 years to overcome cracking. In that case, a significant safety barrier is obtained, to counteract the negative effect of heat and radiation on the strength of the concrete buffer. Also the appliance of a top force (e.g. by screwing a top plate on the mantle of the envelope) can induce beneficial compressive stresses that counteract the tensile stress build-up in the buffer. The presence of the steel envelope reduces the tensile stresses due to the prevention of the expansive behaviour of the buffer and the introduction of beneficial compressive stresses. By reducing the modulus of elasticity of the filler material, the cracking risk near the outer border of the buffer becomes smaller.

Mainly due to the expansive behaviour of the overpack and due to the hindering of the displacement of the filler material due to the heat originating from the radwaste, the SCC filler comes under compression, so no cracking is expected there. Also early-age cracking is not at state in case of the lid, which is confirmed by means of the Half-Scale Tests. On a thermo-mechanical level, the use of a precast lid does not provide additional benefits compared to the use of a freshly cast lid.

2 Future research

This doctoral study illustrates the low cracking risk during the first construction phase of the buffer out of hot cell. However, an early-age cracking risk during the construction stages in hot cell cannot be overlooked due to the insertion of the heat-emitting radioactive waste enclosed by an expandable overpack.

Future research is needed on behalf of different branches of the early-age behaviour of the Supercontainer, originating from different findings, needs and difficulties occurring during this study:

- The proposed SCC composition has a rather high dispersion of the obtained fresh test results. It is known that SCC is quite sensitive to variations in any part of its composition. In order to come to a more robust self-compacting concrete composition, it is advised to add more fine components (filler material, fine aggregates) to the mix, replacing the coarser constituents. As a consequence, the obtained thermal, mechanical and maturity-related properties can change. A repetition of the laboratory characterization program and the simulations via HEAT/MLS is needed to evaluate the early-age cracking risk in case more fine materials is added (recommendation: 50 kg/m³ limestone filler replaces an equal amount of coarse aggregates, size 6/14).
- For now, SCC is considered as the filler material, used to fill the remaining annular gap between the buffer and the overpack under thermal load. Other materials should be considered and investigated on the subject of fresh properties, self-compacting ability, self-healing properties, strength, hardening under thermal load, hardening under irradiation, etc. In Chapter 3, two other possibilities are given for the filler material: a fluid mortar (grout) and a (portlandite) powder with its specific (dis-)advantages. In total, five types of fillers will be developed and tested in laboratory conditions prior to their use in practice, with differences in aggregate size and presence of a swelling agent. It can also be advised to propose and investigate another type of filler material, with the ability to take on or counteract the expansive behaviour of the overpack during the construction stages in hot cell, in such a way that the stress build-up transfer towards the outer surface of the buffer is minimized, and the early-age cracking risk during those construction steps is reduced (e.g. a filler material with a reduced modulus of elasticity).
- To investigate the effect of gamma radiation on hardening cementitious materials, a preliminary study of SCC based mortar samples irradiated by means of a ⁶⁰Co source with a dose rate inferior to 10 Gy/h are conducted. Indications of a compressive strength loss are found, related to the increase in capillary porosity, determined by means of fluorescence microscopy (scale 100:1). The repeatability of those tests should be demonstrated, and additional tests are meaningful and desired. The examination of other mechanical and/or thermal properties of hardening irradiated samples (or of samples that are irradiated after a certain degree of hardening is obtained) should be performed. Also the impact of higher dose rates (superior to 10 Gy/h), the combined effect of gamma radiation and elevated temperatures (more significant to

characterize the heat-emitting radioactive waste), and the behaviour of hardening concrete under thermal load should be taken a look at. Finally, examination by means of fluorescence microscopy should be combined by investigations on an ever smaller scale, e.g. research of the gel pore structure on a nanoscale by means of SEM.

- The analysis of the second part (insertion of a heater source inside the created opening of the buffer, and the warming up of the concrete buffer) and the third part (disconnection of the heating element and the cooling down of the concrete buffer) of the Half-Scale Tests by means of the temperature distribution inside the buffer, and the displacement and deformation of the concrete buffer, is subject for further study. An inspection of the visible parts of the HC's buffer surface is conducted to evaluate whether tangential and/or axial cracks appear due to the insertion of the heater element (with a constant thermal power of 300 W/m). Also tomographical studies (seismic reflection), wave velocity measurements, ultrasound measurements and core taking activities are planned and conducted to examine the bonding and the quality of the interface of the filler and the buffer on one side, and between the filler and the steel overpack on the other side. Also the quality of the lid, with the application of a certain degree of roughness of the contact surface, will be examined. Finally, the effect of elevated temperatures on the compressive strength of the SCC is evaluated by means of cores taken out of the lid and out of a non-heated reference cylinder.
- From the obtained experience derived from the preceding tests, the Half-Scale Test will be repeated in the nearby future, with SCC as the reference concrete composition, and by considering improvements and keeping in mind the difficulties that occurred previously in the first tests. Automation of the addition of limestone filler and superplasticizer to the concrete mix is highly recommended, and also the estimation of the water content of the added limestone aggregates needs to be improved. It is even better to use completely dry aggregates. For the casting and pumping activities, a 'cast in one' method for the fabrication of the buffer needs to be applied in order to avoid the creation of a casting joint. The use of a carbon steel overpack with a lowered coefficient of thermal expansion in combination with a filler (with the ability to counteract the expansive behaviour of the overpack), is highly recommended. Finally the importance of the stainless steel cylindrical envelope, used as formwork, cannot be overlooked: it is advised to maintain the formwork during all steps of the construction procedure (casting of the buffer, during hardening, during heating and during cooling). Due to the expansive nature of the concrete buffer, compressive stresses are induced into the critical tensile stress regions by the steel formwork by hindering the deformation, and crack formation can be counteracted. Therefore, it is advised to remove the steel formwork once the cooling period (after disconnecting the heater source) is over. Once cooled down, the visual inspection of the buffer for crack formation can start and the effect of the formwork can be examined, taking into account that a criss-cross pattern of cracks appeared in the second construction stage of the first Half-Scale Container. Applying a vertical load

on top of the HC, once the heat-source is inserted and the freshly cast lid reached a sufficient hardening state (at least 24 hours), can be advised to induce the previously discussed beneficial compressive stresses into the buffer.

CURRICULUM VITAE AND PUBLICATIONS

Curriculum Vitae

Personalia

Name: Bart Craeye
Date of birth: November 28, 1983
Place of birth: Ronse, Belgium
E-mail: Bart.Craeye@UGent.be
Bart.Craeye@Artesis.be



Education

- 2006 – 2010 PhD studies at the Magnel Laboratory for Concrete Research, Department of Structural Engineering, Ghent University, Belgium.
Teaching activities in Concrete Technology, in Theory of Strength of Materials and in Engineering Projects
- 2004 – 2006 Master studies at the Faculty of Engineering, Department of Structural Engineering, Ghent University, Belgium.
- 2001 – 2004 Bachelor studies at the Faculty of Engineering, Department of Structural Engineering, Ghent University, Belgium.
- 1995 – 2001 Studies (Science-Mathematics) at Viso Cor Mariae, Brakel.

Doctoral Training

Durability of Materials (UGent), Environmental Impact of Radiation and Sound (UGent), Diagnostics and Repair of Structures (UGent), Cement and Cementitious Materials in the Geological Disposal of Radioactive Waste (ITC School Course, Eurajoki, Finland), Geological Disposal of High-Level Waste (ITC School Course, Las Vegas, USA), Heat and Mass Transfer in Building Materials, Components and Buildings (KUL, Postdoctoral course, Leuven, Belgium), Presentation Techniques (UGent).

Publications

AI

Effect of mineral type on autogenous shrinkage of self-compacting concrete.

B. Craeye, G. De Schutter, B. Desmet, J. Vantomme, G. Heirman, L. Vandewalle, Ö. Cizer, S. Aggoun, E.H. Kadri. Accepted for publication in Cement and Concrete Research (2009).

Super Absorbing Polymers as an internal curing agent for mitigation of early-age cracking of high-performance concrete bridge decks.

B. Craeye, M. Geirnaert, G. De Schutter. Submitted to Construction and Building Materials (2009).

Early age behaviour of concrete supercontainers for radioactive waste disposal.

B. Craeye, G. De Schutter, H. Van Humbeeck, A. Van Cotthem. Nuclear Engineering and Design 239 (2009) 23-35.

Conference papers

Early-age cracking behaviour of high-performance concrete bridge decks internally cured with super absorbing polymers.

B. Craeye, M. Geirnaert, G. De Schutter. Proceedings of the 2nd International Symposium on Service Life Design for Infrastructure. Delft, The Netherlands, 4 – 6 October (2010).

Validation of the early-age thermo-mechanical behaviour of SCC Supercontainers for the disposal of High Level radioactive Waste.

B. Craeye, G. De Schutter, W. Wacquier, H. Van Humbeeck, A. Van Cotthem. Proceedings of the 4th International RILEM Symposium on Self-Compacting Concrete. Sherbrooke, Canada, 20 – 22 September (2010).

Thermo-mechanical behaviour of concrete Supercontainers for the disposal of high-level radioactive waste.

B. Craeye, G. De Schutter. Proceedings of the 10th PhD Symposium. Faculty of Engineering, Ghent University, Belgium, 9 December (2009).

Finite element computation of early age thermal cracking in concrete Supercontainers for radioactive waste disposal.

B. Craeye, G. De Schutter, H. Van Humbeeck, W. Wacquier, A. Van Cotthem. Proceedings of the 12th International Conference on Civil, Structural and Environmental Engineering Computing. Madeira, Portugal, 1 – 4 September (2009).

The use of SCC for the containment of High Level Waste.

B. Craeye, G. De Schutter, H. Van Humbeeck, A. Van Cotthem. Proceedings of the 2nd International Symposium on Design, Performance and Use of Self-Consolidating Concrete. Beijing, China, 5 – 7 June (2009).

Concrete buffers for the containment of High Level Radioactive Waste: Casting conditions and early age behaviour.

B. Craeye, G. De Schutter, H. Van Humbeeck, W. Wacquier, A. Van Cotthem. Proceedings of the workshop on Long Term Performance of Cementitious Barriers and Reinforced Concrete in Nuclear Power Plants and Waste Management. Cadarache, France, 30 March – 2 April (2009).

Thermo-hydrromechanical behaviour of the Supercontainer concrete buffer during construction.

B. Craeye, G. De Schutter, W. Wacquier.

Proceedings of the 13th Exchange Meeting on the role of Cementitious Materials for Deep Disposal of High-Level Waste in Boom Clay. ESV Euridice GIE, Club House SCK·CEN, Mol, 29 January (2009).

Concrete containers for containment of vitrified high-level radioactive waste and spent fuel: the Belgian approach.

B. Craeye, G. De Schutter, H. Van Humbeeck, A. Van Cotthem. Proceedings of the 2nd International Conference on Concrete Repair, Rehabilitation and Retrofitting. Cape Town, South Africa, 24 – 26 November (2008).

Creep and shrinkage behaviour of concrete supercontainers for radioactive waste disposal.

B. Craeye, G. De Schutter, H. Van Humbeeck, A. Van Cotthem. Proceedings of the 8th International Conference on Creep, Shrinkage and Durability of Concrete and Concrete Structures. Isa-Shima, Japan, 30 September – 2 October (2008).

Experimental evaluation of mitigation of autogenous shrinkage by means of a vertical dilatometer.

B. Craeye, G. De Schutter. Proceedings of the 8th International Conference on Creep, Shrinkage and Durability of Concrete and Concrete Structures. Isa-Shima, Japan, 30 September – 2 October (2008).

Early age behaviour of concrete supercontainers for radioactive waste disposal

B. Craeye. Proceedings of the 1st Magnel Research Seminar. Elsegem, Belgium, 23 May (2008).

Study of the behaviour of concrete supercontainers for the disposal of heat-emitting radioactive waste.

B. Craeye, G. De Schutter. Proceedings of the 8th PhD Symposium. Faculty of Engineering, Ghent University, Belgium, 5 December (2007).

Development of a SCC Composition for disposal of heat-emitting, radioactive waste in Belgium.

B. Craeye, G. De Schutter, J. Bel, H. Van Humbeeck, A. Van Cotthem. Proceedings of the 5th International RILEM Symposium on Self-Compacting Concrete. Ghent, Belgium, 3 – 5 September (2007).

Experimental evaluation of mitigation of autogenous shrinkage by means of a vertical dilatometer.

B. Craeye, G. De Schutter. Proceeding of the International RILEM Symposium on Volume Changes on Hardening Concrete. Lyngby, Denmark, 20 – 23 August (2006).